Durham University

Durham E-Theses

Origins of overpressure in the Malay Basin and its influence on petroleum systems

Mohammad Jamaal Hoesni

How to cite:

Hoesni, Mohammad Jamaal (2004) Origins of overpressure in the Malay Basin and its influence on petroleum systems. Doctoral thesis, Durham University.

Use policy

The full-text may be used and/or reproduced, and given to third parties in any format or medium, without prior permission or charge, for personal research or study, educational, or not-for-profit purposes provided that:

- a full bibliographic reference is made to the original source
- a https://etheses.durham.ac.uk/id/eprint/1755/ is made to the metadata record in Durham E-Theses
- the full-text is not changed in any way

The full-text must not be sold in any format or medium without the formal permission of the copyright holders.

Please consult the full Durham E-Theses policy for further details.

Academic Support Office, The Palatine Centre, Durham University, Stockton Road, Durham, DH1 3LE
e-mail: e-theses.admin@durham.ac.uk Tel: +44 0191 334 6107
https://etheses.durham.ac.uk

Origins of Overpressure in the Malay Basin and its Influence on Petroleum Systems

By

Mohammad Jamaal Hoesni

2004

A thesis submitted to the University of Durham in partial fulfilment of the requirements for the degree of Doctor of Philosophy .

A copyright of this thesis rests with the author. No quotation from it should be published without his prior written consent and information derived from it should be acknowledged.

28 FEB 2005

Abstract

The origin of overpressure in the Malay Basin is investigated by examining wireline log responses. 2-D basin modelling was carried out to test various hypotheses concerning the origin of overpressure and to reconstruct the overpressure evolution in the basin. The assessment on the influence of overpressure on the petroleum system was also studied through a series of models.

Empirical and soil mechanic methods were used to construct pore pressure profiles from the Malay Basin wells. The profiles gave variable results which do not match the formation pressure in all cases. The differences arise due to several factors, including choice of method, appropriate selection of normal compaction trend, multiple origins of overpressure and interference caused by chemical compaction. With the aid of velocity-density cross-plots and basin models, a systematic approach for identifying the causes for overpressure in the Malay Basin has been established.

Overpressure in the Malay Basin is mainly due to disequilibrium compaction, with potential contribution from chemical compaction processes. The occurrence of chemical compaction is evident from a distinctive profile (rapidly increasing density with almost constant velocity) observed on the velocity-density crossplots, which has not been reported before. The onset of chemical compaction are observed between 105°C to 120°C, which does not necessarily coincide with the top of the overpressure. In the adjacent basins, Baram Delta and West Luconia, chemical compaction is not evident, possibly due to lower geothermal gradients. Worldwide basin comparison indicates the presence of the chemical compaction in some other overpressured basins.

The importance of incorporating chemical compaction in basin modelling has been demonstrated. Modelling can successfully replicate pressure profiles when appropriate porosity-permeability history is considered, taking into account the effect of chemical compaction. Whilst the contribution to overpressure from gas generation is minor compared to disequilibrium compaction (loading stress) there is potential for large gas resources sealed by chemically compacted shales.

Acknowledgments

This research could not have been possible without the assistance and encouragement that I received from many individuals and organizations. I want to take this opportunity to thank them.

First of all, I wish to express my deepest gratitude to PETRONAS for granting study-leave, financial support and the release of data for this research.

I would like to thank my two supervisors Dr Richard Swarbrick and Professor Neil Goulty for their valuable advice and guidance over the course of this study, for many fruitful discussions on the results of my work and for reviewing this thesis.

I would also like to thank Toby Harrold for getting me started with pore pressure prediction, Martin Traugott for helping out with the problems related to pressure prediction and wireline logs, Anthony Mallon on scanning electron microscopy, Chris Johnson on interpretation of XRD results and to all staff in the Geological Sciences Department, especially Dave and Gary on the IT.

I wish to extend my thanks to Yunlai Yang and Andy Aplin of Newcastle Upon-Tyne University for carrying out ShaleQuant analysis on two of the wells, Benoit Erout and Segolene Verrier of Beicip-Franlab for providing Easydepth program and technical assistance on Temispack, and Rick Lahann for providing a copy of his OTC paper.

Many thanks to my colleagues in PRSS (Jalil, Wan Ismail, Ku Izhar, Azriyuddin, Peter, Mazlan, Ramly, Rosmah), PCSB (Mahadir, Ramlee) and PMU (Ismail, Arrifin, Awalludin) for providing much needed data and samples for this study. Also, my sincere appreciation to friends and close relatives back home for sending news and keeping us up-to-date with the current events.

Finally, I would like to thank my family for their patience and understanding during this hectic period. To my wife, Yati, and my four kids, Shaz, Wani, Ashraf and Mimi, a big 'TERIMA-KASIH'. And also, to my mother and mother-in-law for their blessings. Thank you all.

Table of Contents

Abstract ii

Acknowledgments iii

Table of Contents iv

List of Figures x

List of Tables xx

Declaration xxi

Chapter 1: Introduction 1

1.1 Overpressure and Exploration Risk in the Malay Basin 2

1.2 Petroleum Geology of the Malay Basin 3

1.2.1 Geological History 5

1.2.2 Stratigraphy 7

1.2.3 Structural Elements 9

1.2.4 Hydrocarbon Occurrences 11

1.4 Overpressure 13

1.4.1 Occurrence and Distribution in the Malay Basin 13

1.4.2 Origins of Overpressure: Current Understanding 13

1.4.3 Rationale for Carrying out the Research 15

1.5 Thesis Objectives 16

1.5.1 Aims 16

1.5.2 Scope of Work 16

1.6 Thesis Outline 17

Chapter 2: Pore Pressure Prediction From Wireline Logs 19

2.1 Introduction 20

2.2 Pore Pressure: Concept and Terminology 20

2.3 Pressure Detection (Prediction) Methods 22

2.3.1 Pre-Drilling Methods 22

2.3.2 While Drilling Methods 22

2.3.3 Post-Drilling Methods 22

2.4 Wireline Pore Pressure Prediction Methods 23

2.4.1 Equivalent Depth Methods 23

2.4.2 Ratio Methods 26

2.5 Data and Pre-Processing 27

2.6 Pore Pressure Prediction Results 28
2.6.1 North Malay 31
2.6.1.1 NM-1 33
2.6.1.2 NM-3 33
2.6.2 West Malay 35
2.6.2.1 WM-8 35
2.6.2.2 WM-10 37
2.6.3 Northeast Malay 39
2.6.3.1 NE-22 39
2.6.3.2 NE-33 41
2.6.4 Central Malay 44
2.6.4.1 CM-16 44
2.6.4.2 CM-17 45
2.6.5 Southeast Malay 45
2.6.5.1 SE-25 48
2.6.5.2 SE-27 48
2.6.6 South Malay 48
2.6.6.1 SM-29 51
2.6.6.2 SM-30 51
2.7 Factors Affecting the Pore Pressure Estimation 54
2.7.1 Normal Compaction Curves 54
2.7.1.1 Compaction Equation 55
2.7.1.2 Shale Lithology 58
2.7.1.3 Erosion/Uplift 61
2.7.2 Shale Porosity 64
2.7.2.1 Sonic vs Density-Derived Porosity 64
2.7.2.2 Solidity 65
2.7.3 Temperature 68
2.7.4 Stress 68
2.7.5 Non-Mechanical Compaction 70
2.8 Summary and Conclusions 71
Chapter 3: Origins of Overpressure in the Malay Basin 75
3.1 Introduction 76
3.2 Causal Mechanisms 76

3.2.1 Disequilibrium Compaction 78
3.2.2 Volume Change or Unloading 79
3.2.3 Others 79
3.3 Wireline Log Characteristics 79
3.3.1 Normal Compaction 80
3.3.2 Disequilibrium Compaction 82
3.3.3 Unloading 82
3.3.4 Clay Diagenesis 86
3.4 Evidences from Log Signatures in the Malay Basin 86
3.4.1 Disequilibrium Compaction 89
3.4.2 Fluid Expansion 89
3.4.3 Chemical Compaction 93
3.5 Diagenesis and Overpressure 96
3.5.1 Shale Diagenesis in Malay Basin 97
3.5.2 Chemical Compaction Signature 98
3.6 Summary and Conclusions 104
Chapter 4: Origins of Overpressure in the Baram Delta and West Luconia 106
4.1 Introduction 107
4.1.1 Geological Setting of Baram Delta 107
4.1.2 Geological Setting of West Luconia 109
4.2 East Baram Delta 109
4.2.1 Stratigraphy 109
4.2.2 Pore Pressure Prediction 111
4.2.3 Origin 113
4.3 West Baram Delta 113
4.3.1 Stratigraphy 116
4.3.2 Pore Pressure Prediction 116
4.3.3 Origin 121
4.4 West Luconia 122
4.4.1 Stratigraphy 122
4.4.2 Pore Pressure Prediction 126
4.4.3 Origin 129
4.5 Log Recognition of Overpressure Origin 129

4.6 Summary and Conclusions 130
Chapter 5: Numerical Simulation of Overpressure Evolution in the Malay Basin 134
5.1 Introduction 135
5.2 Method and Data Input 136
5.2.1 Basin Subsidence and Compaction 136
5.2.2 Thermal History 138
5.2.3 Pore Pressure and Fluid Flow History 139
5.2.4 Hydrocarbon Generation and Migration 140
5.3 Wells, Cross-Section and Model Assumptions 142
5.3.1 Input Data 142
5.3.2 Calibration Data 146
5.4 Modelling Results 147
5.4.1 Model 1: Mechanical Compaction 147
5.4.2 Model 2: Mechanical-Chemical Compaction 150
5.4.3 Model 3: Mechanical Compaction and Hydrocarbon Generation 156
5.4.4 Model 4: Mechanical-Chemical Compaction and Hydrocarbon Generation 159
5.4.5 Model 5: Lateral Fluid-Flow 162
5.5 Discussion 166
5.6 Summary and Conclusions 167
Chapter 6: Overpressure Influence on the Petroleum Systems in the Malay Basin 169
6.1 Introduction 170
6.1.1 Petroleum System Concept 170
6.1.2 Previous Works 171
6.2 Malay Basin Petroleum Systems 173
6.3 Results of 2D Basin Modelling 177
6.3.1 Thermal Modelling 180
6.3.2 Hydrocarbon Generation 182
6.3.4 Hydrocarbon Migration and Accumulation 186
6.3.5 Validation of the Models 189
6.4 Discussion 192
6.4.1 Vitrinite Reflectance: Suppression or Retardation? 192

6.4.2 Overpressure Generating Mechanisms 193
6.4.3 Porosity Preservation 200
6.4.4 Gas Generation: Direct from Kerogen or Oil Cracking 200
6.4.6 Prospectivity of Deep Overpressured Reservoirs 204
6.5 Summary and conclusions 206
Chapter 7: Synthesis and Discussion 207
7.1 Global Comparisons 208
7.1.1 Sources of Data and Methodology 208
7.1.2 Selected Areas 208
7.2 Bowers (2001) 210
7.3 Lahann et al. (2001) 212
7.4 Tingay et al. (2000) 212
7.5 Mahakam Delta (Indonesia) 214
7.5.1 Overpressure Study 214
7.5.2 Source of Data 214
7.5.3 Velocity-Density Crossplots 214
7.6 Venture Gas Field, Scotian Shelf (Canada) 216
7.6.1 Overpressure Study 216
7.6.2 Source of Data 216
7.6.3 Velocity-Density Crossplots 218
7.7 Halten Terrace (offshore mid-Norway) 218
7.7.1 Overpressure Study 218
7.7.2 Sources of Data 221
7.7.3 Velocity-Density Crossplots 224
7.8 Gulf of Mexico (USA) 224
7.8.1 Overpressure Study 224
7.8.2 Sources of Data 227
7.8.3 Velocity-Density Crossplots 227
7.9 Discussion 227
7.10 Summary and Conclusions 231
Chapter 8: Conclusions 234
8.1 Conclusions I: Origins of Overpressure 235
8.2 Conclusions II: Influence on Petroleum Systems 236
8.3 Future Work 237

References 238
Appendix A: Erosion Estimation from Sonic Logs 263

List of Figures

Figure 1.1 Map of Tertiary basins in Southeast Asia. The main area of study is the Malay Basin. The other basins which have been included are the East Baram, West Baram and Western Luconia. Orange and blue lines are isopachs of 1 km and 4 km thickness, respectively..... 4

Figure 1.2 Extrusion model showing collision between India and Eurasia that resulted in strike-slip faults and basin formation in Southeast Asia proposed by Tapponier et al. (1982). Study area is shown in the red rectangle..... 6

Figure 1.3 Geological section showing major anticlinal features resulted from mid-Miocene basin inversion..... 8

Figure 1.4 High geothermal gradient (averaging 47°C/km) recorded for the Malay Basin (after Yusuff, 1993)..... 8

Figure 1.5 Generalised stratigraphic of the Malay Basin and correlation to the adjacent Penyu and West Natuna basins (after Ramli, 1988; EPIC, 1994)..... 10

Figure 1.6 Summarized hydrocarbon occurrences and structural history of the basin (from EPIC, 1994)..... 10

Figure 1.7 Map showing major oil and gasfields in the Malay Basin. The contours represent sedimentary thickness in kilometres. 12

Figure 1.8 Cross-section of the basin showing top of overpressure..... 12

Figure 1.9 Pressure data for the Malay Basin derived from various sources. The grey dots are mudweight data, blue dots are direct formation pressure from RFT and MDT and the red triangles are leak-off test data..... 14

Figure 2.1 Predicting pore pressure from wireline logs: (a) equivalent depth method and (b) Eaton ratio method. In the equivalent depth method it is assumed that vertical projection to the normal compaction curve corresponds to a line of constant porosity and constant effective stress. In the empirical ratio method it is assumed that the ratio of the measured log value (B) to the log value on the normal compaction curve at the same depth (A) is empirically related to the ratio of the

vertical effective stress at B and A.....24
Figure 2.2 Data pre-processing prior to pore pressure analysis: (a) raw sonic dataset, (b) selecting shale using gamma-ray filter, after removal of bad data points, (c) smoothing the data using moving average of 400 ft (120 m) interval. 29
Figure 2.3 Location map of the Malay Basin showing wells selected for this study. The wells are grouped according to geographic distribution. Contours represent Tertiary sediment thickness in km.....30
Figure 2.4 Wireline logs from well NM-1 showing departure from normal compaction trend indicating top of overpressure.....32
Figure 2.5 Pore pressure analysis results for NM-1. (a) Equivalent depth method using mean effective stress, EDM (mes), (b) Equivalent depth method using vertical effective stress, EDM (ves), (c) Eaton method (EM).....34
Figure 2.6 Pore pressure analysis results for NM-3. (a) EDM (mes), (b) EDM (ves), (c) EM. 36
Figure 2.7 Pore pressure analysis results for WM-8. (a) EDM (mes), (b) EDM (ves), (c) EM. 38
Figure 2.8 Pore pressure analysis results for WM-10. (a) EDM (mes), (b) EDM (ves), (c) EM. 40
Figure 2.10 Pore pressure analysis results for NE-33. (a) EDM (mes), (b) EDM (ves), (c) EM. 43
Figure 2.11 Pore pressure analysis results for CM-16. (a) EDM (mes), (b) EDM (ves), (c) EM. 46
Figure 2.12 Pore pressure analysis results for CM-17. (a) EDM (mes), (b) EDM (ves), (c) EM. 47
Figure 2.13 Pore pressure analysis results for SE-25. (a) EDM (mes), (b) EDM (ves), (c) EM. 49
Figure 2.14 Pore pressure analysis results for SE-27. (a) EDM (mes), (b) EDM (ves), (c) EM. 50
Figure 2.15 Pore pressure analysis results for SM-29. (a) EDM (mes), (b) EDM (ves), (c) EM. 52
Figure 2.16 Pore pressure analysis results for SM-30. (a) EDM (mes), (b) EDM (ves), (c) EM. 53

Figure 2.17 Pore pressure prediction for well WM-8, using modified Eaton method, which used sonic porosity instead of sonic travel time. (a) Normal compaction curves derived from single (red) and double (green) exponential functions plotted against depth with sonic-derived porosity. (b) Predicted pore pressure for single and double exponential compaction trends. 57

Figure 2.18 Pore pressure prediction for well CM-17, using modified Eaton method. See Figure 2.17 for explanation. 57

Figure 2.19 Calculated pore pressure for Well NM-5 using compaction curve with minimum matrix transit-time. (a) Normal compaction curves with (green line) and without (blue) minimum matrix transit-time. (b) Pore pressure results. 59

Figure 2.20 Calculated pore pressure for Well SM-28 using compaction curve with minimum matrix transit-time. (a) Normal compaction curves with (green) and without (blue) minimum matrix transit-time. (b) Pore pressure results. 59

Figure 2.21 Plot of void ratio versus hydrostatic mean effective stress for shales from NM-6, grouped according to gamma-ray values. Also plotted are various normal compaction curves of varying sediment mechanical parameters. (a) All shales, (b) GR of 70 to 80 API shale, (c) GR of 80 to 90 API shale, (d) GR of 90 to 150 API shale, (e) GR 150-160 API and (f) GR above 160 API shale. 60

Figure 2.22 Predicted pore pressure for CM-16 using the EDM mean effective stress: (a) selecting shale from gamma-ray logs, (b) plot of void ratio versus hydrostatic mean effective stress, (c) predicted pore pressure using the two different compaction coefficient (Cc) values. 62

Figure 2.23 Density profile for wells NM-1 and CM-17. Grey line represents density data from log. Red dots are the calculated density values from the sonic log, There is a good match between the density log and the sonic-derived density in the upper part of well NM-1 and in well CM-17. Density values began to depart below top of overpressure in well NM-1. 66

Figure 2.24 Computed pore pressure for well WM-8 using solidity instead of porosity in EDM (ves) method. (a) solidity (green) and porosity

(blue) trends plotted against vertical effective stress. Also plotted are the derived normal compaction curves for the well. (b) Predicted pressure profiles using solidity (green) compares to porosity (blue). 67

Figure 2.25 Computed pore pressure for well WM-8, using solidity and porosity data, instead of sonic transit-time in Eaton method. (a) solidity (green) and porosity (blue) trends with depth and the estimated normal compaction curves. (b) Predicted pressure profile using solidity and porosity parameters showing better pore pressure prediction obtained using porosity than solidity. 67

Figure 2.26 Minimum horizontal stress (Sh) calculated using Breckels & van Eekelen (1982) data from Brunei and leak-off data from the Malay Basin. 69

Figure 2.27 Predicted pore pressure using Bowers (2001) high pressure correction method. (a) NM-1, (b) SM-30. 72

Figure 2.28 Predicted pore pressure using smectite and illite compaction curves. (a) NM-1, (b) SM-30..... 73

Figure 2.29 Predicted pore pressure using Eaton exponent of 5 (instead of 3) . (a) NM-1, (b) SM-30. 74

Figure 3.1 Schematic historical path for shales undergoing normal compaction: (a) fluid pressure versus depth, (b) shale porosity versus depth, (c) shale porosity versus vertical effective stress, (d) bulk density versus velocity..... 81

Figure 3.2 Schematic evolutionary path expected for overpressured shales that undergoing disequilibrium compaction (red): (a) fluid pressure versus depth, (b) shale porosity with depth, (c) shale porosity versus vertical effective stress, (d) bulk density versus velocity. Grey dots/lines represent expected trend for normally compacted rocks. 83

Figure 3.3 Schematic evolutionary path expected for overpressured shales that results from unloading: (a) fluid pressure versus depth, (b) shale porosity with depth, (c) shale porosity versus vertical effective stress, (d) bulk density versus velocity. 85

Figure 3.4 Example of possible trends expected from overpressured shales undergoing clay diagenesis: (a) fluid pressure versus depth, (b) shale

porosity versus depth, (c) shale porosity versus vertical effective stress, (d) bulk density versus velocity from sonic transit times. 87

Figure 3.5 Velocity vs. density plot of well SE-25 showing no departure from the normal trend between the normally pressured and the overpressured shales. Data from 7000-8000 ft was omitted due to borehole condition resulting in spurious distribution. 90

Figure 3.6 Plots of vertical effective stress against density, velocity and log-derived porosity wells NM-1, NM-3, SM-28 and SM-30. Both actual (grey) and averaged (blue-hydrostatic and red-overpressured) datapoints are shown. The same normal compaction curves (solid lines) are used for each crossplot for all the wells. 91

Figure 3.7 Velocity vs. density crossplots for wells NM-1, NM-3, SM-28 and SM-30. Grey dots represent actual log values and the symbols representing averaged log values to help visualizing the compaction trends. Also plotted on the trend are the estimated borehole temperature and the onset of the overpressure..... 94

Figure 3.8 SEM micrograph of microfabric of overpressured shale at depth 5560 ft in well SM-30 (a) 650x magnification, (b) 2220x magnification. 99

Figure 3.9 SEM micrograph of microfabric of overpressured shale at depth 8150 ft from well SM-30. (a) 650x magnification, (b) 2220x magnification. 100

Figure 3.10 Example of possible trend expected from overpressured shales undergoing chemical compaction. (a) Fluid pressure versus depth, (b) shale porosity versus depth, (c) shale porosity versus vertical effective stress, (d) bulk density versus velocity from sonic transit times. 101

Figure 3.11 Proposed processes for chemical compaction in explaining the velocity-density trend in the Malay Basin. 103

Figure 4.1 Map showing location of the geological provinces in Sabah and Sarawak Basins. The provinces covered in this study are the East Baram, West Baram and West Luconia. 108

Figure 4.2 East Baram Delta: (a) well locations and geological features, (b) lithostratigraphic scheme. 110

Figure 4.3 Results of pressure analysis for well EB-1. (a) EDM (ves), (b) EDM (mes), (c) Eaton..... 112
Figure 4.4 Results of pressure analysis for well EB-3. (EDM (ves), (b) EDM (mes), (c) Eaton..... 114
Figure 4.5 Velocity-density crossplots for (a) well EB-1 and (b) EB-3. Grey dots represent actual log values for the shale. Blue dots are the averaged dataset using moving average of 400 ft interval. Also plotted on the EB-1 trend are temperature intervals, based on geothermal gradient of 24.9°C/km (obtained from well report). 115
Figure 4.6 Sarawak Basin. (a) Map showing location of the studied wells in the West Baram Delta and the West Luconia Province, (b) stratigraphic framework for the West Baram Delta..... 117
Figure 4.7 Pressure analysis results for well WB-6. (EDM (ves), (EDM (mes), (c) Eaton 118
Figure 4.8 Pressure analysis results for well A. (a) EDM (ves), (b) EDM (mes), (c) Eaton..... 119
Figure 4.9 Pressure analysis results for well B. (a) EDM (ves), (b) EDM (mes), (c) Eaton..... 120
Figure 4.10. Velocity-density crossplots for (a) WB-6, (b) Well A, (c) Well B.123
Figure 4.11 Corrected pore pressure using Bowers (1995) method for Well A.. 124
Figure 4.12 Stratigraphy of the West Luconia Province.. 125
Figure 4.13 Pressure analysis results for well WL-1. (a) EDM (ves), (b) EDM (mes), (c) Eaton..... 127
Figure 4.14 Pressure analysis results for well WL-3..... 128
Figure 4.15 Pressure analysis results for well WL-4..... 131
Figure 4.16 Velocity-density crossplot for WL-4. 132
Figure 4.17 Evaluation strategy for determining origin of overpressure. 133
Figure 5.1 Schematic flowchart for a typical basin modelling study (from Ungerer et al., 1990) 137
Figure 5.2 Porosity-depth trend for shales in the Malay Basin. Also plotted for comparison are data from Giles et al. (1998) and Temispack default value for shale..... 137
Figure 5.3 1-D modelling: (a) assigning each layer a set of petrophysical data based percentages of shale content; (b) treating the layers as either

shale (low permeability) or sandstone (permeable). The clay content is derived from ShaleQuant wireline log analysis (blue line/grey dots). (c) Burial history plot for well SM-28. 144

Figure 5.4 Location map showing the wells and the modelled 2D lines. Wells analysed in Chapter 2 are given in red dots, while the remaining wells in the area are in grey. Green and red colours indicates major oil and gas fields, respectively. 145

Figure 5.5 Porosity and permeability data for: (a) well SM-28 and (b) SM-30. Sonic and density-derived shale porosity are plotted as red and blue lines, respectively. The grey lines are data obtained from ShaleQuant log analysis. Porosity and permeability data from measured core samples are plotted as red squares. 148

Figure 5.6 Modelled results for well SM-28 using different shale permeability anisotropy coefficients: (a) pressure, (b) vertical permeability, (c) porosity and (d) density. 149

Figure 5.7 Temporal evolution of (a) pressure, (b) vertical permeability and (c) porosity for a Group L shale in SM-28, which is adjacent to a reservoir section where formation pressure was taken. 151

Figure 5.8 Depth plots of 1-D results for well SM-30 using different permeability anisotropy coefficients. 152

Figure 5.9 History plots of pressure, porosity and vertical permeability of an overpressured shale from Group L in well SM-30. 154

Figure 5.10 Results of 1D modelling with mechanical and chemical compaction for SM-28. The chemical compaction parameters used in the modelling are as listed in the legend. 155

Figure 5.11 Results of 1D modelling for SM-30 using similar chemical compaction parameters as for SM-28 in Figure 5.10. 157

Figure 5.12 Porosity-permeability relationship used in the modelling (red squares) The coloured shapes are ranges of porosity-permeability for shales taken from Neuzil (1994). ShaleQuant result is plotted as grey circles. 158

Figure 5.13 Modelled pressure-depth profile resulting from hydrocarbon generation in wells SM-28 and SM-30. Models run are: Model 3a (oil generation from Type I source rocks with 2% TOC), Model 3b

(gas generation from Type III source rocks with 2% TOC) and Model 3c (gas from primary & secondary cracking of Type I source rocks with TOC 2%). 160

Figure 5.14 Modelled pressure-depth profile resulting from hydrocarbon generation in the mechanical-chemically compacted shales: (a) SM-28 and (b) SM-30. 161

Figure 5.15 Modelled 2-D section (a) seismic section, (b) gridded litho-section. 163

Figure 5.16 Temporal plots of pore pressure for Group L shale (source rock) and sandstone (reservoir) at: (a) Well SM-29 and (b) Kitchen C. Results are for: Model 5a (no HC generation), Model 5b (oil generation) and Model 5c (gas from cracking). 165

Figure 6.1 Typical biomarker fingerprints of two main oil groups in the Malay Basin: lacustrine-derived (a,c,d) and coaly-derived (b,d,f). The fingerprints are presented in forms of whole oil gas chromatograms (a,b), m/z 191 (c,d) and m/z 217 (e,f). 174

Figure 6.2 Cross-plots of TOC vs. Rock-Eval S_2 for shales/coals in the Malay Basin, (a) Groups A/B to I, (b) Groups J-M. Data derived from EPIC (1994). 175

Figure 6.3 Cross-plots of the TOC (from Figure 6.2) against Tmax values. Onset of oil generation zone begins at Tmax of 435°C and end at around 470°C. For Type I kerogen, Tmax values generally less than 450°C, even at late mature stage. 176

Figure 6.4 2-D cross-section of N-S line: (a) seismic profile, (b) gridded section used for basin modelling study. Also shown are the locations of the wells and oil/gas fields (projected). 178

Figure 6.5 Comparing thermal modelling results using rifting heat flow against a constant basal heat flow for well SM-31. 181

Figure 6.6 Present-day measured and modelled temperatures and maturity for wells: (a) NS-3 (km 42), (b) NS-4 (km 53), (c) SM-31 (km 85) and (d) NS-5 (km 123). No significant changes in the modelled temperature and maturity as result of chemical compaction within the Group K, L and M upper shales are noted. 183

Figure 6.7 Modelled present-day temperature distribution using a constant heat

flow of 60 mW/m^2. 185

Figure 6.8 Modelled maturity and kerogen transformation: (a) present-day maturity profile across the N-S section, (b) calculated transformation ratio history for Group L source rock at locations NS-4 (km 53), syncline (km 65) and SM-31 (km 85). 187

Figure 6.9 Modelled present-day oil saturation from Group K, L and M source intervals (TOC of 2%, Type I kerogen). Model (a) was runs with mechanical compaction only and model (b) using both mechanical and chemical compaction. 188

Figure 6.10 Modelled gas saturation resulting from cracking. Source rocks been assigned to Group K, L and M shales (TOC of 2%, Type I kerogen). Model (a) was simulated using mechanical compaction alone and model (b) was run with both mechanical and chemical on the shales. 190

Figure 6.11 Predicted pore pressure in well SM-31 for various models. Best-fit of pore pressure were obtained using mechanical and chemical compaction within the tight shales (source rocks) with hydrocarbon generation. 191

Figure 6.12 Discovered hydrocarbon pools along the modelled section. Green and red represent oil and gas zones, respectively. Wells, pseudo wells or oil/gas fields are NS-1 (km 9), NS-2 (km-33), NS-3 (km 42), NS-4 (km 53), SM-31 (km-85) and NS-5 (km 123). 191

Figure 6.13 Maturity depth profiles for wells (a) NM-1, (b) WM-11, (c) SM-28 (d) SM-30. 194

Figure 6.14 Modelled hydrocarbon saturation from Groups E, H and I coaly source rocks (Type III kerogen with TOC of 20%). No significant hydrocarbon accumulation was observed. 196

Figure 6.15 Modelled oil saturations with Group K,L and M shales as source rocks (Type I kerogen, TOC of 2%). Both mechanical and chemical compaction were applied to all lithologies, assuming two sets of chemical compaction parameters applied to sandy and shaly facies. 196

Figure 6.16 Gas saturation plots modelled at three different geological ages: (a) present-day, (b) 3 Ma and (c) 10 Ma. Arrows (red) indicate

migration direction and the sizes represent the magnitude. 197

Figure 6.17 Modelled pore pressure for wells: (a) SM-31 at km 85, (b) well NS-4 at km 53 and (c) pseudo-well NS-3 at km 41. Models were run using mechanical and chemical compaction, assuming similar chemical compaction parameters for two groups of lithologies, sandy and shaly units. 198

Figure 6.18 Pressure evolution in well SM-31 for the (a) Group L shale, (b) Group L reservoir. 199

Figure 6.19 Modelled porosity evolution for (a) shale and (b) sandy units in SM-31, with and without chemical compaction. 201

Figure 6.20 Plot of iC_4/nC_4 and $\delta^{13}C$ C_2 to distinguish origin of gases in the Malay Basin. The plot is used to distinguish the origin of gases in the Malay Basin (Hoesni and Abolins, 2000). Open circles (blue & green) are taken from various fields in the basin. The closed circles (red) are gas samples from well SM-28 and SM-30. No data are available from well SM-31. 203

Figure 6.21 Velocity-density crossplots of SM-31 showing chemical compaction signature. Chemical compaction begins at temperature of around 110°C with the deviation from the normal compaction trend. This caused a drastic reduction in permeability. 203

Figure 6.22 Comparing velocity-density crossplots of two wells located at different end of the modelled section. The well on the northern end of the line do not exhibit chemical compaction signature. 205

Figure 7.1 Location of the selected examples of overpressured basins 209

Figure 7.2 Velocity-density crossplots for well EI 330-20AS/T, taken from Bowers (2001) 211

Figure 7.3 Velocity-density crossplots for Well B in Lahann et al. (2001), showing illlitization and unloading trend. Data are grouped in depth intervals (feets) 211

Figure 7.4 Velocity-density crossplots for Well A, Baram Delta, Brunei (data from Tingay et al., 2000). Data are grouped as: (a) depth intervals, (b) temperature intervals. 213

Figure 7.5 Sonic and density logs for a Mahakam Delta well, taken from Burrus

et al., 1993.....215
Figure 7.6 Velocity-density crossplots for a Mahakam Delta well. Data were plotted according to depth and temperature intervals. Grey dots are raw log data and coloured dots are the averaged data. 217
Figure 7.7 Wireline logs for well H-22, Venture Gas Field, taken from Mudford and Best (1989).....219
Figure 7.8 Velocity-density crossplots for well H-22. Data were plotted according to depth and temperature intervals.....220
Figure 7.9 Collation of (a) sonic and (b) density log data for the Halten Terrace, from Skar et al. (1998). Blue and brown lines represent maximum boundaries. Red dots are the mid-points data.....222
Figure 7.10 Wireline logs for well 6406/2-6, Halten Terrace. Blue line is the actual log response and the the red dots are the averaged datapoints for the shaly section.....223
Figure 7.11 Velocity-density crossplots for wells data from Skar et al. (1998) for the Halten Terrace. Plotted are the mid-points data only.....225
Figure 7.12 Velocity-density crossplots for well 6406/2-6, Halten Terrace.....226
Figure 7.13 Sonic and density crossplot of a well from the Garden Banks, Gulf of Mexico (data from Geopop; Swarbrick, pers.comm.).....228
Figure 7.14 Velocity-density crossplot for a Garden Banks' well plotted according to: (a) depth intervals, (b) temperature intervals.....229
Figure 7.15 Summary of velocity-density trends for different processes.....233

List of Tables

Table 3.1 Some of the published examples of the proposed origins for overpressure in sedimentary basins.....77

Table 3.2 Interpretation of the origins of overpressure for the Malay basin wells, based on shale pore pressure profile and velocity-density crossplots. D-disequilibrium compaction; U-unloading; C-chemical compaction; N-normal compaction; X-not determinable.....88

Table 5.1 Examples of published porosity-permeability data for shales.....141

Table 5.2 Modelled pressure within the reservoirs (Ksst & Lsst) and the overlying shales (K2 & L2).....164

Table 6.1 Some published examples on the influence of overpressure on petroleum systems.....172

Table 6.2 Stratigraphy and lithology along the modelled 2D section. The source rocks and reservoirs are indicated by * and #, respectively. The range of lithology within each stratigraphic group reflects the lateral and vertical variation...177

Table 6.3 Petrophysical parameters of the lithologies used in the modelling.....179

Table 6.4 Modelling scenarios.....180

Table 6.5 Hydrocarbon properties for migration runs.....189

Table 6.6 Estimated undiscovered oil and gas resources in several petroleum systems within Asia Pacific by U.S. Geological Survey (McCabe et al., 2000)....204

Table 7.1 Location of the selected overpressured basins discussed in Chapter 7.....210

Table 7.2 Estimated temperatures at point of departure in velocity-density crossplots..230

Declaration

The content of this thesis is the original work of the author (other people's work, where included, is acknowleged by reference). It has not been previously submitted for a degree at this or any other university.

M.J.Hoesni

Durham

July 2004

Copyright

The copyright of this thesis rests with the author. No quotation from it should be published without his prior written consent and information derived from it should be acknowledged.

Chapter 1:

Introduction

1.1 Overpressure and Exploration Risk in the Malay Basin

Since the first exploration well in the Malay Basin, Tapis-1, was drilled in 1969, exploration activities have been largely concentrated on the Lower Miocene-Oligocene fluvial-braided sands within compressional anticline traps, where major oil and gas discoveries have been made. These reservoirs are found at depths between 2000 and 3000 m. These wells are relatively shallow, considering that the deepest sediments are located over 12 km below sea level in the basin centre. The major factors influencing the maximum drilling depths are the high geothermal gradient and overpressure in the basin. High temperatures result in deterioration of reservoir quality and make hydrocarbon preservation at depth less likely, while high overpressure poses a major drilling risk in the area, also making the economics of drilling wells less attractive.

Kader (1994) reported that over 80% of the wells drilled in the basin were terminated due to overpressure. Many operators consider the top of overpressure as an economic basement. Statistics of hydrocarbon discoveries in the Gulf Coast, USA reported by Leach et al. (1994) show most of the hydrocarbon accumulations are found above the overpressure. Similar findings apply for the NW Australian Shelf (Zaunbrecher, 1994). One of the reasons for absence of hydrocarbons in high overpressure reservoirs is seal breaching, when pore pressures reach the fracture gradient, and reservoirs that are close to the fracture gradient of 0.85 psi/ft (19.6 kPa) are considered incapable of trapping significant amount of hydrocarbons (Timko and Fertl, 1971; Law and Spencer, 1998). However, hydrocarbons are trapped in reservoirs in some basins where the fracture gradient exceeds 0.9 psi/ft, e.g., Scotian Shelf, Canada and the North Sea (Engelder & Fisher, 1994; White, 2002).

The top of overpressure commonly coincides with the oil window. The deeper highly pressured sequences are normally found where temperatures exceed 150°C. At these high temperatures, liquid hydrocarbons (C_{14+}) are not expected to survive, leaving mainly dry gas, if any. However, in recent deeper wells in the Malay Basin, such as Bergading Deep-1, oils and condensate were preserved within deep overpressured sequences (Fatt, 1999). Other published works have reported liquid

hydrocarbons surviving in high temperature and high pressure reservoirs (Vandenbroucke et al., 1999).

The principal aim of this study is investigate the relationship between overpressure and the hydrocarbon distribution in the Malay Basin. This involved re-evaluating hypotheses on the origins of the overpressure and the influence it might have on the petroleum systems in the Malay Basin. Secondary aims include comparison with another Malaysian Basin, located offshore Borneo, as well as with other overpressured, petroliferous basins around the world.

In the Malay Basin, vast areas below top overpressure remain to be explored. There is a need to understand the origin and distribution of overpressure in the Malay Basin and application of new technology for pressure prediction is needed to reduce uncertainty in both pressure prediction and hydrocarbon reserve expectations. Recent success stories in recovering hydrocarbons from highly overpressured reservoirs in other basins, such as Elgin, Franklin and Shearwater Fields, Central North Sea (Blehaut et al., 1999; Gilham et al., 2003), Thunder Horse and Bullwinkle, US Gulf of Mexico (O'Connell et al., 1993; Flemings et al., 2001) serve to make deeper overpressured targets in the Malay Basin look attractive.

1.2 Petroleum Geology of the Malay Basin

The Malay Basin is located on the Sunda Shelf, with water depths of about 50 to 80 m. The basin is bounded by the Pattani Basin to the north and West Natuna Basin to the south (Figure 1.1*)*. The basin is about 500 km long and 250 km wide, trending NW-SE. It is one of the most prolific hydrocarbon basins in Southeast Asia, with estimated hydrocarbon reserves discovered to date in excess of 2.4 billion barrels of oil and 36.6 trillion cubic feet of gas (Zainul et al., 1999).

Regional geology of the basins in Malaysia can be found in some published journals and unpublished oil companies' report. Comprehensive reviews and summaries of these works have recently been compiled and published in "The Petroleum Geology and Resources of Malaysia" (PETRONAS, 1999).

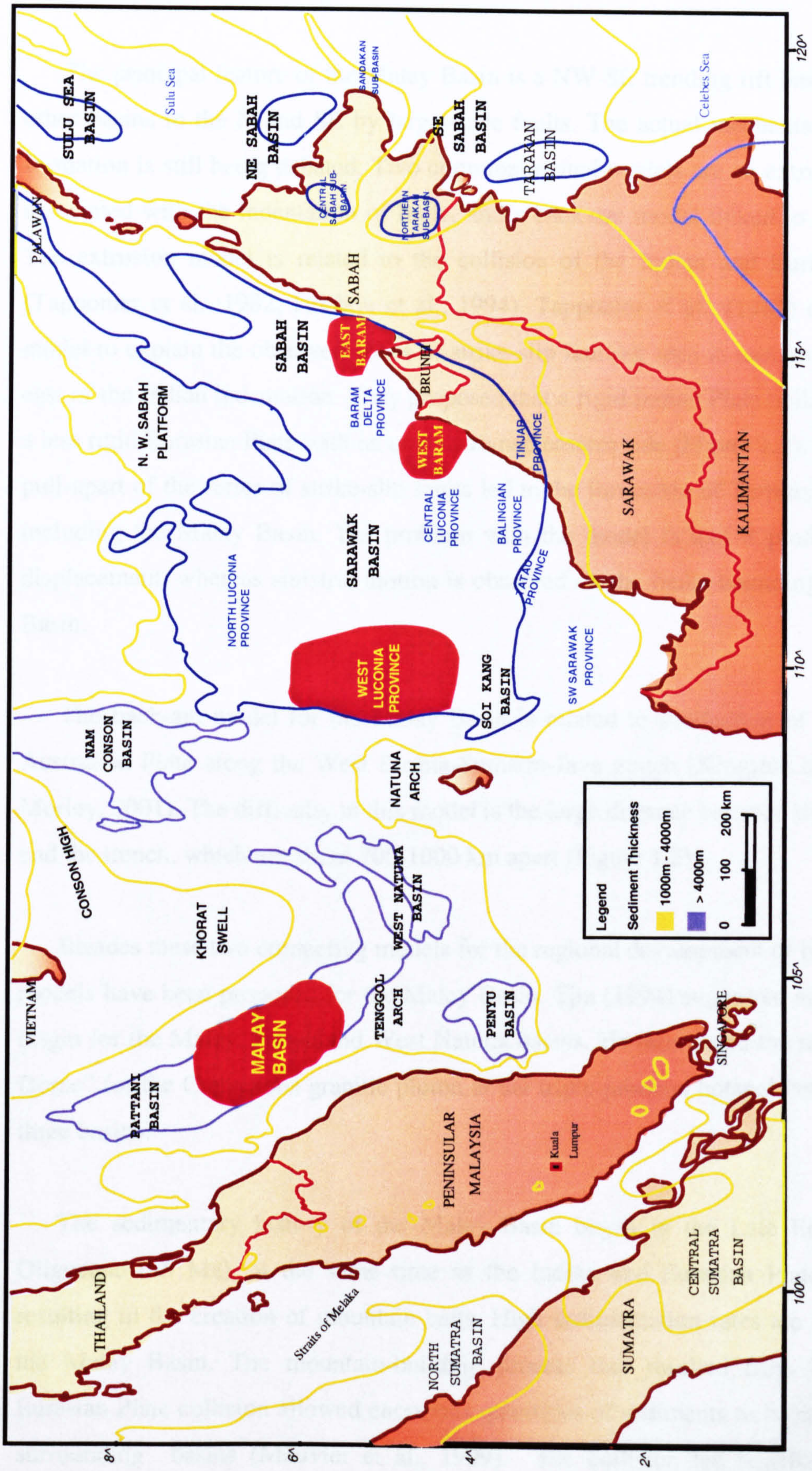


Figure 1.1 Map of Tertiary basins in Southeast Asia. The main area of study is the Malay Basin. The other basins which have been included are the East Baram, West Baram and Western Luconia. Orange and blue lines are isopachs of 1 km and 4 km thickness, respectively.

1.2.1 Geological History

The principal feature of the Malay Basin is a NW-SE trending rift basin linked to other basins to the N and SE by large-scale faults. The actual mechanism for basin formation is still being debated. Two commonly cited models are an extrusion model associated with the indentation of India, and a back-arc model linked to subduction. The extrusion model is related to the collision of the Indian and Eurasian plates (Tapponier et al., 1982; Huchon et al., 1994). Tapponier et al., (1982) developed a model to explain the observed series of strike-slip faulting seen in eastern Asia to the east of the Indian indentation. They proposed that a rigid Indian Plate collided against a less rigid Eurasian Plate with an unconstrained eastern side (Figure 1.2). Subsequent pull-apart of the series of strike-slip faults led to the formation of Tertiary rift basins, including the Malay Basin. The problem with the model is that it predicts dextral displacement, whereas sinistral motion is observed on the faults bounding the Malay Basin.

The back-arc model for the Malay Basin is related to subduction of the Indian-Australian Plate along the West Burma-Sumatra-Java trench (Kingston et al., 1983; Morley, 2001). The difficulty in this model is the large distance between the extension and the trench, which are about 700-1000 km apart (Figure 1.2)

Besides these two competing models for the regional development of basins, other models have been proposed for the Malay Basin. Tjia (1994) suggested an aulacogen origin for the Malay, Penyu and West Natuna basins. He introduced the term "Malay Dome" for the Cretaceous granitic pluton at the triple-junction hotspot between these three basins.

The sedimentary history of the Malay Basin began in the Late Eocene-Early Oligocene (45 Ma), at the same time as the Indian and Eurasian Plates collided, resulting in the creation of mountain belts. High sedimentation rates are recorded in the Malay Basin. The mountain-building process that resulted from the Indian-Eurasian Plate collision allowed enormous quantities of sediments to be shed into the surrounding basins (Metivier et al., 1999). The collision led to rifting and the formation of a series of grabens and half-grabens, with topography filled by

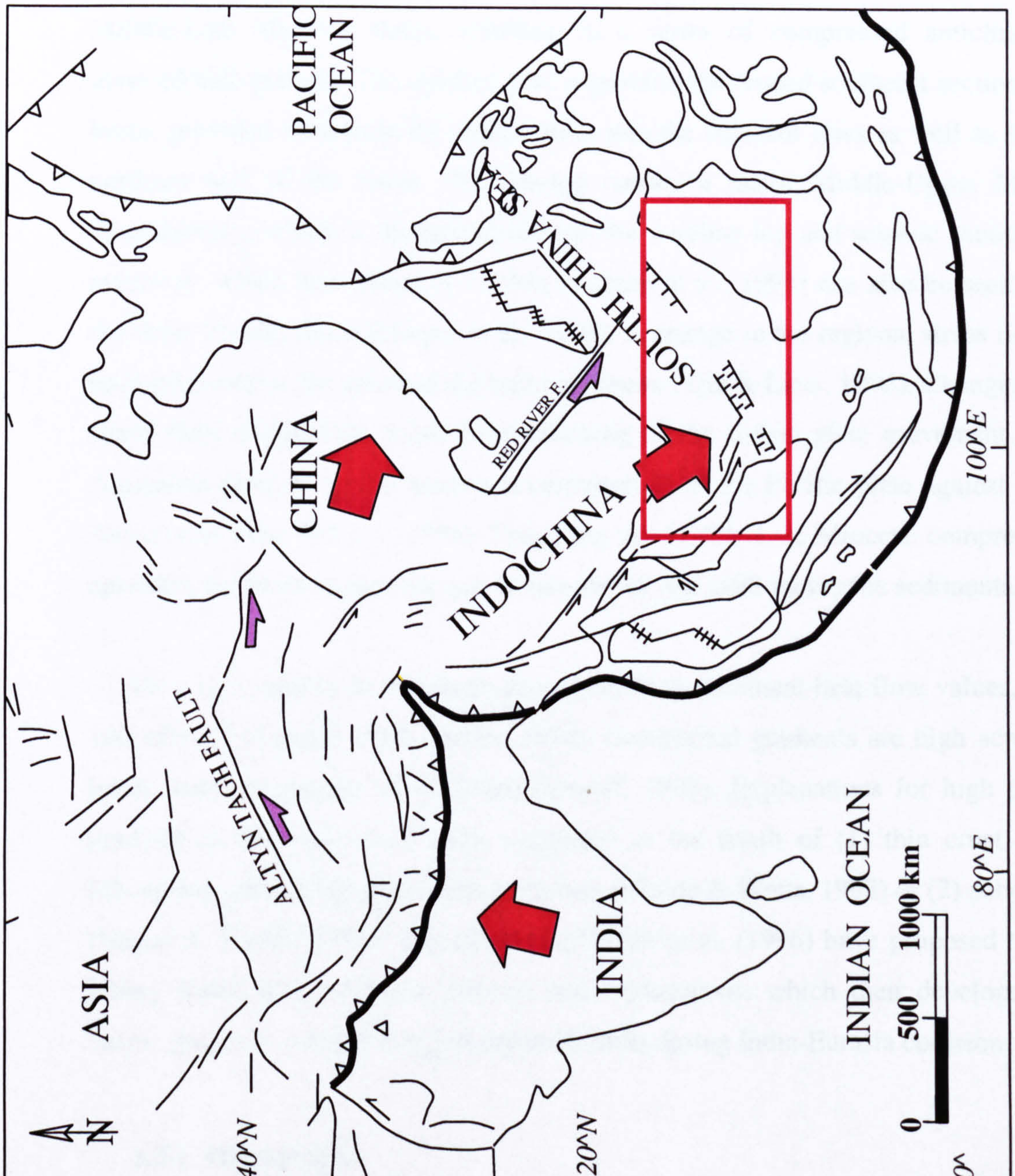


Figure 1.2 Extrusion model showing collision between India and Eurasia that resulted in strike-slip faults and basin formation in Southeast Asia proposed by Tapponier et al. (1982). Study area is shown in the red rectangle.

Oligocene and Lower Miocene sediments, mainly fluvial and lacustrine deposits. This syn-rift succession was followed by further subsidence interpreted as due to thermal sagging, infilled by deposits that mainly comprise of coastal plain sediments.

Following the rift and post-rift phases, major structural inversion occurred in Middle-Late Miocene times, resulting in a series of compressed anticlines and inverted half-grabens. The uplifted part, especially the eroded southeast section of the basin, provided sediments for redeposition into the adjacent lows as well as into the northern half of the basin. The erosion caused a major Middle-Upper Miocene unconformity, which is distinguishable on the wireline log and seismic section. The inversion, which been dated at 7.8 Ma (Yakzan et al., 1994) can also be seen across the West Natuna Basin (Ginger et al., 1993). A change in the regional stress field has been proposed as the cause of the basin inversion (Tjia & Liew, 1996). Changes in the stress field might arise either from blocking of the Indian plate movement by the Australian plate or due to westward convergence of the Pacific plate against the SE Asian crust (Tjia & Liew, 1996). Following the Middle-Late Miocene compressional episodes, the basin underwent gentle subsidence and infill by marine sediments.

Heat flow studies in this basin show very high basement heat flow values, above 100 mWm^{-2} (Yusoff, 1984; Halim, 1994). Geothermal gradients are high across the basin, with an average of 47°C/km (Yusoff, 1993). Explanations for high thermal gradient in the basin have been suggested as the result of (1) thin crust due to lithospheric stretching and crustal extension (Madon & Watts, 1998) or (2) subduction (Nagao & Uyeda, 1995). Tjia (1994) and Ngah et al. (1996) have proposed that the Malay Basin was originally formed from aulacogens, which then developed into basins proper as a result of reactivation of faults during India-Eurasia collision.

1.2.2 Stratigraphy

Stratigraphic subdivision of the Malay Basin used in this study is based on the Esso Production Malaysia Inc (EPMI) "group" scheme. These "groups" are identified and correlated using seismic stratigraphy, where the seismic sequence boundaries

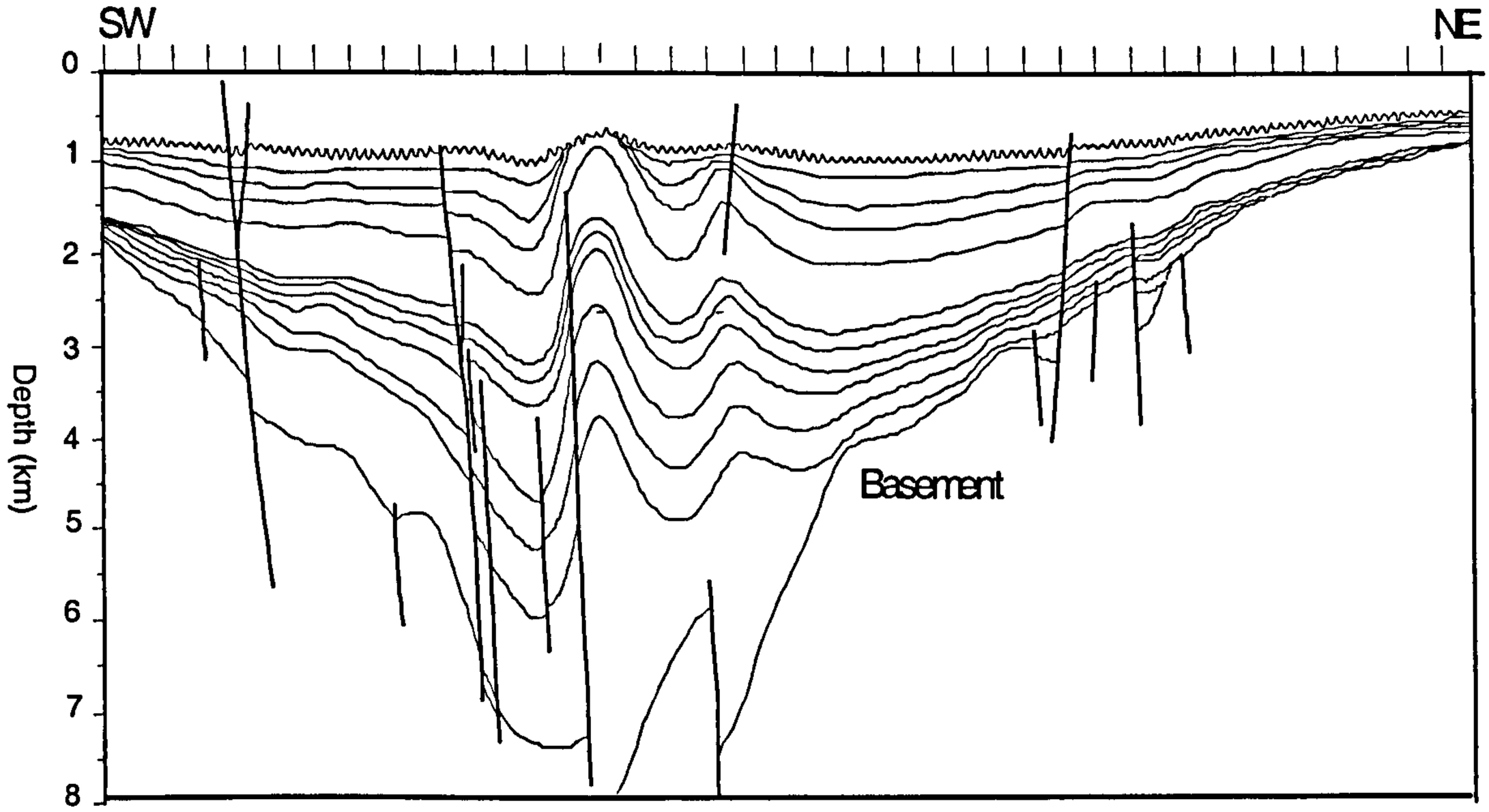


Figure 1.3 Geological section showing major anticlinal features resulted from mid-Miocene basin inversion.

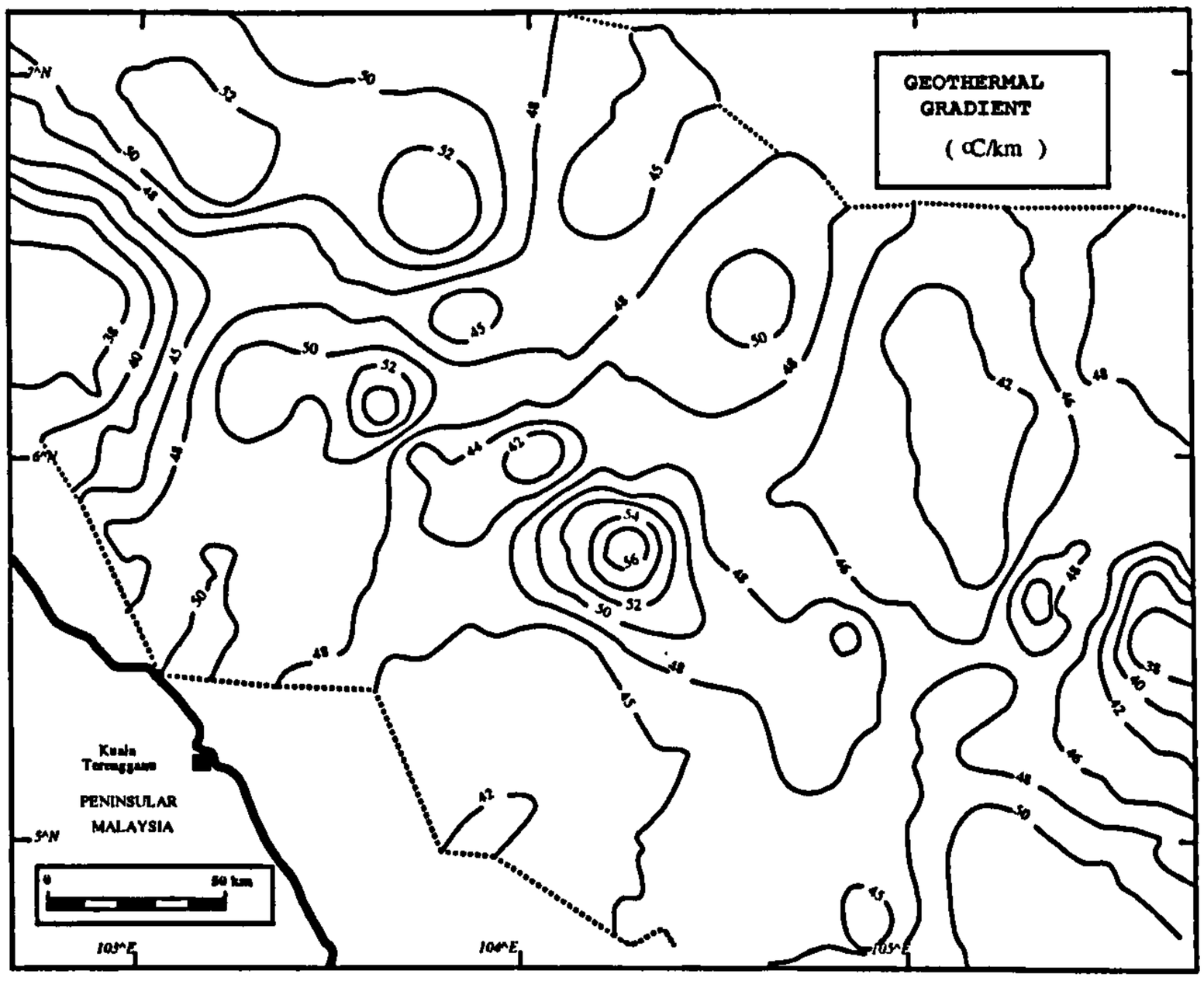


Figure 1.4 High geothermal gradient (averaging 47°C/km) recorded for the Malay Basin (after Yusuff, 1993).

represent erosional surfaces. The nomenclature for this stratigraphic subdivision was originally developed for EPMI's operating areas in the eastern part of the basin. The sequences are labelled alphabetically from M (Oligocene) to A (Recent). Outside the EPMI operating areas, other nomenclatures have been developed and can be found in some well reports and published papers (see Madon et al., 1999b). The correlation between these nomenclatures is summarised in Figure 1.5.

Over 12 km of sediments were deposited above the pre-Tertiary basement, comprising metasediments, as well as igneous and carbonate rocks. Several exploration wells have penetrated these basement rocks at the basin margin. These basement carbonates are potential candidates for giving rise to high inorganic CO_2 gas in some of the fields in the area. These gases were tapped through deep faults (Waples & Ramly, 1996). The basement granites in the area have been dated by K/Ar dating to be of Jurassic-Cretaceous age (EPMI, 1976). The early graben fill consists mainly of continental red beds.

Poor recovery of foraminifera and nannofossils from well cuttings and excellent recovery of palynomorphs indicate that the palaeowater depths are quite shallow (less than 100 m depth). Early marine influence was first recorded during early Miocene in the south-eastern part of the basin. Full marine conditions (holomarine) for the basin were only achieved during Pliocene times.

1.2.3 Structural Elements

The basin is asymmetrical in shape, having a steeper south-western flank than its north-eastern flank. The rifting is thought to have begun in the Early Oligocene (~ 45 Ma), and could possibly be older as suggested by Tjia & Liew (1996).

The early extensional features, such as half-grabens and major basement faults, can be seen on seismic sections over the northern and western part of the basin. In the south-eastern part of the basin, most of the extensional features are overprinted by the later compressional event, which formed E-W folds and anticlines (Figure 1.6).

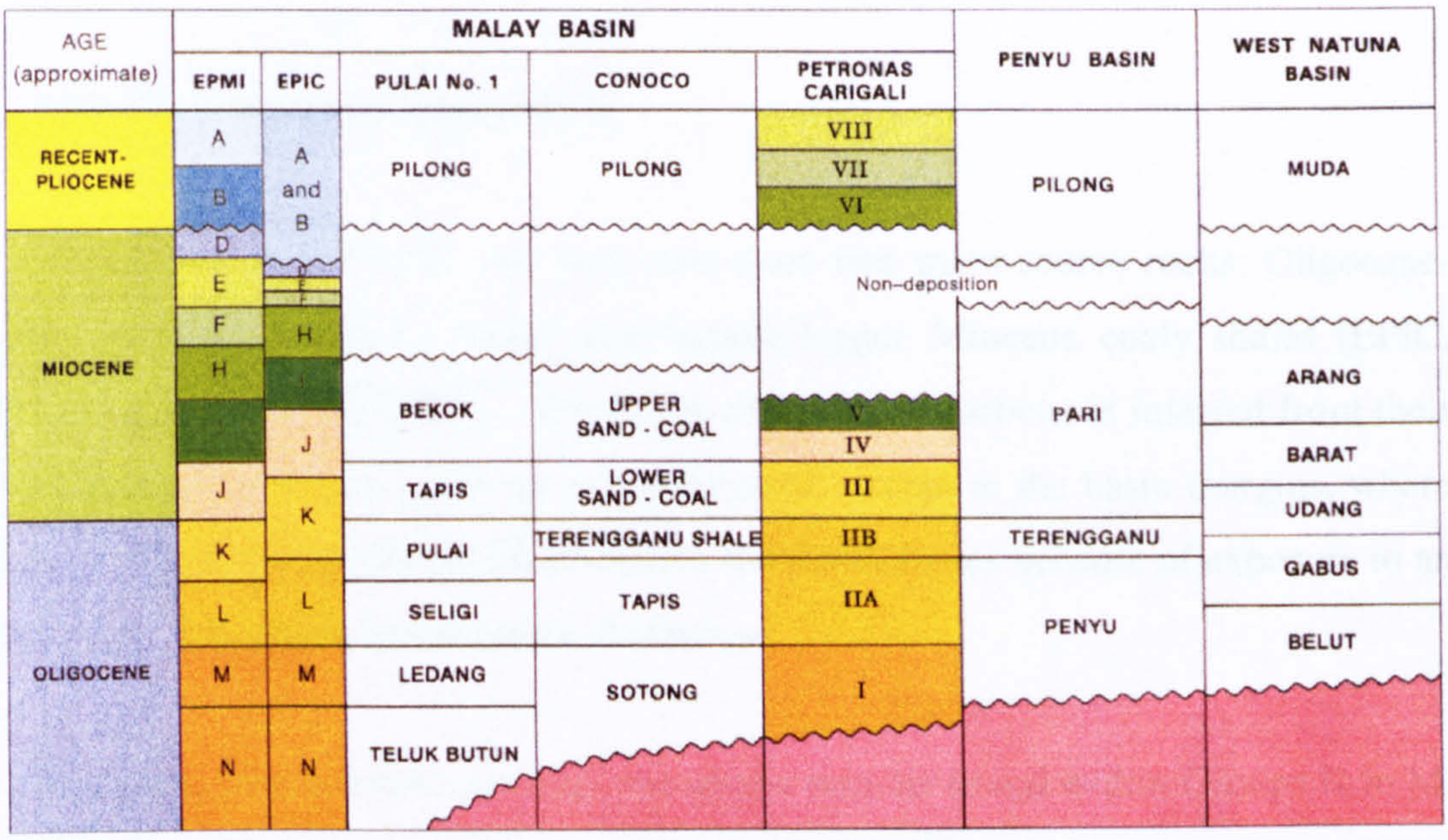


Figure 1.5 Generalised stratigraphic of the Malay Basin and correlation to the adjacent Penyu and West Natuna basins (after Ramli, 1988; EPIC, 1994).

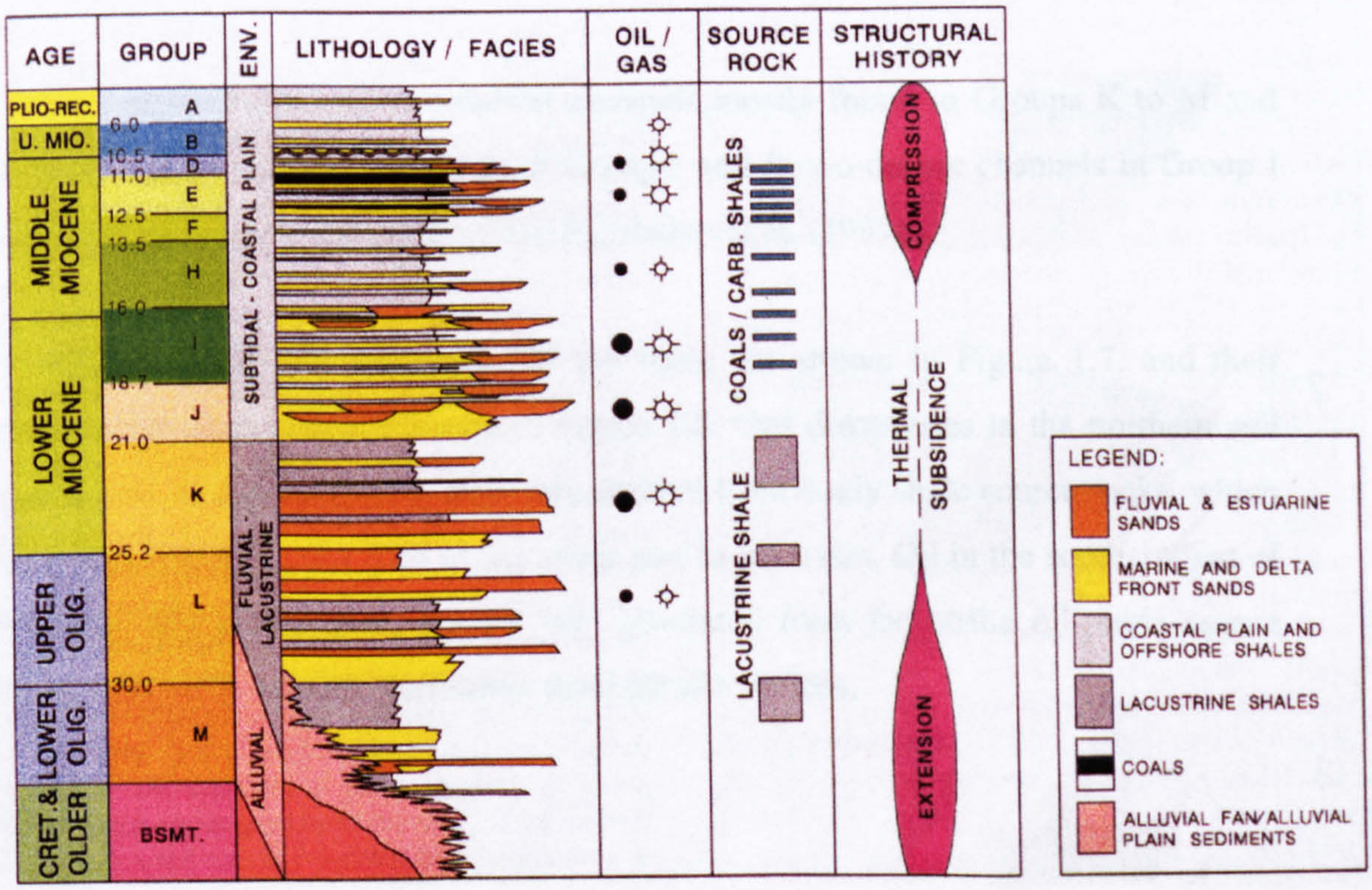


Figure 1.6 Summarized hydrocarbon occurrences and structural history of the basin (from EPIC, 1994).

The maximum contemporary compressive stress was thought to be orientated between NE-SW and ENE-WSW (Ngah et al., 1996).

1.2.4 Hydrocarbon Occurrences

Oil and gas in the basin are generated from two main source rocks: Oligocene-Lower Miocene lacustrine shales and Middle-Upper Miocene coaly shales (EPIC, 1994; McCaffrey et al., 1998). The origin of the hydrocarbons is inferred from their properties as the source rocks are not penetrated, except at the basin margins, where the source quality is probably lower than in the distal shales because of exposure to an oxidising environment and dilution of clastics.

Oligocene-Lower Miocene lacustrine shales may be found within Groups K to M. The source materials are made up of oil-prone algal (Type I) kerogen. Coaly shales containing mainly terrigeneous (Type III) kerogen are found in fluvio-deltaic source rocks from Groups E and I (Figure 1.6)

The reservoirs range from fluvial channels mostly found in Groups K to M and shoreface and subtidal shelf sands of Group J and fluvio-deltaic channels in Group I and younger (Figure 1.6) as described by Madon et al. (1999a).

Major oil and gas discoveries in the basin are shown in Figure 1.7, and their stratigraphic occurrence is shown in Figure 1.6. Gas discoveries in the northern and central part of the basin were primarily derived from coaly shale source rocks, which have been buried deeper than in any other part in the basin. Oil in the southern part of the basin and at the basin margin was generated from lacustrine oil-prone source rocks, with some minor contribution from paralic sources.

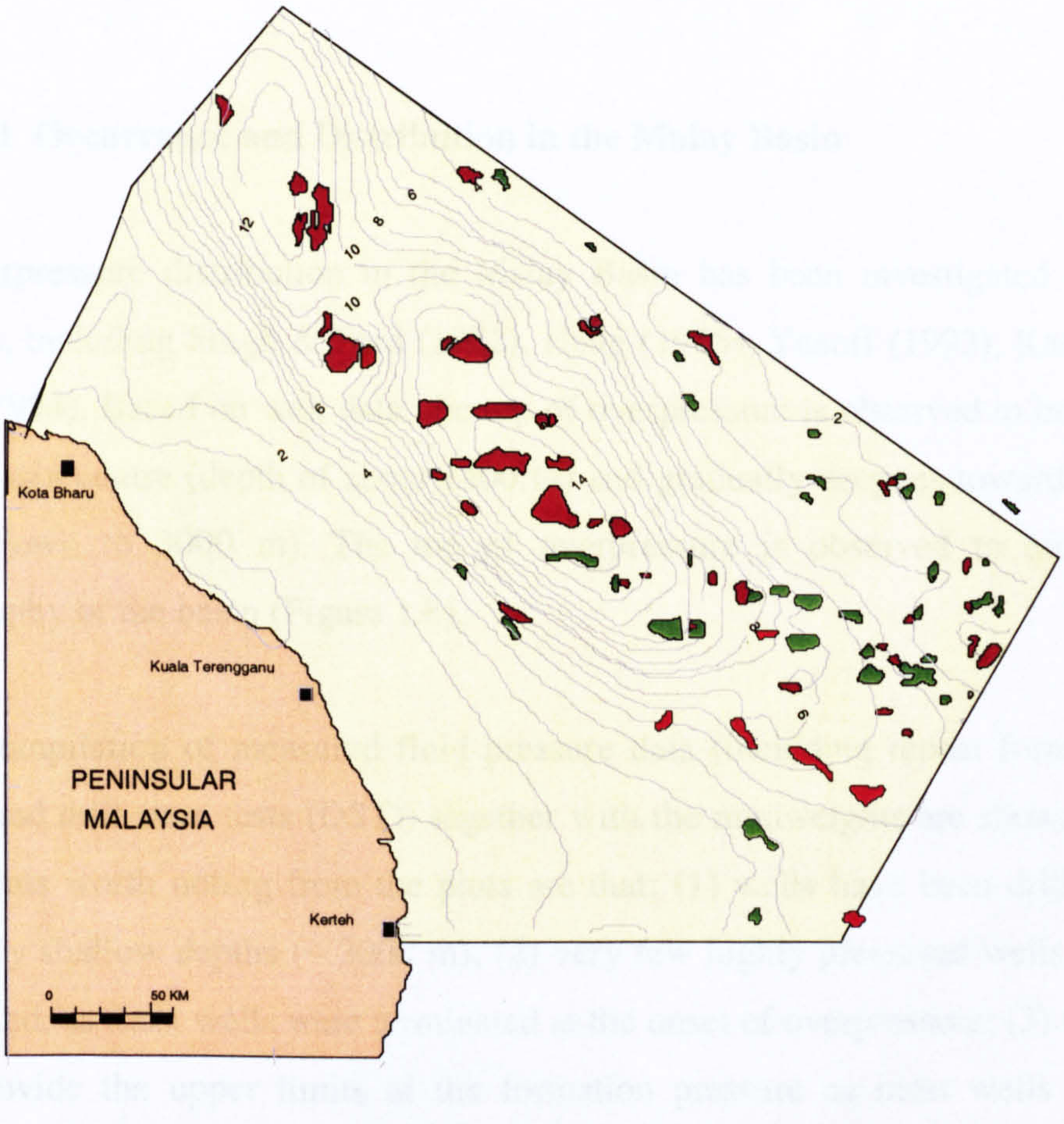


Figure 1.7 Map showing major oil and gasfields in the Malay Basin. The contours represent sedimentary thickness in kilometres.

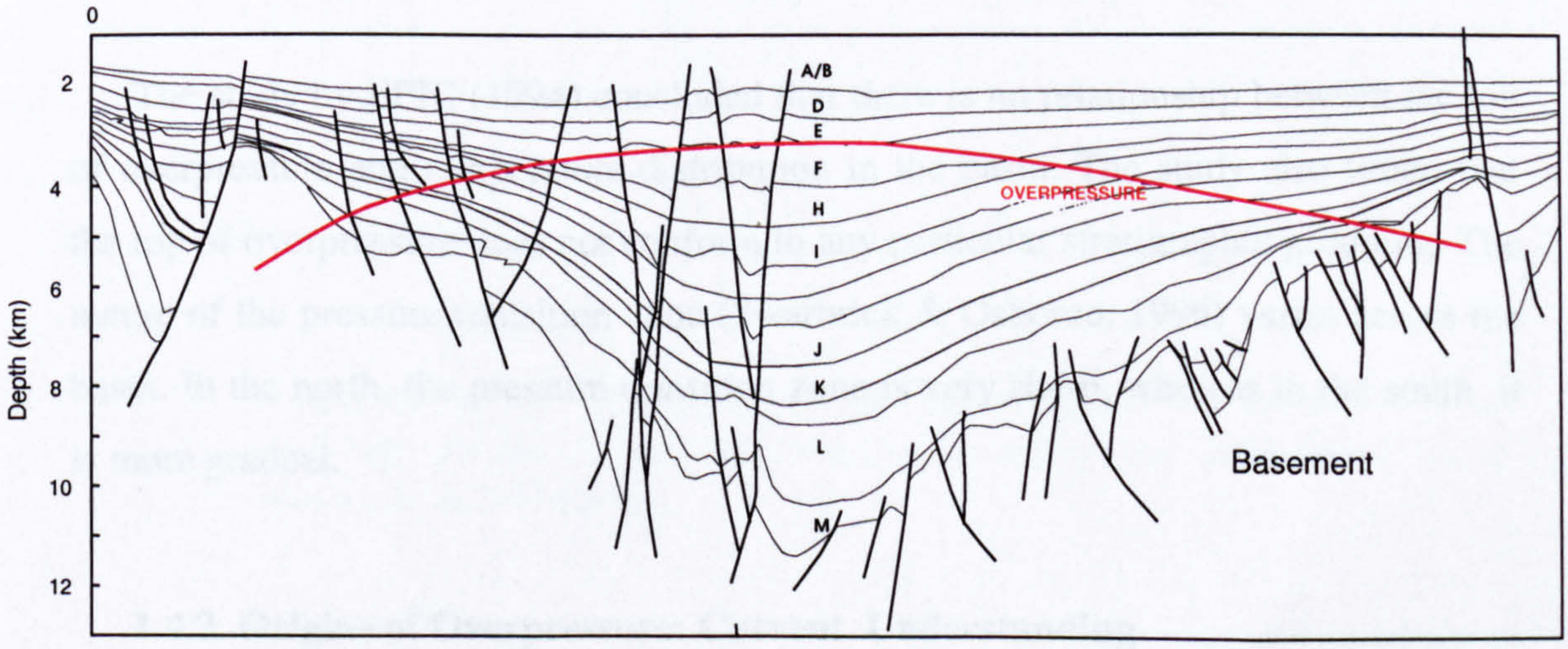


Figure 1.8 Cross-section of the basin showing top of overpressure.

1.4 Overpressure

1.4.1 Occurrence and Distribution in the Malay Basin

Overpressure distribution in the Malay Basin has been investigated by several workers, including Singh & Ford (1982), Heng (1985), Yusoff (1993), Kader (1994), EPIC (1994). Based on well data, the top of overpressure is observed to be shallower in the basin centre (depth of about 1400 m) and gradually deepens towards the basin flank (down to 3000 m). The top of overpressure is observed to cross-cut the stratigraphy of the basin (Figure 1.8).

A compilation of measured fluid pressure data (including repeat formation tests (RFT) and drill stem tests (DST)) together with the mudweights are shown in Figure 1.9. Points worth noting from the plots are that: (1) wells have been drilled to only relatively shallow depths (~ 3000 m); (2) very few highly pressured wells have been penetrated, as most wells were terminated at the onset of overpressure; (3) mudweight data provide the upper limits of the formation pressure as most wells are drilled slightly overbalanced for safety reasons. Also, in the southeast part of the basin swelling clays caused drilling problems, which resulted in the usage of higher mudweight than the actual formation pressure.

The study by EPIC (1994) concluded that there is no relationship between the top of overpressure and temperature distribution in the basin. The study also found that the top of overpressure does not conform to any particular stratigraphic grouping. The nature of the pressure transition zone (Swarbrick & Osborne, 1996) varies across the basin. In the north, the pressure transition zone is very sharp, whereas in the south it is more gradual.

1.4.2 Origins of Overpressure: Current Understanding

Several causes of overpressure have been postulated for the Malay Basin (Heng, 1985; EPIC, 1994). Disequilibrium compaction as a result of rapid burial of Tertiary sediments is the most favoured explanation for the origin of overpressure in the basin.

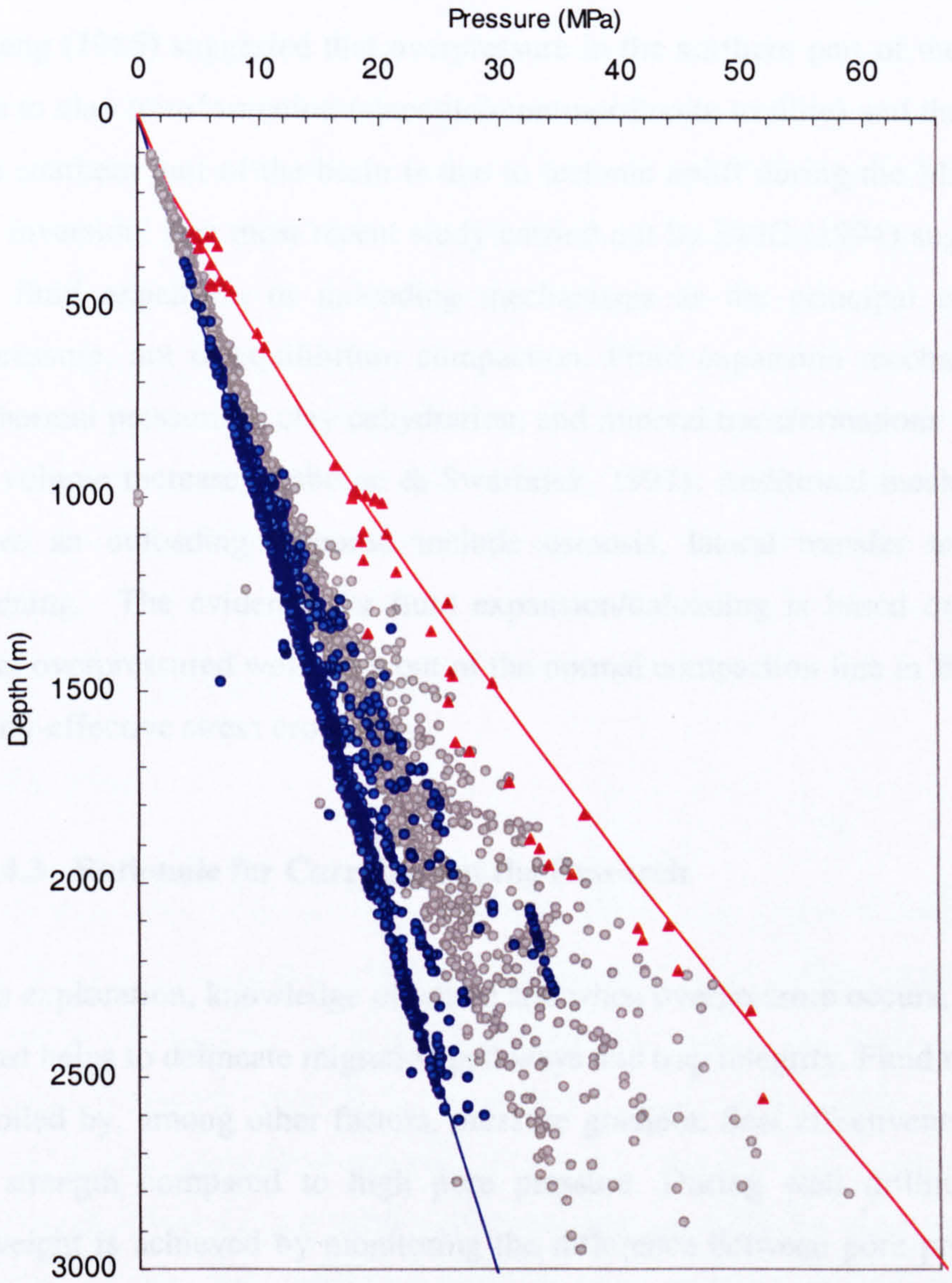


Figure 1.9 Pressure data for the Malay Basin derived from various sources. The grey dots are mudweight data, blue dots are direct formation pressure from RFT and MDT and the red triangles are leak-off test data.

Rapid deposition of low-permeability sediments inhibit expulsion of fluids, so the sediments are undercompacted and the pore fluids become overpressured (Dickinson, 1953).

Heng (1985) suggested that overpressure in the northern part of the Malay Basin is due to clay transformation (smectite/montmorillonite to illite) and the overpressure in the southern part of the basin is due to tectonic uplift during the Middle Miocene basin inversion. The most recent study carried out by EPIC (1994) suggested one or more fluid expansion or unloading mechanisms as the principal contributors to overpressure, not disequilibrium compaction. Fluid expansion mechanisms include aquathermal pressuring, clay dehydration, and mineral transformations which involve fluid volume increase (Osborne & Swarbrick, 1997). Additional mechanisms which involve an unloading response include osmosis, lateral transfer and framework weakening. The evidence for fluid expansion/unloading is based on the fact that several overpressured wells plot out of the normal compaction line in Bower's (1995) velocity-effective stress crossplots.

1.4.3 Rationale for Carrying out the Research

In exploration, knowledge of where and when overpressure occurs, or occurred in the past helps to delineate migration pathways and trap integrity. Fluid movements are controlled by, among other factors, pressure gradient. Seal effectiveness depends on rock strength compared to high pore pressure. During well drilling, a balanced mudweight is achieved by monitoring the difference between pore pressure and the fracture pressure. This will helps to minimise well inflow and mud losses and to avoid kicks. During production, the pressure information is vital in planning field depletion, especially in compartmentalised fields.

In recent years, volumes of papers discussing topics on overpressure have been published (Law et al., 1998; Mitchell & Grauls, 1998; Huffman & Bowers, 2002). Greater awareness on the subjects and better understanding of the interaction between geological processes and overpressure development has helped in better pore prediction. Several pore pressure prediction methods have been developed and some

may require local calibration. With the large amount of data from the Malay Basin, such published works can be applied to the basin to help in better understanding and predicting the overpressure. Complete suites of wireline logs available in the Malay Basin provide a good opportunity to study the overpressure generating processes through wireline logs. The almost complete sonic and density logging of some wells enables a direct study to distinguish between the mechanism of compaction disequilibrium and unloading processes, as proposed by Bowers (1995). This will help to explain the origins of the overpressure, not only for this basin but also for other basins which share a similar geologic setting.

In this thesis, work is reported on the application of several pore pressure prediction methodologies to help in determining the origins and behaviour of pore pressure and sedimentary processes in the basin.

1.5 Thesis Objectives

1.5.1 Aims

The objectives of this study are two-fold. Firstly, the origin of overpressure in the Malay Basin is investigated. This is largely accomplished through examining wireline log responses from representative wells located throughout the basin. Secondly, using a 2D basin modelling program, the overpressure in the Malay Basin can be simulated. The models are constrained and calibrated using measured rock properties. Series of models with different parameters were run to test the influence of overpressure on the petroleum system. The reliability of the predicted models was then compared to the actual well data or drilling results.

1.5.2 Scope of Work

Recognizing mechanisms contributing to the overpressure in a basin is a challenging task. Most often, the absence of some processes are used to infer the likely origins of overpressure in the basin. A number of papers discuss the characteristics of wireline log responses for different overpressure origins (Bowers,

1995; Lahann, 2002; Swarbrick, 2002). In this study, I have attempted to understand the origin of overpressure in the Malay Basin by examining and predicting pore pressure using wireline logs, and applying empirical models and a soil mechanics approach.

Numerical basin modelling is used here to integrate geological, geophysical and geochemical processes to simulate overpressure in the basin and aid in understanding the influence of overpressure on hydrocarbon migration and trapping in the basin.

1.6 Thesis Outline

This thesis is divided into eight chapters, with three appendices. Chapter 1 provides a general overview of the study, highlighting the needs for carrying out the research, the background, and the scope of the work.

In Chapter 2 several methods of pore pressure prediction have been tested on the Malay Basin wells, including both traditional methods and a soil-mechanics approach. Results from each method are compared, highlighting key factors that arise that may result in the differences in the results.

Chapter 3 discusses the origins of the overpressure in the Malay Basin. The causal mechanisms are inferred from the wireline logs behaviour and rock properties. Shale cuttings have been subjected to XRD and SEM analyses.

Chapter 4 presents an overpressure investigation on several selected wells from the Baram Delta and Western Luconia provinces from Sabah and Sarawak Basins. These basins are much in contrast to the Malay Basin in term of basin history, and provide an excellent comparison study to better understand key factors contributing to overpressure in these basins.

In Chapter 5, basin modelling has been used to reconstruct the overpressure evolution in the Malay Basin. The modelling tool allows a quick ways of testing different hypotheses with regard to events and factors leading to the overpressure

development in the basin. The models help to establish the relative significance of difference causal mechanisms for overpressure in the area.

Chapter 6 discusses the possible influence of overpressure on the petroleum systems in the Malay Basin, including kerogen maturation, fluid migration and trap integrity.

Chapter 7 provides a synthesis on the results achieved from Chapter 2 to Chapter 6 and discusses the findings in context of global perspectives. Finally, Chapter 8 summarizes the findings and results of all the chapters.

Chapter 2:

Pore Pressure Prediction From Wireline Logs

2.1 Introduction

Direct measurement of pore fluid pressure is limited to rocks with high permeability. Wireline pressure measurements such as the Repeat Formation Test (RFT) and Modular Dynamics Tester (MDT) and measurement by a Drill Stem Test (DST), which is a production test, are not performed on low permeability rocks such as shales because of the long times required to achieve flow. Indirect estimation of pore pressure in shales can be obtained from wireline logs.

The objectives of this chapter are (1) to describe how wireline logs are used to predict pore pressure in the shales and to pick top of overpressure; (2) to evaluate the suitability of different pore prediction methods for analysis of overpressure in the Malay Basin; and (3) to determine the factors influencing pore pressure prediction results.

This chapter is divided into four parts. The first part provides an overview of the concept of pore pressure. The second part describes various wireline methods for pore pressure estimation. The different approaches used by these methods are discussed. The third part presents the pore pressure estimation results of several representative wells from the Malay Basin. The differences in the results obtained by different methods and how they compare with the observed formation pressures are highlighted. The results of a few representative wells from different part of the basin is discussed in this chapter. The final part discusses possible causes for variation in pore pressure results and highlights some keys issues that have influenced the results.

2.2 Pore Pressure: Concept and Terminology

Pore fluid pressure is defined as the pressure experienced by the fluids in the rock pores at any particular depth. For a normally pressured rock, the pore fluid is assumed to be in hydrostatic equilibrium up to the surface and the pore pressure is given by:

$$P_f = \rho g z \quad (2.1)$$

where

P_f = pore fluid pressure at depth z,

ρ = the fluid density, and

g = gravitational acceleration.

Hydrostatic pressure gradient

The pressure gradient (P_f/z) associated with normal pressures is commonly referred to as hydrostatic. The pressure imposed on these fluids within the interconnected pores is equivalent to the weight of the overlying water column extended vertically to the surface. The hydrostatic pressure gradient ranges from 0.433 psi/ft (9.795 MPa/km) for freshwater to 0.519 psi/ft (11.74 MPa/km) for saturated saltwater, according to Exploration Logging Inc. (1981). However, in the Malay Basin, the hydrostatic pressure gradient is in the range of 0.426 - 0.433 psi/ft (EPIC, 1994). The low hydrostatic pressure gradient is due to the high temperature gradient in the basin, leading to lower density at any depth.

Lithostatic pressure gradient

The vertical stress exerted on the sediment at any given depth corresponds to the total weight of the overlying rock formations. This stress is sometimes refers to as overburden stress or lithostatic pressure. Often, for simplicity, the lithostatic gradient is taken as 1.0 psi/ft (0.023 MPa/m) correspond to the average bulk density of 2.3 g/cc. The actual lithostatic pressure gradient varies with depth, dependent upon the density of the rocks and the fluids. In offshore areas, the shallow, less consolidated sediments have lower bulk density than 2.3 g/cc, and so the lithostatic gradient is lower than 1.0 psi/ft.

Overpressure

Overpressure refers to the excess pressure above normal or hydrostatic pore pressure. High pore pressure sequences are often associated with abnormally high porosities for the depth of burial.

Terzhagi (1923) defined effective stress (σ) as the difference between normal stress (S) and pore pressure (P_f).

$$\sigma = S - P_f \quad (2.2)$$

Basically, effective stress is the grain-to-grain contact stress, the magnitude of which controls mechanical compaction in rocks. In normally compacted rock, porosity is reduced with increasing effective stress.

2.3 Pressure Detection (Prediction) Methods

Prediction of overpressure can be carried out at different stages during exploration: before drilling (pre-drill), during drilling and after-drilling (post-drill). More comprehensive discussion can be found in Mouchet and Mitchell (1989).

2.3.1 Pre-Drilling Methods

Prediction before drilling can be achieved using seismic velocity analysis. Seismic pressure prediction relies on detecting changes in interval velocity with depth (Dutta, 2002). These changes reflect the properties of the overpressured rock, which in most cases are undercompacted. In frontier areas, seismic pressure prediction provides the only mean of predicting the overpressure. In moderately explored basin, the use of integrated basin modelling could assist in predicting overpressure ahead of drill.

2.3.2 While Drilling Methods

Pore pressure can be monitored during drilling from the following parameters: d-exponent, measurement while drilling (MWD), mud gas, background gas, connection and trip gas, gas analysis, mud temperature and shale density,

2.3.3 Post-Drilling Methods

Post-drilling methods involve the use of wireline log data to estimate the pore

pressure downhole. The results will help in planning for future exploration wells in the area. It also helps to better understand the origin of overpressure in the area. This thesis focuses on the use of wireline logs in pore pressure analysis.

2.4 Wireline Pore Pressure Prediction Methods

The most commonly used methods to estimate pore pressure from wireline logs are the equivalent depth and Eaton ratio methods (Mouchet & Mitchell, 1989). These methods are sometimes refers to as vertical and horizontal methods, respectively (Traugott, 1997), according to the direction of extrapolation from the measured depth position to the normal compaction curve (Figure 2.1). A brief description of the methods is given below. Full details of the procedures can be found in the source references.

The Eaton method is empirical, whilst the equivalent depth method is deterministic and relies on the assumption that shales of equal porosity and similar composition have been subjected to the same maximum vertical effective stress, regardless of their burial depth. The assumption is valid provided that any overpressure has only been created by disequilibrium compaction, and provided that the ratios between the principal effective stresses do not vary with depth (Goulty, 2004).

2.4.1 Equivalent Depth Methods

Two published equivalent depth methods were tested for the Malay Basin wells. The first technique is the equivalent depth method (Forster and Whelan, 1966) that follows procedures first introduced by Rubey and Hubbert (1959) and later developed by Hart et al. (1995), in which sonic-derived shale porosity is related to vertical effective stress. This method will be referred to as EDM(ves) method throughout this thesis:

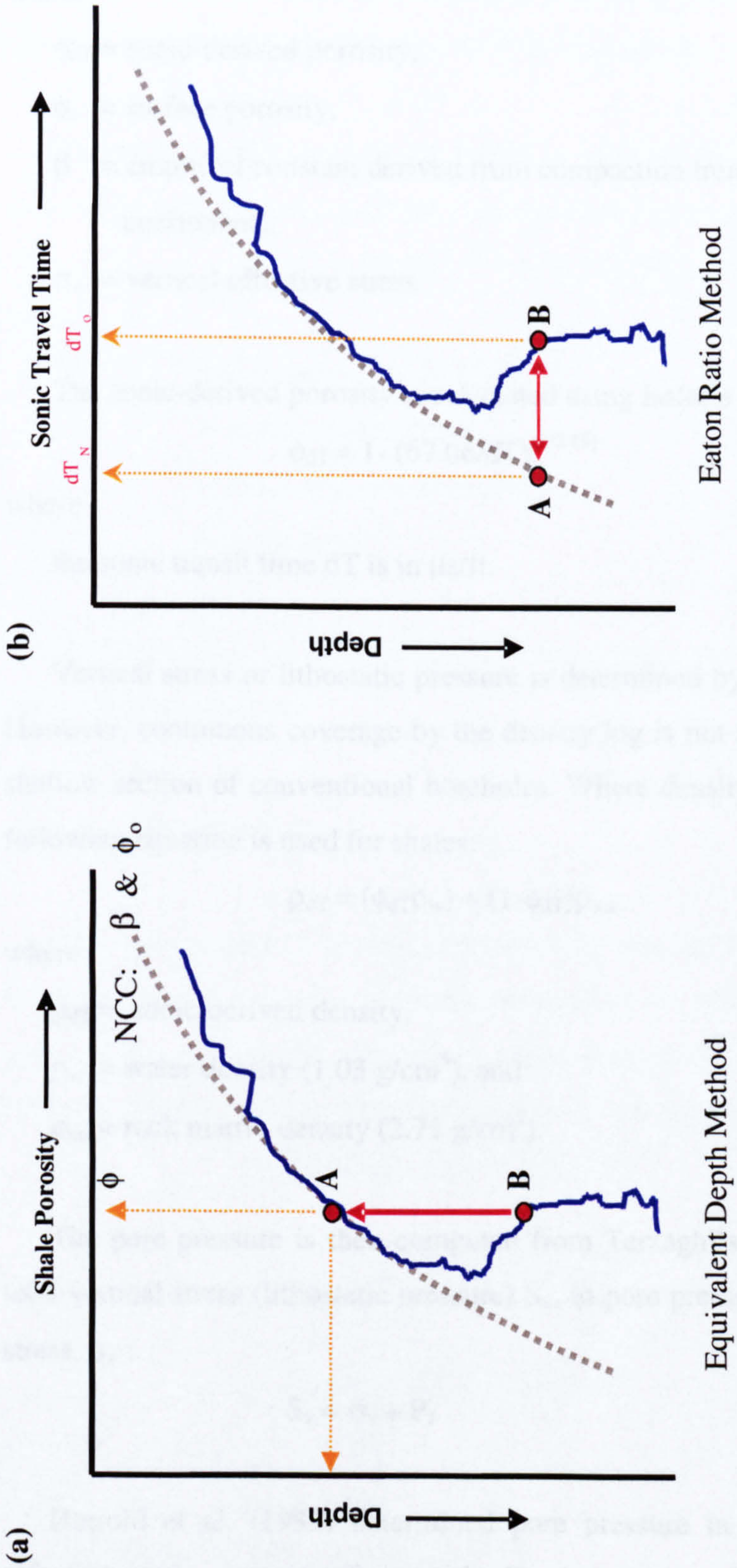


Figure 2.1 Predicting pore pressure from wireline logs: (a) equivalent depth method and (b) Eaton ratio method. In the equivalent depth method it is assumed that vertical projection to the normal compaction curve corresponds to a line of constant porosity and constant effective stress. In the empirical ratio method it is assumed that the ratio of the measured log value (B) to the log value on the normal compaction curve at the same depth (A) is empirically related to the ratio of the vertical effective stress at B and A.

$$\phi_{dT} = \phi_o e^{-\beta\sigma_v} \text{ or } \sigma_v = 1/\beta \ln(\phi_o/\phi_{dT}) \quad (2.3)$$

where

ϕ_{dT} = sonic-derived porosity,

ϕ_o = surface porosity,

β = empirical constant derived from compaction trend (compaction coefficient),

σ_v = vertical effective stress.

The sonic-derived porosity is calculated using Issler's (1992) relation:

$$\phi_{dT} = 1 - (67.06/dT)^{(1/2.19)} \quad (2.4)$$

where

the sonic transit time dT is in μs/ft.

Vertical stress or lithostatic pressure is determined by integrating the density log. However, continuous coverage by the density log is not available, particularly in the shallow section of conventional boreholes. Where density data are not available, the following equation is used for shales:

$$\rho_{dT} = (\phi_{dT}\rho_w) + (1-\phi_{dT})\rho_{ma} \quad (2.5)$$

where

ρ_{dT} = sonic-derived density,

ρ_w = water density (1.03 g/cm^3), and

ρ_{ma} = rock matrix density (2.71 g/cm^3).

The pore pressure is then computed from Terzaghi's law (equation 2.2) relating total vertical stress (lithostatic pressure) S_v, to pore pressure, P_f and vertical effective stress, σ_v :

$$S_v = \sigma_v + P_f \quad (2.6)$$

Harrold et al. (1999) determined pore pressure in the shales from the mean effective stress, instead of vertical effective stress. Mean stress was computed assuming both horizontal stresses are equal. Horizontal stress can be determined either using leak-off data or using an empirical relationship, such as used by Breckels

& van Eekelen (1982) from a Brunei data set. Harrold et al. (1999) used gamma-ray as shale classifier. Results using different shales grouping are discussed in Chapter 2.7.1. In this study, shales are treated as a single group and the averaged log values (for 400 foot depth intervals) were used in the analysis.

The detailed method can be found in Harrold (2000). The method is herein referred to as EDM (mes) method. The equation can be approximated as follows:

$$P_{sh} = 16.6D^{1.145} + 0.5S_v - 0.5P_{hyd} - 1.5\sigma_m \quad (2.7)$$

where

P_{sh} = hydrostatic pressure (MPa)

S_v = vertical stress (MPa),

σ_m = mean effective stress (MPa)

D = depth (km).

In determining the mean effective stress (mes), the two horizontal stresses are assumed to be identical.

2.4.2 Ratio Methods

The ratio method of Eaton (1975) uses the ratio of the observed log reading and the expected log value for normally pressured rock to determine the pore pressure. The method commonly uses sonic transit-time (dT), resistivity (R) and seismic interval velocity (V) data. The equations can be summarized as follows:

$$P_p = P_{OB} - (P_{OB}-P_n)(dT_n/dT)^{EE} \quad (2.8)$$

$$P_p = P_{OB} - (P_{OB}-P_n)(R/R_n)^{EE} \quad (2.9)$$

$$P_p = P_{OB} - (P_{OB}-P_n)(V/V_n)^{EE} \quad (2.10)$$

where

P_p = predicted pore pressure gradient

P_{OB}= overburden gradient

P_n = normal (hydrostatic) pore pressure gradient

dT_n= normal sonic travel time

dT = observed sonic travel time

R_n = resistivity on normal trend

R = observed resistivity

V = velocity on normal trend

Vn = observed velocity

EE = Eaton Exponent (sonic=3; resistivity=1.2; velocity = 3)

2.5 Data and Pre-Processing

A total of 32 Malay Basin wells were analysed for wireline pore pressure prediction analysis.

The data used in this study are:

- Wireline logs, in digital and hardcopy format. The logs consist of calliper, gamma ray, sonic, density, resistivity and neutron. Not all of these logs are available in some of the wells.
- Pressure data from RFT, FIT, mudweights and Leak-Off Pressure.
- Final well drilling reports for general lithology and stratigraphy of each well.

Wireline logs data were provided in two formats: digital ASCII and hardcopy printed-paper. Data from hardcopy are either (1) taken directly from the log for clean shale section only, or (2) digitised prior to pore pressure analysis.

In this study, the sonic log is preferred over density for calculating shale compaction or porosity, because of its availability downhole, because it is more responsive towards overpressure (showing clear reversal signalling top of overpressure) and also because it is less influenced by the borehole conditions. The neutron porosity log tends to overestimate shale porosity because its response is sensitive to clay bound water.

Prior to analysis, the wireline log data were first checked for possible shifts between different logging runs. The vertical distribution of shales is then extracted

from the wireline log using the gamma-ray log as a lithological indicator. The data were screened further using the calliper log to remove those intervals that appeared to be affected by adverse borehole conditions. The resultant sonic data were then processed by application of a "moving average filter", applying a smoothing interval of 400 ft (120 m). A moving average filter helps to reduce noise and uncertainty in due to data scattering within the logs (Figure 2.2).

2.6 Pore Pressure Prediction Results

Predicted pore pressures in several Malay Basin wells are summarised in this chapter. The variations in the results arise from different methods and other external factors are discussed in Chapter 2.7 below. Results from three methods (EDM (mes); EDM (ves); Eaton method (using sonic)) are discussed.

For confidentiality, the well names are coded. The identity of each well and the unpublished well reports may be obtained directly from PETRONAS. All well reports used in this study will only be referenced as unpublished reports and are not listed in the references.

For the purposes of discussion and result presentation, the wells are grouped into six main areas following grouping by Fatt (1999). These areas are based on their play types and geographical locations. The groups are North Malay (NM), West Malay (WM), East Malay (EM), Central Malay (CM), Southeast Malay (SE) and South Malay (SM) (Figure 2.3).

Wireline log signatures for the upper Miocene-Pliocene shallow interval (post-unconformity) are found to be different from the remaining section down well. Example, in well NM-1, it is impossible to get a single normal compaction curve to fits shales below and above the unconformity (see Figure 2.4). The upper Miocene-Pliocene (Group A/B) appears to have a long transit-time, corresponding to high porosities. This may suggest that these Group A/B sediments are less consolidated. Other possibilities that may also contribute to these contrasting log signatures are (1) lithological variation between the non-marine shales (pre-unconformity sediments)

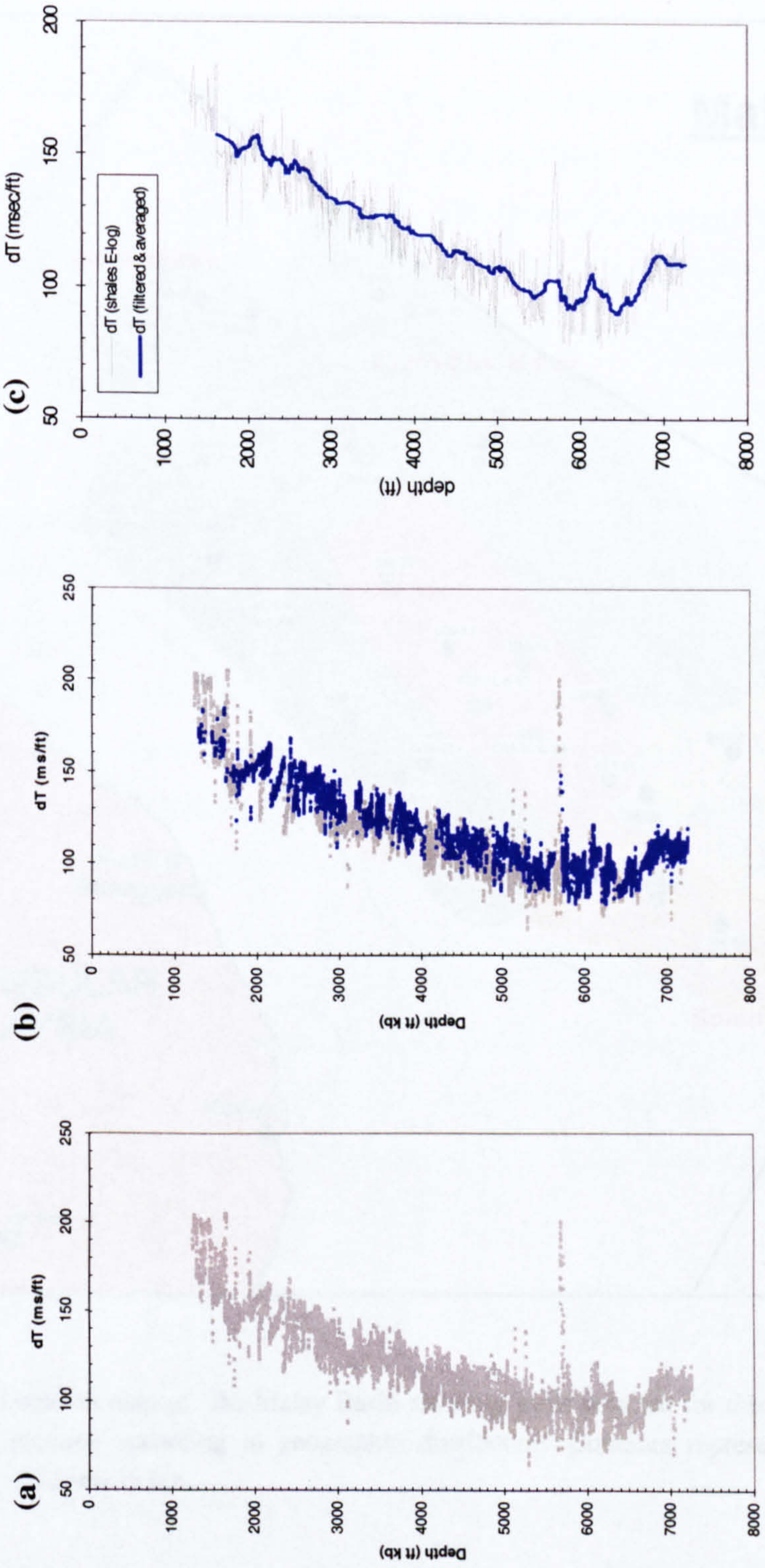


Figure 2.2 Data pre-processing prior to pore pressure analysis: (a) raw sonic dataset, (b) selecting shale using gamma-ray filter, after removal of bad data points, (c) smoothing the data using moving average of 400 ft (120 m) interval.

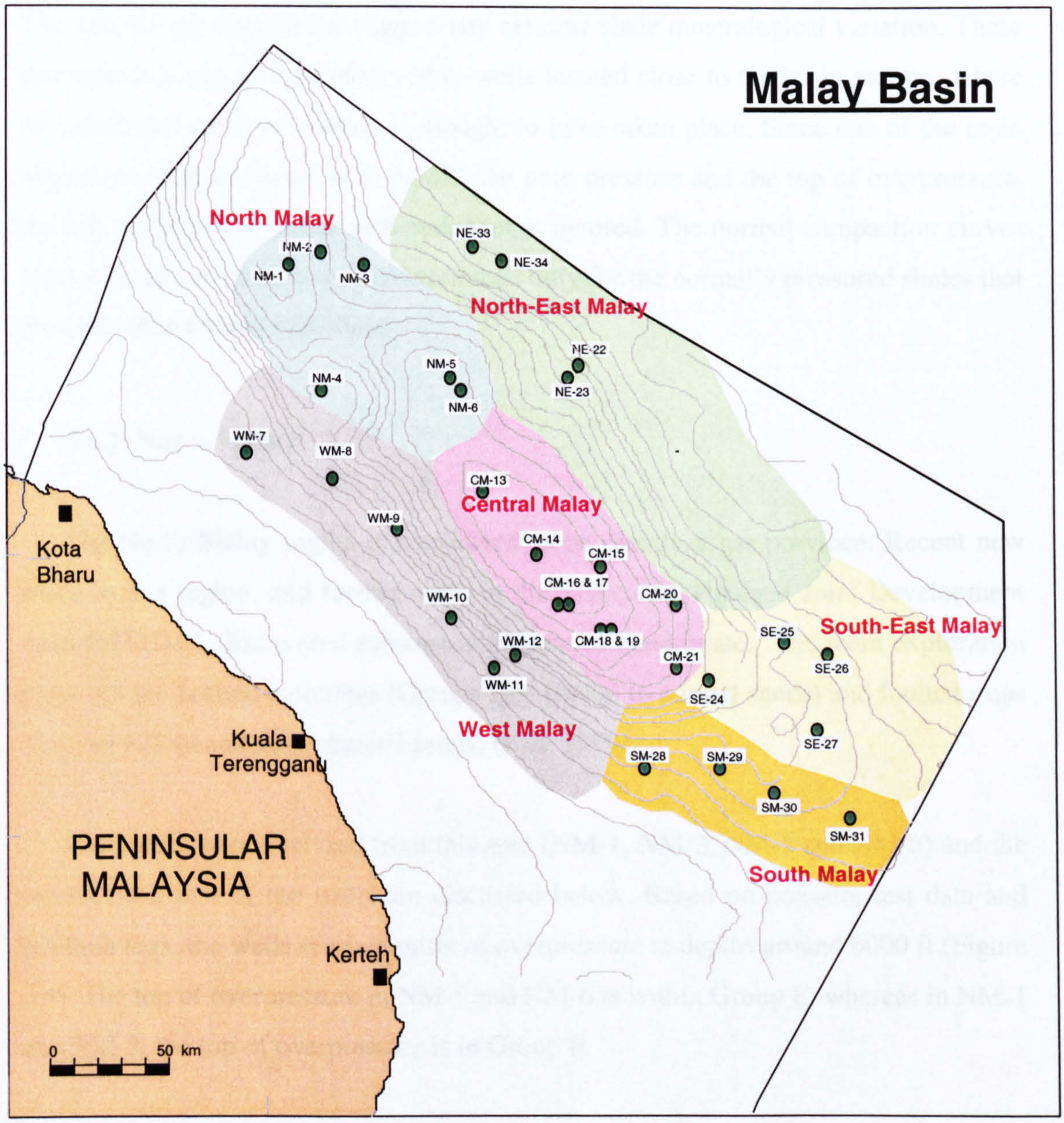


Figure 2.3 Location map of the Malay Basin showing wells selected for this study. The wells are grouped according to geographic distribution. Contours represent Tertiary sediment thickness in km.

and full marine shales of Group A/B, (2) overcompaction of Oligocene-middle Miocene shales that were more deeply buried prior to erosion down to the unconformity surface. The exact causes has not been investigated during this study. The gamma-ray logs do not suggest any extreme shale mineralogical variation. These discrepancies can also be observed in wells located close to the basin margin, where no significant uplift or erosion is thought to have taken place. Since one of the main objectives of this chapter is to predict the pore pressure and the top of overpressure, the log variation for Group A/B sediment is ignored. The normal compaction curves for pore pressure prediction are determined only for the normally pressured shales that are older than Group A/B shales.

2.6.1 North Malay

The North Malay region is considered to be mainly a gas province. Recent new wells in this region, and further north in the Malaysian-Thailand Joint Development Area (MTJDA), discovered substantial amount of condensate. The main exploration plays are the faulted anticlines (Groups D/E fluvial to coastal sands) and faulted traps (Groups H/I meandering channel sands) (Fatt, 1999).

Four wells were analysed from this area (NM-1, NM-3, NM-5 and NM-6) and the results from two of the wells are discussed below. Based on pressure test data and wireline logs, the wells reached onset of overpressure at depths around 6000 ft (Figure 2.4). The top of overpressure in NM-5 and NM-6 is within Group E, whereas in NM-1 and NM-3, the top of overpressure is in Group F.

Groups A and B consist predominantly of claystones with stringers of sandstones. Group D is made up of interbeds of claystones, sandstones and minor coals. Higher amounts of coals are found in the underlying Group E, in addition to the interbedded shales and sandstones. Group F is made up of thick shale sequence with minor sandstone and coaly intervals. Thickening of the Group F sequence is observed towards the north. The Group H sequence penetrated in wells NM-1 and NM-3 consists of thick shales at the top and more sandy and coaly beds towards the base. In these wells, the strong deflection of the sonic log from the normal trend indicates

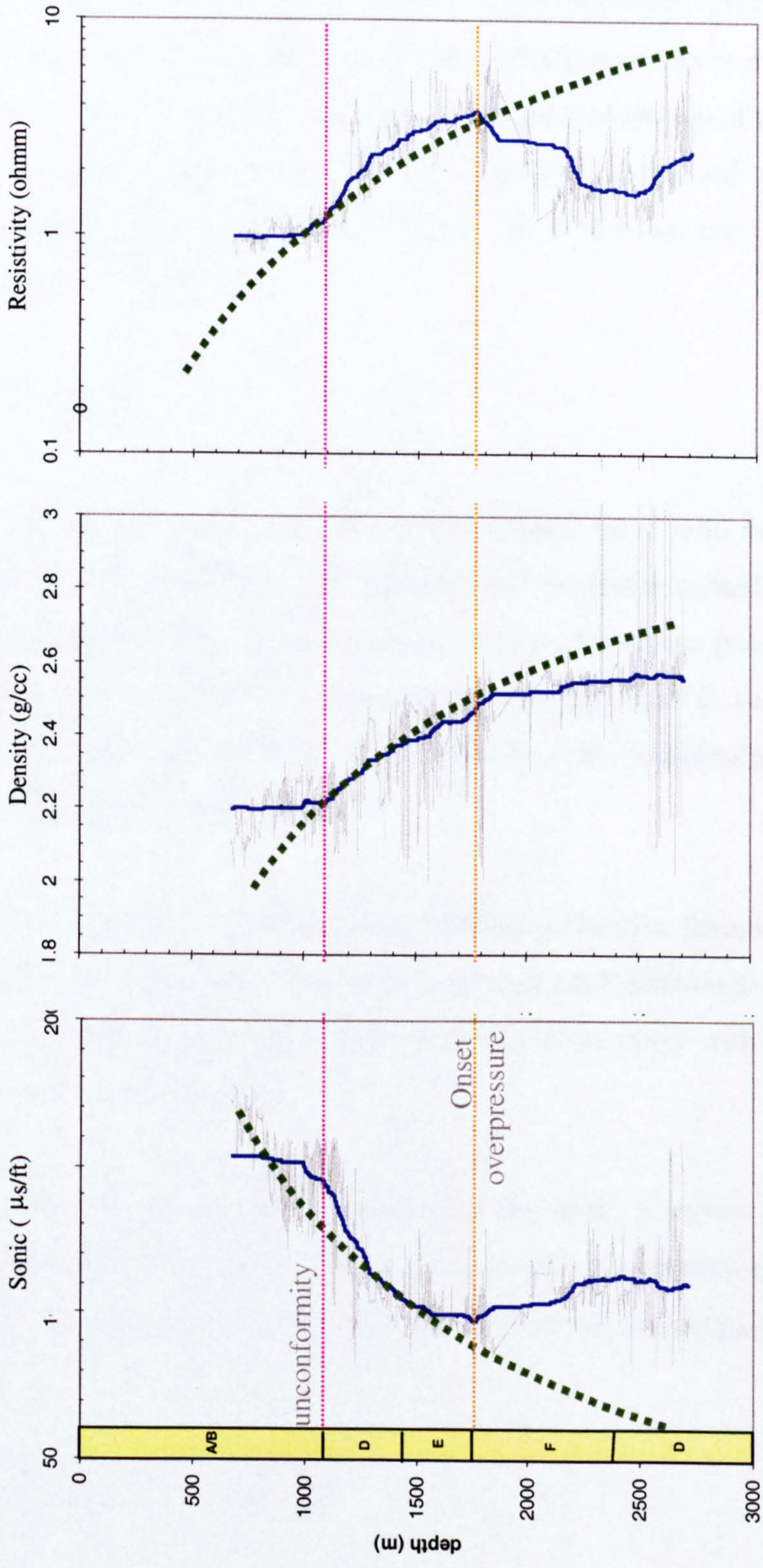


Figure 2.4 Wireline logs from well NM-1 showing departure from normal compaction trend indicating top of overpressure.

undercompacted shales, and correspond to the top of overpressure.

Deflection of the sonic log in the two northern wells (NM-1 and NM-3) occurs at the onset of overpressure (estimated from formation pressure), while in the two southern wells (NM-5 and NM-6), the deflection occurs at much shallower depth. As a result, all three methods provide a better pick of the top of the overpressure for NM-1 and NM-3. Assuming sonic log deflection correspond to overpressure, then the pore pressures in the shales in NM-5 and NM-6 are not in equilibrium with pore pressures in the sands.

2.6.1.1 NM-1

The well report from this well mentioned good hole condition from the top to 6152 feet, below which hole rugosity and mudcake caused deterioration in density logs. High mudweight was necessary due to high pore pressure encountered below 6000 ft. Mudweight was increased to 17.4 ppg at 9016 ft, because of loss of returrns. Drilling was terminated as the drillers had no confidence in achieving full mud circulation beyond that depth.

The well report indicated development of ferroan dolomite below 8000 ft depth, which was suggested to be a product of a clay dehydration process. Also reported was an increased illite:smectite ratio in mixed layer clays with depth. The detail XRD results are not available.

Pore pressure prediction results for this well is shown in Figure 2.5. Predicted pore pressure from EDM (mes) matched with the formation, whereas the other two methods underpredicted the pore pressure at the deeper part of the well (8000 ft to TD).

2.6.1.2 NM-3

Well NM-3 was drilled on a fault bounded structure. The well was drilled using mudweight of 9 to 10 ppg until 7126 ft. At 7126 ft, well experienced a kick with an

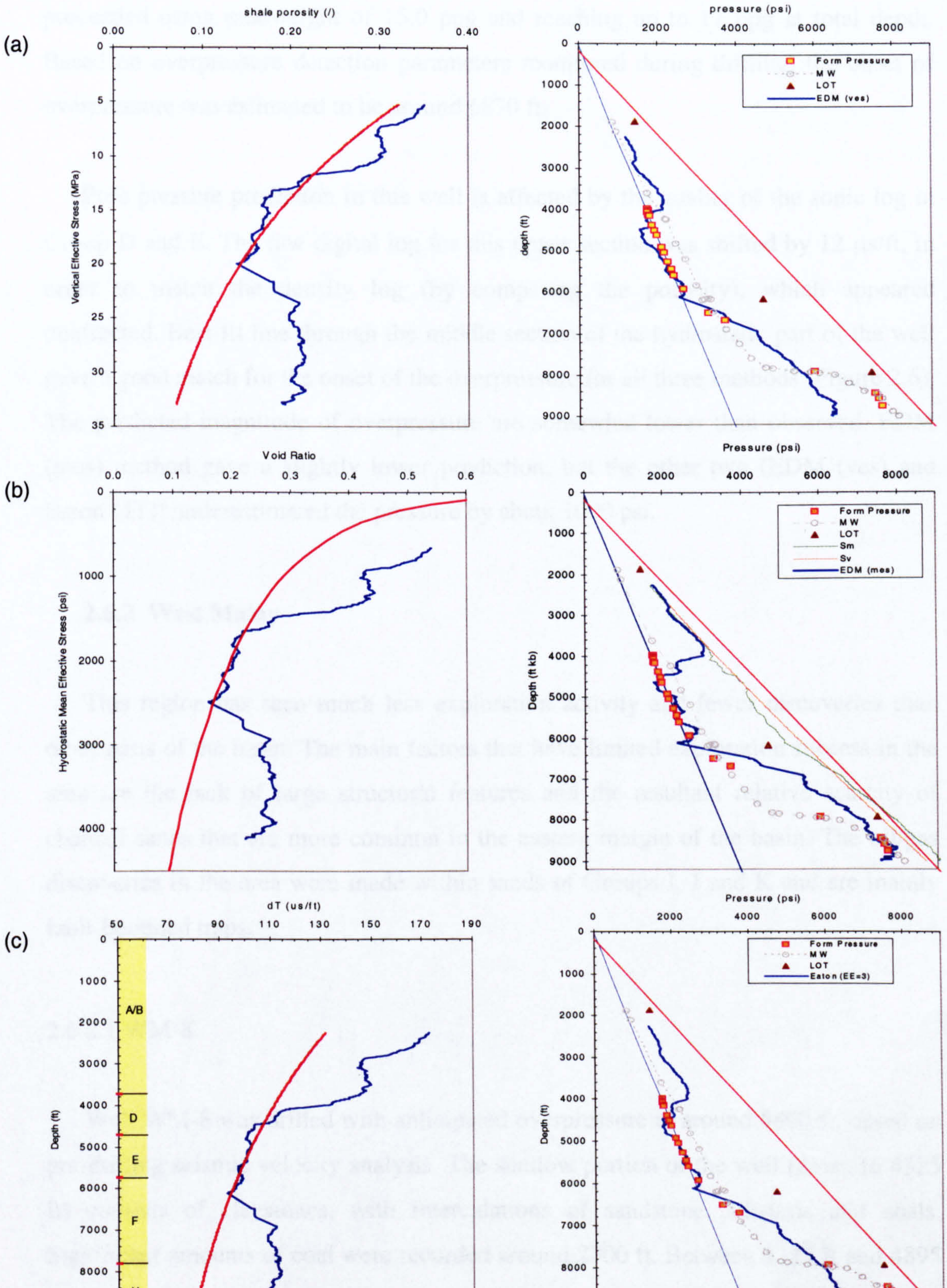


Figure 2.5 Pore pressure analysis results for NM-1. (a) Equivalent depth method using mean effective stress, EDM (mes), (b) Equivalent depth method using vertical effective stress, EDM (ves), (c) Eaton method (EM).

estimated pressure of 1900 psi and was killed with 14.5 ppg mud. Drilling then proceeded using mudweight of 15.0 ppg and reaching up to 17 ppg at total depth. Based on overpressure detection parameters monitored during drilling, the onset of overpressure was estimated to be around 6870 ft.

Pore pressure prediction in this well is affected by the quality of the sonic log in Group D and E. The raw digital log for this upper section was shifted by 12 μs/ft, in order to match the density log (by comparing the porosity), which appeared unaffected. Best-fit line through the middle section of the hydrostatic part of the well gave a good match for the onset of the overpressure for all three methods (Figure 2.6). The predicted magnitude of overpressure are somewhat lower than observed. EDM (mes) method gave a slightly lower prediction, but the other two (EDM (ves) and Eaton (dT)) underestimated the pressure by about 1000 psi.

2.6.2 West Malay

This region has seen much less exploration activity and fewer discoveries than other parts of the basin. The main factors that have limited exploration success in the area are the lack of large structural features and the resultant relative scarcity of channel sands that are more common in the eastern margin of the basin. The oil/gas discoveries in the area were made within sands of Groups I, J and K and are mainly fault-bounded traps.

2.6.2.1 WM-8

Well WM-8 was drilled with anticipated overpressure at around 5800 ft, based on pre-drilling seismic velocity analysis. The shallow portion of the well (down to 4325 ft) consists of claystones, with intercalations of sandstone, siltstone and coals. Significant amounts of coal were recorded around 2900 ft. Between 4325 ft and 4895 ft, interbedded claystones and siltstones with coals seams and minor dolomitic stringers make up the lithology. Below 4895 ft, the lithology mainly consists of claystones with local interbeds of siltstone, sandstone and coal stringers.

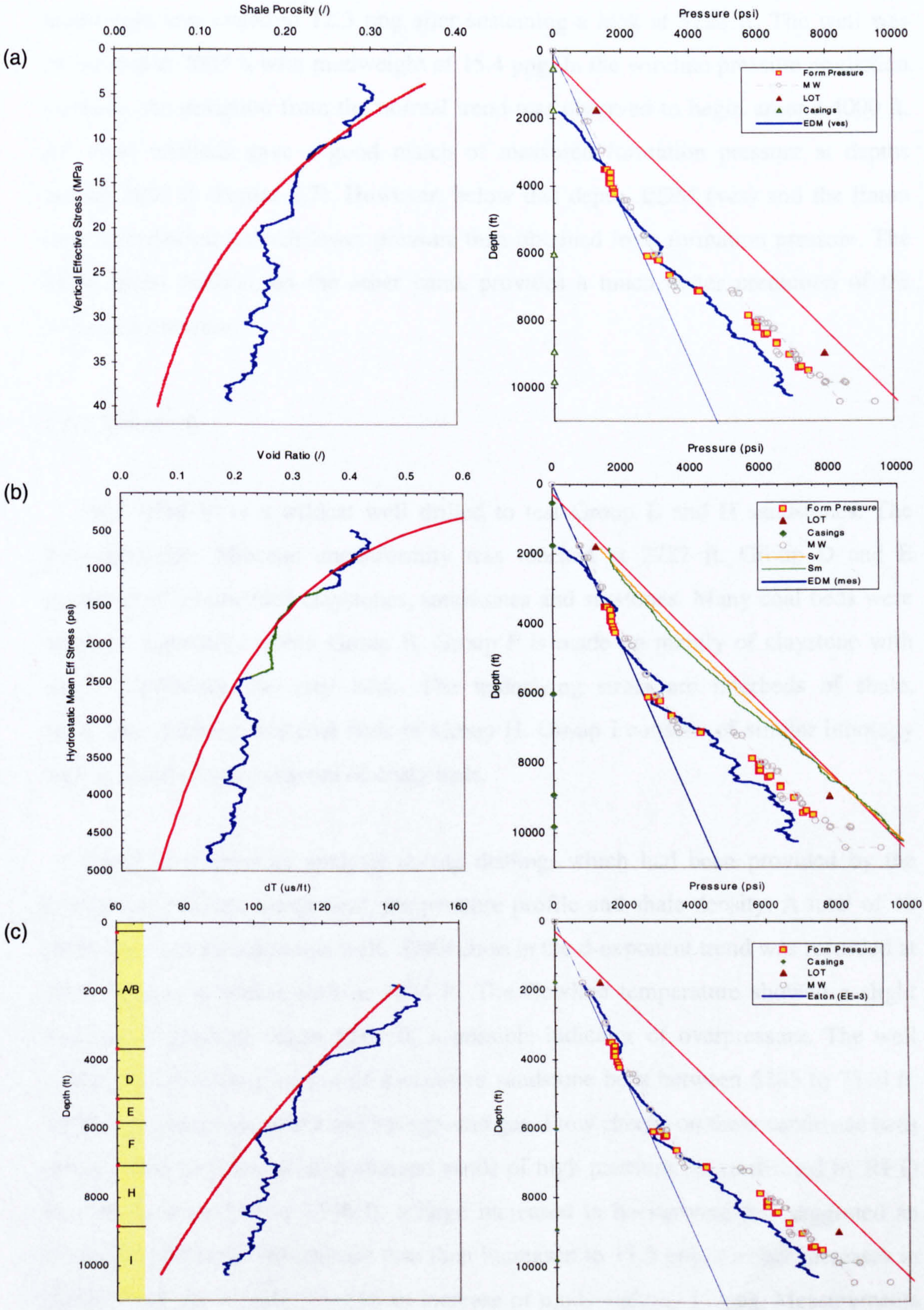


Figure 2.6 Pore pressure analysis results for NM-3. (a) EDM (mes), (b) EDM (ves), (c) EM.

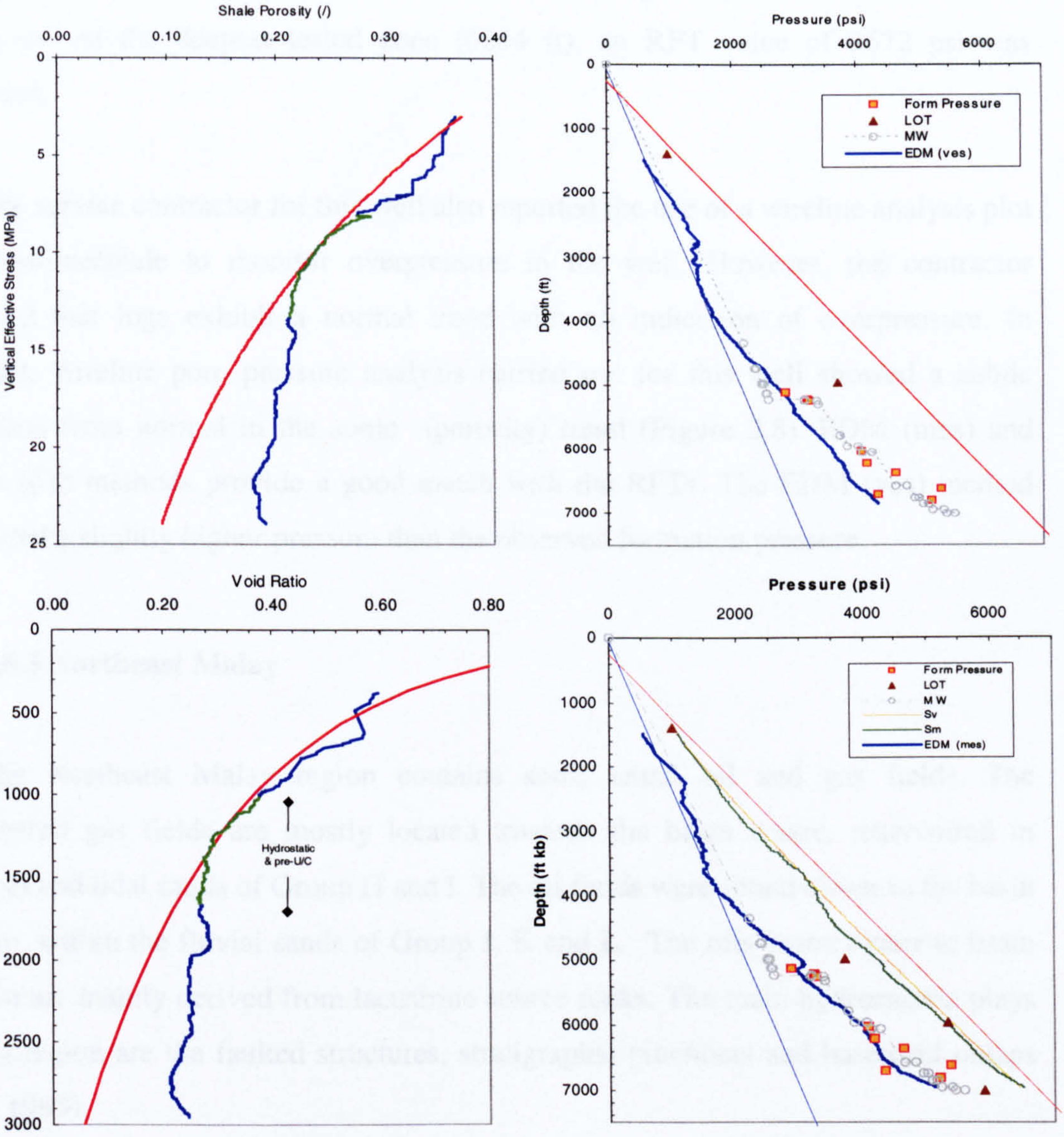
The well was drilled with a mudweight of 9.0 ppg from 1420 ft and subsequent mudweight was raised to 12.3 ppg after sustaining a kick at 5228 ft. The well was terminated at 7003 ft with mudweight of 15.4 ppg. In the wireline pressure prediction methods, the deviation from the normal trend was observed to begin around 4000 ft. All three methods gave a good match of measured formation pressure at depths around 5000 ft (Figure 2.7). However, below this depth, EDM (ves) and the Eaton method predicted a much lower pressure than obtained from formation pressure. The EDM (mes) method, on the other hand, provides a much better prediction of the formation pressure.

2.6.2.2 WM-10

Well WM-10 is a wildcat well drilled to test Group E and H sandstones. The Pliocene/Upper Miocene unconformity was reached at 2727 ft. Group D and E consisted of interbedded claystones, sandstones and siltstones. Many coal beds were reported, especially within Group E. Group F is made up mainly of claystone with minor sandstones and coal beds. The underlying strata are interbeds of shale, sandstone, siltstone and coal beds of Group H. Group I consists of similar lithology with a slightly higher amount of coaly beds.

Continuous pressure analysis during drilling, which had been provided by the contractor, includes d-exponent, temperature profile and shale density. A total of 40 RFTs were attempted in this well. Deflection in the d-exponent trend was recorded at 7546 ft, with a further shift at 7874 ft. The flowline temperature showed a slight increase in gradient below 6562 ft, a possible indicator of overpressure. The well report indicated the presence of successive sandstone beds between 6185 to 7546 ft, which gave large gas peaks and background gas. Flow checks on these sandstone beds showed that they are isolated charged sands of high pressure (as confirmed by RFT) but low volume. Below 7546 ft, a large increased in background gas suggested an overpressured zone. Mudweight was then increased to 11.5 ppg. Further increases in background gas at 7841 ft led to an increase of mudweight to 12 ppg. Measurements of shale cuttings showed a slight decrease in density around 7382 to 7792 ft, suggesting an overpressured zone. RFT measurements showed a normally pressured

(a)



(b)

(c)

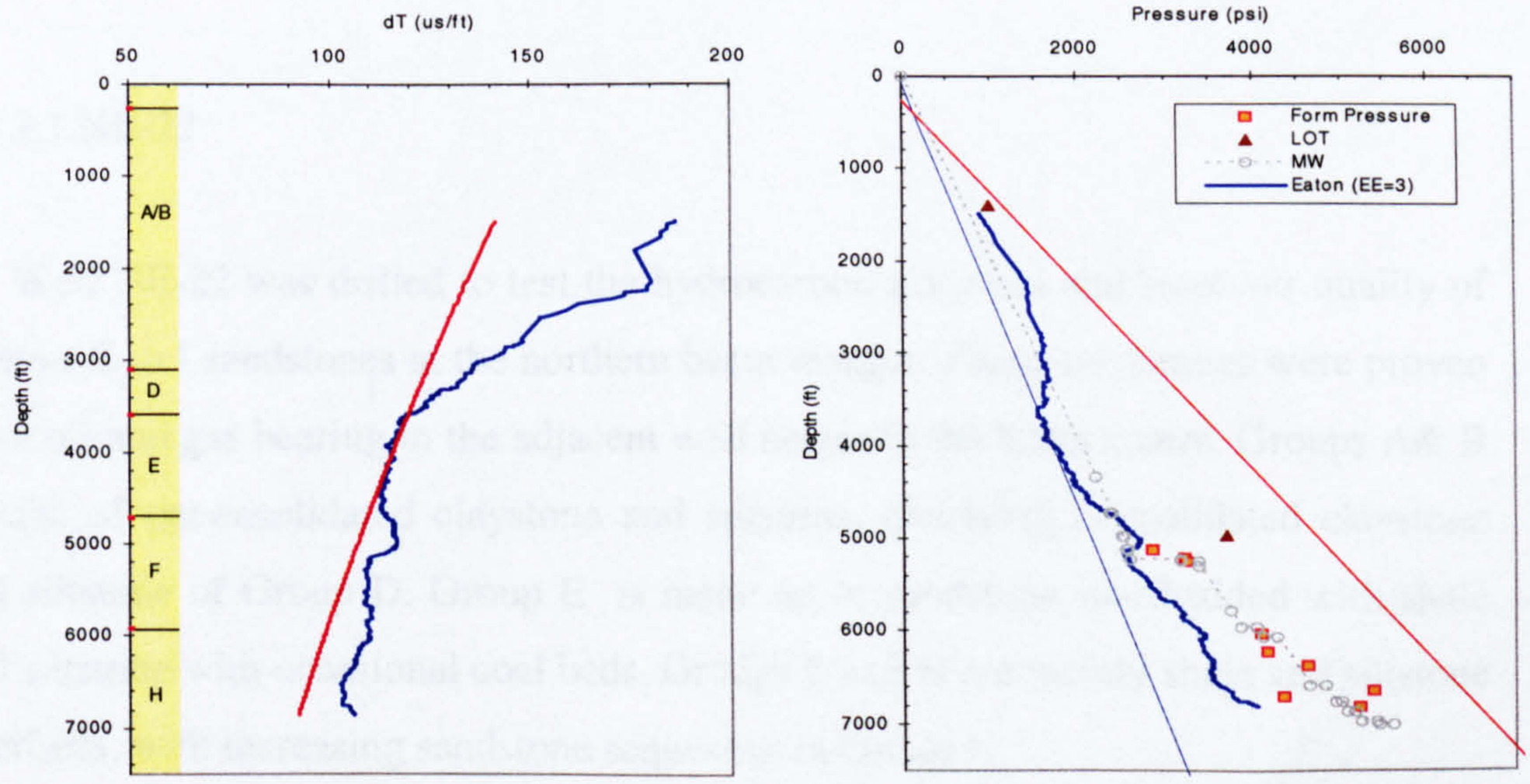


Figure 2.7 Pore pressure analysis results for WM-8. (a) EDM (mes), (b) EDM (ves), (c) EM.

sequence down to 6178 ft. Below 6178 ft, RFT readings indicate above than normal pressures. At the deepest tested zone (6834 ft), an RFT value of 3672 psi was recorded.

The service contractor for this well also reported the use of a wireline analysis plot of claystone/shale to monitor overpressure in the well. However, the contractor reported that logs exhibit a normal trend with no indication of overpressure. In contrast, wireline pore pressure analysis carried out for this well showed a subtle deviation from normal in the sonic (porosity) trend (Figure 2.8). EDM (mes) and Eaton (dT) methods provide a good match with the RFTs. The EDM (ves) method predicted a slightly higher pressure than the observed formation pressure.

2.6.3 Northeast Malay

The Northeast Malay region contains some small oil and gas fields. The discovered gas fields are mostly located towards the basin centre, reservoired in channel and tidal sands of Group H and I. The oil fields were found closer to the basin margin, within the fluvial sands of Group J, K and L. The oils found closer to basin margin are mainly derived from lacustrine source rocks. The main hydrocarbon plays in this region are the faulted structures, stratigraphic pinchouts and basement onlaps (Fatt, 1999).

2.6.3.1 NE-22

Well NE-22 was drilled to test the hydrocarbon potential and reservoir quality of Groups E to I sandstones at the northern basin margin. These sandstones were proven to be oil and gas bearing in the adjacent well nearer to the basin centre. Groups A& B consist of unconsolidated claystone and siltstone, overlying consolidated claystone and siltstone of Group D. Group E is made up of sandstone interbedded with shale and siltstone with occasional coal beds. Groups F and H are mainly shale and siltstone interbeds, with increasing sandstone sequences in Group I.

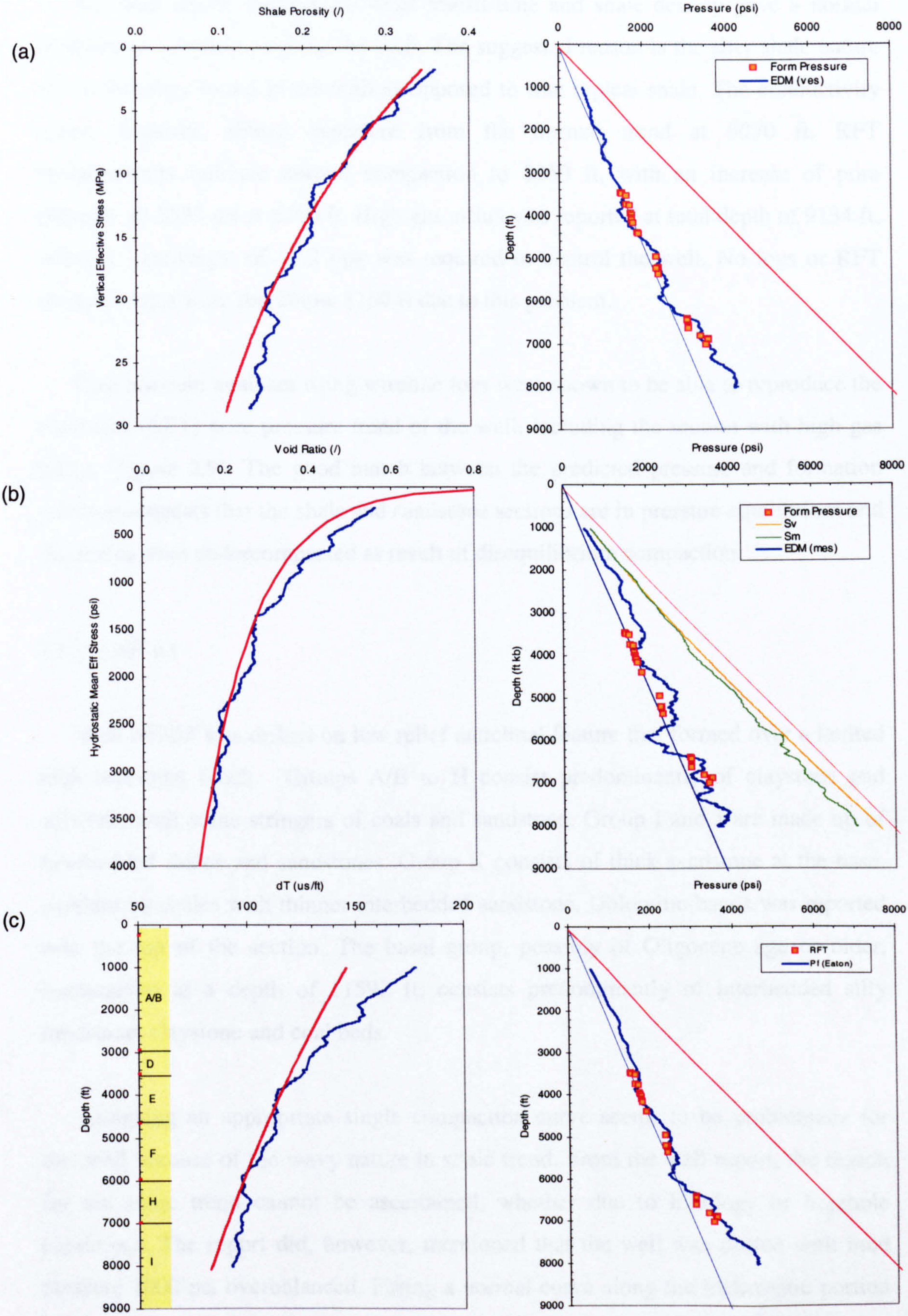


Figure 2.8 Pore pressure analysis results for WM-10. (a) EDM (mes), (b) EDM (ves), (c) EM.

The well report showed the sonic transit-time and shale density gave a normal compaction trend throughout the well. The suggested reason is the silty shale nature of the lithology found in the well as opposed to true typical shale. The conductivity curve, however, shows departure from the normal trend at 6070 ft. RFT measurements indicate normal compaction to 5250 ft, with an increase of pore pressure to 3553 psi at 6400 ft. High gas influx was reported at total depth of 9134 ft, where a mudweight of 15.2 ppg was required to control the well. No logs or RFT measurements were run below 8760 ft due to this problem.

Pore pressure analyses using wireline logs were shown to be able to reproduce the measured (RFT) pore pressure trend of the well, including the section with high gas influx (Figure 2.9). The good match between the predicted pressure and formation pressure suggests that the shale and sandstone sections are in pressure equilibrium and the shales were undercompacted as result of disequilibrium compaction.

2.6.3.2 NE-33

Well NE-33 was drilled on low relief anticlinal feature that formed over a faulted high basement block. Groups A/B to H consist predominantly of claystone and siltstone, with some stringers of coals and sandstone. Group I and J are made up of interbedded shales and sandstones. Group K consists of thick sandstone at the base, overlain by shales with thinner interbedded sandstone. Dolomitic bands was reported near the top of the section. The basal group, possibly of Oligocene age or older, encountered at a depth of 11592 ft, consists predominantly of interbedded silty sandstone, claystone and coal beds.

Assigning an appropriate single compaction curve seems to be problematic for this well because of the wavy nature in sonic trend. From the well report, the reason for the sonic trend cannot be ascertained, whether due to lithology or borehole conditions. The report did, however, mentioned that the well was drilled with mud pressure 1000 psi overbalanced. Fitting a normal curve along the hydrostatic portion of the shale below the unconformity (Top D) gave a much higher predicted pore pressure at total depth in all the three methods (Figure 2.10). Several overpressured

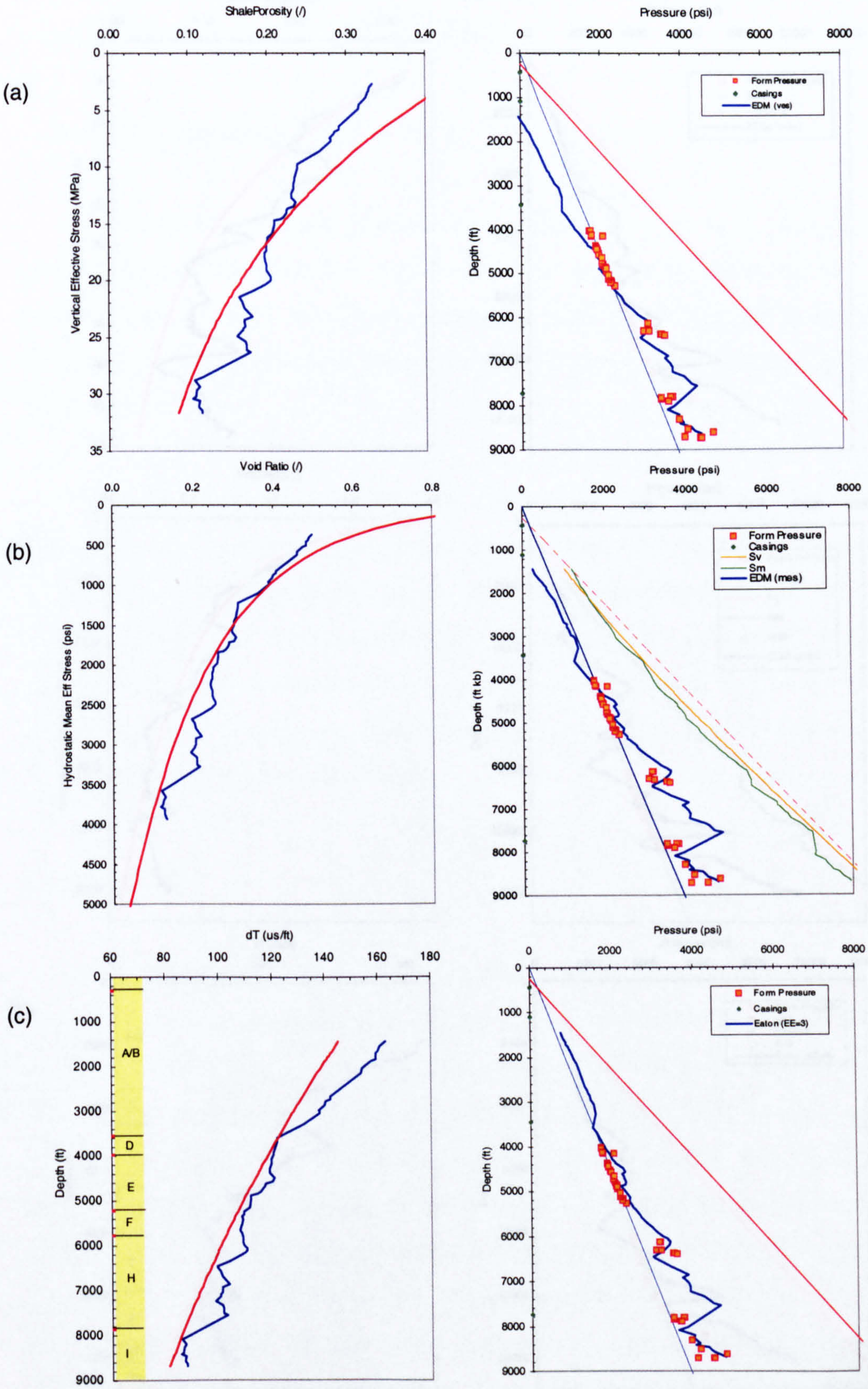


Figure 2.9 Pore pressure analysis results for NE-22. (a) EDM (mes), (b) EDM (ves), (c) EM.

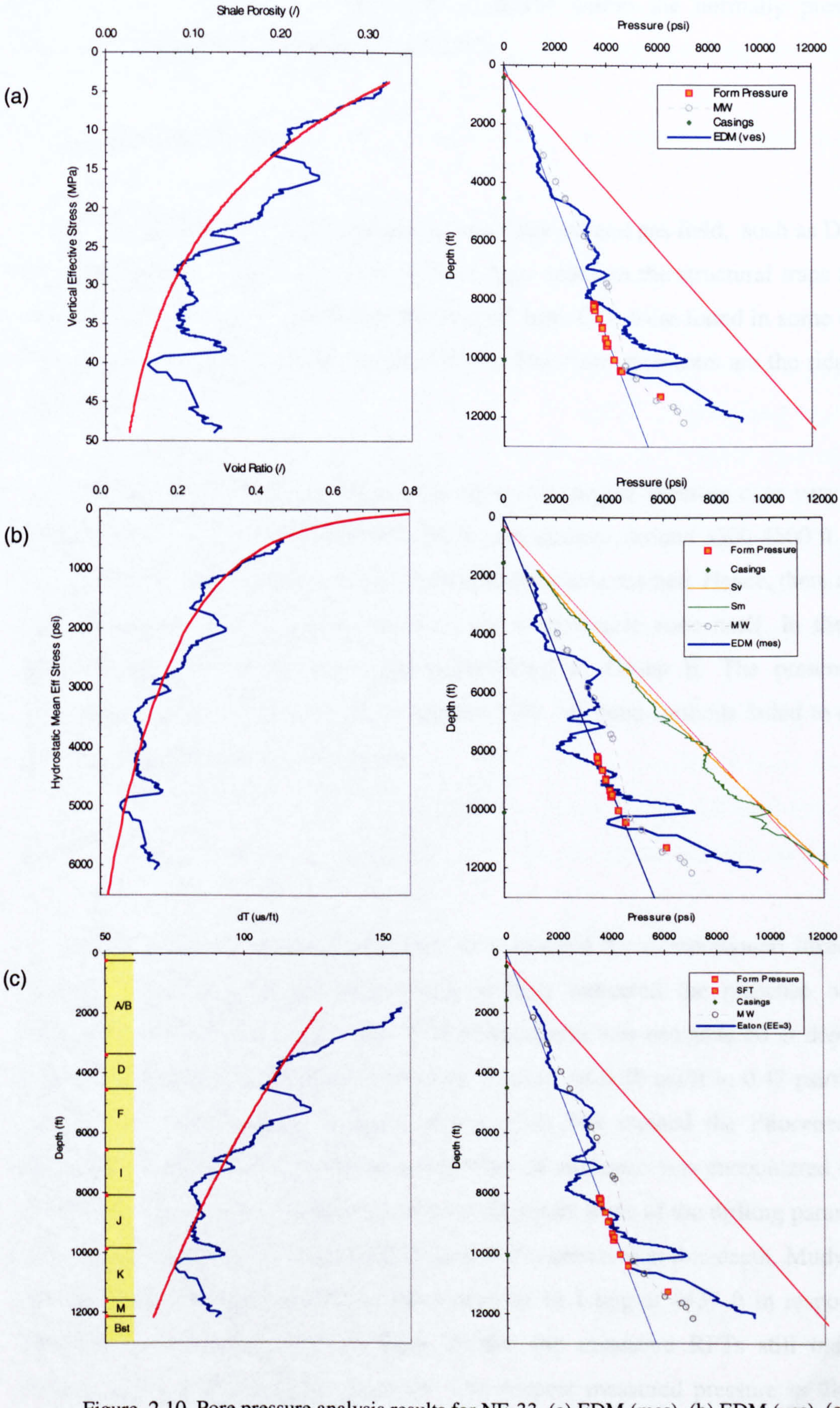


Figure 2.10 Pore pressure analysis results for NE-33. (a) EDM (mes), (b) EDM (ves), (c) EM.

and underpressured sections were also predicted within the normally pressured sequence determined from the RFTs and SFTs.

2.6.4 Central Malay

The Central Malay region contains several large oil and gas field, such as Dulang and Semangkok. The main discoveries have been made in the structural traps found within Groups E and H. Significant amounts of high CO_2 were found in some of the fields making it less economic for production. The main reservoirs are the tidal and fluvial sands.

The main problem in this area is the rapid rise in pore pressure over very short depth intervals. The onset of overpressure is very shallow, around 3500-4500 ft. Most wells were terminated as soon as top of overpressure was reached. Hence, there are no pressure profiles that extend deeper into the overpressure zone itself. In the four studied wells, the overpressure was encountered in Group E. The presence of overpressure was not apparent from wireline logs. All three methods failed to detect the onset of overpressure in the wells.

2.6.4.1 CM-16

Well CM-16 was terminated as soon as it reached the overpressured formation. Pressure detection methods used during drilling indicated the presence of two overpressured intervals in the well. Mild overpressure was encountered at depths of 3100 to 3900 ft with an estimated pressure gradient of 0.46 psi/ft to 0.47 psi/ft. The contractor reported this as a result of the uplift that created the Pliocene/upper Miocene unconformity. The deeper overpressured sequence was encountered below 4600 ft. According to the contractor in the well report, none of the drilling parameters other than gas analysis provided indications of overpressure at this depth. Mudweight was raised to 10.6 ppg at 4264 ft and further to 11.1 ppg at 4437 ft in response to increase in background gas. At these depths, the measured RFTs still indicated normally pressured sandstone intervals. The deepest measured pressure in the well was 2310 psi at depth of 4745 ft.

All the three wireline pore pressure prediction methods used for this well show a very subtle change in pore pressure (Figure 2.11). The onset of a deep overpressured sequence close to total depth is not apparent in any of the three methods. This suggests the pore pressure in the sandstone has recently been inflated and is much higher than in the overlying shale.

2.6.4.2 CM-17

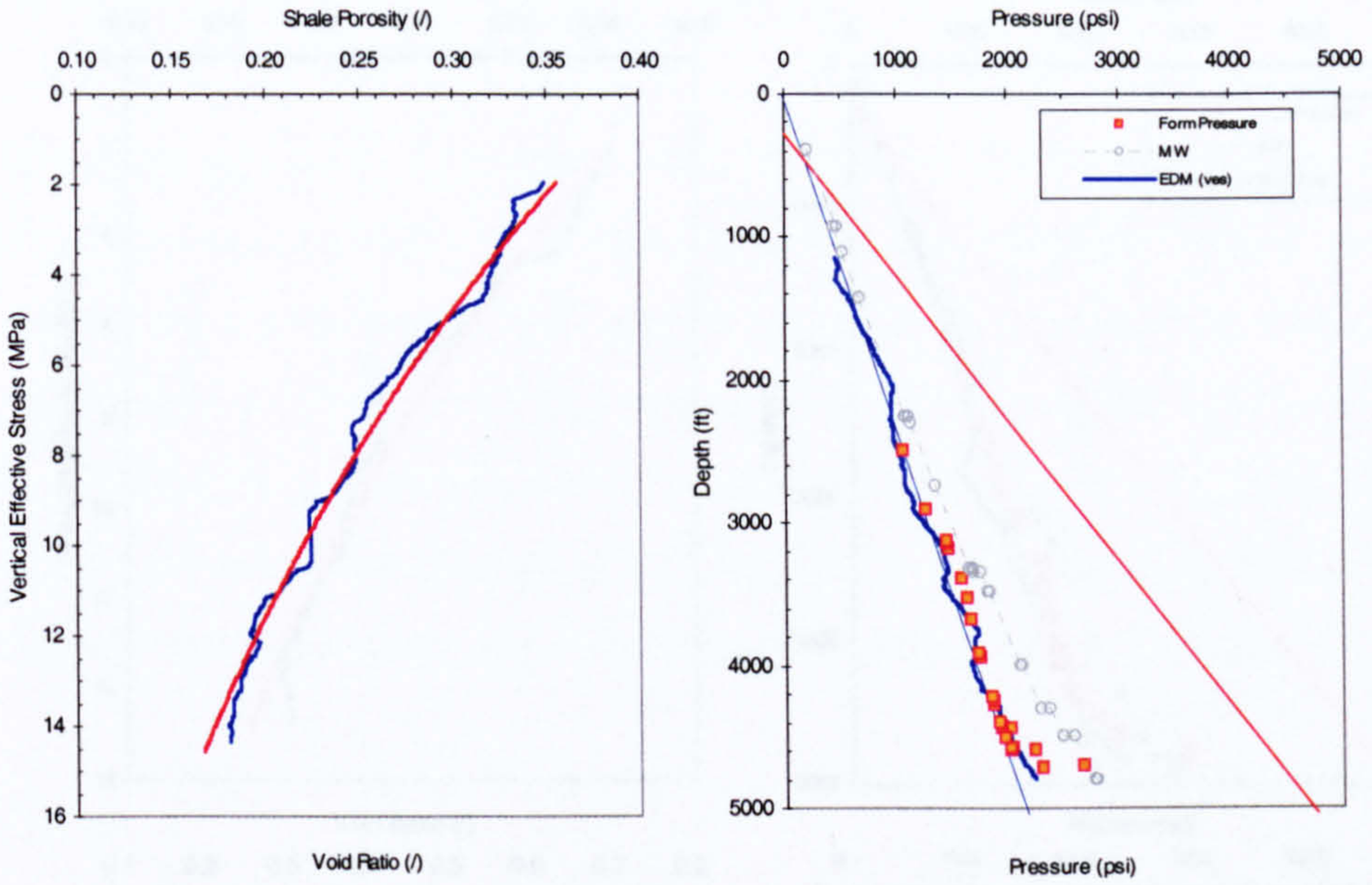
Well CM-17 was drilled close to CM-16 on the same structure. The lithology and pore pressure profile are very similar to CM-16. Two similar overpressured sequences were penetrated. The shallower overpressured section was in the depth interval 3175 to 3290 ft. The deeper overpressured section was penetrated at a depth of 4450 ft, where the mudweight was raised to 10.2 ppg, following an increase in gas readings. Closer to total depth, the mudweight was increased further to 13 ppg after the RFT measurements indicated the well was being drilled slightly underbalanced. The well was terminated prior to reaching the Group F at 4896 ft.

All three wireline pressure prediction methods gave similar results to those predicted for CM-16 (Figure 2.12). The predicted pore pressures for the shales within the overpressured section are much lower than the pore pressure in the sandstone as determined from the RFT.

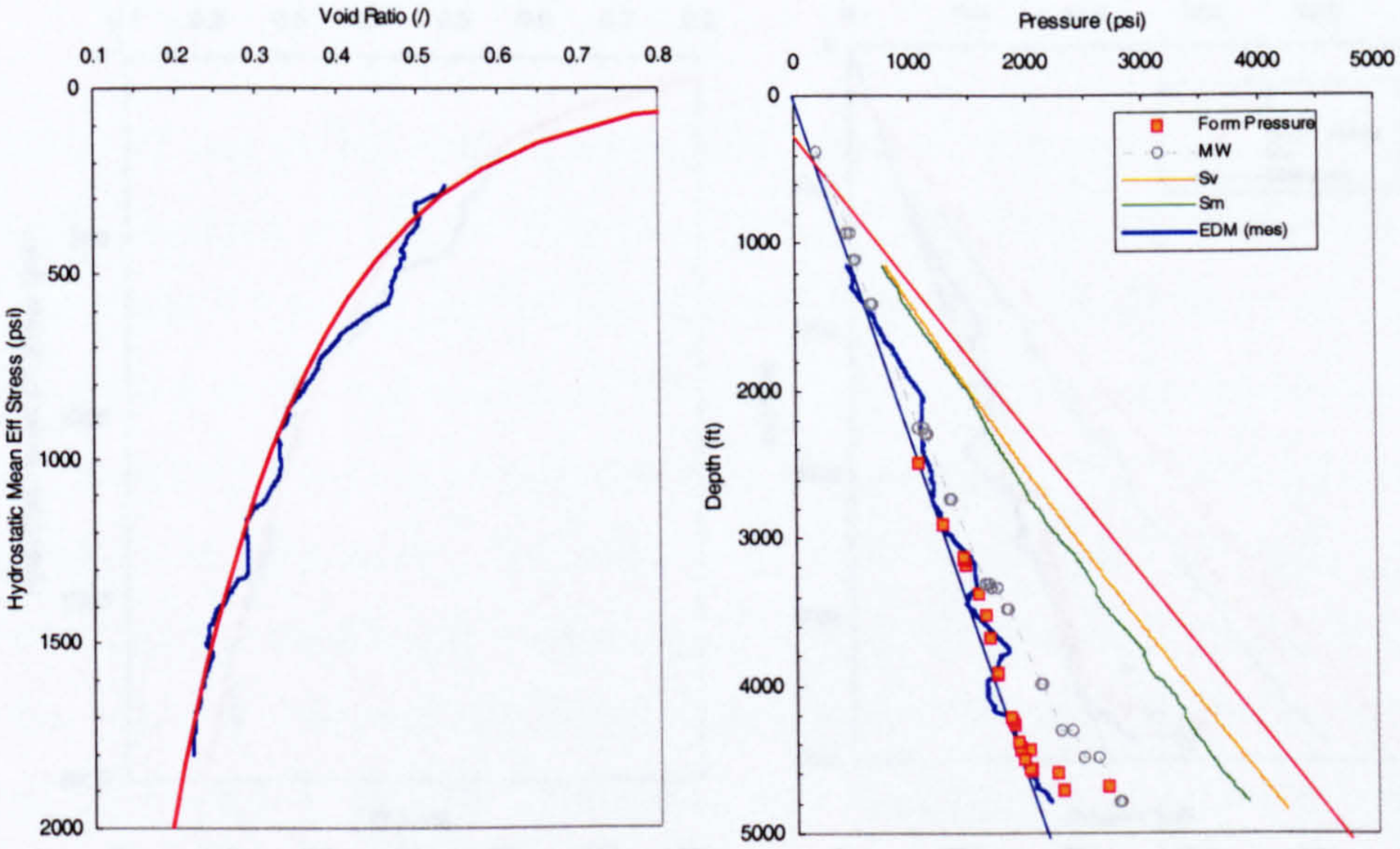
2.6.5 Southeast Malay

The Southeast Malay region is considered the most prolific part of the Malay Basin for oil production. Several large oil fields (>200 MMSTB) have been discovered, such as Guntong, Seligi and Tapis (Fatt, 1999). The main reservoirs are the Group J and K sands (EPIC, 1994). These large oil accumulations are the results of two main factors: (1) optimum burial depths of the Oligocene-Lower Miocene lacustrine shales for oil generation; and (2) the existence of large compressional anticlines containing fluvial-braided sand reservoirs.

(a)



(b)



(c)

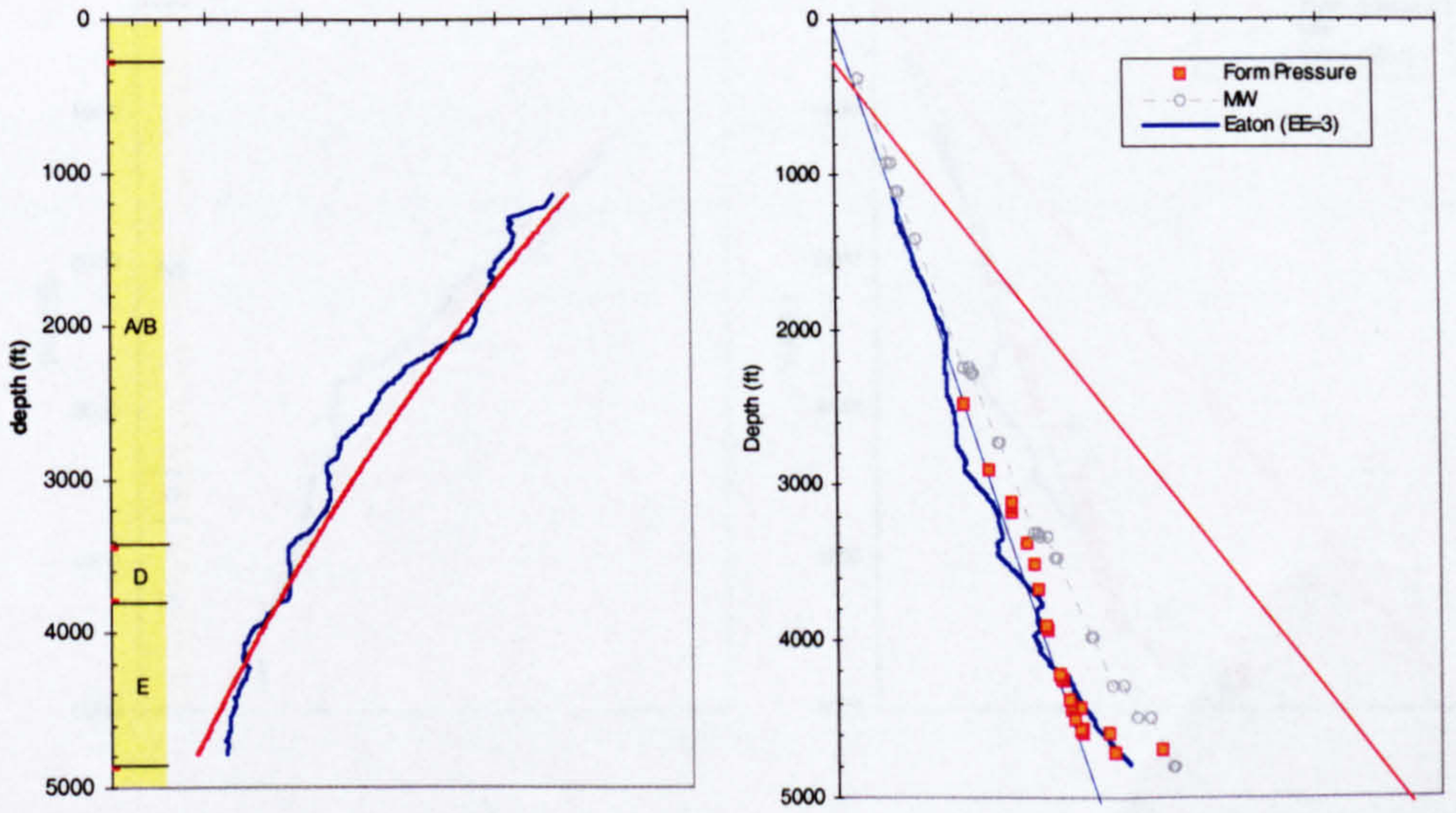


Figure 2.11 Pore pressure analysis results for CM-16. (a) EDM (mes), (b) EDM (ves), (c) EM.

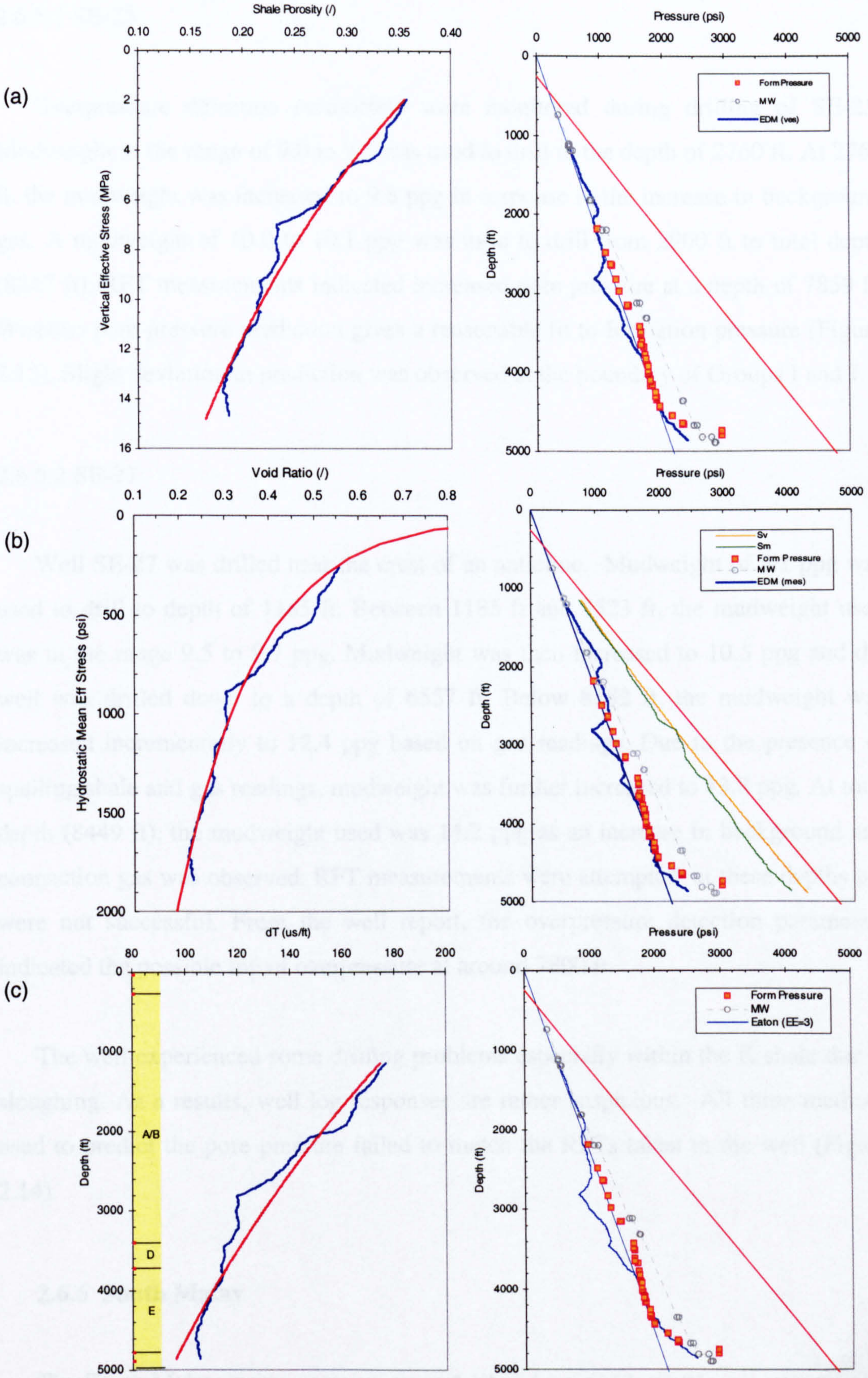


Figure 2.12 Pore pressure analysis results for CM-17. (a) EDM (mes), (b) EDM (ves), (c) EM.

2.6.5.1 SE-25

Overpressure detection parameters were monitored during drilling of SE-25. Mudweight in the range of 9.0 to 9.5 was used to drill to the depth of 2760 ft. At 2760 ft, the mudweight was increased to 9.8 ppg in response to the increase in background gas. A mudweight of 10.0 to 10.1 ppg was used to drill from 2900 ft to total depth (8247 ft). RFT measurements indicated increased pore pressure at a depth of 7859 ft. Wireline pore pressure prediction gives a reasonable fit to formation pressure (Figure 2.13). Slight deviation in prediction was observed at the boundary of Groups I and J.

2.6.5.2 SE-27

Well SE-27 was drilled near the crest of an anticline. Mudweight of 9.1 ppg was used to drill to depth of 1185 ft. Between 1185 ft and 5523 ft, the mudweight used was in the range 9.5 to 9.7 ppg. Mudweight was then increased to 10.5 ppg and the well was drilled down to a depth of 6557 ft. Below 8282 ft, the mudweight was increased incrementally to 12.4 ppg based on gas readings. Due to the presence of spalling shale and gas readings, mudweight was further increased to 13.8 ppg. At total depth (8449 ft), the mudweight used was 14.2 ppg as an increase in background and connection gas was observed. RFT measurements were attempted at these depths but were not successful. From the well report, the overpressure detection parameters indicated the possible top of overpressure at around 7800 ft.

The well experienced some drilling problems especially within the K shale due to sloughing. As a results, well log responses are rather suspicious. All three methods used to predict the pore pressure failed to match the RFTs taken in the well (Figure 2.14).

2.6.6 South Malay

The South Malay region contains several oil and gas fields that are currently under production (Angsi, Duyong, Malong-Sotong-Anding). The main reservoirs are found in Group I and K channel sands.

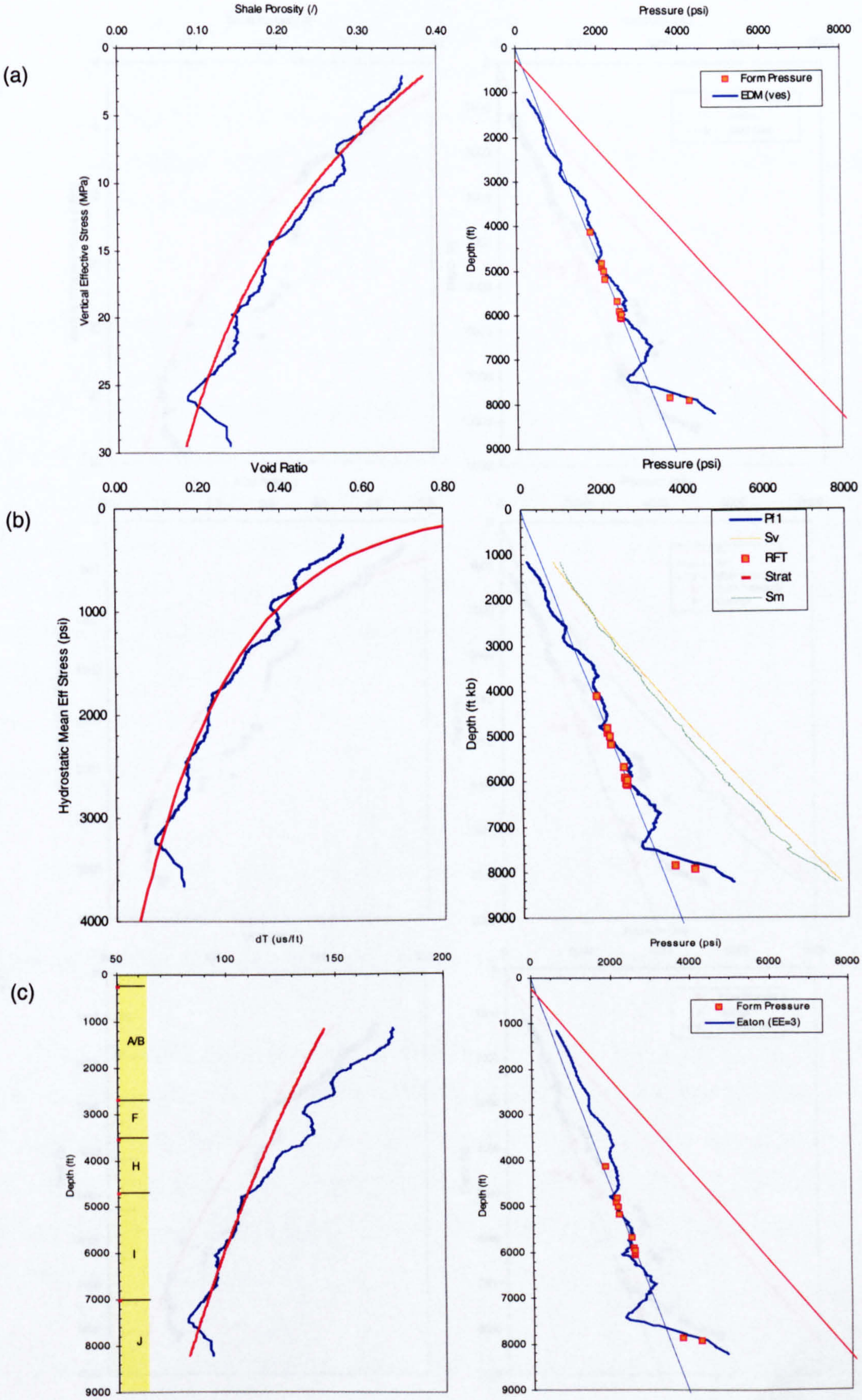


Figure 2.13 Pore pressure analysis results for SE-25. (a) EDM (mes), (b) EDM (ves), (c) EM.

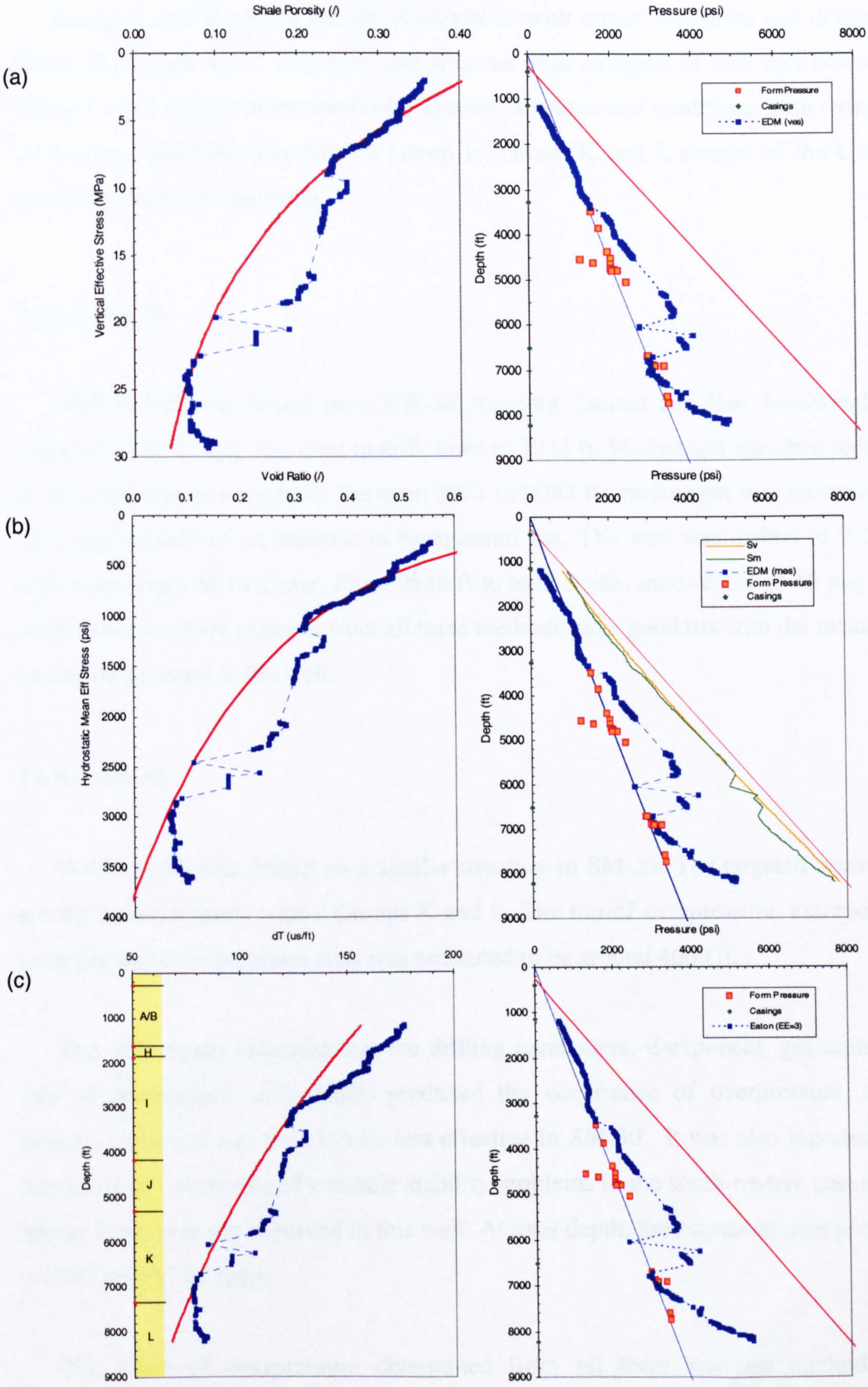


Figure 2.14 Pore pressure analysis results for SE-27. (a) EDM (mes), (b) EDM (ves), (c) EM.

Group A and B consist mainly of claystone with minor sandstone and dolomite. Group H is made up of claystone and siltstone with stringers of coal and dolomite. Group I and J consist of interbeds of claystone, siltstone and sandstone, with stringers of coal and dolomite occurring in Group I. Group K and L consist of thick shale overlying massive sandstone.

2.6.6.1 SM-29

Well SM-29 was drilled on a NW-SE trending, faulted anticline. Mudweight in range of 9.5 to 11 ppg was used to drill down to 7934 ft. Mudweight was then reduced to 10.5 ppg due to a washout. Between 8921 to 9083 ft, mudweight was increased to 11.5 ppg because of an increase in background gas. The well was drilled to 9725 ft with mudweight of 14.2 ppg. From 9886 ft to total depth, mudweight of 15 ppg was used. Predicted pore pressure from all three methods gave good fits with the measured formation pressure in the well.

2.6.6.2 SM-30

Well SM-30 was drilled on a similar structure to SM-29. The targeted reservoirs are the massive sands within Groups K and L. The top of overpressure, extrapolated from the wireline formation tests was estimated to be around 4600 ft.

The well report indicated that the drilling parameters, d-exponent, gas units and rate of penetration, successfully predicted the occurrence of overpressure. Shale density, however, was found to be less effective in SM-30. It was also reported that the common occurrence of borehole stability problems in the south-eastern part of the Malay Basin was not observed in this well. At total depth, the estimated pore pressure is 7093 psi (15.83 ppg).

The onset of overpressure determined from all three wireline methods are consistent with the observed trend of formation pressures (Figure 2.16). Due to the shallow occurrence of overpressure and relatively short interval of normally pressured section below the unconformity, the normal compaction curves are based on the

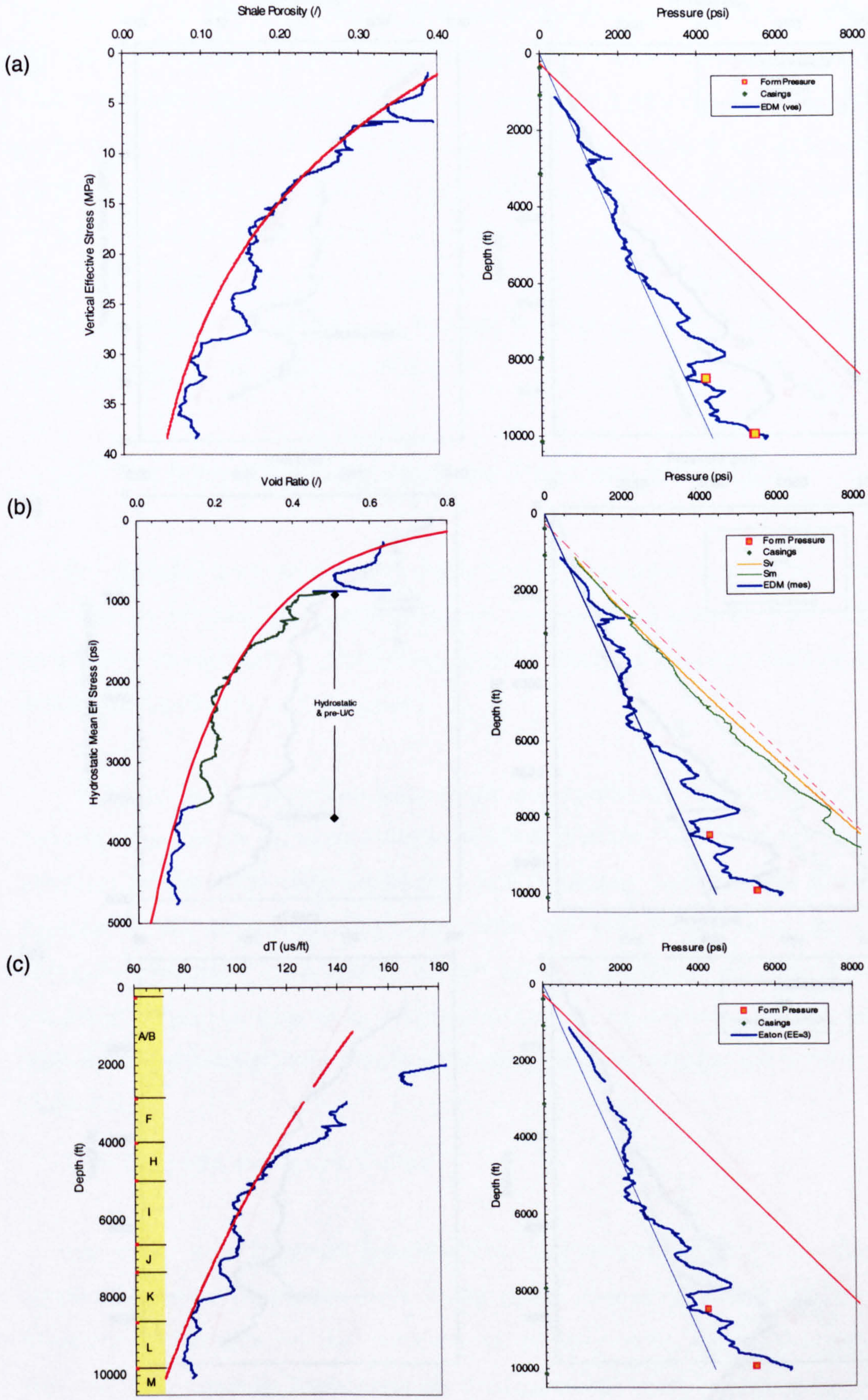


Figure 2.15 Pore pressure analysis results for SM-29. (a) EDM (mes), (b) EDM (ves), (c) EM.

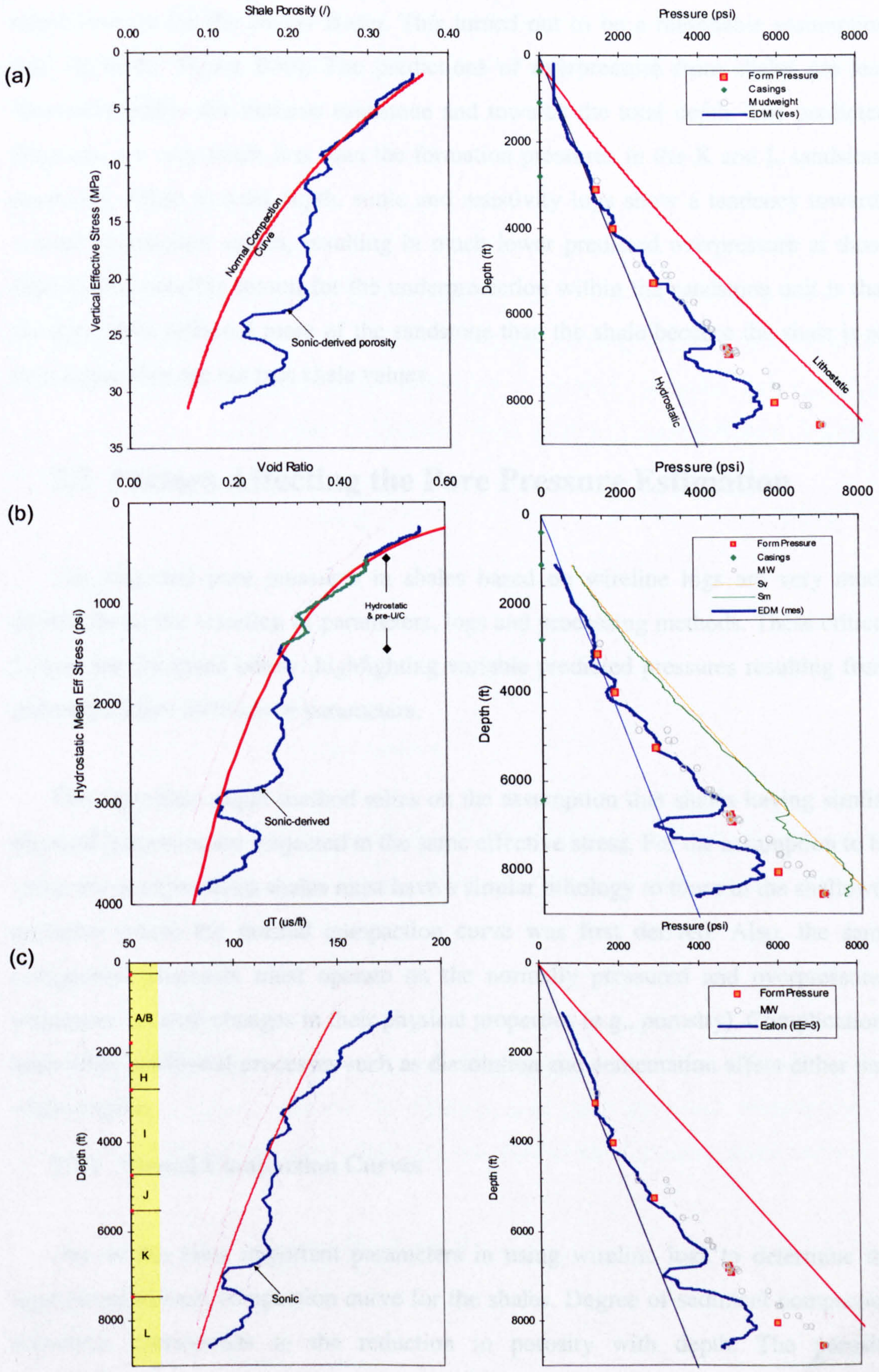


Figure 2.16 Pore pressure analysis results for SM-30. (a) EDM (ves), (b) EDM (mes), (c) EM.

best-fit curves for the Malay Basin. This turned out to be a reasonable assumption (see Appendix Figure B30). The predictions of overpressure from shales are less successful within the massive sandstone and towards the total depth. The predicted pressures are very much less than the formation pressures in the K and L sandstone reservoirs. Close to total depth, sonic and resistivity logs show a tendency towards normal compaction values, resulting in much lower predicted overpressure at those depths. One possible reason for the underprediction within the sandstone unit is that the log values reflected more of the sandstone than the shale because the shale is so thin; hence they are not true shale values.

2.7 Factors Affecting the Pore Pressure Estimation

The predicted pore pressures in shales based on wireline logs are very much dependent on the selection of parameters, logs and processing methods. These critical factors are discussed below, highlighting variable predicted pressures resulting from different chosen methods or parameters.

The equivalent depth method relies on the assumption that shales having similar physical properties are subjected to the same effective stress. For the assumption to be valid, the overpressured shales must have a similar lithology to those in the shallower sequence where the normal compaction curve was first derived. Also, the same compaction processes must operate on the normally pressured and overpressured sequences to cause changes in their physical properties (e.g., porosity). Complications arise when additional processes such as dissolution and cementation affect either part of the section.

2.7.1 Normal Compaction Curves

One of the most important parameters in using wireline logs to determine the appropriate normal compaction curve for the shales. Degree of sediment compaction downhole corresponds to the reduction in porosity with depth. The porosity parameters can either be derived directly from laboratory measurement or computed from porosity logs. The compaction curves (porosity or porosity parameters) vary according to lithological composition, temperature gradient and stress history.

Published shale compaction curves are therefore basin-specific, as reflected by different published curves and depth-porosity relationship (Rieke & Chilingarian, 1974; Giles et al., 1998).

2.7.1.1 Compaction Equation

There are numerous compaction curves for shales that have been published to date, ranging from simple exponential to double exponential. The earliest compaction law was introduced by Athy (1930), which relates porosity to depth. This empirical exponential law requires local calibration with relatively homogeneous lithology intervals:

$$\phi = \phi_o e^{-cz} \qquad (2.11)$$

where

ϕ = porosity at depth z,

ϕ_o = the surface porosity,

c = compaction coefficient constant.

Hubbert & Rubey (1959) modified Athy's compaction law by substituting the depth (z) with effective stress (σ) to reflect the changes of porosity due to loading stress rather than burial depth:

$$\phi = \phi_o e^{-c\sigma} \qquad (2.12)$$

The above relationships (porosity and porosity-parameters) have been used in the wireline pore pressure analysis. In addition, soil mechanic-based relationship of Skempton (1970) and Burland (1990) was also used in the equivalent depth method:

$$e = e_{100} - \beta \ln(\sigma_v/\sigma_{100}) \qquad (2.13)$$

where

e_{100}= void ratio at 100 kPa,

β = compression coefficient

σ_{100}= effective stress of 100 kPa

An alternative to a simple exponential function is the double exponential found in Temispack (Beicip-Franlab, 1997) and Giles et al. (1998). In Temispack, the porosity-effective stress relationship is defined as

$$\phi = \phi_1 + \phi_a e^{(\sigma/\sigma a)} + \phi e^{(\sigma/\sigma b)} \quad (2.14)$$

where

ϕ_1, ϕ_a and ϕ_b = empirically defined porosity coefficients

σ_a and σ_b = exponent factors of effective stress.

Examples from two wells (WM-8 and CM-17) are presented here. In the case of well WM-8, using a double exponential compaction trend provides a much better pore pressure prediction compared to a single exponential trend in a modified Eaton method (Figure 2.17). For well CM-17, due to its shallower depth, no significant differences were detected (Figure 2.18).

There are other published porosity-depth relationships in the literature, including Falvey & Deighton's (1982) inverse porosity relationship, Baldwin & Butler's (1985) power law, Liu & Roaldset's (1994) parabolic equation and many others. These equations were not tested in this study.

Heasler & Kharitonova (1996) have proposed the inclusion of a minimum rock matrix transit time in the sonic transit time (dT) vs depth (z) relationship:

$$dT = dT_o e^{(-bz)} + c \quad (2.15)$$

where,

$dT_{o=}$ surface sonic transit-time

b = exponential decay constant

c = rock matrix transit time (at zero porosity)

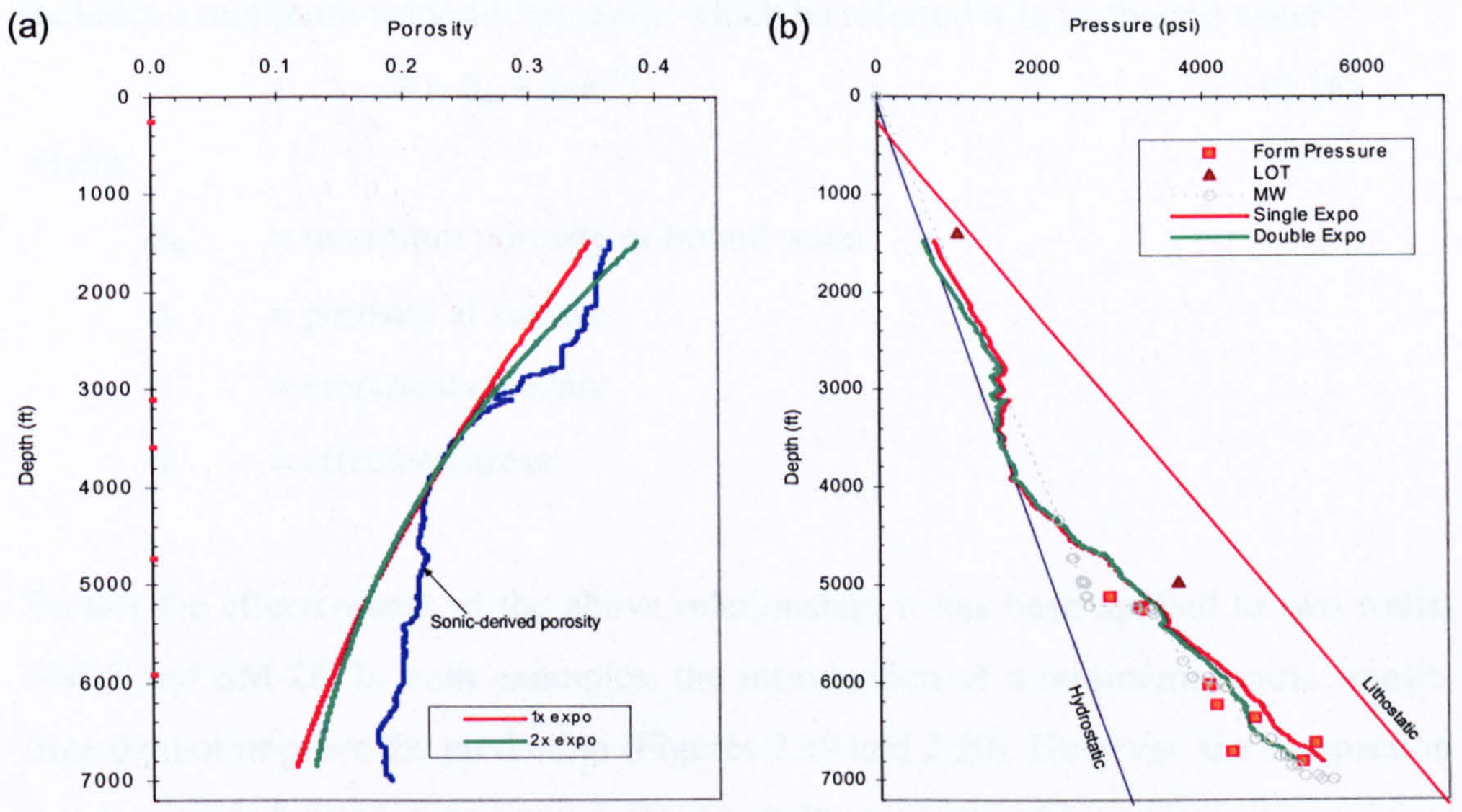


Figure 2.17 Pore pressure prediction for well WM-8, using modified Eaton method, which used sonic porosity instead of sonic travel time. (a) Normal compaction curves derived from single (red) and double (green) exponential functions plotted against depth with sonic-derived porosity. (b) Predicted pore pressure for single and double exponential compaction trends.

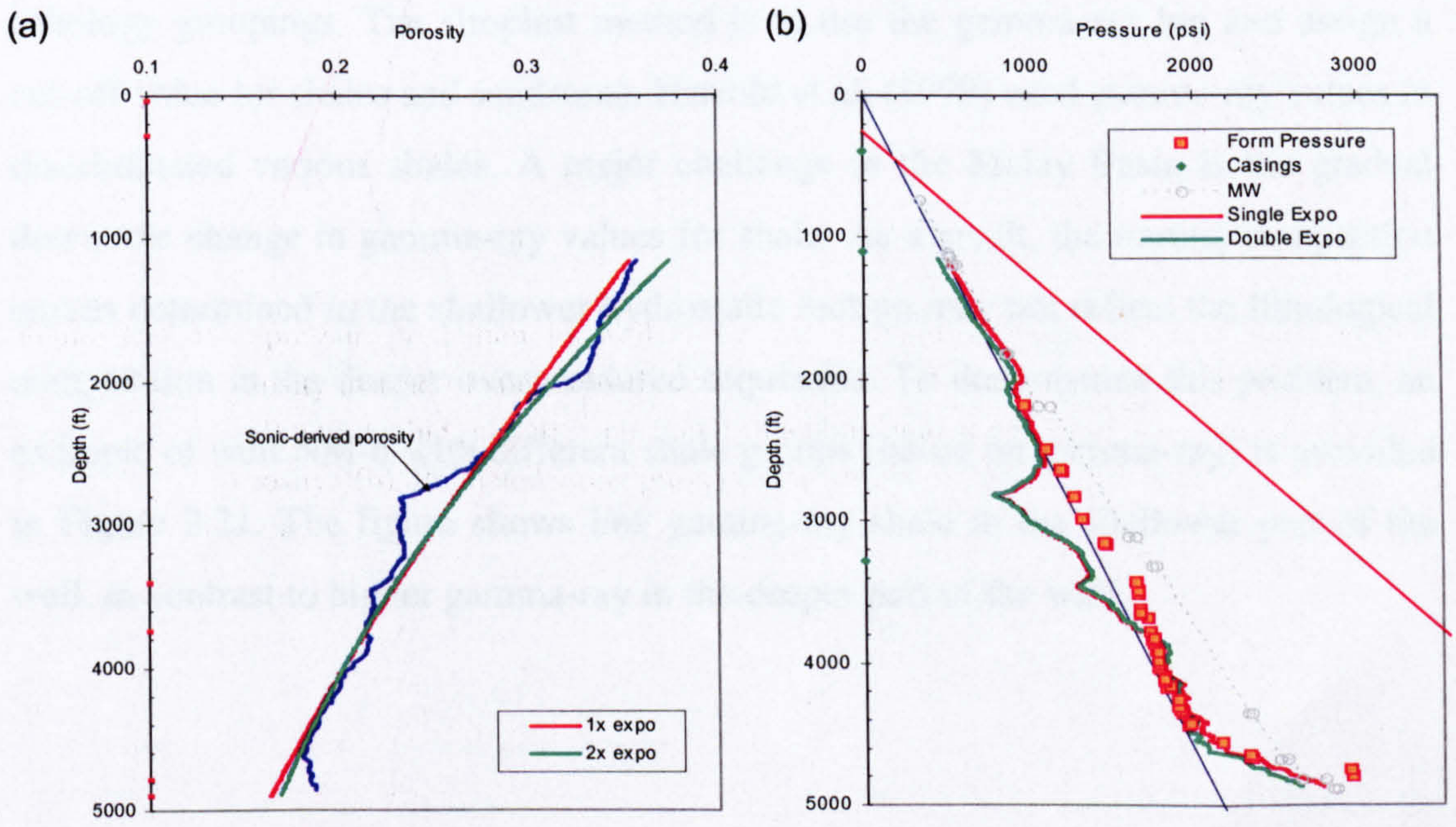


Figure 2.18 Pore pressure prediction for well CM-17, using modified Eaton method. See Figure 2.17 for explanation.

Similarly, in an empirical porosity-effective stress relationship, Lahann (2002) includes a minimum value for porosity, which he referred it to as 'bound water':

$$\phi = \phi_m + \phi_o e^{-c\sigma} \quad (2.16)$$

where,

ϕ_m = minimum porosity or bound water

ϕ_o = porosity at surface

c = empirical constant

σ = effective stress

To test the effectiveness of the above relationship, it has been applied to two wells, NM-5 and SM-28. In both examples, the introduction of a minimum matrix transit-time did not improve the prediction (Figures 2.19 and 2.20). However, the compaction trends provide better approximations to the shallower parts of the wells.

2.7.1.2 Shale Lithology

Lithology exerts an important control on the log responses and the normal compaction curves. A number of ways have been proposed to discriminate various lithology groupings. The simplest method is to use the gamma-ray log and assign a cut-off value for shales and sandstone. Harrold et al. (1999) used gamma-ray values to discriminated various shales. A major challenge in the Malay Basin is the gradual downhole change in gamma-ray values for shale. As a result, the normal compaction curves determined in the shallower hydrostatic section may not reflect the lithological composition in the deeper overpressured sequences. To demonstrate this problem, an example of well NM-6 with different shale groups (based on gamma-ray) is provided in Figure 2.21. The figure shows low gamma-ray shale in the shallower part of the well, in contrast to higher gamma-ray in the deeper part of the well.

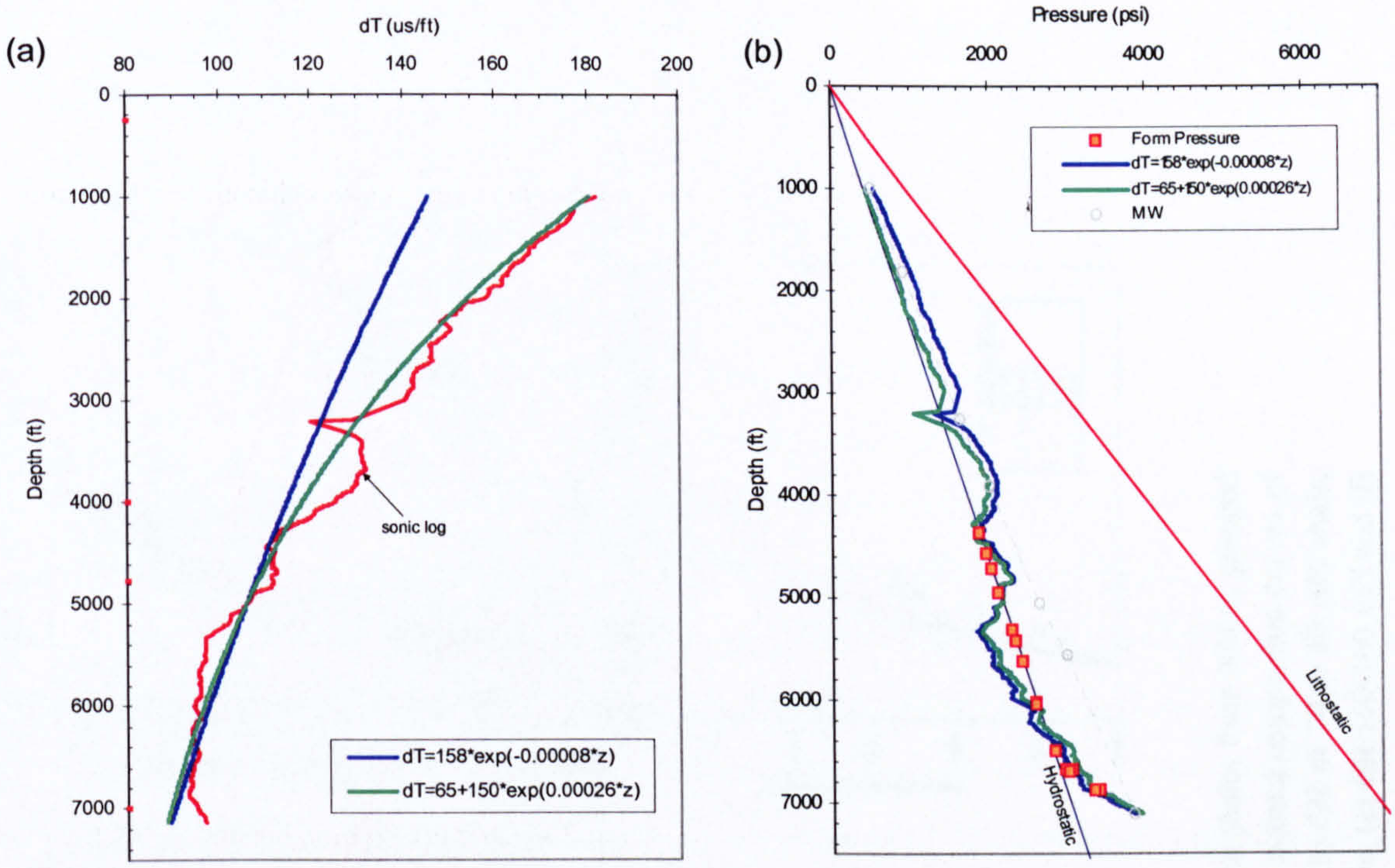


Figure 2.19 Calculated pore pressure for Well NM-5 using compaction curve with minimum matrix transit-time. (a) Normal compaction curves with (green line) and without (blue) minimum matrix transit-time. (b) Pore pressure results.

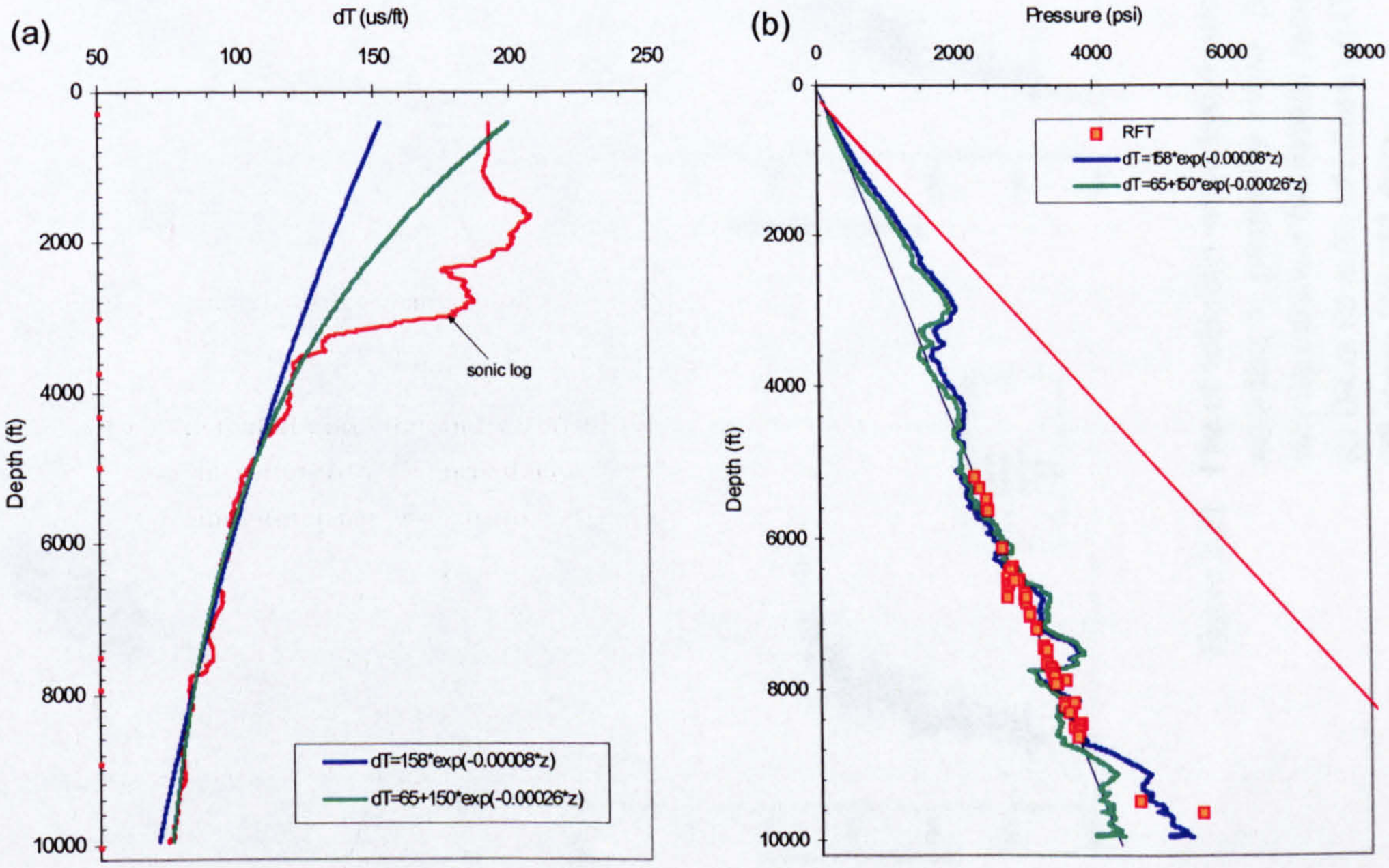


Figure 2.20 Calculated pore pressure for Well SM-28 using compaction curve with minimum matrix transit-time. (a) Normal compaction curves with (green) and without (blue) minimum matrix transit-time. (b) Pore pressure results.

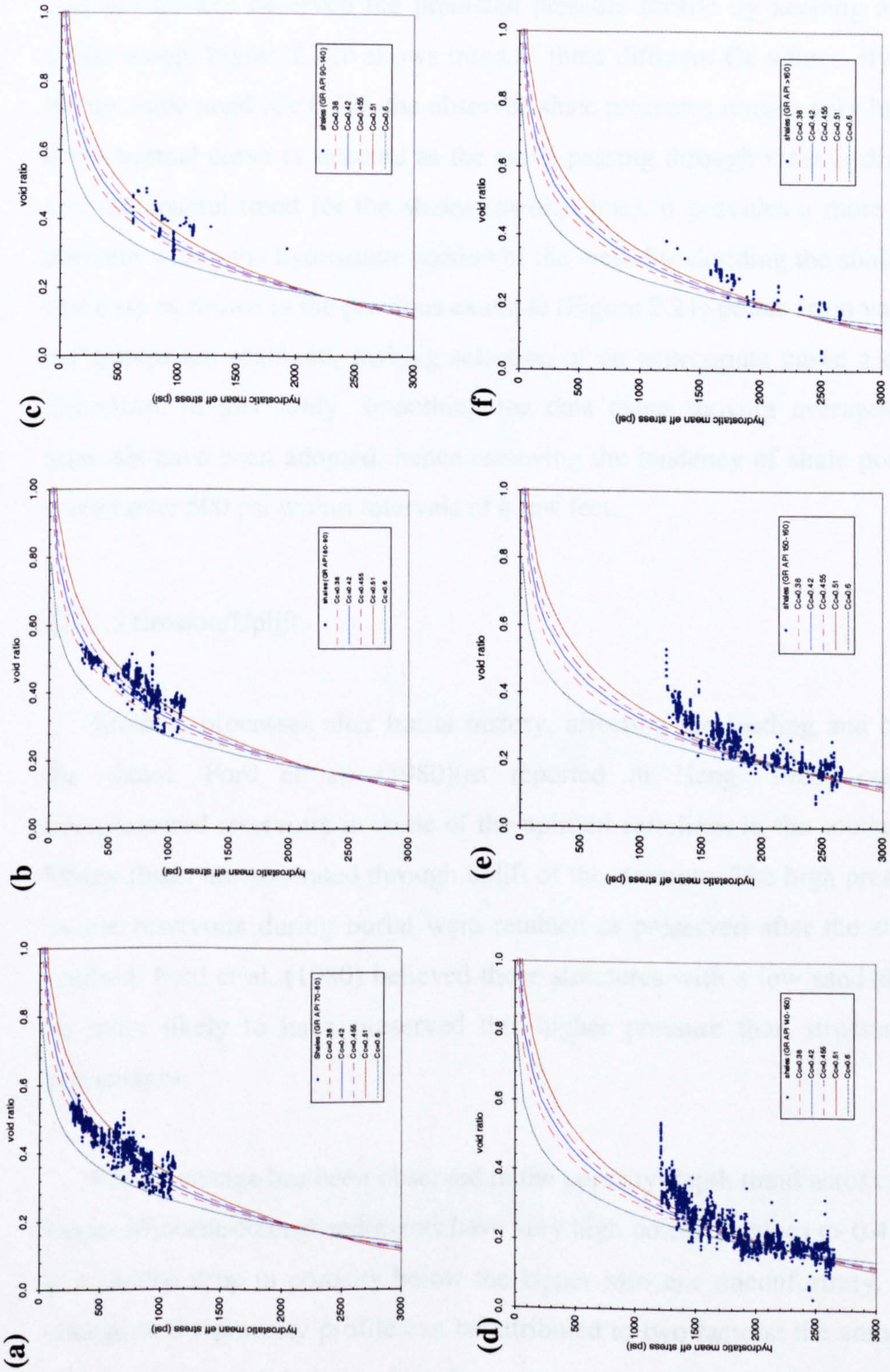


Figure 2.21 Plot of void ratio versus hydrostatic mean effective stress for shales from NM-6, grouped according to gamma-ray values. Also plotted are various normal compaction curves of varying sediment mechanical parameters. (a) All shales, (b) GR of 70 to 80 API shale, (c) GR of 80 to 90 API shale, (d) GR of 90 to 140 API shale, (e) GR 150-160 API and (f) GR above 160 API shale.

Selecting an appropriate normal compaction curve has implications for the pressure estimation. Harrold et al. (1999) selected the lowest curve for each shale group (classified according to gamma-ray response). To demonstrate this, we will vary the e_{100} and Cc and observed the predicted pressure profile by keeping all shales as a single group. Figure 2.22b shows trend of three different Cc values. By selecting the lowest shale trend (Cc 0.32), the observed shale pressures remain very high. However, if the normal curve is selected as the curve passing through most hydrostatic points, i.e., the general trend for the shales (median line), it provides a more realistic pore pressure within the hydrostatic section of the well. Subdividing the shales may not be that easy as shown in the previous example (Figure 2.21) points from various gamma-ray groups are scattered, making selection of an appropriate curve a daunting task. Therefore, in this study, smoothing the data using moving averages over 400 ft intervals have been adopted, hence removing the tendency of shale pore pressure to scatter over 500 psi within intervals of a few feet.

2.7.1.3 Erosion/Uplift

Tectonic processes alter burial history, affecting the loading and compaction of the shales. Ford et al. (1980)(as reported in Heng, 1985) considered that overpressured reservoirs in some of the uplifted anticlines in the southern part of the Malay Basin are generated through uplift of the structure. The high pressures reached by the reservoirs during burial were retained or preserved after the structures were uplifted. Ford et al. (1980) believed those structures with a low sand-shale ratio will be more likely to have preserved this higher pressure than structures with sand percentages.

Abrupt change has been observed in the porosity-depth trend across the basin. The Upper Miocene-Recent sediments have very high porosity values (> 0.4 %) and there is a sudden drop in porosity below the Upper Miocene unconformity. These sudden change in the porosity profile can be attributed to two factors: the amount of erosion and the change in lithology. Significant erosion has been recorded in the southeastern part of the basin, resulting in removal of Group D to H sediments. In the north, however, sedimentation was reported to be continuous, based on paleontological and

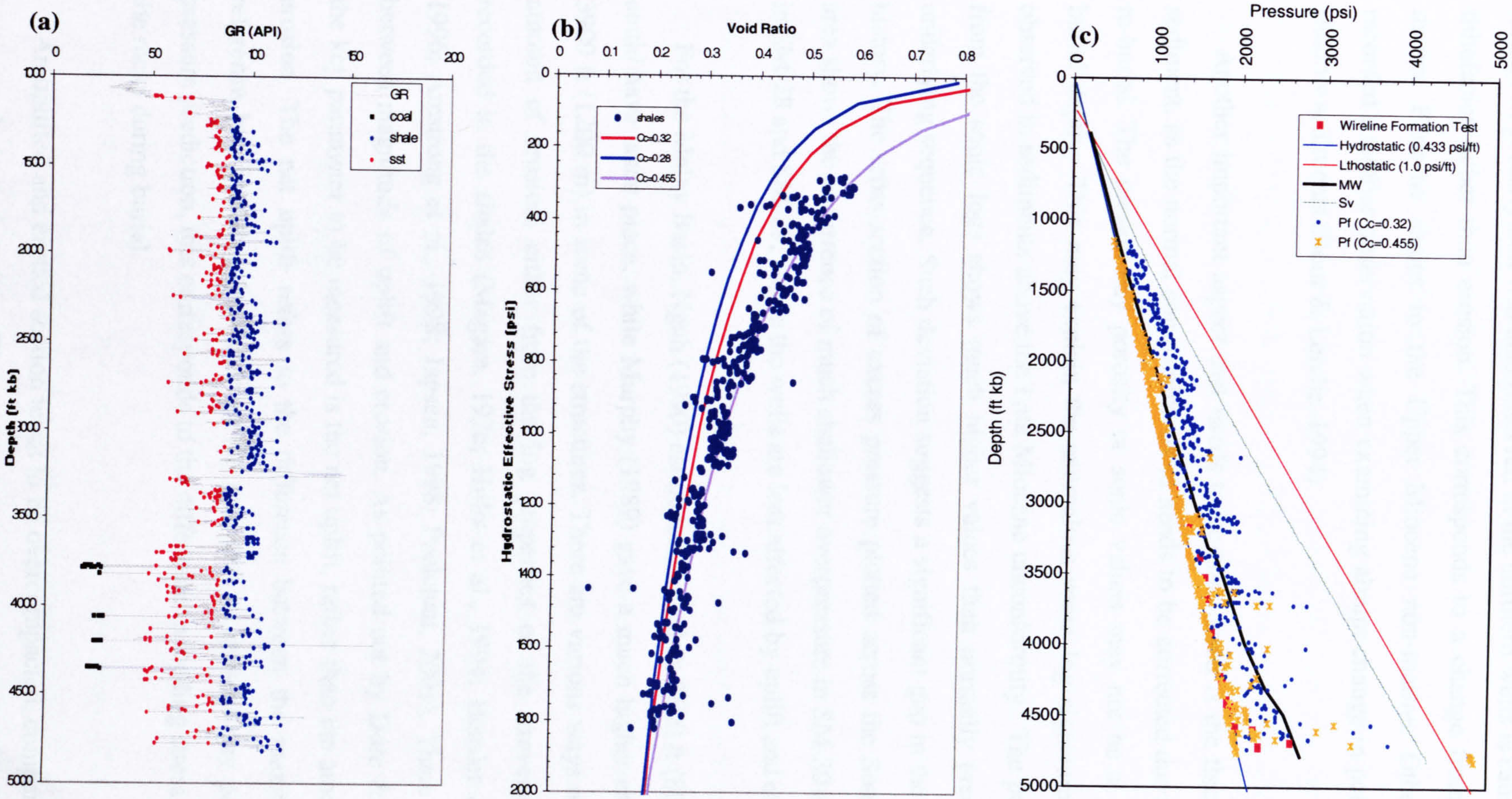


Figure 2.22 Predicted pore pressure for CM-16 using the EDM mean effective stress: (a) selecting shale from gamma-ray logs, (b) plot of void ratio versus hydrostatic mean effective stress, (c) predicted pore pressure using the two different compaction coefficient (Cc) values.

seismic sequence interpretation (EPIC, 1994). This may suggest that the abrupt change in porosity that was also observed in the northern wells is caused by change in lithofacies rather than erosion. This corresponds to a change from unconsolidated marine Pliocene shales to the Upper Miocene non-marine. Other authors have recorded a similar observation when examining abrupt change in porosity profiles in shallow sediments (Bour & Lerche, 1994)

Another important aspect that needs to be considered is the thickness of eroded sediment, as the normal compaction trend needs to be corrected due to the uplift and re-burial. The present-day porosity or sonic values may not be at their maximum burial depth. This may explain the anomalous sonic log signatures that are often observed in sediments above the Late Miocene unconformity. The porosities derived from the sonic logs shows much higher values than normally predicted from the underlying sequence. Such deviation suggests a significant gap in the sediment burial history. The cross-section of excess pressure plotted across the South Malay Basin area shows the occurrence of much shallower overpressure in SM-30 and SM-31, than in SM-28 and SM-29, where the wells are less affected by uplift and erosion.

For the Malay Basin, Ngah (1990) estimated more than 2600 ft (800 m) of erosion could have taken place, while Murphy (1989) gave a much higher estimated of over 3900 ft (1200 m) in some of the structures. There are various ways of estimating the amount of erosion, either from the log properties or the irreversible parameters recorded in the shales (Magara, 1976; Hillis et al., 1994; Heasler & Kharitonova, 1996; Amstrong et al., 1998; Japsen, 1998; Poelchau, 2001). There is a difference between magnitude of uplift and erosion. As pointed out by Dore & Jensen (1996), the key parameter to be measured is the net uplift, rather than the amount of uplift or erosion. The net uplift refers to the difference between the maximum depth the reference bed has been buried to in the past and its present day position. In pore pressure prediction, this corresponds to the difference in loading stress experienced by the rocks during burial.

An uplifted and eroded section tends to be overcompacted, compared to a normal, continuously buried section. The sonic transit-time of the normal compaction curve for the Malay Basin has been derived using the Heasler & Kharitonova (1996) fitting

technique. The curve was determined on the hydrostatic portions of the wells located on the western side of the basin. These wells are known not to be affected by the erosion (e.g., WM-10 and SM-28). The shale matrix transit-time for shale was determined as 63 us/ft. Magara (1976) used 68 us/ft, while Heasler & Kharitonova (1996) used a value of 64-66 us/ft for shale matrix transit-time. As for the surface transit-time, i.e. transit-time for water, a value of 202 us/ft was determined for the Malay Basin. Magara (1976) proposed values in the range of 180-210 us/ft. The normal compaction curve determined for the basin is

$$dT=63+150e^{(-0.00026z)} \quad (2.17)$$

where

dT = sonic transit –time (μs/ft)

z = depth (ft)

Plots of sonic transit-time versus depth, together with the best-fit line for the well and the normal compaction curve derived for the Malay Basin are presented in Appendix A. The differences observed between the best-fit line and the normal compaction curve give some idea of the amount of net uplift that has occurred within the well. Wells in the North Malay, West Malay and South Malay do not appear to show much difference. Wells from the Central Malay shows the most pronounced net uplift, estimated in the range 600 to 700 ft. Wells in the NE Malay and SE Malay appears to be slightly undercompacted. In view of the small net uplift observed in most of the wells, the influence of uplift and erosion on overpressure development in the basin is probably minor.

2.7.2 Shale Porosity

2.7.2.1 Sonic vs Density-Derived Porosity

The porosity used in this study is derived from sonic transit-time, based on Issler (1992) parameters. The relationship is suitable for non-calcareous, low Total Organic Carbon content shale. The use of these parameters in this study is supported by the direct comparison between the sonic-derived porosity (using Issler's equation) and the

density-derived porosity in the normally pressured sequence. The density-derived porosities were computed assuming 2.71 g/cc and 1.0 g/cc for matrix and fluid density, respectively. Figure 2.23 shows the comparison of these values in two wells.

In deeper overpressured sequences, the sonic and density porosities did not match. The sonic and density log responses in overpressured sequence have been shown to vary (Hermanrud et al., 1998; Tingay et al., 2000). Hermanrud et al. (1998) suggested the sonic log response is affected by the microfracturing in the rock due to stress reduction. However, Bowers & Katsube (2002) pointed that the pore pressures in the Haltenbanken area are well below overburden, making it less likely to cause microfracturing. They proposed that the sonic and density logs responded to the changes occurring in bulk and transport properties in the shale. The sonic log records the rock transport properties, which are govern by the flexibility of the connecting pores to the changes in stress. The bulk porosity is recorded by density log, regardless of the relative properties of porosity in connecting and storage pores. The difference between the sonic and density log responses can then be use to identify the contribution of fluid expansion mechanisms to the development of overpressure (Bowers, 2001).

2.7.2.2 Solidity

Holbrook et al. (1995) and Heppard et al. (1998) used solidity instead of porosity in their pore pressure prediction. Solidity (i.e., 1-ϕ), introduced by Baldwin & Butler (1985), is empirically derived for his power-law compaction curve. According to Holbrook et al., (1995) and Heppard et al. (1998), solidity provides a better relationship with effective stress compared to porosity. To test this, well WM-8 has been subjected to wireline pore pressure analysis using solidity rather than porosity or void ratio (in the Eaton and EDM methods). In the EDM (ves) method, using solidity data did not show improvement in the pore pressure prediction results (Figure 2.24). In the modified Eaton method (using solidity instead of sonic transit-time and with the same Eaton exponent of 3), the predicted pore pressure shows some minor improvement (Figure 2.25).

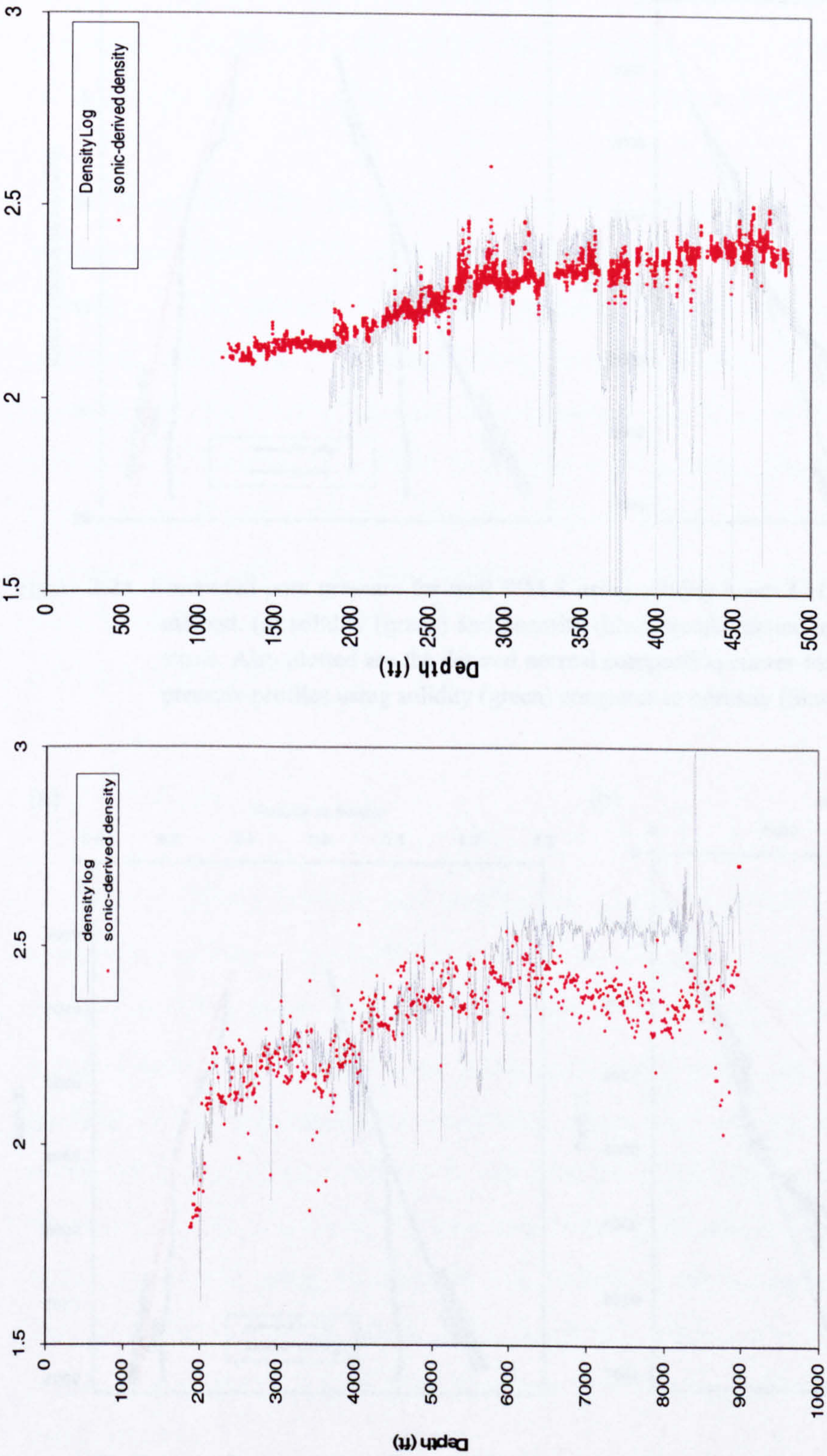


Figure 2.23 Density profile for wells NM-1 and CM-17. Grey line represents density data from log. Red dots are the calculated density values from the sonic log, There is a good match between the density log and the sonic-derived density in the upper part of well NM-1 and in well CM-17. Density values began to depart below top of overpressure in well NM-1.

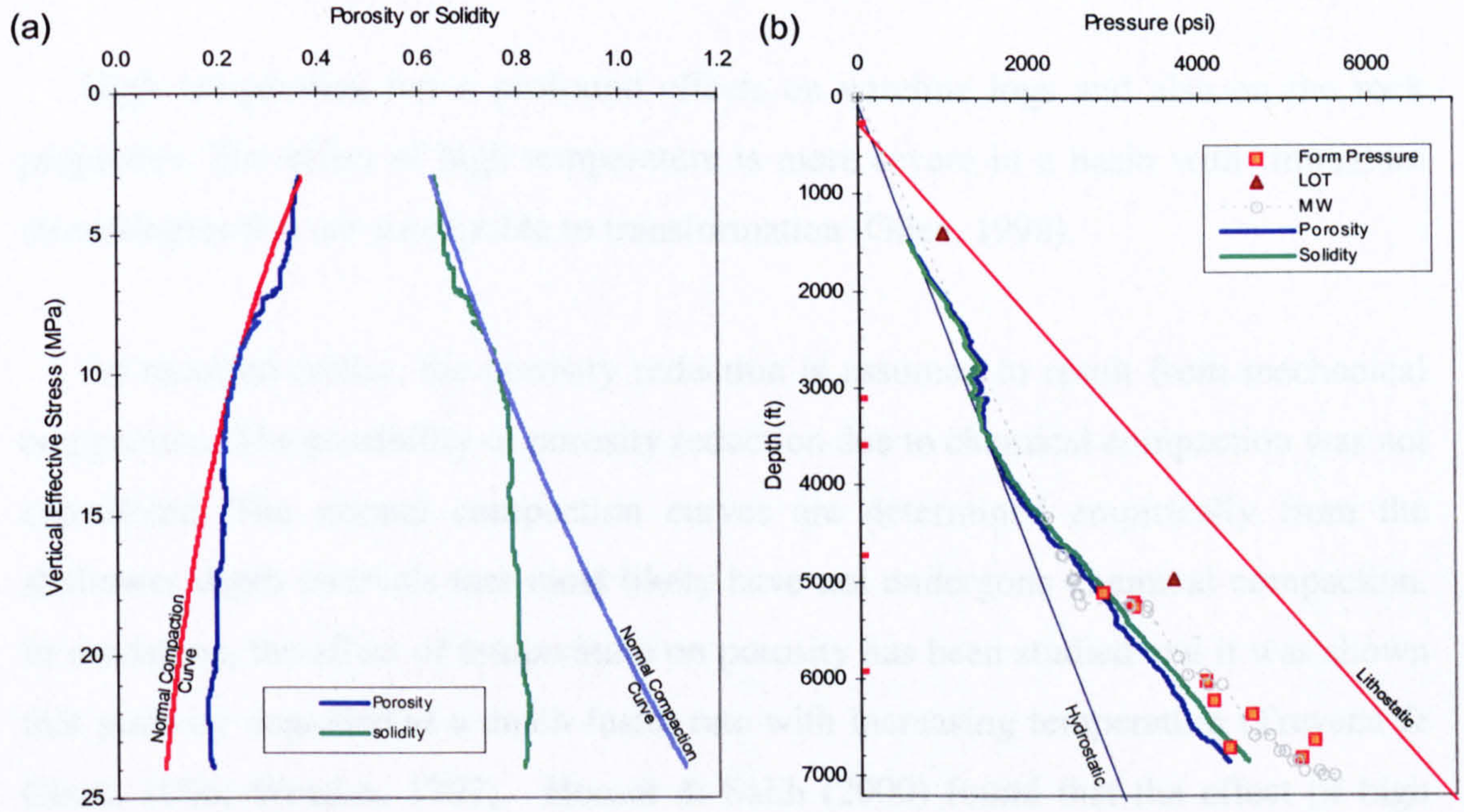


Figure 2.24 Computed pore pressure for well WM-8 using solidity instead of porosity in EDM (ves) method. (a) solidity (green) and porosity (blue) trends plotted against vertical effective stress. Also plotted are the derived normal compaction curves for the well. (b) Predicted pressure profiles using solidity (green) compares to porosity (blue).

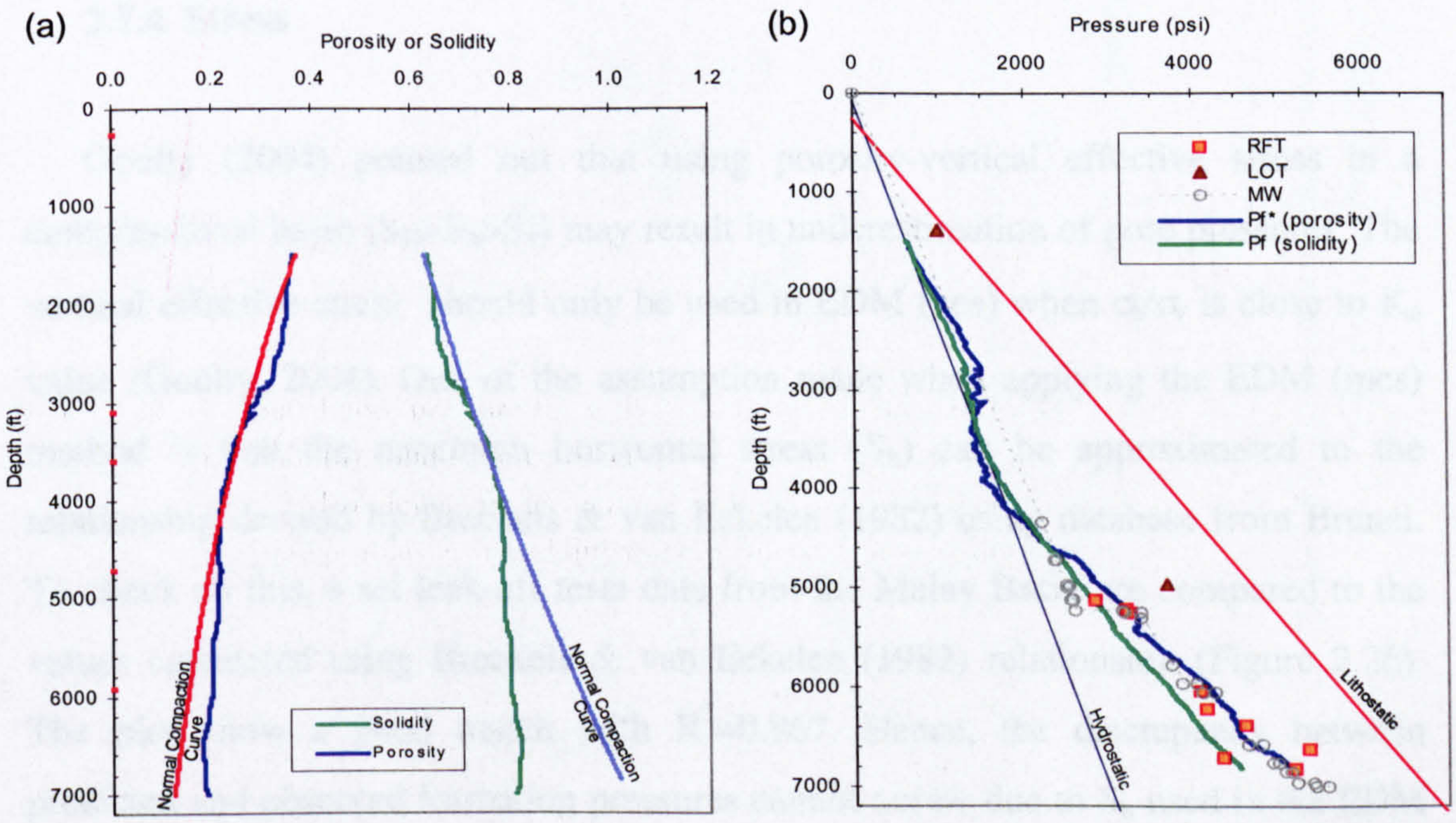


Figure 2.25 Computed pore pressure for well WM-8, using solidity and porosity data, instead of sonic transit-time in Eaton method. (a) solidity (green) and porosity (blue) trends with depth and the estimated normal compaction curves. (b) Predicted pressure profile using solidity and porosity parameters showing better pore pressure prediction obtained using porosity than solidity.

2.7.3 Temperature

High temperature has a profound effects on wireline logs and also on the rock properties. The effect of high temperature is more severe in a basin with immature mineralogies that are susceptible to transformation (Giles, 1998).

As reported earlier, the porosity reduction is assumed to result from mechanical compaction. The possibility of porosity reduction due to chemical compaction was not considered. The normal compaction curves are determined empirically from the shallower depth intervals that most likely have not undergone chemical compaction. In sandstone, the effect of temperature on porosity has been studied and it was shown that porosity degraded at a much faster rate with increasing temperature (Trevena & Clark, 1986; Worden, 1997). Hoesni & Salih (2000) found that the effect of high geothermal gradient on the sandstone porosity in the Malay Basin to be statistically significant. However, the effect of temperature on the shales porosity in the basin has not been investigated.

2.7.4 Stress

Goulty (2004) pointed out that using porosity-vertical effective stress in a compressional basin ($S_H>S_h>S_v$) may result in underestimation of pore pressures. The vertical effective stress should only be used in EDM (ves) when σ_h/σ_v is close to K_o value (Goulty, 2004). One of the assumption made when applying the EDM (mes) method is that the minimum horizontal stress (S_h) can be approximated to the relationship derived by Breckels & van Eekelen (1982) using database from Brunei. To check on this, a set leak-off tests data from the Malay Basin are compared to the values calculated using Breckels & van Eekelen (1982) relationship (Figure 2.26). The plot show a good match with R^2=0.967. Hence, the discrepancy between predicted and observed formation pressures cannot not be due to S_h used in the EDM (mes) method.

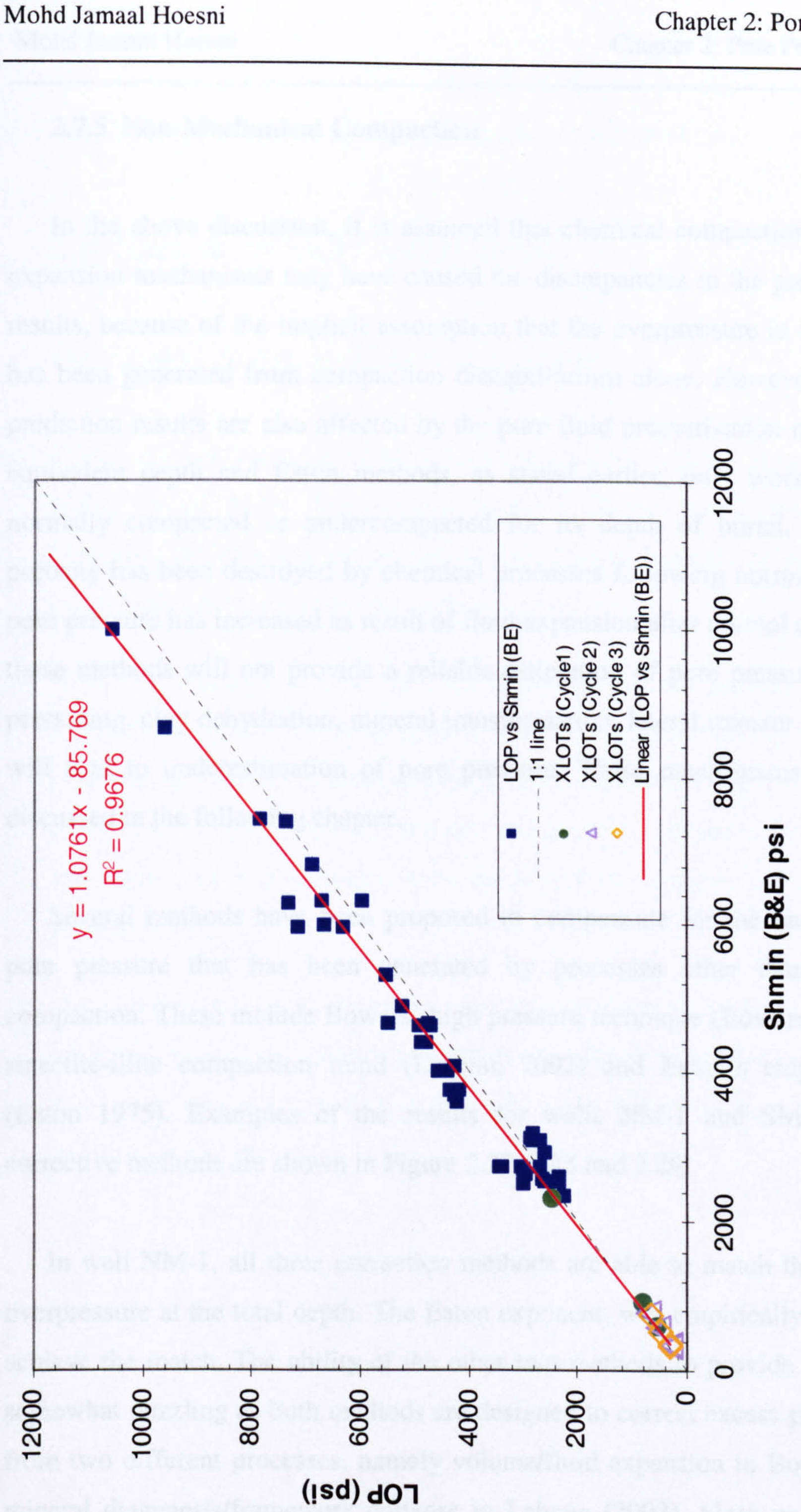


Figure 2.26 Minimum horizontal stress (Sh) calculated using Breckels & van Eekelen (1982) data from Brunei and leak-off data from the Malay Basin.

2.7.5 Non-Mechanical Compaction

In the above discussion, it is assumed that chemical compaction effects or fluid expansion mechanisms may have caused the discrepancies in the pressure prediction results, because of the implicit assumption that the overpressure in the Malay Basin has been generated from compaction disequilibrium alone. However, pore pressure prediction results are also affected by the pore fluid pressurization mechanisms. The equivalent depth and Eaton methods, as stated earlier, only work if the shale is normally compacted or undercompacted for its depth of burial. In cases where porosity has been destroyed by chemical processes following normal compaction or pore pressure has increased as result of fluid expansion after normal compaction, then these methods will not provide a reliable estimation of pore pressure. Aquathermal pressuring, clay dehydration, mineral transformation, lateral transfer and cementation will lead to underestimation of pore pressure. These mechanisms will be further discussed in the following chapter.

Several methods have been proposed to compensate for the underestimation of pore pressure that has been generated by processes other than disequilibrium compaction. These include Bowers' high pressure technique (Bowers, 1995; 2001), a smectite-illite compaction trend (Lahann, 2002) and Eaton's empirical exponent (Eaton 1975). Examples of the results for wells NM-1 and SM-30 using these corrective methods are shown in Figure 2.27, 2.28 and 2.29.

In well NM-1, all three correction methods are able to match the observed high overpressure at the total depth. The Eaton exponent, was empirically adjusted to 5 to achieve the match. The ability of the other two methods to provide a good match is somewhat puzzling as both methods are designed to correct excess pressure resulting from two different processes, namely volume/fluid expansion in Bowers (2001) and mineral diagenesis/framework collapse in Lahann (2002). More on these processes will be discuss in Chapter 3. At the moment, based on the results, both processes discussed by Bowers (2001) and Lahann (2002) appear identical.

In well SM-30, all three correction methods gave a good match with the formation pressure down to depth of 8000 ft. None of these methods, however, able to predict

low effective stress in the deepest formation test in this well.

2.8 Summary and Conclusions

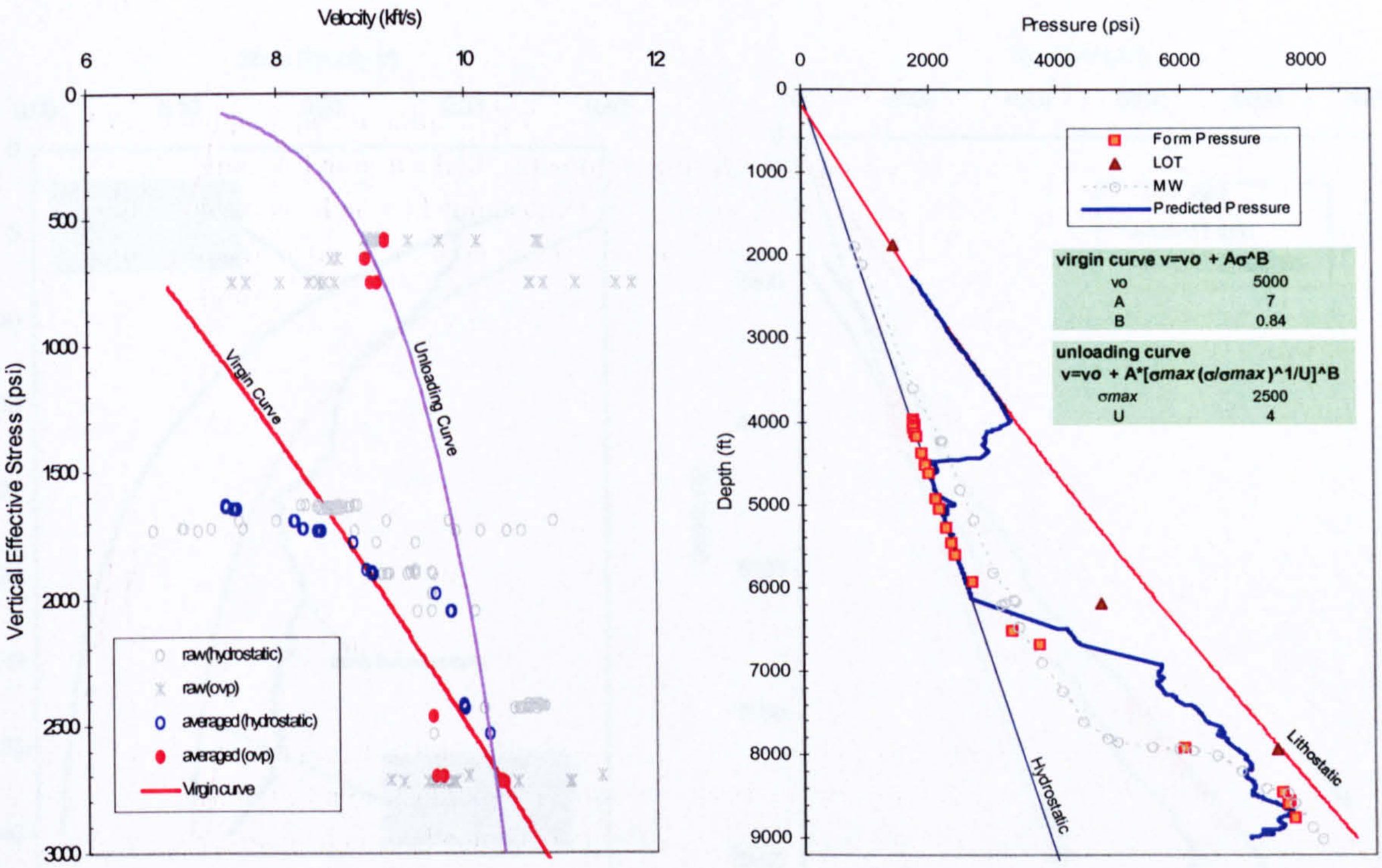
The primary conclusions of this chapter are that:

(a) Three different methods of pore pressure prediction gave mixed results for the Malay Basin wells. Mismatched between the predicted pore pressure and formation pressure are mainly due to selection of normal compaction trend, log quality and processes contributing to the overpressure.

(b) Where overpressure is resulted from disequilibrium compaction, the three tested methods provide a reasonable good-fit with the formation pressure. Otherwise, the methods resulted in underprediction of pore pressure. In some cases (e.g., well NM-1 and WM-8), however, the equivalent depth method using mean effective stress provides a good-match with the formation pressure, where the other two methods failed.

(c) The underestimation in predicted pore pressure can be corrected using methods proposed by Bowers (2001), Lahann et al., (2001) and Eaton (1975). However, these correction methods do not works for wells that are strongly affected by non-mechanical compaction.

(a)



(b)

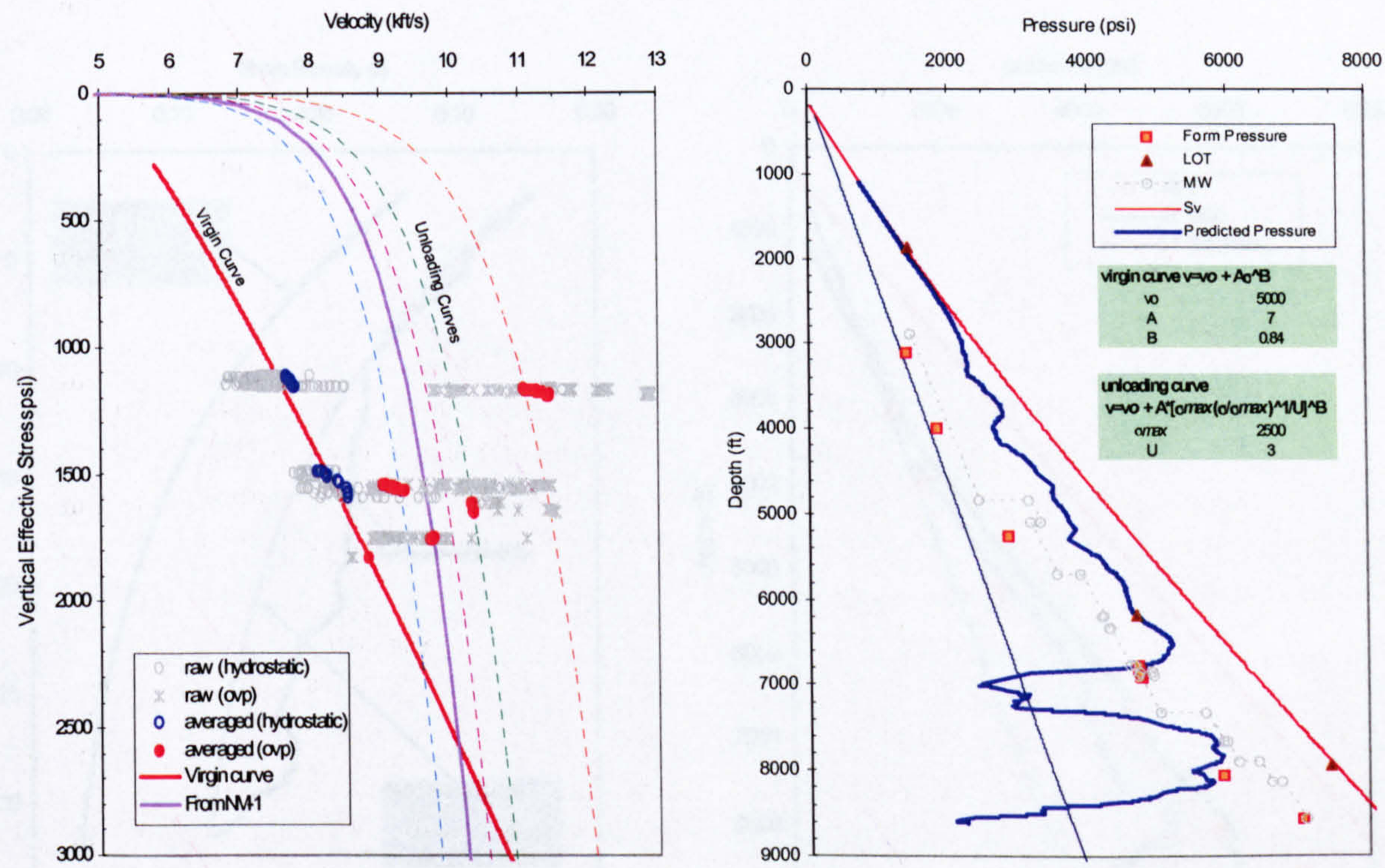


Figure 2.27 Predicted pore pressure using Bowers (2001) high pressure correction method. (a) NM-1, (b) SM-30.

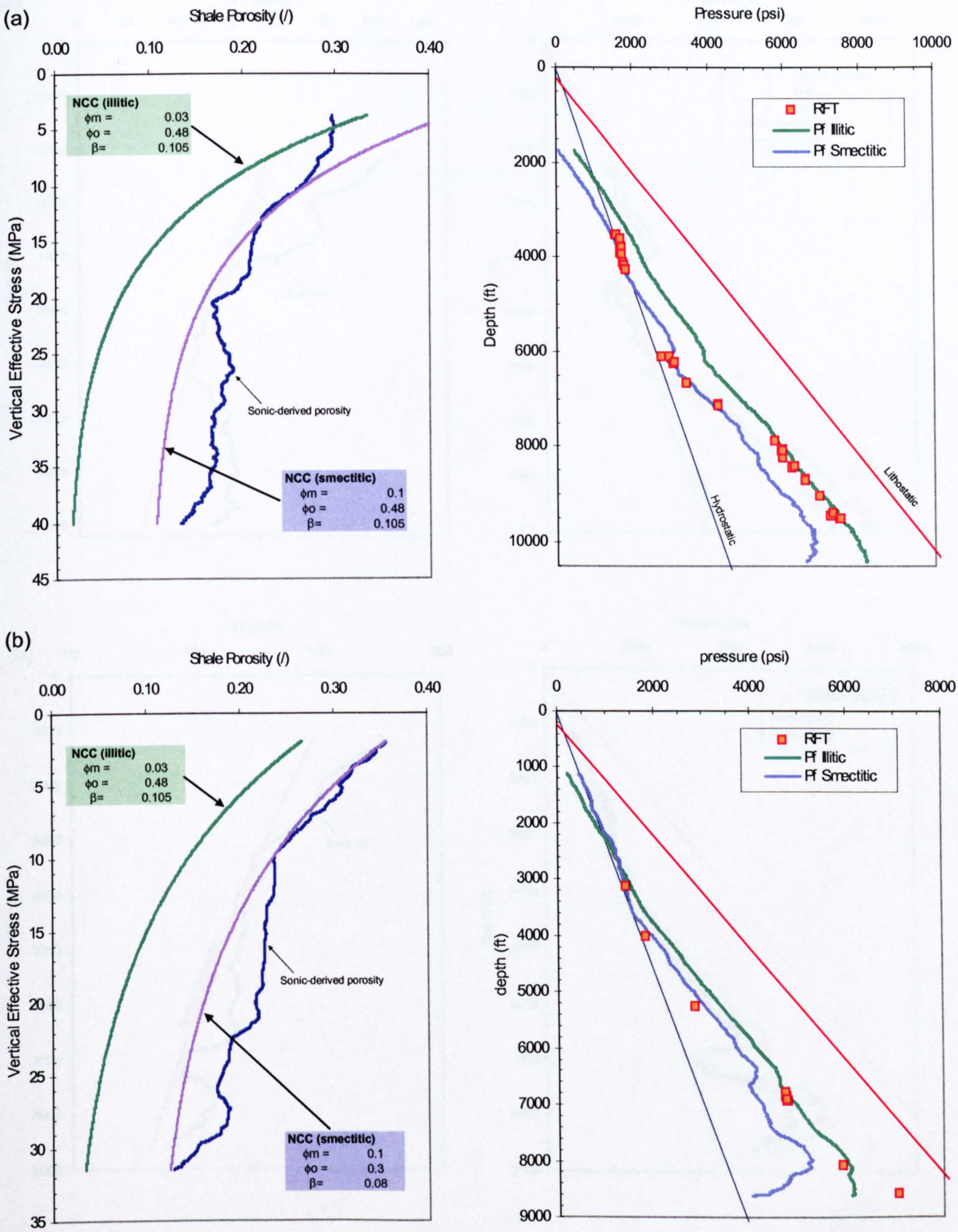


Figure 2.28 Predicted pore pressure using smectite and illite compaction curves. (a) NM-3, (b) SM-30.

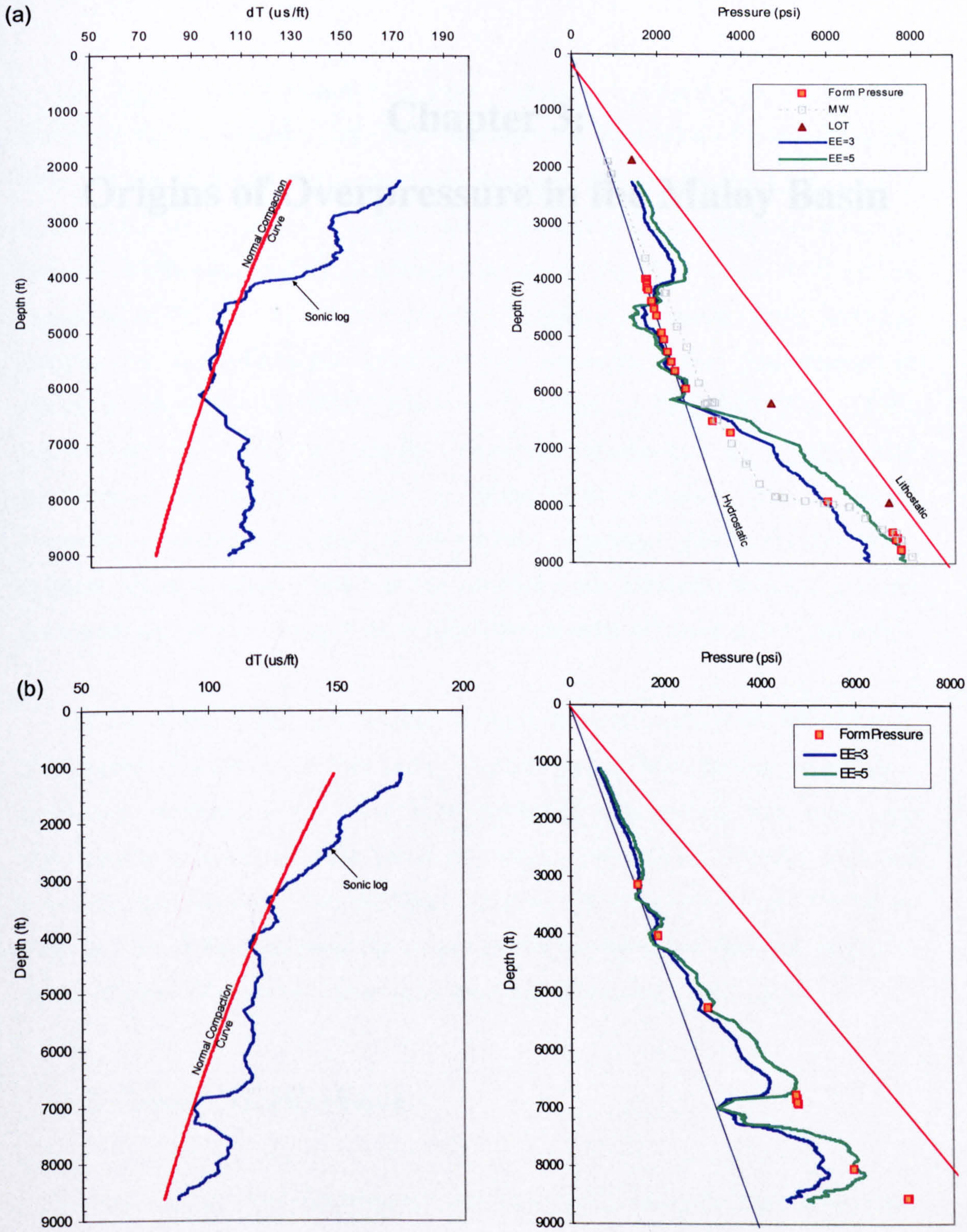


Figure 2.29 Predicted pore pressure using Eaton exponent of 5 (instead of 3) . (a) NM-1, (b) SM-30.

Chapter 3:

Origins of Overpressure in the Malay Basin

3.1 Introduction

The origins of overpressure have been studied and grouped into several main classes by various workers. Hall (1993) described the generation of overpressure by either internal or external processes, while Bowers (1995) described the mechanisms as disequilibrium compaction (loading) and fluid expansion (unloading). Swarbrick & Osborne (1998) discussed the mechanisms as result either from stress, fluid volume expansion or fluid movement and buoyancy. Slavin & Smirnova (1998) preferred grouping the mechanisms into synsedimentary processes against post-sedimentary processes. Deming et al. (2002), following discussion by Bredehoeft et al. (1994), summarized two different thought processes responsible for overpressure development. He referred to them as 'static' and 'dynamic'. Static refers to overpressure generated as a result of the presence of pressure seals or barriers, while dynamic refers to overpressure that has resulted from imbalance between pressure generation and pressure dissipation, in which the presence of barrier is not a necessity.

The aim of this chapter is to discuss the origin of overpressure in the Malay Basin. The chapter is divided into four parts. The first part reviews various overpressure generating mechanisms that have been published. The second part deals with characteristic features of these processes, identifiable through wireline logs and downhole measurements. The third part discusses the observations from the Malay Basin and the deductions about the origins of overpressure. The final part highlights the significance of chemical compaction on overpressure study in the basin.

3.2 Causal Mechanisms

A brief description of published schemes for overpressure-generating mechanisms is given in Table 3.1

Table 3.1 Some of the published examples of the proposed origins for overpressure in sedimentary basins.

Reference	Study Areas	Note
Disequilibrium Compaction		
Bredehoeft & Hanshaw (1968)	Gulf Coast	Disequilibrium compaction
Mudford & Best (1989)	Venture Field, Nova Scotia	Minor contribution from hydrocarbon generation
Burrus, Schneider & Wolf (1994)	North Sea, Norway Gulf Coast Mahakam Delta	Compaction disequilibrium responsible for at least 80% of the observed overpressure
Buryakorvsky, Djevanshir & Chilingar (1995)	Caspian Sea	Due to high sedimentation rate and high argillaceous rocks
Hart, Flemings & Despande (1996)	Eugene Island block 330, Gulf Coast	Disequilibrium compaction accounts for 75% of the observed overpressure
Gordon & Fleming, 1998	Gulf of Mexico	Sediment loading.
Yardley, 1998	Central Graben, North Sea	As result of rapid Late Tertiary burial, rather than lateral transfer.
Harrold, Swarbrick & Goulty (1999)	Southeast Asia	Disequilibrium compaction
Fluid Expansion		
Alnes & Lilburn (1998)	Gulf Coast	Dynamic aquathermal expansion
Hydrocarbon Generation		
Spencer, 1987	Rocky Mountains	Volume expansion when kerogen matures to oil, and later to gas
Hunt, Whelan, Eglinton & Cathles (1994)	U.S. Gulf Coast	Gas generation as main causes of overpressure
Zaunbrecher (1994)	Barrow and Exmouth sub-basins, Australia	Mainly hydrocarbon generation with some contribution from disequilibrium compaction
Burrus, Osadetz, Wolf, Doligez, Visser & Dearborn (1996)	Williston Basin	Overpressure in organic-rich Bakken shales are due to hydrocarbon generation
Holm, 1996	Central Graben	In Kimmeridge Clay source rock
Marco-Toledo, Stumpf-Verney & Fontes (1998)	Campos Basin	Mainly hydrocarbon generation and complemented by disequilibrium compaction
Lee & Deming (2002)	Anardako Basin	Overpressure from gas generation with gas capillary seals.
Tectonic		
Kho, Hemmings & Have (1994)	Baram Delta, Malaysia	Inflation overpressure caused by shale diapirism
Yassir & Bell (1996)	Beaufort-Mackenzie Basin, Canada	Lateral tectonic compression
Hennig, Yassir, Addis & Warrington (2002)	Papua New Guinea	Tectonic compression
van Ruth, Hillis, Tingate	Cooper Basin, Australia	Horizontal stress

& Swarbrick (2003)		
Clay Diagenesis		
Bruce (1984)	Gulf of Mexico	Smectite to illite
Lahann et al. (2001)	U.S. Gulf Coast	Smectite to illite transformation
Multiple Origins/ Others		
Buhrig (1989)	Viking Graben	Rapid loading, aquathermal pressuring and hydrocarbon generation in a relatively closed system
Ward, Coghill & Broussard (1994).	Central Graben, North Sea	Disequilibrium compaction (above ~3.5 km) and fluid expansion mechanisms (below 3.5 km)
Wensaas, Shaw, Gibbons, Aagaard & Dypvik (1994)	Gullfaks Area, North Sea	Disequilibrium compaction and gas leakage form Jurassic reservoirs.
Mantaring, Matsuda & Okamoto (1994)	Baram Delta, Malaysia	Undercompacted claystone, uplifted reservoirs and fluid-transfer in shallower sand intervals.
Howes (1998)	NW Java, Indonesia	Hydrocarbon column, compaction disequilibrium, kerogen transformation and hydraulic head
Lander, 1998	North Sea	Diagenetic alteration of sandstones as possible causes

3.2.1 Disequilibrium Compaction

Normal pore pressure is achieved when the pore pressure is in static equilibrium up to the surface. During low sedimentation rates, fluid can be expelled fast enough to maintain hydrostatic equilibrium. When this balance is upset by a high rate of sedimentation in combination with low permeability overburden, overpressure is developed. In this situation, the compaction process is halted or retarded, resulting in undercompaction. These process is commonly referred to as disequilibrium compaction. The overpressure means that less of the overburden load is supportedly by the matrix than in a normally pressured sediment, reducing the grain-to-grain contact stress (also termed "effective stress"). Loading stresses are applied to the sediment in vertical and horizontal direction. Vertical loading is due to sediment weight. Horizontal confining stresses arises from gravitational loading during passive subsidence, but additional horizontal stresses may be superimposed by tectonic compression (Yassir, 1998, van Ruth et al., 2003). Sheldon & Wheeler (2003) pointed out that changes in pore fluid chemistry as a result of pressure solution could also lead to a increase in horizontal stress.

Disequilibrium compaction has been acknowledged by many workers to be the

most dominant cause of overpressure (Table 3.1). Rapidly subsiding basins containing low permeability sediments such as Tertiary deltas on continental margins, are typical environments for overpressure generated by disequilibrium compaction. Disequilibrium compaction may also be triggered as a result of seal formation or faulting that prevents efficient dewatering. Seals may be formed by illitisation in shales (Freed & Peacor, 1989), by capillary sealing by gas (Revil et al., 1998), or by mineral diagenesis, such as quartz dissolution and precipitation resulting in seal banding (Tigert & Al-Shaieb, 1990).

3.2.2 Volume Change or Unloading

There are several processes that may contribute to the increase in fluid volume. These include hydrocarbon generation (Meissner, 1978; Barker, 1990), clay dehydration (Burst, 1959; Bruce, 1984; Colten-Bradley, 1987), aquathermal expansion (Barker, 1972), lateral transfer (Traugott, 1996; Stump et al., 1998; Yardley & Swarbrick, 2000) and osmosis. These processes could potentially lead to a reduction in effective stress without any increase in porosity. With exception of hydrocarbon generation particularly gas, many of these volume change reactions produce very small amounts of overpressure (Swarbrick & Osborne, 1998; Swarbrick et al., 2002).

3.2.3 Others

Several others processes have been proposed. These processes are minor and are unlikely to have generated significant overpressure in the Malay Basin. They include hydraulic head, buoyancy (and uplift and erosion).

3.3 Wireline Log Characteristics

The characteristics of overpressure on wireline log responses relate to the relationship between sediment porosity and pore pressure (Swarbrick, 2002). Where disequilibrium compaction is the generating mechanism, porosity is higher than expected for normally pressured sediment at the same depth. Assuming continuous

burial, the porosity will correspond to current effective stress.

However, where fluid volume expansion is involved, the effective stress is likely to have been higher that at present, with the volume increase having reduced effective stress and only a very small increase in porosity related to the elasticity of the sediment.

The observed discrepancy between the predicted pore pressure from the equivalent depth method (EDM) and measured formation pressure has been used as an indication of additional pressuring mechanisms besides disequilibrium compaction (Hart et al., 1995; Mudford, 1988). Bowers (2001) and Lahann (2002) have adopted a more sophisticated method involving a velocity-density cross plot to differentiate between overpressure that arises from disequilibrium compaction and fluid expansion mechanisms (Bowers, 2001) and/or clay diagenesis (Lahann, 2002).

3.3.1 Normal Compaction

The characteristics of overpressured sediments can be viewed by understanding the mechanics of compaction. In normally compacted rocks, the porosity loss in fine-grained sediments is primarily driven by mechanical compaction involving increases in effective stress at grain contacts, due to both increasing gravitational loading stress during burial and superimposed changes in horizontal (tectonic) stress related to fluctuating plate stresses. Where the pore pressure remains normal, on the hydrostatic pressure gradient (Figure 3.1a), the reduction in porosity with depth takes place along the "normal compaction curve" (Figure 3.1c). The normal compaction behaviour for shale mudrocks is largely controlled by its clay fraction, i.e. the proportion of rock volume less than two microns grain size (Aplin et al., 1995). Density and velocity, which are related to porosity, will also follow the normal compaction curve. Examples of the published velocity-density relationships for shale are:

Gardner et al. (1974) $\rho = 1.75\ V^{0.265}$

Castagna et al. (1993) $\rho = -0.0261V^2 + 0.373V + 1.458$

where

ρ = density (g/cm^3)

V = velocity (km/s)

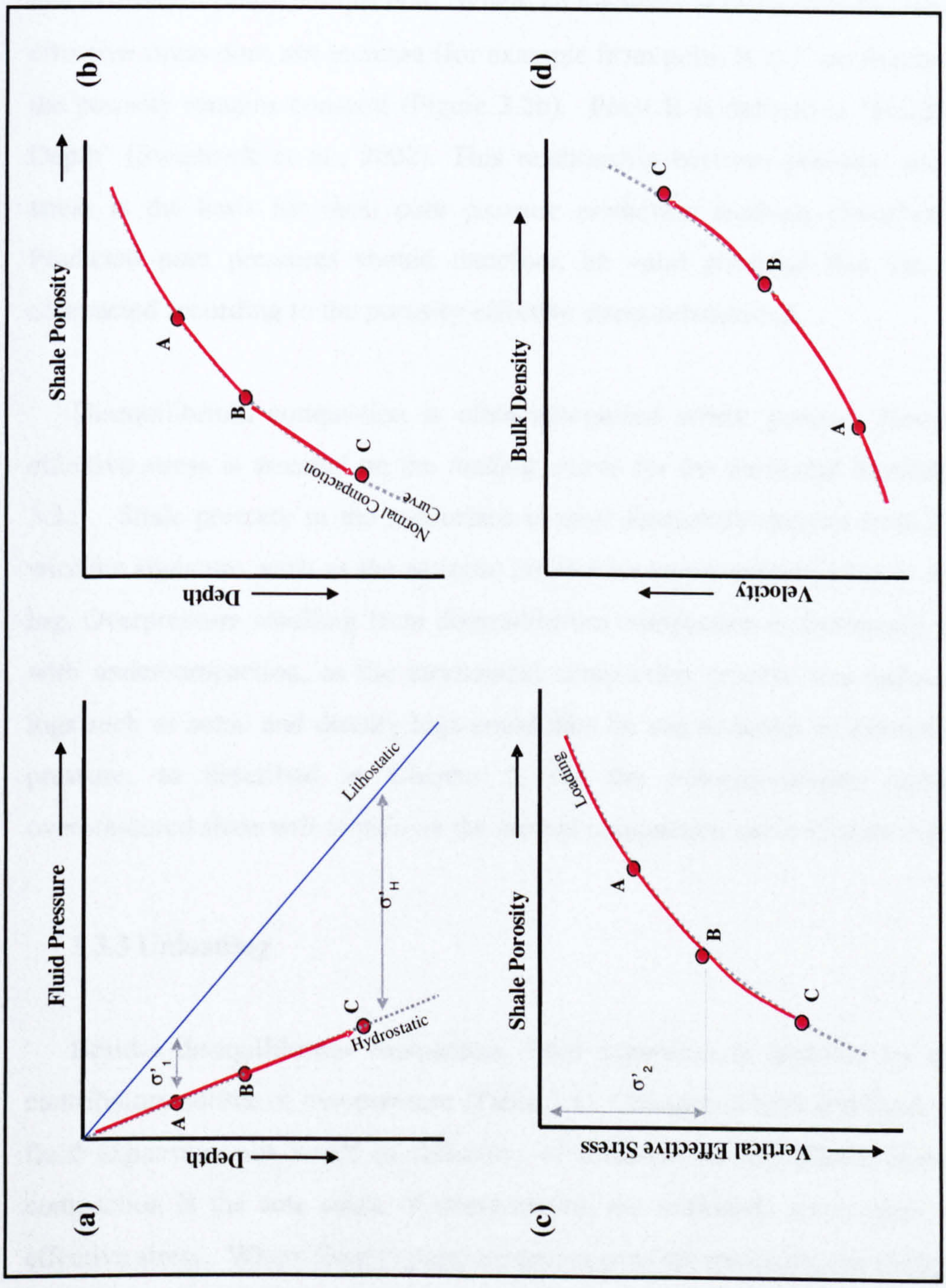


Figure 3.1 Schematic historical path for shales undergoing normal compaction: (a) fluid pressure versus depth, (b) shale porosity versus depth, (c) shale porosity versus vertical effective stress, (d) bulk density versus velocity. Points A,B and C represent different stages of sedimentary burial (see text for explanation).

3.3.2 Disequilibrium Compaction

Where low permeability prevents complete dewatering, the effective stress is lower than expected for the depth of burial. The resulting overpressure is therefore due to disequilibrium compaction. Where all the water is retained in the sediment, the effective stress does not increase (for example from point B to C on Figure 3.2a) and the porosity remains constant (Figure 3.2b). Point B is defined as 'Fluid Retention Depth' (Swarbrick et al., 2002). This relationship between porosity and effective stress is the basis for most pore pressure prediction methods (Swarbrick, 2002). Predicted pore pressures should therefore, be valid provided that the sediments compacted according to the porosity-effective stress relationship.

Disequilibrium compaction is often recognised where porosity plotted against effective stress is arrested on the loading curve for the particular lithology (Figure 3.2c). Shale porosity in the subsurface is most frequently derived from a borehole wireline signature, such as the acoustic travel time (sonic velocity) log or the density log. Overpressure resulting from disequilibrium compaction is commonly associated with undercompaction, as the mechanical compaction process was halted. Porosity logs such as sonic and density logs could then be use to detect or estimate the pore pressure, as described in Chapter 2. On the velocity-density crossplot, the overpressured shale will remain on the normal compaction curve (Figure 3.2d).

3.3.3 Unloading

Besides disequilibrium compaction, fluid expansion is regarded by many as a contributory source of overpressure (Table 3.1). Changes in rock and fluid volume by fluid expansion can result in reduction of effective stress. Where disequilibrium compaction is the sole cause of overpressure, the sediments are at their maximum effective stress. Where fluid expansion mechanisms are the cause, the sediments have been at a higher effective stress in the past. These mechanisms are referred to as "unloading" mechanisms by Bowers, (1995).

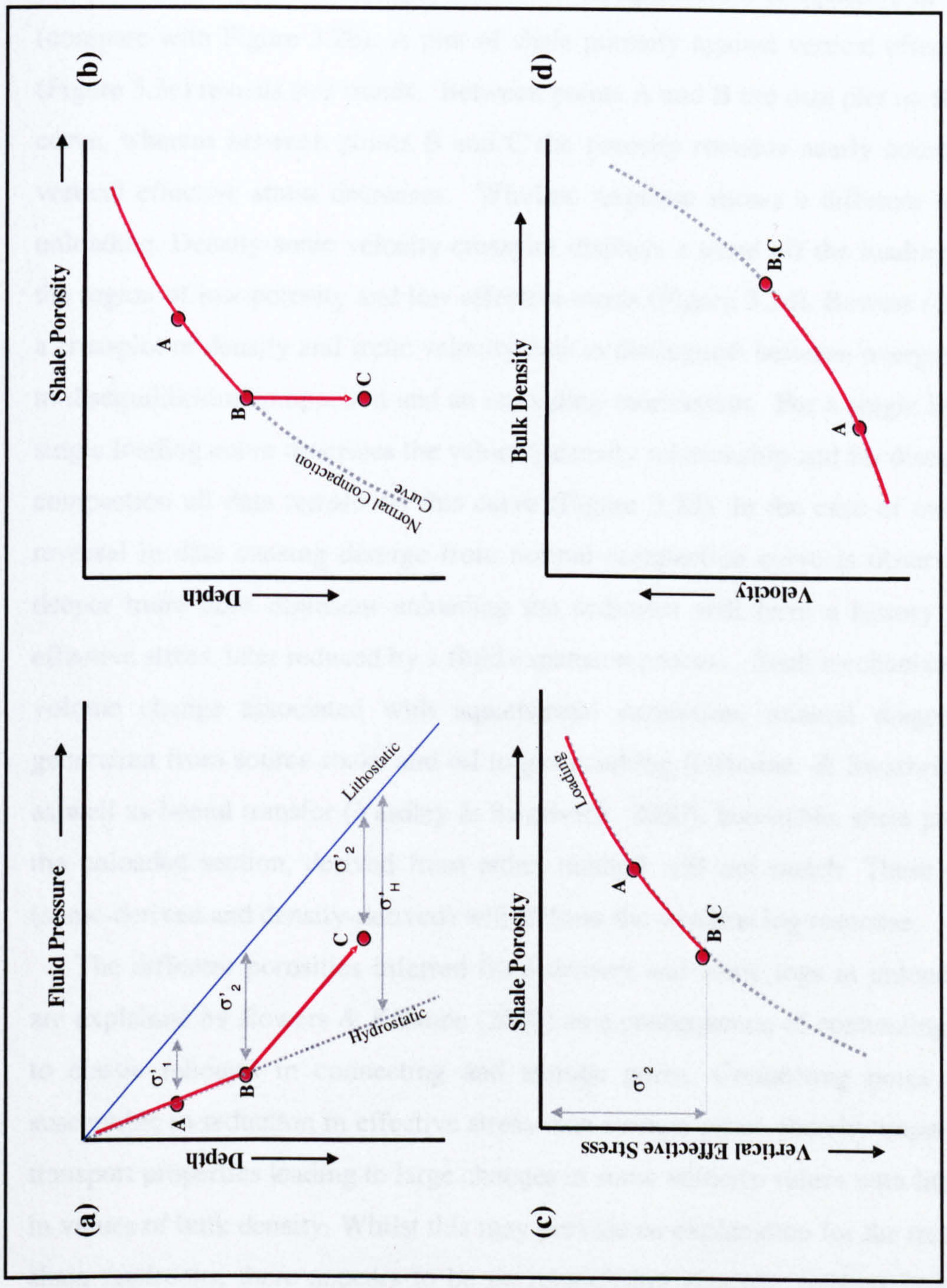


Figure 3.2 Schematic evolutionary path expected for overpressured shales that undergoing disequilibrium compaction (red): (a) fluid pressure versus depth, (b) shale porosity with depth, (c) shale porosity versus vertical effective stress, (d) bulk density versus velocity. Grey dots/lines represent expected trend for normally compacted rocks. Points A,B and C represent different stages of sedimentary burial (see text for explanation).

A pore pressure profile in which the effective stress reduces with increasing depth is shown in Figure 3.3a. Provided that the lithology remains the same, the transition zone between points B and C is due to a contribution to the overpressure from unloading. A plot of density-derived shale porosity against depth (Figure 3.3b) does not differentiate between overpressure from disequilibrium compaction or unloading (compare with Figure 3.2b). A plot of shale porosity against vertical effective stress (Figure 3.3c) reveals two trends. Between points A and B the data plot on the loading curve, whereas between points B and C the porosity remains nearly constant as the vertical effective stress decreases. Wireline response shows a different trend from unloading. Density-sonic velocity crossplot displays a trend off the loading curve in the region of low porosity and low effective stress (Figure 3.3d). Bowers (1995) used a crossplot of density and sonic velocity data to distinguish between overpressure due to disequilibrium compaction and an unloading mechanism. For a single lithology, a single loading curve describes the velocity-density relationship and for disequilibrium compaction all data remain on this curve (Figure 3.2d). In the case of unloading, a reversal in data causing diverge from normal compaction curve is observed. If the deeper trend does represent unloading the sediment will have a history of higher effective stress, later reduced by a fluid expansion process. Such mechanisms include volume change associated with aquathermal expansion, mineral diagenesis, gas generation from source rocks and oil to gas cracking (Osborne & Swarbrick, 1997), as well as lateral transfer (Yardley & Swarbrick, 2000). Inevitable, shale porosity for the unloaded section, derived from either method will not match. These porosities (sonic-derived and density-derived) will follows the wireline log response.

The different porosities inferred from density and sonic logs in unloaded shales are explained by Bowers & Katsube (2002) as a consequence of contrasting response to elastic rebound in connecting and storage pores. Connecting pores are more susceptible to reduction in effective stress than storage pores, thereby impacting their transport properties leading to large changes in sonic velocity values with little change in values of bulk density. Whilst this may provide an explanation for the trend seen in shale mudrocks, there appears to be no relationship between velocity and effective stress in chalk mudrocks (Lubanzadio et al., 2002).

Fluid expansion mechanisms for overpressure reduce the principal effective stresses, with only recovery of the elastic component of compaction. The shortfall

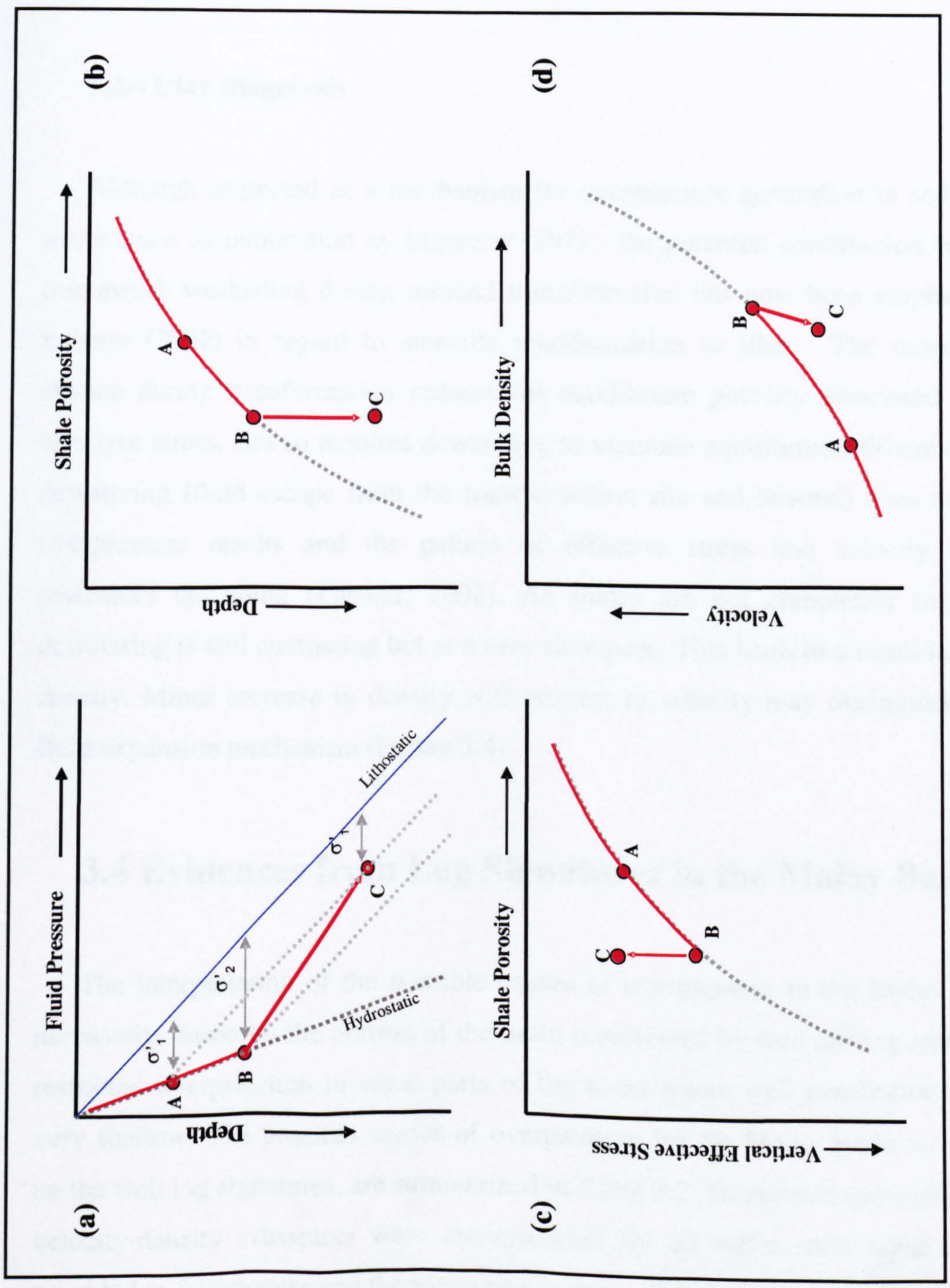


Figure 3.3 Schematic evolutionary path expected for overpressured shales that results from unloading: (a) fluid pressure versus depth, (b) shale porosity with depth, (c) shale porosity versus vertical effective stress, (d) bulk density versus velocity.

between the measured and predicted pore pressure have been used as an estimation of the contribution to the overall overpressure resulting from fluid expansion. Hart et al. (1995), for example, estimated that about 25 % of the overpressure in a Gulf Coast well may be attributed to an unspecified fluid expansion process.

3.3.4 Clay Diagenesis

Although neglected as a mechanism for overpressure generation in sedimentary rocks since its publication by Meissner (1978), the potential contribution from rock framework weakening during mineral transformation has now been emphasised by Lahann (2002) in regard to smectite transformation to illite. The mineralogical change during transformation reduces the equilibrium porosity associated with the effective stress, and so requires dewatering to maintain equilibrium. Where complete dewatering (fluid escape from the transformation site and beyond) does not occur, overpressure results and the pattern of effective stress and velocity variation resembles unloading (Lahann, 2002). As shales are not completely impervious, dewatering is still continuing but at a very slow pace, This leads to a small increase in density. Minor increase in density with respect to velocity may distinguish it from fluid expansion mechanism (Figure 3.4).

3.4 Evidences from Log Signatures in the Malay Basin

The interpretation of the possible causes of overpressure in the Malay Basin is necessarily based on the portion of the basin represented by well drilling results. This restricted interpretation in some parts of the basin where well penetration has been very shallow. The possible causes of overpressure for the Malay Basin wells, based on the well log signatures, are summarized in Table 3.2. To assist in the interpretation, velocity-density crossplots were reconstructed for all wells, with some examples provided in this chapter and the remaining wells included in Appendix D.

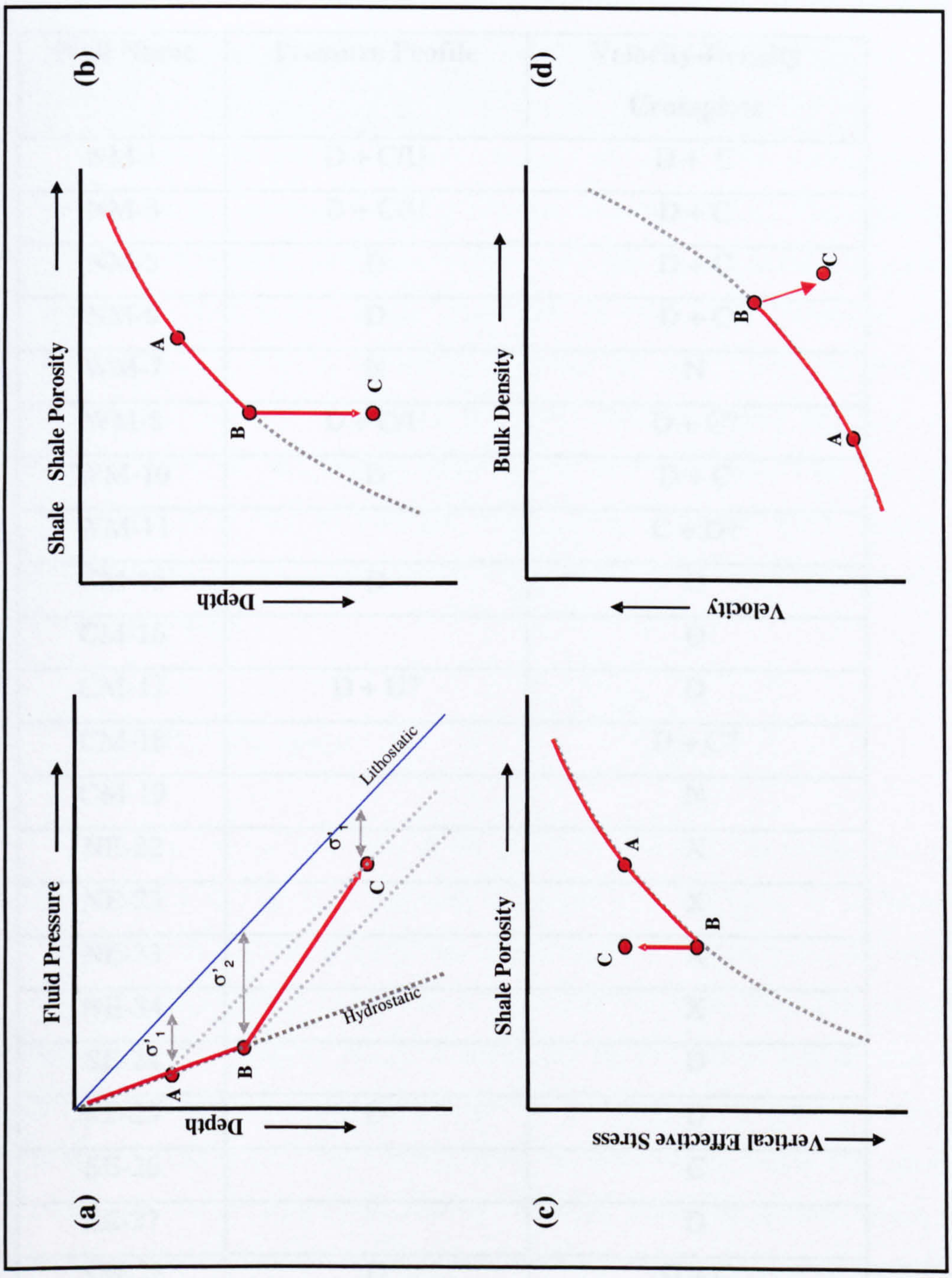


Figure 3.4 Example of possible trends expected from overpressured shales undergoing clay diagenesis: (a) fluid pressure versus depth, (b) shale porosity versus depth, (c) shale porosity versus vertical effective stress, (d) bulk density versus velocity from sonic transit times.

Table 3.2 Interpretation of the origins of overpressure for the Malay basin wells, based on shale pore pressure profile and velocity-density crossplots. D-disequilibrium compaction; U-unloading; C-chemical compaction; N-normal compaction; X-not determinable.

Well Name	Pressure Profile	Velocity-Density Crossplots
NM-1	D + C/U	D + C
NM-3	D + C/U	D + C
NM-5	D	D + C
NM-6	D	D + C
WM-7	N	N
WM-8	D + C/U	D + C?
WM-10	D	D + C
WM-11		C + D?
CM-15	D	D
CM-16		D
CM-17	D + U?	D
CM-18		D + C?
CM-19		N
NE-22		X
NE-23		X
NE-33		X
NE-34		X
SE-24		D
SE-25	D	D
SE-26		C
SE-27		D
SM-28	D	D + C
SM-29	D	D
SM-30	C + D	C + D
SM-31	C + D	C+ D

3.4.1 Disequilibrium Compaction

Since disequilibrium compaction process involves only mechanical compaction, predicted pore pressure using EDM methods for wells undergoing this process should fit with the formation pressure. Wells that gave a close match between the predicted and measured pore pressure are CM-15, CM-16, CM-17, SE-25, and SE-27.

An example of velocity-density crossplot for well SE-25 is shown on Figure 3.5. To help recognise broad trends in the data from well SE-25, averaged data using a smoothing filter were plotted as in the pore pressure estimations. In addition, upper and lower bounds are shown, these are derived from Gardner's and Bower's relationships for velocity to density in shales (Bowers, 2001). Estimated downhole temperatures are also included on the plots. Data from well SE-25 show no major reversal from the compaction trend. Scatter in the datapoints for the interval from 7000-8000 ft is due to enlarged borehole (as evidence from caliper log). The overpressured shales (depth below 8000 ft) are shown on the plot to remain on compaction trend.

3.4.2 Fluid Expansion

Velocity-density crossplots of the overpressured shale do display unloading trend (faster drops in velocity compared to density) as in Figure 7c in Bowers (2001). However, velocity and density data plotted against vertical effective stress for some wells do show the characteristic of an unloading limb. Examples of velocity and density against vertical effective stress for NM-1, NM-3, SM-28 and SM-30 are shown in Figure 3.6. Scatter in the hydrostatically pressured sections reflect variations in shale composition. The vertical effective stress for the shales was estimated using direct pressure measurements from the adjacent sandstone section, which is within $\pm$ 10 feet of the pressure measurements (with the exception of well D, $\pm$ 50 feet), i.e. assumes equilibration of pore pressures between sandstone and shale. The plots show that the deeper, overpressured shales in each well lie on the unloading curves, at lower effective stress. These plots appear to suggest an unloading origin for the overpressure. What is striking, however, is that in all cases the density of the deeper

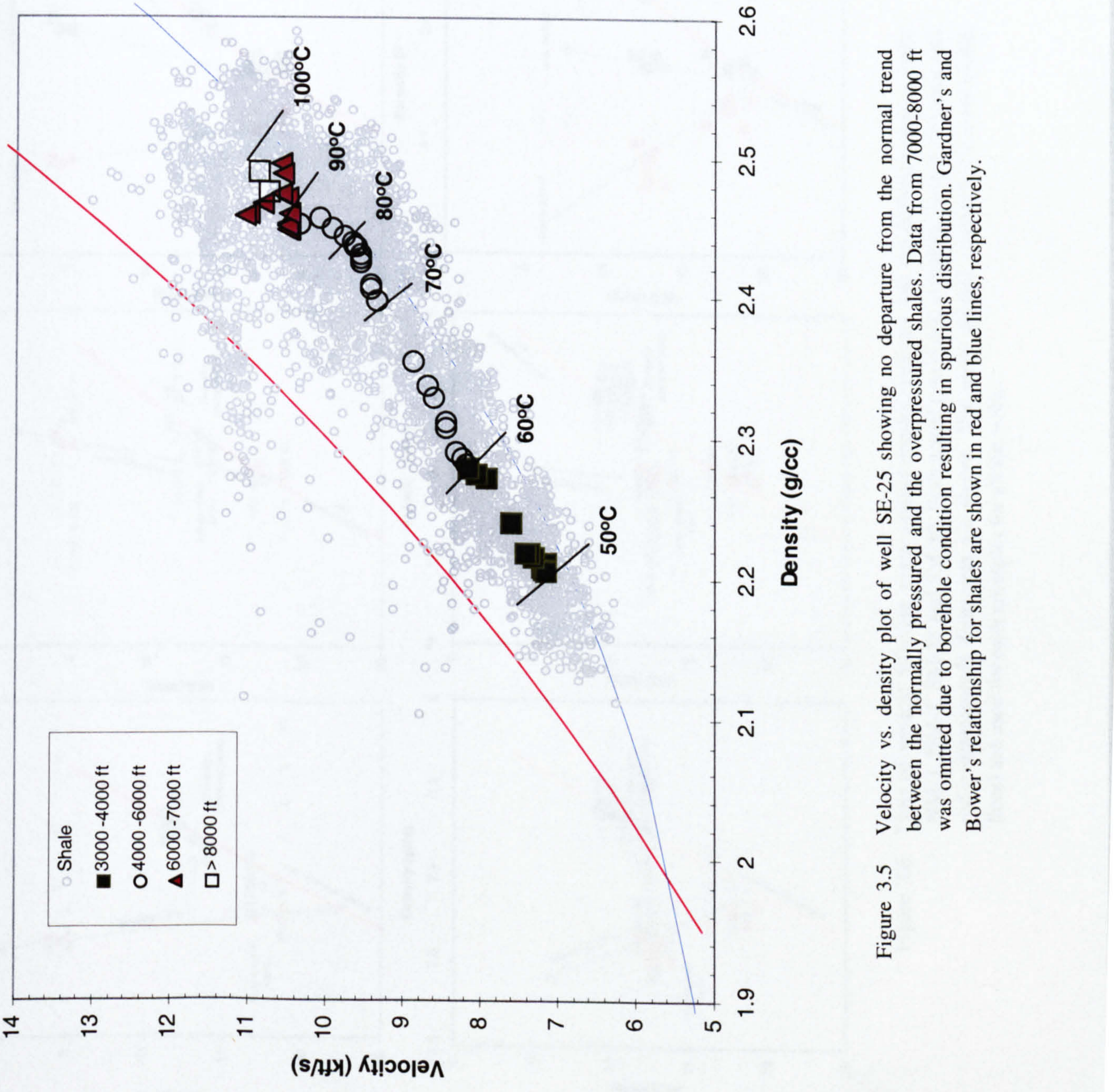


Figure 3.5 Velocity vs. density plot of well SE-25 showing no departure from the normal trend between the normally pressured and the overpressured shales. Data from 7000-8000 ft was omitted due to borehole condition resulting in spurious distribution. Gardner's and Bower's relationship for shales are shown in red and blue lines, respectively.

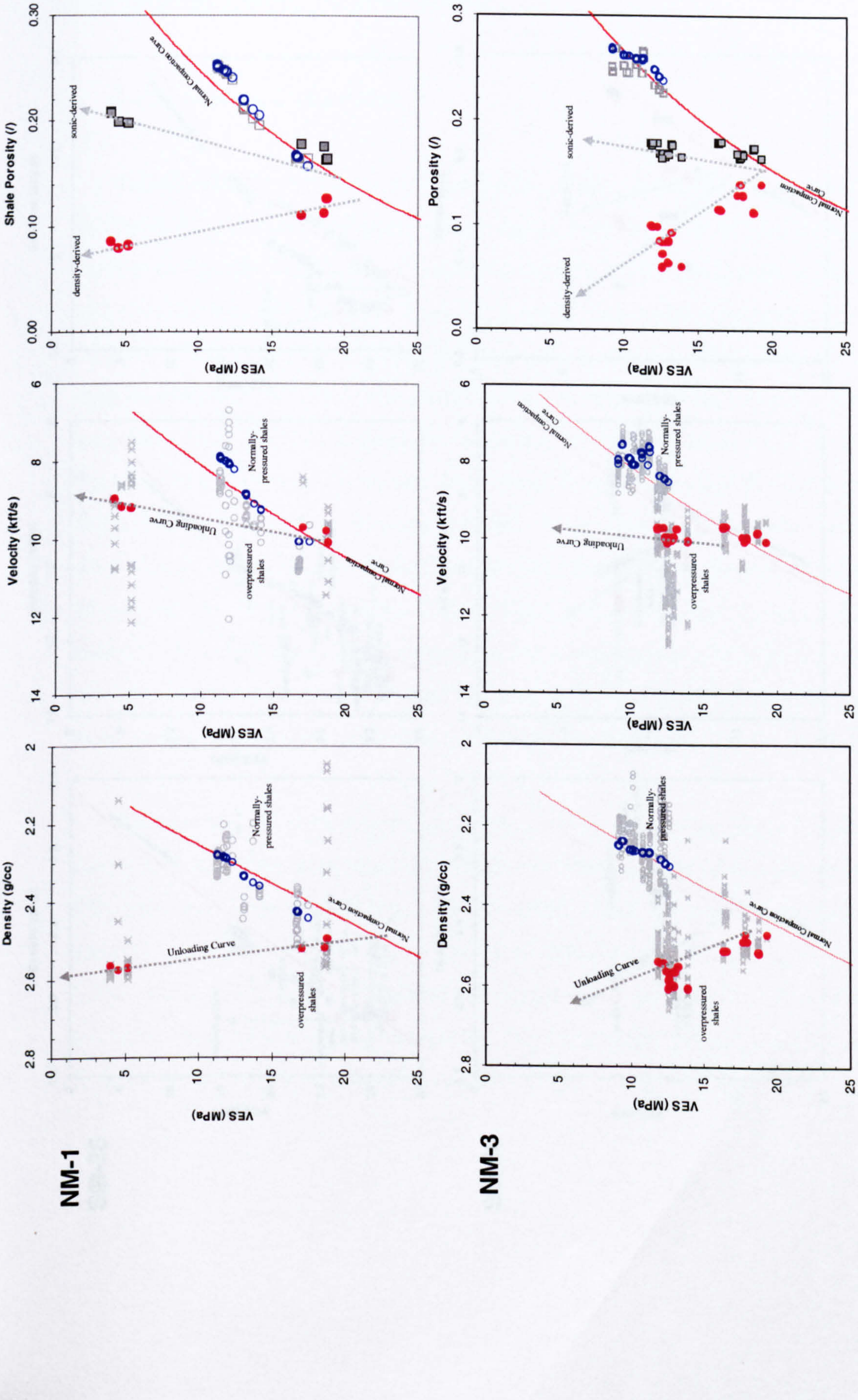


Figure 3.6 Plots of vertical effective stress against density, velocity and log-derived porosity wells NM-1, NM-3, SM-28 and SM-30. Both actual (grey) and averaged (blue-hydrostatic and red-overpressured) datapoints are shown. The same normal compaction curves (solid lines) are used for each crossplot for all the wells.

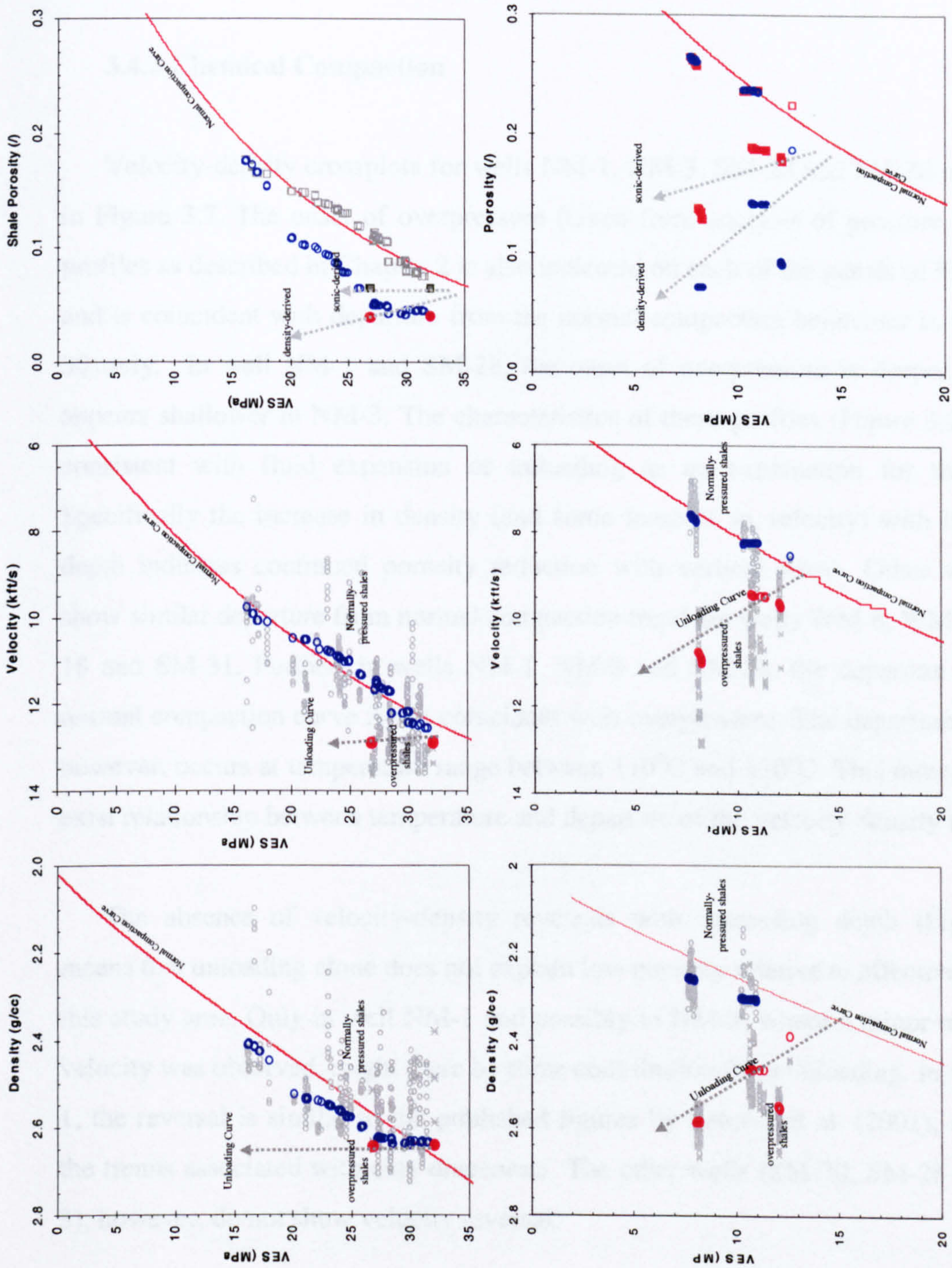


Figure 3.6 Continued.

sediments increases as the overpressure increases, creating a strong departure between the velocity and density responses, as shown in the shale porosity vs. vertical effective stress plot (Figure 3.6c). The observed increase in density is more consistent with mineral diagenesis than volume expansion.

3.4.3 Chemical Compaction

Velocity-density crossplots for wells NM-1, NM-3, SM-28 and SM-30 are shown in Figure 3.7. The onset of overpressure (taken from analysis of pressure vs. depth profiles as described in Chapter 2 is also indicated on each of the panels of Figure 3.7, and is coincident with departure from the normal compaction behaviour in well SM-30 only. In well NM-1 and SM-28, the onset of overpressure is deeper, while it appears shallower in NM-3. The characteristics of these profiles (Figure 3.7) are not consistent with fluid expansion or unloading as an explanation for the trends. Specifically the increase in density (and some increase in velocity) with increasing depth indicates continued porosity reduction with vertical stress. Other wells that show similar departure from normal compaction trend are wells WM-8, WM-10, CM-18 and SM-31. Further, in wells NM-1, NM-3 and SM-28, the departure from the normal compaction curve is not coincident with overpressure. The departure in trend, however, occurs at temperature range between 110°C and 120°C. This indicates there exist relationship between temperature and departure of the velocity-density trend.

The absence of velocity-density reversals with increasing depth (Figure 3.7) means that unloading alone does not explain low porosity relative to effective stress in this study area. Only in well NM-1 and possibly in NM-3, where a minor reversal in velocity was observed, might there be some contribution from unloading. In well NM-1, the reversal is similar to the published figures by Lahann et al. (2001), similar to the trends associated with clay diagenesis. The other wells (SM-30, SM-28 and NM-3), however, do not show velocity reversal.

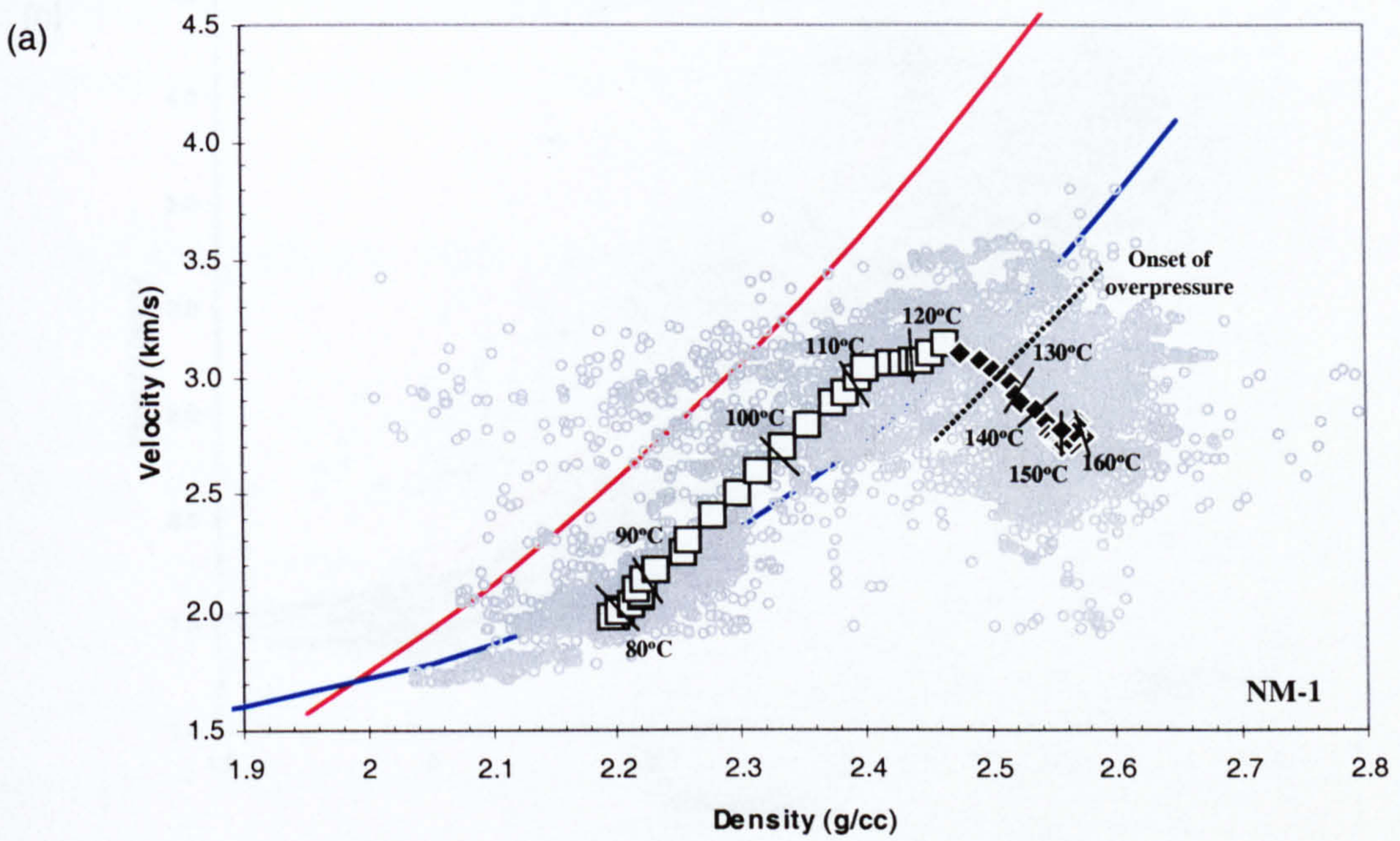
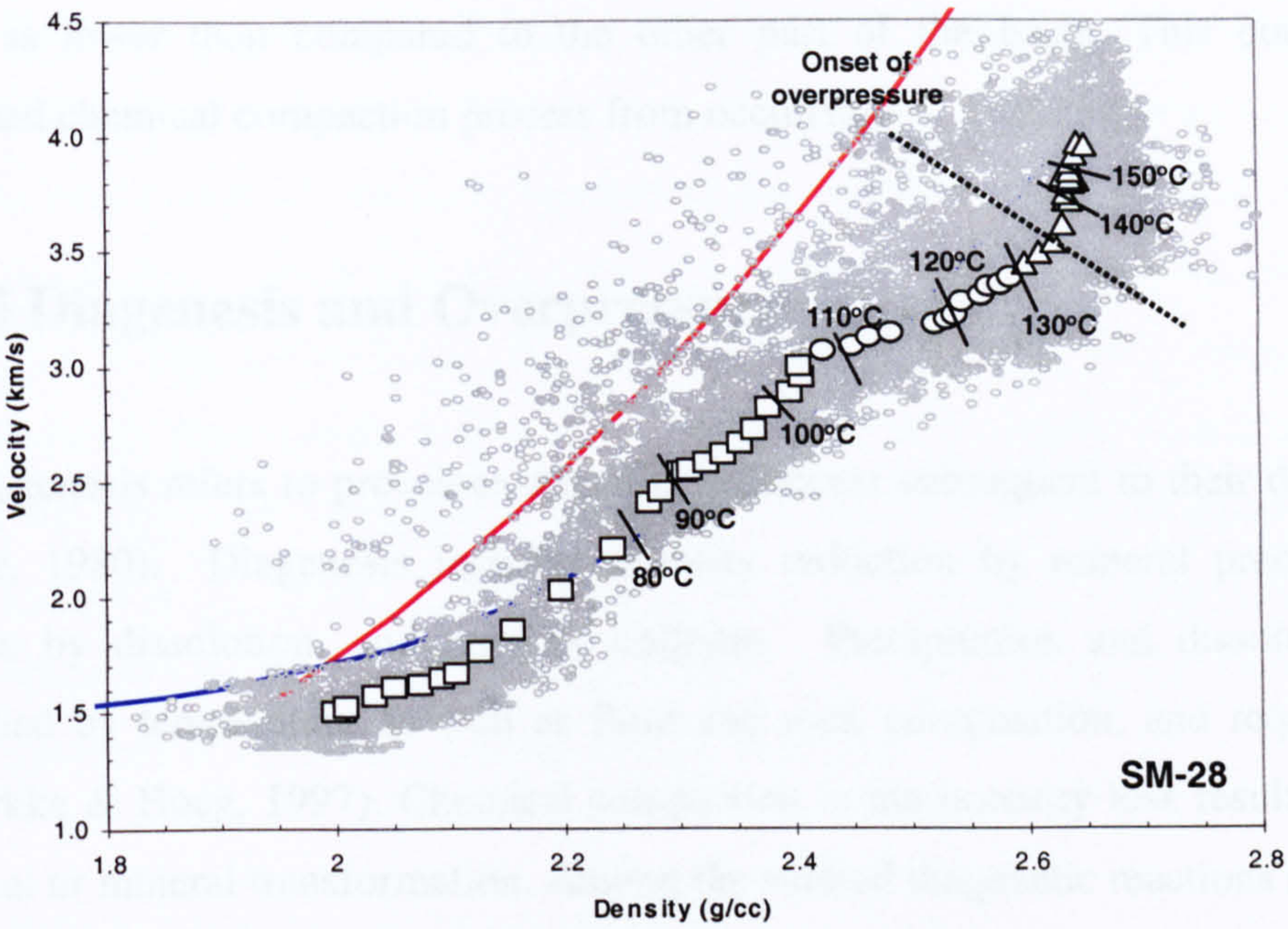


Figure 3.7 Velocity vs. density crossplots for wells (a) NM-1, (b) NM-3, (c) SM-28 and (d) SM-30. Grey dots represent actual log values and the symbols representing averaged log values to help visualizing the compaction trends. Also plotted on the trend are the estimated borehole temperature and the onset of the overpressure. Red and blue lines are Gardner's and Bower's relationship for shales, respectively.

(c)



(d)

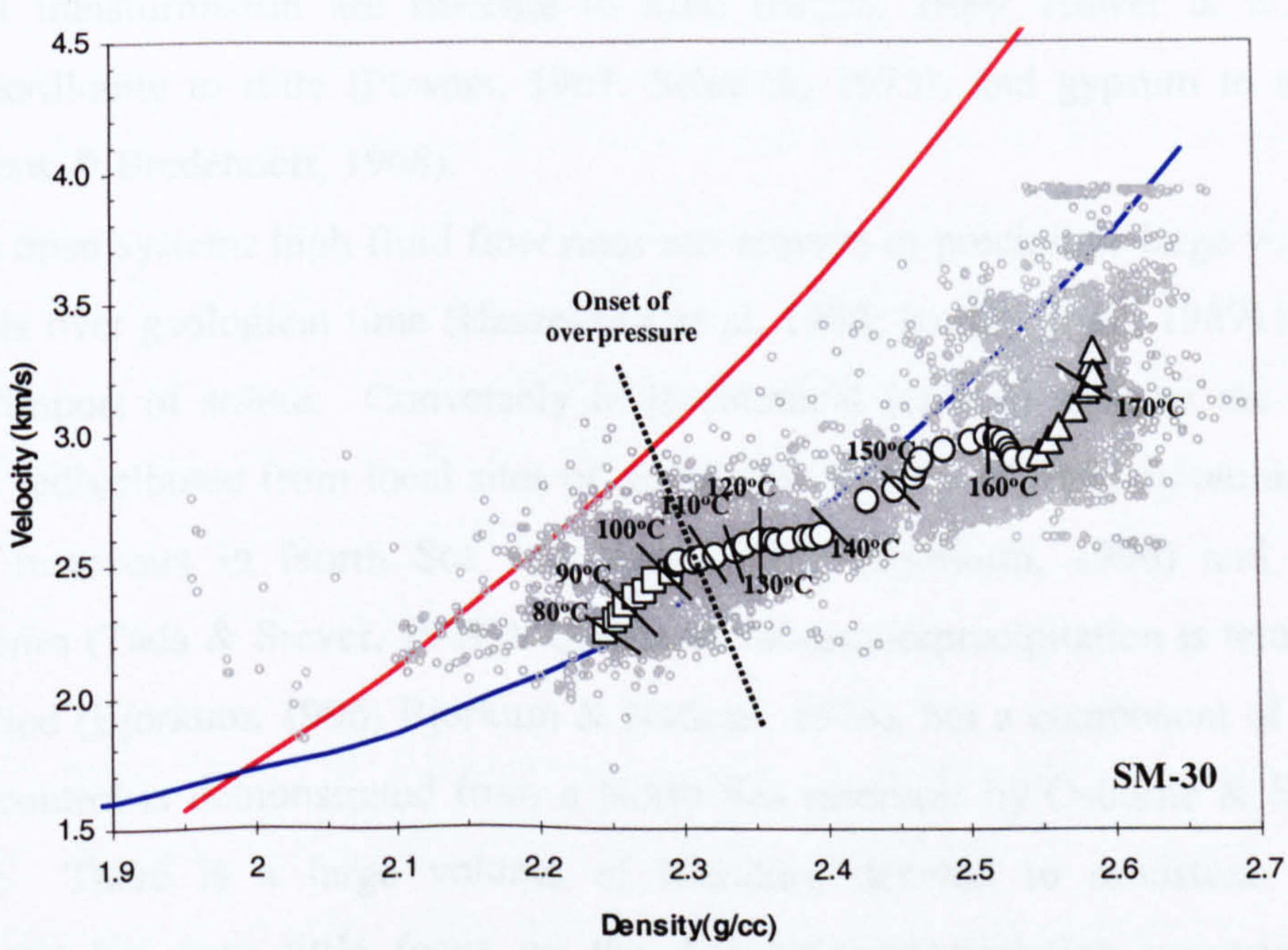


Figure 3.7 Continued.

Wells from Central Malay do not show any sign of clay diagenesis or chemical compaction, although the area exhibits high geothermal gradient, which could promotes chemical compaction. On the hand, geothermal gradient in the Southeast Malay is lower than compared to the other part of the basin. This could have prevented chemical compaction process from occurring.

3.5 Diagenesis and Overpressure

Diagenesis refers to processes affecting sediments subsequent to their deposition (Berner, 1980). Diagenesis includes porosity reduction by mineral precipitation, increase by dissolution, and porosity collapse. Precipitation and dissolution are controlled by temperature as well as fluid and rock composition, and require time (Bjorlykke & Hoeg, 1997). Chemical compaction is the porosity loss resulting from chemical or mineral transformation. Among the studied diagenetic reactions involving mineral transformation are smectite to illite (Bruce, 1984; Hower et al., 1976), montmorillonite to illite (Powers, 1967; Schmidt, 1973), and gypsum to anhydrite (Hanshaw & Bredehoeft, 1968).

In open systems high fluid flow rates can remove or precipitate large volumes of minerals over geological time (Haszeldine et al, 1984; Burley et al., 1989) involving export/import of solute. Conversely in isochemical (closed) systems the solute is merely redistributed from local sites of dissolution to sites of reprecipitation (e.g., in quartz reservoirs in North Sea and mid-Norway (Bjorkum, 1996) and in chalk limestones (Tada & Siever, 1989)). Quartz dissolution/reprecipitation is temperature-controlled (Bjorkum, 1996; Bjorkum & Nadeau, 1998), but a component of effective stress control is demonstrated from a North Sea reservoir by Osborne & Swarbrick (1999). There is a large volume of literature devoted to sandstone reservoir diagenesis but very little focus on the dissolution/precipitation occurring within shales. The complex chemical alterations taking place in shales are not well understood. Lahann et al. (2001), however, have studied the smectite to illite transformation in shales in relation to stress, and concluded that the vertical effective stress is reduced as a consequence of redistribution of load during transformation.

In an open or partially open system, chemical diagenesis promotes redistribution of mass between shales and sandstones. The transfer of potassium and aluminium from the dissolution of K-feldspar in the sandstone facilitates precipitation of illite and quartz within the shales (Awwiller, 1993). These movements can be by advection or diffusion (Haszeldine, et al., 1984; Thyne, 2001). In a closed system, dissolution of a less stable mineral results in precipitation of a more stable mineral elsewhere within the shales. Dissolution processes within the system weaken the framework leading to further compaction. The precipitation of cement will strengthen the framework but significantly reduce the permeability or hydraulic conductivity and prevent dissipation of overpressure (Bjorkum & Nadeau, 1998; Tenthorey, et al., 1998; Nadeau et al., 2002). This pressure sealing will further enhance overpressure during continued burial as fluid retention is improved when loading continues, as well as any contribution from other fluid expansion processes.

3.5.1 Shale Diagenesis in Malay Basin

The geothermal gradient in the Malay Basin is high at 50°C/km, leading to temperatures of over 100°C at depths of only 1.5 km. For the shales in each well, the temperatures are indicated on Figure 3.7. What is striking in all cases is the departure from the mechanical compaction trends at temperatures between 100 to 120°C. High temperatures have been shown to promote porosity reduction, resulting in rapid degradation of reservoirs (Trevena & Clark, 1986; Worden et al., 1997). There is no comparable literature on shales.

O'Brien & Slatt (1990) examined a suite of geopressured samples under a scanning electron microscope (SEM) and found randomness in shale fabrics within the geopressured section. This randomness in fabric orientation resulted from undercompaction, with high fluid pressure preventing further collapse of the clay framework. Naturally, similar observations would be expected for the suite of samples from well SM-30.

Shale cuttings from well SM-30 were examined with an SEM in order to study microstructures and fabrics of the samples. The cuttings were broken perpendicular to

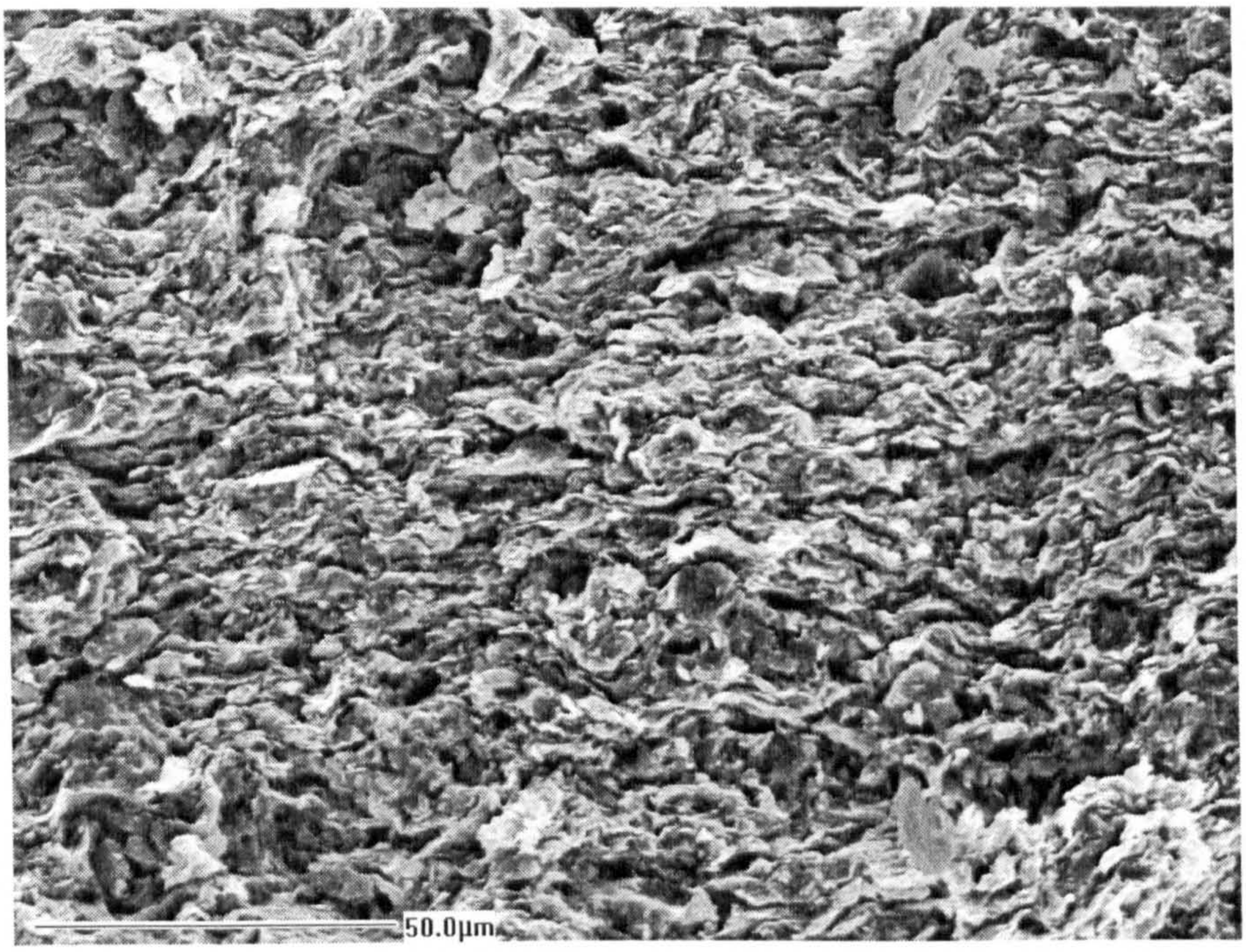
the bedding and glued on to the SEM stubs before coating with gold. The minerals were identified using energy dispersive x-ray analysis (EDX). SEM results show that the shale fabric for the deeper overpressured sequence (Figure 3.9) has more strongly oriented clays compared to the shallower overpressured sequence (Figure 3.8). These observations suggest that the deeper sequence is not undercompacted, consistent with post-compaction reduction in effective stress by some unloading mechanism.

3.5.2 Chemical Compaction Signature

Pore pressure and velocity-density trends associated with chemical compaction can be summarized as in Figure 3.10. Shales undergo normal compaction from point A to B. Point B is where the fluid isolation depth is reached leading to pressure build-up. Under disequilibrium compaction conditions, the maximum pressure gradient is parallel to the overburden (dotted line in Figure 3.10a). However, reduction in porosity caused by chemical compaction increases the pressure further and reduces the effective stress (Figure 3.10b and c). These changes will cause deviation in velocity-density with large increase in density.

The wireline log signature resulting from chemical compaction is illustrated using data from well SM-30 (Figure 3.11). They consist of two parts: (1) a sharp increase in density (Trend A), followed by (2) sharp increase in velocity (Trend B). Two possible mechanisms been proposed to helps understand the observed Trend A and Trend B.

First, the trend can be explained as results of matrix framework collapse and partial dewatering. The process begins with clay diagenesis. During clay diagenesis, partial transfer of stress to pore water causes reduction in effective stress. The bulk density should remain constant. However, if some of the pore water is allowed to escape, hence maintaining some overpressure, then the bulk density will increase (Trend A). Velocity, on the other hand, is highly influenced by cracks and grain boundaries. The effect of the cracks can be minimized if they are saturated with water and high effective pressures (Mavko et al., 1998), which occur in the deeper section of the well (Trend B).



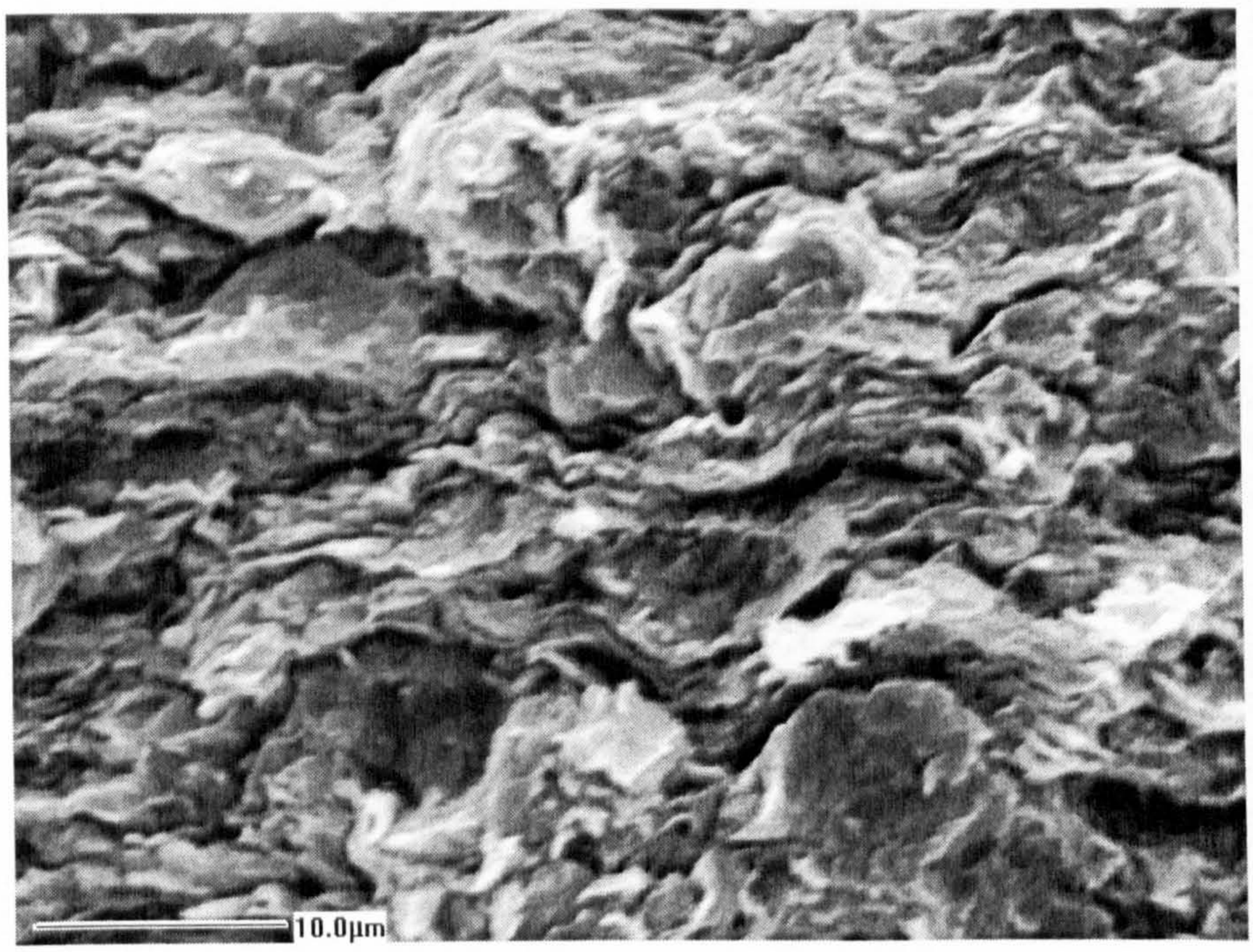
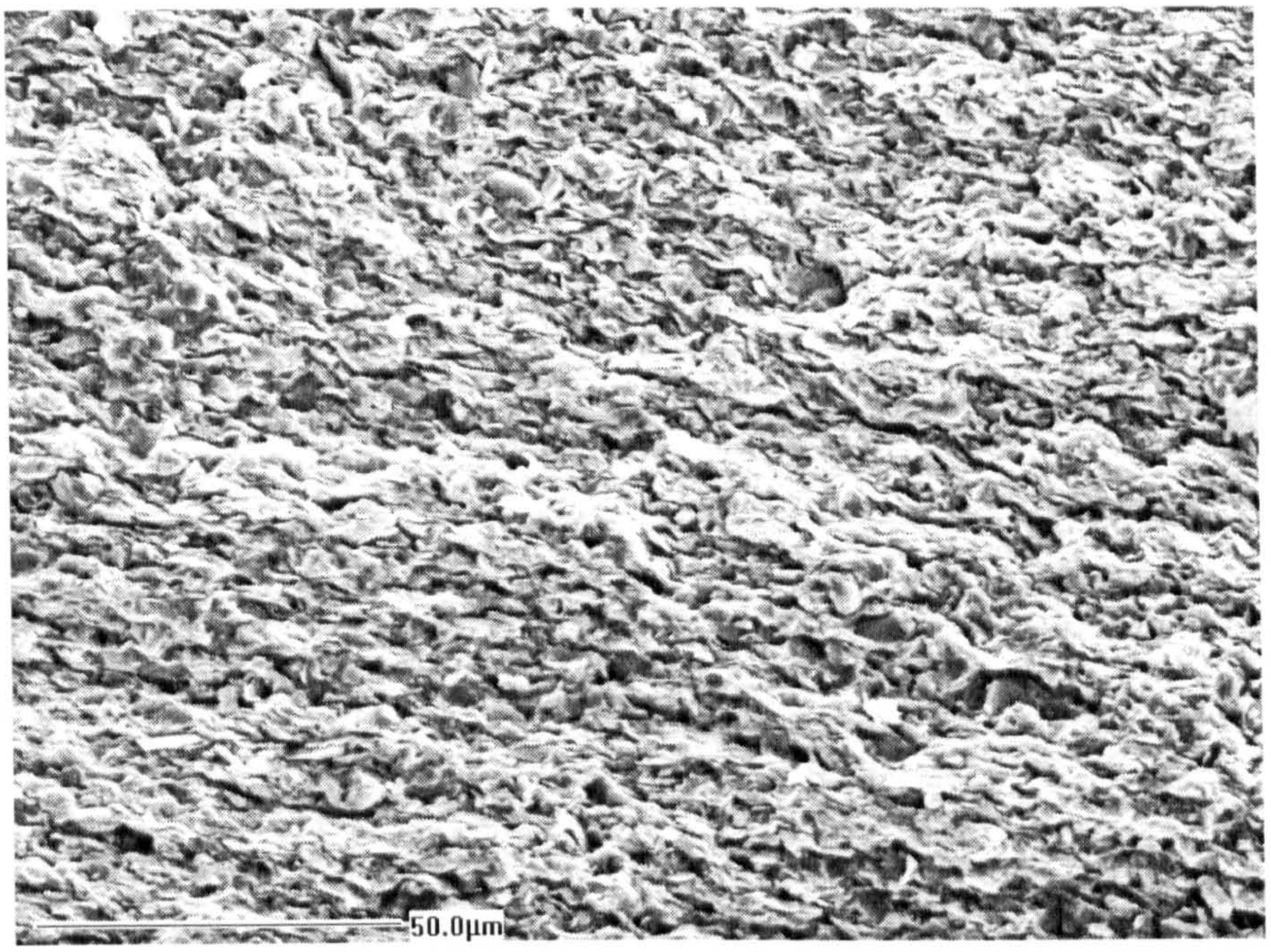


Figure 3.8 SEM micrograph of microfabric of overpressured shale at depth 5560 ft in well SM-30 (a) 650x magnification, (b) 2220x magnification.



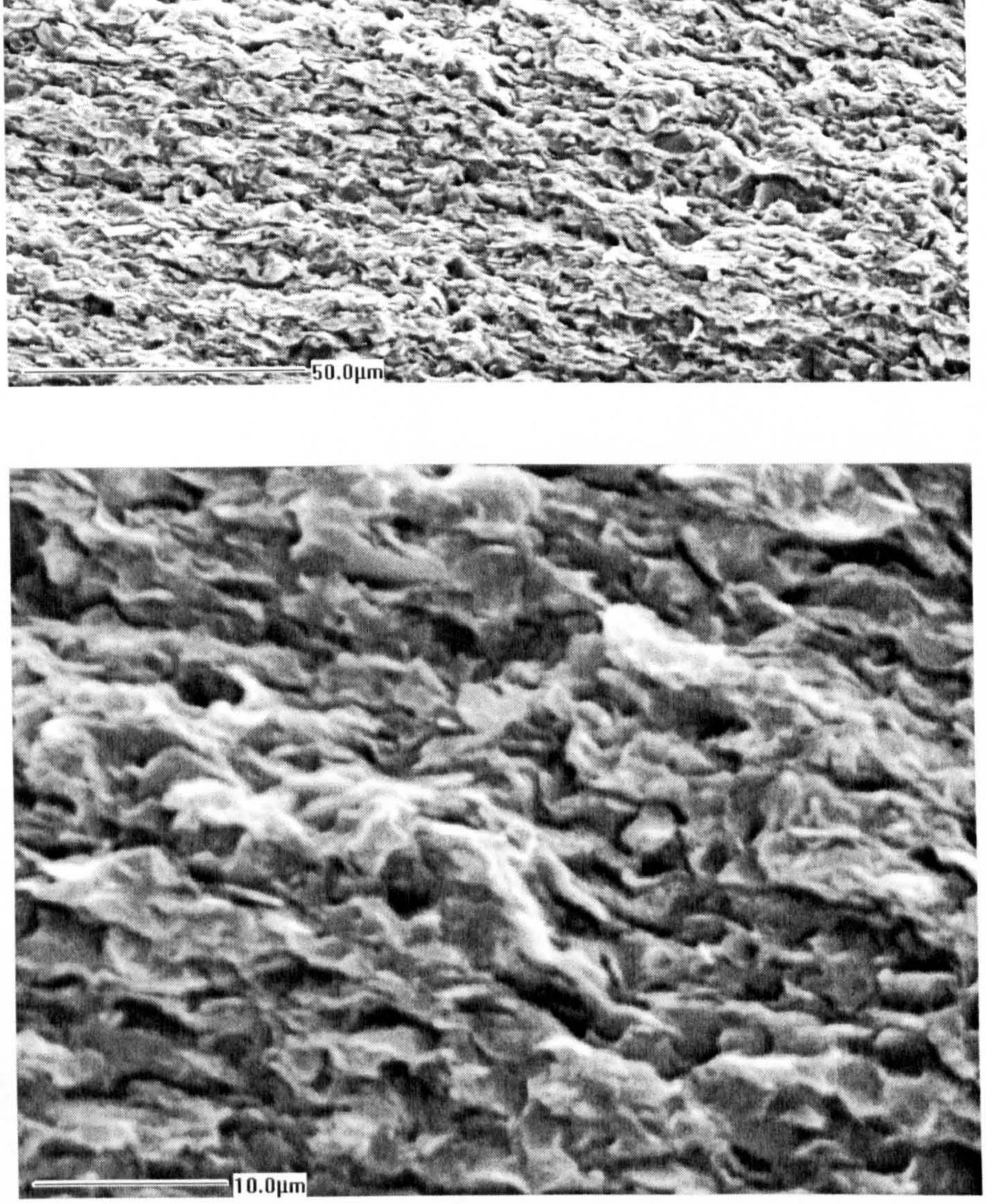


Figure 3.9 SEM micrograph of microfabric of overpressured shale at depth 8150 ft from well SM-30. (a) 650x magnification, (b) 2220x magnification.

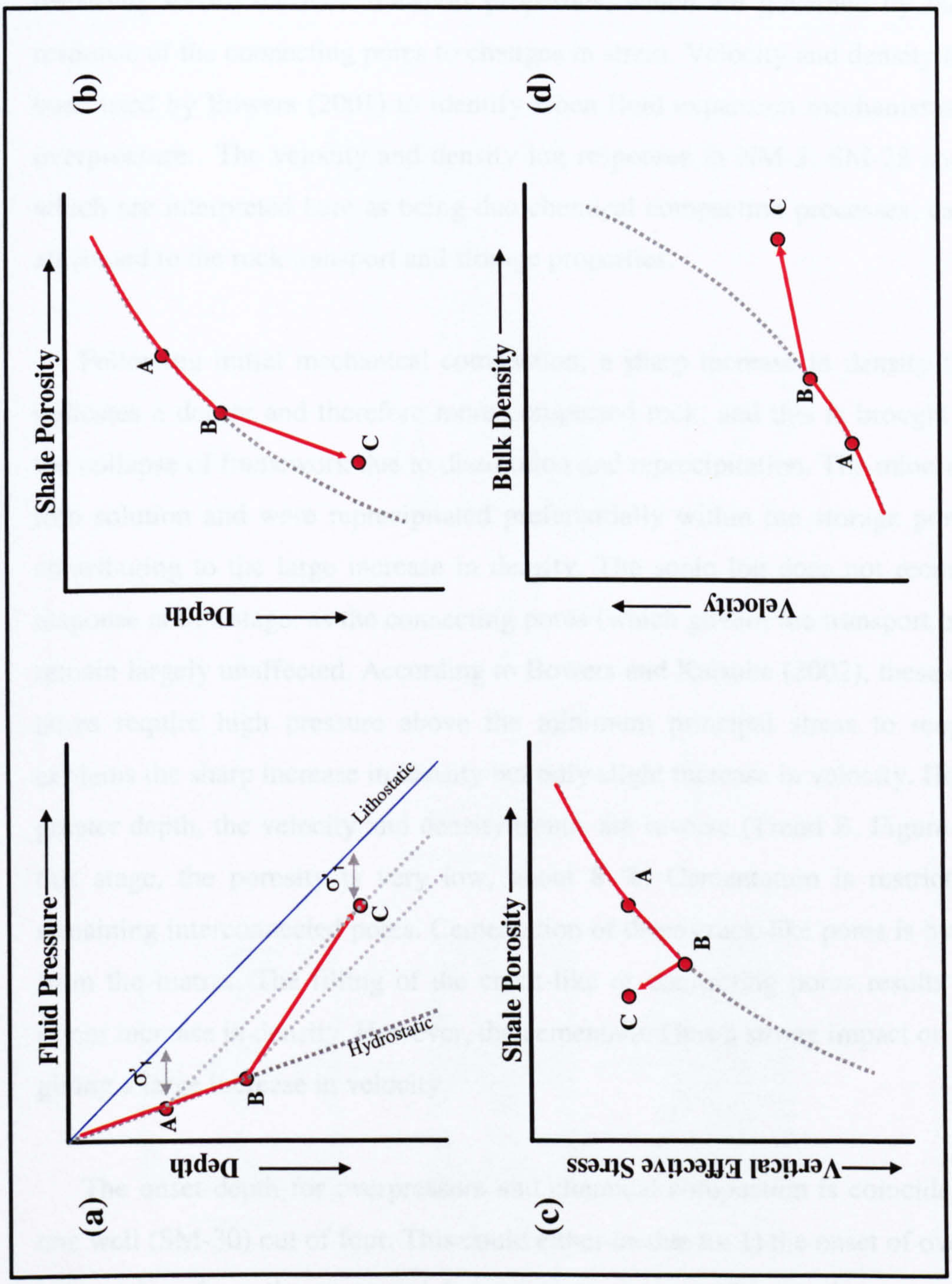


Figure 3.10 Example of possible trend expected from overpressured shales undergoing chemical compaction. (a) Fluid pressure versus depth, (b) shale porosity versus depth, (c) shale porosity versus vertical effective stress, (d) bulk density versus velocity from sonic transit times.

An alternative explanation is related to sequential filling of the pore space in the shales. Bowers & Katsube (2002) discuss the response of different wireline porosity tools to overpressure. Sonic and resistivity logs are more responsive to overpressure caused by fluid expansion than neutron and density logs. This is because sonic and resistivity record the rock transport properties, which are governed by the flexible response of the connecting pores to changes in stress. Velocity and density logs have been used by Bowers (2001) to identify when fluid expansion mechanisms generate overpressure. The velocity and density log responses in NM-3, SM-28 and SM-30, which are interpreted here as being due chemical compaction processes, can also be attributed to the rock transport and storage properties.

Following initial mechanical compaction, a sharp increase in density (Trend A) indicates a denser and therefore more compacted rock, and this is brought about by the collapse of framework due to dissolution and reprecipitation. The minerals moved into solution and were reprecipitated preferentially within the storage pores, hence contributing to the large increase in density. The sonic log does not record a large response at this stage, as the connecting pores (which govern the transport properties) remain largely unaffected. According to Bowers and Katsube (2002), these crack-like pores require high pressure above the minimum principal stress to reopen. This explains the sharp increase in density but only slight increase in velocity. However, at greater depth, the velocity and density trends are reverse (Trend B, Figure 3.11). At this stage, the porosity is very low, about 8 %. Cementation is restricted to the remaining interconnected pores. Cementation of these crack-like pores is by diffusion from the matrix. The filling of the crack-like or connecting pores results in only a minor increase in density. However, the cementation has a strong impact on the sonic, giving a large increase in velocity.

The onset depth for overpressure and chemical compaction is coincident only in one well (SM-30) out of four. This could either be due to: 1) the onset of overpressure being taken from the measured formation pressures within sandstones, which may differ from the shales (not supported by data in Figure 2), or 2) overpressure is not related to the porosity reduction by chemical compaction, but is a consequence of mechanical processes such as loading and sediment permeability. Nevertheless the reduction in porosity by chemical compaction, especially the blocking of connecting

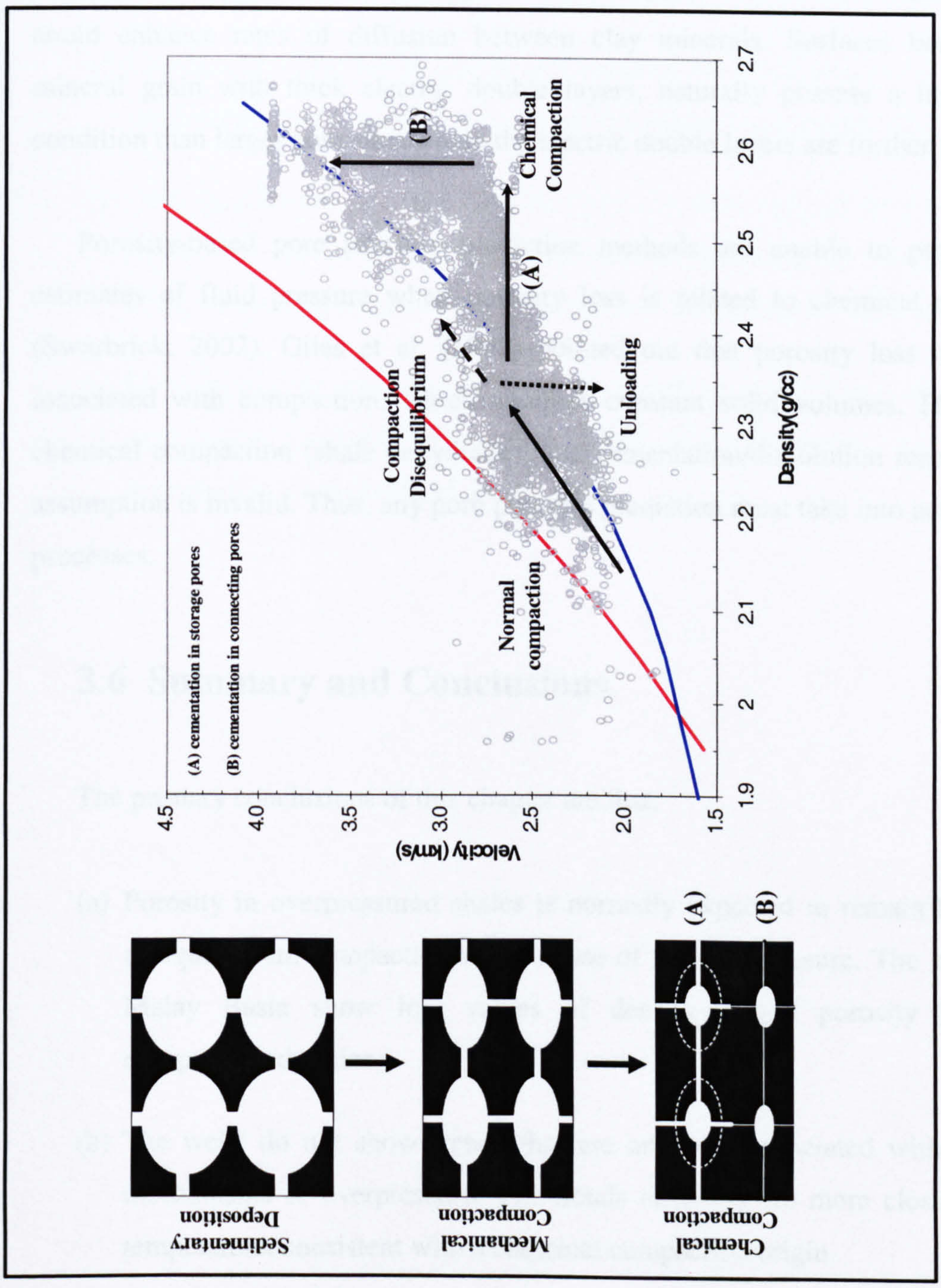


Figure 3.11 Proposed processes for chemical compaction in explaining the velocity-density trend in the Malay Basin.

pores, will undoubtedly result in low permeability and the potential for overpressure.

Several reasons could be proposed for the preference of filling/precipitation of storage pores prior to filling/precipitation in the connecting pores. As discussed by Weyl (1959), clay minerals have high surface charge, and hence thick water films that could enhance rates of diffusion between clay minerals. Surfaces between clay mineral grain with thick electric double layers, naturally possess a higher stress condition than larger pore sites where the electric double layers are further apart.

Porosity-based pore pressure prediction methods are unable to provide good estimates of fluid pressure when porosity loss is related to chemical compaction (Swarbrick, 2002). Giles et al. (1998) pointed out that porosity loss is normally associated with compaction, which assumes constant solid volumes. However, in chemical compaction (shale dehydration and cementation/dissolution reactions), this assumption is invalid. Thus, any pore pressure prediction must take into account these processes.

3.6 Summary and Conclusions

The primary conclusions of this chapter are that:

(a) Porosity in overpressured shales is normally expected to remain high where disequilibrium compaction is the cause of the overpressure. The wells in the Malay Basin show low values of density-derived porosity within the overpressured shales.

(b) The wells do not show trends that are normally associated with unloading mechanisms of overpressure. The trends observed are more close related to temperature, consistent with a chemical compaction origin.

(c) The chemical compaction trend can be explained either by shale framework collapse with partial dewatering or by the sequential cementation of the storage pores and connecting pores.

(d) Traditional porosity-based pore pressure prediction methods work well only where rocks behave according to principles governing mechanical compaction. These methods do not take into account reduction in porosity due to chemical compaction. Since porosity is related to effective stress, the pore pressures in overpressured shales in this setting will be underestimated.

(e) Chemical compaction in shales will enhance the effectiveness of the seal in the area, and plays a major role in controlling the overpressure dissipation.

(f) High geothermal gradient can facilitate the development of pressure seals within the shales by chemical compaction, resulting in subsequent more effective development of overpressure due to addition of overburden stress.

(g) Overpressure in this study area is believed to result from disequilibrium compaction (shallow and deep) caused by rapid burial, as well as a contribution from chemical compaction.

Chapter 4:

Origins of Overpressure in the Baram Delta and West Luconia

4.1 Introduction

Basins offshore Sabah and Sarawak, in East Malaysia are divided into several geological provinces (Figure 4.1) which are characterized by differences in tectonic and sedimentation histories. The Baram Delta, which includes the Champion Delta Complex in Brunei, is bounded by the West Baram Line to the west and by the Jerudong-Morris Fault to the east. The portion of the basin that lies in Sarawak is referred to as the West Baram Delta, while the part that lies in the Sabah is called East Baram Delta Province. West Luconia is a paleodeltaic system of similar size to the present Baram Delta.

This chapter discusses the results of pore pressure prediction in the shale from wireline log responses in shales in several overpressured wells in the basins. The results are examined and compared to the Malay Basin wells (Chapter 2) in order to understand and deduce the origin of overpressure in the Baram Delta and West Luconia.

4.1.1 Geological Setting of Baram Delta

The basins in East Malaysia evolved from the opening of the South China Sea basin. The sea-floor spreading in the South China Sea created several drifted micro-continental blocks, which then collided with Borneo. The collision resulted in fold thrust belts of northern Borneo during the Oligocene. The collision also led to several regional unconformities, including the lower Middle Miocene Deep Regional Unconformity (DRU). The uplifted fold belts provided clastic sediments to the Sabah and Sarawak continental margins (Hutchison et al., 2000).

The Baram Delta complex begin prograding into the Sabah-Sarawak continental margin during the Middle Miocene, overlying the deformed deepwater sediments of the Crocker Formation (Oligocene-Late Miocene) and Rajang Group (Paleocene-Oligocene).

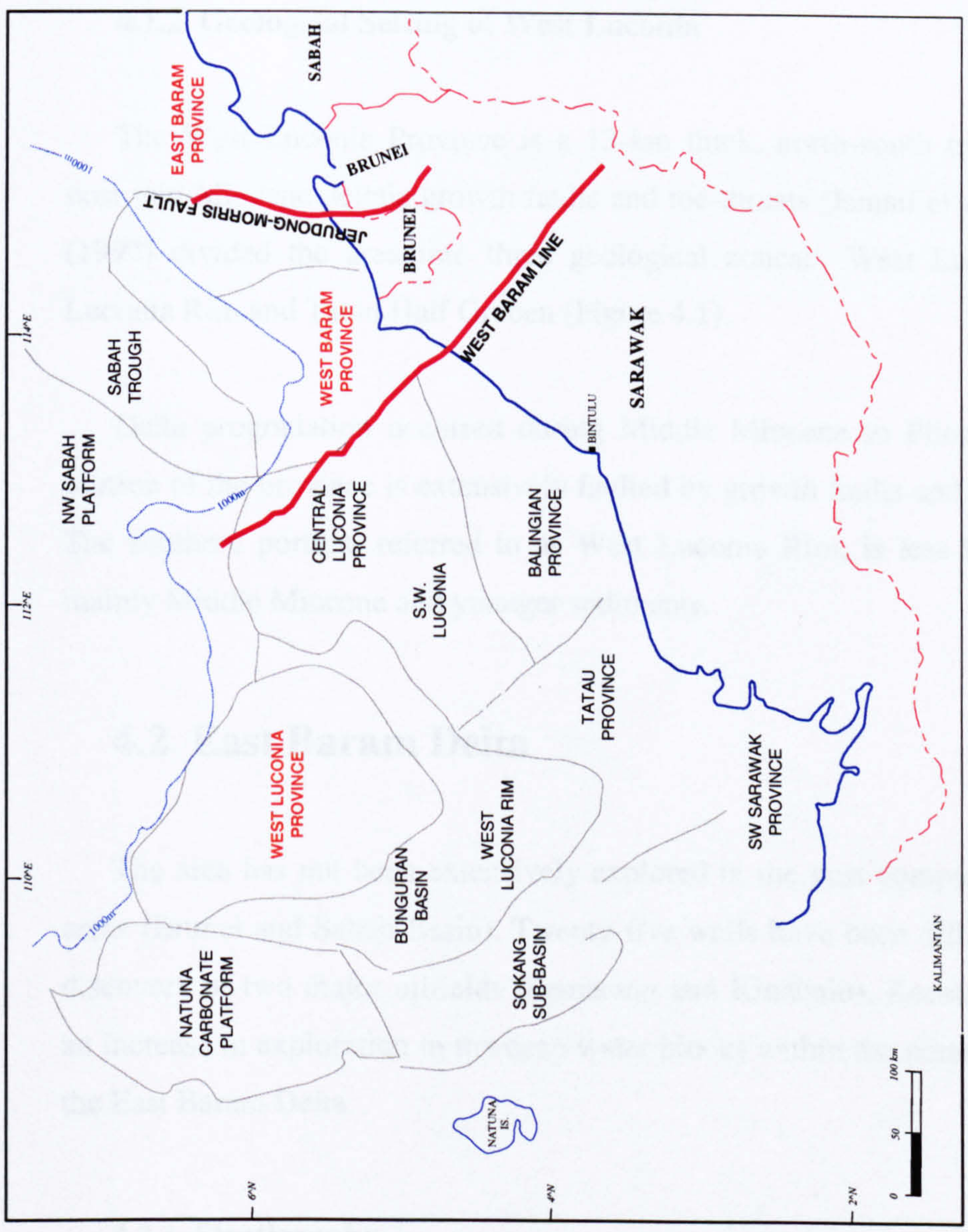


Figure 4.1 Map showing location of the geological provinces in Sabah and Sarawak Basins. The provinces covered in this study are the East Baram, West Baram and West Luconia.

Growth faults downthrown basinwards are the dominant feature in West Baram Delta Province. Wrench compressive tectonism in early Late Miocene time resulted in a series of NE trending folds and some reverse faults. The intersection between growth faults and compressional anticlines provide an excellent hydrocarbon traps. (Scherer, 1980; Sandal, 1996; Tan et al., 1999).

4.1.2 Geological Setting of West Luconia

The West Luconia Province is a 13-km thick, north-south trending basin, with post mid-Miocene deltaic growth faults and toe-thrusts (Ismail et al., 1994). Ganesan (1997) divided the area into three geological zones: West Luconia Delta, West Luconia Rim and Tatau Half Graben (Figure 4.1).

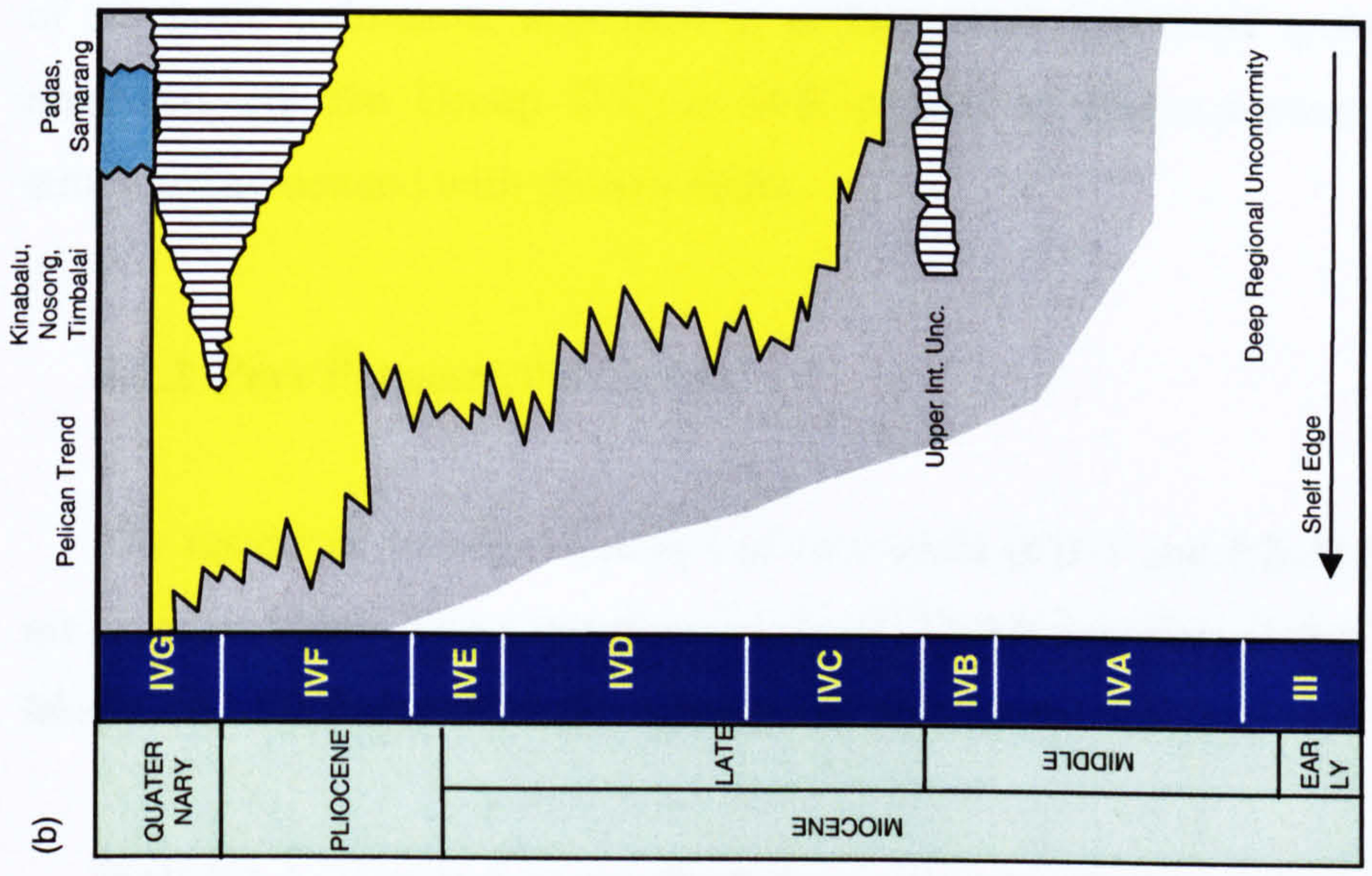
Delta progradation occurred during Middle Miocene to Pliocene. The northern portion of the province is extensively faulted by growth faults and rollover anticlines. The southern portion, referred to as West Luconia Rim, is less faulted and consist mainly Middle Miocene and younger sediments.

4.2 East Baram Delta

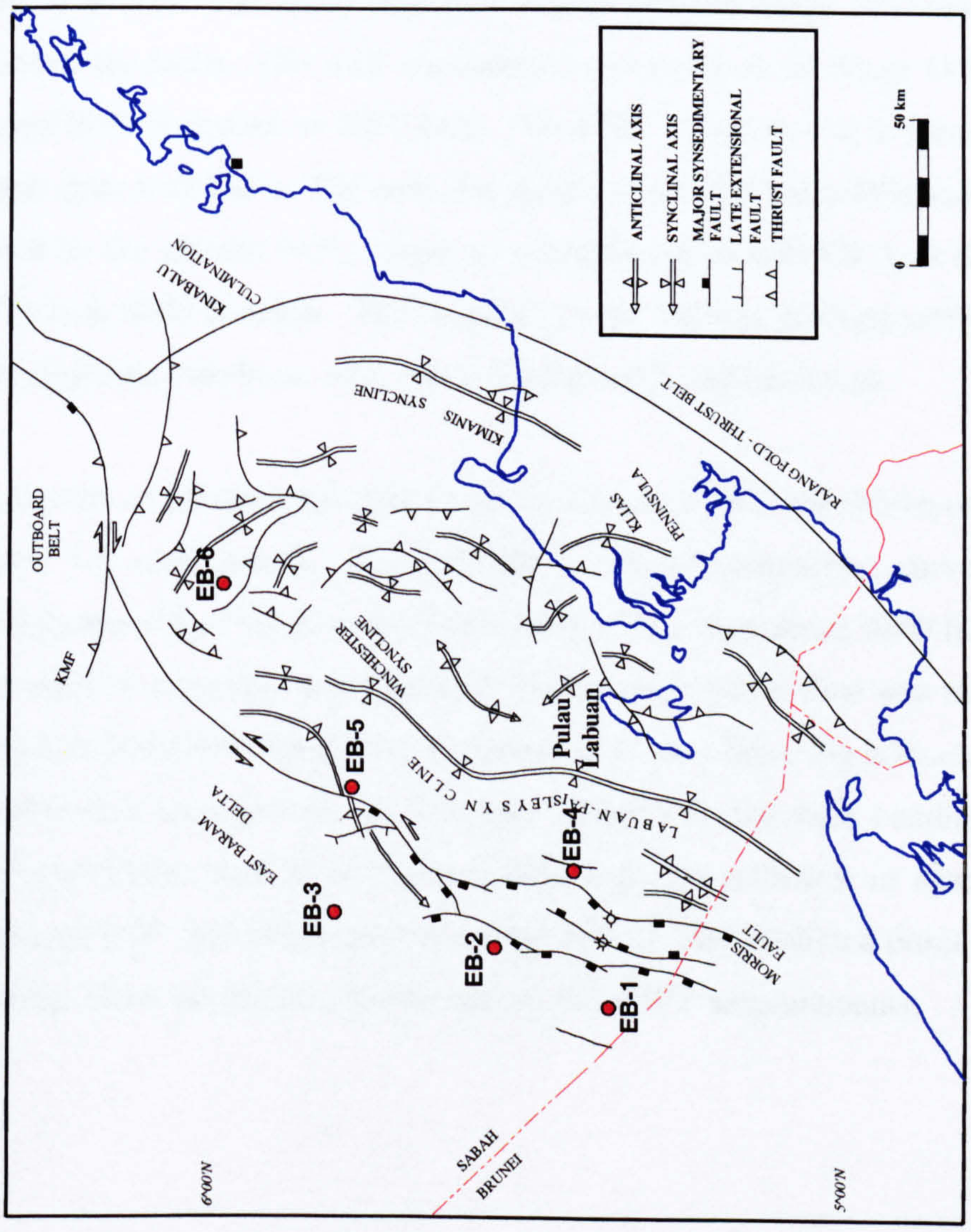
The area has not been extensively explored in the past compared to the adjacent areas (Brunei and Sabah Basin). Twenty-five wells have been drilled resulting in the discovery of two major oilfields (Samarang and Kinabalu). Recently, there has been an increase in exploration in the deep water blocks within the outer shelf and slope of the East Baram Delta.

4.2.1 Stratigraphy

The East Baram stratigraphy follows that of the Sabah Basin, where they are subdivided into 'Stages'. These stages are separated by unconformities (Figure 4.2) caused by tectonic collision and uplift of the basin margin. The stages are designated from the oldest, Stage IVA (Oligocene), to Stage IVG (Recent) (Levell, 1987). Stages



(b)



(a)

Figure 4.2 East Baram Delta: (a) well locations and geological features, (b) lithostratigraphic scheme.

I to III comprise deep marine pre-lower Middle Miocene sediments. Stage IV consists of siliclastic sediments, deposited as deltaic, shelf and slope sediments. The main reservoirs are the Group IVC to IVE coastal to fluvio-marine sands, found in structures associated with growth faults.

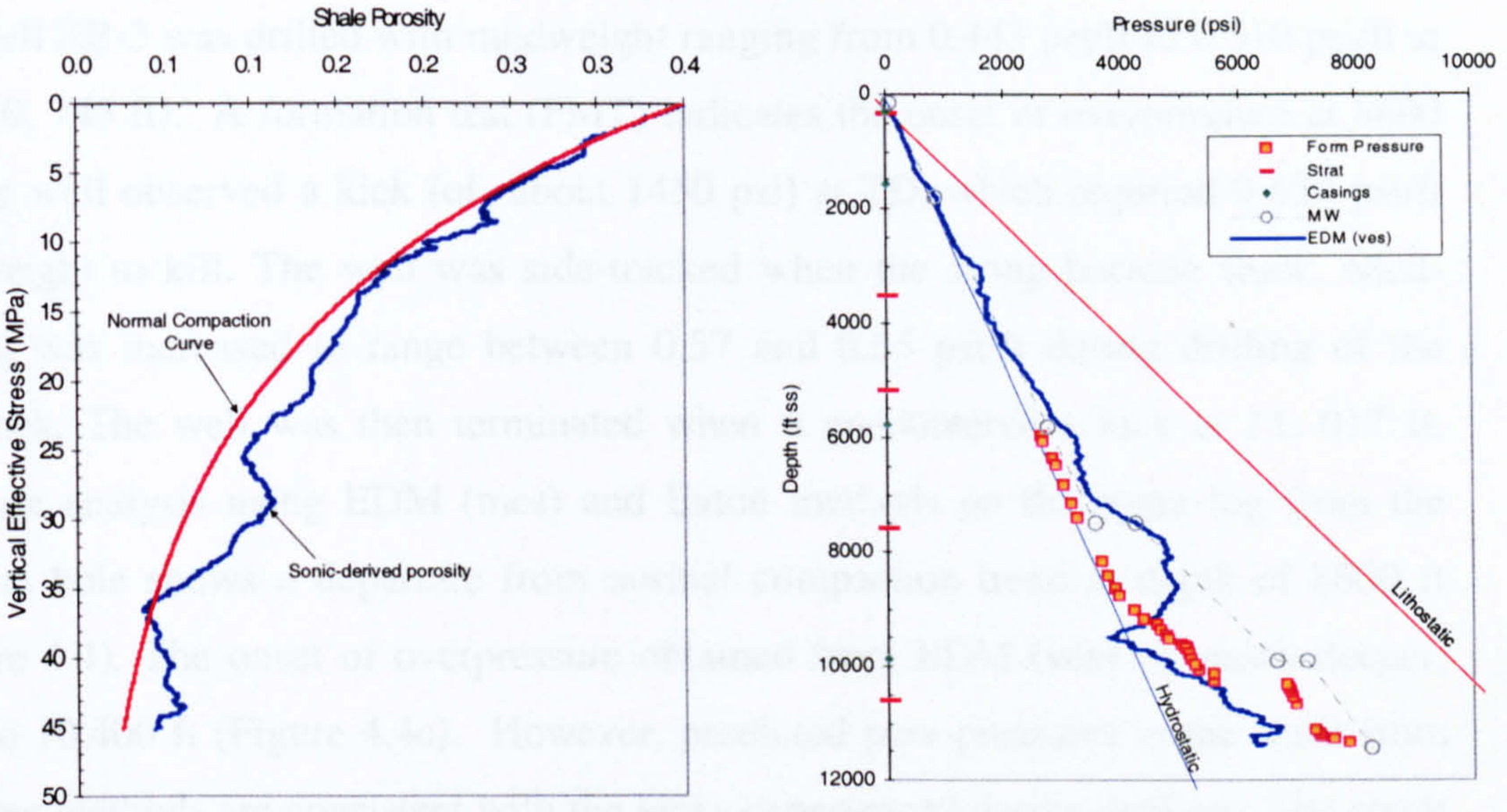
4.2.2 Pore Pressure Prediction

The results of pressure analysis of two wells (EB-1 and EB-3) from East Baram are presented here. The same three methods (EDMs and Eaton) that were used in the Malay Basin (Chapter 2) were applied on these two wells.

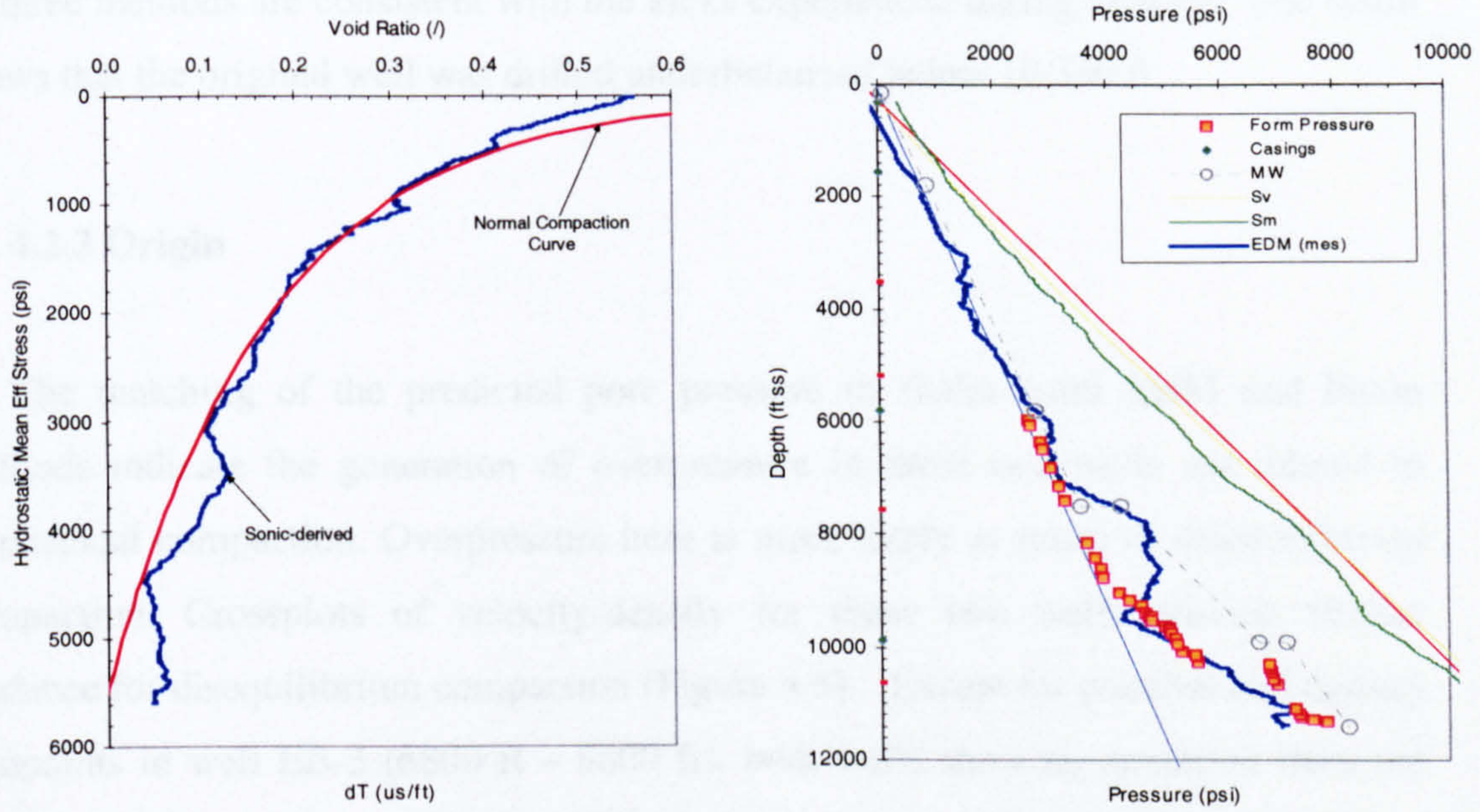
Well EB-1 (Figure 4.3) was drilled on a similar structural trend to the Champion field in Brunei. The main objective was to test the Stage IVC reservoirs that are bounded by faults. The well encountered overpressure in Stage IVC at a depth of around 9000 ft (based on RFT data). Well EB-3 (Figure 4.4) is located 51 km (31.7 miles) from well EB-1. The well was drilled to test the Stage IVE and IVD reservoirs sealed by the growth fault. Onset of overpressure in well EB-3, as determined from RFTs is at 8600 ft depth. The lithology in the wells is predominantly sandstone and silty claystone interbeds, with minor lignitic coals and limestone.

Results of pressure analysis for wells EB-1 and EB-3 are shown on Figure 4.3 and Figure 4.4, respectively. For well EB-1, normal compaction curves were derived through best fits of sonic or sonic-derived porosity logs above 9500 ft. Below 9500 ft, a reversal in sonic log was observed. Higher sonic travel-time was recorded between 7000 ft to 8000 ft of Stage IVC. Unfortunately, no calliper log is available to ascertain whether this corresponds to lithology changes or borehole conditions. All three methods (EDMs and Eaton) gave similar pressure estimates in agreement with the measured RFT formation pressures (Figure 4.3). The predicted onset of overpressure is about 500 ft deeper than that projected from RFT measurements.

(a)



(b)



(c)

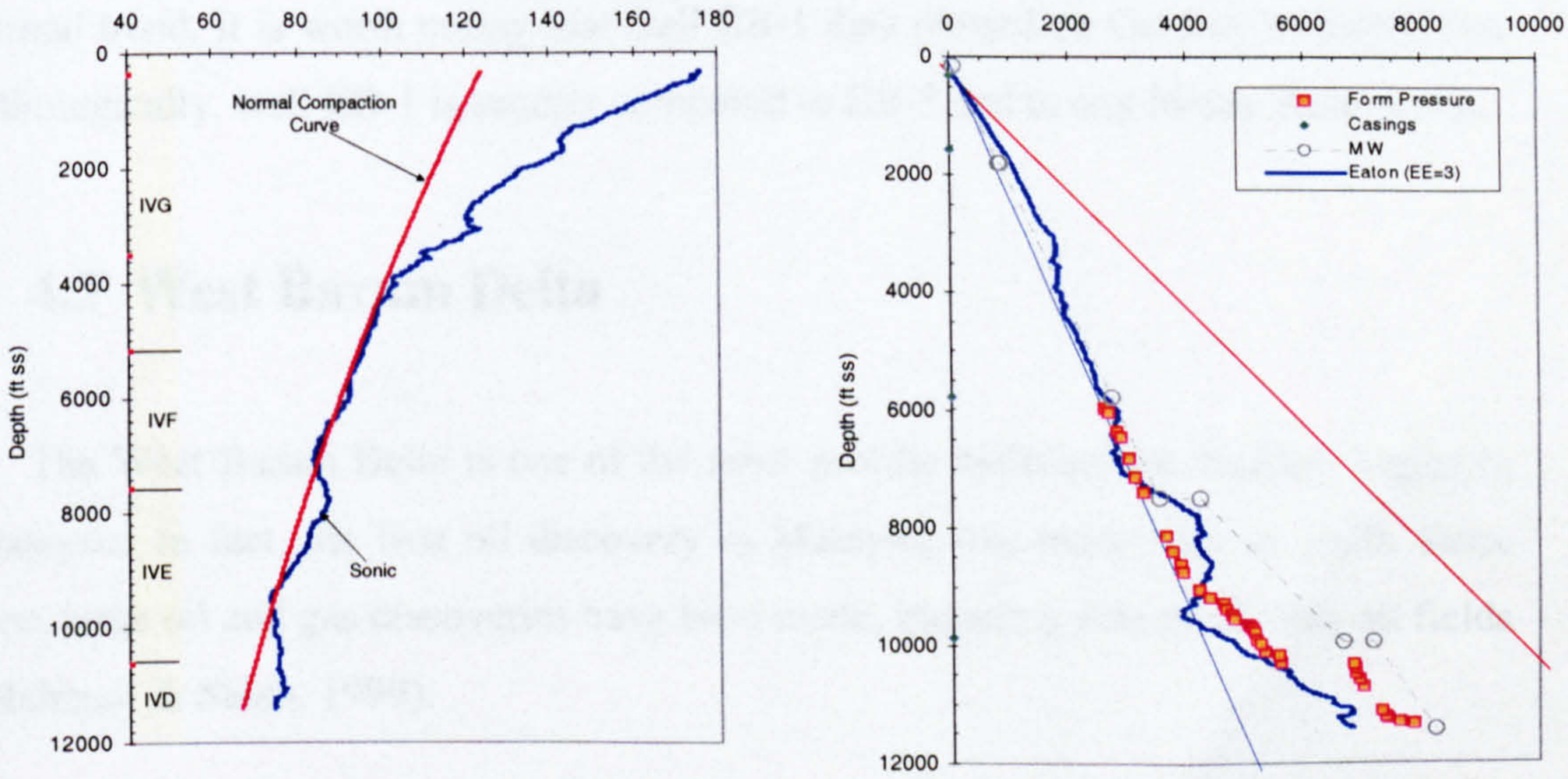


Figure 4.3 Results of pressure analysis for well EB-1. (a) EDM (ves), (b) EDM (mes), (c) Eaton.

Well EB-3 was drilled with mudweight ranging from 0.443 psi/ft to 0.510 psi/ft at TD (10, 745 ft). A formation test (FMT) indicates the onset of overpressure at 8600 ft. The well observed a kick (of about 1450 psi) at TD, which required 0.650 psi/ft mudweight to kill. The well was side-tracked when the string became stuck. Mud-weight was increased to range between 0.57 and 0.65 psi/ft during drilling of the sidetrack. The well was then terminated when it encountered a kick at 11, 017 ft. Pressure analysis using EDM (mes) and Eaton methods on the sonic log from the original hole shows a departure from normal compaction trend at depth of 8600 ft (Figure 4.4). The onset of overpressure obtained from EDM (ves) is much deeper, around 10,400 ft (Figure 4.4c). However, predicted pore pressures in the shale from all three methods are consistent with the kicks experienced during drilling. The result shows that the original well was drilled underbalanced below 10,350 ft.

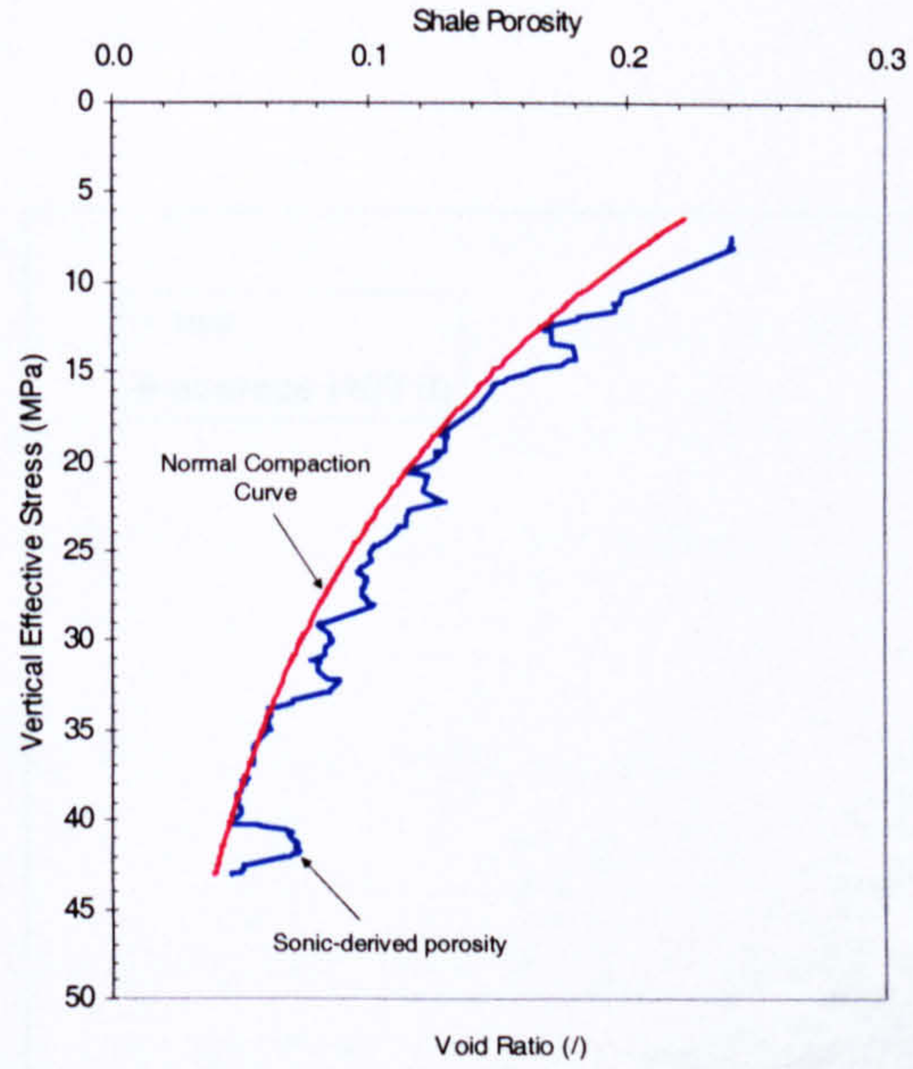
4.2.3 Origin

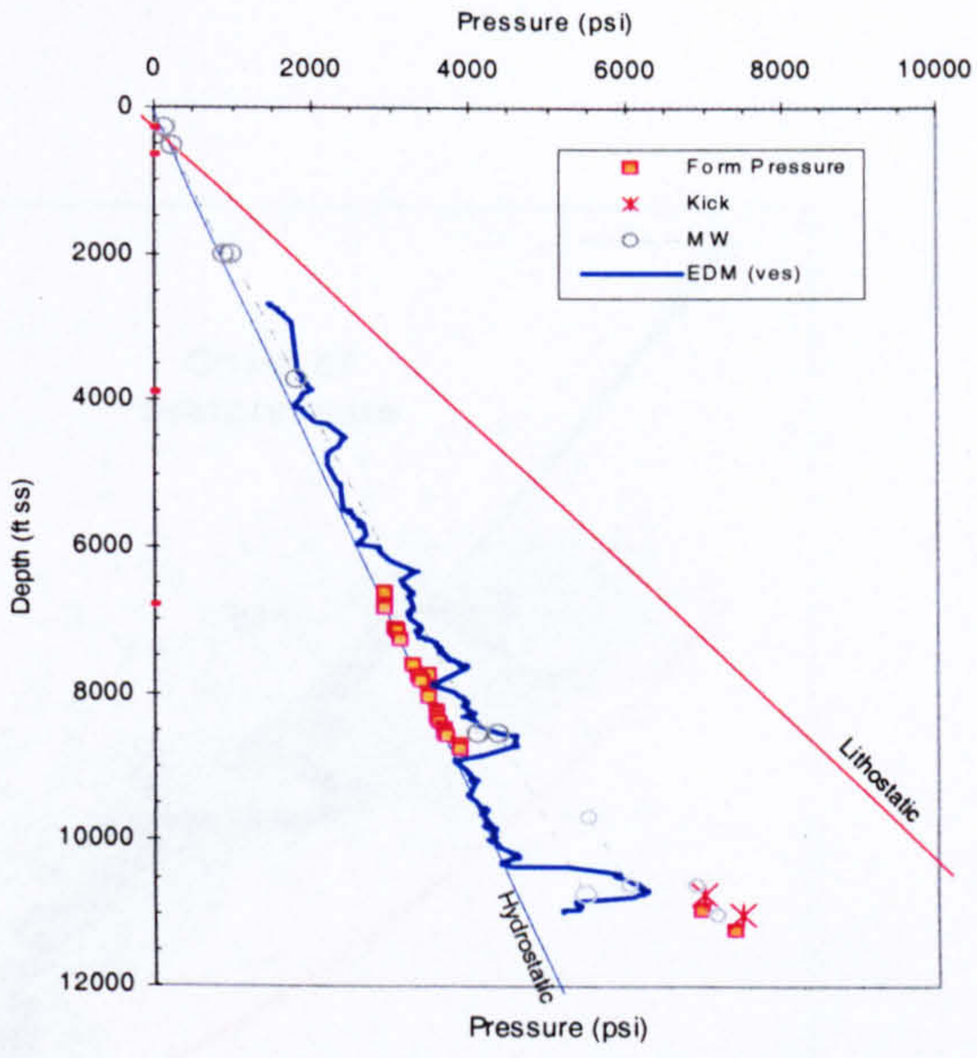
The matching of the predicted pore pressure in shales from EDM and Eaton methods indicate the generation of overpressure in these two wells are related to mechanical compaction. Overpressure here is more likely as result of disequilibrium compaction. Crossplots of velocity-density for these two wells provide further evidence for disequilibrium compaction (Figure 4.5). Except for possible bad density datapoints in well EB-3 (6800 ft – 8800 ft), both wells show no deviation from the normal trend. It is worth noting that well EB-1 data plotted on Gardner's shale trend. Lithologically, well EB-1 is sandier compared to EB-3 and to any Malay Basin wells.

4.3 West Baram Delta

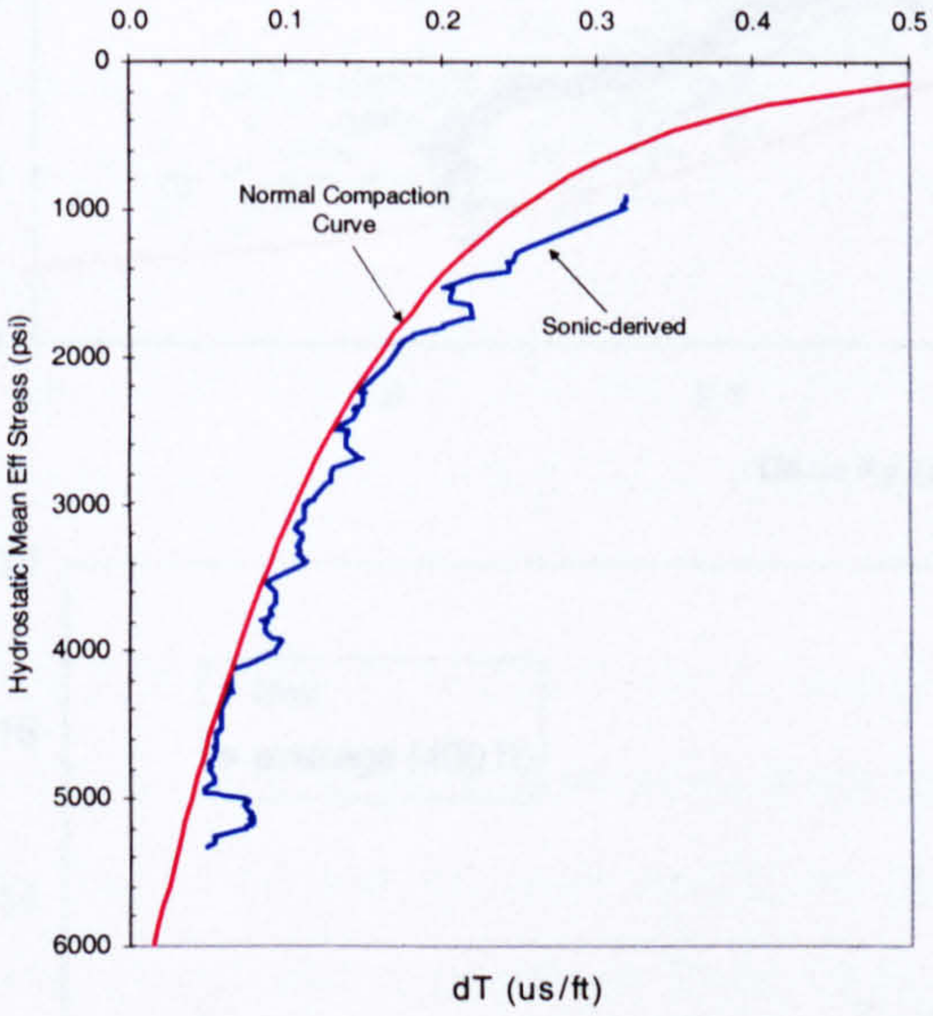
The West Baram Delta is one of the most prolific hydrocarbon–bearing basins in Malaysia. In fact, the first oil discovery in Malaysia was made here in 1910. Since then, large oil and gas discoveries have been made, including nine producing oil fields (Mahmud & Saleh, 1999).

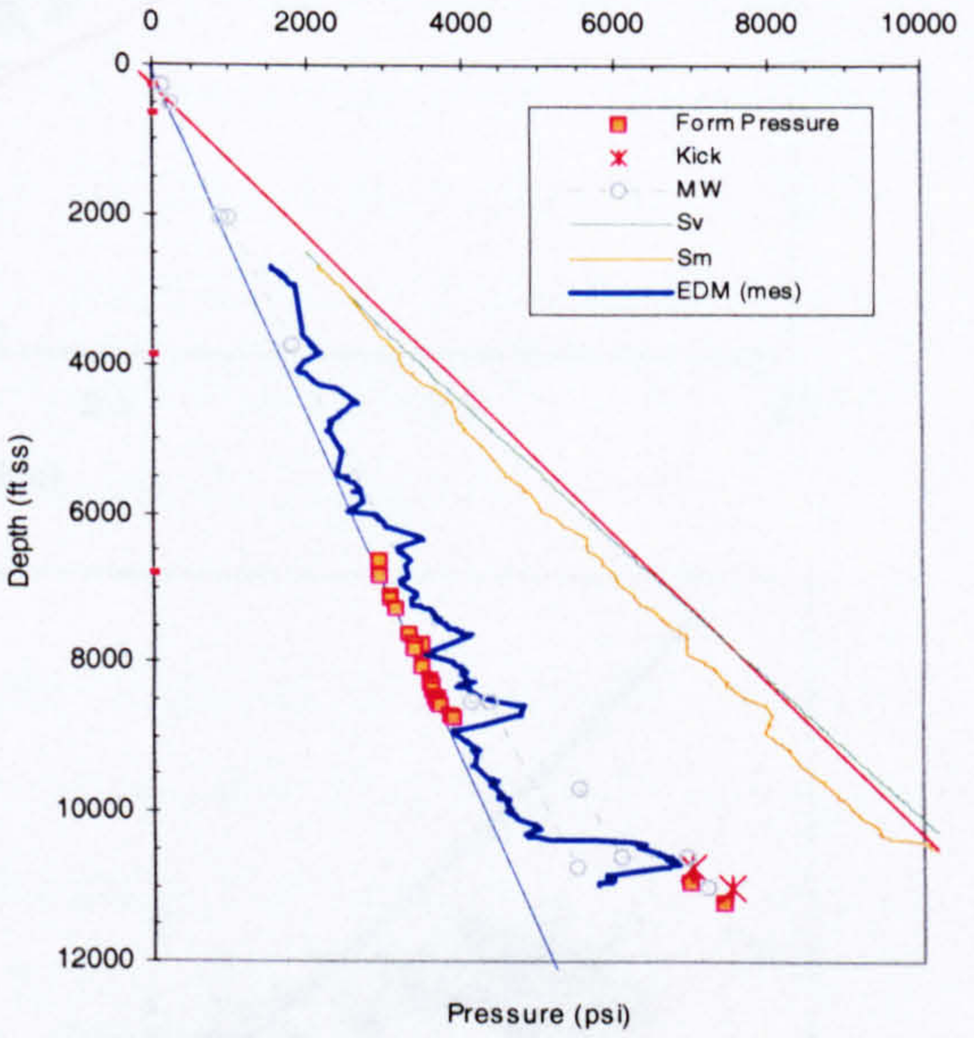
(a)



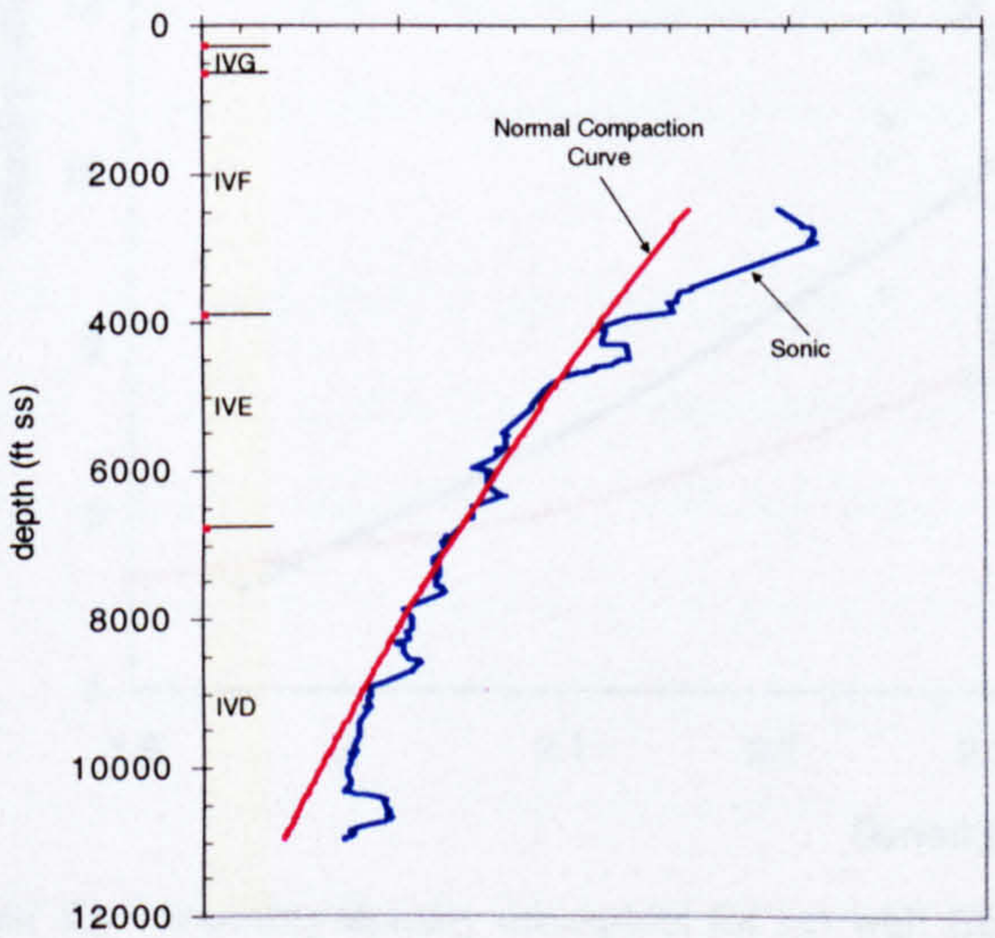


(b)





(c)



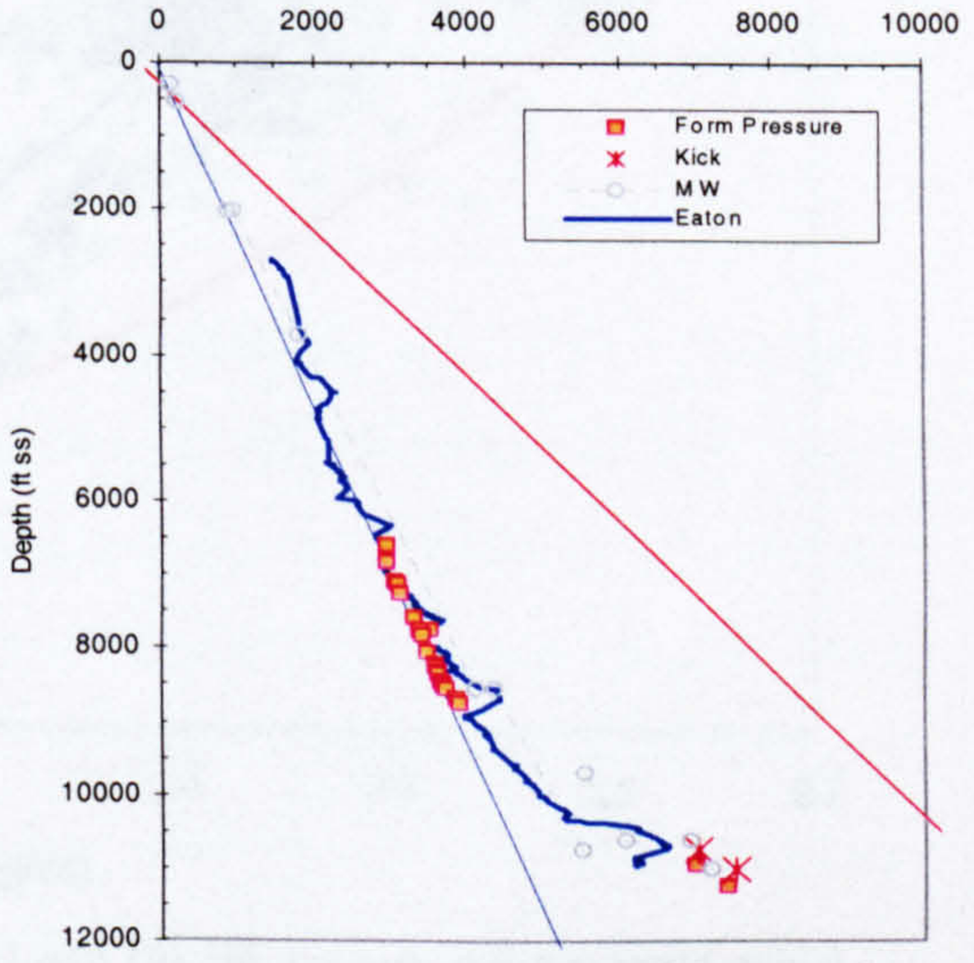


Figure 4.4 Results of pressure analysis for well EB-3. (EDM (ves), (b) EDM (mes), (c) Eaton

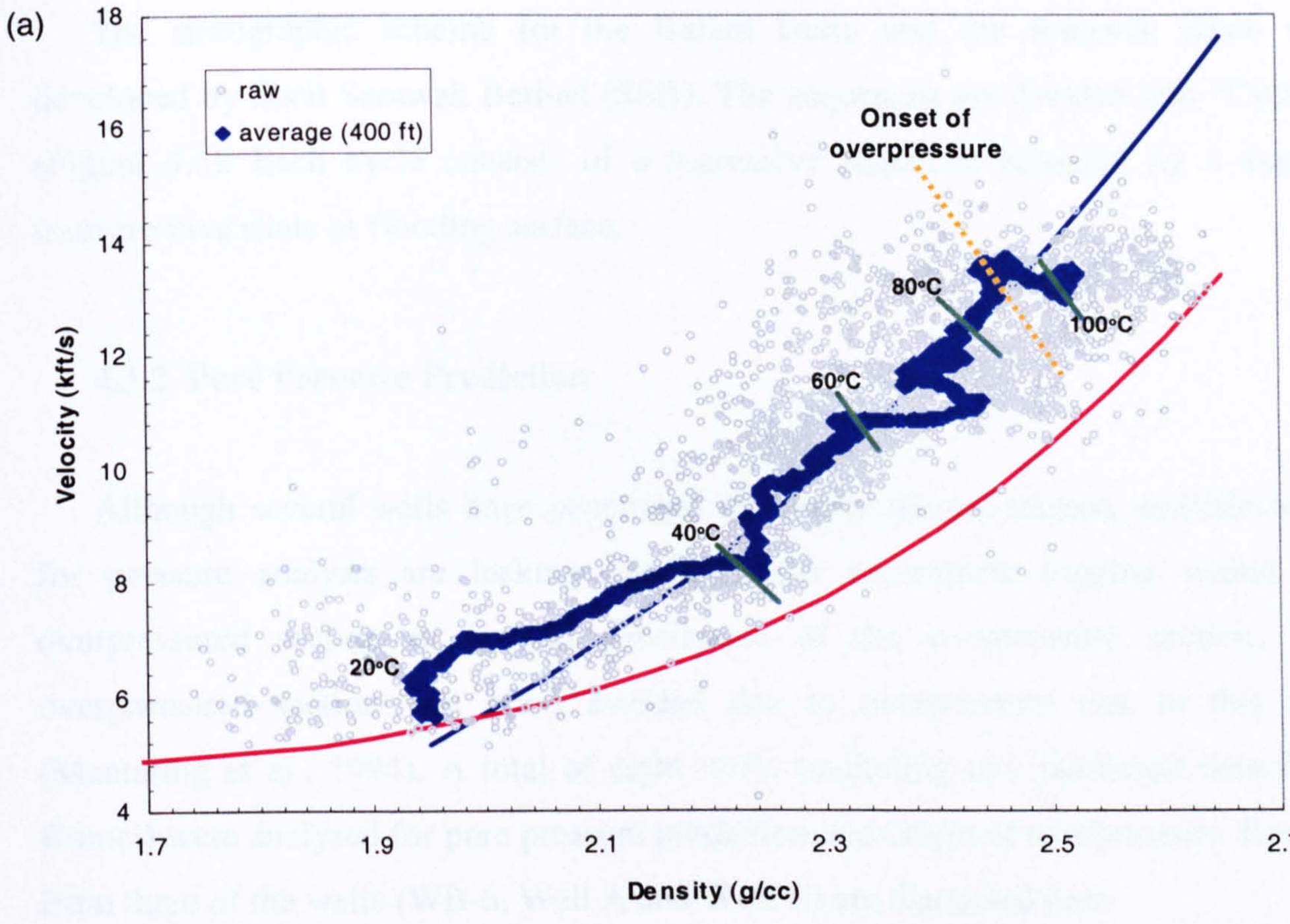


Figure 4.5 Velocity-density crossplots for (a) well EB-1 and (b) EB-3. Grey dots represent actual log values for the shale. Blue dots are the averaged dataset using moving average of 400 ft interval. Also plotted on the EB-1 trend are temperature intervals, based on geothermal gradient of 24.9°C/km (obtained from well report). Gardner's and Bower's relationship for shales are shown in blue and red lines, respectively.

4.3.1 Stratigraphy

The stratigraphic scheme for the Baram Delta and the Sarawak basin was developed by Shell Sarawak Berhad (SSB). The sequences are divided into "Cycles" (Figure 4.6). Each cycle consists of a regressive sequence bounded by a marine transgressive shale or flooding surface.

4.3.2 Pore Pressure Prediction

Although several wells have penetrated the overpressured section, suitable wells for pressure analysis are lacking due to either incomplete logging within the overpressured section or limited penetration of the overpressure section. The overpressured section was often avoided due to overpressure risk in this area (Mantaring et al., 1994). A total of eight wells (including two published data from Brunei) were analysed for pore pressure prediction and origin of overpressure. Results from three of the wells (WB-6, Well A and Well B) are discussed here.

Well WB-6 was drilled to Cycle V, where significant oil and gas-filled sequences were encountered. Wireline formation tests show that onset of overpressure is around 9000 ft. Predicted pore pressure results for shale are given in Figure 4.7. In all three methods, the predicted pressures from shales below 9000 ft are consistently lower than the measured formation pressures. The shale pore pressure and the formation pressure were observed to be lithostatic parallel.

Well A and Well B are two examples taken from offshore Brunei (Tingay et al., 2000). Well A is reported to encounter overpressure at 5905 ft (1800 m) and top of overpressure around 8202 ft (2500 m). These depths coincide with the deviations seen on both sonic and density logs (Figure 4.8). Normal compaction curves were fitted to data above 5905 ft (1800 m), where the pore pressure is interpreted as hydrostatic (supported by RFTs). Predicted pressures in shales, using the three methods are given in Figure 4.8. The EDM (ves) and Eaton methods give pore pressures that are consistently lower than the observed formation pressure. EDM (mes), on the other hand, provides a good match with the formation pressure. In well B, a sharp increase

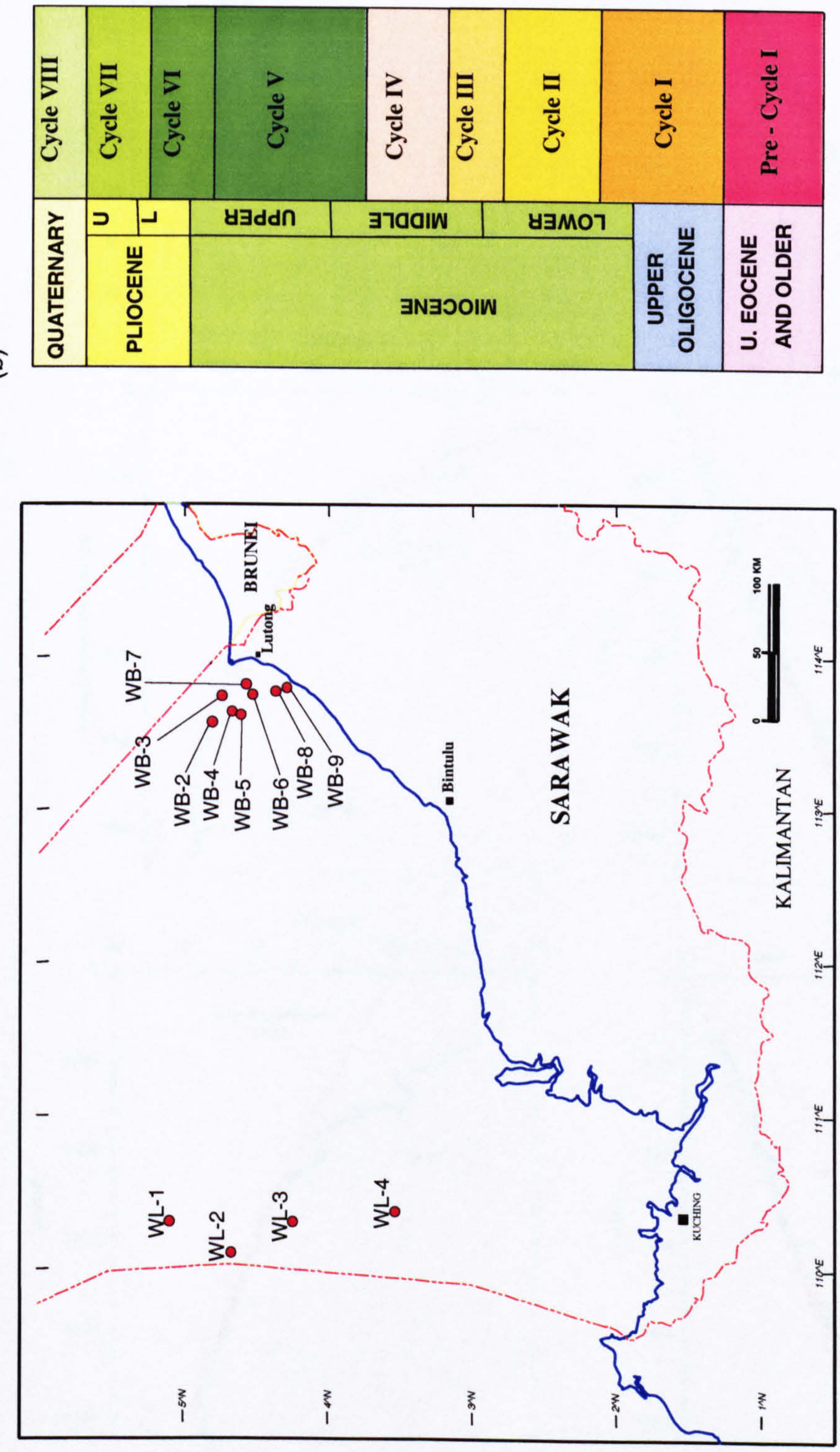
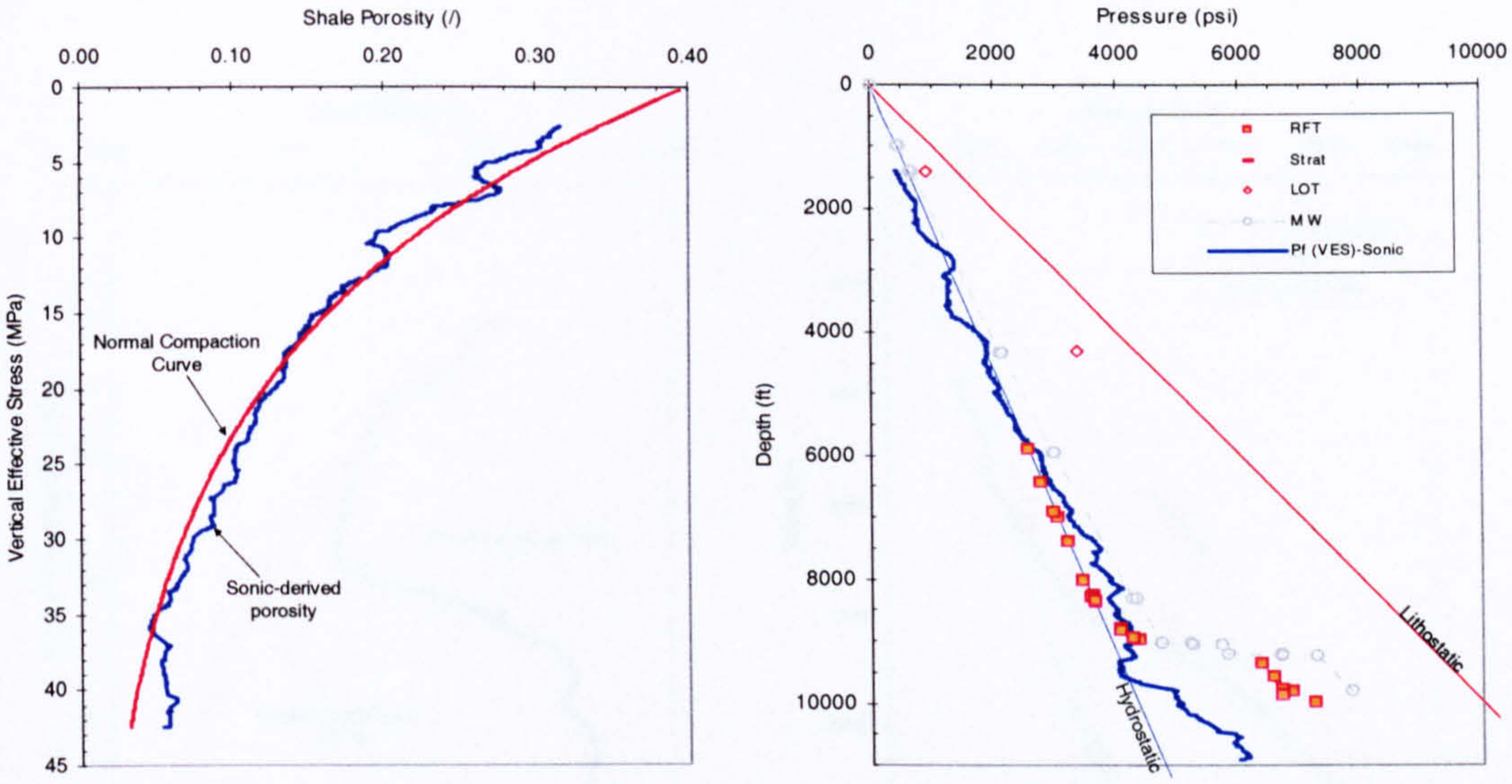
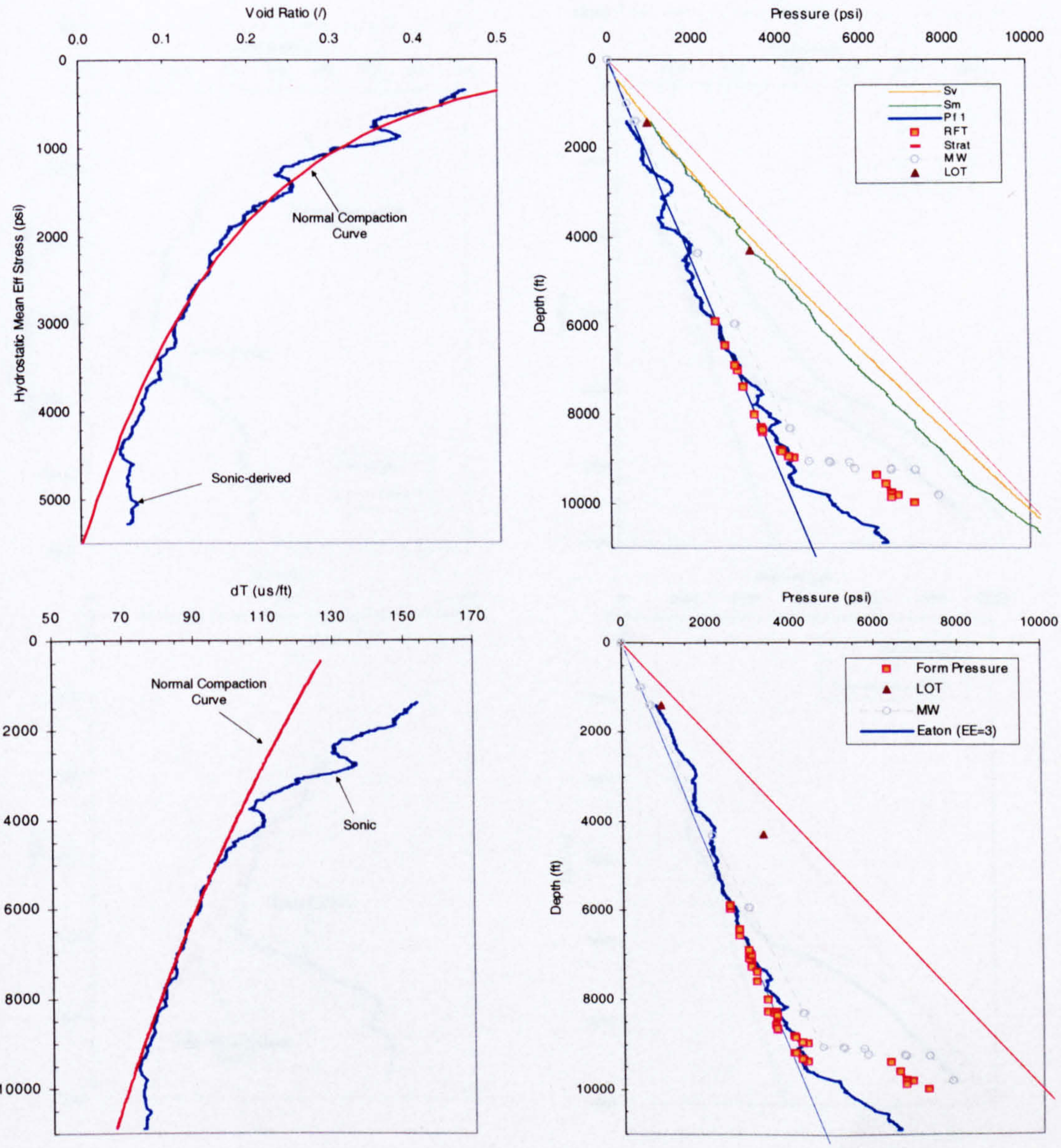


Figure 4.6 Sarawak Basin. (a) Map showing location of the studied wells in the West Baram Delta and the West Luconia Province, (b) stratigraphic framework for the West Baram Delta.

(a)



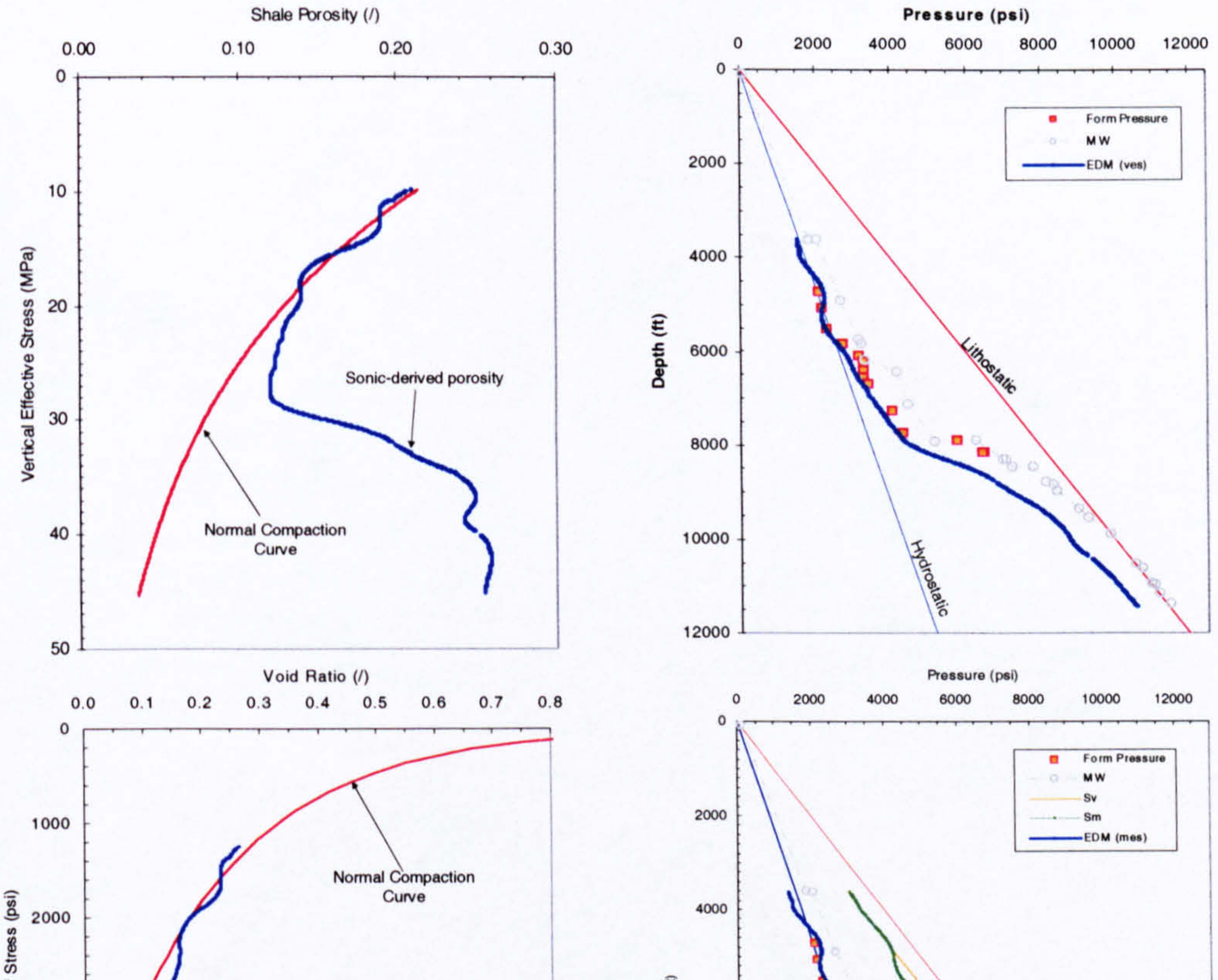
(b)



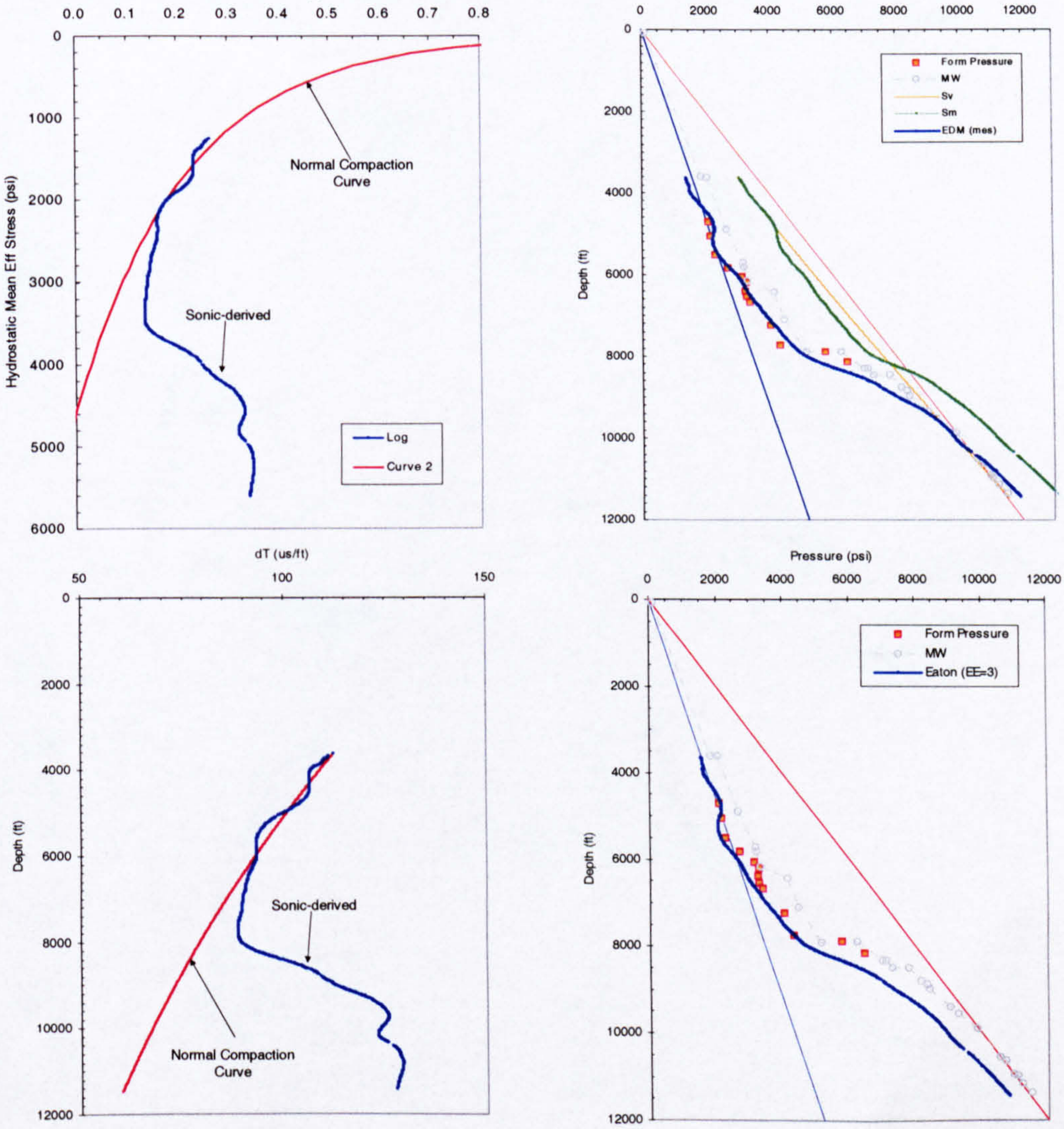
(c)

Figure 4.7 Pressure analysis results for well WB-6. (EDM (ves), (EDM (mes), (c) Eaton

(a)



(b)



(c)

Figure 4.8 Pressure analysis results for well A. (a) EDM (ves), (b) EDM (mes), (c) Eaton. Log and pressure data from Tingay et al. (2000).

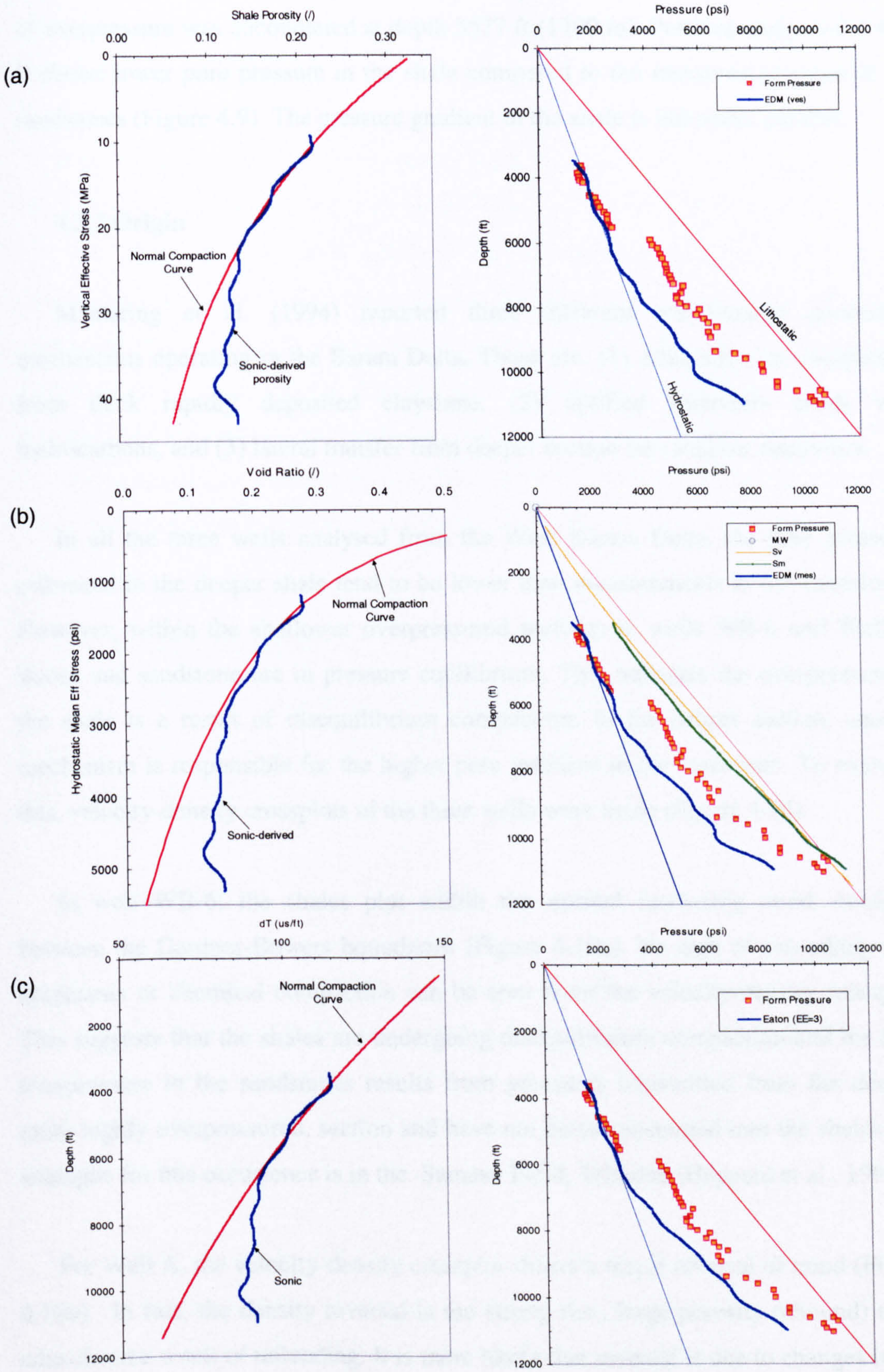


Figure 4.9 Pressure analysis results for well B. (a) EDM (ves), (b) EDM (mes), (c) Eaton. Log and pressure data from Tingay et al. (2000).

of overpressure was encountered at depth 5577 ft (1700 m). Pressure analysis for well B shows lower pore pressure in the shale compared to the measured pressure in the sandstones (Figure 4.9). The pressure gradient in the shale is lithostatic parallel.

4.3.3 Origin

Mantaring et al. (1994) reported three different overpressure generating mechanisms operating in the Baram Delta. These are: (1) disequilibrium compaction from thick rapidly deposited claystone, (2) uplifted reservoirs sands with hydrocarbons, and (3) lateral transfer from deeper section into shallow reservoirs.

In all the three wells analysed from the West Baram Delta, the pore pressures estimated in the deeper shale tend to be lower than measurements in the sandstones. However, within the shallower overpressured sections in wells WB-6 and Well B, shales and sandstone are in pressure equilibrium. This indicates the overpressure in the shale is a result of disequilibrium compaction. In the deeper section, another mechanism is responsible for the higher pore pressure in the reservoirs. To examine this, velocity-density crossplots of the three wells were made (Figure 4.10).

In well WB-6, the shales plot within the normal increasing trend, confined between the Gardner-Bowers boundaries (Figure 4.10a). No sign of unloading, clay diagenesis or chemical compaction can be seen from the velocity-density crossplot. This suggests that the shales are undergoing disequilibrium compaction and the high overpressure in the sandstones results from pressures transmitted from the deeper, more highly overpressured, section and have not been transmitted into the shales. An analogue for this occurrence is in the Samaan Field, Trinidad (Heppard et al., 1998).

For Well A, the velocity-density crossplot shows a major reversal of trend (Figure 4.10b). In fact, the density reversal is too strong (i.e., large porosity rebound) to be considered a result of unloading. It is more likely that reversal is due to changes in the shale lithology, rather than volume expansion or unloading. A high pressure correction method (Bowers, 1995), which been applied on the overpressured section gave a better match of predicted pressure (Figure 4.11). This suggests that Bowers

(1995) correction method is also applicable for disequilibrium compaction origin that involved facies changes.

Well B, unlike Well A, does not exhibit an unloading trend (Figure 4.10c). Instead, it follows a normal trend along the Bowers lower shale limit. A shift in trend at the shallower depth (4000 ft - 5000 ft) may be due to a lithology change or bad density data, neither of which could be verified from the available data. The main conclusion on the origin of overpressure for Well B is that the shales are undergoing undercompaction as a result of disequilibrium compaction, while higher pressures in the sandstone are the results of pressure transmission from the deeper section. In fact, the high pressures are thought to have bled off from the downthrown section of the fault blocks (Swarbrick, personal communication, 2004).

4.4 West Luconia

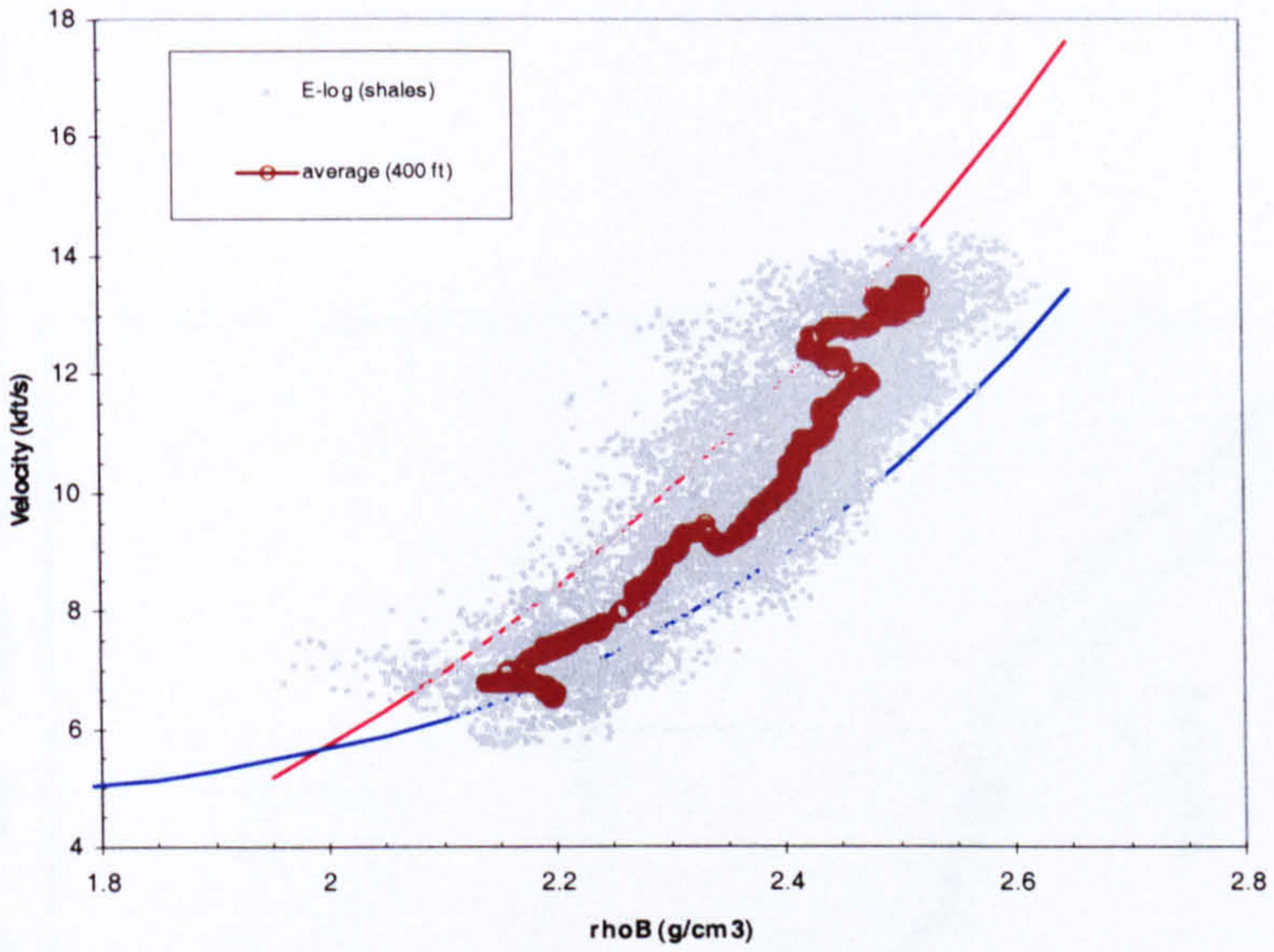
The area has been considered as underexplored with only nine exploration wells having been drilled to date. High CO_2 and overpressure are consider as the main exploration risks in the area.

4.4.1 Stratigraphy

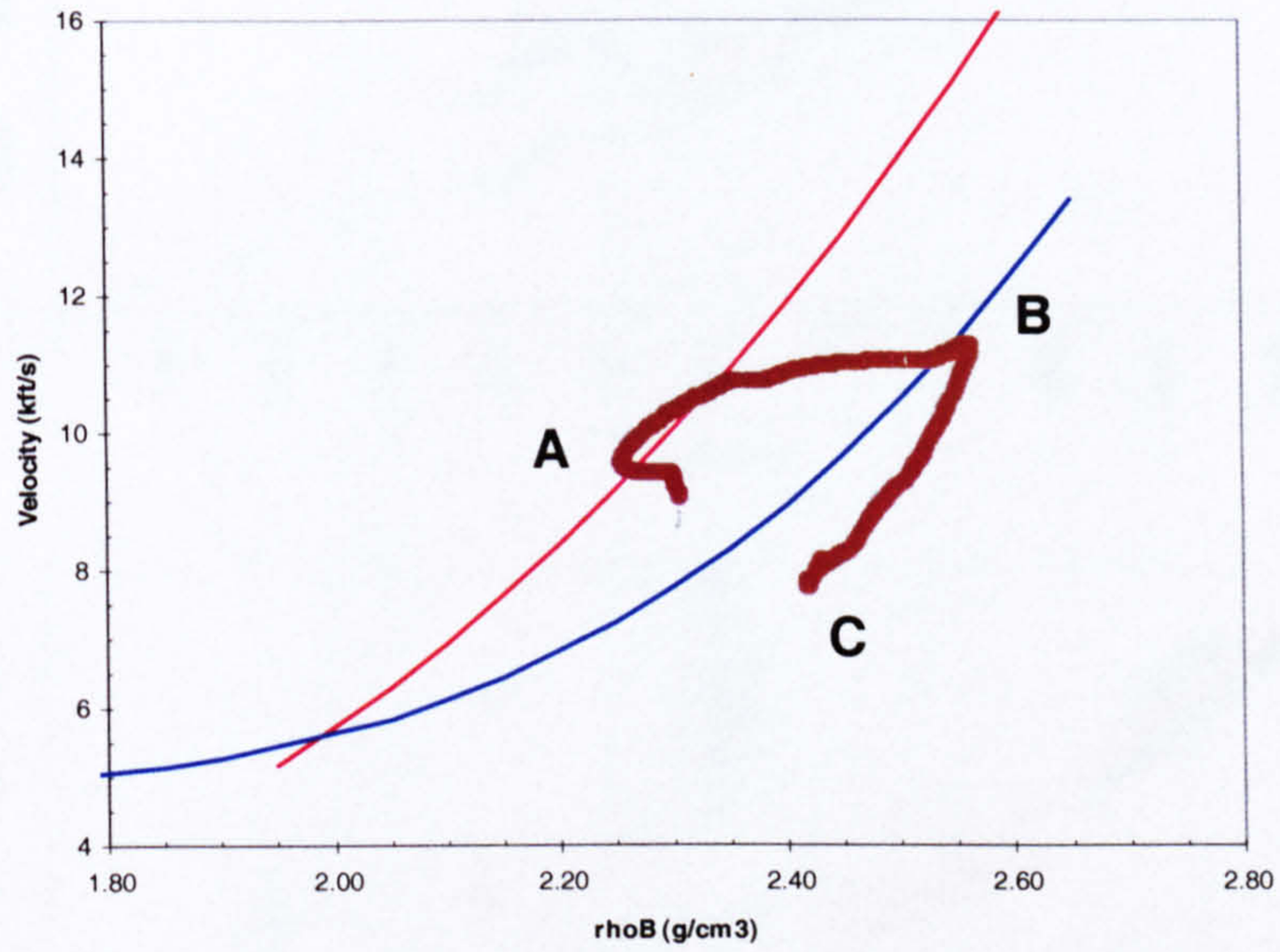
The stratigraphic scheme for West Sarawak follows that of Shell's 'Cycle' concept (Figure 4.12). Each cycle represent regional regressive units that were separated by transgressive units. The stratigraphy in the Sarawak Basin is divided into eight sedimentary cycles, where transgressive marine shale intervals representing cycle breaks (Ho, 1978).

The Oligocene-Early Miocene Cycles I and II represent north-eastward prograding coastal deposits, overlying the Rajang Group Accretionary Prism. Most of these Cycle I and II sediments were removed during a major unconformity at the end of Cycle II. Onlap deposition and renewed faulting towards the end of Cycle III resulted in thick Cycle III accumulation in half-grabens. Continuous subsidence during Cycle IV gave rise to the West Luconia deltaic depocentre and extensive

(a)



(b)



(c)

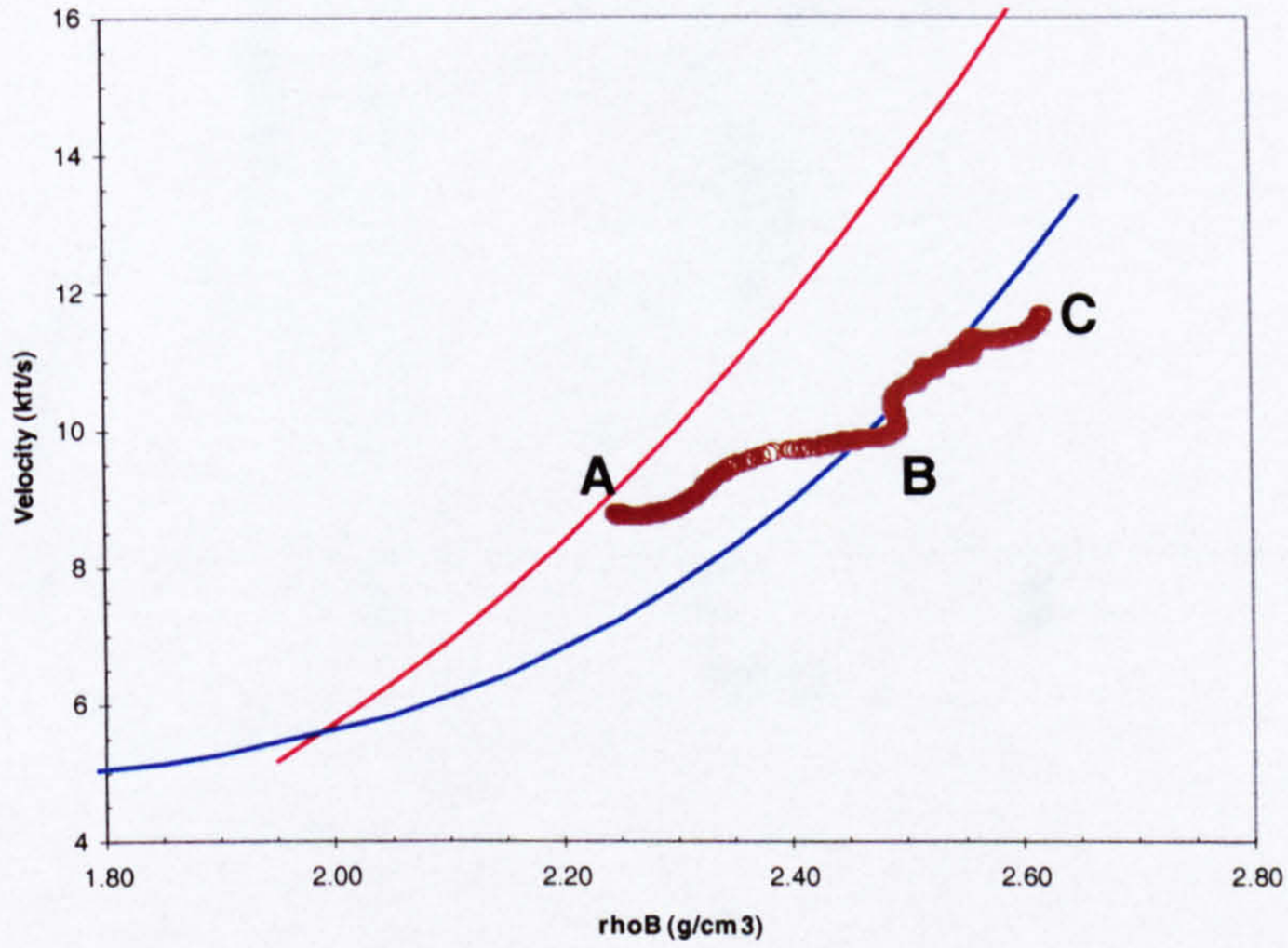


Figure 4.10. Velocity-density crossplots for (a) WB-6, (b) Well A, (c) Well B. Points A, B and C marked major changes in the velocity-density trend (see text for explanation). Red and Blue lines are Gardner's and Bower's relationship for shales, respectively.

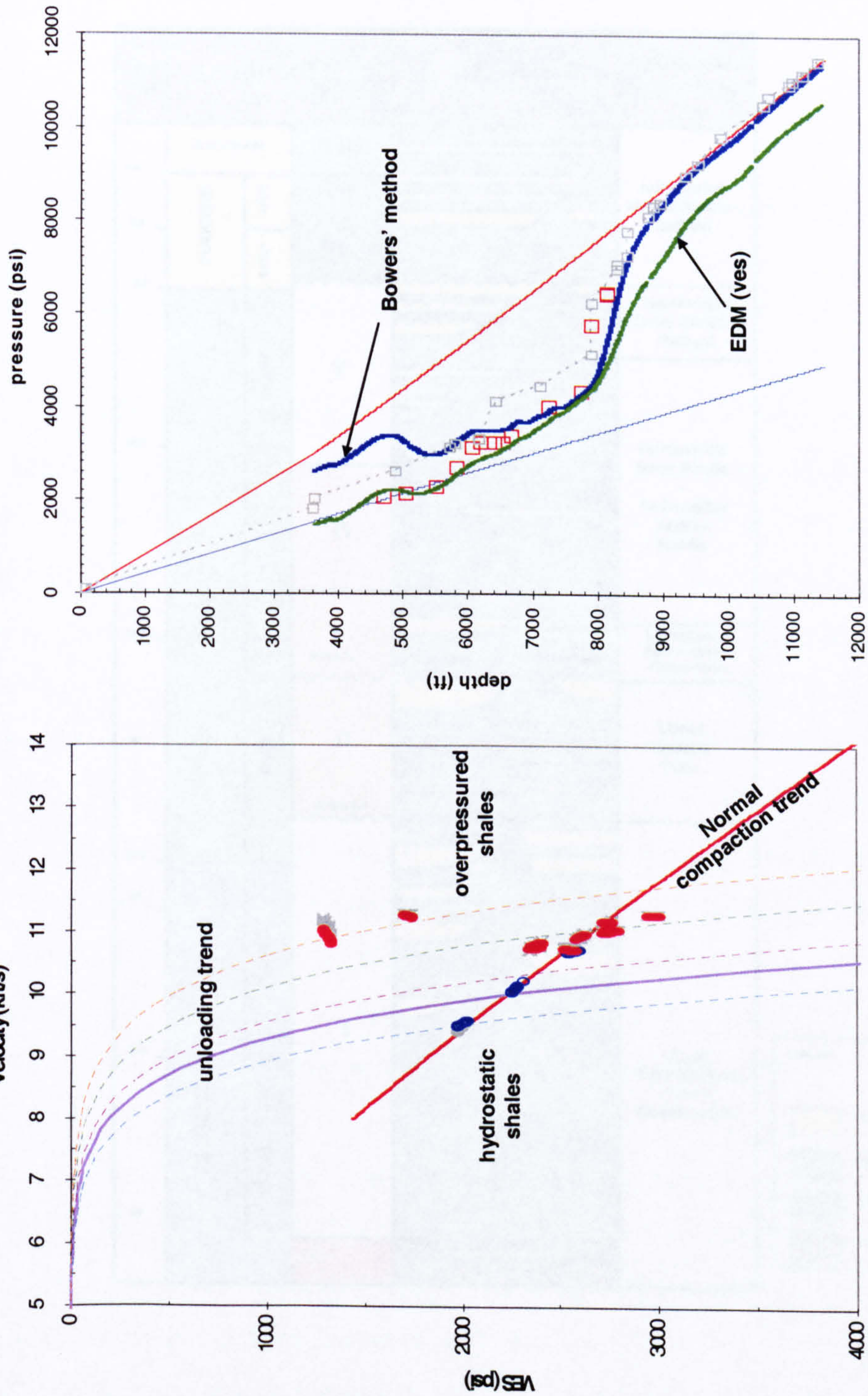


Figure 4.11 Corrected pore pressure using Bowers (1995) method for Well A.

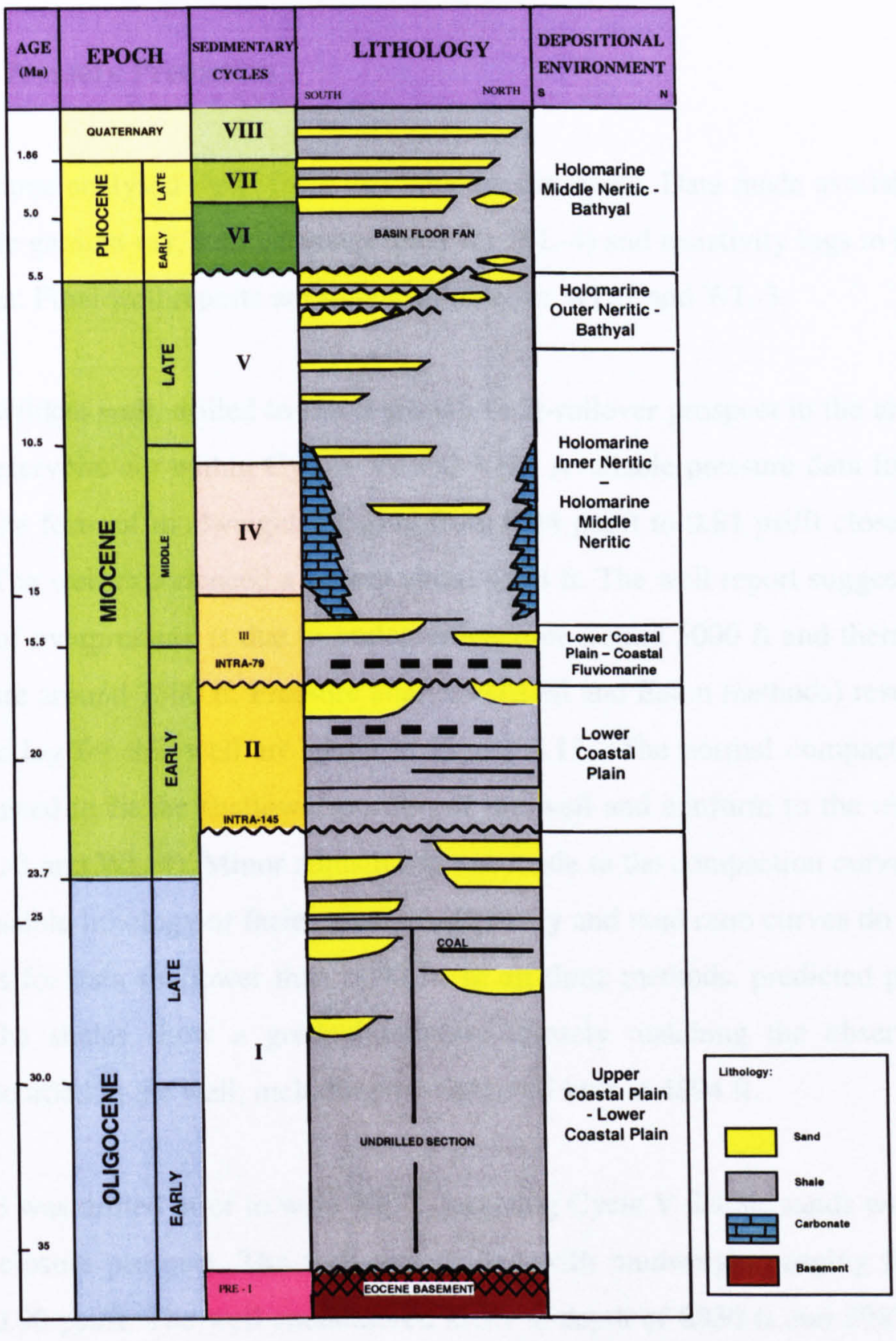


Figure 4.12 Stratigraphy of the West Luconia Province..

carbonate development on structural highs, which was then followed by deposition of Cycle V marine clastics. Gas discoveries and oil shows are found in Cycle V and VI sands, with a high amount of inert gases (CO_2 and N_2).

4.4.2 Pore Pressure Prediction

Results of three analysed wells from this area are discussed. Data made available for this study are gamma-ray, sonic, density (only for WL-4) and resistivity logs in the hardcopy format. Final well reports are only available for WL-2 and WL-3.

WL-2 is a wildcat well, drilled to test a growth fault-rollover prospect in the area. The targeted reservoirs are within Cycles VI and VII. Available pressure data from the well is in the form of mudweight, ranging from 0.44 psi/ft to 0.81 psi/ft close to TD (7546 ft). The well experienced a kick at about 4894 ft. The well report suggested that the onset of overpressure is due to undercompaction around 5000 ft and there is hard geopressure around 7500 ft. Pressure analysis (EDM and Eaton methods) results using the sonic log for this well are given in Figure 4.13. The normal compaction curve was adjusted to fit the shallower portion of the well and conform to the other two wells (WL-3 and WL-4). Minor adjustment was made to the compaction curve to account for possible lithology or facies changes. Porosity and void ratio curves do not allow good fits for data shallower than 3000 ft. In all three methods, predicted pore pressures in the shales show a gradual increase, closely matching the observed mudweights recorded in the well, including the observed kick at 4894 ft.

Well WL-3 was drilled prior to well WL-2, targeting Cycle V deltaic sands with a four-way dip closure prospect. The well was drilled with mudweight ranging from 0.46 psi/ft to 0.90 psi/ft. The well encountered kicks at depth of 8830 ft and 8987 ft. The well report suggested the onset of overpressure due to undercompaction at a depth of 7000 ft. The sonic log was only available to a depth of 8000 ft. Complication arising from overpressure prevented further logging beyond that depth. Results of pressure analysis for this well is shown in Figure 4.14. A steady increase in sonic velocity over the depth interval of 3800 to 6300 ft provides a good trend for the normal compaction curve. All methods show a gradual, lithostatic parallel increase in

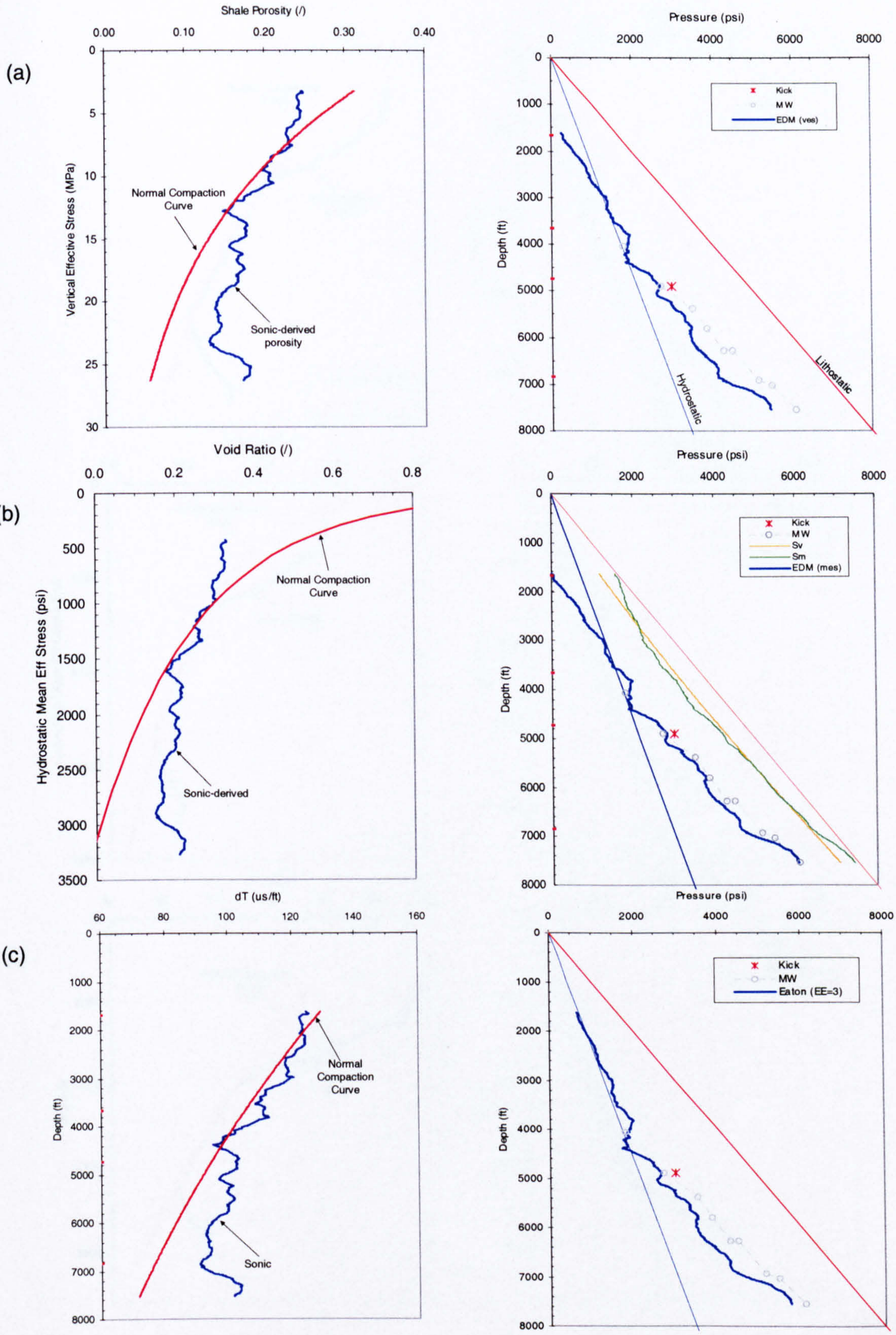
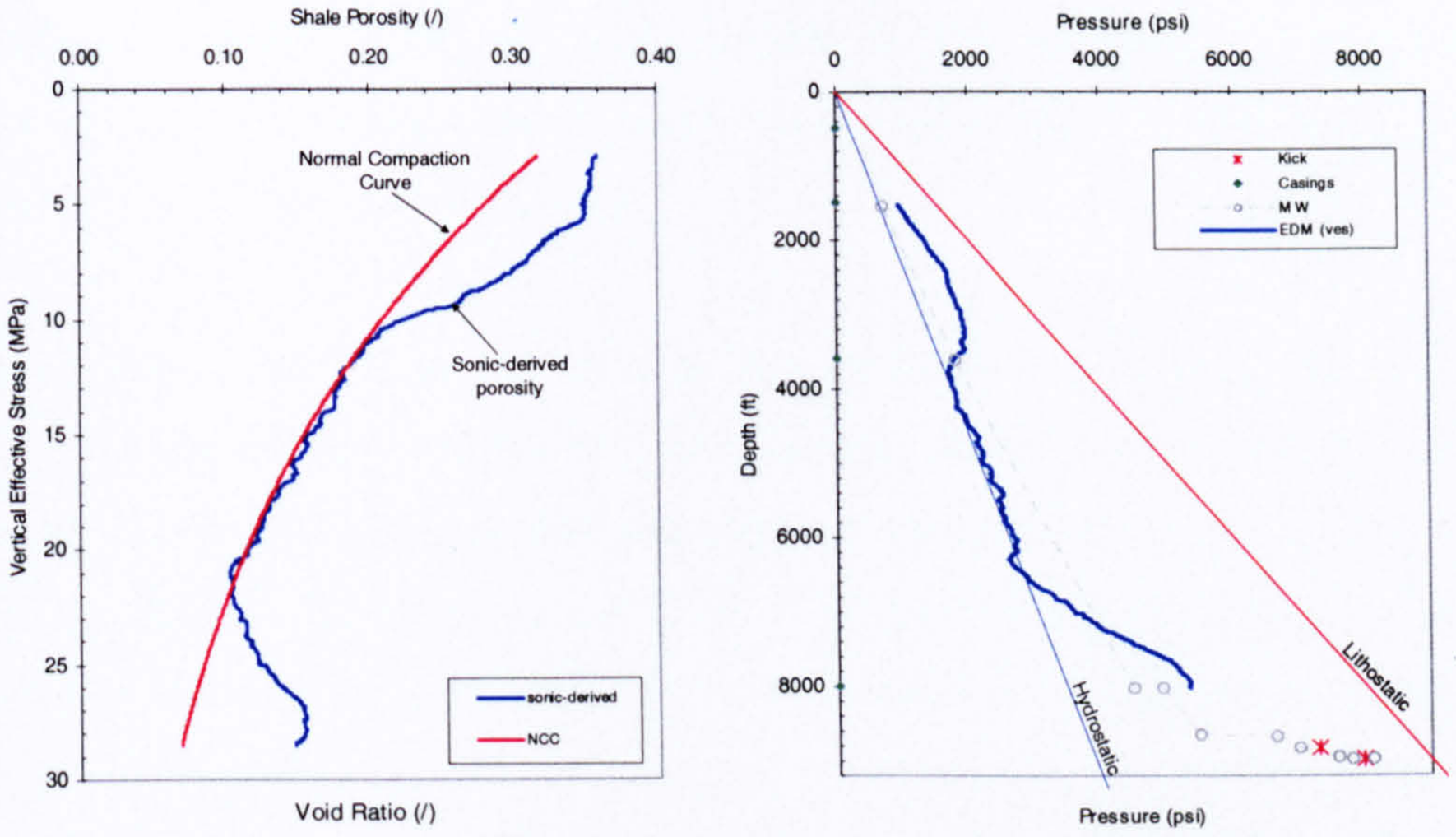
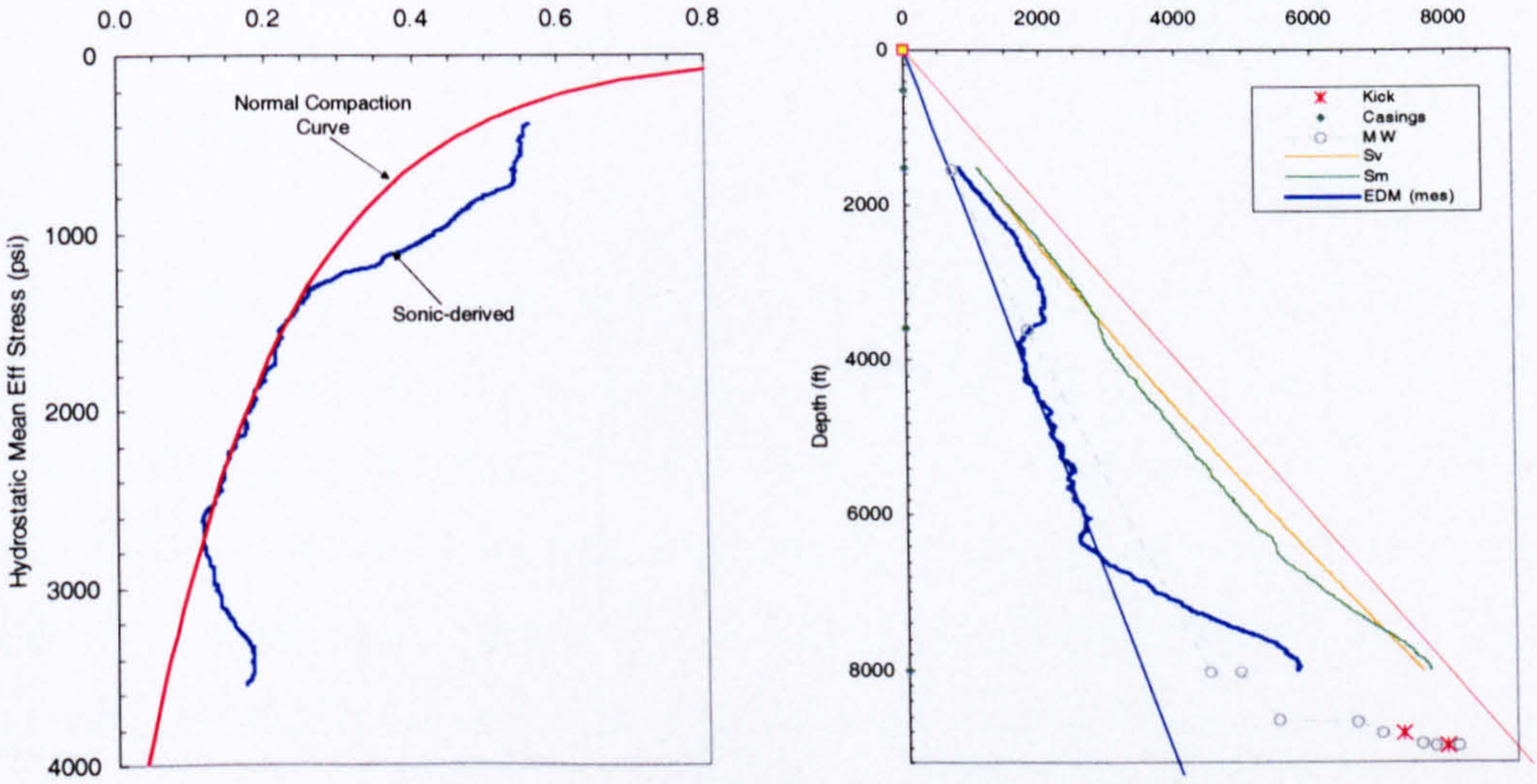


Figure 4.13 Pressure analysis results for well WL-1. (a) EDM (ves), (b) EDM (mes), (c) Eaton.

(a)



(b)



(c)

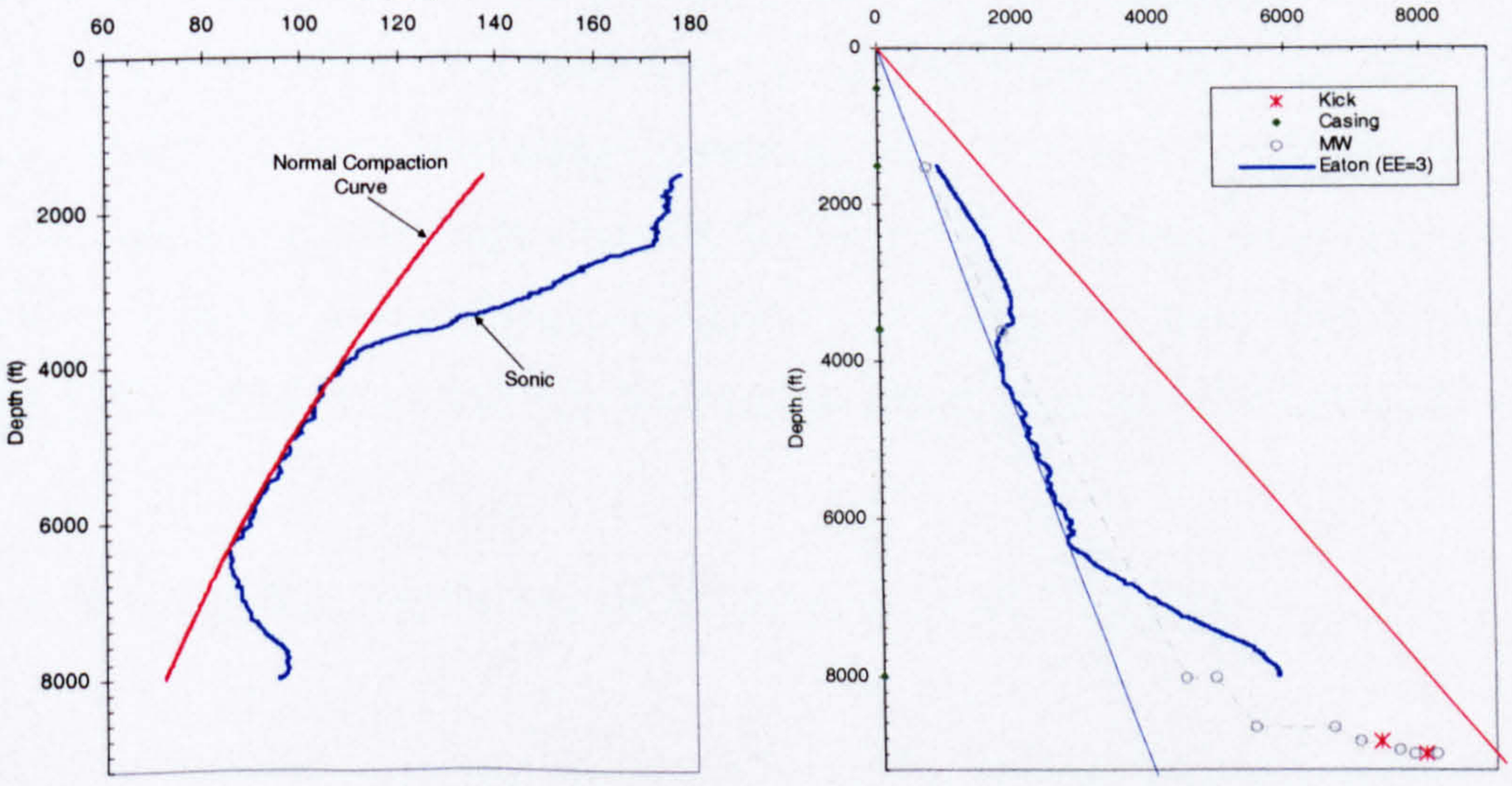


Figure 4.14 Pressure analysis results for well WL-3.

pressure with depth, from the onset at 6400 ft. Extrapolation of the predicted overpressure trend shows a good match with mudweight and two kicks, which occurred in the deeper part of the well.

Well WL-4 contain only mudweight data as subsurface pressure data. No well report is available. However, the well does contain density data for velocity-density crossplot. Pressure analysis in this well suggests the onset of overpressure to be at depth of 3000 ft. EDM (mes) and EDM (ves) gave predicted pressures close to mudweight values. The Eaton method, however, predicted much higher values than anticipated. (Figure 4.15).

4.4.3 Origin

Results from pore pressure analysis in all three wells shows agreement with the measured formation pressures. Pressure equilibrium between the shales and the sandstones suggest that disequilibrium compaction is the most likely overpressure generating mechanism in the area. The velocity-density crossplot for WL-4 shows a steady increasing trend, parallel to the Bowers boundary (Figure 4.16). The data, however fall outside the expected range for shale, whereas the data for all the other wells in this study lie inside the range. Possible shift in log reading (sonic or density) may be an explanation. The trend does not display any deviation from the normal compaction trend that would suggest unloading, diagenesis or chemical compaction as the overpressure generating mechanism. The most likely explanation for overpressure in WL-4 is due to disequilibrium compaction. Unfortunately, there is no density log available for wells WL-2 and WL-3 to confirm the origin of overpressure in the area.

4.5 Log Recognition of Overpressure Origin

Based on the pressure and wireline log analysis conducted for the Malay, Baram and West Luconia basins, a flowchart has been developed to enable determination on overpressure origin in the basin (Figure 4.17). Overpressure resulting from disequilibrium compaction, fluid expansion, clay diagenesis, lateral transfer and chemical compaction can be recognized by combination of prediction methods and

well log signatures.

4.6 Summary and Conclusions

The primary conclusions of this chapter are that:

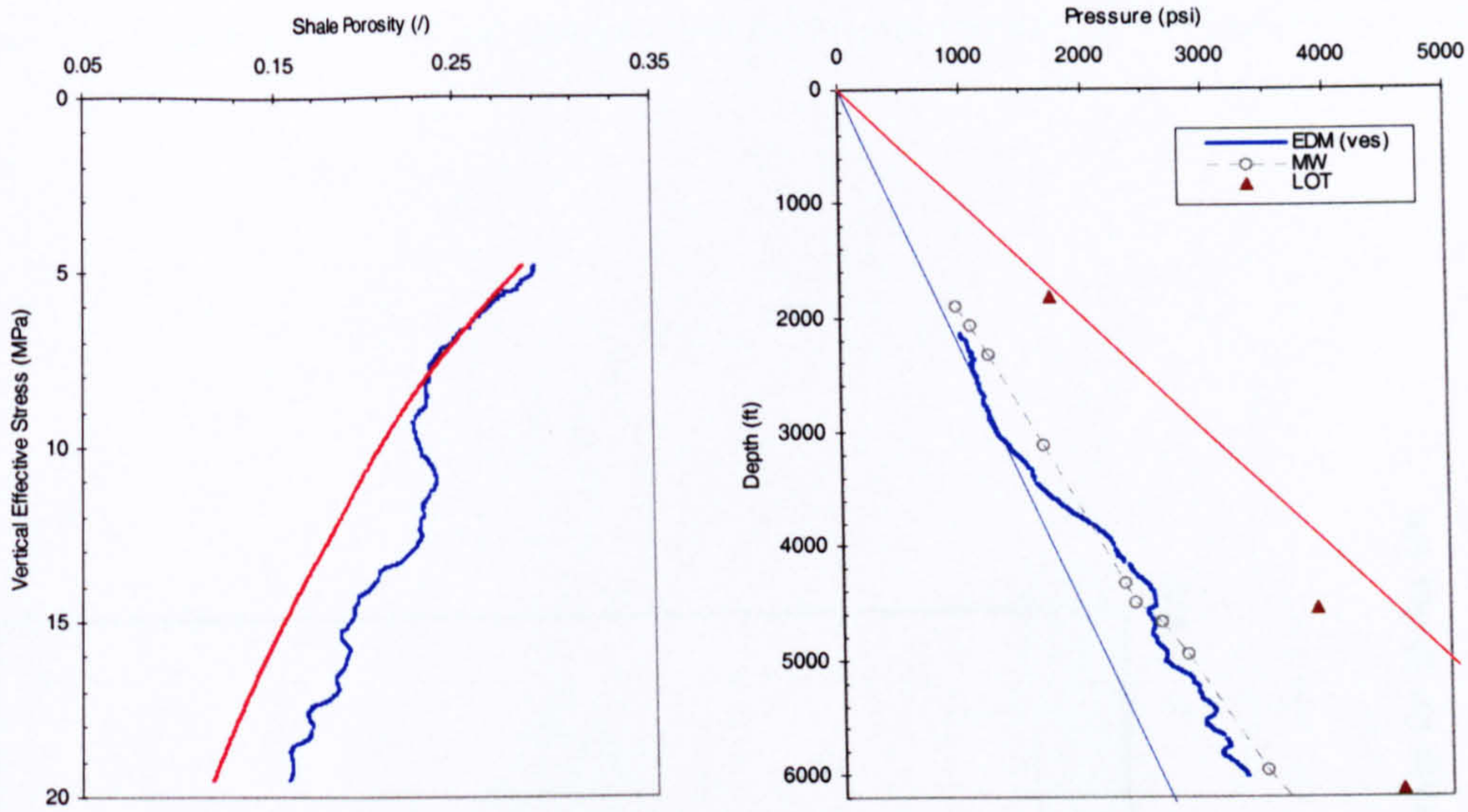
(a) The overpressure in the East Baram wells (EB-2 and EB-3) was generated through disequilibrium compaction. High sedimentary deposition rates due to uplift and deformation prior to middle Late Miocene unconformity contributed much to the overpressure in East Baram.

(b) Disequilibrium compaction and lateral transfer have been deduced for shales in the West Baram (Sarawak and Brunei) wells. Predicted pore pressures in the shales are lower than the formation pressures measured in the sandstones, so processes other than disequilibrium compaction must be involved. Lithology changes may also result in underprediction in pore pressure estimation, giving a similar reversal trend on the velocity-density plot.

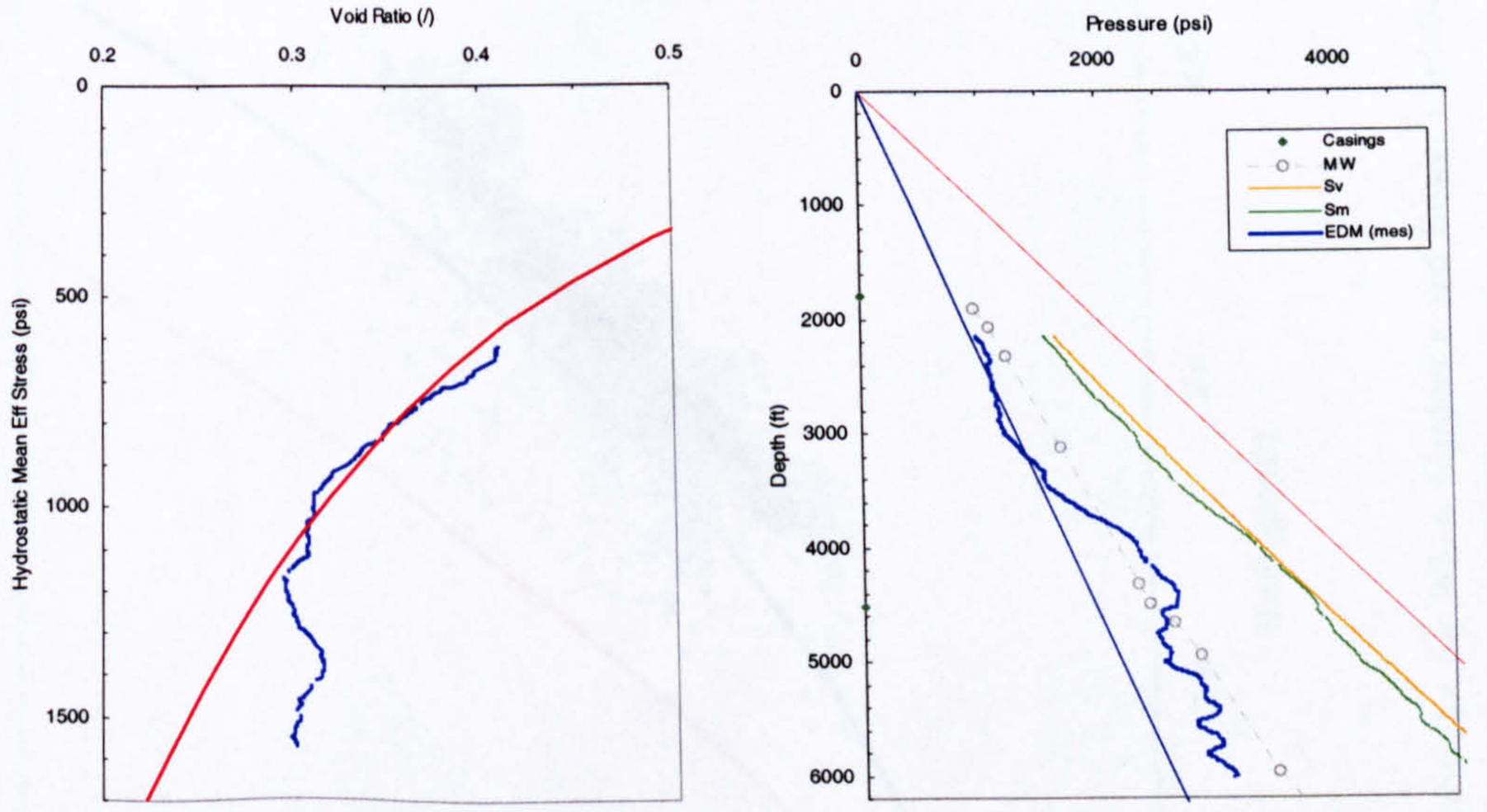
(c) Wells from West Luconia indicate overpressure resulting from disequilibrium compaction. Wireline pore pressure estimation methods gave a good match with the measured formation pressures. The velocity-density plot for one single well shows no deviation or reversal.

(d) No evidence of chemical compaction or clay diagenesis was recorded in the any of the studied wells from East Baram, West Baram and West Luconia. The lower geothermal gradient (25°C to 40°C) in these basins, compared to the Malay Basin (50°C), is suggested to be the reason for the absence of chemical compaction within the shales.

(a)



(b)



(c)

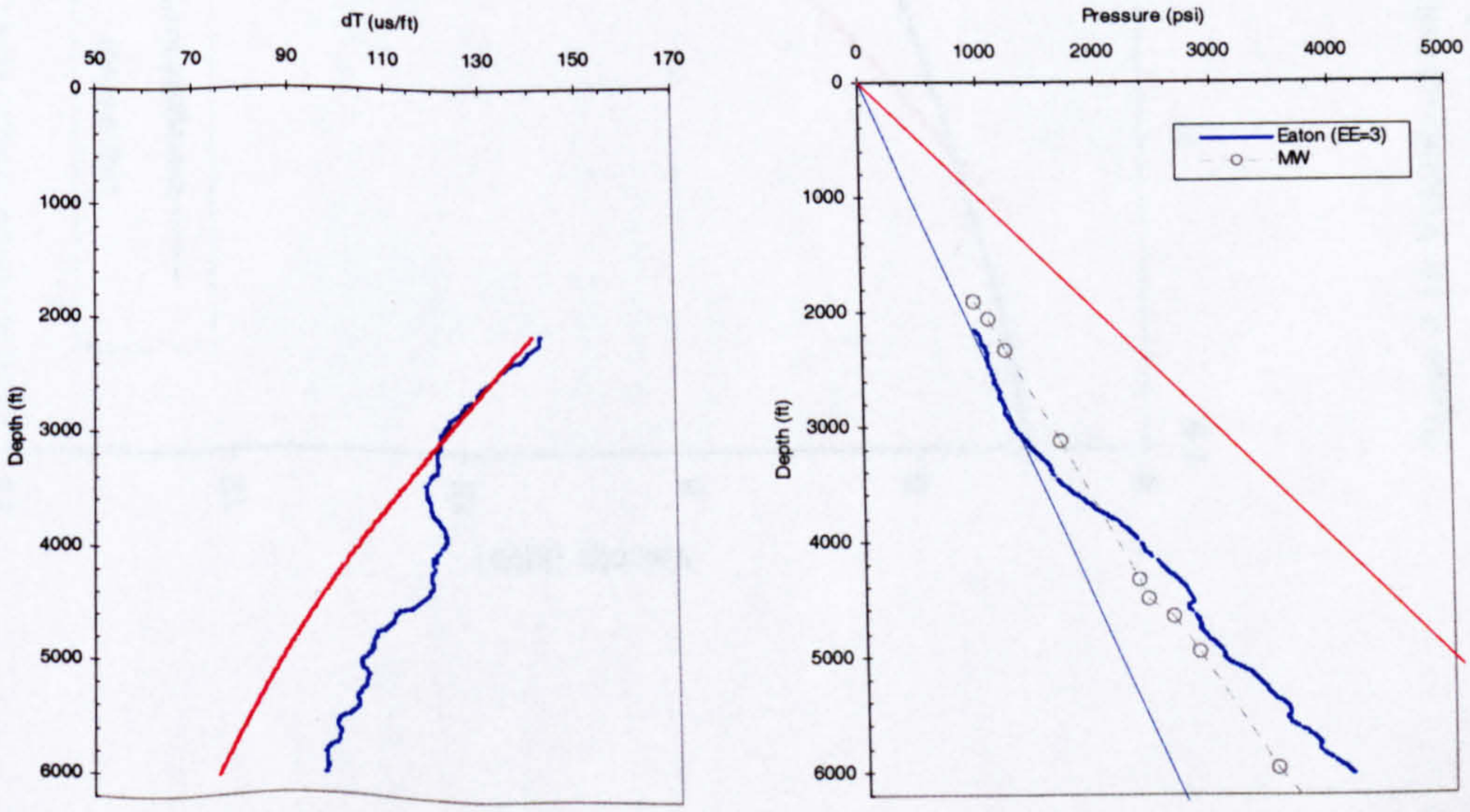


Figure 4.15 Pressure analysis results for well WL-4.

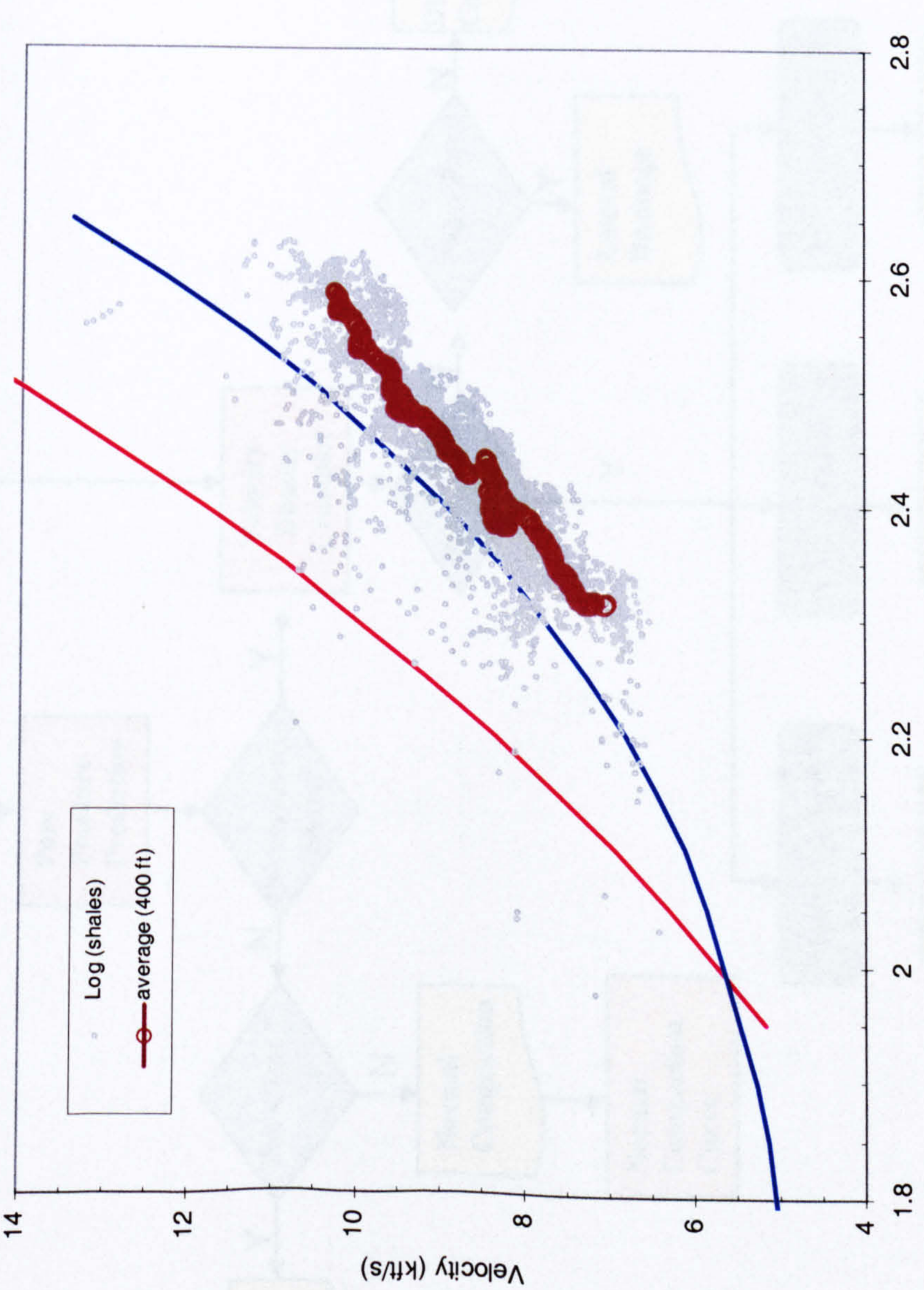


Figure 4.16 Velocity-density crossplot for WL-4. Gardner's and Bower's relationship for shales are shown as red and blue lines, respectively.

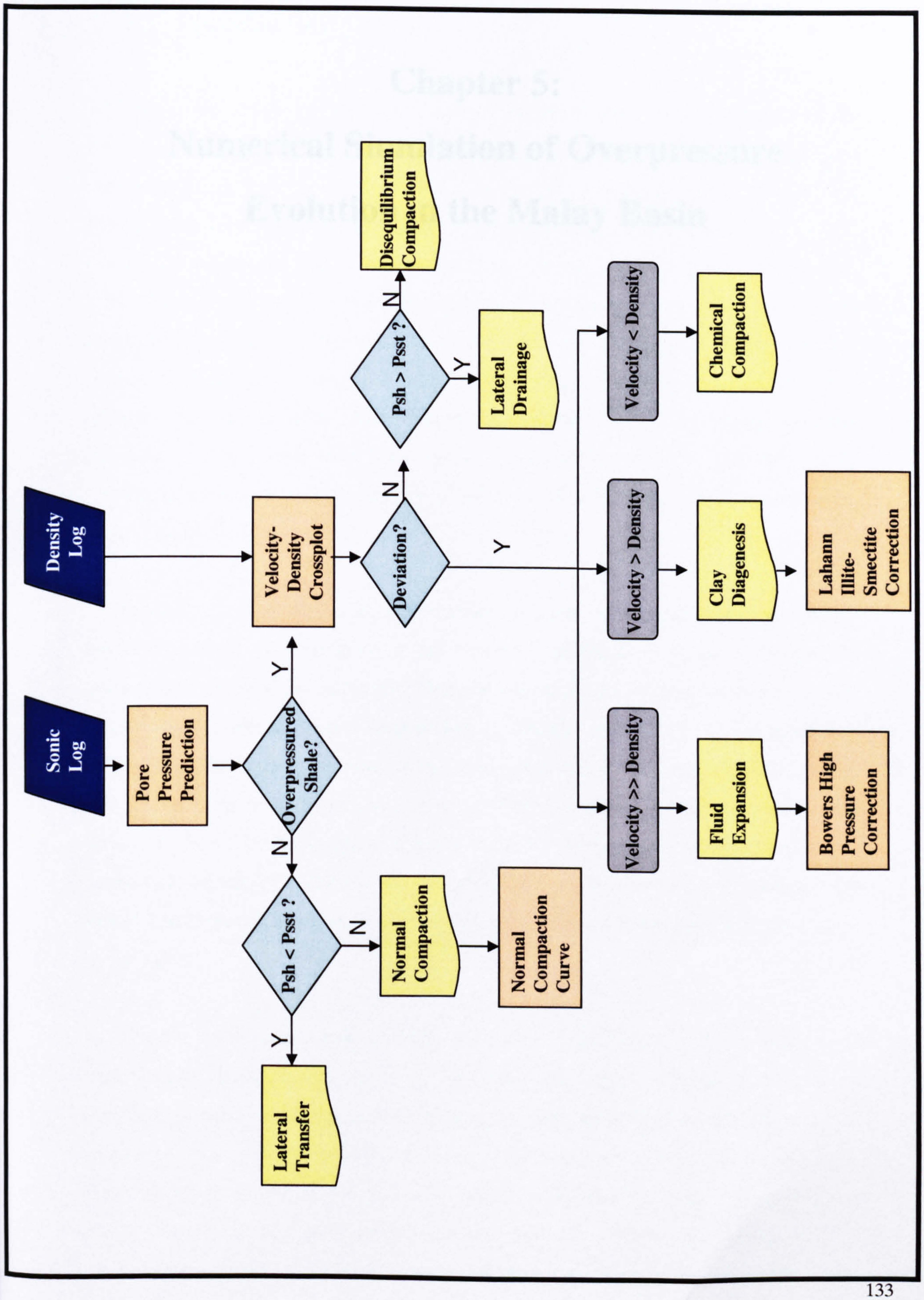


Figure 4.17 Evaluation strategy for determining origin of overpressure.

Chapter 5:

Numerical Simulation of Overpressure Evolution in the Malay Basin

5.1 Introduction

Basin modelling has now becoming a standard tool in oil exploration. Its functional ability to integrate various coupled geological, geophysical and geochemical processes together with increasing knowledge about basin and hydrocarbon formation, and supported by exponential growth in computing ability, has led to widespread use of basin modelling (Hermanrud, 1993; Illife & Dawson, 1996; Giles et al., 1998). It was initially introduced to allow reconstruction of burial and thermal maturity evolution of different source rocks through geologic time. The timing of oil and gas generation and expulsion is critical with respect to the formation of structural traps, to allow assessment of the hydrocarbon type and charge available for plays. Fluid flow modelling has also been developed (e.g., Bethke, 1985). Recent developments in basin modelling allow coupled fluid flow and geomechanical modelling in 3-D.

In view of the numerous input parameters required in running a basin modelling simulation, users must be made aware how each of these parameters subsequently affect the outcome of the end result. There is non-uniqueness in the solutions for each model. This chapter explores several key parameters available in basin modelling software, particularly in relation to the reconstruction of overpressure in the Malay Basin. The purpose of this chapter is to address the following questions: (1) Could disequilibrium compaction process account for the high overpressure in the deeper section of the studied wells? (2) If not, what are the other possible mechanisms? (3) What is the role of chemical compaction in relation to the generation of overpressure in the basin?

Shale is much more prone to overpressure due to its low permeability. Since two-dimensional basin modelling is a very time-consuming process and involves significant amounts of unknown parameters and assumptions, one-dimensional modelling was first undertaken to study different wells across the basin. One-dimensional modelling also allows rapid testing of various lithological properties for easier comparison of results against the observed data. Sensitivity analysis in one-dimensional modelling is very much quicker than two-dimensional modelling. Once

data were obtained, 2-D basin modelling was then undertaken by incorporating the parameters from the 1-D studies. 3-D modelling was beyond the scope of this thesis, as only 2-D Temispack software was available.

There are three main parts to this chapter. The first part presents the methods used in the basin modelling simulation and data requirements. The second part introduces the wells and the cross-section used in this study, together with the assumptions in running these models. The last part discusses the results of the simulation. Four potential mechanisms for overpressure have been examined, namely, disequilibrium compaction, hydrocarbon generation, lateral transfer and chemical compaction.

5.2 Method and Data Input

Both 1-D and 2-D basin modelling runs were carried out using the same 2-D software, Temis2D version 3.0. Only a single column was used in the 1-D modelling. In addition, by limiting 1-D run to a single-phase fluid flow model, a much faster computational time was achieved, compared to a 2-D run.

Temis2D is a finite-volume commercial software that enables the user to simulate basin subsidence, thermal history and hydrocarbon generation and migration as in a sedimentary basin. The details of the algorithms and the modelled processes are given in Ungerer et al. (1990) and Burrus et al. (1991), and in several other publications referenced herein. The rest of this section is a brief description of the modelling processes and the essential input data.

5.2.1 Basin Subsidence and Compaction

Temis2D used a "forward backstripping" method in the computation of subsidence and burial histories. The sedimentary columns are first backstripped to determine the porosity-depth relationships for relevant lithologies, so subsequent forward modelling is based on these predetermined porosity-depth relationships. If the sedimentary thickness does not match the original section, the porosity-depth relationships are assumed to be no longer applicable. This is certainly the case in

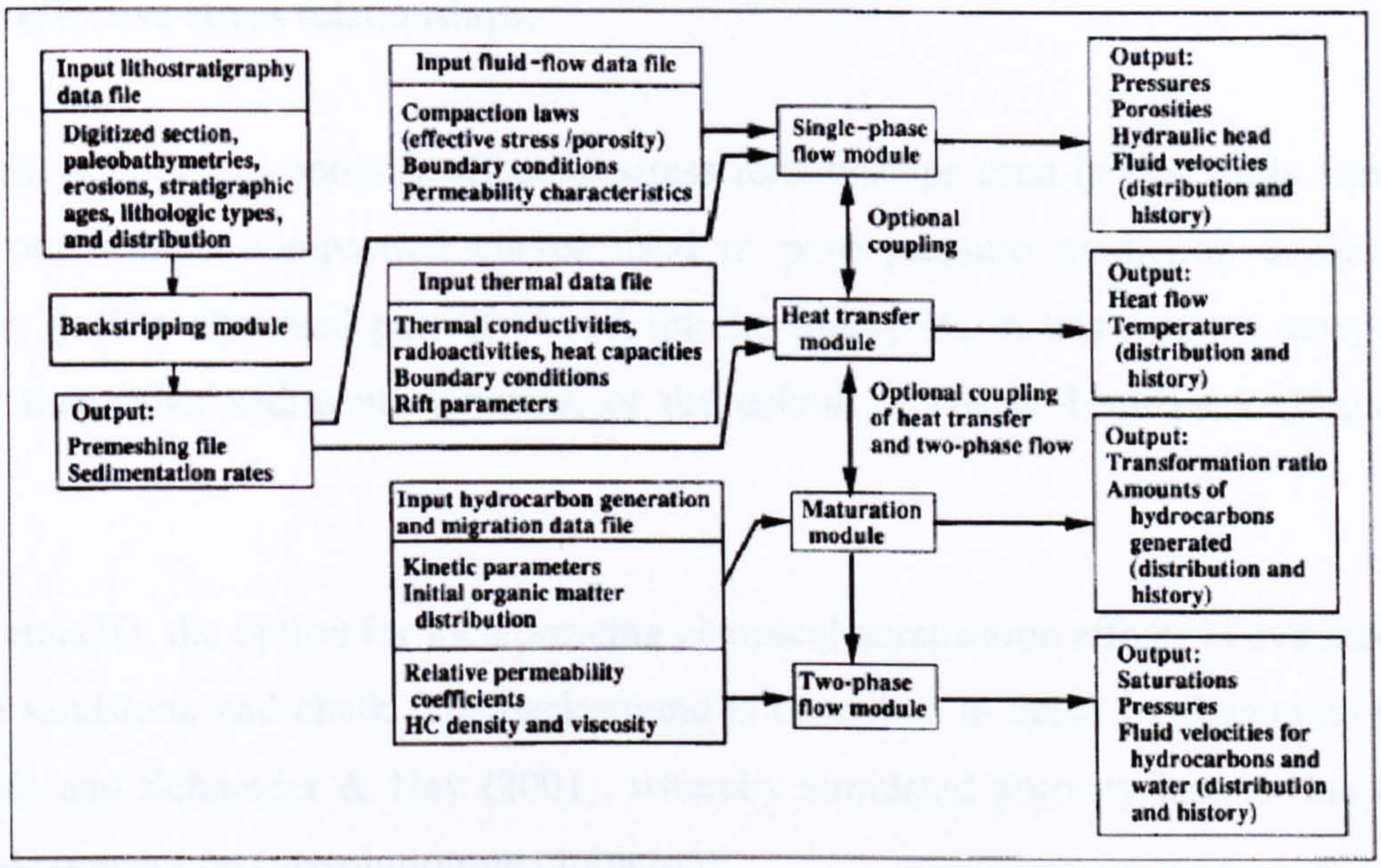


Figure 5.1 Schematic flowchart for a typical basin modelling study (from Ungerer et al., 1990)

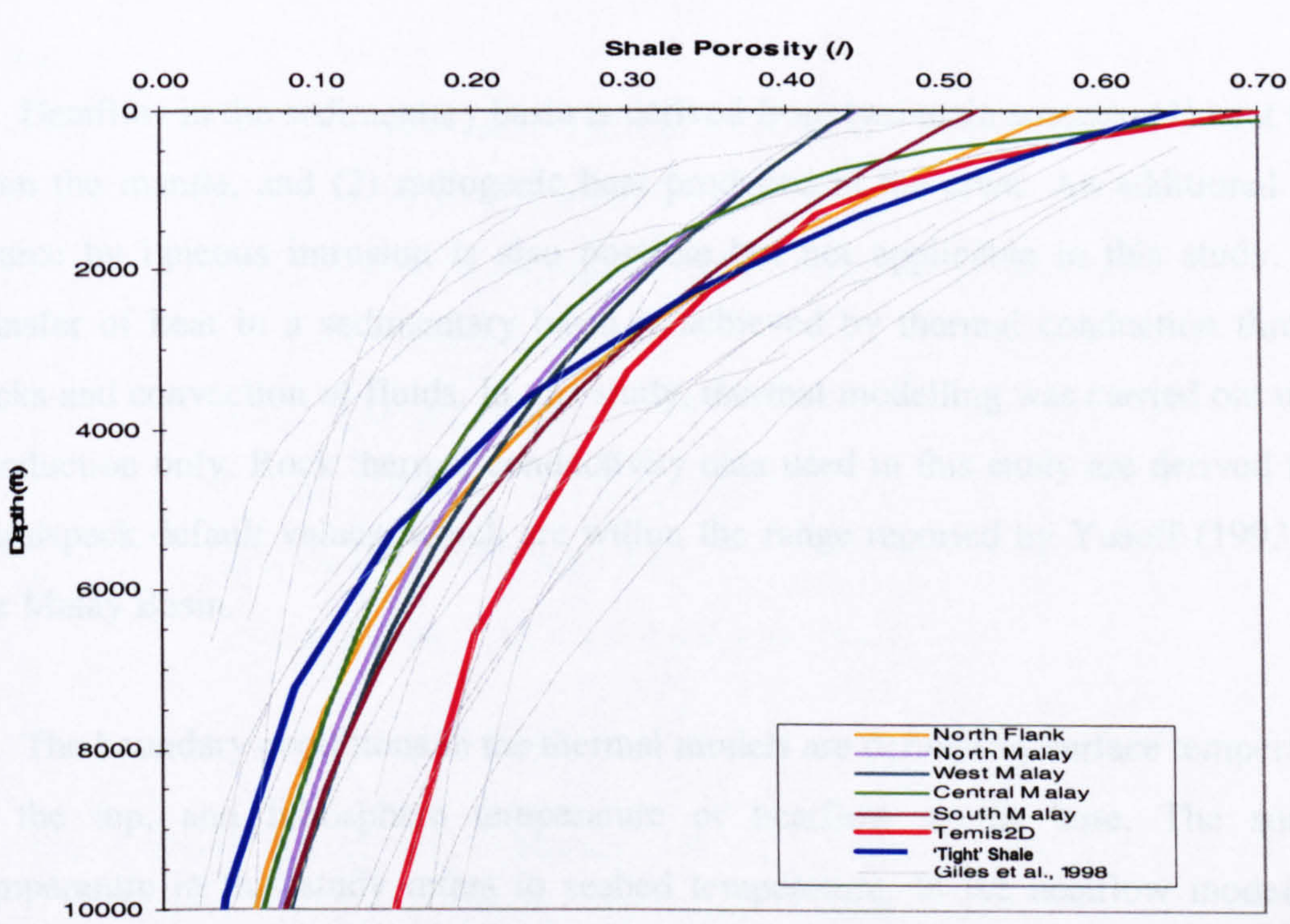


Figure 5.2 Porosity-depth trend for shales in the Malay Basin. Also plotted for comparison are data from Giles et al. (1998) and Temispack default value for shale.

overpressured sequences, where undercompacted rocks are no longer subjected to the normal porosity-depth relationships. Sediment compaction is then governed by porosity-effective stress relationships.

Porosity-depth and porosity-effective stress relationships used in this study were taken from normal compaction curves used in pore pressure prediction analysis (Chapter 2). The observed porosity trend for the Malay Basin has a much steeper gradient than other sedimentary basins, or the default values in Temispack (Figure 5.2).

In Temis2D, the option for incorporating chemical compaction effects is available for both sandstone and chalk. The background is described in detail by Schneider et al. (1996) and Schneider & Hay (2001), whereby simulated porosity loss is due to chemical compaction (dissolution-precipitation).

5.2.2 Thermal History

Heatflow in the sedimentary basin is derived from two main sources: (1) heat flow from the mantle, and (2) radiogenic heat produced in the crust. An additional heat source by igneous intrusion is also possible but not applicable in this study. The transfer of heat in a sedimentary basin is achieved by thermal conduction through rocks and convection of fluids. In this study, thermal modelling was carried out using conduction only. Rock thermal conductivity data used in this study are derived from Temispack default values, which are within the range reported by Yusoff (1993) for the Malay Basin.

The boundary conditions in the thermal models are defined by surface temperature at the top, and lithosphere temperature or heatflow at the base. The surface temperature in this study refers to seabed temperature. In the heatflow model, the magnitude of heatflow can either be constant or varies with geological history, such as in rifting. With the current Temis2D (ver 3.0), it is not possible to run rifting heatflow in the fluid flow mode. Hence, a constant heatflow model was used. A test was carried out to examine the difference between using a rifting and a constant heat flow and the

result indicates they do not differ very much (see Chapter 6.3.1).

The thermal models are constrained by present-day temperature and paleotemperature indicators, such as vitrinite reflectance. The temperature was computed using the transient heatflow model, rather than steady-state. Transient heatflow takes into account the thermal blanketing effect due to rapid burial, as well as the cooling of sediments resulted from dumping of colder sediment on the top. Vitrinite reflectance was computed using kerogen Type III hydrogen-poor vitrinite.

5.2.3 Pore Pressure and Fluid Flow History

Fluid flow and the resulting pore pressure are modelled using effective stress-porosity relationships. The fluid movement is computed using Darcy's law, which has been adapted to include rock with very low permeability:

$$V_x = -(K.K_x)/\mu_x * \text{grad}(((P+P_c)/\rho_x.g)-Z) \qquad (5.1)$$

where

V_x is the rate of fluid movement for phase x (water, oil, gas),

K is the intrinsic permeability (in m^2),

K_x is the relative permeability of phase x (water, oil ,gas),

μ_x is the viscosity (in Pa.s),

P is the pore pressure,

P_c is the lithology capillary pressure,

ρ_x is the fluid volume (in kg/m^3),

g is the gravitational acceleration (in m/s^2).

The permeability of the sediments can be computed from porosity using a standard Kozeny-Carman relationship. However, two other options are available, (1) a linear porosity-permeability relationship, and (2) the users empirical input.

The Kozeny-Carman equation relates permeability to specific surface area and porosity. For permeable sediments ($\phi > 0.10$), the equation is a given as:

$$K= 0.2\phi^3 / (S_o^2 (1-\phi)) \quad (5.2)$$

where,

K is permeability in m^2,

S_o is the specific surface area in m2/m3,

ϕ is the porosity.

For low permeability sediments (ϕ<0.10), a modified Kozeny-Carman equation is used:

$$K=20\phi^5 / (S_o^2 (1-\phi)) \quad (5.3)$$

Neuzil (1994) published permeability data for shales, ranging from 10^{-15} m^2 to 10^{-22} m^2 (1 nD=10^{-21} m^2). The anisotropy in permeability of the lithologies is taken into account by assigning various anisotropy coefficients to the lithologies. The anisotropy coefficient varies from 0.5 to 10^{-2} for the vertical permeability and about 1 for the horizontal permeability. Table 5.1 listed some examples of measured and modelled data that have been published.

5.2.4 Hydrocarbon Generation and Migration

Hydrocarbon generation is modelled from each source rock which has been assigned with a specific kerogen kinetics scheme. The kerogen conversion to hydrocarbons is governed by multiple parallel first-order kinetics, as described by Arrhenius' law:

$$k=Ae^{-(E/RT)} \quad (5.4)$$

where,

k is the rate constant in s^{-1},

E is the activation energy per mole,

R is the universal gas constant (0.001987 kcal/mol),

A is the frequency factor in s^{-1},

T is the temperature in Kelvin.

Table 5.1 Examples of published porosity-permeability data for shales.

Samples	Lithology	Location	Porosity (*f*)	Permeability (m^2)	So (m^2/m^3)	Kh/Kv	References	Notes
Venture B-13	Shale	Scotian Shelf	4.8	6.7E-23			Katsube et al., 1990	Measured
Venture B-52	Shale	Scotian Shelf	5.7	4E-21			Katsube et al., 1990	Measured
Dunlin,	Shales	N. Viking	0.1	1E-21	2E8	500	Burrus, et al., 1991	Modelled
Sd5-Sh95	mixed	Mahakam	0.1	2E-20		1	Burrus et al., 1992	Modelled
Sd5-Sh93-OM2	mixed	Mahakam	0.1	2E-20		1	Burrus et al., 1992	Modelled
Mahakam	Shale	Mahakam	0.17	4E-20	1E8	1	Burrus et al., 1993	Modelled
Bakken Shale	Shale	Williston Basin	0.15	4E-18	1E8	100	Burrus et al., 1993	Modelled
Lower Toarcian	Shale	Paris Basin	0.12	3E-18	3.2E7	10	Burrus et al., 1993	Modelled
Cretaceous +	Shale	Tampen Spur		3.7E-20	1E8	333	Moretti & Deacon,	Modelled
Draupne	Shale	Tampen Spur		3.7E-20	1E8	10	Moretti & Deacon,	Modelled
Heather	Shale	Tampen Spur		3.7E-20	1E8	10	Moretti & Deacon,	Modelled
Drake	Shale	Tampen Spur		3.7E-20	1E8	10	Moretti & Deacon,	Modelled
Faults	Barrier	Tampen Spur		3.7E-20	1E8	10	Moretti & Deacon,	Modelled
c	Si15-Sh85	Williston Basin	0.10	4E-21		1	Burrus et al., 1996	Modelled
d '	Sd30-Sh60-	Williston Basin	0.10	4E-19		1	Burrus et al., 1996	Modelled
e	Si50-Sh50	Williston Basin	0.10	4E-21		2	Burrus et al., 1996	Modelled
e'	Sd50-Si20-	Williston Basin	0.10	4E-20		2	Burrus et al., 1996	Modelled
f	Sd50-Si50	Williston Basin	0.10	4E-16		1	Burrus et al., 1996	Modelled
Post-Turonian	Shale	Barrow	0.10	6E-18		100	Bekele et al., 2001	Modelled
Muderong Sh	Shale	Barrow	0.10	6E-19		100	Bekele et al., 2001	Modelled
Barrow Gp	Shale	Barrow	0.10	6E-18		100	Bekele et al., 2001	Modelled
Tithonian Sh	Shale	Barrow	0.10	6E-19		100	Bekele et al., 2001	Modelled
Kim/Oxfordian	Shale	Barrow	0.10	2E-20		100	Bekele et al., 2001	Modelled

Note: 1 nD = 10^{-21} m^2

For the purpose of modelling hydrocarbon generation, default values for kerogen Type I and Type III Mahakam were assigned to the Oligocene-Miocene lacustrine shale and middle Miocene coaly shale, respectively. These are believed to be the closest analogues to the Malay Basin source rocks.

Source rock data have been compiled from various unpublished reports to build a source rock model for the basin modelling. Statistical analyses on these data show that the average total organic carbon content (TOC) is 2% and 20% for the shales and the coaly shales, respectively. The coals naturally have a much higher TOC, averaging around 55% (see Chapter 6.2 later). Original total organic carbon (TOC_o) and original hydrogen index (HI_o) for different source rocks were roughly estimated on basis of measured TOC and HI, thermal maturity and original kerogen quality. For coals and coaly shales, the average TOC_o is 20%, and average HI_o is 300 mg hydrocarbons/g TOC.

5.3 Wells, Cross-Section and Model Assumptions

Two wells in the south of the basin were selected for a detailed study. These wells (SM-28 and SM-30) show signatures of chemical compaction (Chapter 3). A cross-section (Section EW) passing through one of the wells was also selecting for modelling. This section extends down to the basin depocentre where the inferred source rocks are subjected to highest maturity and overpressure.

5.3.1 Input Data

Results of pore pressure analysis of wells SM-28 and SM-30 have been discussed in Chapter 2. The formation tops are taken from well completion reports and well-log information. For the non-penetrated sequence, sedimentary thickness was derived from unpublished regional studies carried out by Petronas Carigali (1994) and Esso Production Malaysia Inc (EPIC, 1994).

Formation ages are adopted from the EPIC report, with the exception of the Top D marker horizon. The eroded thickness for the Malay Basin, estimated from the

wireline log is less than 700 ft (Chapter 3). The paleobathymetric depths are kept as constant (500 ft), in view of the stable shelf position prevailing throughout the geological history (Yakzan et al., 1994; Madon & Watts, 1998). The relative sea-level change through time was based on eustatic curves (Haq et al., 1987).

A cross-section, Section EW, was interpreted and depth-converted from a regional seismic line transversing east-west in the southern part of the basin (Figure 5.4). Another line (Section NE), perpendicular to Section EW, will be discussed in the next Chapter. Several wells that are located along these sections provide data for model calibration. The lines also pass between a number of oil and gasfields, which are located on both sides of the section. They provide further information on petroleum systems for the modelling.

In 1-D well modelling, lithologies are estimated from gamma-ray logs. In addition, the wireline logs of these two wells were sent to University of Newcastle-upon-Tyne for ShaleQuant analysis. ShaleQuant provides information on the amount of clay fraction (< 2μm) present in shaley rocks, and estimates of shale permeability from wireline logs, based on artificial neural networks (Yang et al., 2004). These results served as additional data in constraining the models.

Both gamma-ray log and ShaleQuant's clay fraction results were used to subdivide lithostratigraphy in SM-28 and SM-30 (Figure 5.3). To avoid excessive computation time and uphold software stability, the thickness of the cells are kept between 23 and 60 m in 1-D models and between 40 and 200 m in 2-D models. Also, a more regular grid will helps to improve computation time. There are several approaches to assigning the compaction and petrophysical values of the sediments. The simplest is to assign the default values based on the amount of shale and sandstone. An alternative is to group the layers into two categories: low permeability sediment (for clay content exceeding 40%) and high permeability sediments (Figure 5.3). Since the focus is to investigate the shale behaviour in relation to overpressure, the shale properties are modelled while the high permeability sediments are assigned as sandstone using default values in Temispack. The later approach has been adopted in this study.

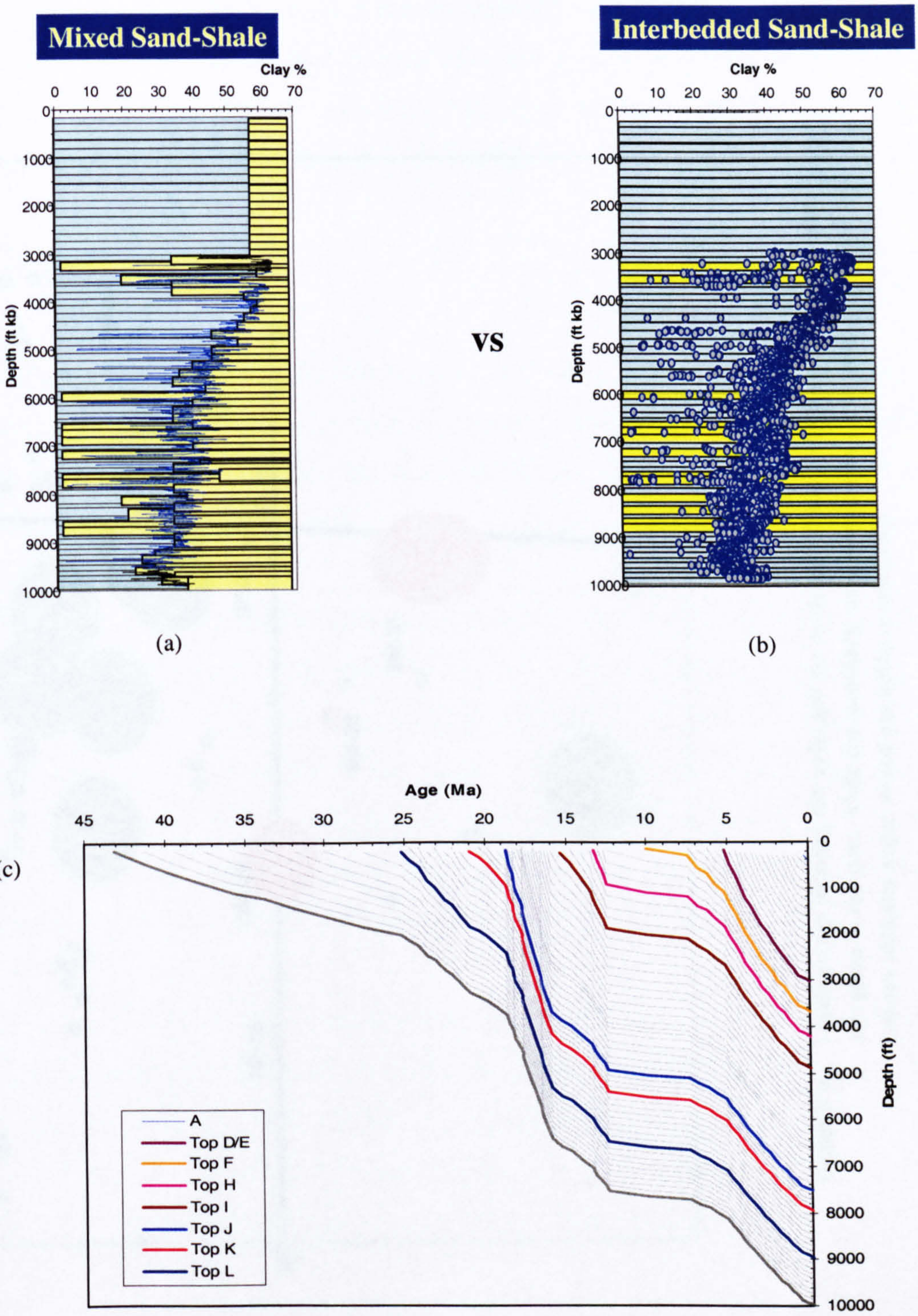


Figure 5.3 1-D modelling: (a) assigning each layer a set of petrophysical data based percentages of shale content; (b) treating the layers as either shale (low permeability) or sandstone (permeable). The clay content is derived from ShaleQuant wireline log analysis (blue line/grey dots). (c) Burial history plot for well SM-28.

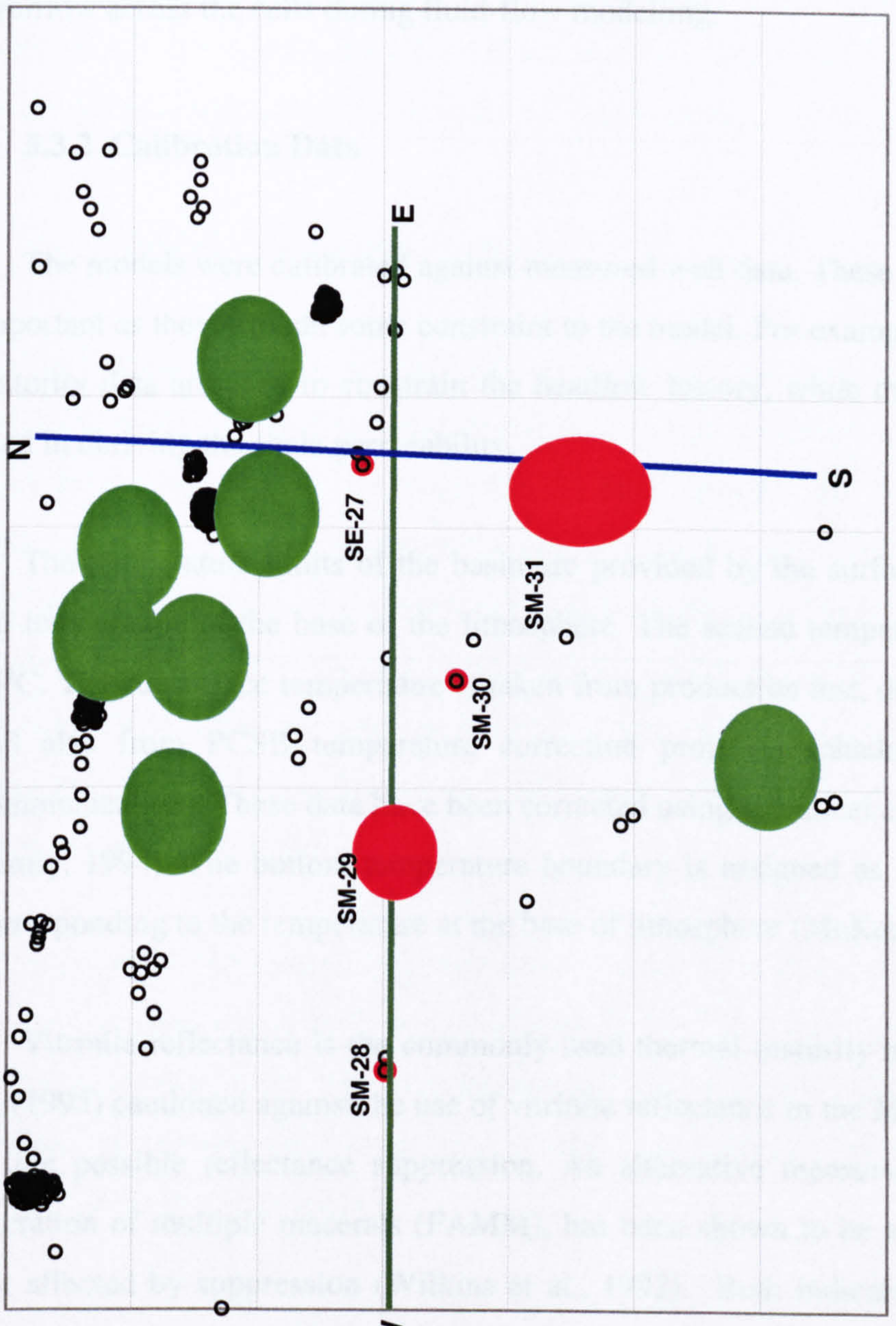


Figure 5.4 Location map showing the wells and the modelled 2D lines. Wells analysed in Chapter 2 are given in red dots, while the remaining wells in the area are in grey. Green and red colours indicates major oil and gas fields, respectively.

For the 2-D models, lateral lithological variations are based on the sand-shale percentages taken from PCSB regional study report (Leslie et al., 1994). Section EW (Figure 5.4) consists of 13 main horizons corresponding to the top of stratigraphic groupings. Additional stratigraphic horizons were added between the main horizons to avoid large contrasts in thickness between the layers which could result in large overflow across the cells during fluid-flow modelling.

5.3.2 Calibration Data

The models were calibrated against measured well data. These calibration data are important as they provide some constraint to the model. For example, temperature and maturity data are used to constrain the heatflow history, while the pressure data are used in deriving the shale permeability.

The temperature limits of the basin are provided by the surface temperature and the temperature at the base of the lithosphere. The seabed temperature was taken as 15°C. The subsurface temperature is taken from production test, drill stem test (DST) and also from PCSB temperature correction project (Mahadir Ramly, personal communication). These data have been corrected using statistical approach (Waples & Ramly, 1994). The bottom temperature boundary is assigned as 1330°C at 120 km, corresponding to the temperature at the base of lithosphere (McKenzie, 1978).

Vitrinite reflectance is the commonly used thermal maturity indicator. Waples et al. (1995) cautioned against the use of vitrinite reflectance in the Malay Basin because of the possible reflectance suppression. An alternative measurement, fluorescence alteration of multiple macerals (FAMM), has been shown to be more reliable and is not affected by suppression (Wilkins et al., 1992). Both indicators are used in this study.

Porosity and permeability data for measured core are collated from unpublished well reports. No data are available for the shales. Shale porosity is derived from sonic and density logs. Shale permeability is calculated from ShaleQuant log analysis (Figure 5.5). Pressure data from wireline tools (RFT) and mudweights were available

for both wells.

5.4 Modelling Results

Overpressure resulting from disequilibrium compaction depends on the rate of sediment loading against the rate of fluid escaping. These two processes are coupled by the porosity reduction and the sediment permeability.

5.4.1 Model 1: Mechanical Compaction

As mentioned earlier, the porosity reduction process in Temispack is modelled using the porosity-effective stress double exponential relationship given in Equation 2.13. From Chapter 2, it was found that the porosity-depth and the porosity-effective stress relationship for the shales in the Malay Basin is significantly different from the published examples and the Temispack default values (see Figure 5.2). Therefore, it is necessary to establish the relationship for the Malay basin rather than to rely on the default values. The porosity coefficient and the exponent factors in Equation 2.13 were adjusted to fit the density-derived porosity data from the normally pressured shale section in the wells.

A series of 1-D models was run by varying the vertical permeability of the shales (at 10% porosity) from 10^{-20} m^2 (10 nD) to 10^{-22} m^2 (0.1 nD) in order to recreate the observed overpressure. The vertical permeability (Kv) was varied by changing the vertical anisotropy coefficient (C_v), while the intrinsic permeability (K) were determined from Equation 5.3:

$$Kv = K \times C_v \qquad (5.5)$$

Pressure profiles modelled by varying shale permeability (over four–orders of magnitude) are shown on Figure 5.6. Modelling results showed that shales with permeability of less than 1nD (10^{-21} m^2) may generate the amount of overpressure observed below 8900 ft in Group L. However, the result also indicates that shallower shale exhibited higher pressure compared to the adjacent sandstone if they have a

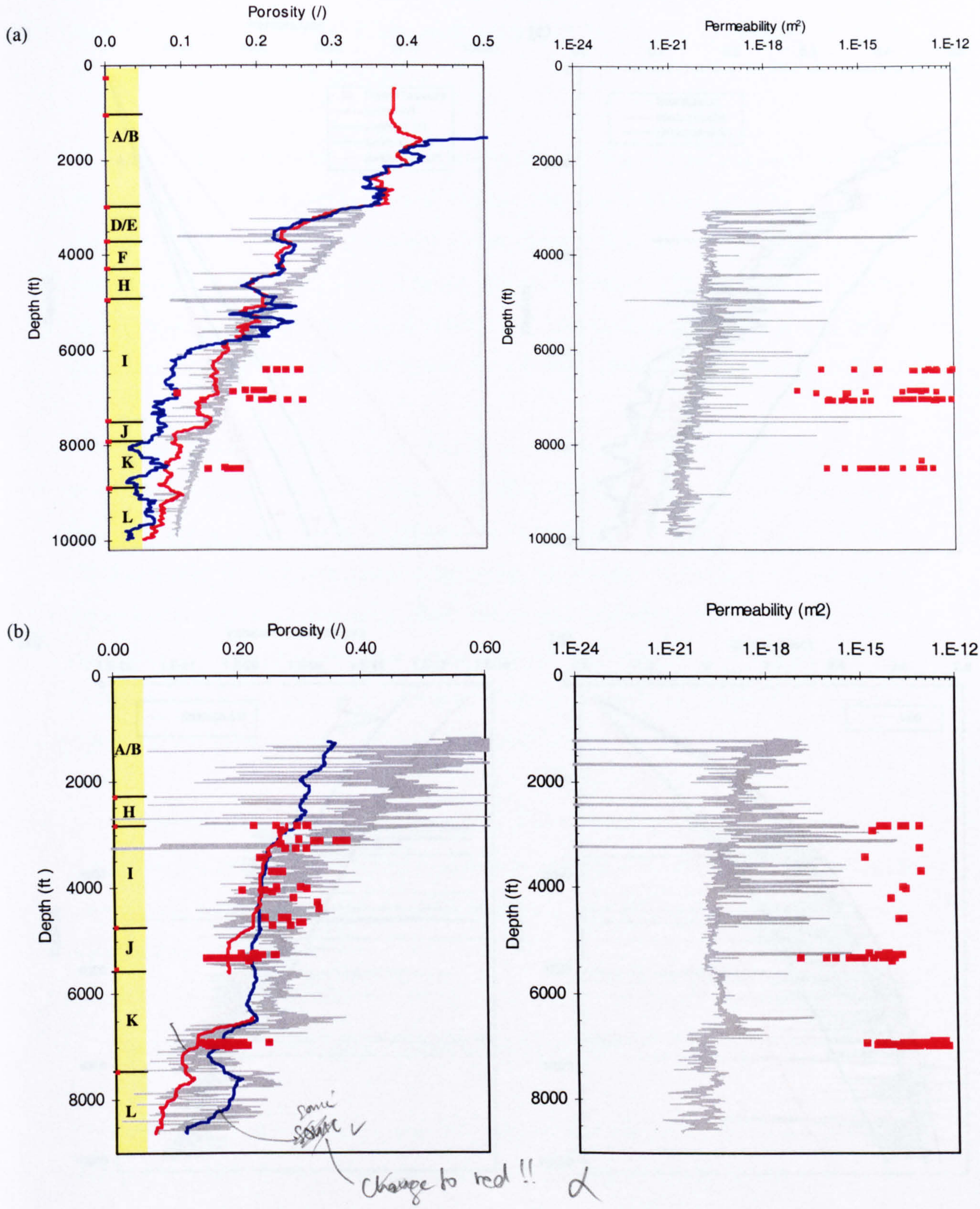


Figure 5.5 Porosity and permeability data for: (a) well SM-28 and (b) SM-30. Sonic and density-derived shale porosity are plotted as red and blue lines, respectively. The grey lines are data obtained from ShaleQuant log analysis. Porosity and permeability data from measured core samples are plotted as red squares.

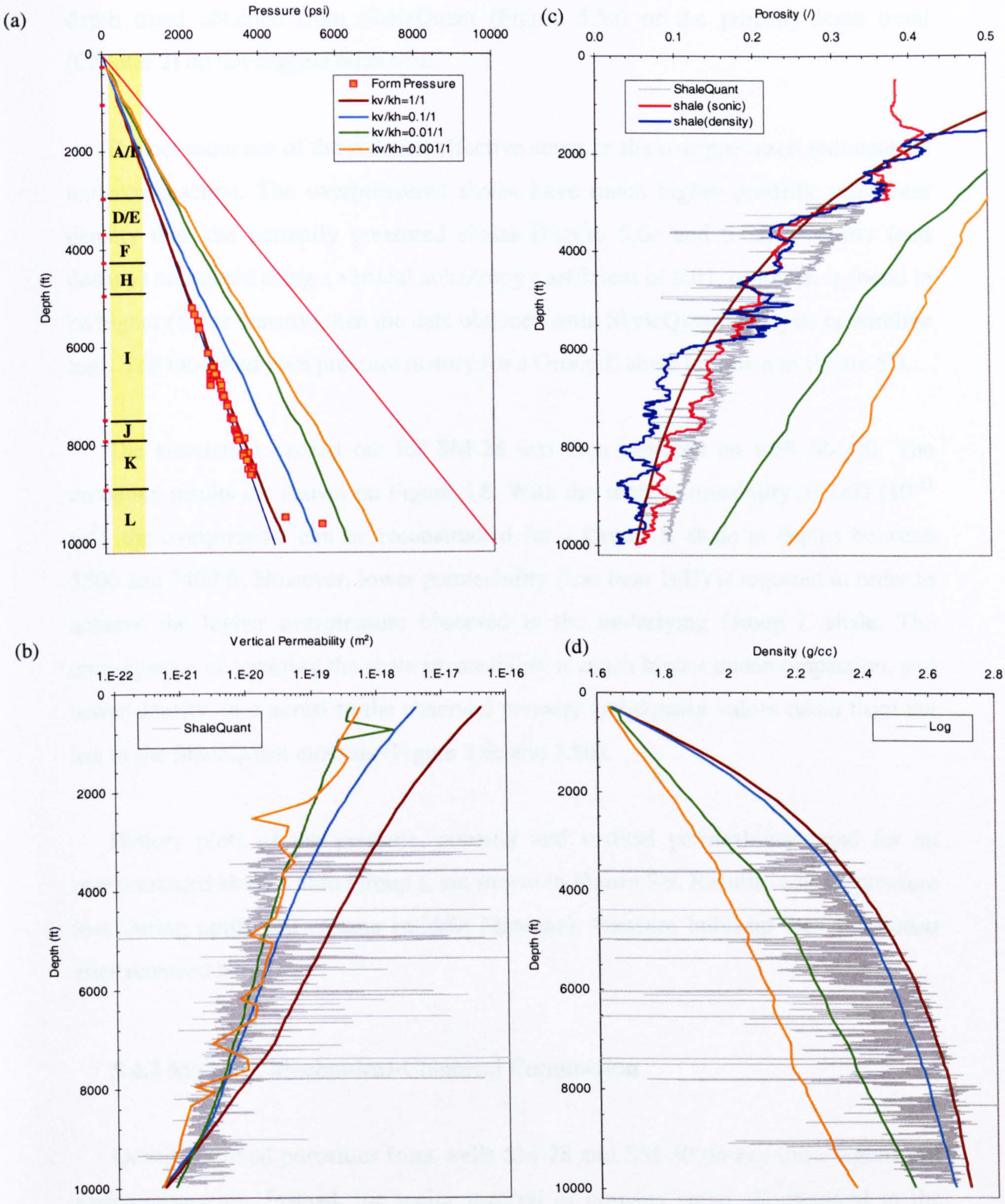


Figure 5.6 Modelled results for well SM-28 using different shale permeability anisotropy coefficients: (a) pressure, (b) vertical permeability, (c) porosity and (d) density.

similar permeability trend to the underlying shales within Group L. The permeability-depth trend obtained from ShaleQuant (Figure 5.5a) or the porosity-depth trend (Chapter 2) do not suggest otherwise.

The consequence of the reduced effective stress in the overpressured sediments is undercompaction. The overpressured shales have much higher porosity and lower density than the normally pressured shales (Figure 5.6c and 5.6d). Porosity (and density) calculated using a vertical anisotropy coefficient of 0.01, or lower, is found to be higher (lower density) than the data obtained from ShaleQuant Analysis or wireline logs. The modelled pore pressure history for a Group L shale is shown in Figure 5.7.

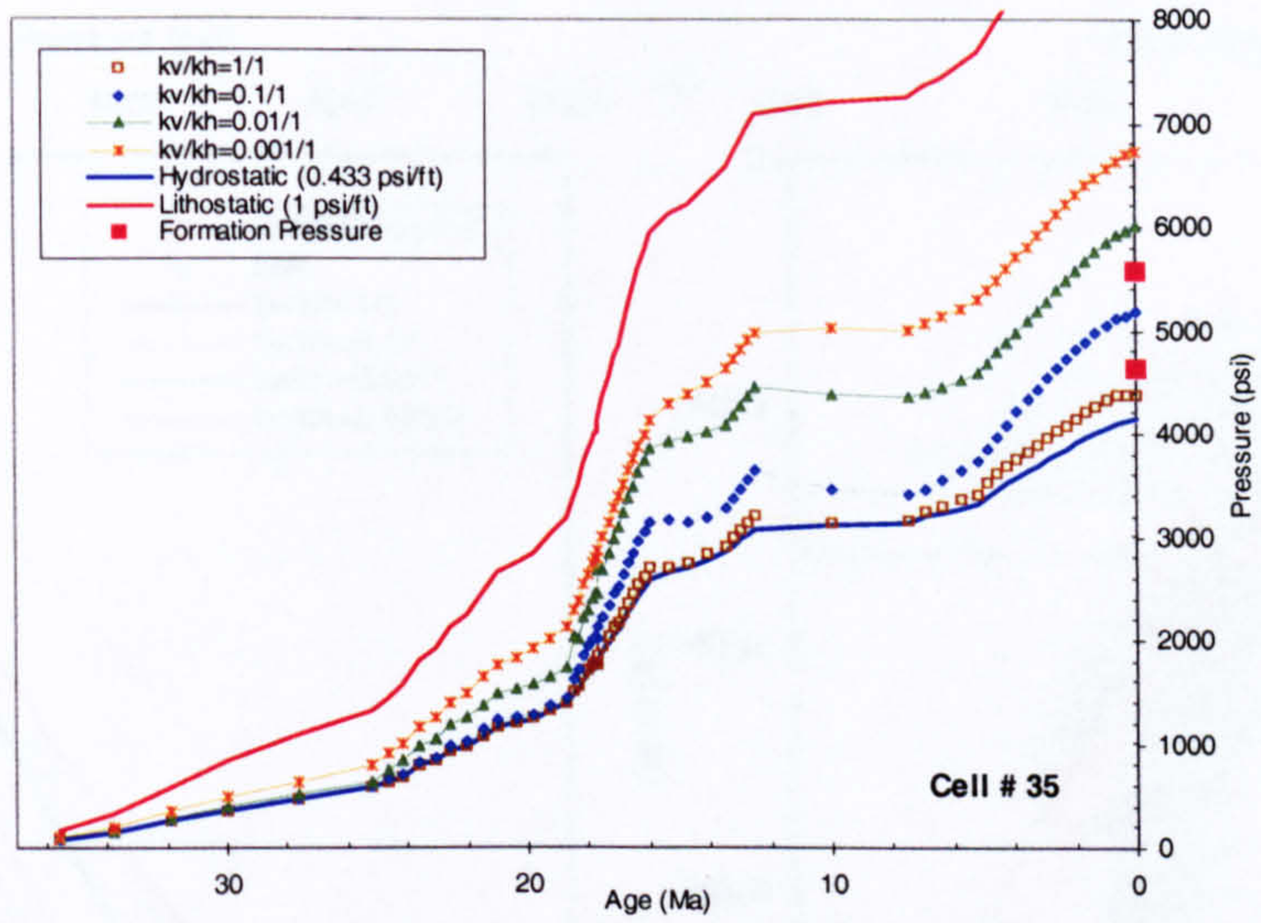
The simulation carried out for SM-28 was then repeated on well SM-30. The modelled results are shown on Figure 5.8. With the shale permeability of 1nD (10^{-21} m^2), the overpressure can be reconstructed for a Group K shale at depths between 5500 and 7400 ft. However, lower permeability (less than 1nD) is required in order to achieve the higher overpressure observed in the underlying Group L shale. The consequence of lowering the shale permeability is much higher undercompaction, and lower density, in contrast to the observed porosity and density values taken from the log or the ShaleQuant analysis (Figure 5.8c and 5.8d).

History plots of the pressure, porosity and vertical permeability trend for an overpressured shale within Group L are shown in Figure 5.9. Results indicate pressure loss during uplift and erosion (middle Miocene). Pressure build-up then proceeded after renewed burial.

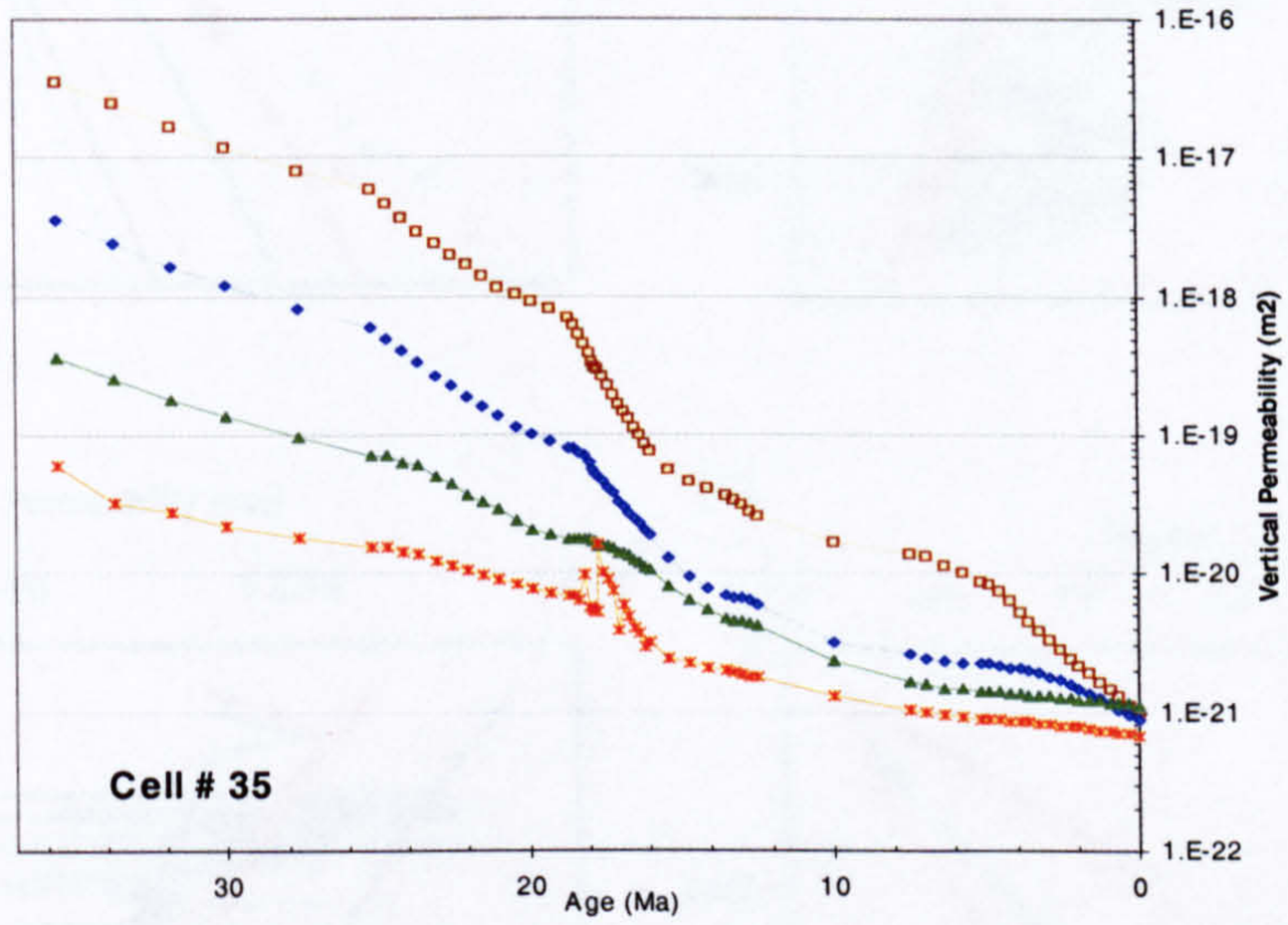
5.4.2 Model 2: Mechanical-Chemical Compaction

Density-derived porosities from wells SM-28 and SM-30 do not show significant undercompaction. Instead, the major reversal in porosity trend is observed in the sonic log or sonic-derived porosity. Hermanrud et al. (1998) have commented on this differences for North Sea shales, which they attributed to the differences in log response toward the fabric in normally and overpressured shales. To rectify the overestimation of the modelled porosity for the overpressured shales, Schneider et al.

(a)



(b)



(c)

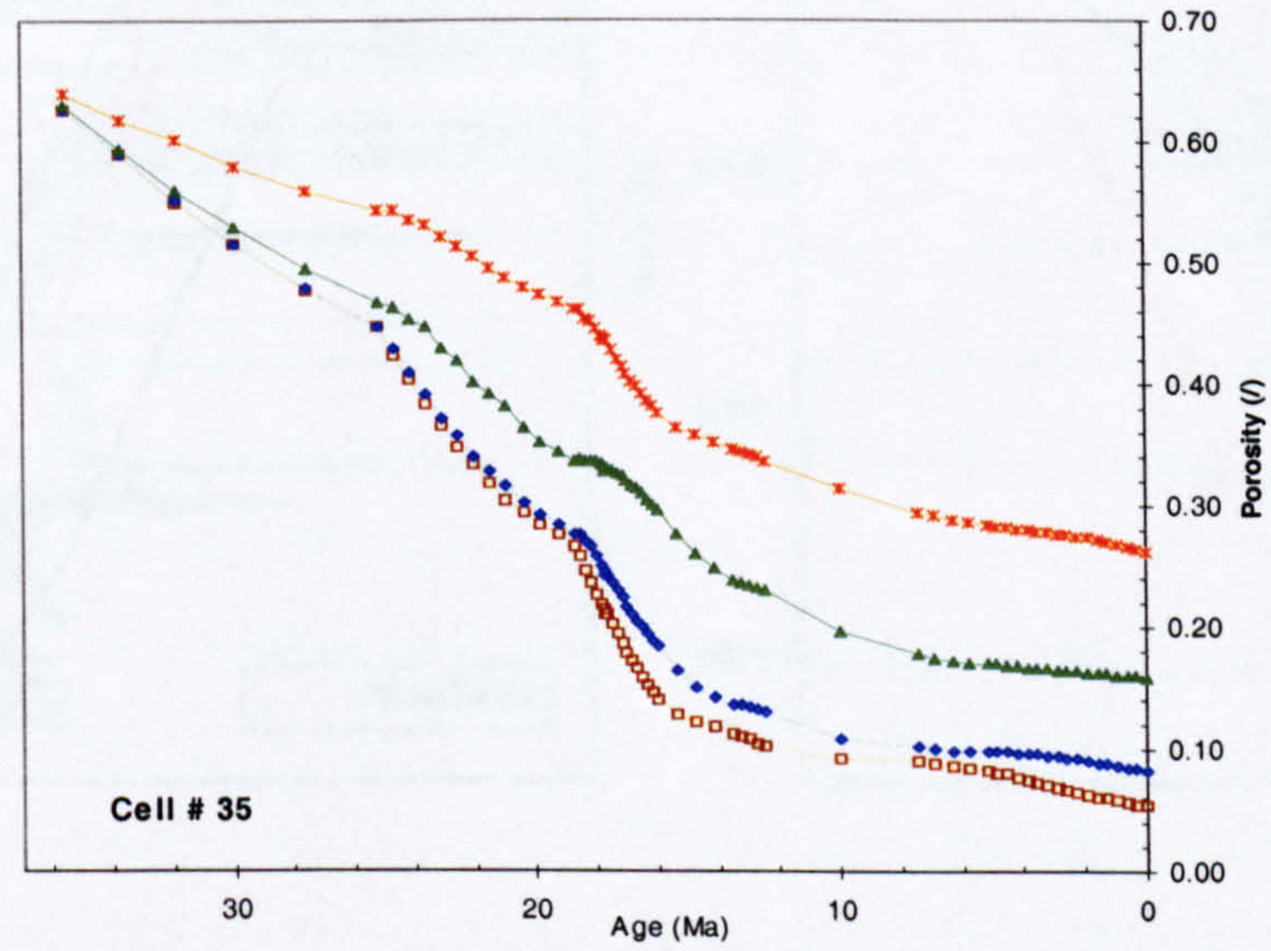


Figure 5.7 Temporal evolution of (a) pressure, (b) vertical permeability and (c) porosity for a Group L shale in SM-28, which is adjacent to a reservoir section where formation pressure was taken.

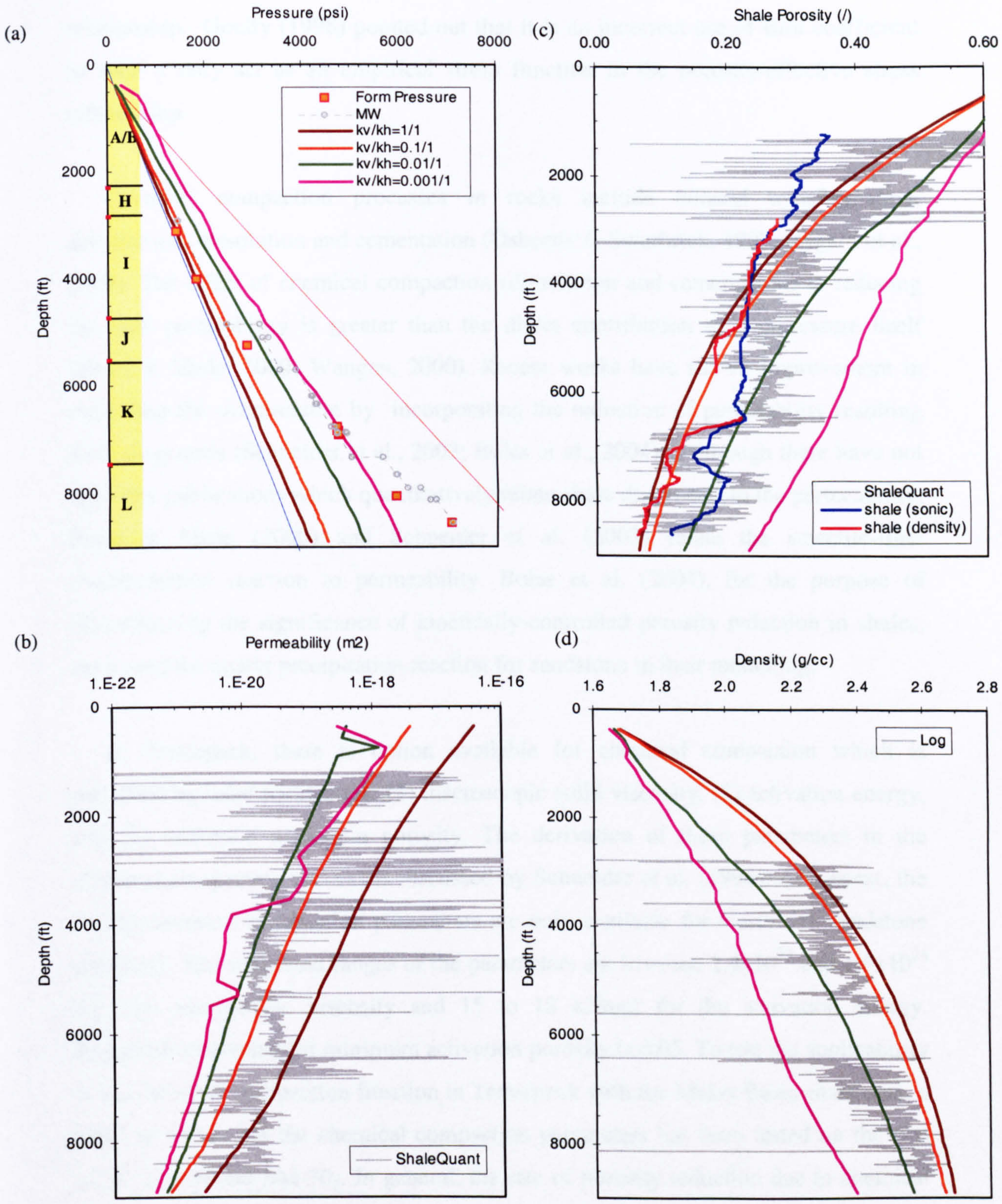


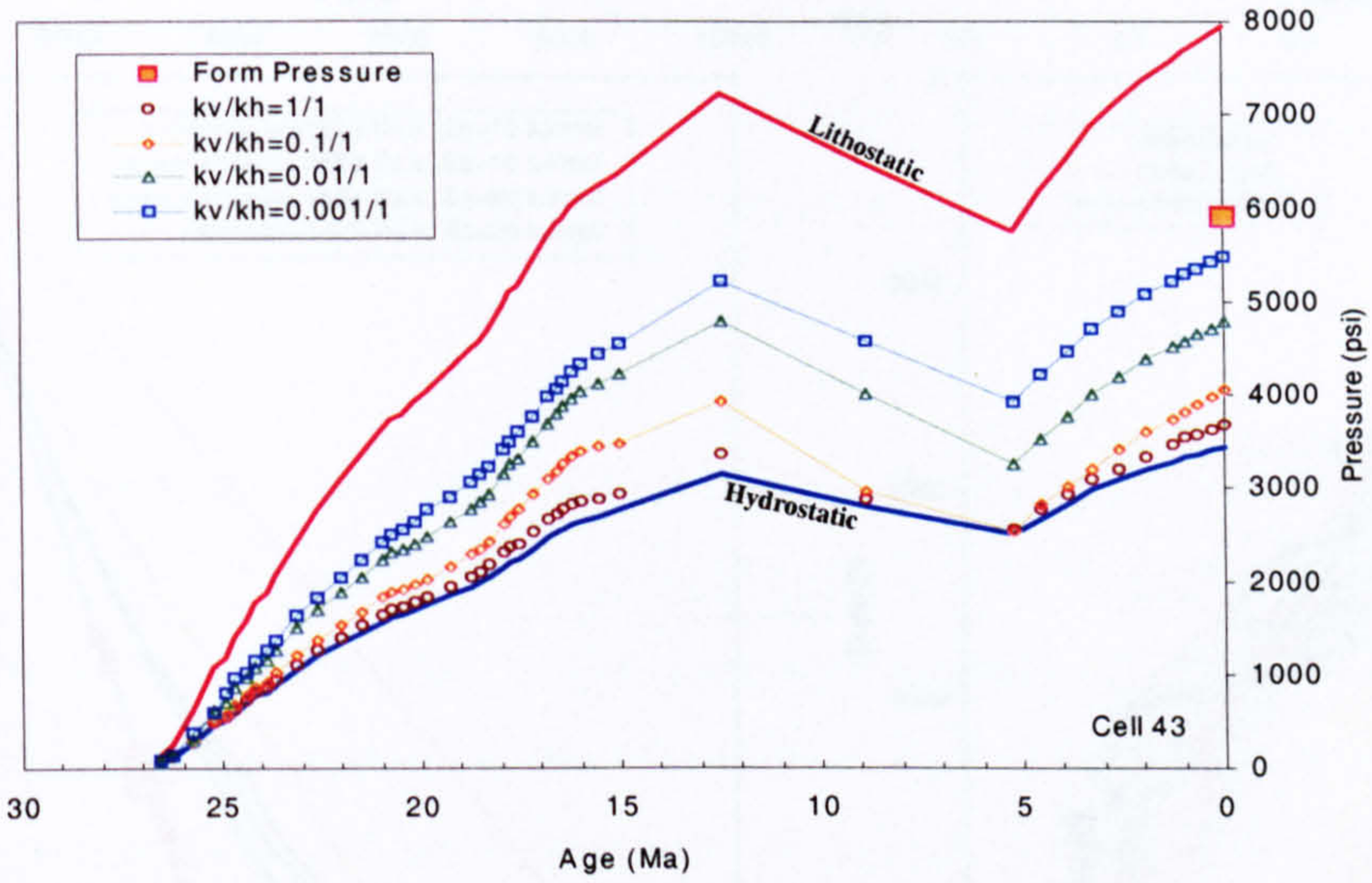
Figure 5.8 Depth plots of 1-D results for well SM-30 using different permeability anisotropy coefficients.

(1993) and Burrus (1998) introduced Biot coefficient into the porosity-effective stress relationship. Goulty (1998) pointed out that it is an incorrect use of Biot coefficient as such it only act as an empirical stress function in the porosity-effective stress relationship.

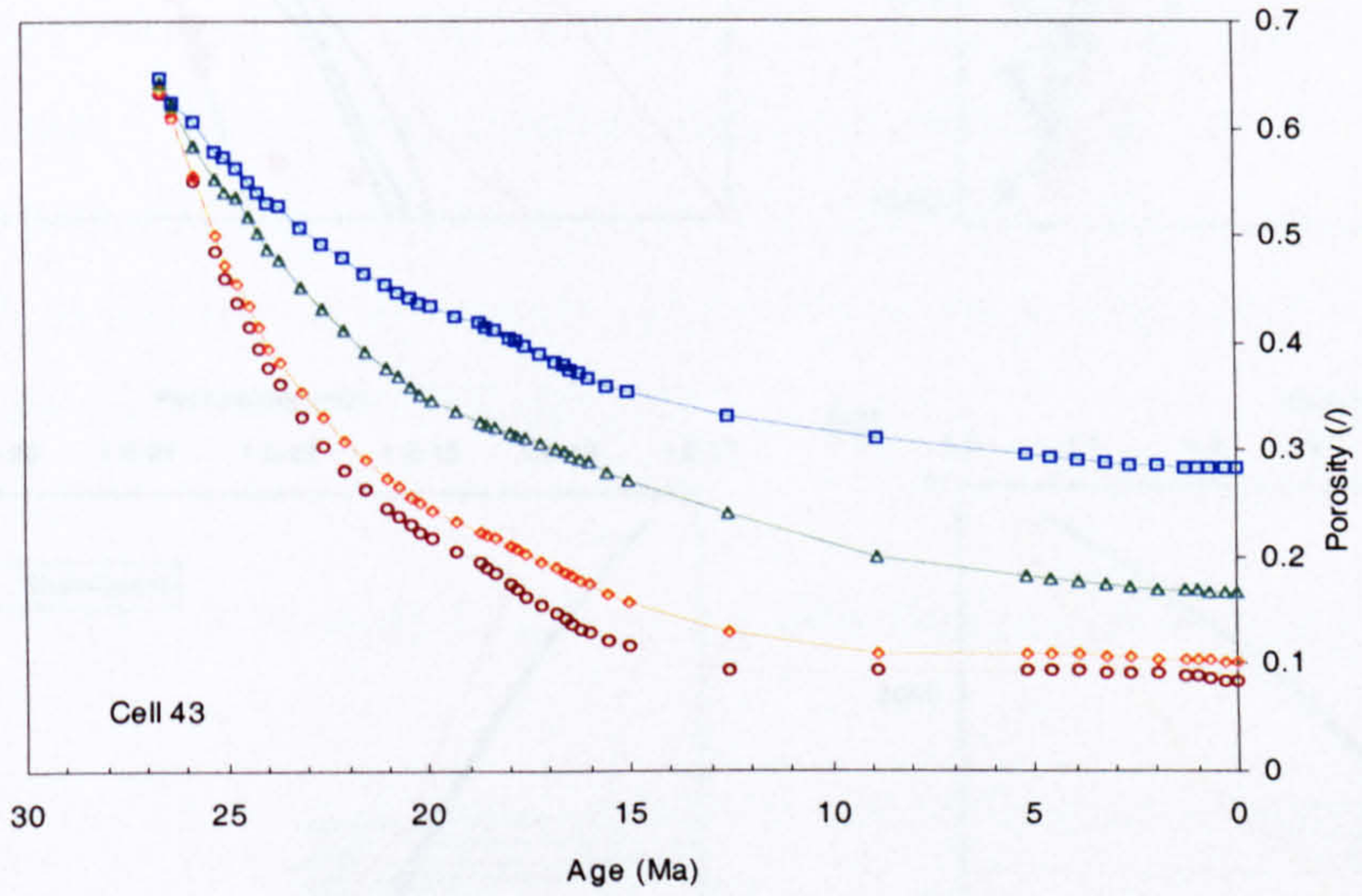
Chemical compaction processes in rocks include mineral transformation, dehydration, dissolution and cementation (Osborne & Swarbrick, 1999; Nygard et al., 2004). The effect of chemical compaction (dissolution and cementation) in reducing the rock permeability is greater than the direct contribution to overpressure itself (Bruel & Made, 2000; Wangen, 2000). Recent works have shown improvement in modelling the overpressure by incorporating the reduction of permeability resulting from diagenesis (Schneider et al., 2003; Bolas et al., 2004). Although there have not been any publications which quantitatively relate shale diagenesis to the permeability, Bruel & Made (2000) and Schneider et al. (2003) relate the smectite-illite transformation reaction to permeability. Bolas et al. (2004), for the purpose of demonstrating the significance of kinetically-controlled porosity reduction in shales, have used the quartz precipitation reaction for sandstone in their modelling.

In Temispack, there is option available for chemical compaction which is described by three parameters: (1) macroscopic solid viscosity, (2) activation energy, and (3) minimum activation porosity. The derivation of these parameters in the chemical compaction process is discussed by Schneider et al. (1996). At present, the default chemical compaction parameters are only available for North Sea sandstone and chalk. The suggested ranges of the parameters are between $2.4x10^{23}$ and $1.6x10^{24}$ Pa.s for microscopic viscosity and 15 to 18 kJ/mol for the activation energy. Recommended value for minimum activation porosity is 0.05. To test the applicability of the chemical compaction function in Temispack with the Malay Basin shale data, a series of values for the chemical compaction parameters has been tested on the two wells (SM-28 and SM-30). In general, the rate of porosity reduction due to chemical compaction increases with lower viscosity and/or higher activation energy. The aim is to use the chemical compaction parameters in Temispack to reproduce the observed overpressure and produce agreement with the density-derived porosity and ShaleQuant permeability.

(a)



(b)



(c)

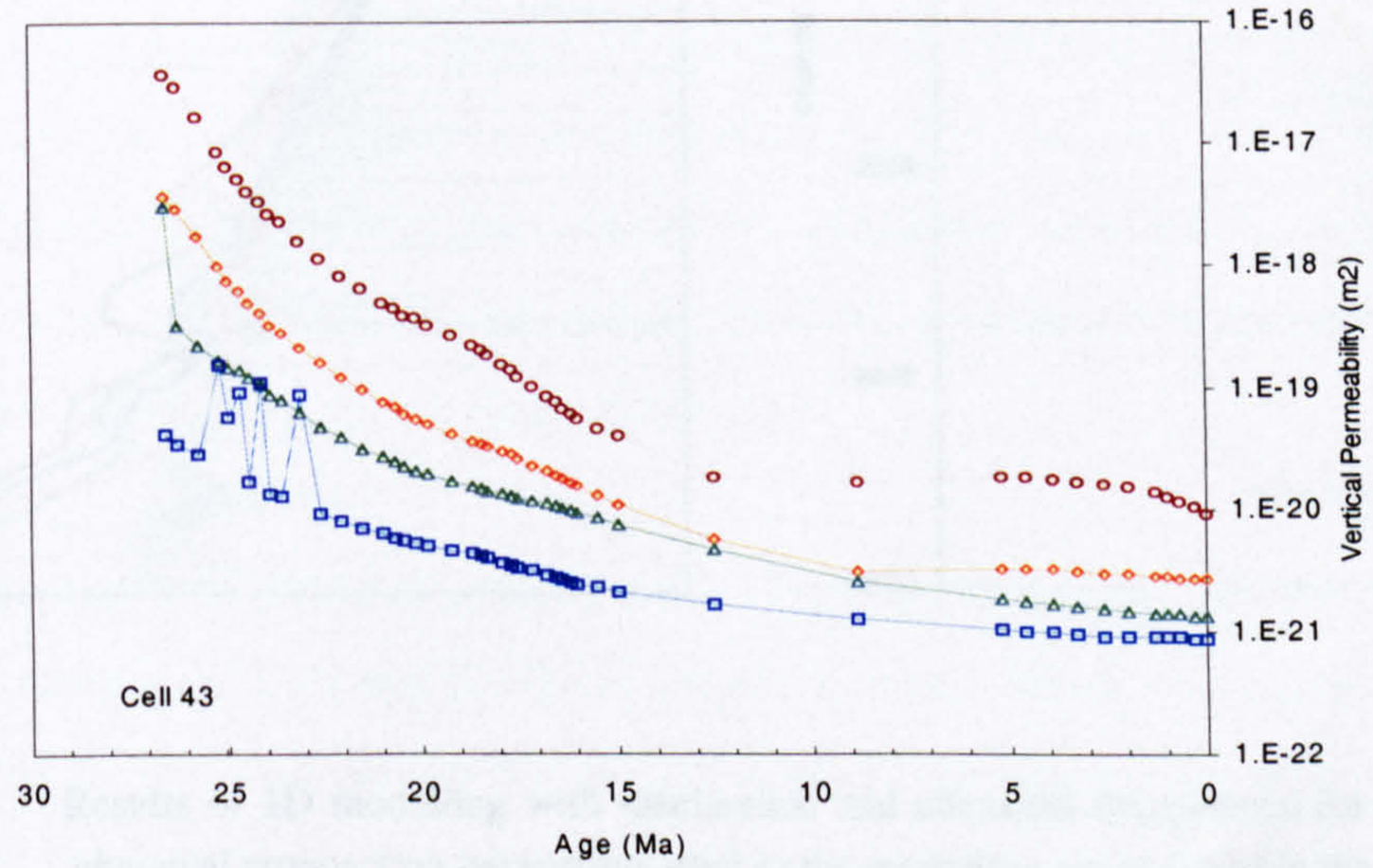


Figure 5.9 History plots of pressure, porosity and vertical permeability of an overpressured shale from Group L in well SM-30.

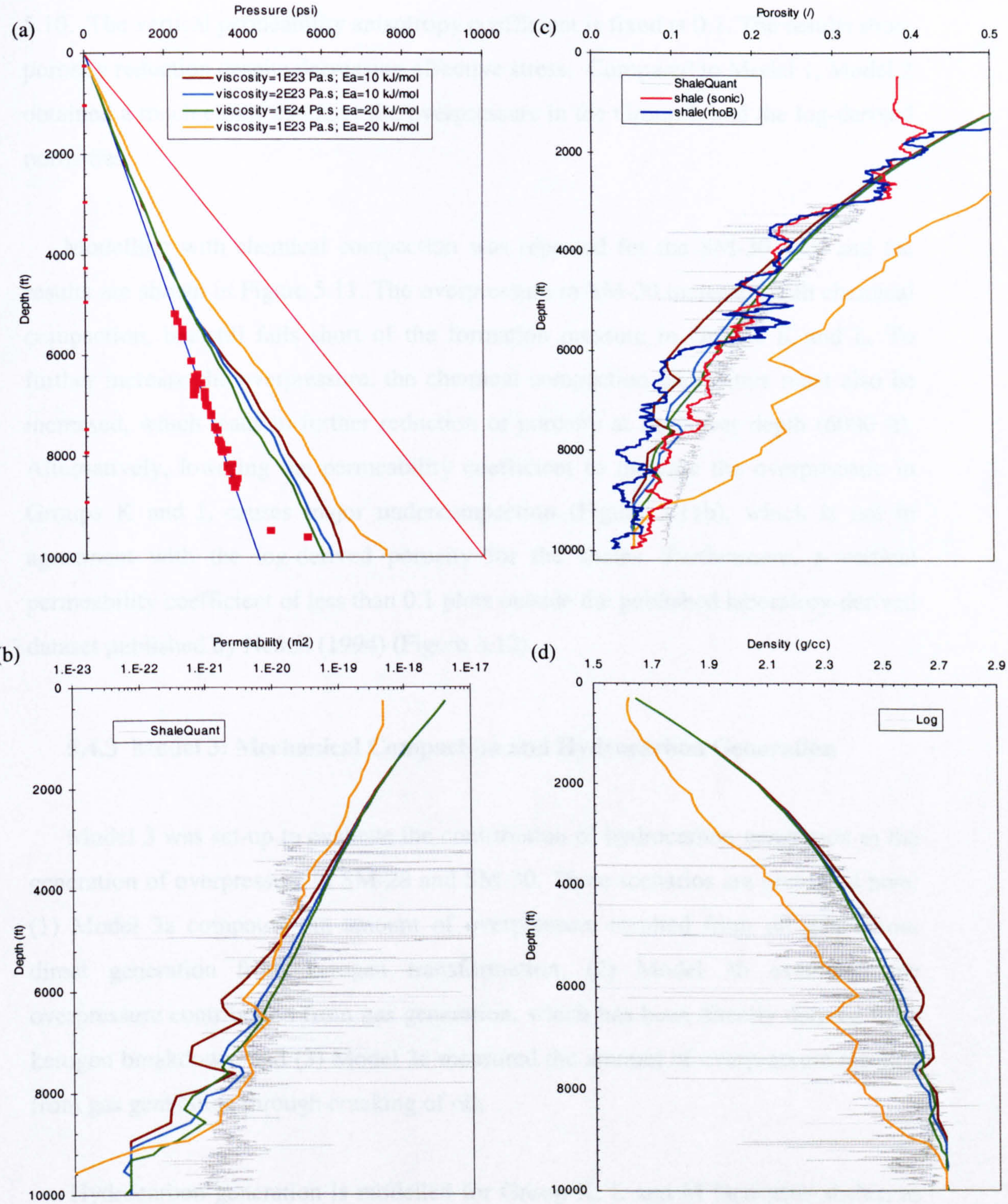


Figure 5.10 Results of 1D modelling with mechanical and chemical compaction for SM-28. The chemical compaction parameters used in the modelling are as listed in the legend.

Simulated 1D results for SM-28 using chemical compaction are shown in Figure 5.10. The vertical permeability anisotropy coefficient is fixed at 0.1. The results show porosity reduction despite decreasing effective stress. Compared to Model 1, Model 2 obtained a much closer match to the overpressure in the Group L and the log-derived porosities.

Modelling with chemical compaction was repeated for the SM-30 well and the results are shown in Figure 5.11. The overpressure in SM-30 increases with chemical compaction, but still falls short of the formation pressure in Groups K and L. To further increase the overpressure, the chemical compaction parameters must also be increased, which leads to further reduction of porosity at shallower depth (6000 ft). Alternatively, lowering the permeability coefficient to increase the overpressure in Groups K and L causes major undercompaction (Figure 5.11b), which is not in agreement with the log-derived porosity for the shales. Furthermore, a vertical permeability coefficient of less than 0.1 plots outside the published laboratory-derived dataset published by Neuzil (1994) (Figure 5.12).

5.4.3 Model 3: Mechanical Compaction and Hydrocarbon Generation

Model 3 was set-up to evaluate the contribution of hydrocarbon generation to the generation of overpressure in SM-28 and SM-30. Three scenarios are presented here: (1) Model 3a computed the amount of overpressure resulted from oil generation, direct generation from kerogen transformation, (2) Model 3b examined the overpressure contribution from gas generation, which has been directly derived from kerogen breakdown, and (3) Model 3c measured the amount of overpressure resulted from gas generation through cracking of oil.

Hydrocarbon generation is modelled for Group K, L and M lacustrine shales, as the overpressure in SM-28 and SM-30 is detected within Group J and older. The coaly source rocks in the younger formation are ignored. In Model 3a, source rocks are assigned as Type I kerogen, having total organic carbon (TOC) of 2%. Kerogen kinetic for Type I is taken from the Temispack database. In Model 3b, gas generation were derived from similar source rocks in Model 3a, but having kerogen kinetics of

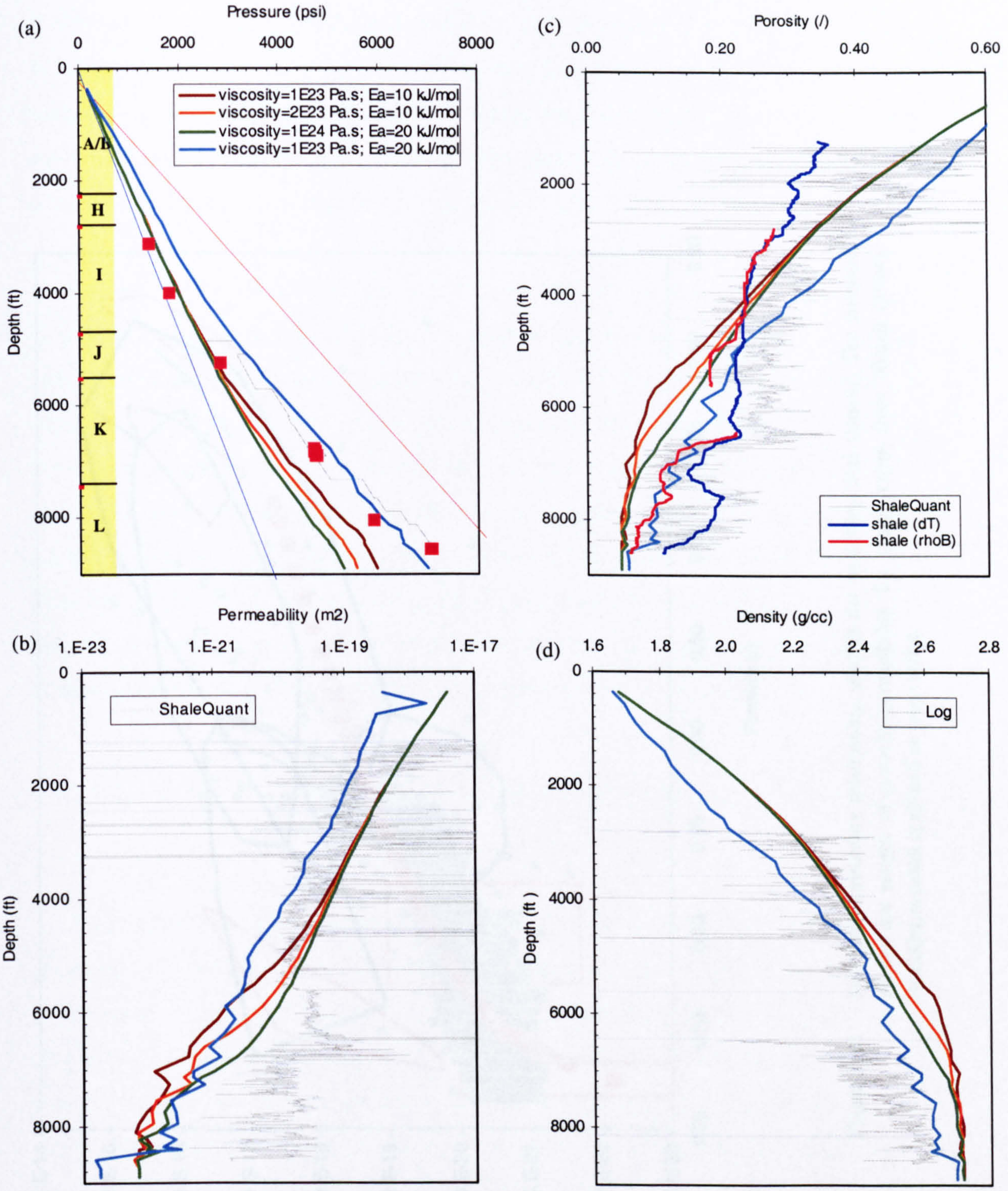


Figure 5.11 Results of 1D modelling for SM-30 using similar chemical compaction parameters as for SM-28 in Figure 5.10.

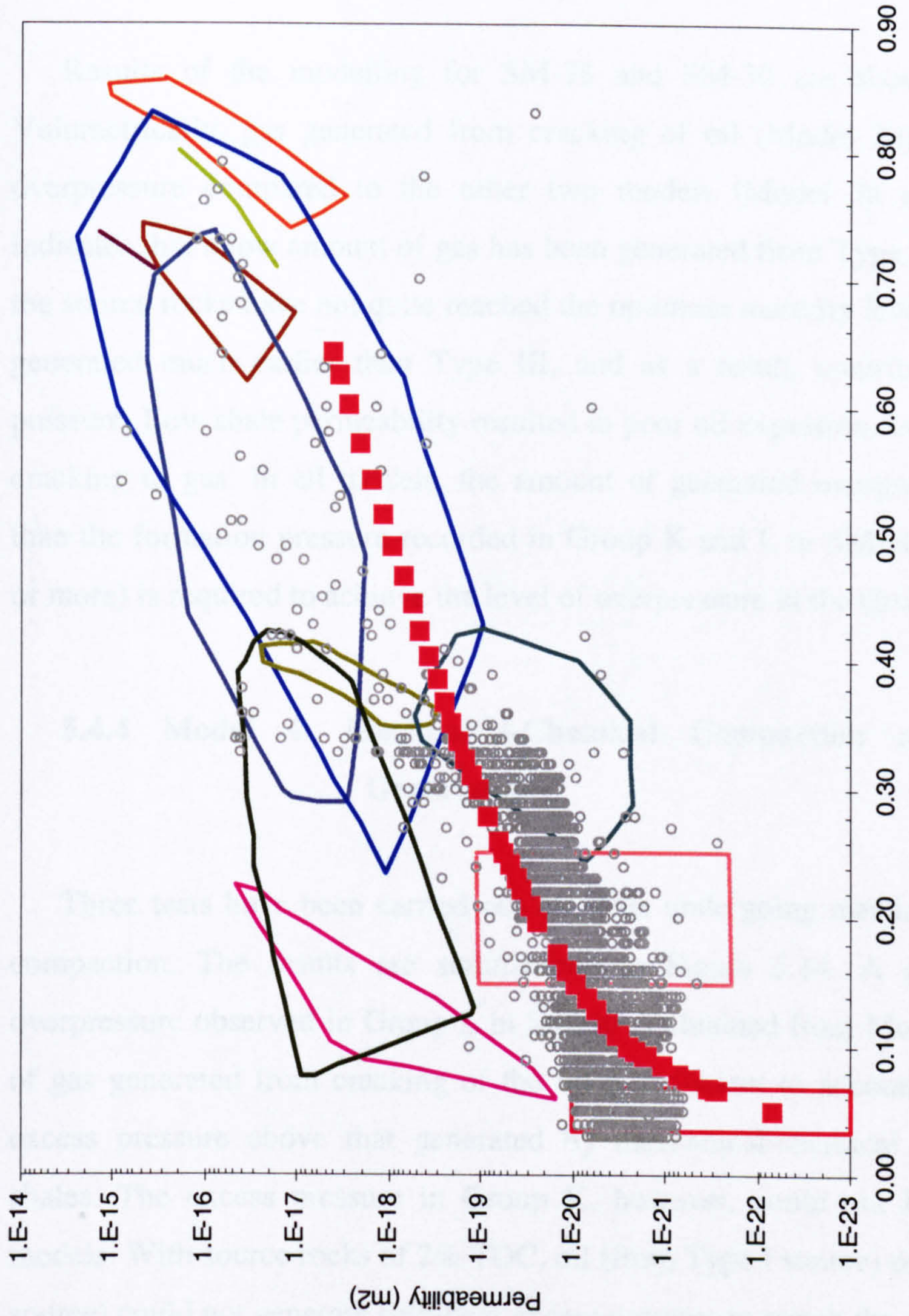


Figure 5.12 Porosity-permeability relationship used in the modelling (red squares) The coloured shapes are ranges of porosity-permeability for shales taken from Neuzil (1994). ShaleQuant result is plotted as grey circles.

Type III kerogen. Type I kerogen does not generate a significant amount of gas, hence it is more appropriate to use Type III kerogen. Also, it is possible the Group K, L and M shales in the southern part of the Malay Basin are more coaly/terrigeneous compared to the eastern part of the basin, where the lacustrine source rocks are more developed. For Model 3c, gas generation were modelled as result of cracking of the oil, which have been generated from Type I source rocks (TOC of 2%).

Results of the modelling for SM-28 and SM-30 are shown in Figure 5.13. Volumetrically, gas generated from cracking of oil (Model 3c) resulted in higher overpressure compared to the other two models (Model 3a and 3b). Model 3b indicates that a low amount of gas has been generated from Type III kerogen because the source rocks have not quite reached the optimum maturity level. Type I, however, generated much earlier than Type III, and as a result, contributed higher excess pressure. Low shale permeability resulted in poor oil expulsion, eventually lead to the cracking to gas. In all models, the amount of generated overpressure is still lower than the formation pressure recorded in Group K and L in SM-30. Higher TOC (5% or more) is required to achieve the level of overpressure in the Group K and L.

5.4.4 Model 4: Mechanical-Chemical Compaction and Hydrocarbon Generation

Three tests have been carried out on shale undergoing mechanical and chemical compaction. The results are summarized in Figure 5.14. A good match to the overpressure observed in Group L in SM-30 is obtained from Model 3c. The amount of gas generated from cracking of the oil is sufficient to account for the additional excess pressure above that generated by mechanical-chemical compaction in the shales. The excess pressure in Group K, however, could not be replicated in all models. With source rocks of 2% TOC, oil (from Type I source) or gas (from Type III source) could not generate sufficient excess pressure to match the amount measured in Group L.

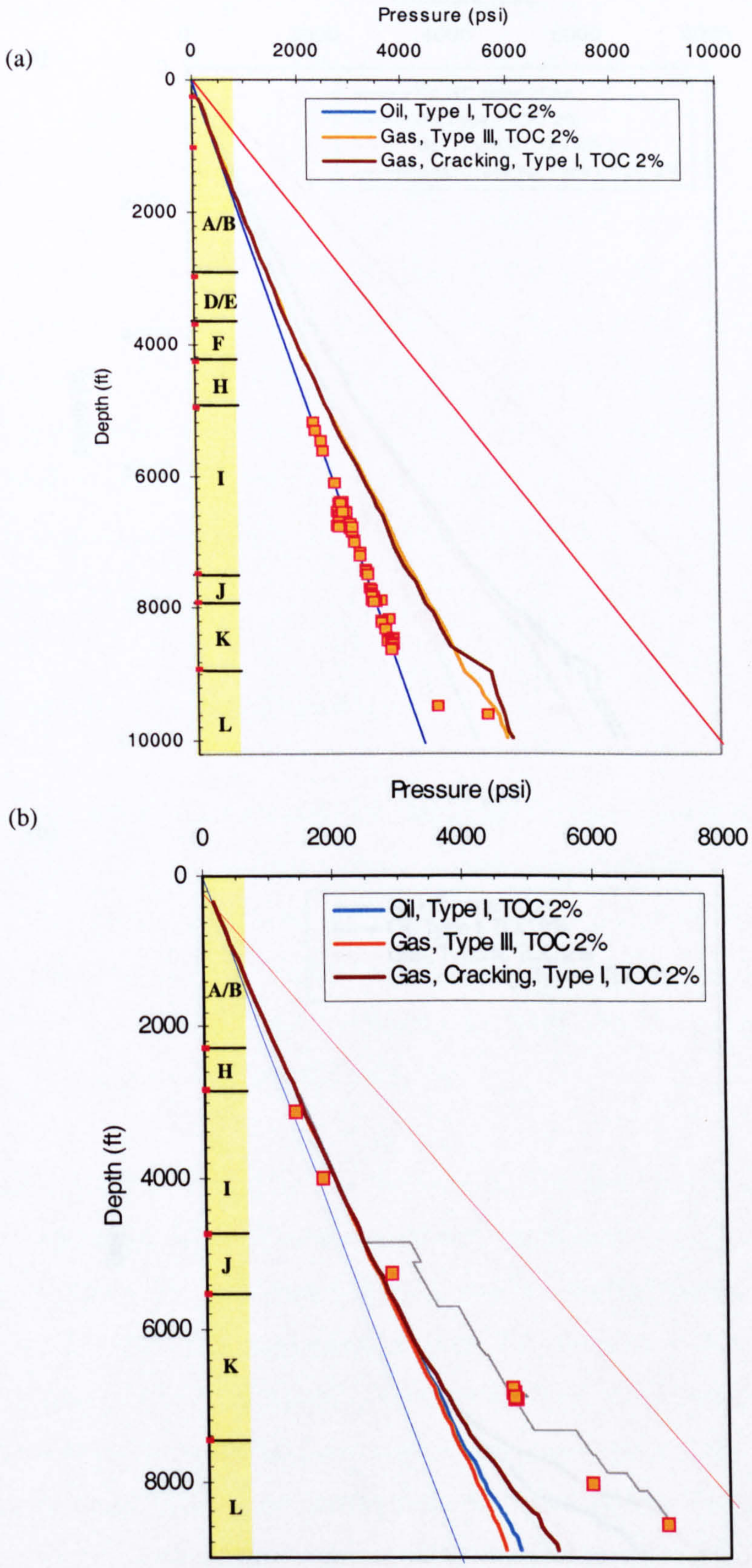


Figure 5.13 Modelled pressure-depth profile resulting from hydrocarbon generation in wells SM-28 and SM-30. Models run are: Model 3a (oil generation from Type I source rocks with 2% TOC), Model 3b (gas generation from Type III source rocks with 2% TOC) and Model 3c (gas from primary & secondary cracking of Type I source rocks with TOC 2%).

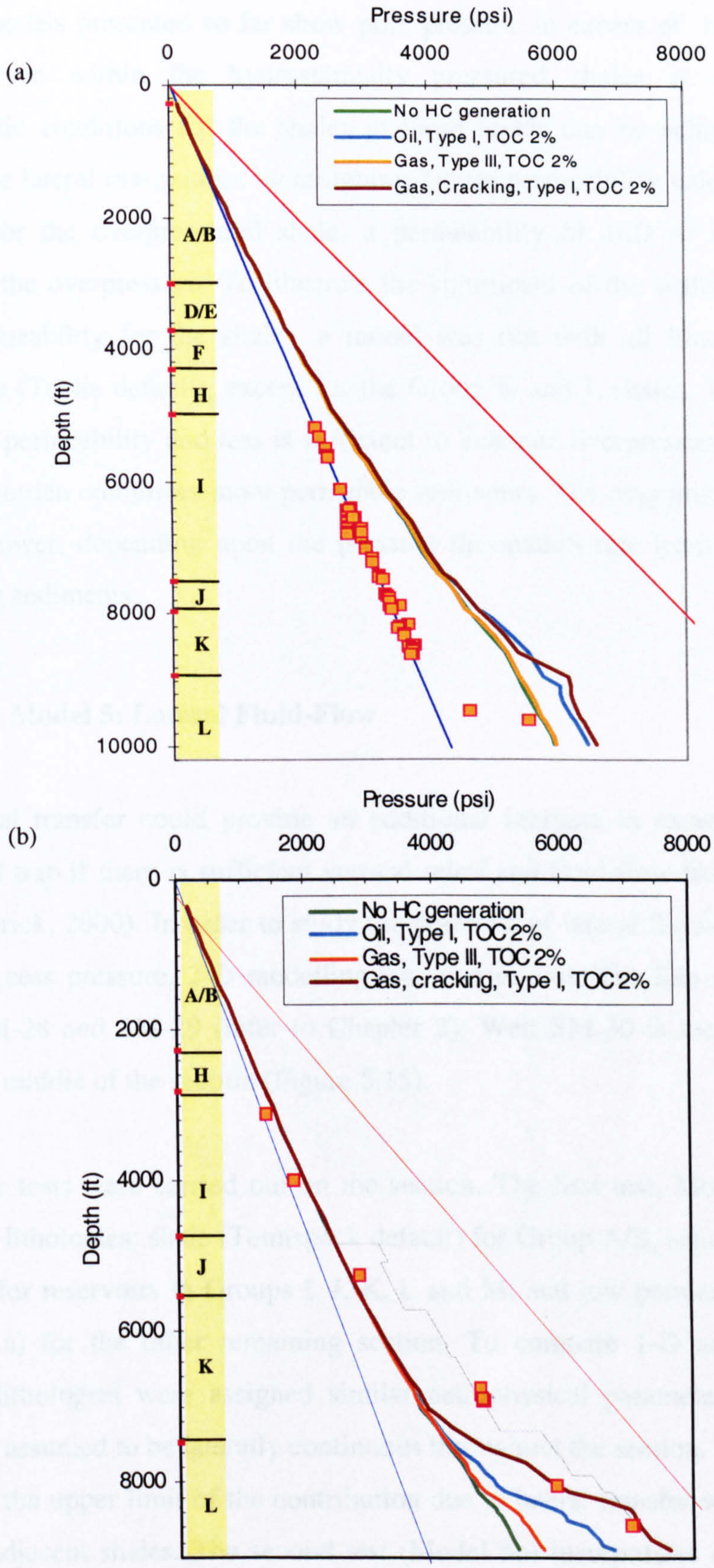


Figure 5.14 Modelled pressure-depth profile resulting from hydrocarbon generation in the mechanical-chemically compacted shales: (a) SM-28 and (b) SM-30.

All models presented so far show pore pressure in excess of hydrostatic for the shales, even within the hydrostatically pressured shales at shallower levels. Hydrostatic conditions for the shales at these levels can be achieved by allowing vertical or lateral dissipation, by assigning higher permeability values to the shallow shales. For the overpressured shale, a permeability of 1nD or less is needed to simulate the overpressure. To illustrate the significant of the sealing requirement of 1nD permeability for the shales, a model was run with all lithology replaced as sandstone (Temis default), except for the Group K and L shales. The result showed that 1nD permeability and less is sufficient to generate overpressure, even though all the overburden comprises more permeable sediments. The magnitude of overpressure will be lower, depending upon the pressure dissipation rate from the shales to the overlying sediments.

5.4.5 Model 5: Lateral Fluid-Flow

Lateral transfer could provide an additional increase in excess pressure at the structural trap if there is sufficient vertical relief and fluid-flow from depth (Yardley & Swarbrick, 2000). In order to study the potential of lateral fluid-flow to contribute to the excess pressure, 2-D modelling was carried out. The line selected intersects wells SM-28 and SM-29 (refer to Chapter 2). Well SM-30 is located about 10 km from the middle of the section (Figure 5.15).

Three tests were carried out on the section. The first test, Model 5a, used three different lithologies: shale (Temispack default) for Group A/B, sandstone (Temispack default) for reservoirs in Groups I, J, K, L and M, and low permeability shale (from Model 1a) for the other remaining section. To compare 1-D and 2-D modelling results, lithologies were assigned similar petrophysical parameters. The sandstone units are assumed to be laterally continuous throughout the section. The objective is to evaluate the upper limit of the contribution due to lateral transfer within the reservoir and its adjacent shales. The second test (Model 5b) incorporates oil generated from Group K, L and M source rocks (Type I kerogen with TOC of 2 wt. %). The third test (Model 5c) modelled gas generation (from cracking of oil from Model 5a) in well SM-28 and SM-29.

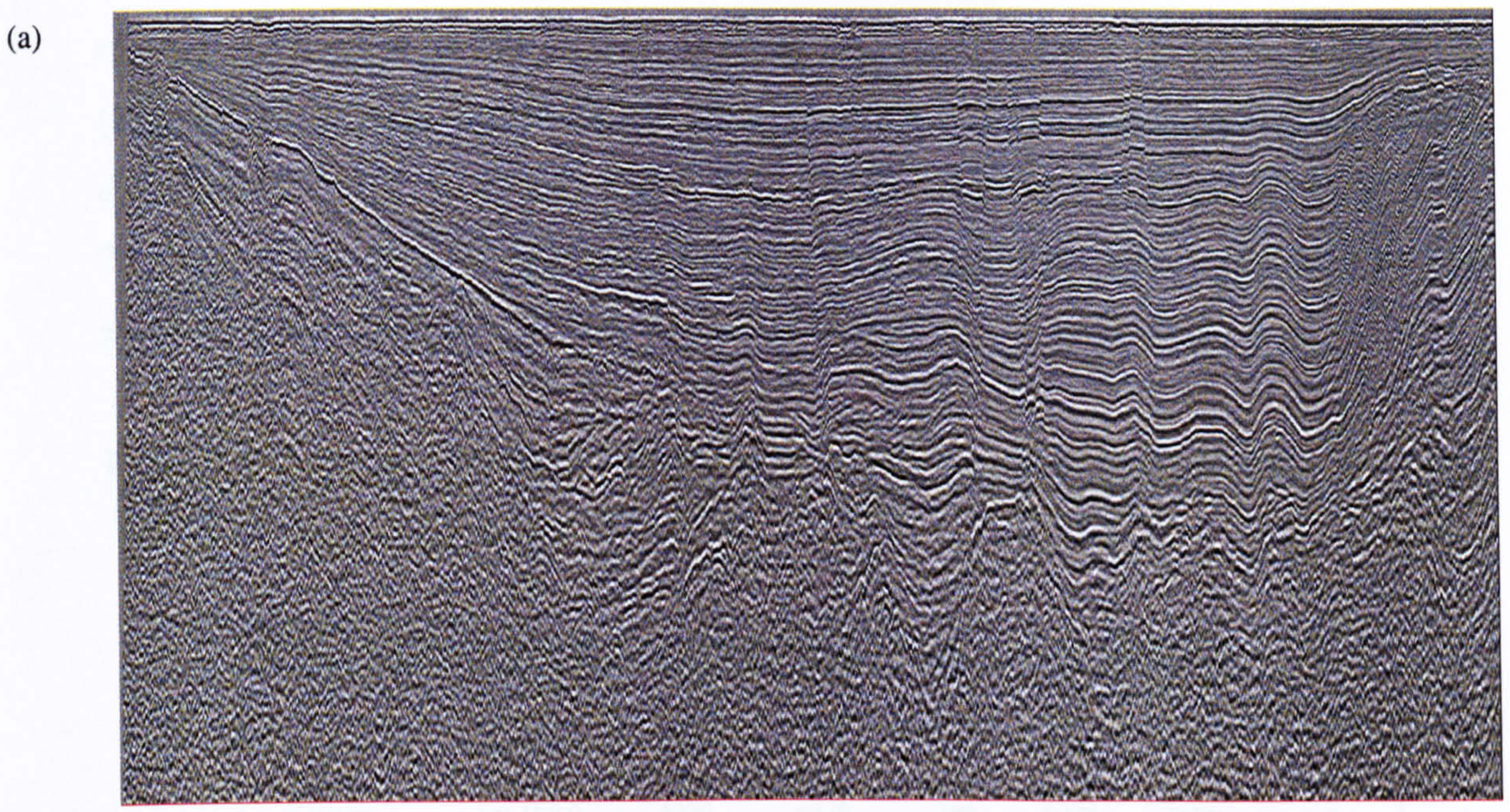


Figure 5.15 Modelled 2-D section (a) seismic section, (b) gridded litho-section.

Calculated pore pressures in Group K and L shales (K2 & L2) and the underlying reservoirs (Ksst & Lsst) at five locations were monitored. The five locations include the crestal part (Well SM-28 and SM-29) and the synclines (Kitchen-A, B & C) (Figure 5.15). The results are summarized in Table 5.2. The results show the pressure differences between the Group L reservoir and the overlying shale are greater at SM-29 than in the adjacent syncline (Kitchen-C). Overpressure generation due to gas generation is much higher (about 500 psi) than from the oil generation.

Table 5.2 Modelled pressure within the reservoirs (Ksst & Lsst) and the overlying shales (K2 & L2).

Model 5a: Fluid-flow

Well	Location	K2	Ksst	Ksst-K2	L2	Lsst	Lsst-L2
SM-28	km 103.3	4042	4216	174	4627	4774	147
Kitchen-A	km 110.5	4313	4471	158	4838	4975	137
Kitchen-B	km 132.3	4070	4280	210	4664	4847	183
SM-29	km 135.8	3936	4137	201	4512	4701	189
Kitchen-C	km 155.9	4093	4379	286	5495	5501	6

Model 5b: Oil Generation (Type I)

Well	Location	K2	Ksst	Ksst-K2	L2	Lsst	Lsst-L2	Lsst (run6f-6e)
SM-28	km 103.3	4103	4263	160	4703	4833	130	59
Kitchen-A	km 110.5	4407	4518	111	4910	5035	125	60
Kitchen-B	km 132.3	4140	4328	188	4741	4907	166	60
SM-29	km 135.8	3998	4185	187	4403	4762	359	61
Kitchen-C	km 155.9	4166	4428	262	5644	5561	-83	60

Model 5c: Gas (cracking)

Well	Location	K2	Ksst	Ksst-K2	L2	Lsst	Lsst-L2	Lsst (run6g-6e)
SM-28	km 103.3	4223	4376	153	4925	5102	177	328
Kitchen-A	km 110.5	4526	4631	105	5140	5303	163	328
Kitchen-B	km 132.3	4327	4686	359	4886	5301	415	454
SM-29	km 135.8	4100	4651	551	4836	5265	429	564
Kitchen-C	km 155.9	4634	4989	355	5812	5924	112	423

pressure in psi

Temporal plots of the modelled pressure for the Group L shale and reservoirs are shown on Figure 5.16. Pressure buildup accelerated in the last 10 Ma. The amount of overpressure generated by lateral transfer (less than 600 psi) is not sufficient to account for the high overpressure (3500 psi) observed at SM-30.

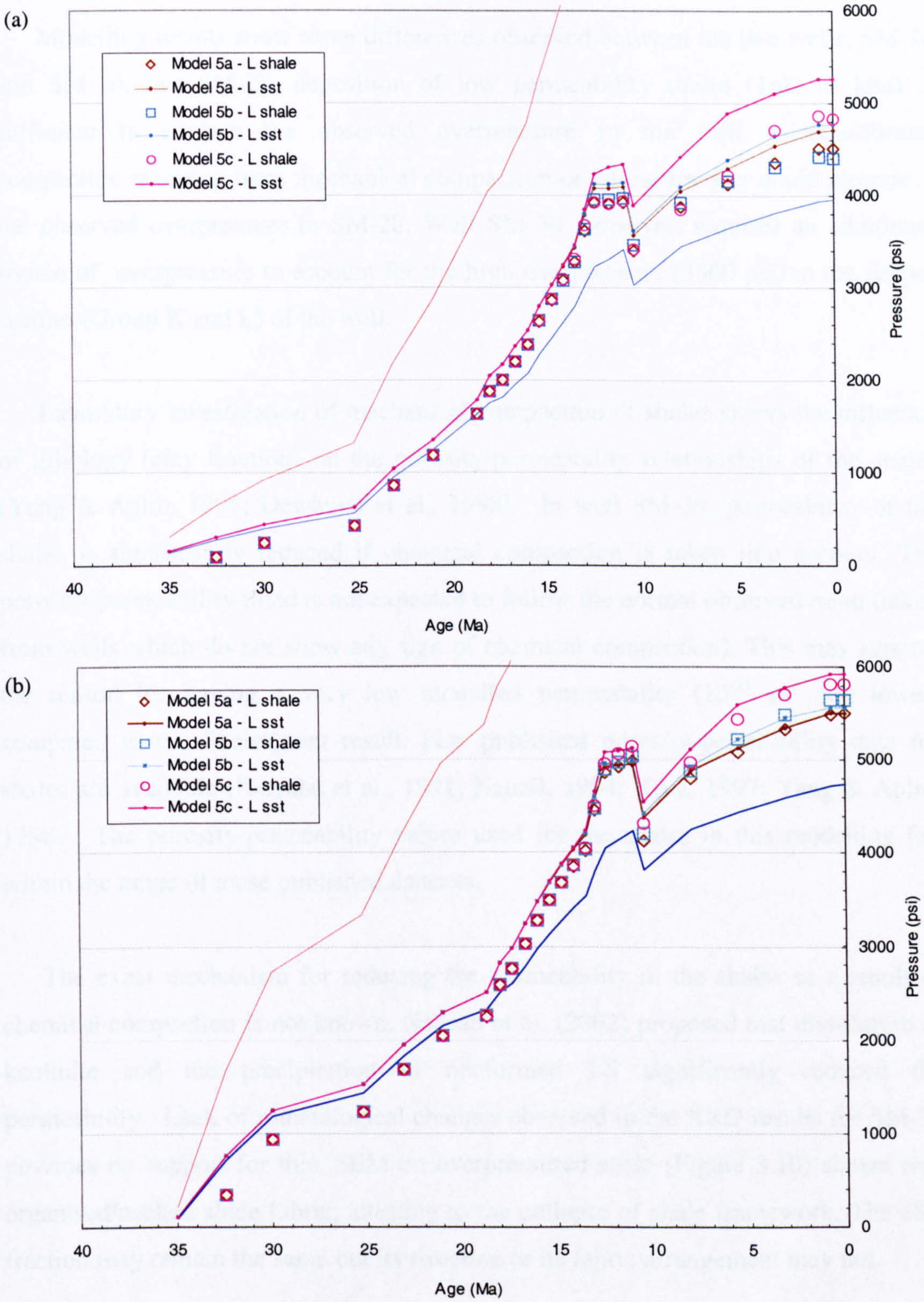


Figure 5.16 Temporal plots of pore pressure for Group L shale (source rock) and sandstone (reservoir) at: (a) Well SM-29 and (b) Kitchen C. Results are for: Model 5a (no HC generation), Model 5b (oil generation) and Model 5c (gas from cracking).

5.5 Discussion

Modelling results show some differences observed between the two wells, SM-28 and SM-30. For SM-28, deposition of low permeability shales (1nD or less) is sufficient to explain the observed overpressure in the well. Disequilibrium compaction resulting from mechanical compaction or lateral transfer could reproduce the observed overpressure in SM-28. Well SM-30, however, requires an additional source of overpressure to account for the high overpressure (3500 psi) in the deeper section (Group K and L) of the well.

Laboratory investigation of mechanical compaction of shales shows the influence of lithology (clay fraction) on the porosity-permeability relationships of the shales (Yang & Aplin, 1998; Dewhurst et al., 1998). In well SM-30, permeability of the shales is significantly reduced if chemical compaction is taken into account. The porosity-permeability trend is not expected to follow the normal observed trend (taken from wells which do not show any sign of chemical compaction). This may support the reason for having a very low modelled permeability (10^{-21} m^2 and lower) compared to the ShaleQuant result. Few published porosity-permeability data for shales are available (Katsube et al., 1991; Neuzil, 1994; Kooi, 1997; Yang & Aplin, 1998). The porosity-permeability values used for the shales in this modelling fall within the range of these published datasets.

The exact mechanism for reducing the permeability in the shales as a result of chemical compaction is not known. Nadeau et al. (2002) proposed that dissolution of kaolinite and the precipitation of neoformed I-S significantly reduced the permeability. Lack of mineralogical changes observed in the XRD results for SM-30 provides no support for this. SEM on overpressured shale (Figure 3.10) shows well organised/packed shale fabric, attesting to the collapse of shale framework. The clay fraction may remain the same but its structure or its fabric arrangement may not.

In Chapters 2 and 3, velocity-density plots of wells SM-28 and SM-30 do not show typical unloading or clay diagenesis trend. Swarbrick et al. (2002) have shown that the amounts of overpressure generated from fluid expansion caused by clay

diagenesis and quartz cementation are relatively low (less than 1000 psi) for a typical low permeability seal (1nD). Gas generation (either directly from kerogen or cracking of the oil), on the other hand, provides the most effective mechanism for volume expansion and overpressure generation. In well SM-30, porosity-permeability loss during chemical compaction may have induced disequilibrium compaction and volume expansion, enhancing further the excess pressure in the well. The evidence for volume expansion does not show up in the velocity-density plots because of the continuous reduction in porosity with effective stress due to chemical compaction. Unloading trends are visible when the shales have been compacted (subjected to maximum effective stress) prior to volume expansion. In the event, where both processes proceed simultaneously, the unloading signature does not show up in the velocity-density plot.

5.6 Summary and Conclusions

The modelled results using Temis2D suggest the following:

(1) Rapid deposition of fine grained sediments (low permeability in order of 1nD) is able to generate overpressure from disequilibrium compaction. The high geothermal gradient in the area is conducive for the creation of effective pressure seals through chemical compaction, which helps to generate higher excess pressure in the basin.

(2) Fixed porosity-permeability history for shales is not suitable for modelling fluid-flow and overpressure in areas where shales are known to be affected by chemical compaction, such as the Malay Basin. Fixed porosity-permeability history results in very high undercompaction, leading to much higher fluid retention, sealing and geothermal gradient than observed.

(3) A temperature-controlled porosity-permeability history for the shales will takes into account the effect of chemical compaction. A much more sophisticated porosity-permeability relationship is preferable, where the influence of time-temperature is included.

(4) The modelling results provide better understanding of the origin and the timing of overpressure in the Malay Basin. Overpressure in the southern part of the basin resulted from disequilibrium compaction with a contribution from hydrocarbon generation, and was enhanced by chemical compaction which created an effective seal in the shales of Groups K and L.

Chapter 6:

Overpressure Influence on the Petroleum Systems in the Malay Basin

6.1 Introduction

The development of overpressure can have a significant impact on the petroleum system of a basin through temperature distribution, seal integrity, fluid migration and reservoir quality. This chapter examines the possible influences of overpressure on the petroleum system in the Malay Basin, based on the findings from earlier Chapters 2, 3 and 5. The 2-D modelling work is continued in this chapter, in order to investigate temporal and spatial relationships between overpressure and geological processes leading to hydrocarbon accumulations in the basin.

This chapter is divided into four main parts. The first part introduces the concept of the petroleum system and presents some of the research findings on the effect of overpressure on the petroleum system. The next part provides an overview on the current understanding of the known petroleum systems within the Malay Basin. The third part discusses the results of the 2-D basin modelling reconstruction of overpressure and hydrocarbon generation along a section in the southern part of the basin. The occurrence of several oil and gas pools along the section is compared to the results of several simulations aimed at testing the influence of overpressure on hydrocarbon migration and accumulation. The role of chemical compaction on overpressure has also been investigated. The final part consists of a discussion and summary of this chapter.

6.1.1 Petroleum System Concept

Magoon & Dow (1994) defined a petroleum system as '*a natural system that encompasses a pod of active source rock and all related oil and gas and which includes all the geologic elements and processes that are essential if a hydrocarbon accumulation is to exist*'. The elements are made up of source rock, reservoir rock, seal rock and overburden rock. The processes are the trap formation, hydrocarbon generation, migration and accumulation.

A petroleum system is first identified from the known accumulation of oil or gas. The presence of oil or gas indicates the existence of one or more petroleum systems.

Effective source rocks are determined from the amount and type of organic matter and the level of thermal maturity (Peters & Casa, 1994). Reservoir rocks provide the storage space for the generated hydrocarbons, while the seal rock provides the necessary mean of retaining the hydrocarbons and preventing them from escaping to the surface.

Overburden rock provides the necessary sedimentary load in creating optimum thermal and pressure conditions for source rocks maturation and hydrocarbon expulsion. In addition, overburden rock is necessary to create a seal.

6.1.2 Previous Works

Overpressure has been documented to influence the elements and the processes operating within the petroleum system. Table 6.1 listed some examples.

Within the source rock, various studies have reported the occurrence of lower than normal vitrinite reflectance (McTavish, 1978, 1998; Carr, 1999; Zou & Peng, 2001) and retardation of hydrocarbon generation process (Price & Wenger, 1992; Torre, et al., 1997). Vitrinite reflectance increases with depth as the result of re-orientation of aromatic structure during burial, and high temperature facilitates removal of the non-aromatic structures. In the presence of overpressure, non-aromatic structures are retained within the vitrinite preventing aromatic structures from re-arranging themselves and resulting in lower reflectance. Within the oil window, generated hydrocarbons tend to exude into vitrinite structures causing bitumen staining and leading to further suppression.

While numerous works discuss the positive influence of overpressure on vitrinite reflectance, there is an equal amount of studies suggesting otherwise. Khorasani and Michelsen, 1994 and He et al., 2002, amongst others showed that there is no significant retardation in vitrinite reflectance due to overpressure. He et al. (2002) studied vitrinite reflectance suppression in the Jurassic section in the Barrow Sub-basin concluded that the overpressure in the area does not influence thermal maturity and hydrocarbon generation in that basin.

Table 6.1 Some published examples on the influence of overpressure on petroleum systems.

Reference	Areas	Affected Elements/Processes	Observations
McTavish (1978)	Northern North Sea	Maturation	Retard vitrinite maturation
Carr (1991) Carr (1998)	Yinngehai Basin, South China Ula Field, Central Graben Po Basin, Italy	Maturation	Retard maturation Incorporate modified kinetic model (PresRo) into basin model to simulate effects of overpressure on organic maturation
Torre et al., 1997.			Retard maturation and hydrocarbon maturation.
Inan (1992)	Thrace Basin, Northwestern Turkey	Source maturation & hydrocarbon migration	Observed kinky vitrinite reflectance-depth well profile within the undercompacted shales. Preserved porosity in undercompacted shales caused delay in hydrocarbon expulsion (low saturation). Hence, cracked into gas. However, the normally pressure shales at basin margin charged two small fields.
Fang et al., 1996	Yinggehai Basin, China		Low Vro and retention of hydrocarbon
Waples & Okui (1992)		Expulsion efficiency	Overpressuring will result in a decrease in expulsion efficiency of oil. This will lead to greater amount of oil cracked to gas. However, in returning to normal pressure, oil expulsion will improve drastically (highly efficient). Since gas will be expelled preferentially over oil and water, overpressured source rock at high maturity will have high expulsion efficiency for gas.
Darby et al. (1997)		Reservoir quality	Control the movement of diagenetic fluids
Caillet et al. (1998)	Ekofisk, Norway	Reservoir quality & seal	Implication on trapping mechanism and hydrocarbon distribution. Hydrodynamic restriction within chalk. Hydrocarbon generation and migration pre-dates overpressure, hence preservation of porosity.
Osborne & Swarbrick (1999)	Central Graben, North Sea	Reservoir quality	Overpressure (low effective stress) prevents extensive quartz cenments, which are found in high effective stress (low or no overpressure) at same depth and temperature.
Cayley (1987)	Central Graben	Hydrocarbon migration	Influence the hydrocarbon migration
Fertl & Leach (1990)	Gulf Coast, USA Baram Delta, Malaysia West Turkmen, USSR?	Hydrocarbon distribution	

Pressure has been suggested to have a retarding effect on the rate of chemical reaction (Carr, 1999; Osborne & Swarbrick, 1997). Citing Le Chatelier's principle as the reason, these authors suggested that the rate of chemical reaction decreases with increase in pressure. However, there are also contradictory reports of the effect of pressure on chemical reaction. For example, Ko & Hesse (1992) found that the rate of illitization in the overpressured shales is faster than in the normally pressured section.

6.2 Malay Basin Petroleum Systems

Biomarker fingerprinting of the oils in the Malay Basin shows two main origins with some mixing between them (EPIC, 1994; Creaney et al., 1994; McCaffrey et al., 1998). The coal-derived oils contain high pristane/phytane ratio, high C29 sterane relative to C27 and C28, high oleanane and bicadinanes, low diasterane/sterane ratio, low gammacerane/hopane ratio, low Ts/(Ts + Tm) ratio (Figure 6.1). Lacustrine-derived oils show waxy GC traces, with low pristane/phytane ratio. The biomarker abundances are lower than in the coaly-derived oils. They consist of high (but variable) gammacerane and high diasterane/sterane.

Two petroleum systems (Upper Oligocene-Middle Miocene and Upper Miocene) contribute to the hydrocarbon accumulations and hydrocarbon generation and migration in the Malay Basin. The Upper Oligocene petroleum system includes Group M, K, L and J shales that contributed mainly oil and some gases in the southern part and the flank of the basin. The Upper Miocene petroleum system contains coals and coaly shales that contributed to mostly gas with some oil in the northern and central part of the basin.

Proprietary geochemical well reports and some published studies (Creaney et al., 1994; McCaffrey et al., 1998) for the oils in the Malay Basin showed that the main source rocks are the Group K, L and M shales, which contain Type I lacustrine organic matter. The younger source rocks are the coals and the coaly shales found in Group E, H and I. These source rocks contain Type III organic matter.

Cross-plots of TOC content and S_2 values from Rock-Eval pyrolysis are shown on Figure 6.2. These data were taken from the EPIC (1994) study of the Malay Basin. The TOC of Group K shales can be as high as 5%, with an average value around 2%. The S_2 values range from 5 to 20 mg HC/g rock, with an average of 5 mg HC/g rock. It is worth nothing that the TOC and S_2 values could have been higher if they had been taken from immature samples. These data were taken from shales that are within the oil generation window (Figure 6.3).

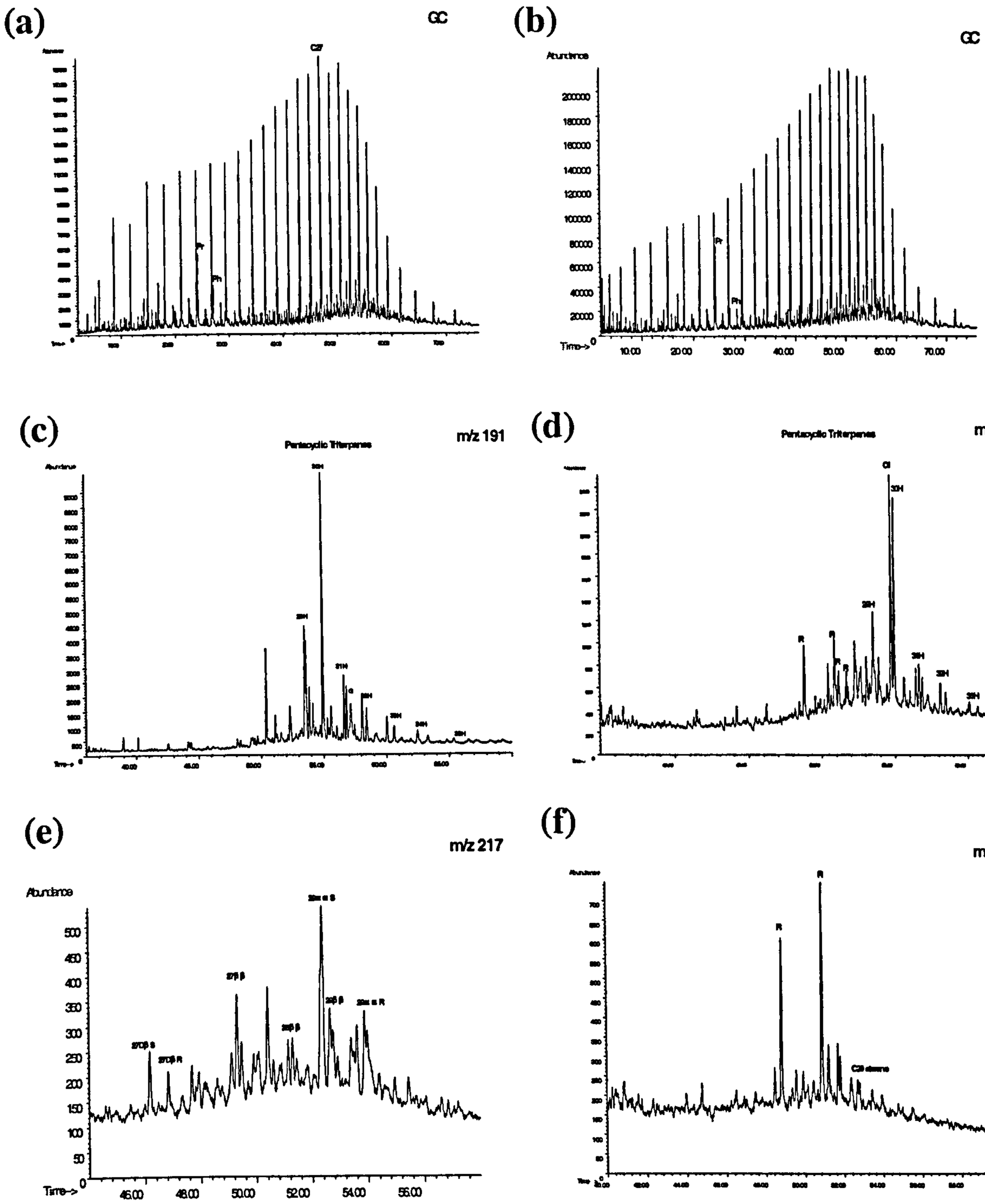
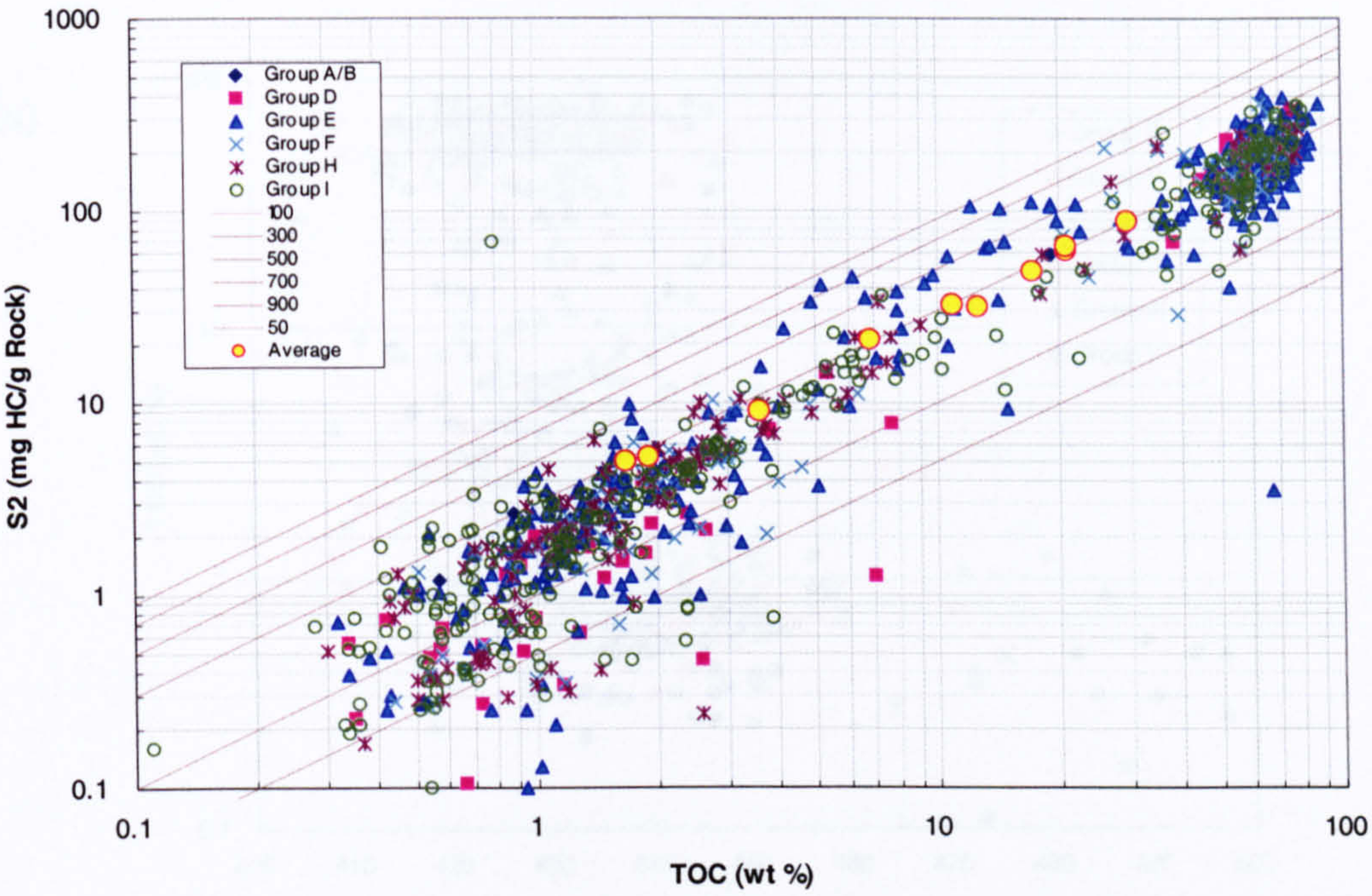


Figure 6.1 Typical biomarker fingerprints of two main oil groups in the Malay Basin: lacustrine-derived (a,c,d) and coaly-derived (b,d,f). The fingerprints are presented in forms of whole oil gas chromatograms (a,b), m/z 191 (c,d) and m/z 217 (e,f).

(a)



(b)

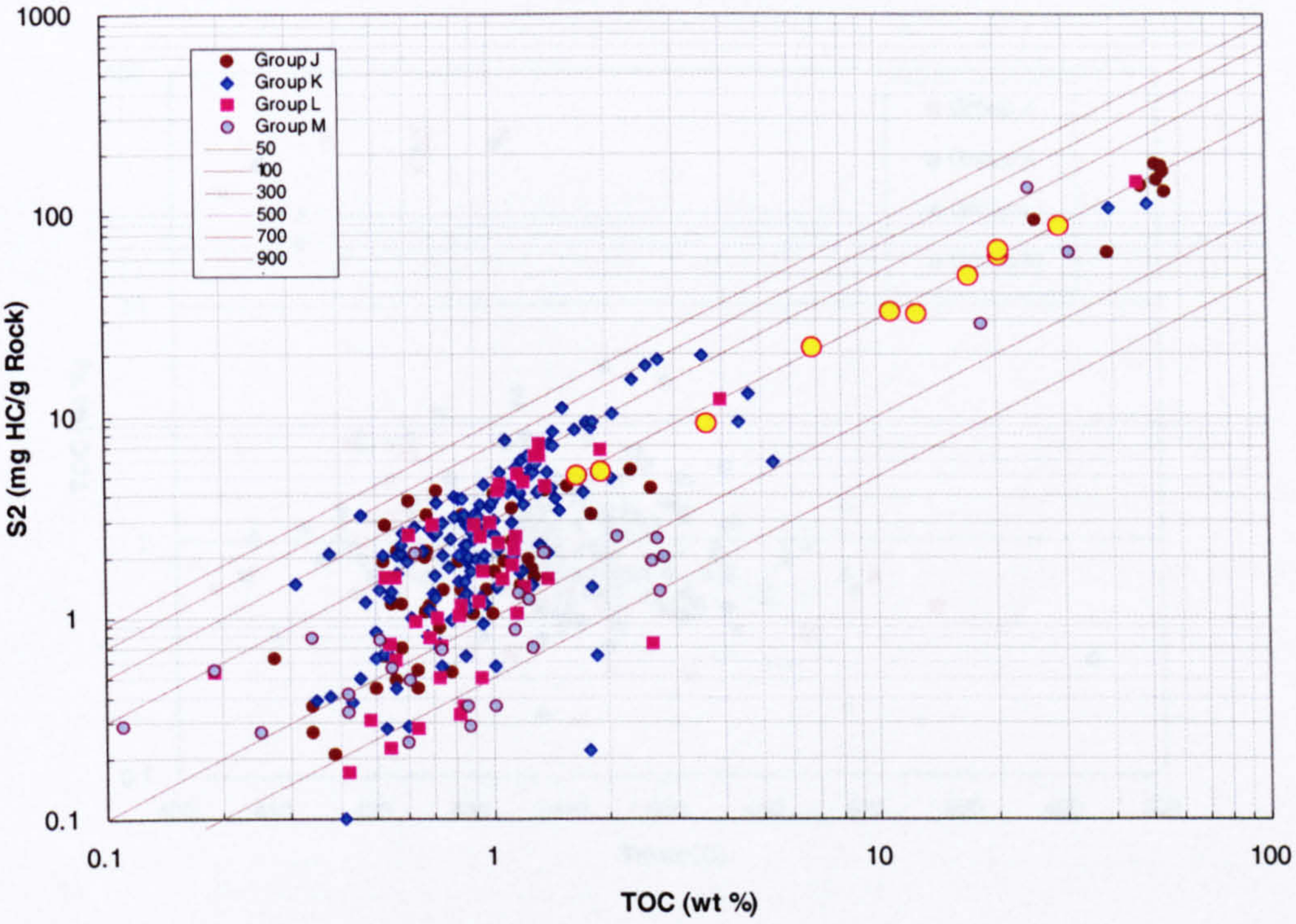
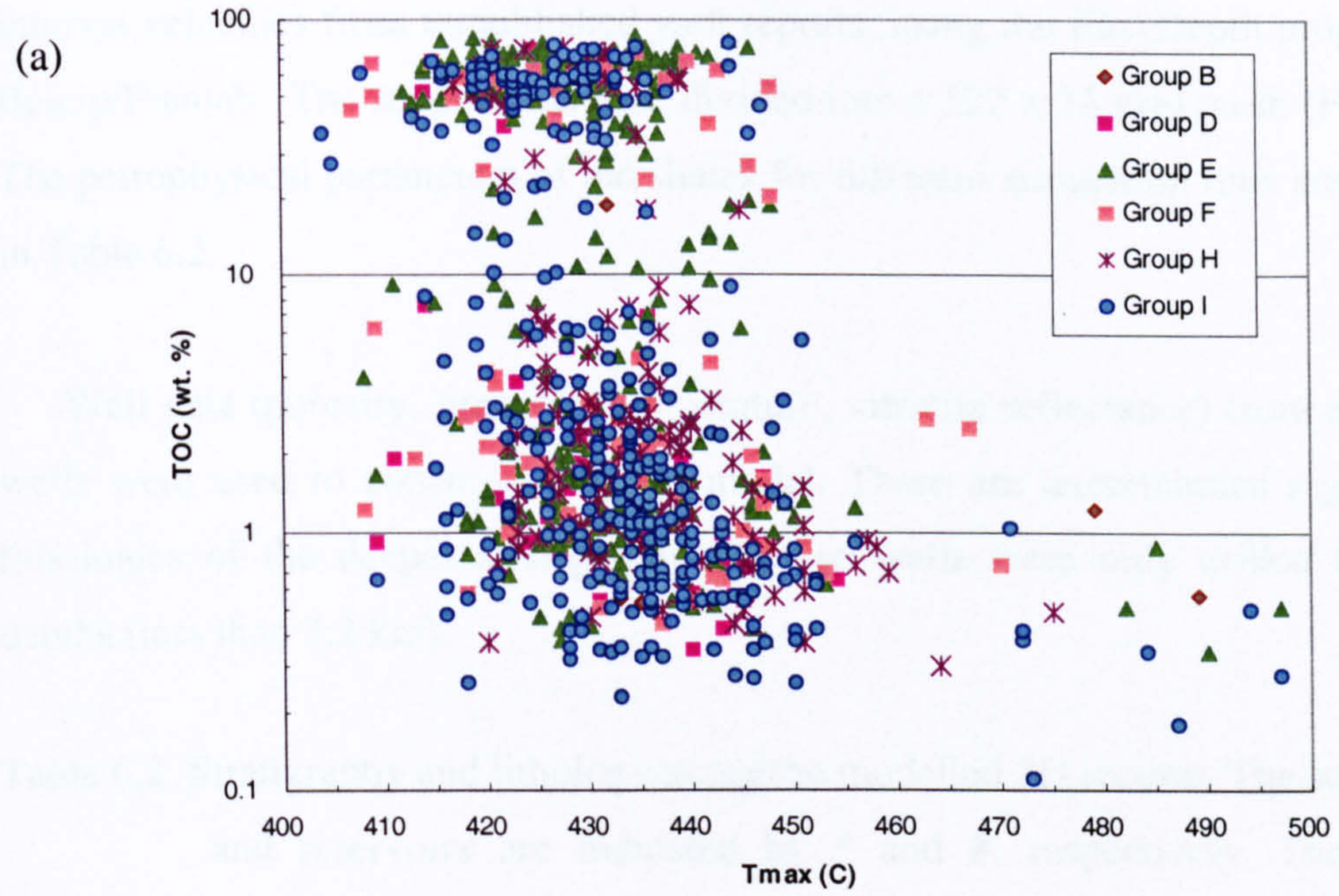


Figure 6.2 Cross-plots of TOC vs. Rock-Eval S_2 for shales/coals in the Malay Basin, (a) Groups A/B to I, (b) Groups J-M. Data derived from EPIC (1994).



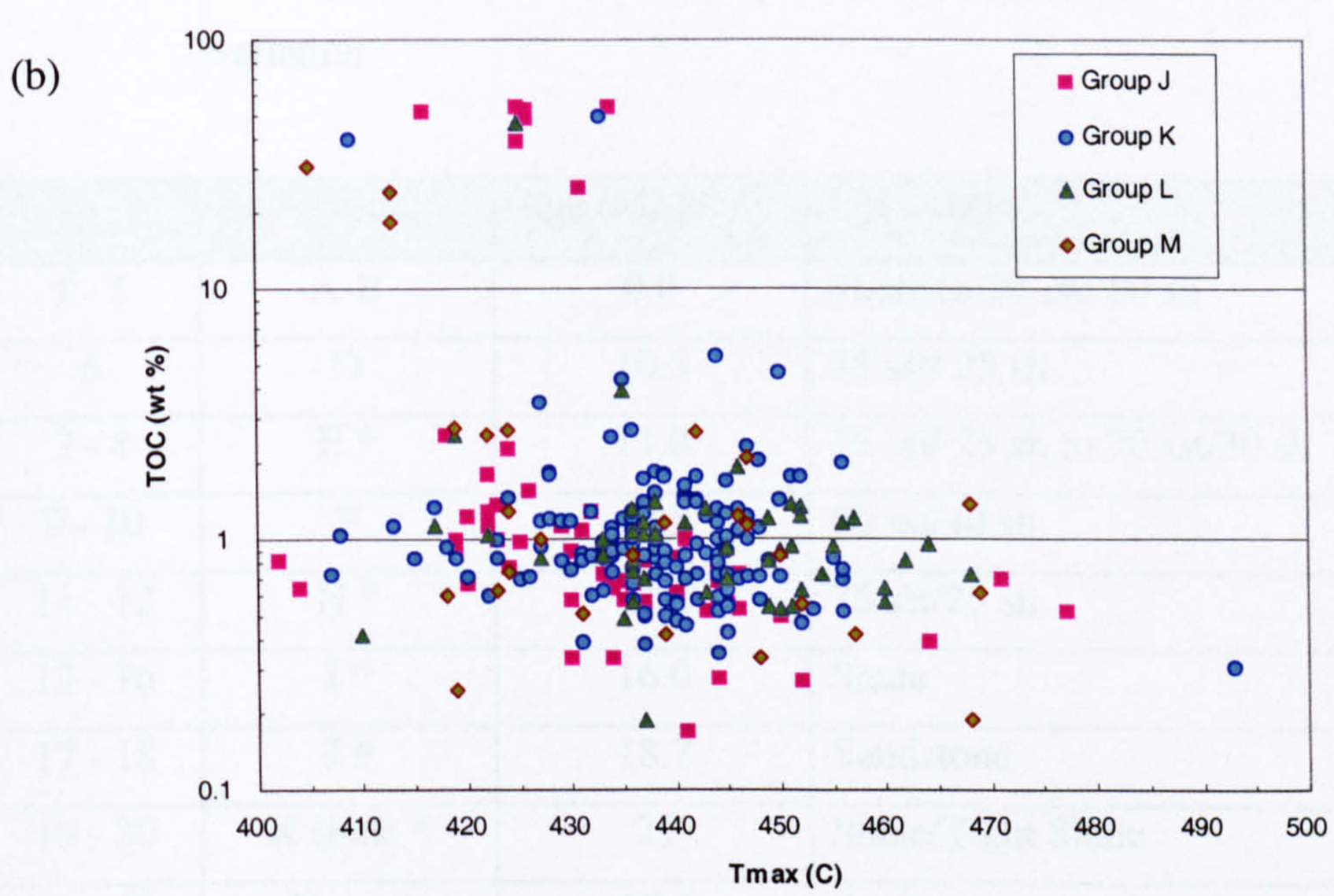


Figure 6.3 Cross-plots of the TOC (from Figure 6.2) against Tmax values. Onset of oil generation zone begins at Tmax of 435°C and end at around 470°C. For Type I kerogen, Tmax values generally less than 450°C, even at late mature stage.

6.3 Results of 2D Basin Modelling

The regional seismic line was first interpreted and then depth converted with interval velocities from unpublished well reports, using the EasyDepth program from Beicip/Franlab. The section was then divided into a 122 x 34 grid mesh (Figure 6.4). The petrophysical parameters of the shales for different simulation runs are presented in Table 6.2.

Well data (porosity, pressure, temperature, vitrinite reflectance) from exploration wells were used to constrain the 2-D model. There are uncertainties regarding the lithologies of the deeper stratigraphy because wells were only drilled to shallow depths (less than 3.2 km).

Table 6.2 Stratigraphy and lithology along the modelled 2D section. The source rocks and reservoirs are indicated by * and #, respectively. The range of lithology within each stratigraphic group reflects the lateral and vertical variation.

No.	Stratigraphy	Age (Ma)	Lithology
1 - 5	A-B	0.0	Shale to 20 sst/ 80 sh
6	D	10.5	75 sst/ 25 sh
7 - 8	E *	11.0	75 sst/ 25 sh to 70 sst/30 sh
9 - 10	F	12.5	60 sst/40 sh
11 - 12	H *	13.5	75 sst/25 sh
13 - 16	I *	16.0	Shale
17 - 18	J #	18.7	Sandstone
19 - 20	K shale *	21	Shale/Tight Shale
21 - 22	K sst #	25.2	Sandstone
23 - 24	L shale *	30.0	Shale/Tight Shale
25 – 26	L sst #	35.0	Sandstone
27 - 34	M *	40.0	Shale/Tight Shale to 50 sst/50 sh

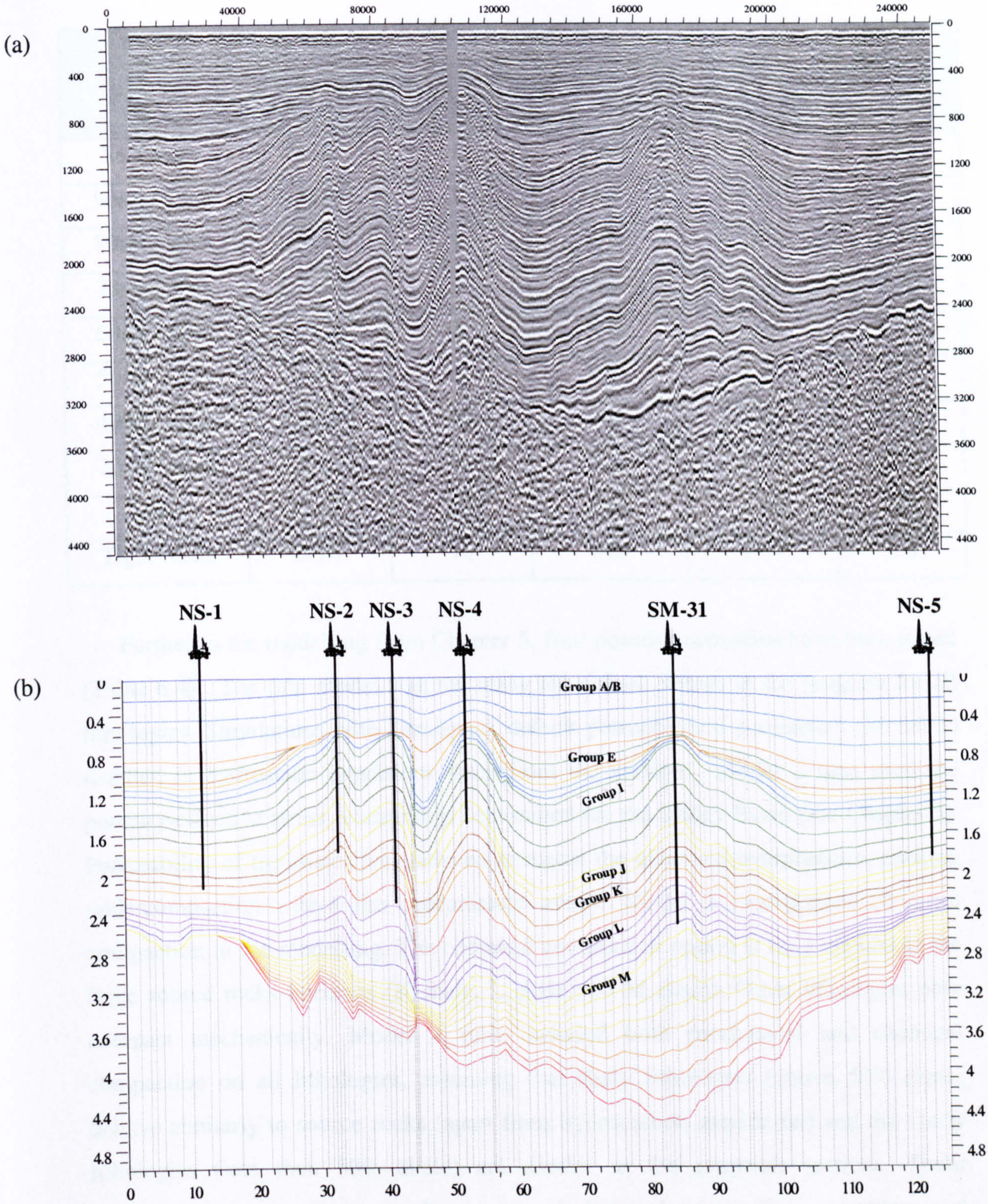


Figure 6.4 2-D cross-section of N-S line: (a) seismic profile, (b) gridded section used for basin modelling study. Also shown are the locations of the wells and oil/gas fields (projected).

Table 6.3 Petrophysical parameters of the lithologies used in the modelling.

Lithology	Specific Surface Area (m^2/m^3)	Kh/Kv (permeability anisotropy)	Heat Capacity (J/kg/C)	Thermal Conductivity (W/M/C)	Density (g/cm^3)
Sandstone	$5x10^5$	1	1000	3.5	2.65
90sst / 10sh	$8.5x10^5$	1	984	3.20	2.67
80sst / 20sh	$1.4x10^6$	1	968	2.94	2.68
70sst / 30sh	$2.5x10^6$	1	952	2.73	2.70
60sst / 40sh	$4.2x10^6$	1	936	2.54	2.71
50sst / 50sh	$1x10^6$	1	950	2.50	2.73
40sst / 60sh	$1.2x10^7$	10	904	2.23	2.74
20sst / 80sh	$3.5x10^7$	10	872	1.99	2.77
Shale	$1x10^8$	10	840	1.80	2.8
Tight Shale	$1x10^8$	10	840	1.80	2.8

Further to the modelling from Chapter 5, four possible scenarios have been tested (Table 6.4). The first model was run using the default values in the program for all lithologies. Simulations with Temispack default petrophysical parameters (Model 1) resulted in hydrostatic conditions throughout the section. Model 2 runs used the porosity-effective stress relationship determined for the Malay Basin (see Chapter 5). Permeability of the shales was reduced to match the observed overpressure, creating undercompaction within the overpressure zones. Model 3 incorporates chemical compaction in the modelling. The chemical compaction option is only applied to the three source rocks horizons (K shale, L shale and M shale). Other lithologies only compact mechanically. Model 4 runs included both mechanical and chemical compaction on all lithologies, assuming that shaly lithologies (above 50% shale) behave similarly to source rocks (apart from hydrocarbon generation) and the sandy lithologies (less than 50% shale) are similar to the reservoir sections. These assumptions are necessary to allow a set of chemical compaction parameters and porosity-depth curves to be used for shaly and sandy units. An option of averaging the compaction parameters for the mixed lithologies has not been attempted in this study.

Table 6.4 Modelling scenarios

Model	Simulation
1a	Normal compaction, default lithology
1b	Normal compaction, default lithology, oil generation
1c	Normal compaction, default lithology, oil cracking (gas)
2a	Undercompaction, fluid-flow only
2b	Undercompaction, oil generation
2c	Undercompaction, gas generation
2d	Undercompaction, oil cracking (gas)
3a	Chemical compaction (source rocks), fluid-flow only
3b	Chemical compaction (source rocks), oil generation
3c	Chemical compaction (source rocks), gas generation
3d	Chemical compaction (source rocks), oil cracking (gas)
4a	Chemical compaction (all lithologies), fluid-flow only
4b	Chemical compaction (all lithologies), oil generation
4c	Chemical compaction (all lithologies), oil cracking (gas)

6.3.1 Thermal Modelling

Surface heat flow in this basin ranges from 85 to 105 mW/m^2 (Yusoff, 1993; Halim, 1994). The high heat-flow areas are towards the basin axis as well in the northern part of the basin. Yusoff (1993) suggested the role of subsurface fluid as partly responsible for transporting high heat into the basin.

Differences in model output between a rifting and a constant heat-flow thermal history has been studied by modelling. Both models were simulated with the same lithological parameters. However, changes to the thickness of the thermal basement (crust and mantle) have been made to accommodate the effect of rifting. The rifting model was run using a β factor (stretching coefficient) of 2, similar to those determined for the Malay Basin by Madon & Watts (1998). The rifting phase was simulated from 45 Ma to 35 Ma. The temperature and maturity data were used to calibrate these models. An example of result is shown on Figure 6.5. Temperature and

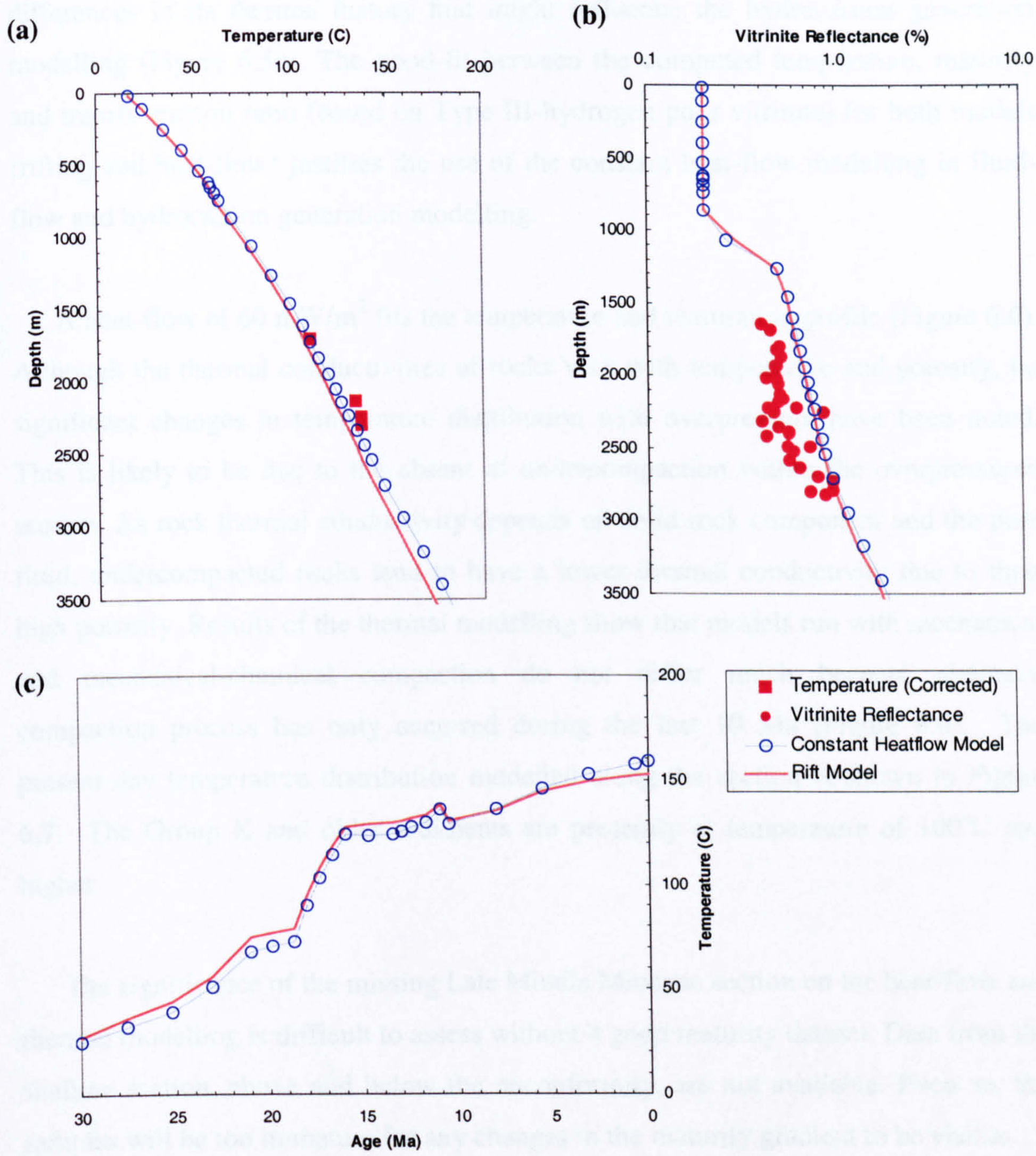


Figure 6.5 Comparing thermal modelling results using rifting heat flow against a constant basal heat flow for well SM-31.

maturity depth profiles for well SM-31 show minor differences between the two models. The plot of temperature evolution for a Group L shale shows no significant differences in its thermal history that might influence the hydrocarbon generation modelling (Figure 6.5c). The good-fit between the computed temperature, maturity and transformation ratio (based on Type III-hydrogen poor vitrinite) for both models (rifting and heat-flow) justifies the use of the constant heat-flow modelling in fluid-flow and hydrocarbon generation modelling.

A heat-flow of 60 mW/m^2 fits the temperature and maturation profile (Figure 6.6). Although the thermal conductivities of rocks vary with temperature and porosity, no significant changes in temperature distribution with overpressure have been noted. This is likely to be due to the absent of undercompaction within the overpressured section. As rock thermal conductivity depends on solid rock component and the pore fluid, undercompacted rocks tend to have a lower thermal conductivity due to their high porosity. Results of the thermal modelling show that models run with mechanical and mechanical-chemical compaction do not differ much because chemical compaction process has only occurred during the last 10 Ma (Figure 6.6). The present-day temperature distribution modelled along the section is shown in Figure 6.7. The Group K and older sediments are presently at temperature of 100°C and higher.

The significance of the missing Late Middle Miocene section on the heat-flow and thermal modelling is difficult to assess without a good maturity dataset. Data from the shallow section, above and below the unconformity, are not available. Even so, the samples will be too immature for any changes in the maturity gradient to be visible.

6.3.2 Hydrocarbon Generation

Major source rock intervals recognized are Oligocene-Miocene lacustrine shales (Groups M, L and K) and Miocene coaly shales (Groups E, H and I). Based on the Rock-Eval and TOC analysis, the Group K, L and M source rocks and the Group E, H and I source rocks) were set at 2% and 20% TOC, respectively. Although the majority of the datapoints (Figure 6.3) for Group K and L fall below 2% TOC, most of these

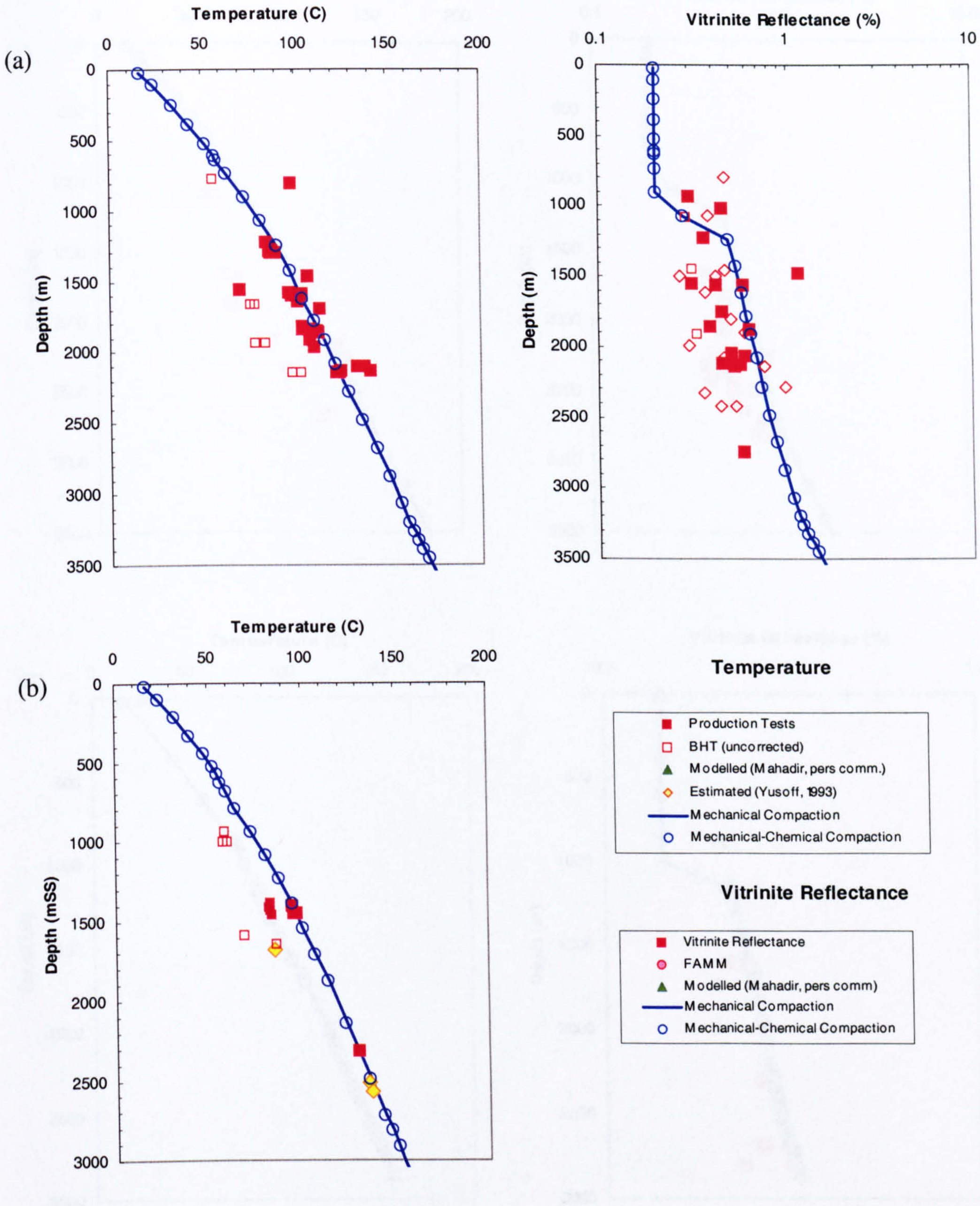


Figure 6.6 Present-day measured and modelled temperatures and maturity for wells: (a) NS-3 (km 42), (b) NS-4 (km 53), (c) SM-31 (km 85) and (d) NS-5 (km 123). No significant changes in the modelled temperature and maturity as result of chemical compaction within the Group K, L and M upper shales are noted.

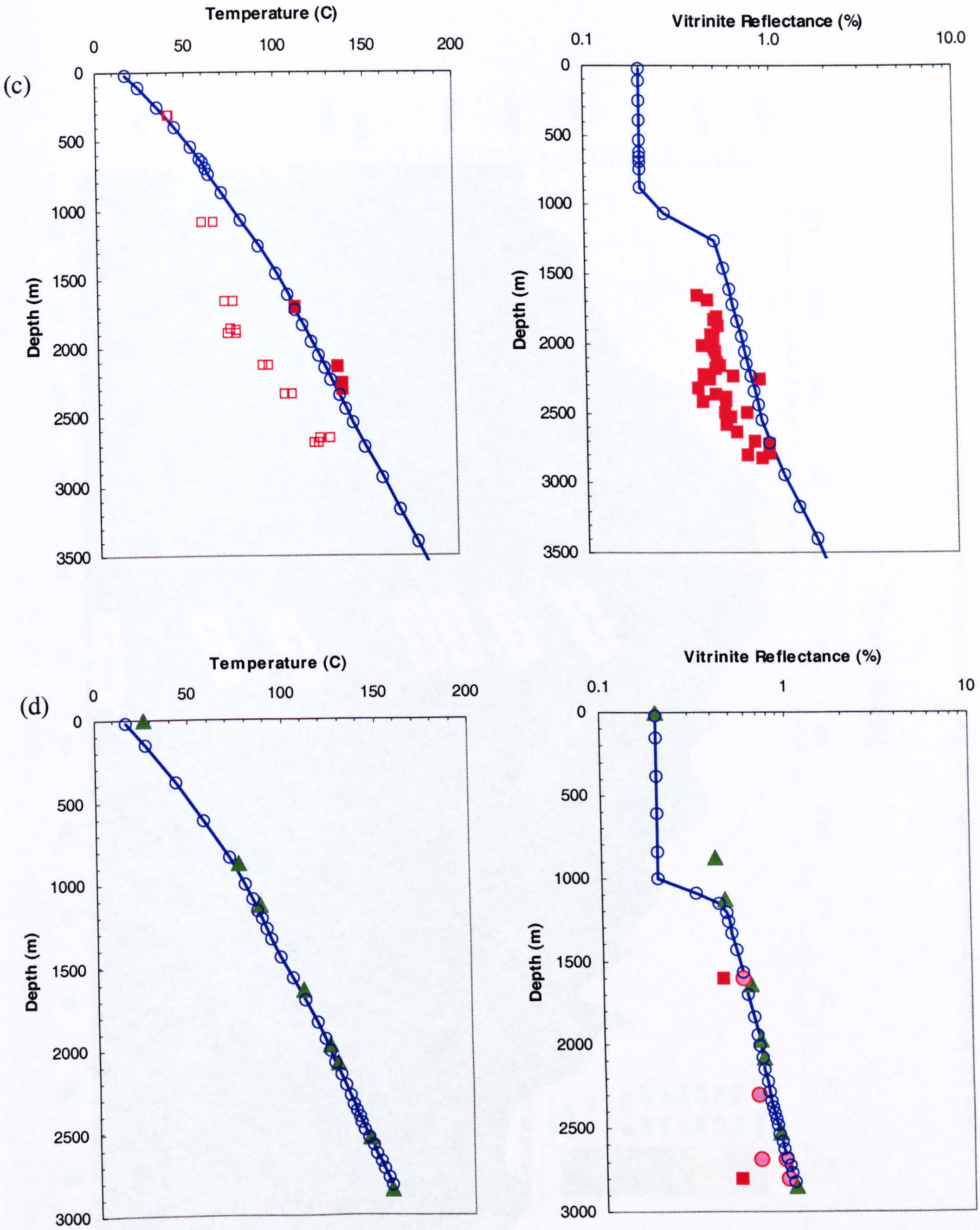


Figure 6.6 Continued

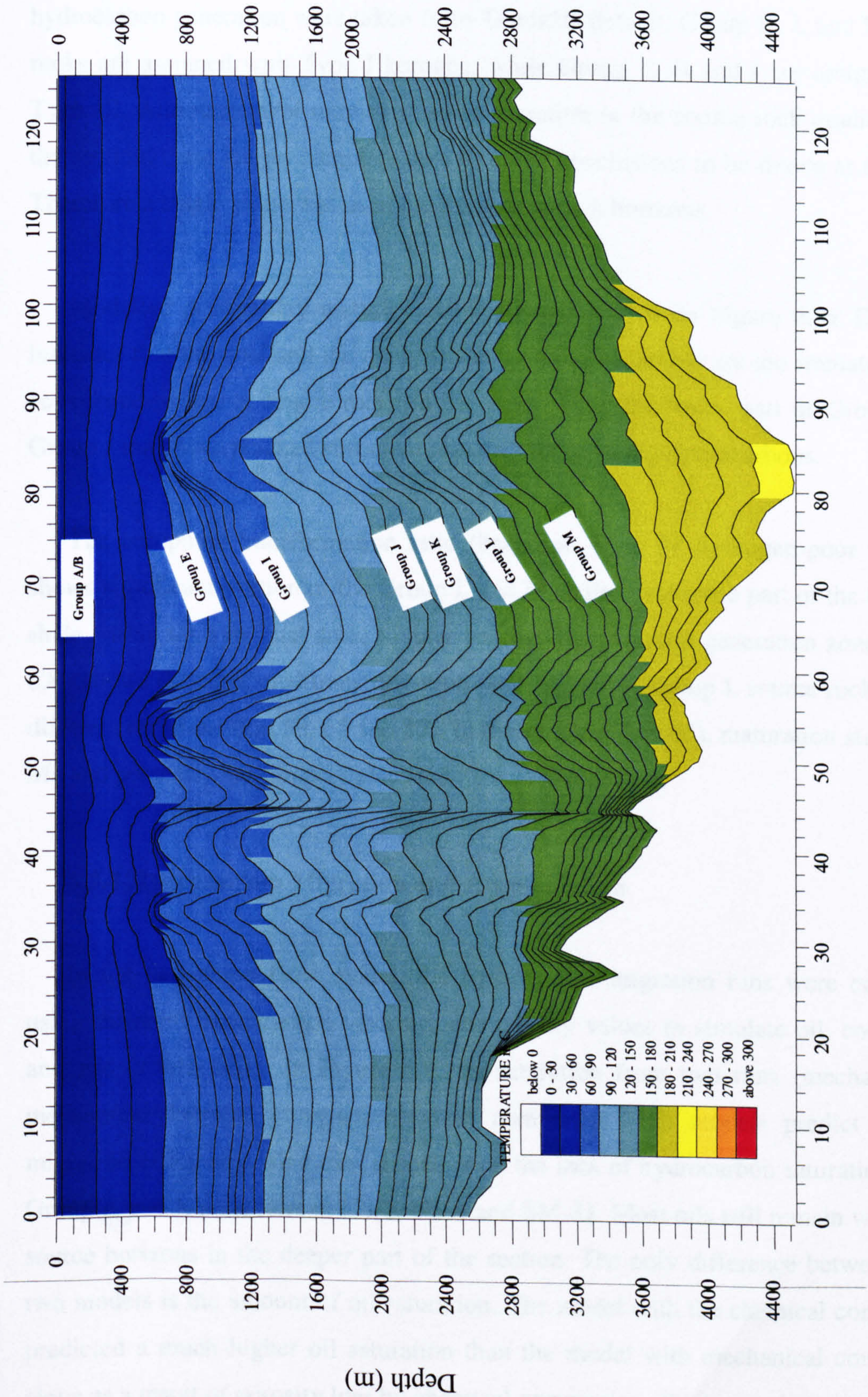


Figure 6.7 Modelled present-day temperature distribution using a constant heat flow of 60 mW/m^2.

data were measured on mature shales.

Kinetics data (activation energy distribution and Arrhenius constant) for hydrocarbon generation were taken from Temis2D default. Group K, L and M source rocks are assigned with Type I kerogen, while Group E, H and I are assigned with Type III. Although there may exist some variation in the source rock quality across the section, there are no complete data to allow conclusions to be drawn at this time. Therefore a single value was used for the source rock horizons.

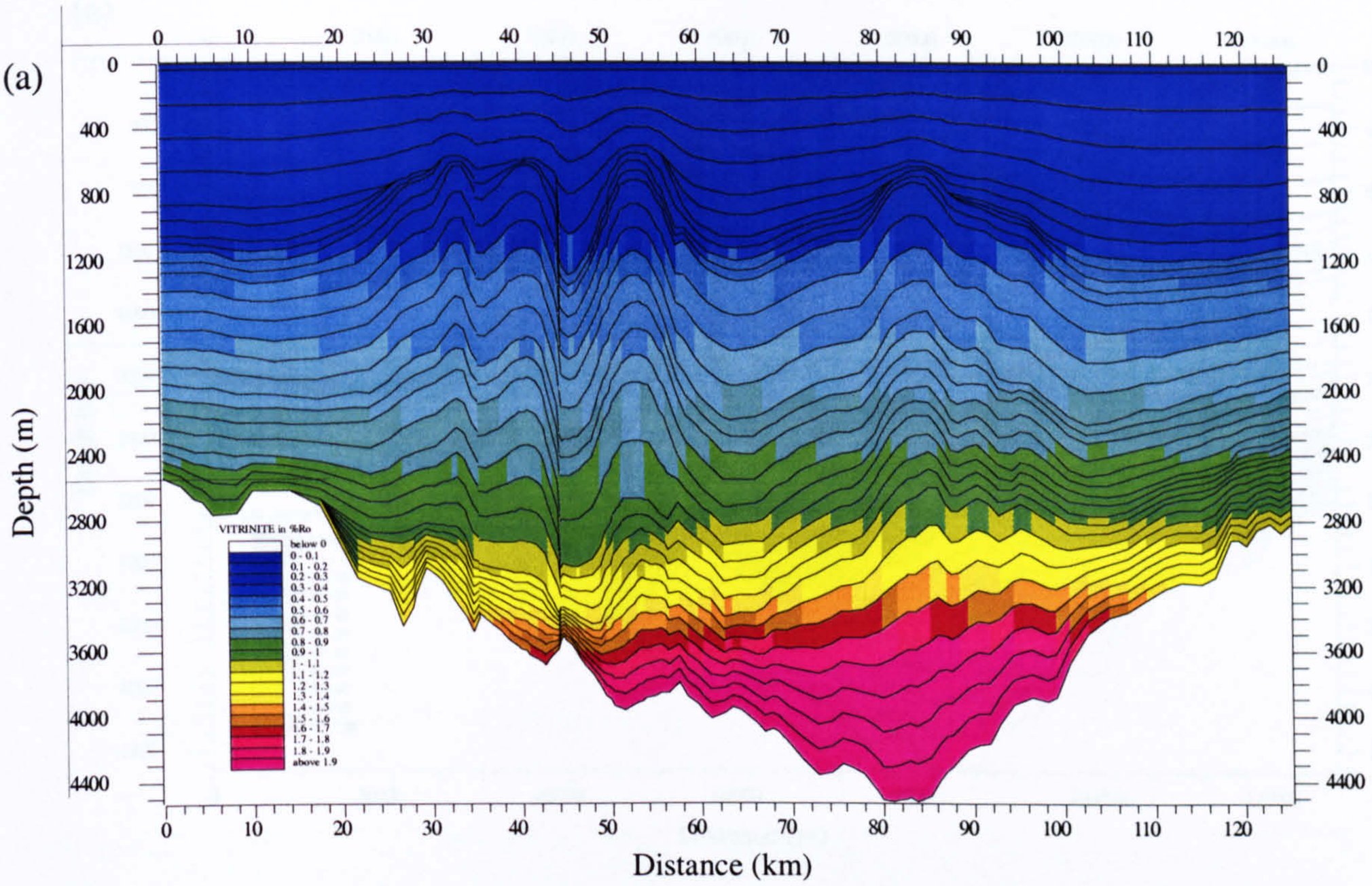
Modelled present-day maturity distribution is shown on Figure 6.8a The result indicates that the coal and the coaly shales in Group E and H are too immature to be considered as active source rocks in the area . Only the lower part of Group I and Group J may have reached sufficient maturity for sourcing hydrocarbons.

The computed transformation ratio (based on Type IV hydrogen-poor vitrinite) shows significant portion of the Group L and M shales, and some part of the Group K shale within the synclinal areas to have reached hydrocarbon generation zone. Figure 6.8b shows the computed transformation ratio history of Group L source rock at three different locations (km 53, 65 and 85). In the syncline (km 65), maturation starts at 16 Ma and presently has almost exhausted its source potential.

6.3.4 Hydrocarbon Migration and Accumulation

In the two-phase flow model, the hydrocarbon migration runs were conducted using different hydrocarbon viscosity and density values to simulate oil, condensate and gas (Table 6.5). In Figure 6.9, oil saturation from two runs (mechanical vs mechanical-chemical compaction) were compared. Both models predict low oil migration efficiency. This can be seen from the lack of hydrocarbon saturation in the Group K and L reservoirs at NS-3, NS-4 and SM-31. Most oils still remain within the source horizons in the deeper part of the section. The only difference between these two models is the amount of oil saturation. The model with the chemical compaction predicted a much higher oil saturation than the model with mechanical compaction alone as a result of porosity loss by chemical compaction. The trapped or unexpelled

(a)



(b)

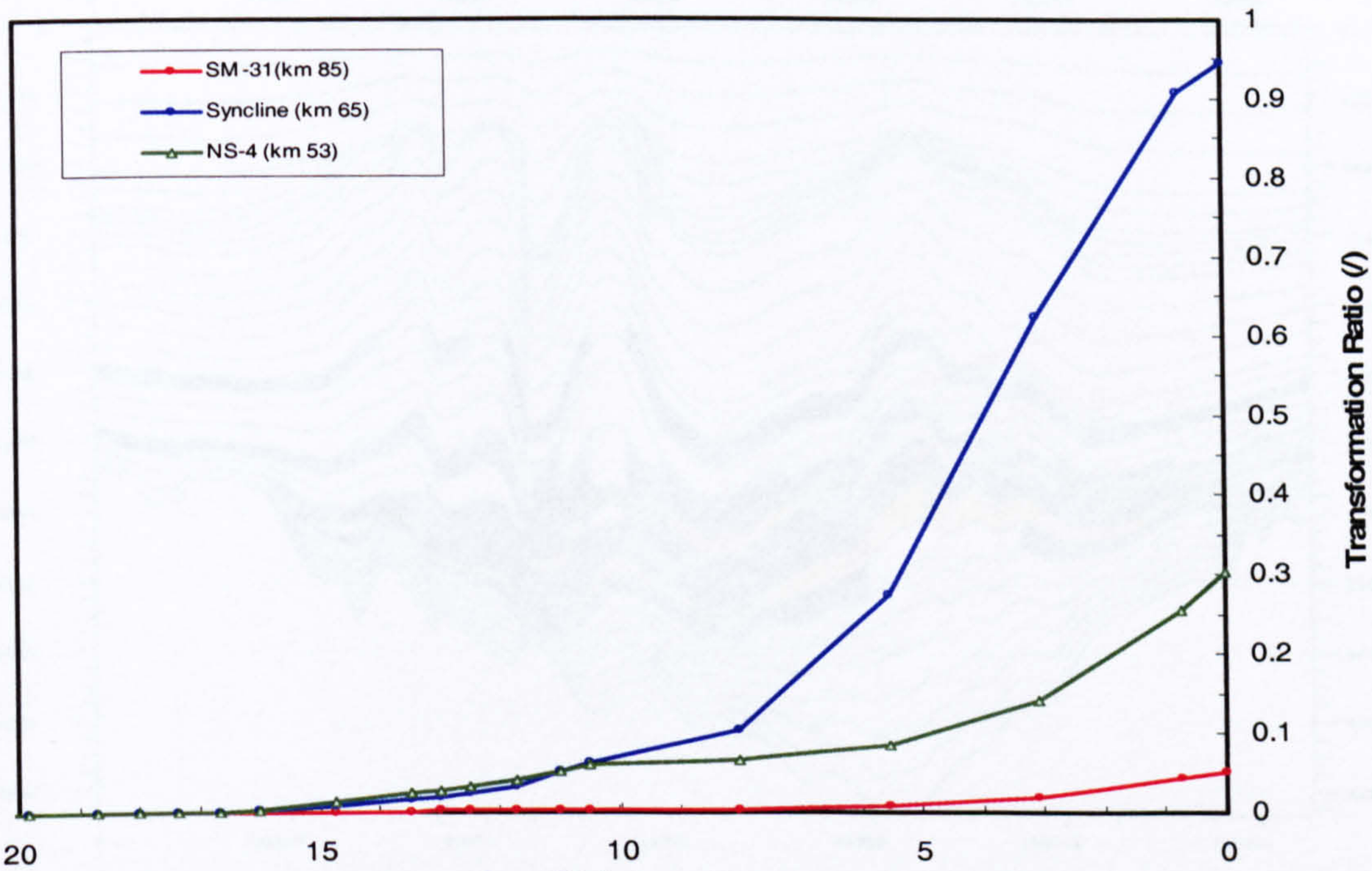


Figure 6.8 Modelled maturity and kerogen transformation: (a) present-day maturity profile across the N-S section, (b) calculated transformation ratio history for Group L source rock at locations NS-4 (km 53), syncline (km 65) and SM-31 (km 85).

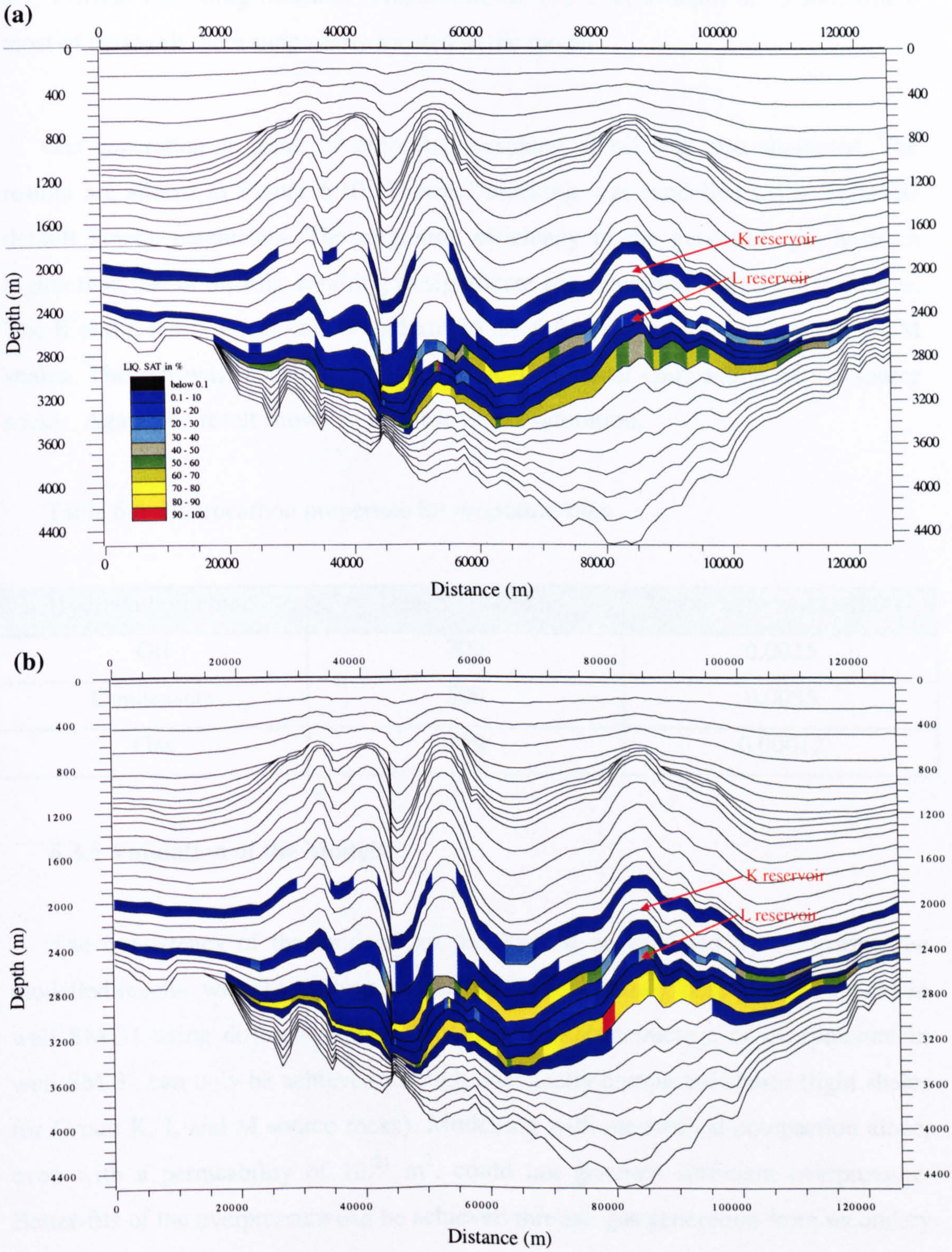


Figure 6.9 Modelled present-day oil saturation from Group K, L and M source intervals (TOC of 2%, Type I kerogen). Model (a) was runs with mechanical compaction only and model (b) using both mechanical and chemical compaction.

oils in the deeper part of the section will be subjected to secondary cracking. In Figure 6.7, thermal modelling indicates temperature of 150°C at a depth of 3 km, where most of these oils were supposedly located in the model.

Gas generation as result of secondary cracking of oil was also simulated. The results are shown in Figure 6.10. Thermal cracking was modelled using Temis2D default kinetic parameters. The migration efficiency of the generated gas is much higher than that of the oils, resulting in significant gas saturation within the structures. The K and L reservoirs at km-53 and km-85 are fully charged by the Group L and M shales. The run was repeated using mechanical-chemical compaction of the source rocks. Again, the result shows an increase in gas saturation.

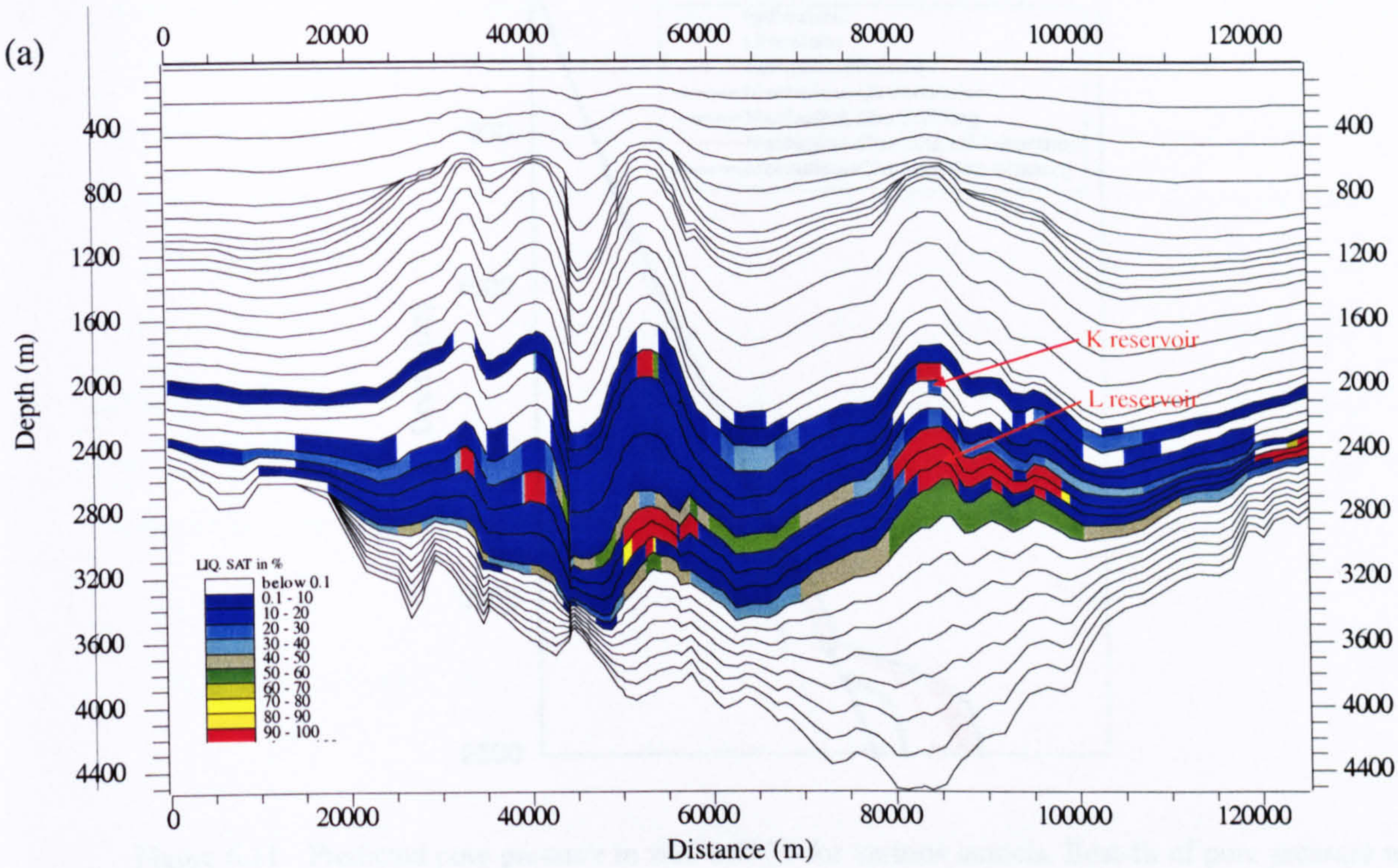
Table 6.5 Hydrocarbon properties for migration runs

Hydrocarbon Phase	Density (kg/m^3)	Viscosity (Pa.s) at 100°C
Oil	700	0.0035
Condensate	500	0.0035
Gas	250	0.00012

6.3.5 Validation of the Models

The consistency of the models can be checked or validated by comparing the modelled results with the drilling results. Figure 6.11 shows pore pressure results in well SM-31 using different compaction models. Reconstruction of overpressure in well SM-31 can only be achieved through chemically compacted shales (tight shales for Group K, L and M source rocks). Modelling with mechanical compaction alone, even with a permeability of 10^{-21} m^2, could not generate sufficient overpressure. Better-fits of the overpressure can be achieved through gas generation from secondary cracking of hydrocarbons.

Another example of model consistency check is to compare the result of hydrocarbon migration with the drilling results. Figure 6.12 summarizes the hydrocarbon discoveries and production along the modelled section. Major oil and



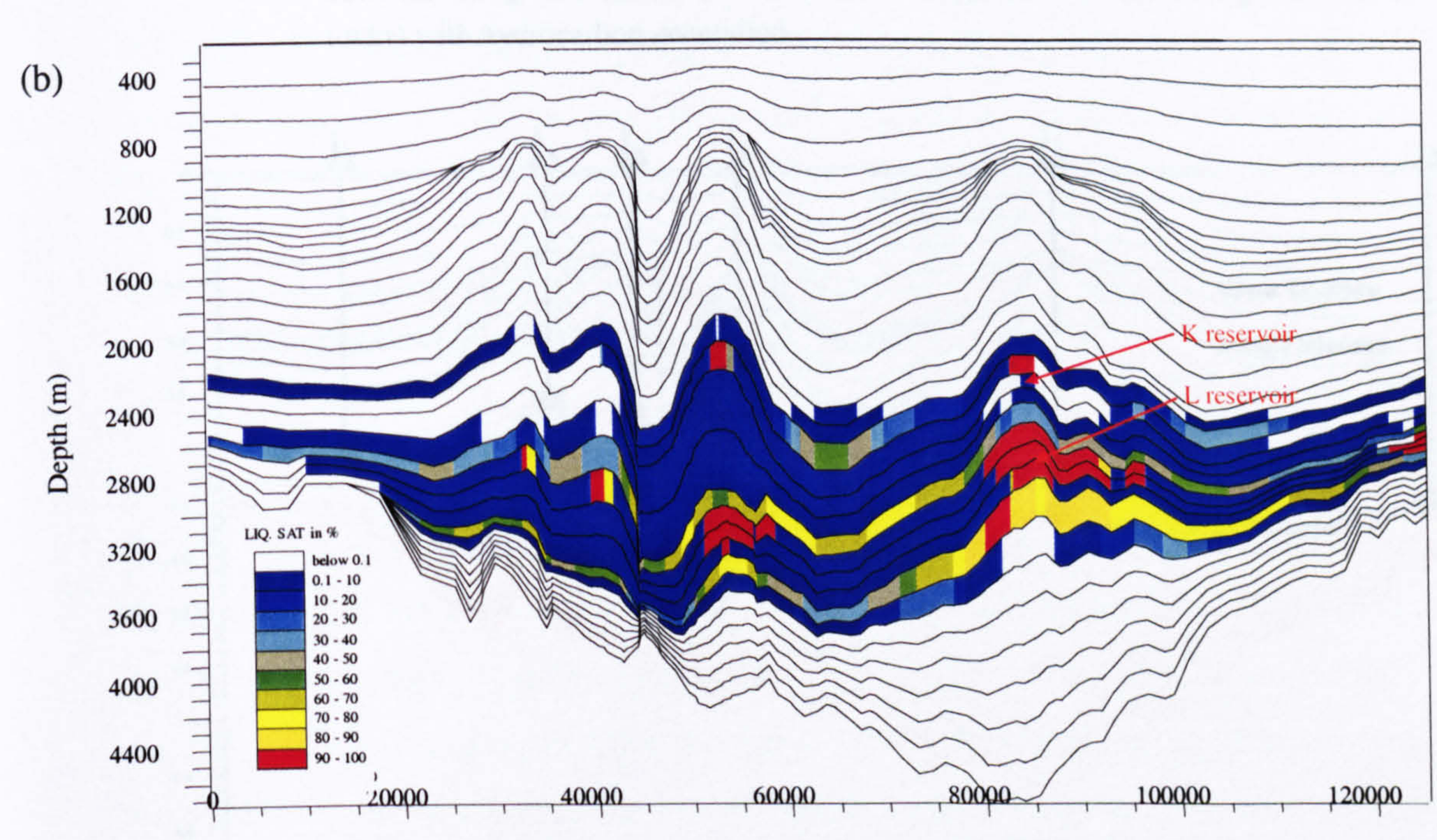


Figure 6.10 Modelled gas saturation resulting from cracking. Source rocks been assigned to Group K, L and M shales (TOC of 2%, Type I kerogen). Model (a) was simulated using mechanical compaction alone and model (b) was run with both mechanical and chemical on the shales.

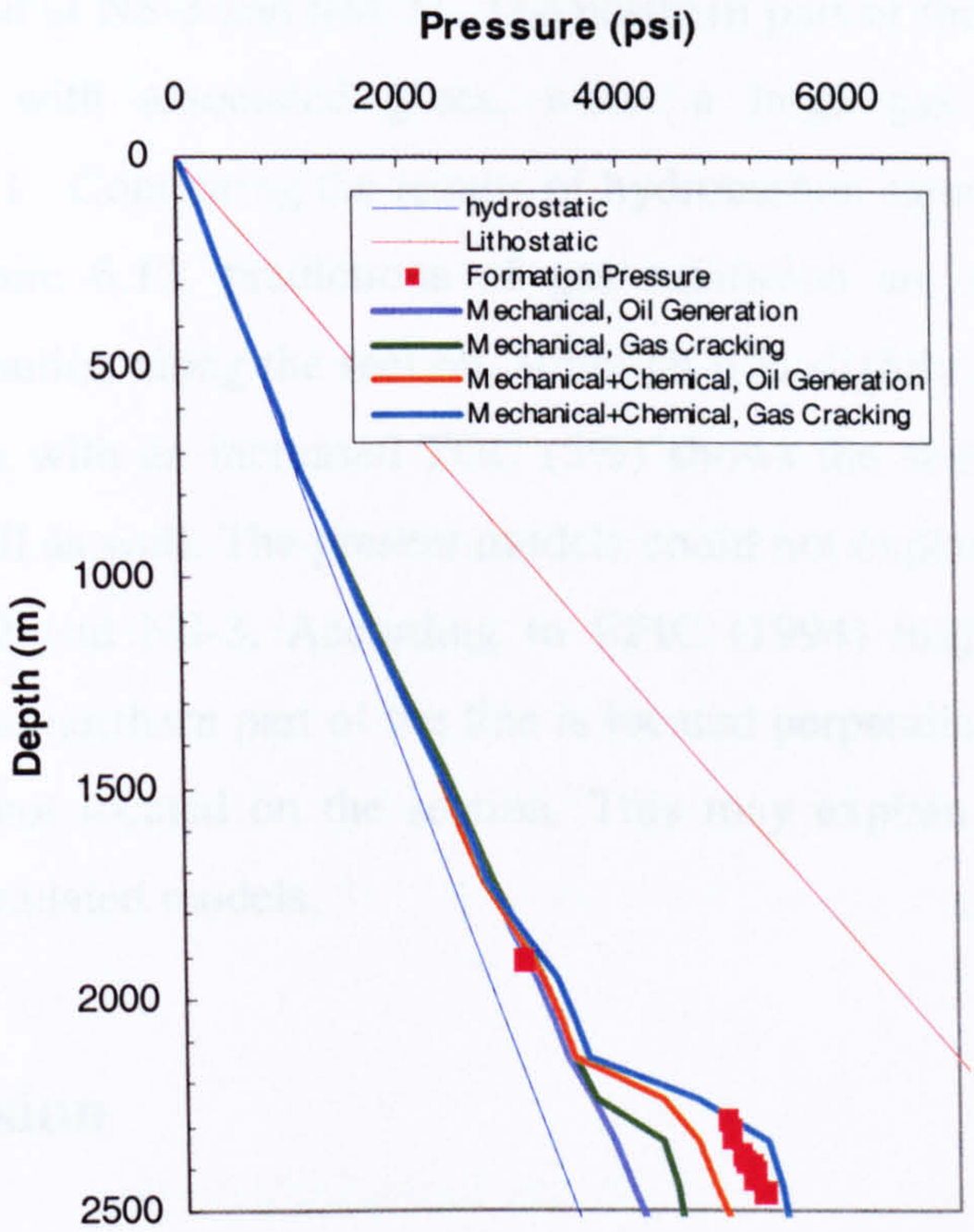


Figure 6.11 Predicted pore pressure in well SM-31 for various models. Best-fit of pore pressure were obtained using mechanical and chemical compaction within the tight shales (source rocks) with hydrocarbon generation.

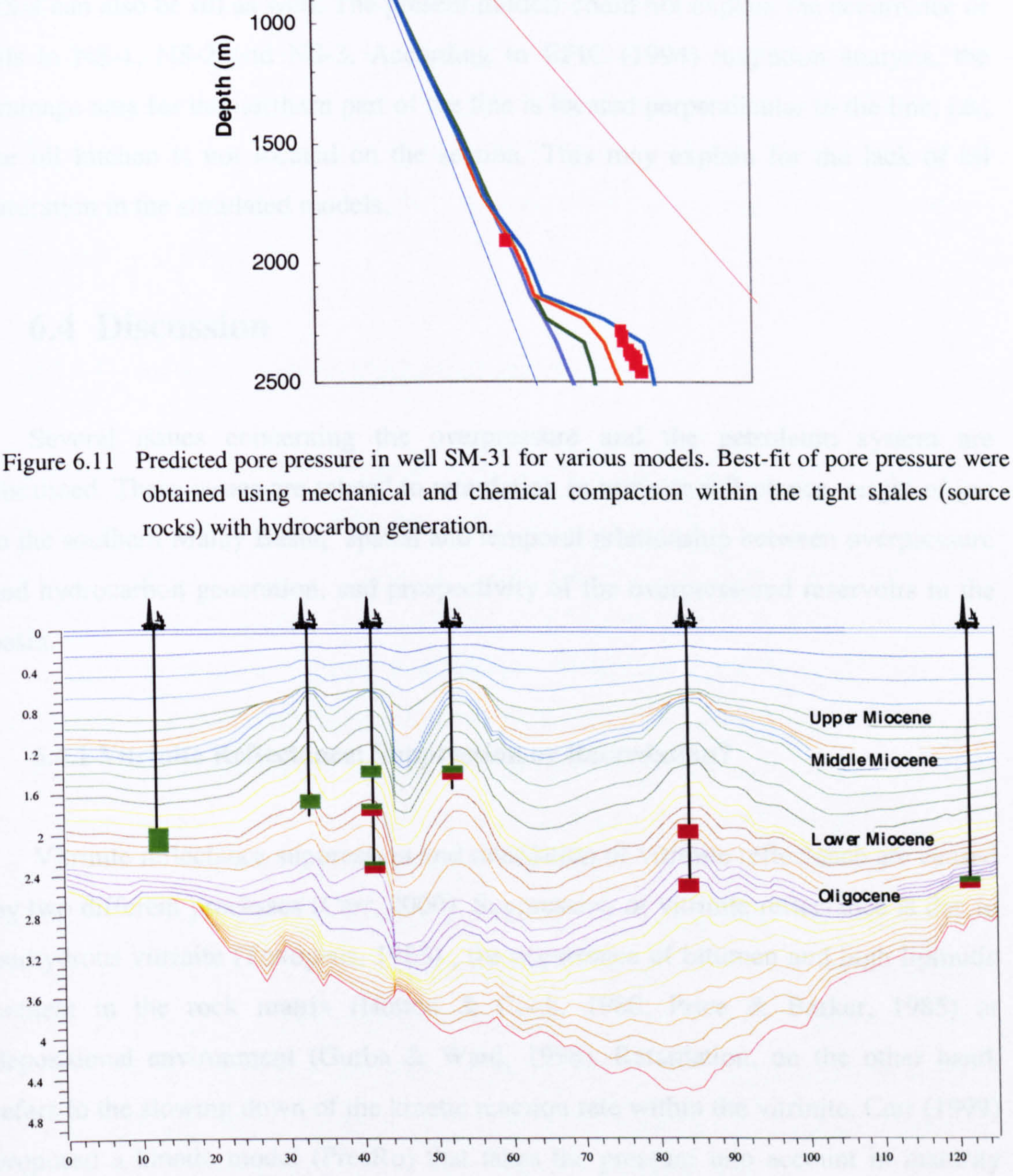


Figure 6.12 Discovered hydrocarbon pools along the modelled section. Green and red represent oil and gas zones, respectively. Wells, pseudo wells or oil/gas fields are NS-1 (km 9), NS-2 (km-33), NS-3 (km 42), NS-4 (km 53), SM-31 (km-85) and NS-5 (km 123).

gas fields are located at NS-3 and SM-31. The northern part of the section consists of predominantly oil with associated gases, while a large gas accumulation was discovered at SM-31. Comparing the results of hydrocarbon saturation on Figure 6.9 and 6.10 with Figure 6.12, predictions of gas saturation are consistent with the observed gas distribution along the section, although it is slightly deeper in NS-3 and NS-4. A model run with an increased TOC (5%) shows the shallower reservoirs in NS-4 can also be fill as well. The present models could not explain the occurrence of oils in NS-1, NS-2 and NS-3. According to EPIC (1994) migration analysis, the drainage area for the northern part of the line is located perpendicular to the line, i.e., the oil kitchen is not located on the section. This may explain for the lack of oil saturation in the simulated models.

6.4 Discussion

Several issues concerning the overpressure and the petroleum system are discussed. These issues are related to retardation in vitrinite reflectance, origin of gas in the southern Malay Basin, spatial and temporal relationship between overpressure and hydrocarbon generation, and prospectivity of the overpressured reservoirs in the basin.

6.4.1 Vitrinite Reflectance: Suppression or Retardation?

Vitrinite reflectance suppression and retardation of vitrinite reflectance are caused by two different processes (Carr, 2000). Suppression of vitrinite reflectance is due to perhydrous vitrinite (Toxopeus, 1983) , the occurrence of bitumen and high liptinitic content in the rock matrix (Hutton & Cook, 1980; Price & Barker, 1985) or depositional environment (Gurba & Ward, 1998). Retardation, on the other hand, refers to the slowing down of the kinetic reaction rate within the vitrinite. Carr (1999) proposed a kinetic model (PresRo) that takes the pressure into account in maturity calculation.

Low vitrinite reflectance readings may also be attributed to sample preparation and measurement. The problems are normally associated with measuring the vitrinite

wisps, due to their smaller size, compared to coaly fragments. Vitrinite wisps are also vulnerable to poor polishing and scratches compared to the coaly fragments.

Vitrinite reflectance data from four wells (NM-1, WM-11, SM-28 and SM-30) are plotted in Figure 6.13. Also plotted is the 'Fluorescence Alteration of Multiple Macerals' (FAMM) results determined by CSIRO (Australia). FAMM's vitrinite reflectance equivalent data are not prone to suppression problems (Wilkins et al., 1992). In well SM-28 (Figure 6.13c), where profound suppression was observed, they are not related to overpressure as seen by the onset of overpressure at the deeper part of the well. In three other wells (NM-1, WM-11 and SM-30), vitrinite reflectance above and below the onset of overpressure does not show any significant suppression or retardation in maturity.

6.4.2 Overpressure Generating Mechanisms

Model simulation using chemical compaction in the source rocks, coupled with gas generation, was able to generate overpressure of the magnitude observed in the SM-31. However, there is no reason to believe that chemical compaction should only apply to the source rocks. The sandstone (reservoirs) and other mixed lithologies could also undergo chemical compaction. Therefore, models were run with mechanical and chemical compaction for all sedimentary units in the section. The sedimentary units are simplified into two groups: shaly and sandy units. The shaly units (consisting of more than 40% shale) were assigned the chemical compaction parameters of shale (tight shale) and the sandy units (with less than 40% shale) were assigned the chemical compaction parameters of a sandstone. For shales, the activation energy was set at 20 kJ/mol with viscosity of $1x10^{24}$ Pa.s. For sandstone , the activation energy is 15 kJ/mol with viscosity of $1.3x10^{24}$ Pa.s, similar to the Garn Formation in the North Sea (Schneider and Hay, 2001). One model was also run with Groups E-I coaly source rocks to investigate whether chemical compaction and gas generated directly from the coal could generate the overpressure

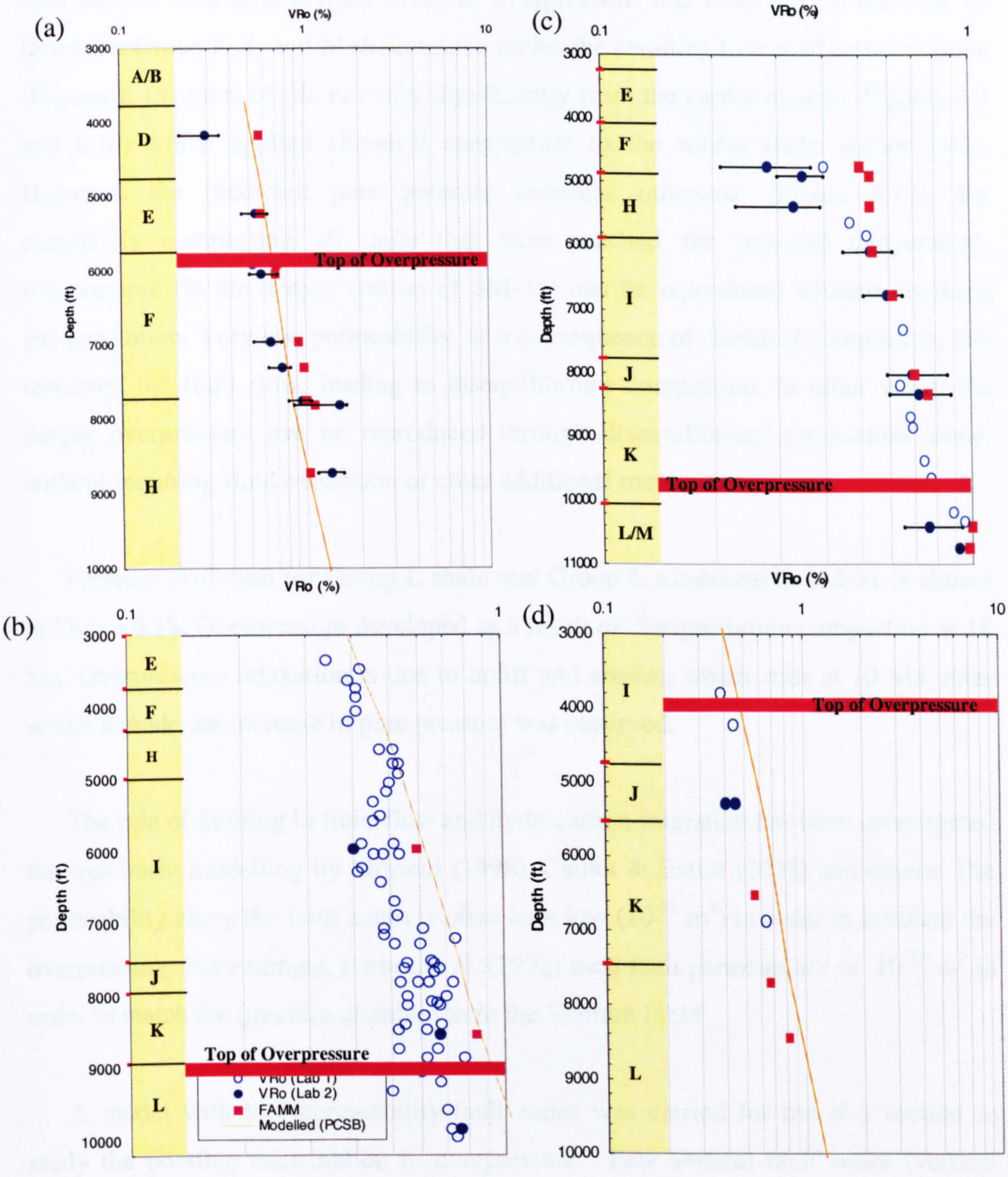


Figure 6.13 Maturity depth profiles for wells (a) NM-1, (b) WM-11, (c) SM-28 (d) SM-30.

For model run using Groups E-I coaly source rocks, the temperature has not reach the optimum level for hydrocarbon generation and chemical compaction. No hydrocarbon saturation (Figure 6.14) or overpressure was observed. In the case of lacustrine Group K, L and M shale source rocks, the resulting hydrocarbon saturations (Figures 6.15 and 6.16) do not vary significantly from the earlier models (Figures 6.9 and 6.10) which applied chemical compaction to the source rocks section only. However, the predicted pore pressure indicates otherwise (Figure 6.17). By chemically compacting all units that have reached the required temperature, overpressure (in the deeper section of SM-31) can be reproduced without invoking gas generation. Very low permeability, as a consequence of chemical compaction, has restricted the fluid flow, leading to disequilibrium compaction. In other word, the deeper overpressure can be reproduced through disequilibrium compaction alone, without requiring fluid expansion or other additional mechanisms.

Pressure evolution for Group L shale and Group L sandstone in SM-31 is shown in Figure 6.18. Overpressure developed as a result of disequilibrium compaction at 18 Ma. Overpressure relaxation is due to uplift and erosion which ends at 10 Ma, after which a moderate increase in pore pressure was observed.

The role of faulting in fluid-flow and hydrocarbon migration has been investigated through basin modelling by Morretti (1998), Caillet & Batiot (2003) and others. The permeability along the fault zones is often kept low (10^{-21} m^2) in order to simulate the overpressure. For example, Forbes et al. (1992) used fault permeability of 10^{-24} m^2 in order to match the pressure distribution in the Venture Field.

A model with low permeability fault zones was carried for the N-S section to study the possible contribution to overpressure. Few vertical fault zones (vertical columns) were included in the modelled section and these were assigned with a shale lithological parameter. The fault permeability values were then varied from 10^{-20} to 10^{-23} m^2. The modelling results indicate shallow overpressure reservoirs can be recreated through low (horizontal) permeability faults with permeability of at least 10^{-23} m^2 due to restriction of lateral flow within the basin. However, the lateral sealing provided by these faults is not sufficient to recreate the high overpressure in the deeper section (such as in SM-31) without the low permeability (vertical) sealing

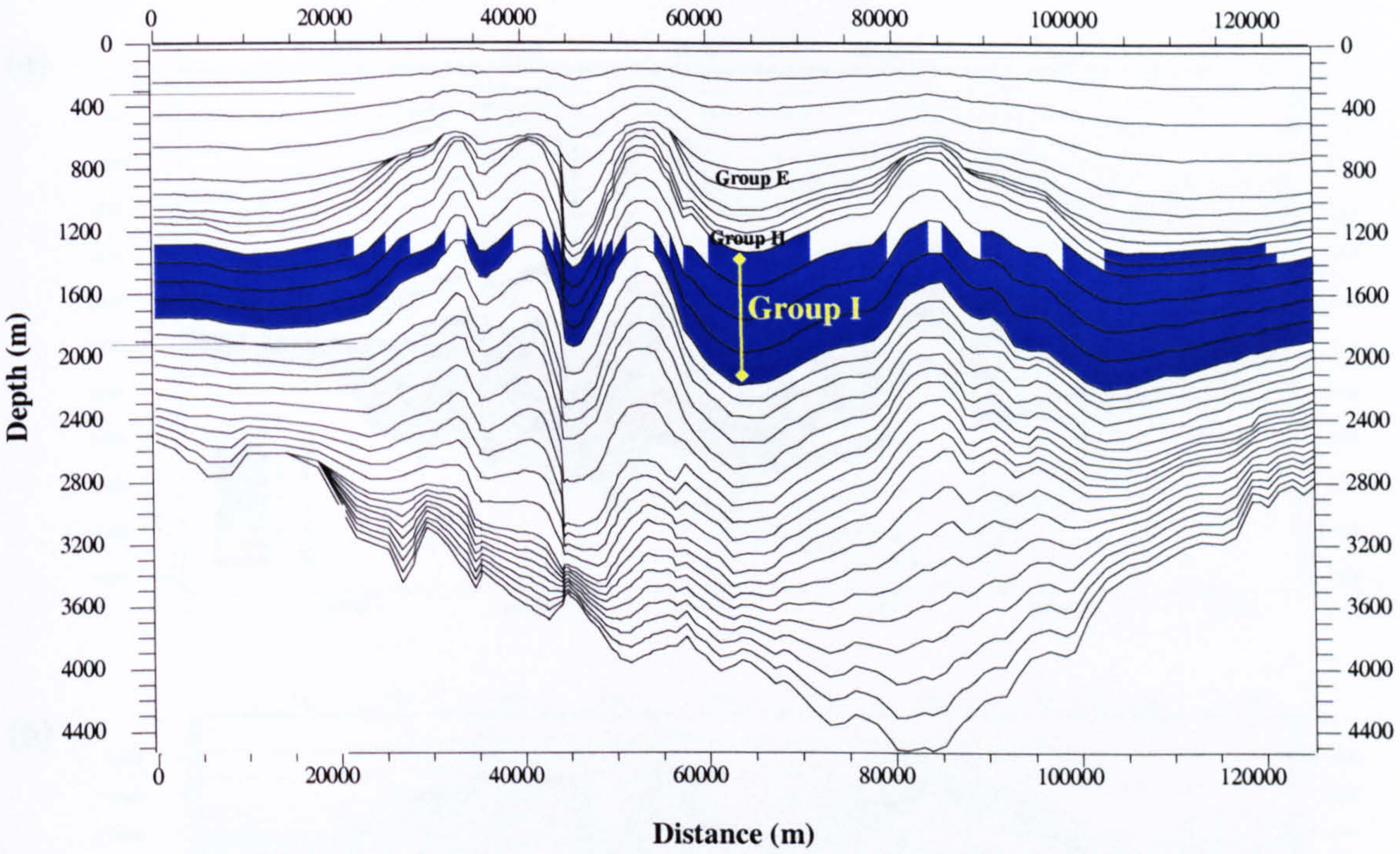


Figure 6.14 Modelled hydrocarbon saturation from Groups E, H and I coaly source rocks (Type III kerogen with TOC of 20%). No significant hydrocarbon accumulation was observed.

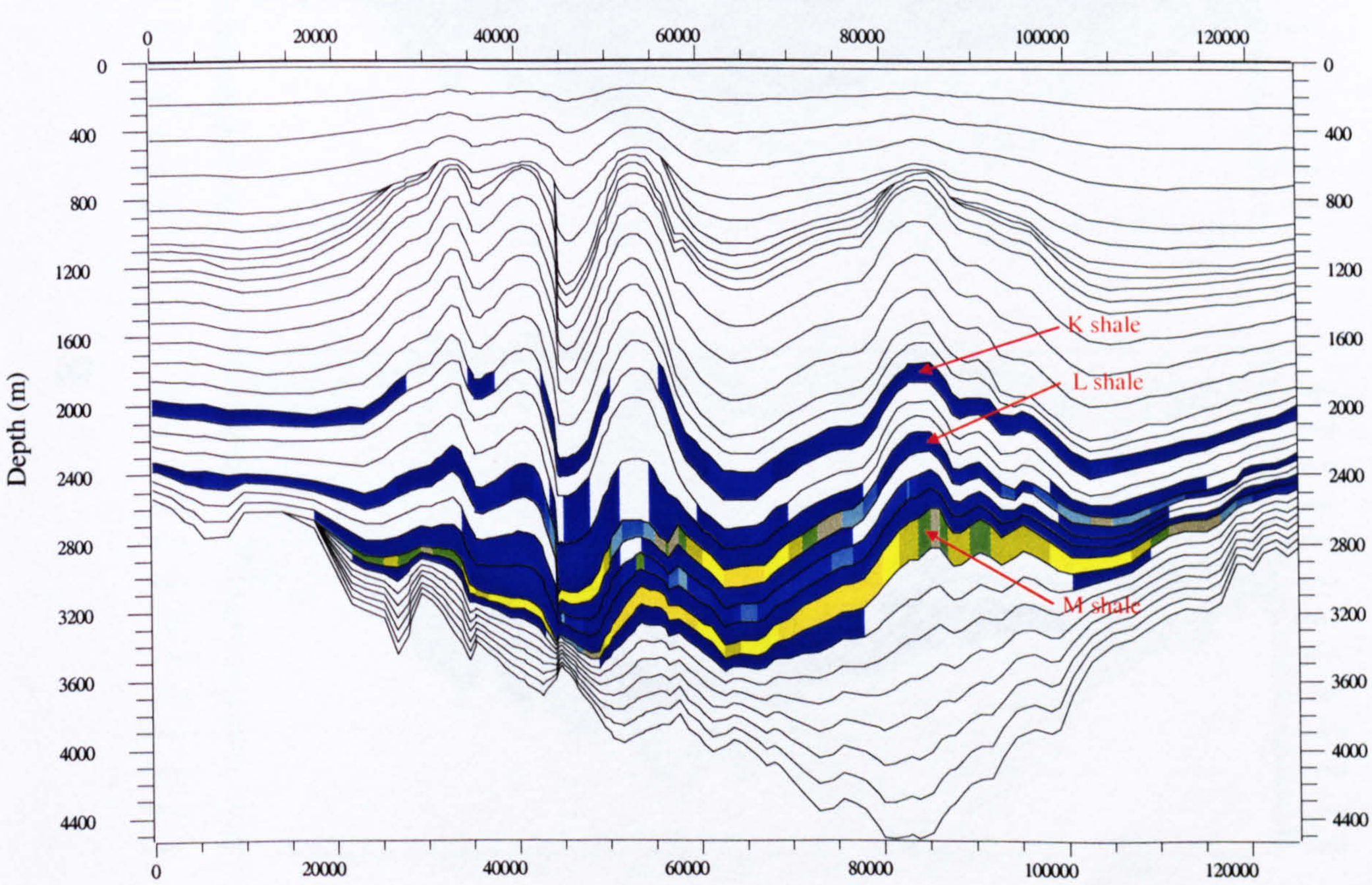


Figure 6.15 Modelled oil saturations with Group K,L and M shales as source rocks (Type I kerogen, TOC of 2%). Both mechanical and chemical compaction were applied to all lithologies, assuming two sets of chemical compaction parameters applied to sandy and shaly facies.

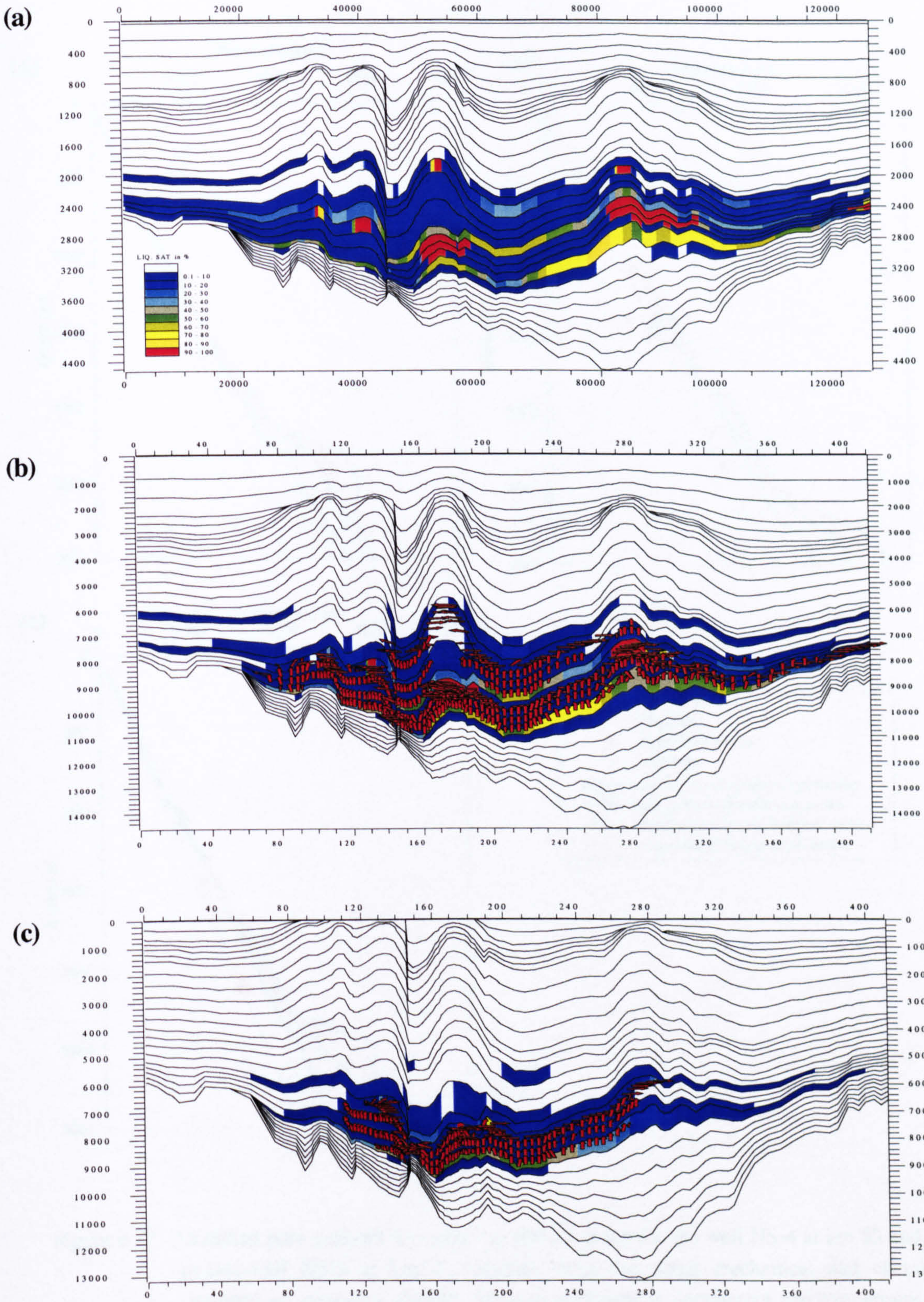


Figure 6.16 Gas saturation plots modelled at three different geological ages: (a) present-day, (b) 3 Ma and (c) 10 Ma. Arrows (red) indicate migration direction and the sizes represent the magnitude.

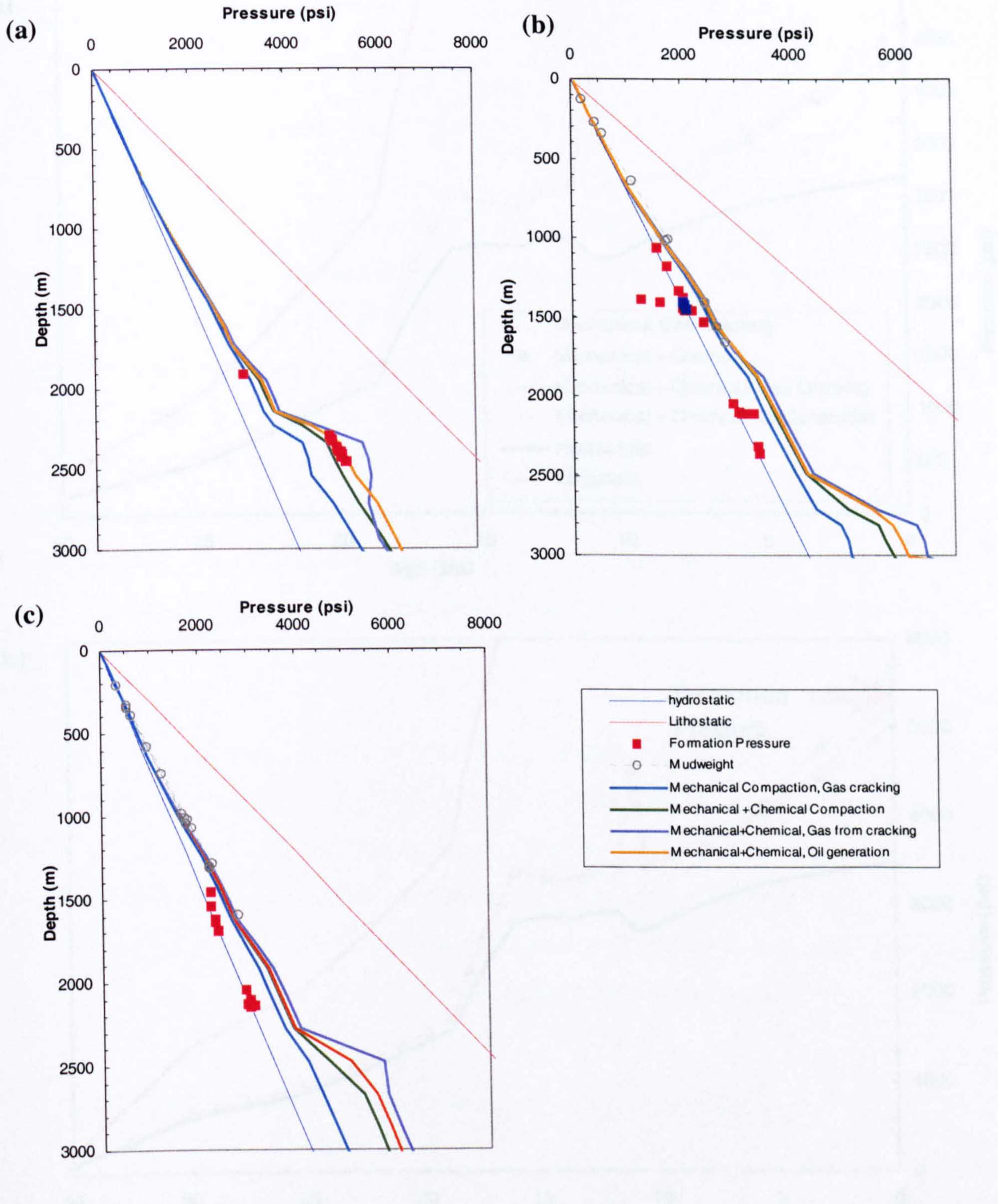


Figure 6.17 Modelled pore pressure for wells: (a) SM-31 at km 85, (b) well NS-4 at km 53 and (c) pseudo-well NS-3 at km 41. Models were run using mechanical and chemical compaction, assuming similar chemical compaction parameters for two groups of lithologies, sandy and shaly units.

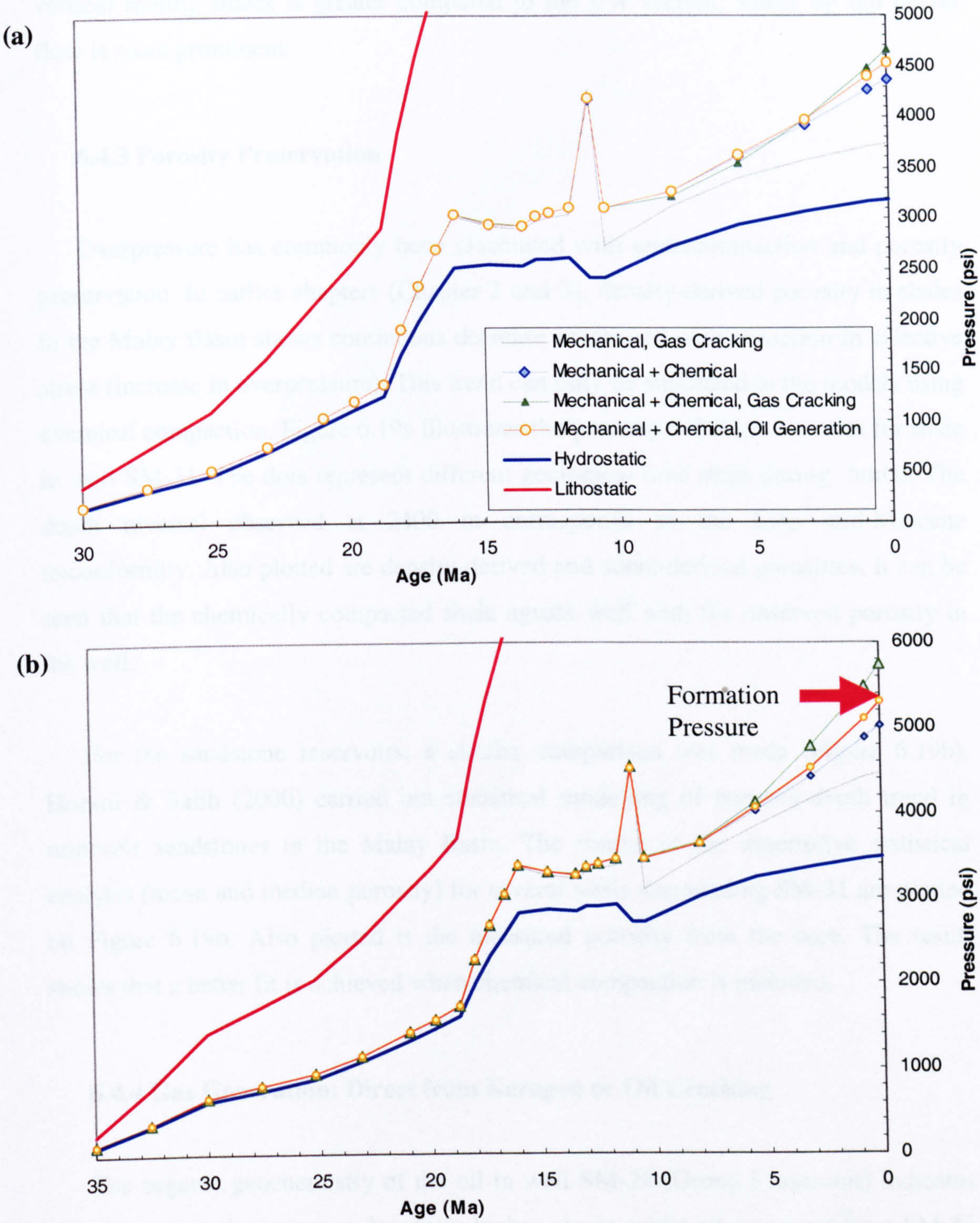


Figure 6.18 Pressure evolution in well SM-31 for the (a) Group L shale, (b) Group L reservoir.

shales (at least 10^{-22} m^2). In the basin parallel section (section NS), the impact of vertical sealing shales is greater compared to the EW section, where up dip lateral flow is more prominent.

6.4.3 Porosity Preservation

Overpressure has commonly been associated with undercompaction and porosity preservation. In earlier chapters (Chapter 2 and 3), density-derived porosity in shales in the Malay Basin shows continuous decrease associated with reduction in effective stress (increase in overpressure). This trend can only be simulated in the models using chemical compaction. Figure 6.19a illustrates the porosity reduction histories for shale in well SM-31. The dots represent different geological time steps during burial. The depth reversal observed at 2400 m corresponds to the Late mid-Miocene unconformity. Also plotted are density-derived and sonic-derived porosities. It can be seen that the chemically compacted shale agrees well with the observed porosity in the well.

For the sandstone reservoirs, a similar comparison was made (Figure 6.19b). Hoesni & Salih (2000) carried out statistical modelling of porosity-depth trend in reservoir sandstones in the Malay Basin. The results of the descriptive statistical analysis (mean and median porosity) for several wells surrounding SM-31 are plotted on Figure 6.19b. Also plotted is the measured porosity from the core. The result shows that a better fit is achieved when chemical compaction is included.

6.4.4 Gas Generation: Direct from Kerogen or Oil Cracking

The organic geochemistry of the oil in well SM-28 (Group I reservoir) indicates that kerogen in the source rock is from higher-plants, while oil recovered from SM-30 well (Group K reservoir) has been shown to be derived from lacustrine organic matter (McCaffrey et al., 1998). Main question now is the origin of the large gas deposits (examples in SM-29 and SM-31) in the southern part of the Malay Basin. Are these gases derived from coaly (Type III) kerogen or lacustrine source rocks? The implication of the former is that a significant part of the Group I coaly source rocks

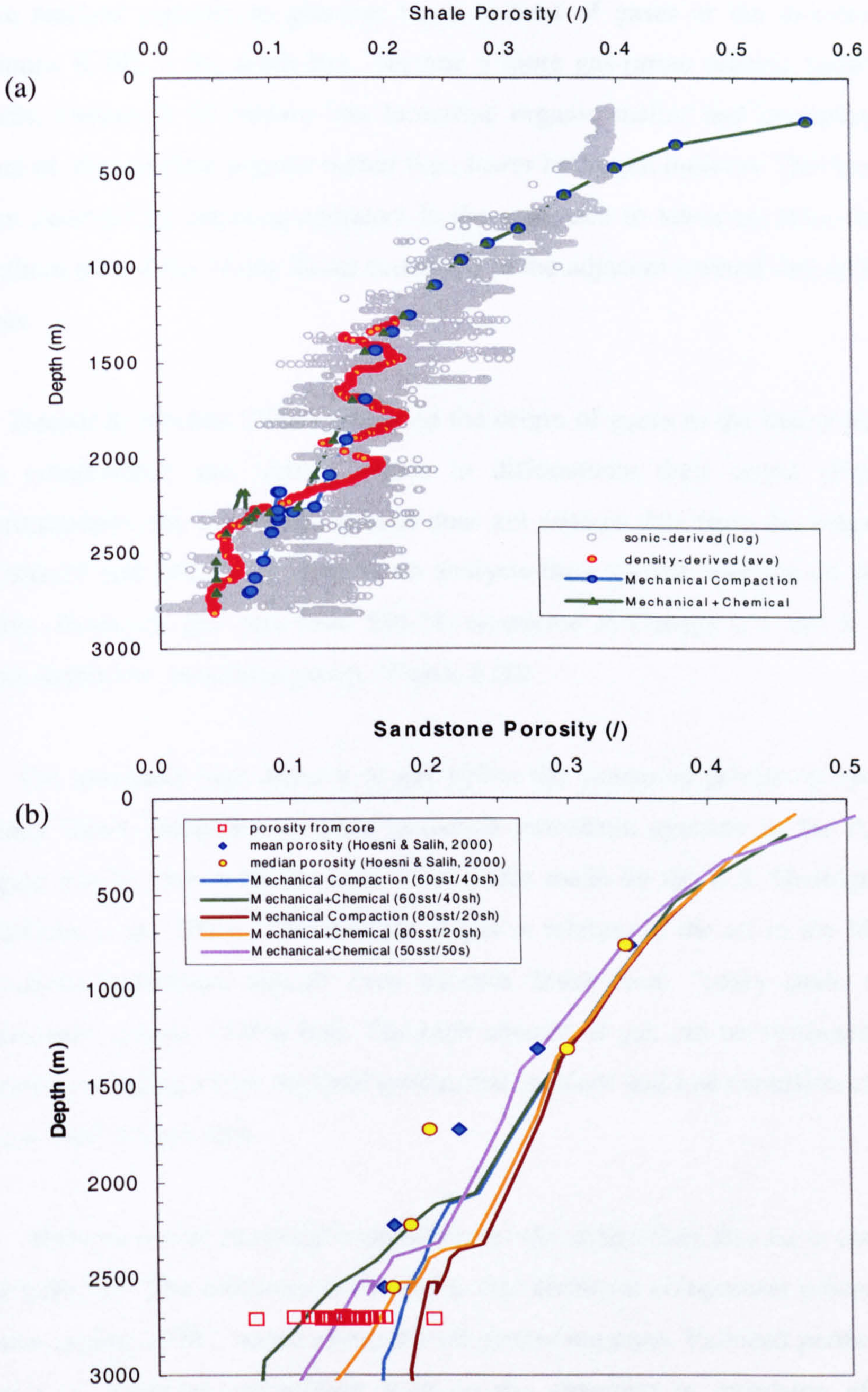


Figure 6.19 Modelled porosity evolution for (a) shale and (b) sandy units in SM-31, with and without chemical compaction.

have reached maturity to generate large amount of gases or the lacustrine system (Groups K-M) in the south has become a more gas-prone organic facies. In other words, Groups K-M contain less lacustrine organic matter and increasingly higher input of higher-plant organic matter (i.e., lower hydrogen indices). This has generally been assumed by previous operators in the area, due to lower oil discoveries in the southern part of the Malay Basin compared to the adjacent (central and south-eastern) areas.

Hoesni & Abolins (2000) discussed the origin of gases in the Malay Basin, using gas composition and isotope values to differentiate their origin (Figure 6.20). Unfortunately, the interpreted dataset does not contain data from the major gasfields of SM-29 and SM-31, as there is no analysis done by the operator on the relevant fields. However, gas data from SM-28, recovered in Groups I, J and K reservoirs, plots within the lacustrine group. (Figure 6.20).

The unusually high amount of gas within the lacustrine petroleum system in the Malay Basin compared to other lacustrine petroleum systems in the Asia Pacific region can be shown by the reserve estimates made by the U.S. Geological Survey (McCabe et al., 2000). The amount of gas in relation to the oil in the Malay Basin lacustrine petroleum system even exceeds those from "coaly shale and coals" petroleum systems (Table 6.6). The high amount of gas can be attributed to several factors, including a high regional geothermal gradient and low expulsion efficiency of a low TOC source rock.

The process of chemical compaction on the shales may also have contributed to the high gas. The explanation for this is that chemical compaction processes, which starts around 110°C, occur within the oil generation zone. Reduced permeability as a result of chemical compaction leads to the reduction in expulsion efficiency or secondary migration, causing the oil to be trapped within the source rocks or in the adjacent sandstones (Figure 6.21). Upon further burial and exposure to higher temperature, these trapped oils were then cracked to gas. Due to high mobility of the gas, migration is possible compared to the oil phase. The chemically compacted shale also helps in reducing vertical migration within the kitchen areas, directing the gas towards the basin flank, and possibly flushing existing hydrocarbons. A model was

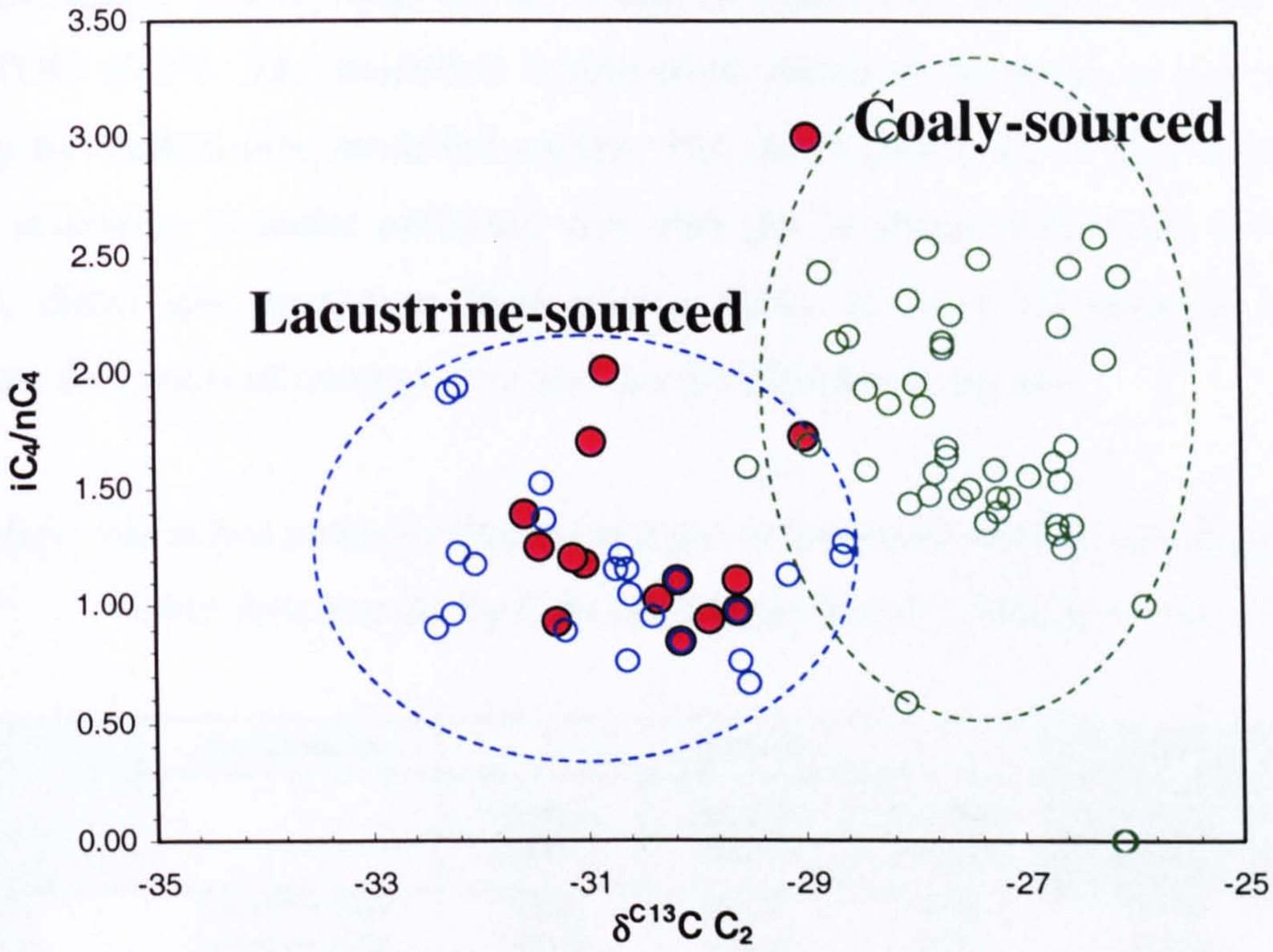


Figure 6.20 Plot of iC_4/nC_4 and $\delta^{13}C$ C_2 to distinguish origin of gases in the Malay Basin. The plot is used to distinguish the origin of gases in the Malay Basin (Hoesni and Abolins, 2000). Open circles (blue & green) are taken from various fields in the basin. The closed circles (red) are gas samples from well SM-28 and SM-30. No data are available from well SM-31.

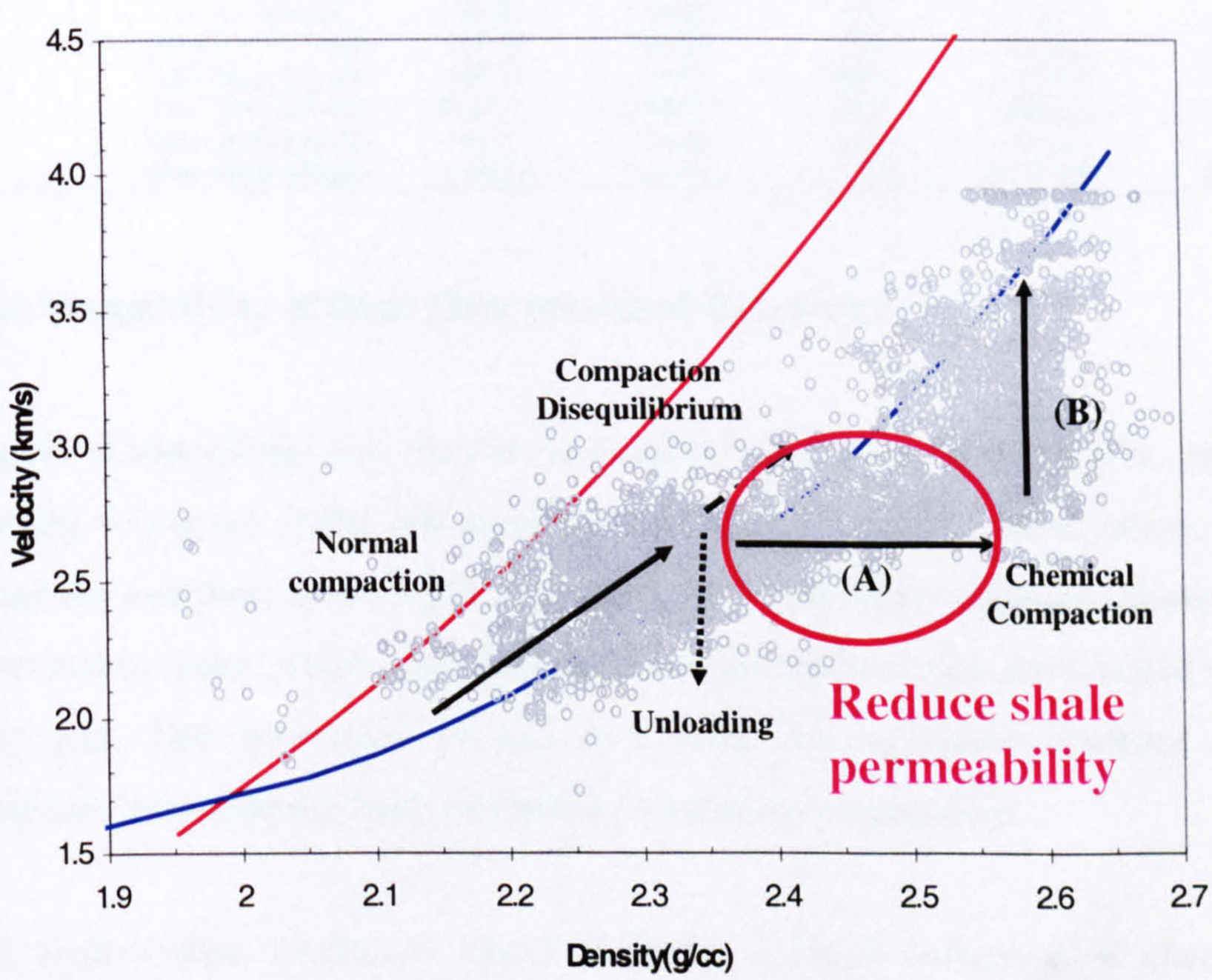


Figure 6.21 Velocity-density crossplots of SM-31 showing chemical compaction signature. Chemical compaction begins at temperature of around 110°C with the deviation from the normal compaction trend. This caused a drastic reduction in permeability. Gardner's and Bower's relationship for shales are shown in red and blue lines, respectively. A and B represent sequential infilling of pore spaces in the shales.

TEXT BOUND INTO

THE SPINE

run with similar source rocks for K, L and M shales but having a kerogen Type III with TOC of 5%. The modelled hydrocarbon phase is assigned as gas of similar density to cracked oils, modelled earlier. The result shows the overpressure with in the L reservoirs is under predicted and also gas is absent within the K reservoir. Hence, direct gas generation from source rocks of Type III kerogen could not replicate the observed overpressure and gas distribution in the area.

Table 6.6 Estimated undiscovered oil and gas resources in several petroleum systems within Asia Pacific by U.S. Geological Survey (McCabe et al., 2000)

Petroleum System Units	Source Rocks	OilField			Gasfield		
		Oil Mean (MMBO)	Gas Mean (MMBO)	NGL Mean (MMBO)	Gas Mean (MMBO)	NGL Mean (MMBO)	Gas/Oil (Oilfield)
North Malay Lacustrine (Oli-Mio)	Lacustrine shale	123.62	594.07	8.33	1167.71	23.32	4.81
South Malay Lacustrine (Oli-Mio)	Lacustrine shale	1002.98	4810.82	67.27	17123.84	342.64	4.80
NW Java Jatibarang/Talang Akar	Lacustrine shale	195.47	391.3	23.5	6187.72	65.5	2.00
S Sumatra Lahat/Talang Akar	Lacustrine shale	468.82	938.49	56.32	17311.77	182.81	2.00
N Sumatra Bampo	Lacustrine shale	111.71	223.34	13.4	8894.01	93.75	2.00
Junggar U Paleozoic	Lacustrine shale	467.25	346.41	20.77	0	0	0.74
Central Sumatra Brown Sh-Sihapas	Lacustrine shale	899.4	539	12.92	3539.18	70.84	0.60
Bohaiwan Tert Lacustrine	Lacustrine shale	2268.01	1135.03	68.17	3503.9	154.66	0.50
Songliao Qingshankou - anticline trap	Lacustrine shale	291.07	96.42	5.79	608.87	26.81	0.33
Songliao Qingshankou - subtle trap	Lacustrine shale	735.2	243.15	14.57	1545.52	68.08	0.33
Ordos Yanchang-Yanan	Lacustrine shale	138.33	19.99	1.2	0	0	0.14
Malay Miocene Coaly	Coaly Shale & Coals	101.23	485.98	6.8	3282.24	65.63	4.80
Balingian Sarawak	Coaly Shale & Coals	529.49	1163.1	69.87	1054.3	46.33	2.20
Baram Delta (Brunei-Sabah)	Coaly Shale & Coals	2137.41	5988.52	359.28	9988.39	439.51	2.80
Junggar Jurassic Coal	Coaly Shale & Coals	96.15	48.05	2.88	901.7	39.7	0.50
Kutei Basin Deltaics	Coaly Shale & Coals	1258.03	3513.65	210.62	32243.05	806.35	2.79

6.4.6 Prospectivity of Deep Overpressured Reservoirs

Results of modelling show that in the southern part of the Malay Basin, chemical compaction within the shales has significantly reduced the shale permeability, which enhanced the overpressure at depth. Reduction of permeability impedes oil expulsion from the source rocks, which upon increased burial (temperature), are cracked to high maturity gas. The generation of gas as a result of secondary cracking of the hydrocarbons subsequently leads to further increase in overpressure.

The hydrocarbon migration model indicates a major influence of chemically compacted shale in enhancing lateral migration. The vertical buoyancy-driven migration is limited by these tight shales, hence limiting the cross-stratal migration of the lacustrine-sourced hydrocarbons. This results in multiple petroleum systems

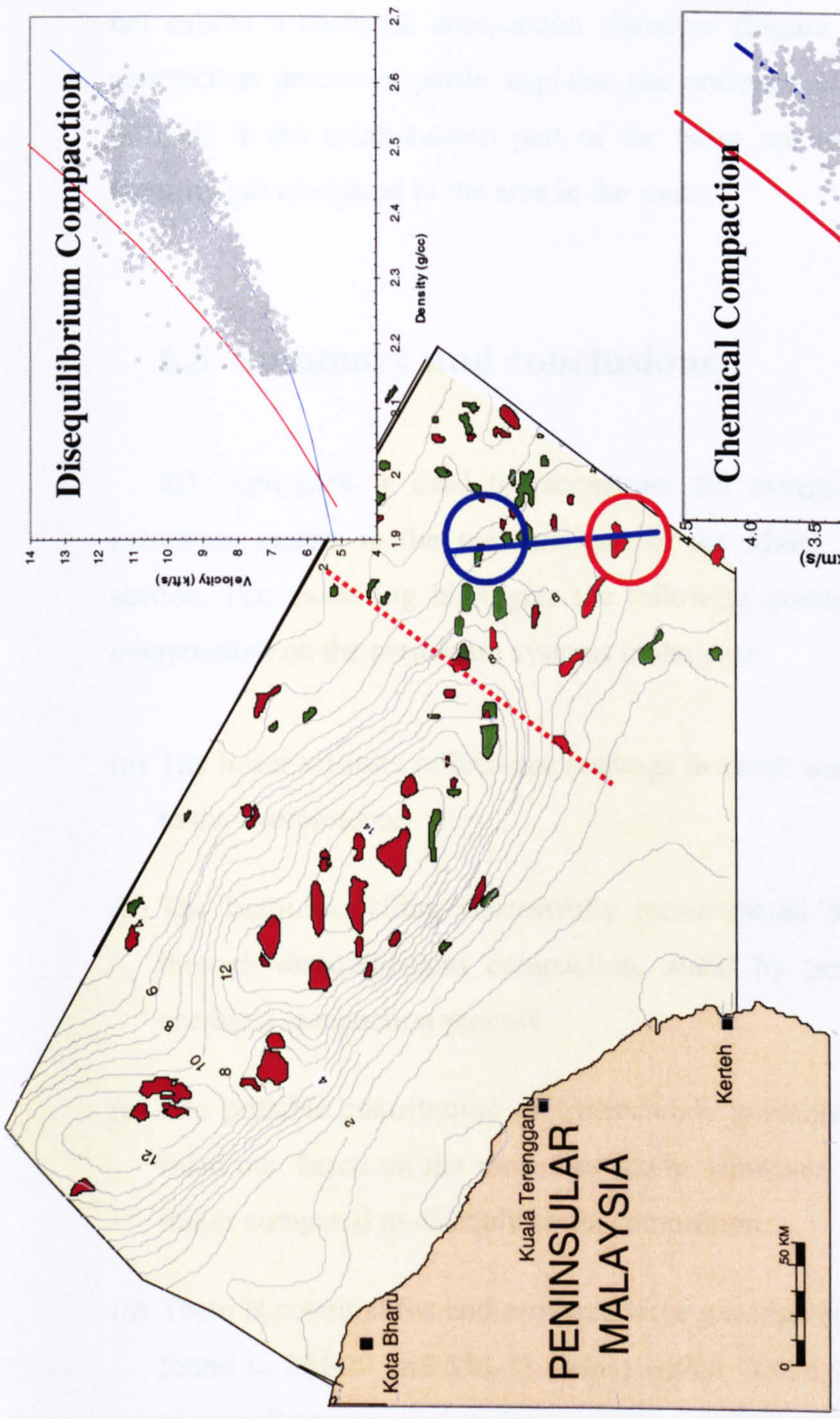


Figure 6.22 Comparing velocity-density crossplots of two wells located at different end of the modelled section. The well on the northern end of the line do not exhibit chemical compaction signature.

confined between the thick shales (e.g., K shale). The potential existence of significant gas accumulations, similar to those in SM-30 and SM-31, are more likely considering the increased effectiveness of the shales to act as top seal after undergoing chemical compaction. In the south-eastern part of the basin, the shales do not exhibit a chemical compaction signature (Figure 6.22). The lack of chemical compaction processes partly explains the presence of oilfields in the area. These oilfields in the south-eastern part of the basin are less prone to flushing of high maturity gas compared to the area in the south.

6.5 Summary and conclusions

2D Temispack is used to reconstruct the overpressure history and study the petroleum system in the southern part of the Malay Basin, along a 125-km long section. The modelling highlights the following points concerning the influence of overpressure on the petroleum systems in the area:

(a) The lower vitrinite reflectance readings in some wells in the basin are not related to the overpressure.

(b) The basin modelling successfully reconstructed the overpressure in the basin through disequilibrium compaction, aided by permeability reduction through chemical compaction process.

(c) The possible contribution of hydrocarbon generation to overpressure cannot be ruled out, based on the modelling study. However, its contribution appears to be minor compared to disequilibrium compaction.

(d) There is potential for undiscovered large gas resources (which are similar to those found in SM-29 and SM-31 fields) within Group K and L reservoirs, sealed by chemically compacted shales.

Chapter 7:

Synthesis and Discussion

7.1 Global Comparisons

In this chapter the velocity-density crossplot and the origin of overpressure in some overpressured sedimentary basins is examined from published data sources. This chapter begins with a brief review of the geological setting of each basin, followed by analysis of the velocity-density crossplot. The objectives of this investigation are (1) to test whether the velocity-density plots used in the Malay Basin are also applicable in distinguishing the origin of overpressure in the other basins, (2) to determine whether the chemical compaction process in the Malay Basin shales is also occurring in other basins or whether it is a basin-specific process for the Malay Basin.

7.1.1 Sources of Data and Methodology

Two essential data elements are required for this analysis: i.e. sonic and density logs. Unfortunately, these logs are not always published within the articles itself. Other supporting data are the pressure data, temperature data and gamma-ray logs.

Sonic and density logs were first digitized and later smoothed using a moving average with filter size of 120 m. Where available, data are first screened using the gamma-ray log to select the shales only. Velocity-density plots are then made for interpretation. One exception is the Halten Terrace area (Skar et al., 1998), where the maximum and minimum limit of the data were first digitized. Mid-points between these maximum and minimum were then selected and plotted on the velocity-density plot.

7.1.2 Selected Areas

Data from four basins were examined (Figure 7.1). They are listed in Table 7.1, together with the source reference of the data.

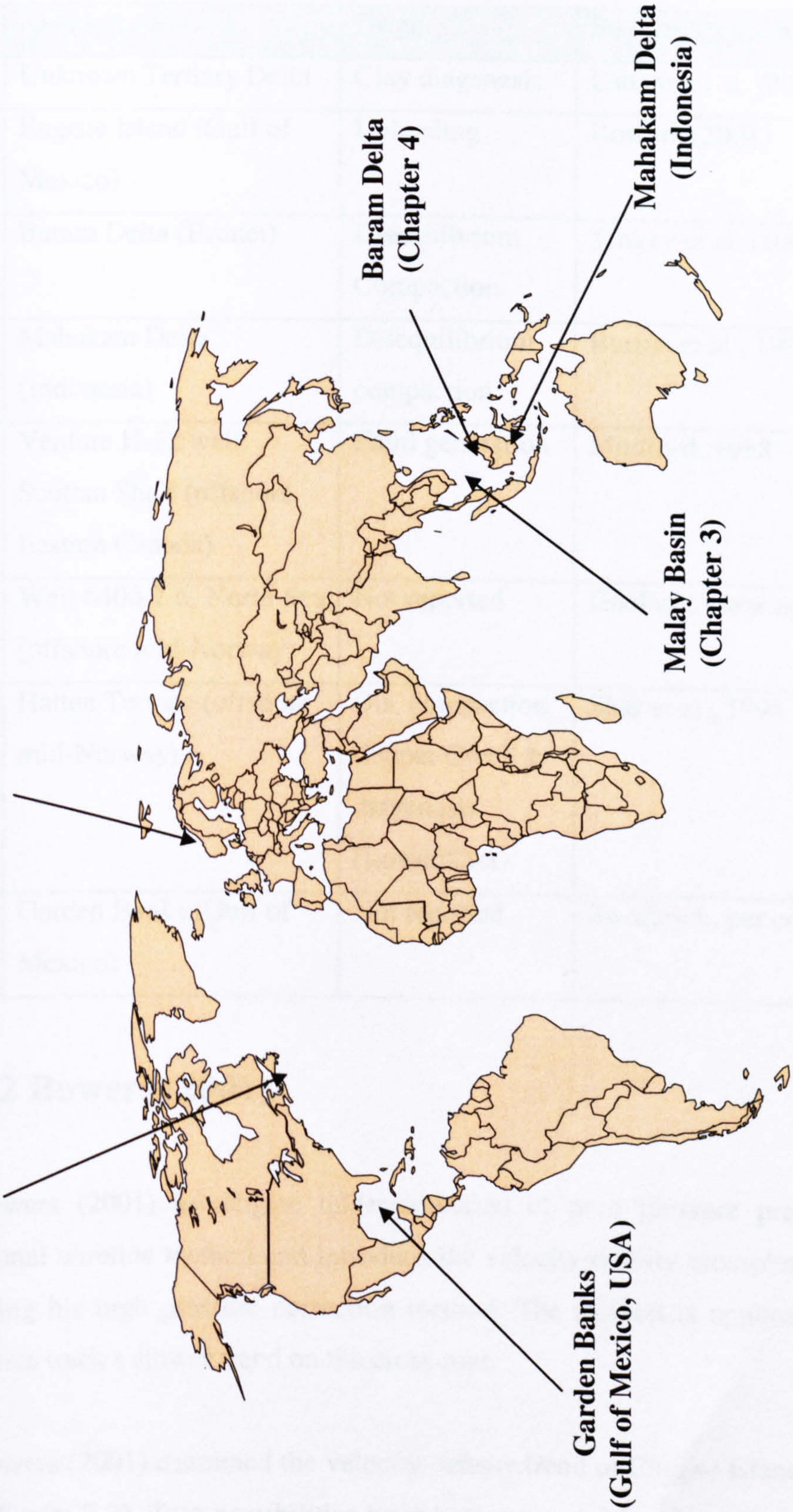


Figure 7.1 Location of the selected examples of overpressured basins.

Table 7.1 Location of the selected overpressured basins discussed in this chapter.

No.	Area Location	Origin	Sources/Reference
1.	Unknown Tertiary Delta	Clay diagenesis	Lahann et al. (2001)
2.	Eugene Island (Gulf of Mexico)	Unloading	Bowers (2001)
3.	Baram Delta (Brunei)	Diseqilibrium Compaction	Tingay et al. (2000)
4	Mahakam Delta (Indonesia)	Disequilibrium compaction	Burrus et al., 1993 – Figure 2
5.	Venture H-22 well, Scotian Shelf (offshore Eastern Canada)	Fluid generation	Mudford, 1988 – Figure 3
6.	Well 6406/2-6, North Sea (offshore mid-Norway)	Not reported	GeoPop; www.npd.no
7.	Halten Terrace (offshore mid-Norway)	Dis. compaction (Upper Cret.) & diagenesis (Lower Cret)	Skar et al., 1998 – Figures 1, 2
6.	Garden Banks (Gulf of Mexico)	Not reported	Swarbrick, per comm

7.2 Bowers (2001)

Bowers (2001) investigate underestimation of pore pressure prediction using traditional wireline method and introduce the velocity-density crossplots as indicator for using his high pressure correction method. The method is applicable when the velocities track a slower trend on the cross-plot.

Bowers (2001) examined the velocity-density trend of Eugene Island 330-A20S/T well (Figure 7.2). Two possibilities have been proposed for the observed reversal in the velocity-density trend (A to C). One suggestion was that point A to C represents various stages of unloading. The second option is related to changes in the lithology

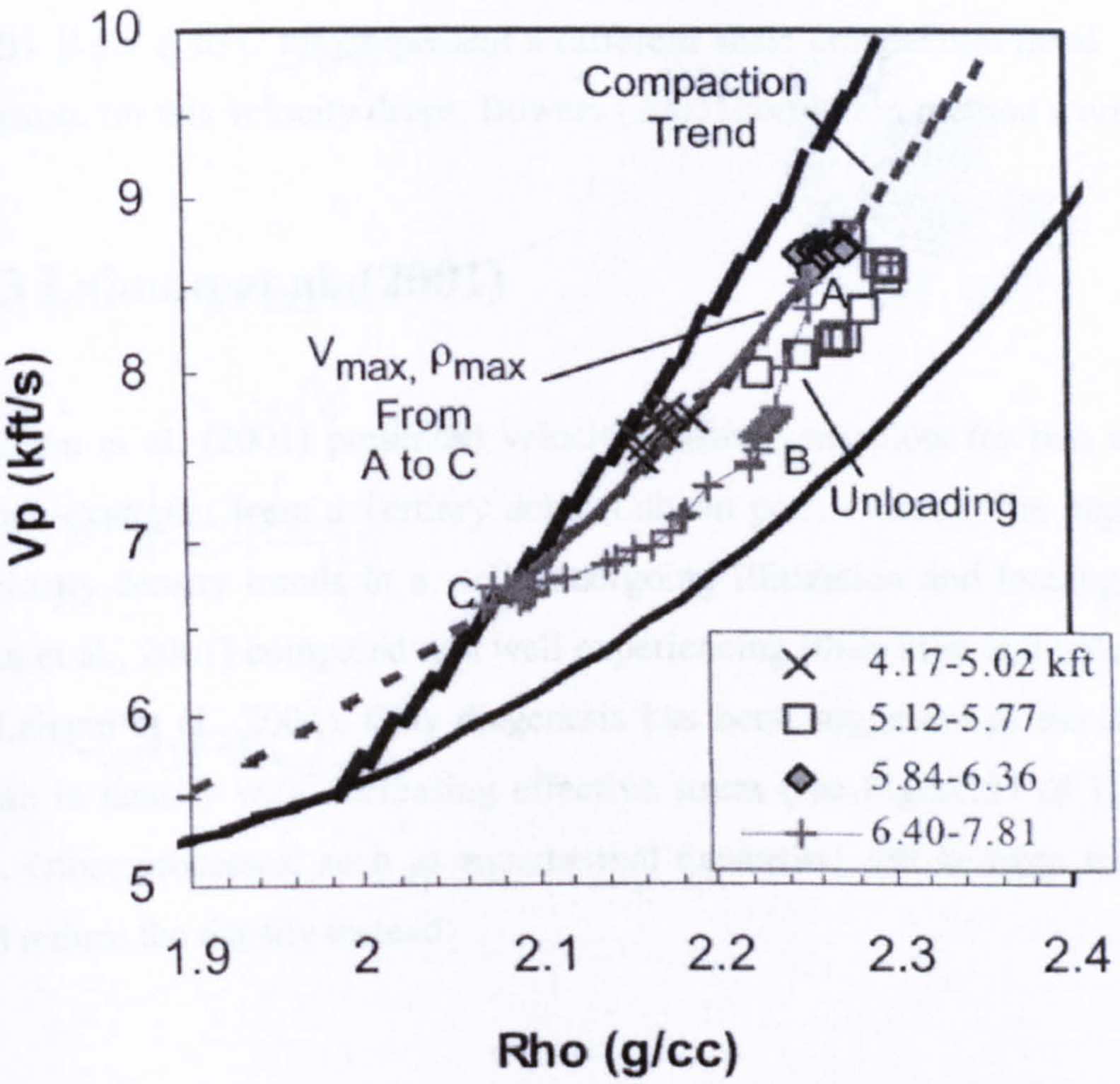


Figure 7.2 Velocity-density crossplots for well EI 330-20AS/T, taken from Bowers (2001)

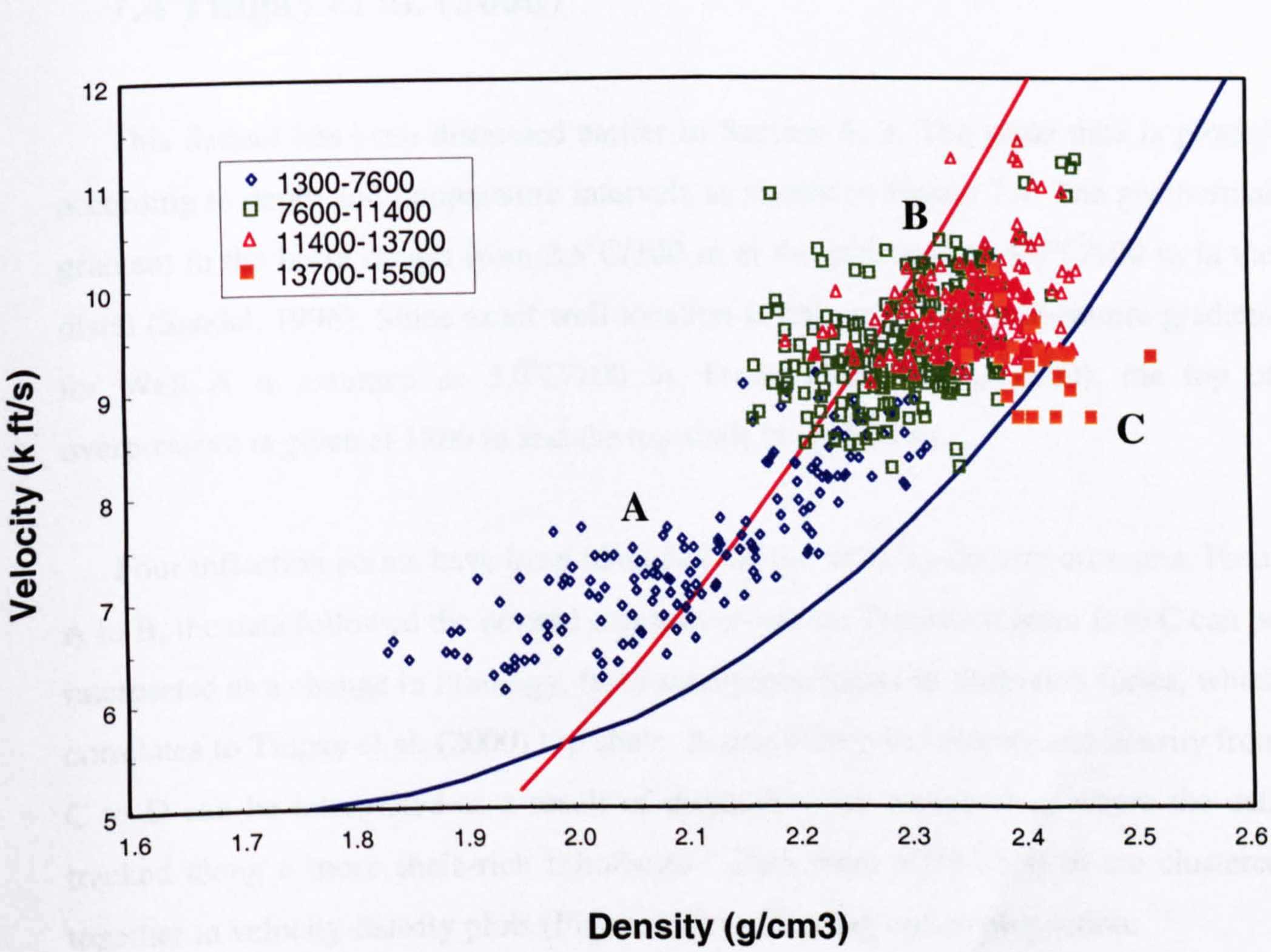


Figure 7.3 Velocity-density crossplots for Well B in Lahann et al. (2001), showing illlitization and unloading trend. Data are grouped in depth intervals (feets).

(A to B). Point B to C may represent a different shale compaction trend. Regardless of the cause for this velocity drops, Bowers (2001) correction method works.

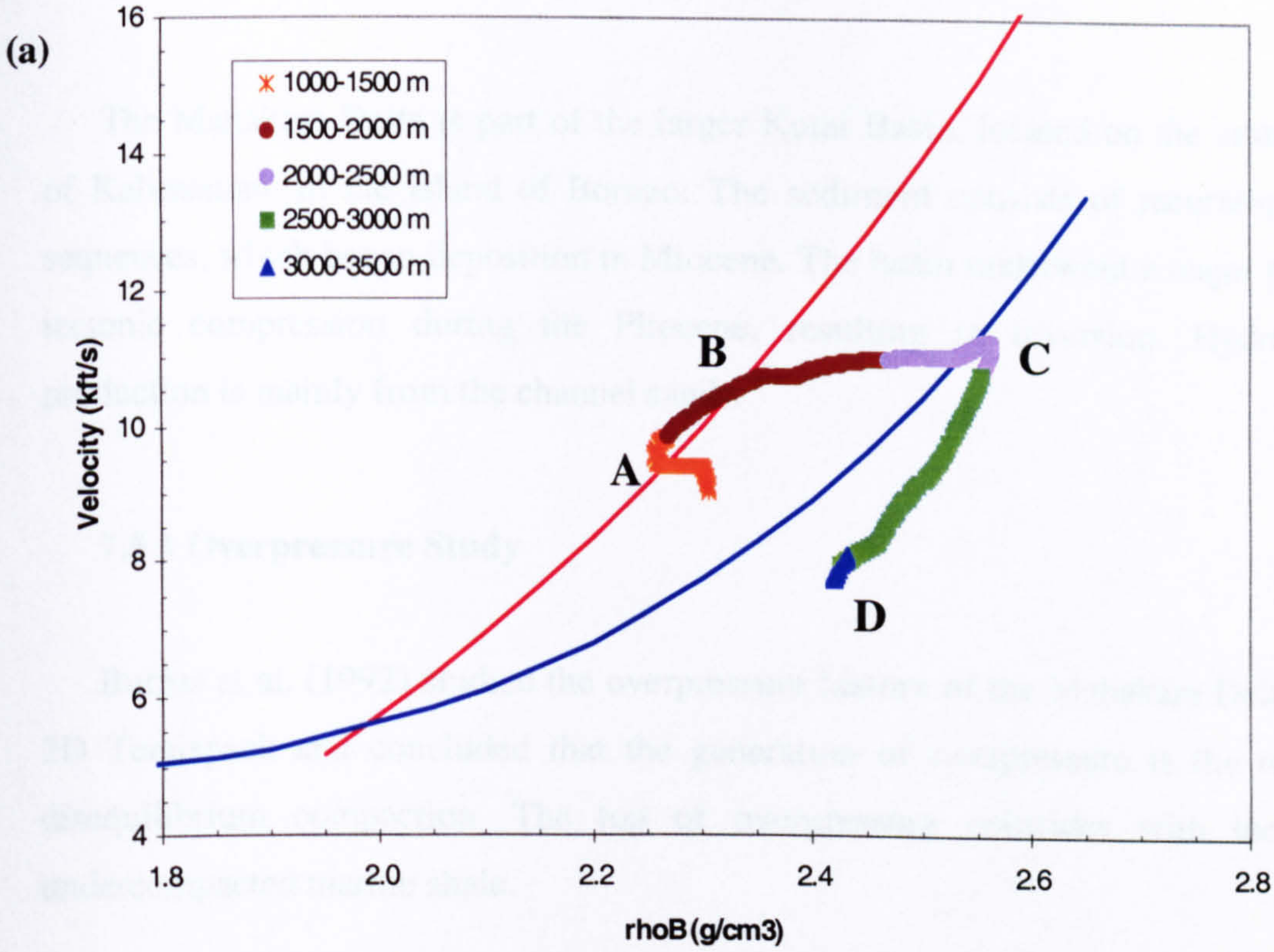
7.3 Lahann et al. (2001)

Lahann et al. (2001) presented velocity-density crossplots for two wells. These wells are examples from a Tertiary delta (Lahann pers. comm). The paper discusses the velocity-density trends in a well undergoing illitization and loading (Well A in Lahann et al., 2001) compared to a well experiencing illitization and unloading (Well B in Lahann et al., 2001). Clay diagenesis has been suggested as the cause for the increase in density with decreasing effective stress (see Figure 11 of Lahann et al., 2001). Other processes, such as aquathermal expansion and kerogen transformation would reduce the density instead.

7.4 Tingay et al. (2000)

This dataset has been discussed earlier in Section 4. 3. The same data is plotted according to depth and temperature intervals as shown in Figure 7.4. The geothermal gradient in the basin ranges from 2.5°C/100 m at the proximal to 4.0°C/100 m in the distal (Sandal, 1996). Since exact well location is unknown, the temperature gradient for Well A is assumed as 3.0°C/100 m. From Tingay et al.(2000), the top of overpressure is given at 1800 m and the top shale is at 2000 m.

Four inflection points have been identified on the velocity-density crossplot. From A to B, the data followed the normal compaction curve. Transition from B to C can be interpreted as a change in lithology, from sand-prone facies to shale-rich facies, which correlates to Tingay et al. (2000) top shale. A major drop in velocity and density from C to D can be interpreted as a result of disequilibrium compaction, where the data tracked along a more shale-rich lithofacies. Data from 3000-3500 m are clustered together in velocity-density plots (Figure 7.4b) indicating undercompaction.



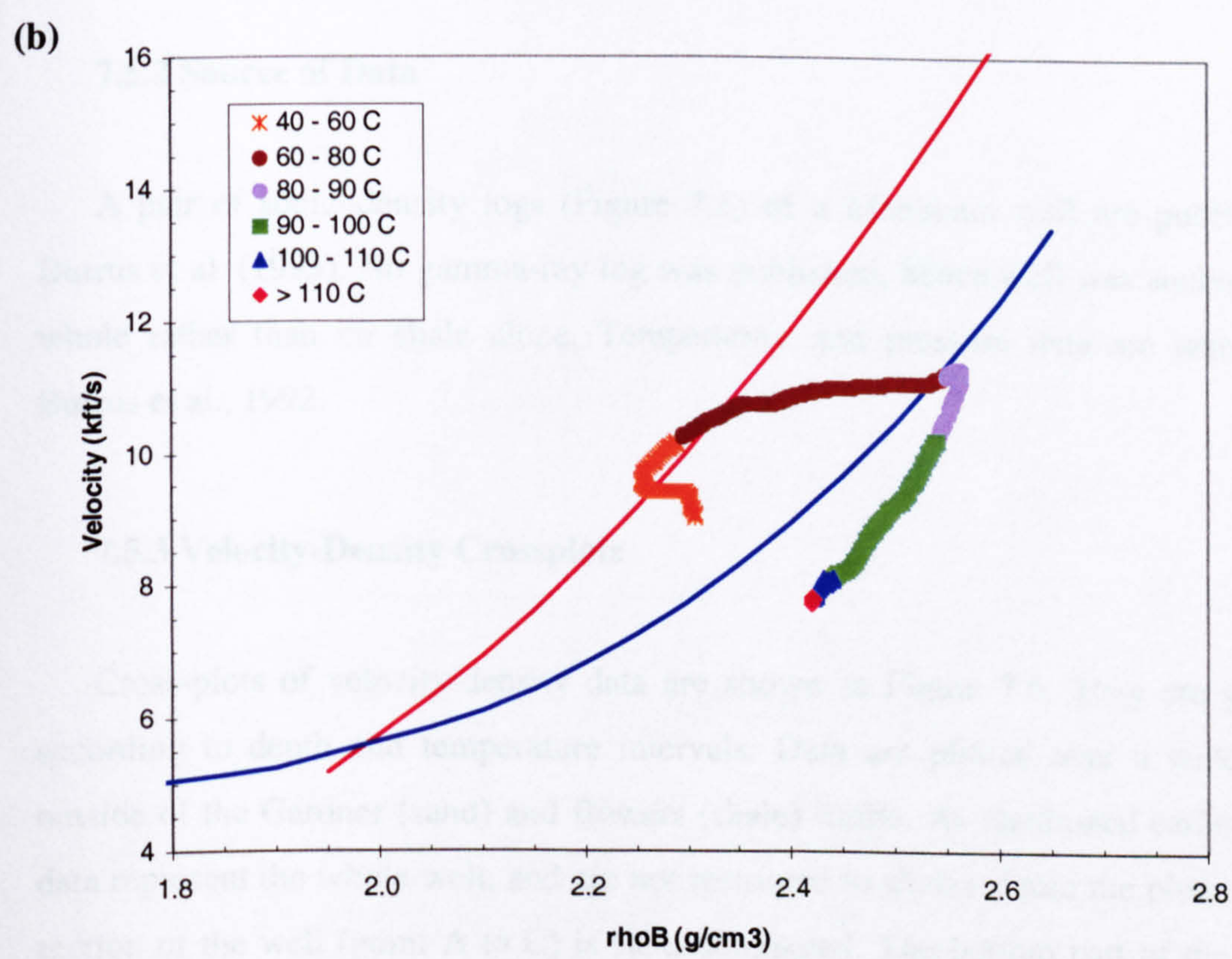


Figure 7.4 Velocity-density crossplots for Well A, Baram Delta, Brunei (data from Tingay et al., 2000). Data are grouped as: (a) depth intervals, (b) temperature intervals.

7.5 Mahakam Delta (Indonesia)

The Mahakam Delta is part of the larger Kutai Basin, located on the eastern part of Kalimantan, in the island of Borneo. The sediment consists of recurrent deltaic sequences, which began deposition in Miocene. The basin underwent a major phase of tectonic compression during the Pliocene, resulting in inversion. Hydrocarbon production is mainly from the channel sands.

7.5.1 Overpressure Study

Burrus et al. (1992) studied the overpressure history of the Mahakam Delta using 2D Temispack and concluded that the generation of overpressure is the result of disequilibrium compaction. The top of overpressure coincides with the thick, undercompacted marine shale.

7.5.2 Source of Data

A pair of sonic–density logs (Figure 7.5) of a Mahakam well are published in Burrus et al. (1993). No gamma-ray log was published, hence well was analysed as a whole rather than on shale alone. Temperature and pressure data are taken from Burrus et al., 1992.

7.5.3 Velocity-Density Crossplots

Cross-plots of velocity-density data are shown in Figure 7.6. They are grouped according to depth and temperature intervals. Data are plotted over a wide-range, outside of the Gardner (sand) and Bowers (shale) limits. As mentioned earlier, these data represent the whole well, and are not restricted to shales. From the plots, the top section of the well (point A to C) is sand-dominated. The bottom part of the well is shale-dominated (point D-E). The density log (Figure 7.5) shows a coarsening upward sequence for the top 2.5 km. Point B represent base of this coarsening upward sequence. Point C to D is interpreted as to represent a major facies change,

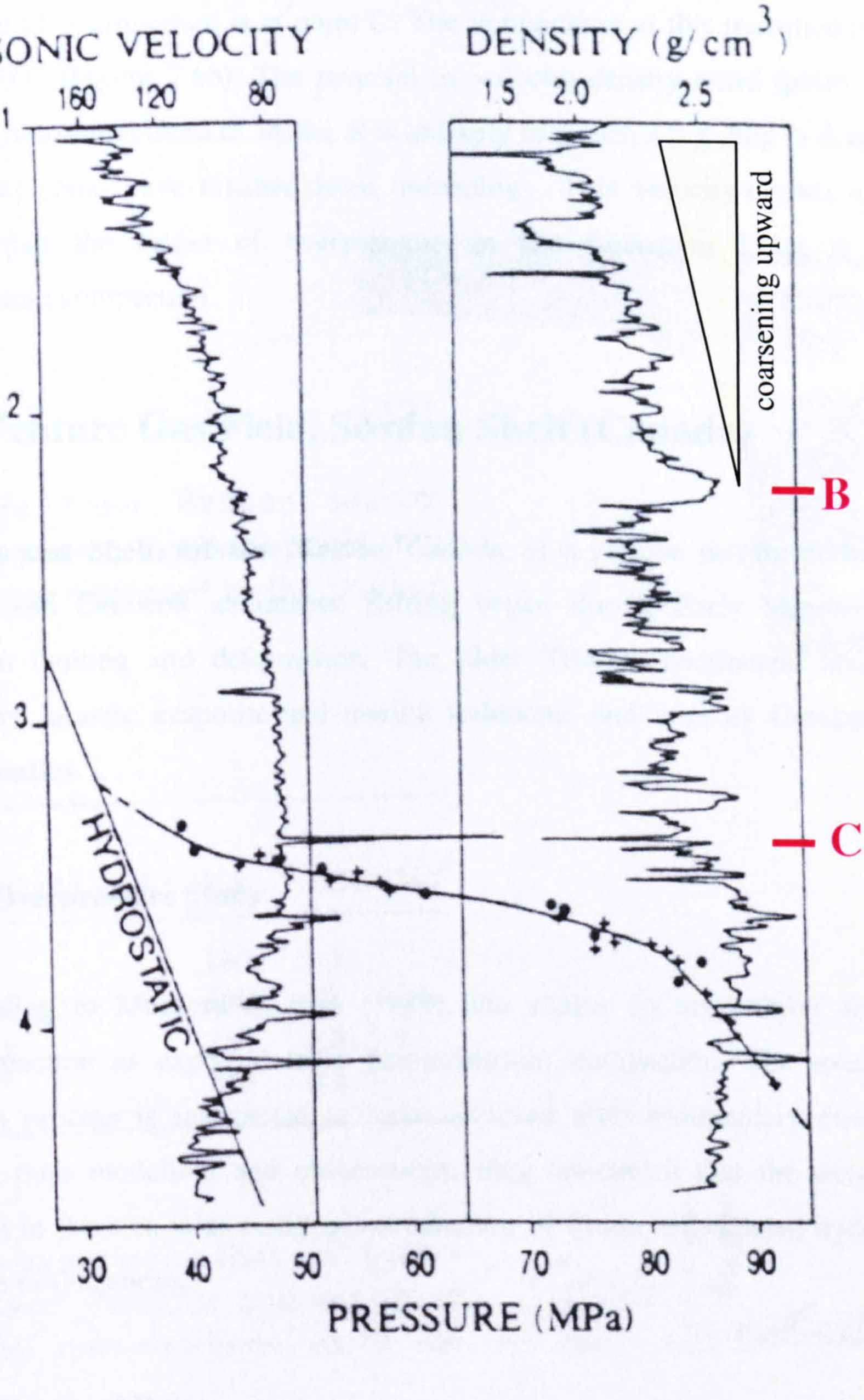


Figure 7.5 Sonic and density logs for a Mahakam Delta well, taken from Burrus et al., 1993. Points B and C marked the change in lithology (see Figure 7.6).

corresponding to the top of marine shales.

The top of overpressure is at point C. The temperature at this transitional zone is around 120°C (Figure 7.6b). The reversal in velocity-density trend (point D to E) represent compaction trend of shales. It is unlikely that such a big drop in density (2.8 to 2.5 g/cc) could have resulted from unloading. This velocity-density crossplot confirms that the origin of overpressure in the Mahakam Delta is due to disequilibrium compaction.

7.6 Venture Gas Field, Scotian Shelf (Canada)

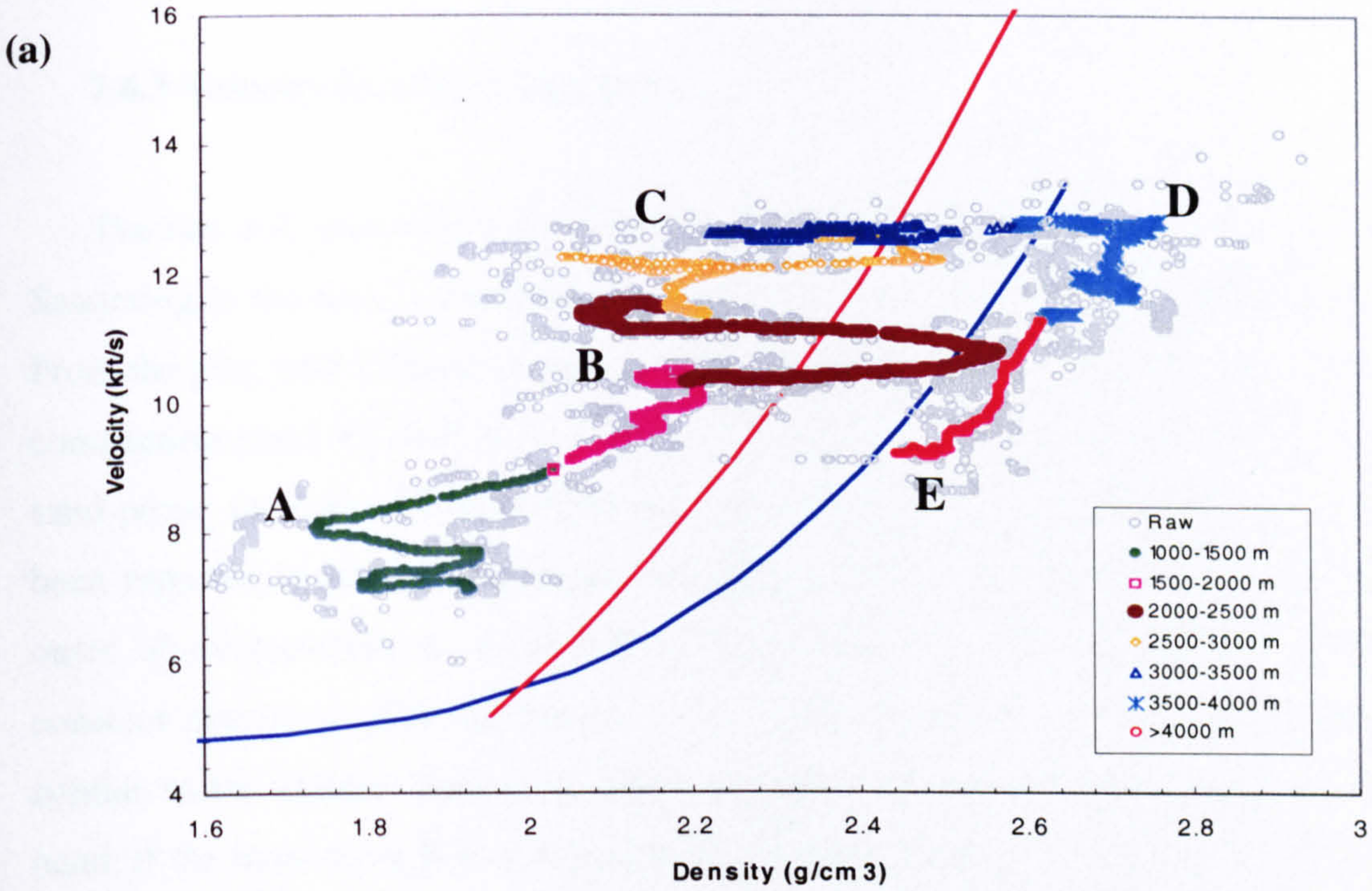
The Scotian Shelf, offshore western Canada, is a passive margin consisting of Mesozoic and Cenozoic sediments. Rifting began during Early Mesozoic times resulted in faulting and deformation. The older Triassic continental clastics are overlain by Jurassic evaporite and marine sediments and later by Cretaceous and Tertiary clastics.

7.6.1 Overpressure Study

According to Mudford & Best (1989), the shales do not exhibit significant undercompaction as expected from disequilibrium compaction. The overpressure generation process is interpreted to have occurred after sedimentary compaction. Based on their modelling and observations, they concluded that the overpressure generation in the area is as result of introduction of fluids, either from hydrocarbon generation or diagenesis.

7.6.2 Source of Data

A suite of wireline logs for well H-22, consisting of resistivity, sonic and density logs was published by Mudford (1988) and Mudford & Best (1989) (Figure 7.7). Unfortunately, no gamma-ray log was available. The well analysis is therefore carried out on the whole well without lithology discrimination. Temperature gradient for the



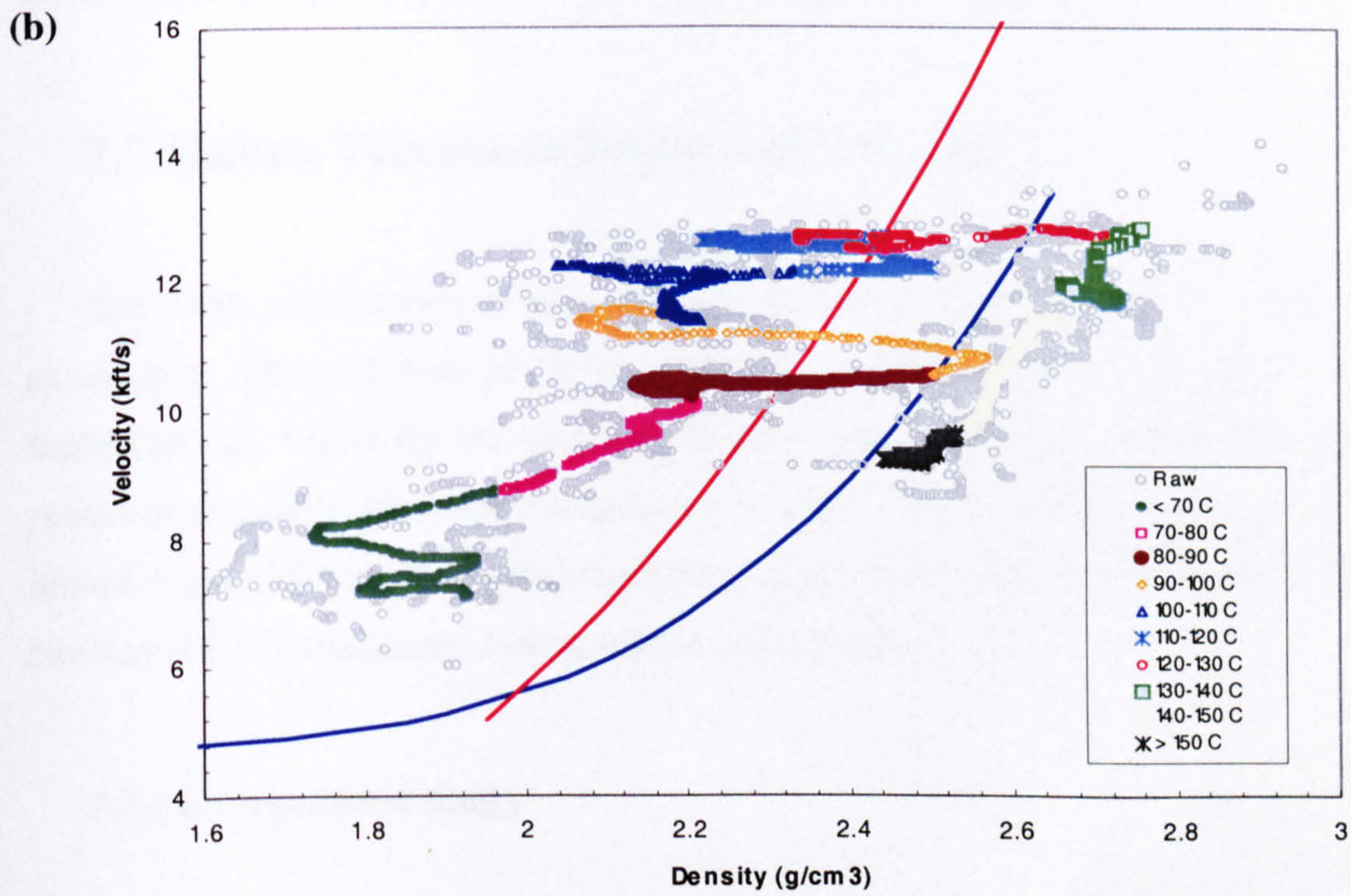


Figure 7.6 Velocity-density crossplots for a Mahakam Delta well. Data were plotted according to depth and temperature intervals. Grey dots are raw log data and coloured dots are the averaged data. Major changes in the velocity-density trend are marked as A to E.

well is derived from temperature data in Mudford & Best (1989).

7.6.3 Velocity-Density Crossplots

The raw and smoothed velocity (sonic) and density data are plotted on Figure 7.8. Scattering in the data is considered as more likely a result of lithological differences. From the plot, four inflections points can be identified. Point A to B follows a normal compaction trend. Point B to C could possibly relate to a change in lithology, from a sand-prone to more clay-rich lithology. No gamma-ray log or facies changes have been reported in the relevant papers (Mudford, 1988; Mudford & Best, 1989). The onset of overpressure is at point B. A significant drop in velocity with relatively constant density is observed from C to D. This observed sonic-density log trend is similar to the classic 'unloading' trend described by Bowers (2001). On the other hand, if the trend from B to C is due to lithological changes, overpressure in this well may well be due to disequilibrium compaction, where point C to D represent a different compaction trend. This could not be confirm with the present data.

7.7 Halten Terrace (offshore mid-Norway)

The main structuration in the area was formed in Late Jurassic as a result of extensional rifting (Jensen & Dore, 1993; Vik & Hermanrud, 1993). This led to faulted-blocks, which are the main hydrocarbon traps in the area. These followed a period of thermal subsidence during Late Cretaceous times. Uplift of Fennoscandian Shield in Late Pliocene/Early Pleistocene times provides sediment sources to the Mid-Norway shelf causing rapid sedimentation and subsidence.

7.7.1 Overpressure Study

Skar et al. (1998) examined well logs and pressure data and concluded that disequilibrium compaction as the cause of overpressure for the upper Cretaceous shales. In lower Cretaceous shale, diagenesis, in addition to disequilibrium compaction is believed to be responsible for the overpressure in the deeper section.

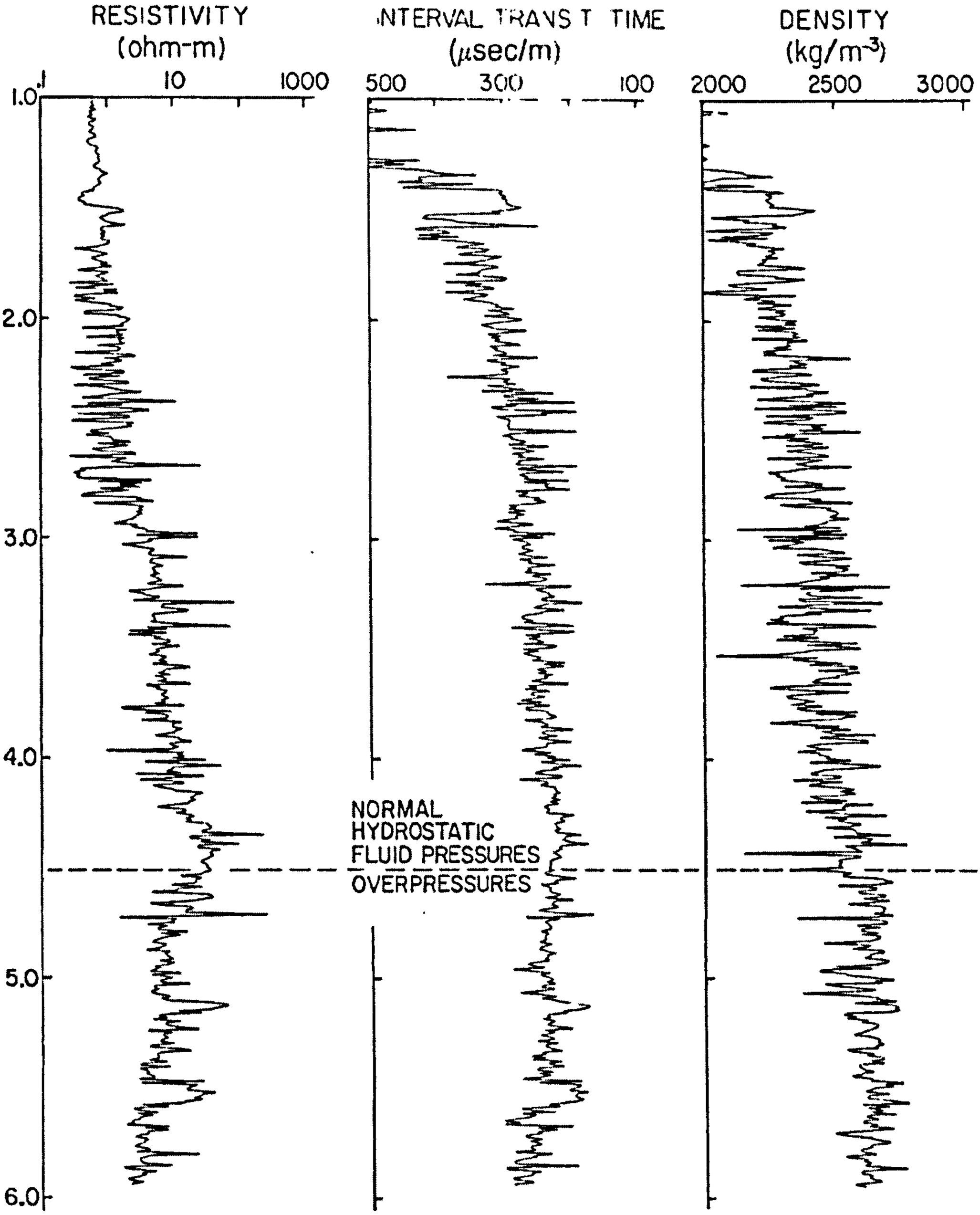
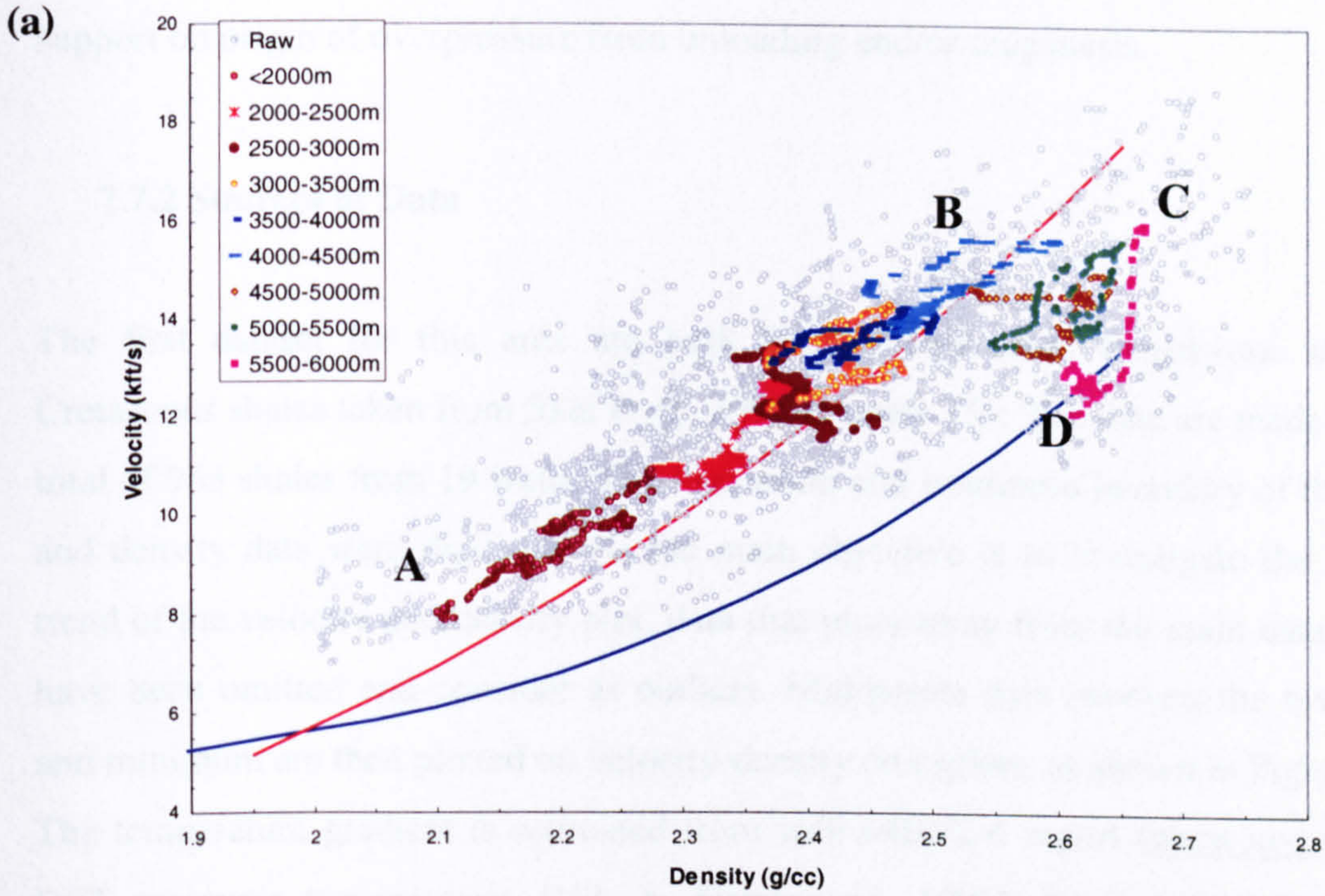


Figure 7.7 Wireline logs for well H-22, Venture Gas Field, taken from Mudford and Best (1989).



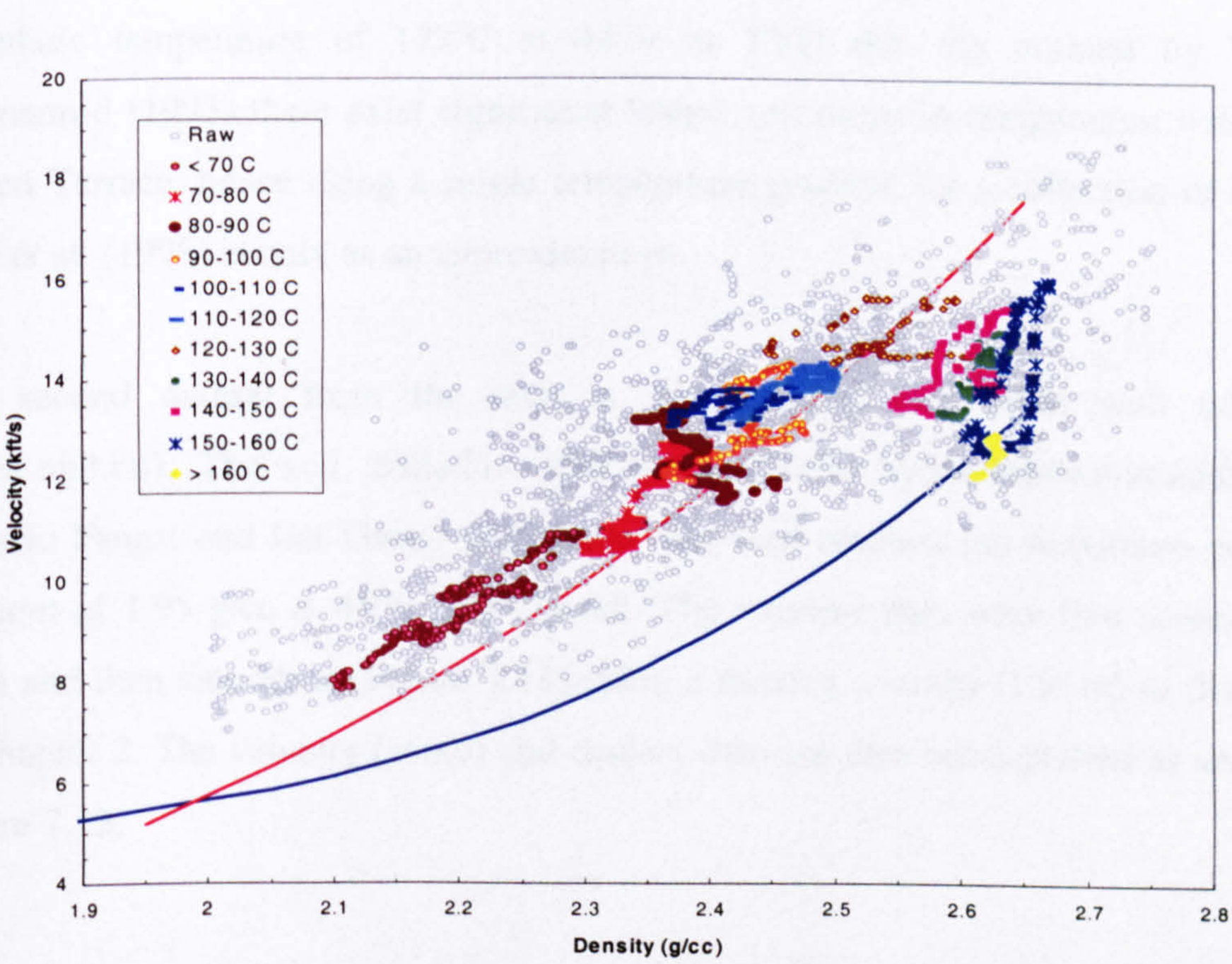


Figure 7.8 Velocity-density crossplots for well H-22. Data were plotted according to depth and temperature intervals. Points A-D marked changes in the velocity-density trend.

Hermanrud et al. (1998) have reported the absent of undercompaction or reversal in density log within the overpressured sequence in offshore Norway, which would support on origin of overpressure from unloading and/or diagenesis.

7.7.2 Sources of Data

The first dataset for this area are bulk density and sonic transit-time data for Cretaceous shales taken from Skar et al., 1998 (Figure 7.9). The data are made up of a total of 963 shales from 19 wells. The maximum and minimum boundary of the sonic and density data were digitized. As the main objective is to investigate the general trend of the velocity and density plot, data that plots away from the main data cluster have been omitted and consider as outliers. Mid-points data between the maximum and minimum are then plotted on velocity-density crossplots, as shown in Figure 7.10. The temperature gradient is estimated from well 6406/2-6 report (www.npd.no) and DST reservoir temperatures (Vik & Hermanrud, 1993). Well 6406/2-6 reached downhole temperature of 177°C at 4479 m TVD rkb. As pointed by Vik & Hermanrud (1993) there exist significant lateral variations in temperature within the Halten Terrace, hence using a single temperature gradient for a collection of data of Skar et al. (1998) is only as an approximation.

The second dataset from the area is wireline log data from well 6406/2-6 (www.npd.no). The well, drilled in 1998, was to test the hydrocarbon potential of the Jurassic Fangst and Bat Group sandstone. The well reached the maximum pressure gradient of 1.95 g/cc at 4479 m TVD rkb. The wireline data were first screened for shale and then smoothed (Figure 7.11) using a moving average (120 m) as described in Chapter 2. The velocity (sonic) and density data are then cross-plotted as shown in Figure 7.12.

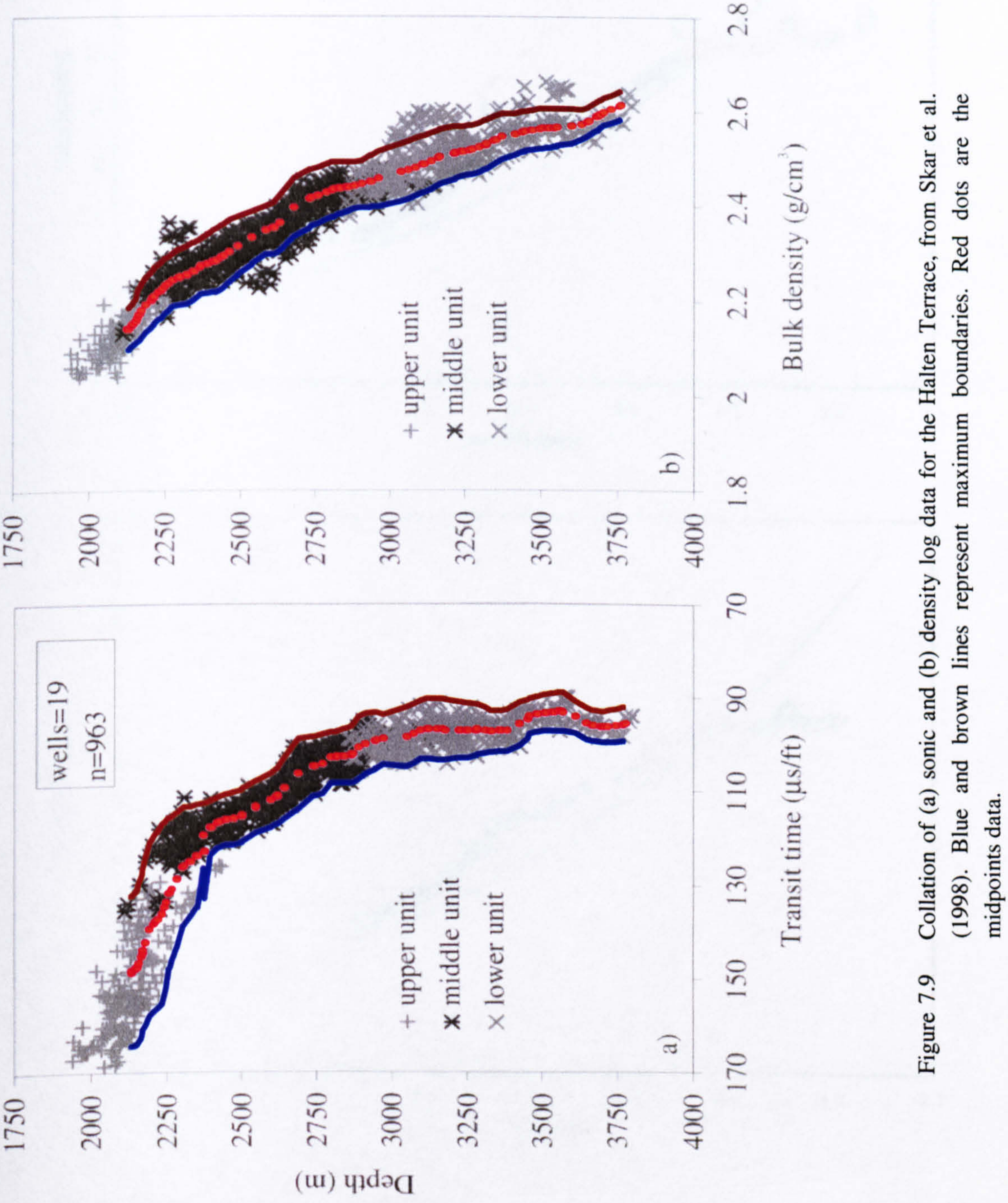
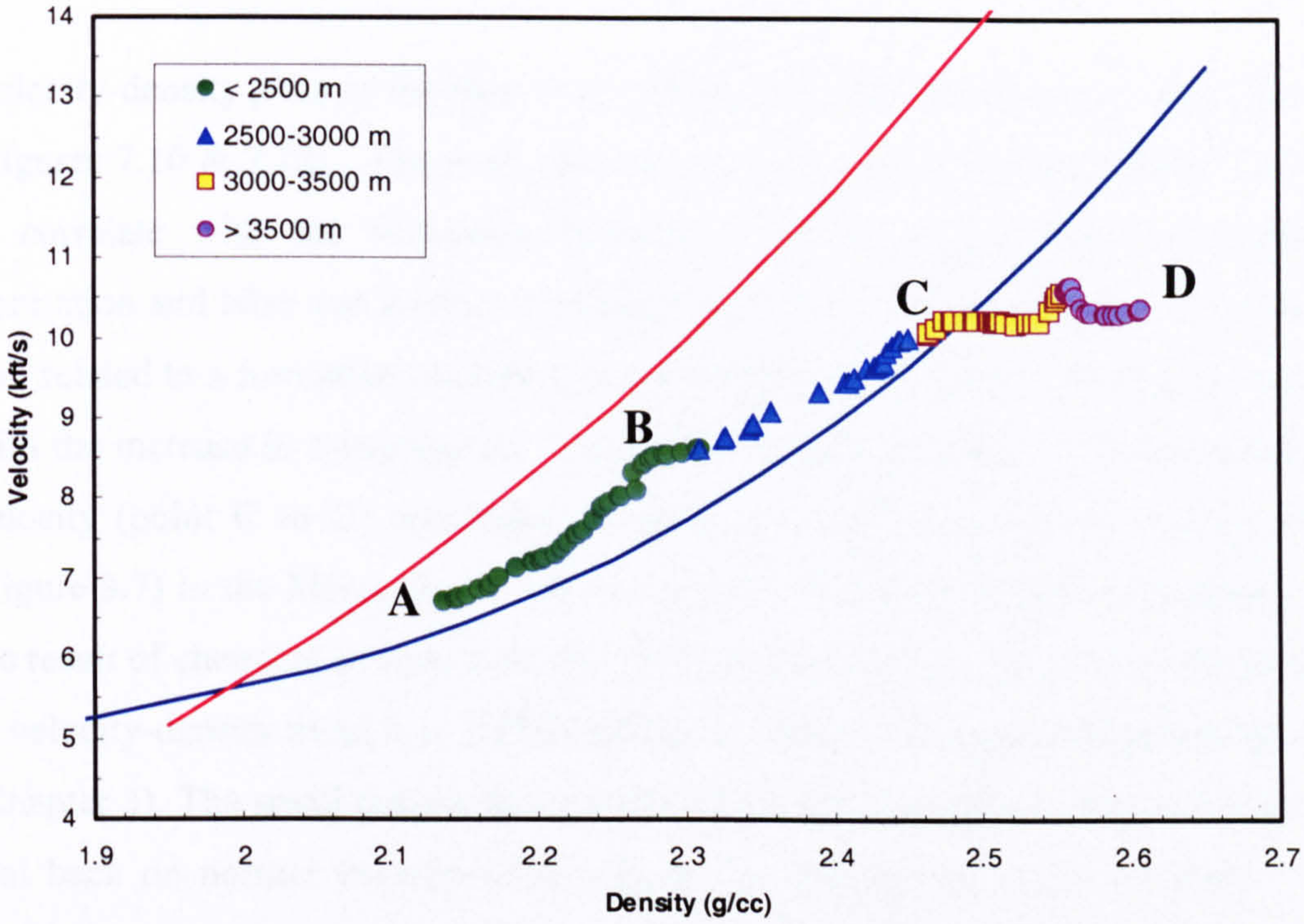


Figure 7.9 Collation of (a) sonic and (b) density log data for the Halten Terrace, from Skar et al. (1998). Blue and brown lines represent maximum boundaries. Red dots are the midpoints data.

(a)



(b)

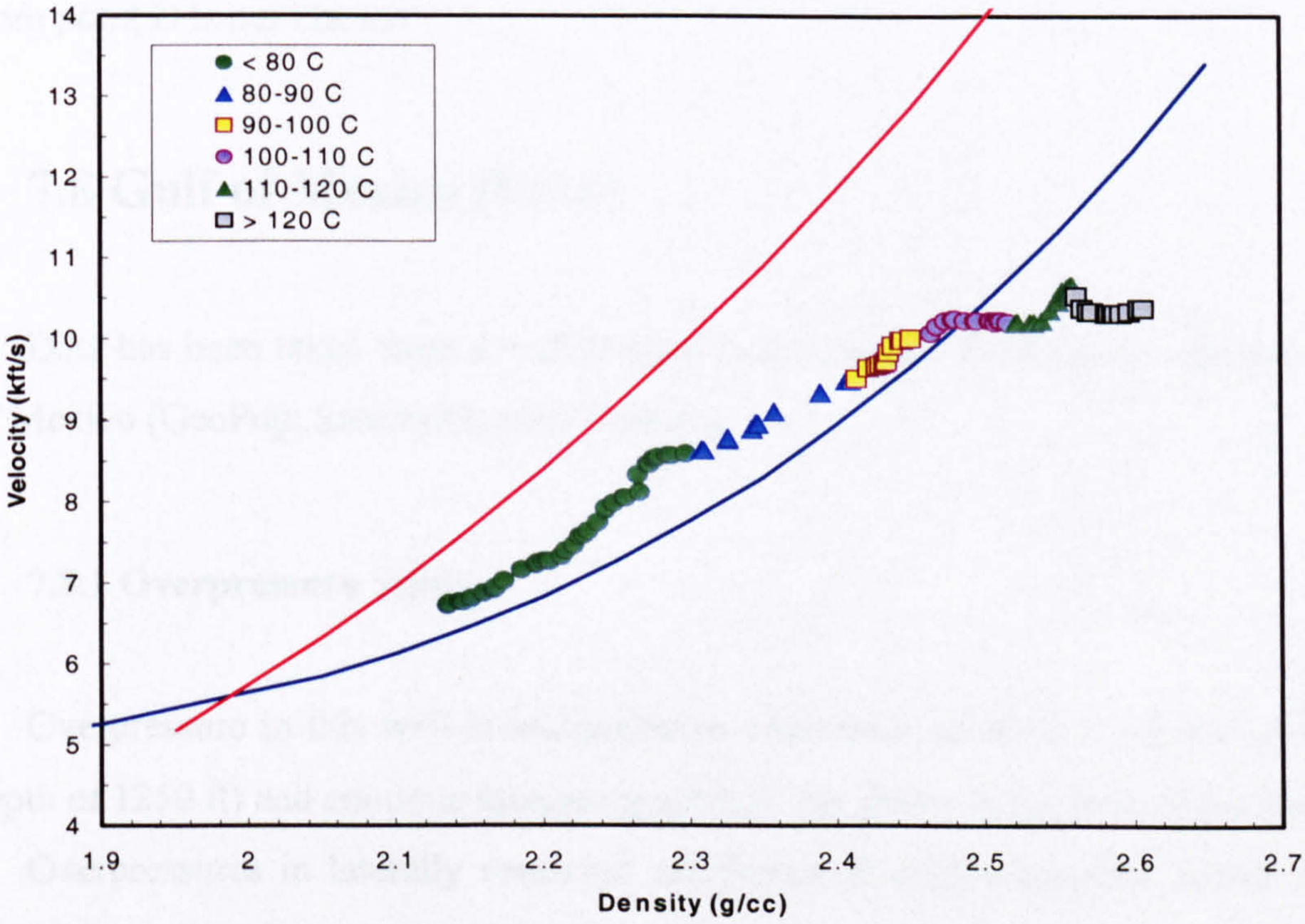


Figure 7.11 Velocity-density crossplots for wells data from Skar et al. (1998) for the Halten Terrace. Plotted are the mid-points data only. Chnages in the velocity-density trend are marked as A-D.

7.7.3 Velocity-Density Crossplots

Velocity-density plots of the Skar et al. (1998) and well 6406/2-6 show a similar trend (Figures 7.10 & 7.12). The plots show two major inflection points (B and C). Point B correlate with the formation boundary between Upper Cretaceous Springar Formation and Nise and Kvitnos Formation in Skar et al. (1998). Point C however, is not related to a formation boundary or known lithology changes. Instead, it coincides with the increase in overpressure. The sharp increase in density with little change in velocity (point C to D) resembles the trend observed in wells SM-30 and SM-31 (Figure 3.7) in the Malay Basin. This trend from C to D is therefore concluded to be the result of chemical compaction. The estimated temperature at point of the departure in velocity-density trend is at 120°C, similar to temperatures in the Malay Basin wells (Chapter 3). The small dataset from depths of 4.5 km and greater (Figure 7.12) which plot back on normal velocity-density trend for compacting shales are noted. These shales are located amongst thick reservoir sandstones. The sudden jump of these data from point D is not known.

7.8 Gulf of Mexico (USA)

Data has been taken from a well located in the Garden Banks area, offshore Gulf of Mexico (GeoPop; Swarbrick pers. Comm.).

7.8.1 Overpressure Study

Overpressure in this well is interpreted to commence at 5000 ft subsea (at water depth of 1250 ft) and continue increasing through the shales to the base of the well.

Overpressures in laterally restricted sandstones at depths between 12800 ft and 15200 ft confirm the estimates from the shales.

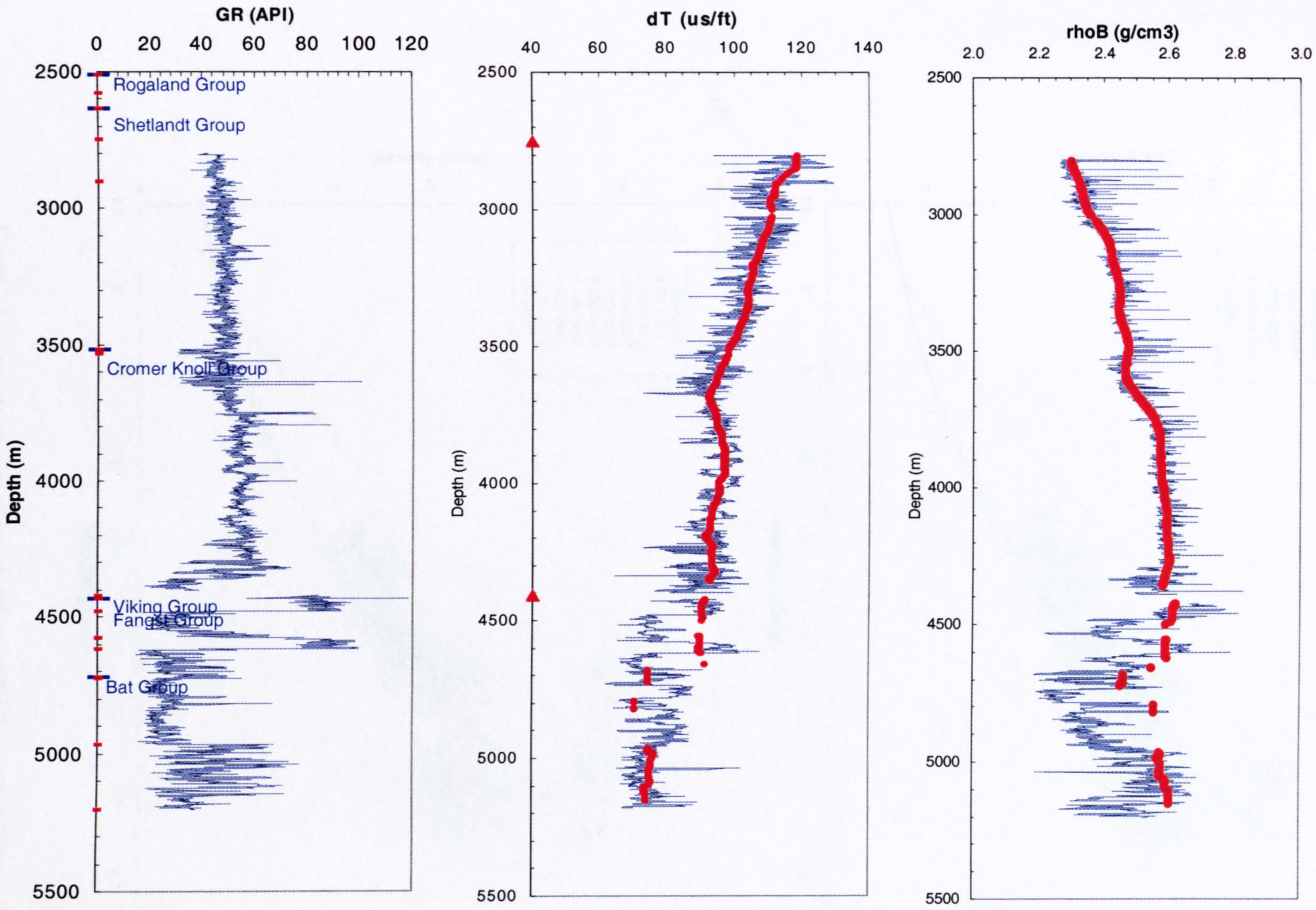


Figure 7.10 Wireline logs for well 6406/2-6, Halten Terrace. Blue line is the actual log response and the the red dots are the averaged datapoints for the shaly section.

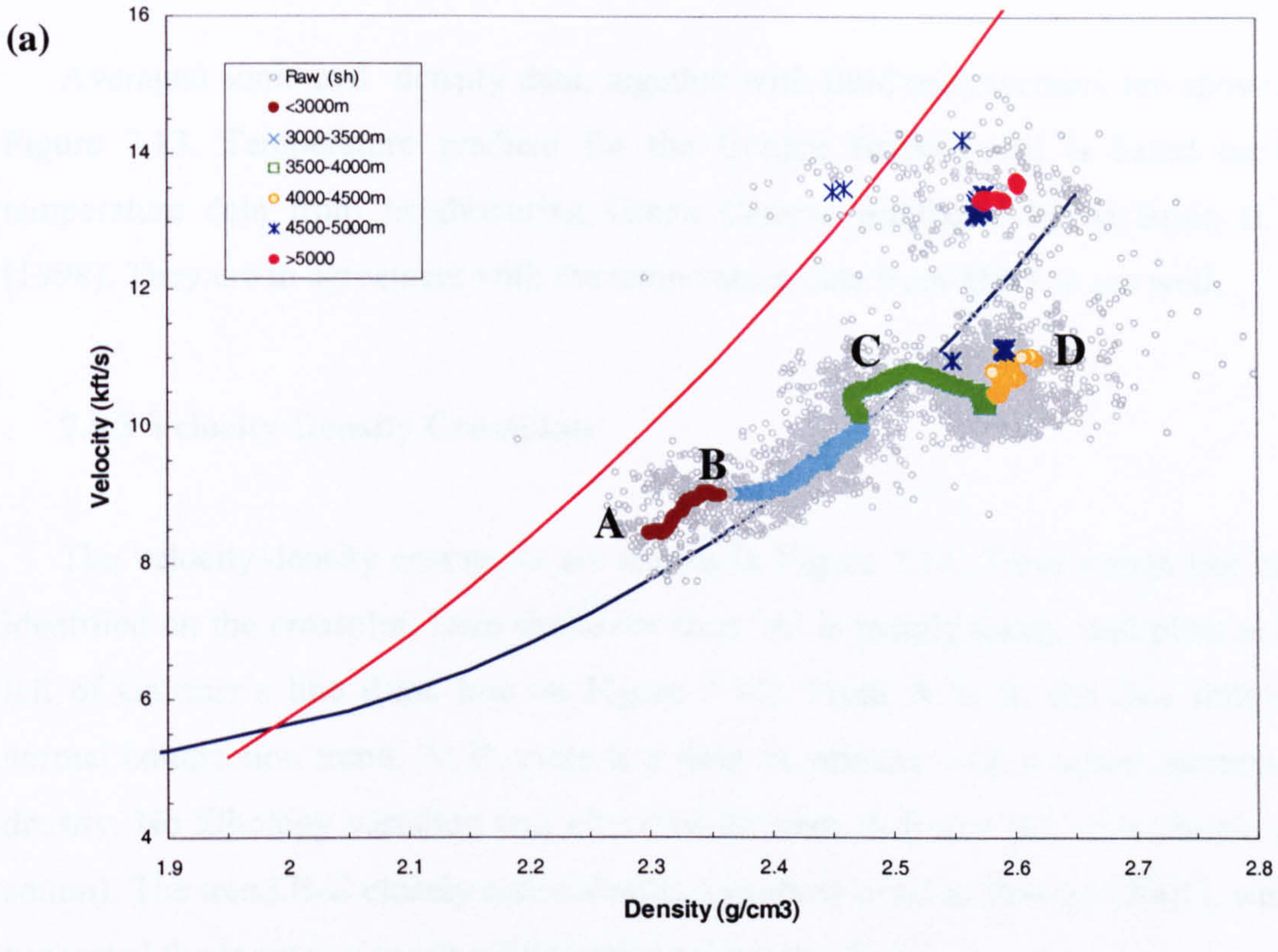


Figure 7.12 Velocity-density crossplots for well 6406/2-6, Halten Terrace.

7.8.2 Sources of Data

Averaged sonic and density data, together with fluid measurement are shown in Figure 7.13. Temperature gradient for the Garden Banks' well is based on the temperature data from neighbouring Green Canyon published by McBride et al. (1998). They are in agreement with the temperature data from MDT in the well.

7.8.3 Velocity-Density Crossplots

The velocity-density crossplots are shown in Figure 7.14. Three points has been identified on the crossplot. Data shallower than 'A' is mainly sandy, and plots to the left of Gardner's line (blue line on Figure 7.14). From A to B, the data follow a normal compaction trend. At B, there is a drop in velocity with a minor increase in density. No lithology variation was observed between A-B and B-C (Swarbrick, per comm). The trend B-C closely resembled the observed trend in Bowers (2001), which suggested the trend as a result of illitization with unloading.

Departure in velocity-density trend (point B) occurs at a temperature of 90°C. In comparison to the other basins, this temperature is low to result in chemical compaction. However, the temperature is within the estimated range for smectite-illite transformation.

7.9 Discussion

Velocity-density crossplots of data from various basins suggest an interplay between the main influential factors controlling the trends: lithology, overpressure generating mechanisms and diagenesis. Lithology changes are characterised by a shift to the left (sandy) and right (very clay-rich) relative to the published trends of Gardner and Bowers. Gardner and Bowers trends are based on data from Gulf of Mexico which has a clay fraction in the region of 40-60% (data in Yang & Aplin, 2004).

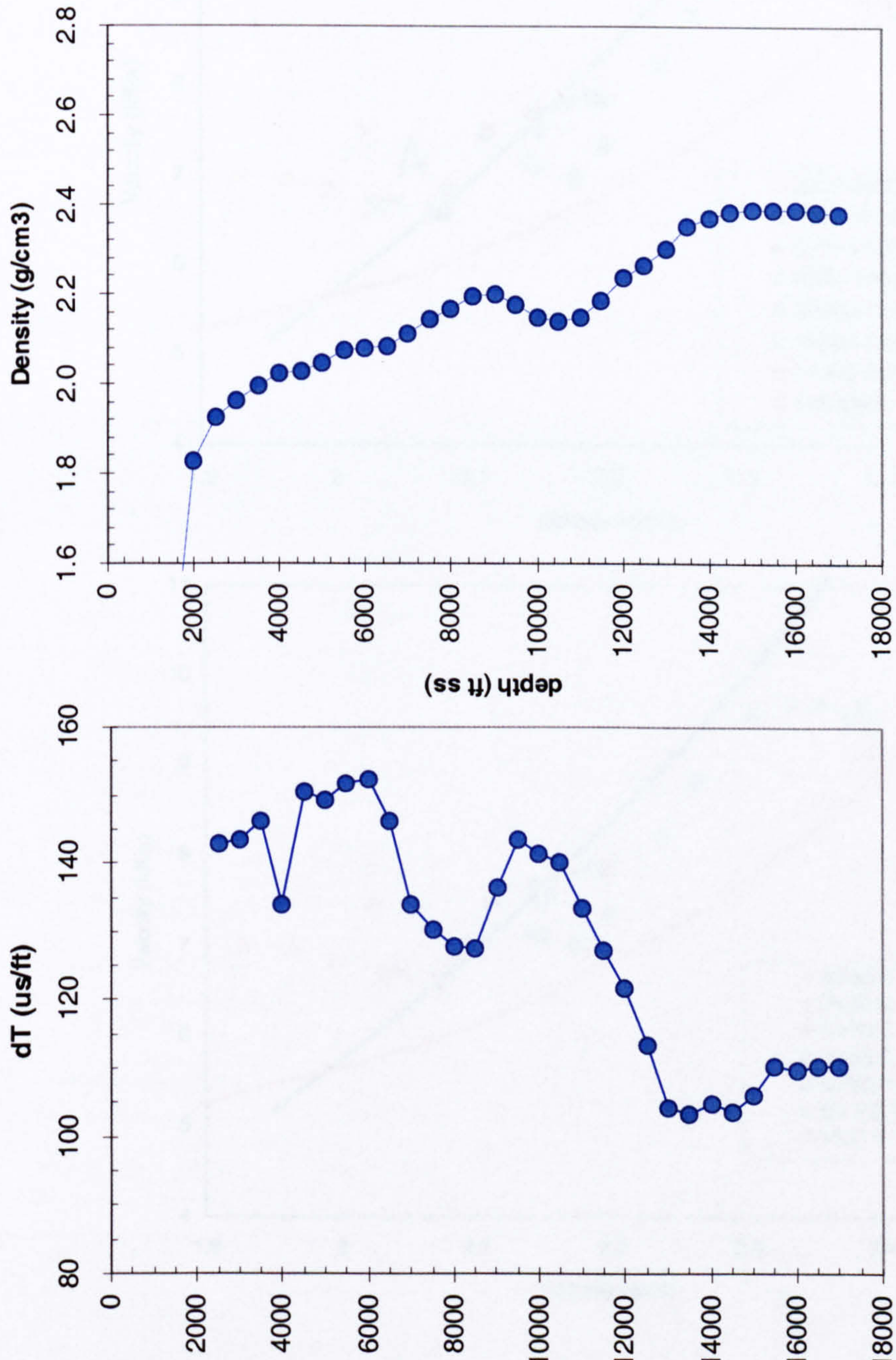


Figure 7.13 Sonic and density crossplot of a well from the Garden Banks, Gulf of Mexico (data from Geopop; Swarbrick, pers.comm.).

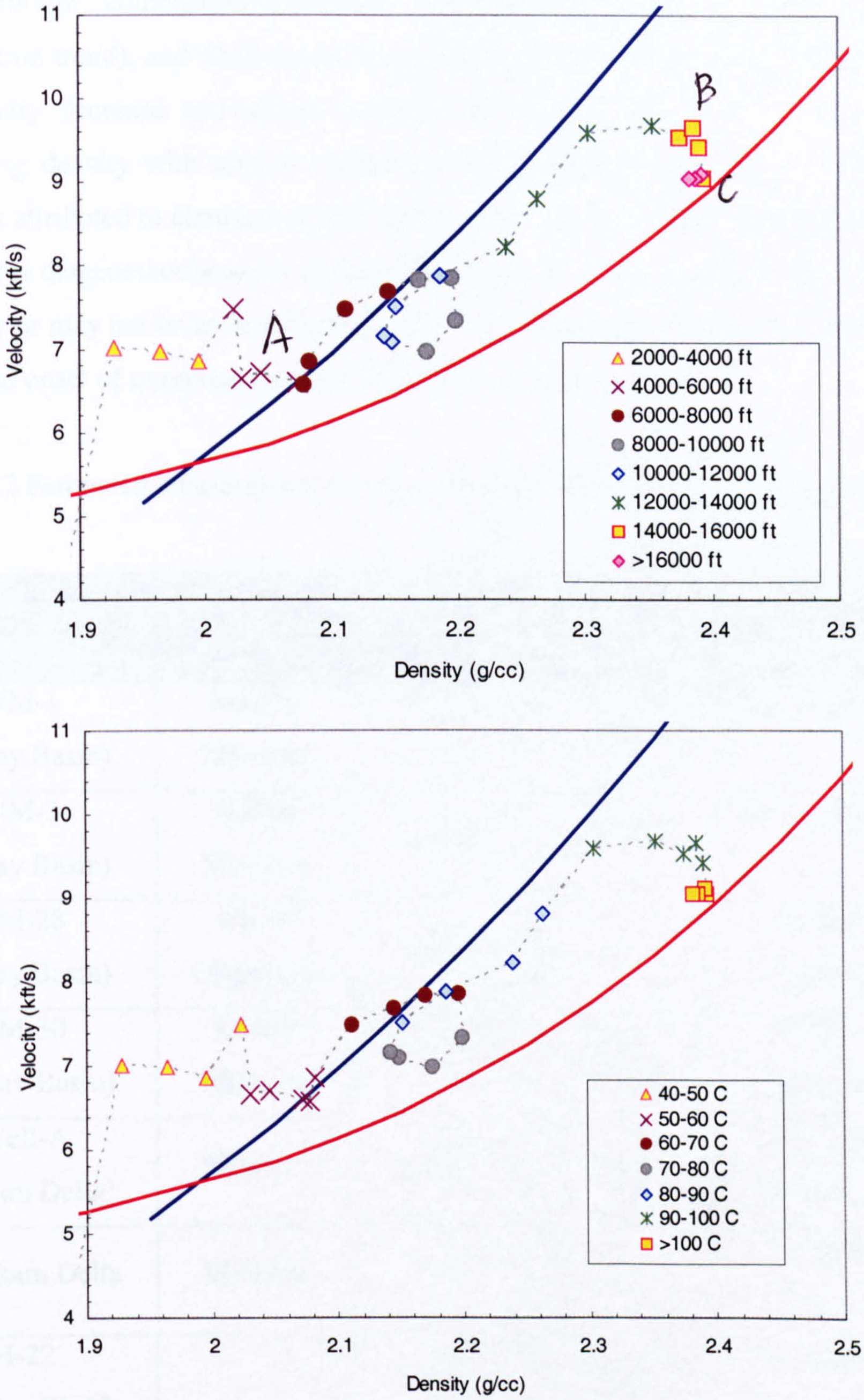


Figure 7.14 Velocity-density crossplot for a Garden Banks' well plotted according to: (a) depth intervals, (b) temperature intervals.

Overpressure generating mechanisms can be distinguished only between disequilibrium compaction (whereby velocity-density data remain on normal compaction trend), and fluid expansion mechanism (whereby an unloading signature of velocity decrease and almost constant density is observed). A new trend of increasing density with almost constant velocity has been observed in this study, which is attributed to chemical compaction and/or clay diagenesis. The temperature at which this diagenesis/chemical compaction trend commences varies from 105-120°C and may or may not be associated with onset of overpressure (well NM-3 has separate trend and onset of overpressure; well SM-30 is coincident).

Table 7.2 Estimated temperatures at point of departure in velocity-density crossplots.

Well (Basin)	Age	Depth (m)	Temperature (C)	Cause for Departure	Reference Figure No.
NM-1 (Malay Basin)	Middle Miocene	1780	120	Clay diagenesis	3.7a
NM-3 (Malay Basin)	Middle Miocene	1400	105	Clay diagenesis	3.7b
SM-28 (Malay Basin)	Upper Oligocene	1710	110	Chemical compaction	3.7c
SM-30 (Malay Basin)	Lower Miocene	1370	105	Chemical compaction	3.7d
Well-A (Baram Delta)	Miocene	2400	80	Change in lithology	7.4
Mahakam Delta	Miocene	3500	120	Change in lithology	7.3
H-22 (Scotian Shelf)		4500	125	Unloading	7.5
Well 6406/2-6 (Halten Terrace)	Lower Cretaceous	3700	120	Chemical compaction	7.9
Garden Banks (Gulf of Mexico)		4000	90	Unloading	7.11

A hybrid trend of moderately decreasing velocity with increasing density is attributed by Lahann et al. (2001) to smectite to illite transformation, a clay diagenesis process. Lahann (2002) estimates the magnitude of overpressure resulting from this process. The hybrid nature of this trend is therefore made up of a chemical compaction process (increase the density with less significant influence on velocity) and unloading (due to a decrease in effective stress). The trends are summarised in Figure 7.15.

7.10 Summary and Conclusions

The velocity-density crossplots from a number of basins around the world have been shown to aid in identification of the origins of overpressure. The results can be summarized as follows:

(a) Onset of overpressure in the Tertiary deltas (Mahakam and Baram) coincide with the lithology change from sand-prone to shale-rich. This lithology changes is clearly marked by shift to the right in the velocity-density crossplot, and is also the control on development of overpressure.

(b) Disequilibrium compaction in Tertiary deltas as result of rapid deposition of fine-grained sediment are not control by temperature. They occurs in wide temperature range, from 80°C (Baram Delta) to 120°C (Mahakam Delta).

(c) An unloading signature is identified from Gulf of Mexico (Eugene Island 330-20AS/T and possibly also from Garden Banks) and Scotian Shelf, offshore Canada.

(d) Trends of sharply increasing density with minor change in velocity are observed in Halten Terrace, offshore Norway. These trends are similar to those seen in some Malay Basin wells. In all cases the onset of trend occurs at between 105-120°C and does not appear to be controlled by overpressure. This trend is interpreted as due to chemical compaction.

(e) A hybrid trend, combining increase in density from chemical processes, and decreasing velocity due to decrease in effective stress (unloading). This trend has

been observed in a Tertiary delta by Lahann et al. (2001) and linked is illite to smectite transformation.

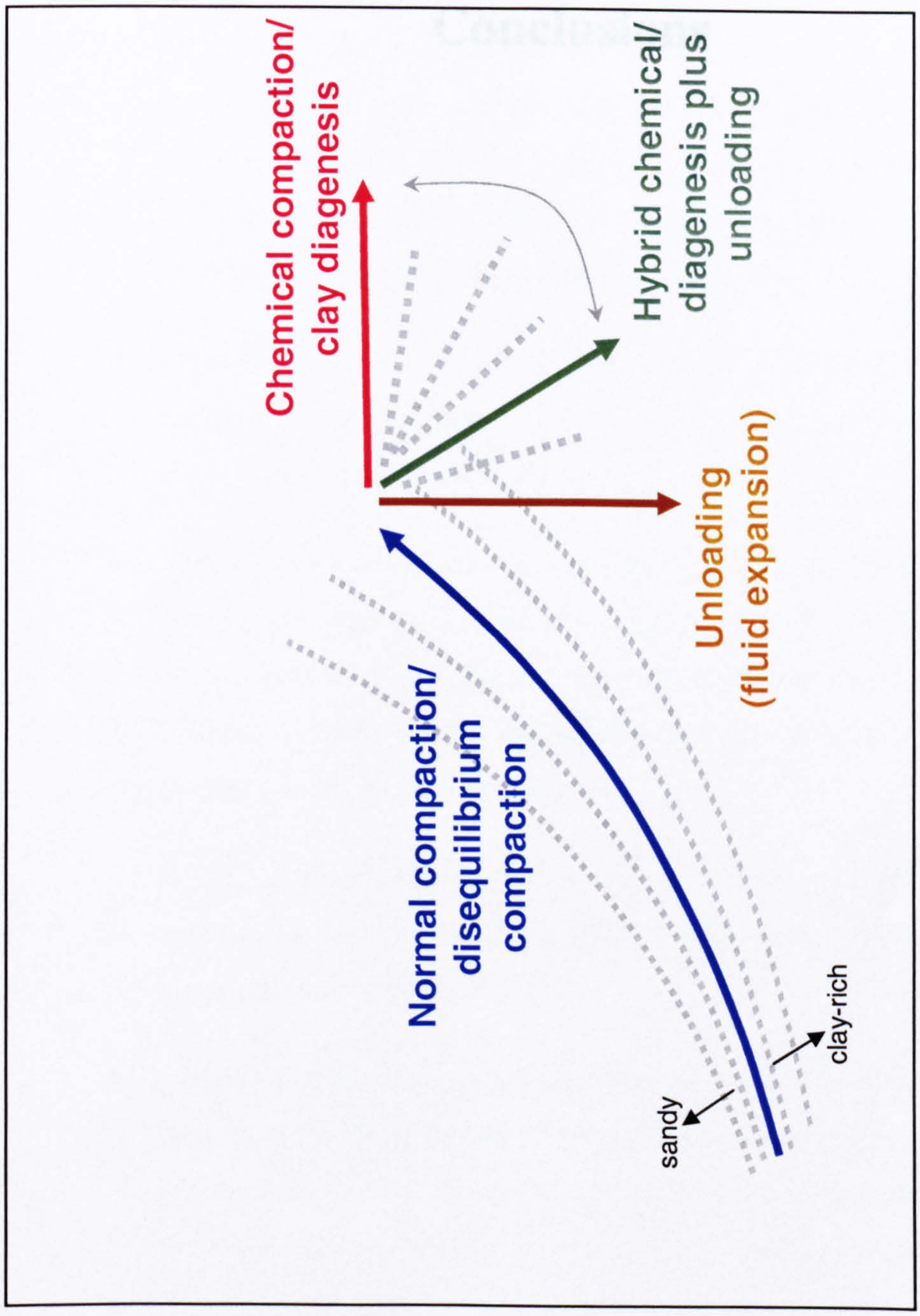


Figure 7.15 Summary of velocity-density trends for different processes.

Chapter 8:

Conclusions

8.1 Conclusions I: Origins of Overpressure

The first objective of this study is to determine the origins of overpressure in the Malay Basin using wireline logs. The following summarizes the main findings from this study:

- In the Malay Basin variable pore pressure profiles are observed. Pore pressure prediction is variable due to: (1) choice of methods (empirical or soil mechanics), (2) difficulties in selection of normal compaction trend, (3) multiple origins of overpressure, and (4) chemical compaction effects.

- Equivalent depth method, a deterministic method of estimating pore pressure in shales, gives closest match with formation pressure data, when mean effective stress is used.

- Malay Basin overpressure results principally from disequilibrium compaction, with a potential (but unquantified) contribution from chemical compaction processes. These processes may involve both shale framework collapse as well as dissolution/reprecipitation involving cementation of storage and (later) connecting pores.

- A distinctive profile on velocity-density crossplots has been established starting at temperatures of 105°C-120°C which identified onset of chemical compaction.

- Disequilibrium compaction and associated lateral transfer can explain the data from the West Baram and West Luconia areas, consistent with rapid sedimentation of the Tertiary deltas. An absence of any chemical signature in the porosity trends is attributed to the low geothermal gradient.

- This study shows the usefulness of velocity-density cross-plots in aiding the interpretation on the causes of overpressure.

- The range of pressure profiles and velocity-density cross-plot trends found in the Malay Basin have been found in basins elsewhere in the world. Here wider variety of mechanical compaction trends are found associated with variable sand and clay content, plus pure unloading signatures associated with fluid expansion mechanisms.

8.2 Conclusions II: Influence on Petroleum Systems

The second objective is to investigate the influence of overpressure on the petroleum system in the Malay Basin. Basin modelling has been used to test several conflicting hypotheses regarding the origins and their control on hydrocarbon distribution in the area. Following is the summary of the main findings:

- Basin modelling using Temis 2D has examined pressure histories resulting from burial (stress), hydrocarbon generation and changes in rock properties due to chemical compaction processes. Modelling can successfully replicate pressure profiles when appropriate porosity-permeability histories are considered, taking into account the effect of chemical compaction.

- The results show initial pressure build-up in the Malay Basin is attributed to rapid sedimentation of fine-grained sediments during the early Miocene. Rapid pressure build-up during the last 10 Ma of syn-sedimentary compaction is due to the present of effective seals created by chemical compaction processes within the shales.

- Whilst contribution to overpressure from gas generation is minor compared to disequilibrium compaction (loading stress) there is potential for large gas resources sealed by chemically compacted shales.

8.3 Future Work

This study has largely benefited from the use of wireline log and basin modelling work. To further substantiate the proposed chemical compaction model, further study and analyses, especially on the shale is recommended. Following is the suggestion for future works:

- Detailed rock properties determination, such as porosity from pore-size distribution (mercury injection), in the shale could further validate the log-derived values used in this study. Other analyses may include cation exchange capacity (CEC), surface area determination and grain-density measurement.

- Although limited XRD analysis has been carried out in this study, the data do not indicate significant changes to the shale mineralogy between normally-pressured and overpressured shales. The possible reason is the use of bulk shale rather than 2μm or 0.2 μm shale fraction, which do not clearly distinguish smectite from illite clays. Hence, a detailed shale mineralogy study in the basin would highlight the extent of illitisation or cementation processes within the basin.

- Further work is also needed to understand the shale responses in the wireline log. The reason behind the reduction in velocity, despite the increase in density during clay diagenesis/chemical compaction, warrants further in-depth study.

- Pore pressure profiles for the shales, generated from wireline log analysis, do not make any distinction between the variation in the shales that might exist due to different facies or composition. Hence, further work is recommended to look into the possible facies control on the variation in pore pressure profiles.

- Continued study on the shale chemical compaction phenomena in the other 'hot' Tertiary basins in Southeast Asia could help us further in understanding the behaviour of shales.

References

Addis, M.A., Hennig, A., and Yassir, N., 1998. Problems in pore pressure detection: distinguishing between overpressures and wellbore instability, AADE Industrial Forum – *Pressure Regime in Sedimentary Basins and Their Prediction*, Sep 1998 Texas.

Alnes, J.R. and Lilburn, R.A., 1998. Mechanisms for generating overpressure in sedimentary basins: a reevaluation: Discussion, *AAPG Bulletin*, v. 82, No. 12, p. 2266-2269.

Amstrong, P.A., Allis, R.G., Funnell, R.H. and Chapman, D.S., 1998. Late Neogene exhumation patterns in Taranaki Basin (New Zealand): evidence from offset porosity-depth trends, *Journal of Geophysical Research*, vol. 103, B12, p. 30,269-30,282.

Aplin, A.C., Yang, Y. and Hansen, S., 1995, Assessment of β, the compression coefficient of mudstones and its relationship with detailed lithology*: Marine and Petroleum Geology*, v. 12, p. 955-963.

Athy, L.F., 1930. Density, porosity and compaction of sedimentary rocks, *AAPG Bull.*, p. 1-24.

Awwiller, D.N., 1993. Illite/smectite formation and potassium mass transfer during burial diagenesis of mudrocks : a study from the Texas Gulf Coast Paleocene-Eocene, *Journal of Sedimentary Petrology*, v.63, no.3, p. 501-512.

Baldwin, B. and Butler, C.O., 1985. Compaction curves, *AAPG Bulletin*, v.69, no. 4, p. 622-626.

Barker, C., 1972, Aquathermal pressuring – the role of temperature in the development of abnormal pressure zone: *AAPG Bulletin*, v. 56, p. 2068-2071.

Barker, C., 1990. Calculated volume and pressure changes during the thermal cracking of oil to gas in reservoirs, *AAPG Bulletin*, v. 74, p. 1254-1261.

Beicip-Franlab, 1997. *Temispack 2.5 User Manual*, 494 p.

Bekele, E.B., Johnson, M.D. and Higgs, W.G., 2001. Numerical modelling of overpressure generation in the Barrow Sub-basin, Northwest Australia, *APPEA Journal*, p. 595-607.

Berner, R.A., 1980. Early diagenesis. A theoretical Approach. Princeton Series in Geochemistry, *Princeton University Press*, 241 p.

Bethke, C.M., 1985. A numerical model of compaction-driven ground-water flow and heat transfer and its application to the paleohydrology of intracratonic sedimentary basins, *J. Geophys. Res.*, 90B, p. 6817-6828.

Bjorkum, P.A. and Nadeau, P.H., 1998. Temperature controlled porosity/permeability reduction, fluid migration, and petroleum exploration in sedimentary basins, *Australian Petroleum Production & Exploration Association Journal*, 38, p. 453-464.

Bjorkum, P.A., 1996. How important is pressure in causing dissolution of quartz in sandstone ?, *Journal of Sedimentary Research*, 66, no.1, p. 147-154.

Bjorlykke, K. and Hoeg, K., 1997. Effects of burial diagenesis on stresses, compaction and fluid flow in sedimentary basins, *Marine and Petroleum Geology*, v. 14., No.3, p. 267-276.

Bjorlykke, K., 1998. Clay mineral diagenesis in sedimentary basins – a key to the prediction of rock properties. Examples from the North Sea Basin, *Clay Minerals*, 33, p. 15-34.

Blehaut, J.F., van Beek, F., Billeau, J.K., Gause, J.K., Kimminau, S., Paardekam, A., Tadcliffe, N., Rademaker, R., Storms, L., Welsh, B.J. and Wittemann, A., 1999. Shearwater prospect development: a high pressure/ high temperature challenge. In: Fleet, A.J. and Boldy, S.A.R. (eds) Petroleum Geology of Northwest Europe: Proceedings of the 5th Conference, p. 1021-1027.

Bolas, H.M.N., Hermanrud, C. and Teige, G.M.G., 2004. Origin of overpressure in shales: Constraint from basin modelling, AAPG Bull., 88, p. 193-211.

Bour, O. and Lerche, I., 1994. Numerical modelling of abnormal fluid pressures in the Navarin Basin, Bering Sea, *Marine and Petroleum Geology*, v. 11, no. 4, p. 491-500.

Bowers, G.L. and Katsube, T.J., 2002. The role of shale pore structure on the sensitivity of wire-line logs to overpressure. In: Huffman, A.R. and Bowers, G.L. (eds), *Pressure Regimes in Sedimentary Basins and Their Prediction*, AAPG Memoir 76, p. 43-60.

Bowers, G.L., 1995. Pore pressure estimation from velocity data; accounting for overpressure mechanisms besides undercompaction, *SPE Drilling and Completions*, June, 1995.

Bowers, G.L., 2001. Determining an appropriate pore-pressure estimation strategy. *Offshore Technology Conference*, Houston, Texas, OTC 13042.

Breckels, I.M., and van Eekelen, H.A.M., 1982. Relationship between horizontal stress and depth in sedimentary basins, *Journal of Petroleum Technology*, v. 34, p. 2191-2198.

Bredehoeft, J., and Hanshaw, B., 1968. On the maintenance of anomalous fluid pressures: I, Thick sedimentary sequences: *Geological Society of America Bulletin*, v. 79, p 1097-1106.

Bredehoeft, J.D., Wesley, J.B and T.D. Foulch, 1994. Simulation of the origin of fluid pressure, fracture generation and the movement of fluids in the Uinta Basin, Utah, *AAPG Bulletin.*, 78, p. 1729-1747.

Bruce, C.H., 1984. Smectite dehydration – its relation to structural development and hydrocarbon accumulation in northern Gulf of Mexico Basin. *AAPG Bulletin*, v.68, No.6, p. 673-683.

Bruel, D and Made, B., 2000. Significance of clay dehydration on overpressure in the Alwyn area, Viking Graben, North Sea, AAPG Annual Meeting Abstract, New Orleans, Lousiana, April 16-19, 2000.

Buhrig, C., 1989, Geopressured Jurassic reservoirs in the Viking Graben: modeling and geological significance: *Marine and Petroleum Geology*, v. 6, no. 48, p. 31-48.

Burland, J.B., 1990. On the compressibility and shear strength of natural clays. *Geotechnique*, 40, p. 329-378.

Burley, S.D., Mullis, J. and Matter, A., 1989. Timing diagenesis in the Tartan reservoir (UK North Sea), constraints from combined cathodoluminescene microscopy and fluid inclusion studies, *Marine and Petroleum Geology*, 6, no.2, p. 98-120.

Burrus, J., 1998, Overpressure models for clastic rocks; their relation to hydrocarbon expulsion: a critical reevaluation, in Law, B.E., G.F. Ulmishek, and V.I. Slavin eds., Abnormal pressures in hydrocarbon environments: *AAPG Memoir 70*, p. 35-64.

Burrus, J.E., Brosse, G.C. de Janvry and Oudin, J., 1992, Basin Modelling in the Mahakam delta based on the integrated 2D model TEMISPACK, *Proc. Indonesian Petroleum Association*, 21st Annual Convention, p. 23-43.

Burrus, J., Kuhfuss, B., Doligez, B. and Ungerer, P., 1991. Are numerical models useful in reconstructing the migration of hydrocarbons? A discussion based on Northern Viking graben. In: England, W.A. and Fleet, A.J. (eds), *Petroleum Migration*, The Geological Society of London, Special Publication 59, p. 89-111.

Burrus, J., Osadetz, K., Gaulier, J.M., Brosse, E., Doligez, B., Choppin de Janvry, G., Barlier, J. and Viser, K., 1993. Source rock permeability and petroleum expulsion efficiency: modelling examples from the Mahakam Delta, the Williston Basin and the Paris Basin. In: Parker, J.R. (ed), *Petroleum Geology of Northwest Europe: Proceeding of the 4th Conference*, 1993 Petroleum Geology '86 Ltd, The Geological Society, London, p. 1317-1332.

Burrus, J., Osadetz, K., Wolf, S., Doligez, B., Visser, K. and Dearborn, D., 1996. A two-dimensional regional basin model of Williston Basin hydrocarbon Systems, *AAPG Bull.*, 80, p. 265-291.

Burrus, J., Schneider, F. and Wolf, S., 1994. Modeling overpressures in sedimentary basins: consequences for permeability and rheology of shales, and petroleum expulsion efficiency, *AAPG International Conference*, Kuala Lumpur, August 21-24, 1994 (abstract).

Burst, J.F., 1959. Post diagenetic clay mineral-environmental relationships in the Gulf Coast Eocene, *Clay and Clay Minerals*, v.6, p. 327-341.

Caillet, G., Bramwell, N. and Meciani, L., 1998, The effect of overpressure on hydrocarbon trapping in the chalk of the greater Ekofisk area (Norway), Overpressures in petroleum exploration; Proc. Workshop, Pau, April 1998- Bull. Centre Rech. Elf Explor. Prod., Mem. 22, 19-26.

Caillet, G. and Batiot, S., 2003. 2D modelling of hydrocarbon migration along and across growth faults: an example from Nigeria. *Petroleum Geoscience,* vol. 9, p. 113-124.

Carr, A.D., 1991. A pressure dependent model for vitrinite reflectance. In: Manning, D., (ed) Advances and application in energy and natural environment, Organic Geochemistry, Manchester Uni Press, p. 285-287.

Carr, A.D., 1999. A vitrinite reflectance kinetic model incorporating overpressure retardation, *Marine and Petroleum Geology,* 16, p. 355-377.

Carr, A.D., 2000. Suppression and retardation of vitrinite reflectance. Part 1 – Formation and significance for hydrocarbon generation. *Journal of Petroleum Geology,* 23, p. 313-343.

Carstens, H., and Dypvik, H., 1981. Abnormal formation pressure and shale porosity, *AAPG Bull.*, 65, p. 344-350.

Castagna, J.P., Batzle, M.L. and Kan, T.K., 1993. Rock physics –The link between rock properties and AVO response, in Offset-Dependent Reflectivity – Theory and Practice of AVO Analysis, Castagna, J.P. and Backus, M. (eds), *Investigations in Geophysics*, No. 8, Society of Exploration Geophysicists, Tulsa, Oklahoma, p. 135-171.

Cayley, G.T. , 1987. Hydrocarbon migration in the Central North sea. In: Brooks, J. and Glennie, K. (eds), *Petroleum Geology of the Northwest Europe*, Graham & Trotman, London, p. 549-555.

Chilingar, G.V., Robertson Jr., J.O. and Rieke III, H.H., 2002. Origin of abnormal formation pressures, In: Chilingar, G.V., Serebryakov, V.A. and Robertson Jr., J.O. (eds), *Origin and Prediction of Abnormal Formation Pressures*, Developments in Petroleum Science 50, p. 21-67.

Chung, K. S., Hemmings, D. and Have, T.T., 1994. Overpressures in the Baram Field, Offshore Sarawak, East Malaysia, AAPG International Conference and Exhibition, Kuala Lumpur, August 21-24, 1994 (abstract).

Colton-Bradley, V.A.C., 1987, Role of pressure in smectite dehydration – effects on geopressure and smectite to illite transition : *AAPG Bulletin*, v. 71, p. 1414-1427.

Creaney, S., Hussein, A.H., Curry, D.J., Bohacs, K.M. and Hassan, R.A., 1994. Source facies and oil families of the Malay Basin, Malaysia, *AAPG Bull.* 78, p. 1139.

Curry, D.J., 1992. Geochemistry and source facies relationships of gases from the Malay Basin, *Exxon Production Research Report* (Unpublished).

Darby, D., William, M., Fallick, A.E. and Haszeldine, R.S., 1997. Illite dates record fluid movement in petroleum basins, *Petroleum Geoscience*, 3, 133-140.

Deming, D., Cranganu, C. and Lee, Y., 2002. Self-sealing in sedimentary basins, *Journal of Geophysical Research*, v. 107, n. B12, 2329.

Dewhurst, D.N., Aplin, A., Sarda, J.P. and Yang, Y., 1998. Compaction-driven evolution of porosity and permeability in natural mudstones: An experimental study, *Journal of Geophysical Research,* vol. 103, No. B1, p. 651-661.

Dickinson, G., 1953. Geological aspects of abnormal reservoir pressures in Gulf Coast Lousiana, *AAPG Bulletin*, v.37, p. 410-432.

Dore, A.G. and Jensen, L.N., 1996. The impact of late Cenozoic uplift and erosion on hydrocarbon exploration, offshore Norway and some other uplifted basins, *Global and Planetary Change*, 12, no. 1-4, p. 415-436.

Dutta, N.C., 2002. Geopressure prediction using seismic data : Current status and the road ahead, Geophysics, v. 67, no. 6, p. 2012-2041

Eaton, B.A., 1975. The equation for geopressure prediction from well logs, Society of Petroleum Engineers of AIME, *paper SPE 5544*, 11 p.

Engelder, T. and Fisher, M.P. , 1994. Influence of poro-elastic behaviour on the magnitude of minimum horizontal stress, Sh, in overpressured parts of sedimentary basins, *Geology*, vol. 22, p. 949-952.

EPIC, 1994. *Regional study of the Malay Basin – Final Portfolios.*, Esso-PETRONAS Integrated Collaborative Study, Esso Production Malaysia Inc. (unpublished report).

EPMI, 1976. Internal report (unpublished).

Exploration Logging Inc., 1981. Theory and evaluation of formation pressures. *The pressure log reference manual*, 250 p.

Falvey, D.A. and Deighton, I., 1982. Recent advances in burial and thermal geohistory analysis, *Journal of the Australian Petroleum Exploration Society*, v.22, p.65-81.

Fang, H., Sitian, L., Yongchuan, S. and Qiming, Z., 1996. Characteristics and origin of the gas and condensate in the Yinggehai Basin, offshore South China Sea: evidence for effects of overpressure on petroleum generation and migration, *Organic Geochemistry*, vol. 24, No.3, p. 363-375.

Fatt, R.W.H., 1999. Petroleum resources, Peninsular Malaysia. In: Leong, K.M. (ed), *The Petroleum Geology and Resources of Malaysia*, PETRONAS, p. 251-272.

Fertl, W., 1976. *Abnormal formation pressure*, Elsevier Scientific Publishing Company, Amsterdam, 382p.

Fertl, W.H. and Leach, W.G., 1990. Formation temperature and formation pressure affect the oil and gas distribution in Tertiary Gulf Coast sediments, *Gulf Coast Association of Geological Societies*, 40, p. 205-216.

Flemings, P., Comisky, J., Liu, X. and Lupa, J.A., 2001. Stress-controlled porosity in overpressured sands at Bullwinkle (CG65), Deepwater Gulf of Mexico, *Offshore Technology Conference*, Houston, Texas, 30 April-3 May, 2001, OTC paper 13103.

Ford, C.H., Wallace, J.F. and Bellis, R.G., 1980. The occurrence and detection of geopressure in the Malay Basin, *Geological Society of Malaysia,* (Unpublished paper).

Forbes, P.L., Ungerer, P. and Mudford, B.S., 1992. A two-dimensional model of overpressure development and gas accummulation in Venture Field, Eastern Canada. *AAPG Bulletin,* 76, p. 318-338.

Forster and Whelan, 1966. Estimation of formation pressures from electrical surveys, offshore Lousiana, *Journal of Petroleum Technology*, Feb, p. 165-171.

Freed, R.L., and Peacor, D.R., 1989, Geopressured shale and sealing effect of smectite to illite transition: *AAPG Bulletin*, v.73, p. 1223-1232.

Ganesan, B.M.S., 1997, Geology and hydrocarbon potential of the offshore Western Sarawak shelfal area: Proceedings ASCOPE 97 conference, vol.2, p. 131-169.

Gardner, G.H.F., Gardner, L.W. and Gregory, A.R., 1974. Formation velocity and density – the diagnostic basics for stratigraphic traps, *Geophysics*, v. 39, n. 6, p. 770-780.

Giles, M.R, Indrelid, S.L.and James, D.M.D., 1998. Compaction – the great unknown in basin modelling. In: Duppenbecker, S.J. and Illife, J.E. (eds) *Basin Modelling: Practice and Progress*, Geological Society, London, Special Publications, 141, p. 15-43.

Gilham, R., Hardacre, K., van der Velde, J.J., Nicolai, C., Hercus, C., de Haas, W. and Sardar, K., 2003. Shearwater: Managing changing uncertainties through field life, Proceedings of the 6th Conference Petroleum Geology of Northwest Europe. (abstract).

Ginger, D.C., Ardjakusuma, W.O., Hedley, R.J. and Pothecary, J., 1993. Inversion history of the West Natuna Basin: examples from the Cumi-Cumi PSC, *Proceedings of the Indonesian Petroleum Association 22nd Annual Convention*, Jakarta, October 1993, p. 635-658.

Gordon, D.S and P.B.Flemings, 1998. Generation of overpressure and compaction-driven fluid flow in a Plio-Pleistocene growth-faulted basin Eugene Island 330, offshore Louisiana, *Basin Research*, 10, p. 177-196.

Goulty, N.R., 1998. Relationship between porosity and effective stress in shales, *First Break*, p. 413-419.

Goulty, N.R., 2004. Mechanical compaction behaviour of natural clays and implications for pore pressure estimation, *Petroleum Geoscience*, v. 10, p. 73-79.

Gurba, L.W. and Ward, C.R., 1998. Vitrinite reflectance anomalies in the high-volatile bituminous coals of the Gunnedah Basin, New South Wales, Australia. *International Journal of Coal Geology*, 36, p. 111-140.

Halim, M.F.A., 1994. Geothermics of Malaysian sedimentary basins, *Bull. Geol. Soc. Malaysia*, 36, p. 162-174.

Hall, P.L., 1993, Mechanisms of overpressuring : an overview. In Manning, D.A.C., Hall, P.L. and Hughes, C.R. (eds). *Geochemistry of clay-pore fluid interactions*, Chapman & Hall, London, p 265-315.

Hanshaw, B. and Bredehoeft, J., 1968. On the maintenance of anomalous fluid pressures, II. Source layer at depth, *Geol. Soc. Am. Bull.*, 79, p. 1107-1122.

Haq, B.U., Hardenbol, J. and Vail, P.R., 1987. Chronology of fluctuating sea levels since the Triassic, *Science*, 235, p. 1156-1167.

Harrold, T.W.D., 2000. *Porosity and effective stress relationships in mudrocks,* PhD Thesis, University of Durham.

Harrold, T.W.D., R.E. Swarbrick, N.R. Goulty, 1999, Pore pressure estimation from mudrock porosities in Tertiary basins, SE Asia, *AAPG Bulletin*, 83, p. 1057-1067.

Hart, B.S., Flemings, P.B. and Deshpande, A., 1995. Porosity and pressure: role of compaction disequilibrium in the development of geopressures in a Gulf Coast Pleistocene basin, *Geology*, v.23, no.1, p. 45-48.

Haszeldine, R.S., Samson, I.M. and Cornford, C., 1984. Quartz diagenesis and convective fluid movement: Beatrice oilfield, UK, North Sea, *Clay Minerals*, 19, p. 391-402.

He, S., Middleton, M., Kaiko, A., Jiang, C. and Li, M., 2002. Two cases of thermal maturity and thermal modeling within the overpressured Jurassic rocks of the Barrow Sub-basin, North West Shelf of Australia, *Marine and Petroleum Geology*, 19, p. 143-159.

Heasler, H.P. and N.A. Kharitonova, 1996. Analysis of sonic well logs applied to erosion estimates in the Bighorn Basin, Wyoming, *AAPG Bull.* 80, No.5, p. 630-646.

Heng, Y.Y., 1985. Abnormal pressure occurrence in the Malay Basin, Esso Production Malaysia Inc., 165 p, (unpublished report).

Hennig, A., Yassir, N., Addis, M.A. and Warrington, A., 2002. Pore-pressure estimation in an active thrust region and its impact on exploration and drilling. In: Huffman, A.R. and Bowers, G.L. (eds), *Pressures regimes in sedimentary basins and their prediction*, AAPG Memoir 76, p. 89-105.

Heppard, P.D., Cander, H.S. and Eggertson, E.B., 1998. Abnormal pressure and the occurrence of hydrocarbons in offshore Eastern Trinidad, west Indies. In: Law, B.E., Ulmishek, G.F. and Slavin, V.I. (Eds), *Abnormal Pressures in Hydrocarbon Environments*, AAPG Memoir 70, p. 215-246.

Hermanrud, C., 1993. Basin modelling techniques-an overview. In: Dore, A.G. et al. (eds), *Basin Modelling: Advances and Applications*, NPF Special Publication 3, Elsevier, Amsterdam., p1-34.

Hermanrud, C., Wensaas, L., Teige, G.M.G., Vik, E., Nordgas Bolas, H.M. and Hansen, S., 1998. Shale porosities from well logs on Haltenbanken (offshore Mid-Norway) show no influence of overpressuring, in Law, B.E., Ulmishek, G.F., and Slavin, V., (eds), *Abnormal Pressures in Hydrocarbon Environment*, AAPG Memoir 70, p. 65-85.

Hillis, R.R., Thomson, K. and Underhill, J.R., 1994. Quantification of Tertiary erosion in the Inner Moray Firth using sonic velocity data from the Chalk and the Kimmeridge Clay, *Marine and Petroleum Geology*, vol. 11, no. 3, p. 283-293.

Hoesni, M.J. and Abolins, P., 2000. Malay Basin Natural Gases: Classification, distribution and geochemical controls, *AAPG International Conference & Exhibition*, Bali, Indonesia (abstract).

Hoesni, M.J. and Salih, A., 2000. Statistical modelling of reservoir porosity in the Malay Basin. *PRSS internal report* (unpublished).

Holbrook, P.W., Maggiori, D.A. and Hensley, R., 1995. Real-time pore pressure and fracture pressure determination in all sedimentary lithologies, *SPE Formation Evaluation*, December, p. 215-222.

Holm, G.M., 1996, The Central Graben – a dynamic overpressure system. In : Glennie, K.W. and Hurst, A.M. (eds), *AD1995 : NW Europe's Hydrocarbon Industry*, Geological Society of London, p. 107-122.

Hower, J., Eslinger, E.V., Hower, M.E. and Perry, E.A., 1976. Mechanism of burial metamorphism of argillaceous sediment: 1. Mineralogical and chemical evidence, *Bulletin of Geological ociety of America*, v. 87, p. 725-737.

Howes, J.V.C., 1998, The recognition of subtle overpressure offshore NW Java, Indonesia- *Overpressures in petroleum exploration*; Proc. Workshop, Pau, April 1998- Bull. Centre Rech. Elf Explor. Prod., Mem. 22, p.167-172.

Hubbert, M.K. and Rubey, W.W., 1959, Role of fluid pressure in mechanics of overthrust faulting : I, Mechanics of fluid filled porous solids and its application to overthrust faulting : *Geological Society of America Bulletin*, v.70, p 115-166.

Huchon, P., Pichon, X.L. And Rangin, C., 1994. Indochina peninsula and the collision of India and Eurasia, *Geology*, 22, no.1, p. 27-30.

Huffman, A.R. and Bowers, G.L. (eds), 2002. *Pressure Regimes in Sedimentary Basins and their Prediction*, AAPG Memoir 76, 238 p.

Hunt, J.M., J.K. Whelan, L.B. Eglinton, and Cathles III, L.M., 1994. Gas generation - a major cause of deep Gulf Coast overpressure: *Oil and Gas Journal*, v. 92, p59-63.

Hutchison, C.S., Bergman, S.C., Swauger, D.A. and Graves, J.E., 2000. A Miocene collisional belt in north Borneo: uplift mechanism and isostatic adjustment quantified by thermochronology, *Journal of the Geological Society,* London, vol. 157, p. 783-793.

Hutton, A.C. and Cook, A.C., 1980. Influence of alginite on reflectance of vitrinite from Joadja, NSW, and some other coals and oil shales containing alginite. *Fuel*, 59, p. 711-714.

Illife, J.E. and Dawson, M.R., 1996. Basin modelling history and predictions. In: Glennie, K. and Hurst, A. (eds), *AD1995: NW Europe's Hydrocarbon Industry*, Geological Society, London, p. 83-105.

Ismail, M.I., Mohamad, A.M., Ganesan, M.S. and Aziz, S.A., 1994. Geology of Sarawak Deepwater and its surroundings, AAPG International Conference and Exhibition, Kuala Lumpur, August 21-24, 1994 (abstract).

Issler, D.R., 1992, A new approach to shale compaction and stratigraphic restoration, Beaufort-Mackenzie Basin and Beaufort Corridor, Northern Canada: *AAPG Bulletin*, v. 76, p. 1170-1189.

Japsen, P., 1998. Regional velocity-depth anomalies, North sea Chalk: a record of overpressure and Neogene uplift and erosion, *AAPG Bulletin*, v.82, no. 11, p. 2031-2074.

Jensen, R.P. and Dore, A.G., 1993. A recent Norwegian Shelf heating event – fact or fantasy?. In: Dore et al. (eds), *Basin Modelling: Advances and Applications*, NPF Special Publication3, p. 85-106.

Kader, M.S., 1994, Abnormal pressure occurrence in the Malay and Penyu basins, offshore Peninsular Malaysia-a regional understanding, *Bulletin Geological Society of Malaysia*, 36, p. 81-91.

Katsube, T.J.B., Mudford, B.S. and Best, M.E., 1991. Petrophysical characteristics of shales from the Scotian Shelf, *Geophysics*, v. 56, no. 10, p. 1681-1688.

Kho, S.C., Hemmings, D. and Have, T.T., 1994. Overpressures in the Baram Field, offshore Sarawak, East Malaysia, *AAPG International Conference and Exhibition*, Kuala Lumpur, Malaysia, August 21-24, 1994 (abstract).

Khorasani, G.G. and Michelsen, J.K., 1994. The effects of overpressure, lithology, chemistry and heating rate on vitrinite reflectance evolution, and its relationship with oil generation, *APEA Journal*, p. 418-435.

Kingston, D.R., Dishroon, C.P. and Williams, P.A., 1983. Global basin classification system, *AAPG Bull.*, 67, p. 2175-2193.

Ko, J. and Hesse, R., 1992. Shale compaction and illite/smectite diagenesis, Beaufort-Mackenzie Basin, Arctic Canada, *AAPG Annual Meeting*, Calgary, Alberta, June 22-25, 1992 (abstract).

Kooi, H., 1997. Insufficiency of compaction disequilibrium as the sole cause of high pore fluid pressures in pre-Cenozoic sediments, *Basin Research*, 9, p 227-241.

Lahann, R., 2002. Impact of smectite diagenesis on compaction modeling and compaction equilibrium . In: Huffman, A.R. and Bowers, G.L. (eds), *Pressure Regimes in Sedimentary Basins and Their Prediction*, AAPG Memoir 76, p. 61-72.

Lahann, R.W., McCarty, D.K. and Hsieh, J.C.C, 2001. Influence of clay diagenesis on shale velocities and fluid-pressure. *Offshore Technology Conference*, Houston, Texas, paper OTC 13046.

Lander, R.H., 1998. Effect of sandstone diagenesis on fluid overpressure development, *AAPG Annual Meeting*, Salt Lake City, Utah, May 17-20, 1998 (abstract).

Law, B.E. and Spencer, C.W., 1998. Abnormal pressure in hydrocarbon environments. In: Law, B.E., Ulmishek, G.F. and Slavins, V.I. (eds), Abnormal Pressures in Hydrocarbon Environments, *AAPG Memoir 70*, p. 1-11.

Law, B.E., Ulmishek, G.F. and Slavins, V.I. (eds), 1998. *Abnormal Pressures in Hydrocarbon Environments*, AAPG Memoir 70.

Leach, W.G., 1994. Distribution of hydrocarbons in abnormal pressure in South Lousiana, U.S.A. In: Fertl, W.H., Chapman, R.E., and Hotz, R.F., (eds), *Studies in Abnormal Pressures*, Elsevier.

Lee, Y. and Deming, D., 2002. Overpressures in the Anardako basin, southwestern Oklahoma: static or dynamic?, *AAPG Bulletin*, v. 86, no. 1, p. 145-160.

Leslie, W.C., Kadir, M.K.A., Ghani, M.A., Kader, A.S., Zakaria, A.A., Abdullah, C.S.H. and Daud, R., 1994. Malay and Penyu Basins Regional Study 1992-1994. PETRONAS Carigali, 4 volumes, Unpublished report.

Liu, G. and Roaldset, E., 1994. A new decompaction model and its application to the northern North Sea, *First Break*, v. 12, p. 81-89.

Lubanzadio, M., Goulty, N.R. and SDwarbrick, R.E., 2002. Variation of velocity with effective stress in chalk; null result from North Sea well data, *Marine and Petroleum Geology,* 19, no. 8, p. 921-927.

Luo, M., Baker, M.R. and LeMone, D.V., 1994. Distribution and generation of the overpressure system, eastern Delaware basin, western Texas and southern New Mexico, *AAPG Bull.*, v.78, p. 1386-1405.

Madon, M., Abolins, P., Hoesni, M.J. and Ahmad, M.B., 1999a. Malay Basin. In: Leong, K.M. (ed), *The Petroleum Geology and Resources of Malaysia*, PETRONAS, p. 171-217.

Madon, M., Karim, R.A. and Fatt, R.W.H., 1999b. Tertiary stratigraphy and correlation schemes. In: Leong, K.M. (ed), *The Petroleum Geology and Resources of Malaysia*, PETRONAS, p. 115-137.

Madon, M.B. and Watts, A.B., 1998. Gravity anomalies , subsidence history and the tectonic evolution of the Malay and Penyu basins, *Basin Research*, 10, p. 375-392.

Magara, K., 1993. Pressure sealing: an important agent for hydrocarbon entrapment. *Journal of Petroleum Science and Engineering*, v. 9, p. 67-80.

Magara, K., 1976. Thickness of removed sedimentary rocks, paleopressure and paleotemperature, southwestern part of Western Canada basin, *AAPG Bulletin*, v. 60, p 554-566.

Magoon, L.B. and Dow, W.G., 1994. The petroleum system. In: Magoon, L.B. and Dow, W.G. (eds), *The Petroleum System-From Source To Trap*, AAPG Memoir 60, p. 3-24.

Mahmud, O.A.B and Saleh, S.B., 1999. Petroleum resources , Sarawak. In: Leong, K.M. (ed), *The Petroleum Geology and Resources of Malaysia*, PETRONAS, p. 453-472.

Mantaring, A., Matsuda, F. and Okamoto, M., 1994. Analysis of overpressure zones at the southern margin of the Baram Delta Province and their implications to hydrocarbon expulsion, migration and entrapment, *AAPG International Conference and Exhibition*, Kuala Lumpur, August 21-24, 1994 (abstract).

Marco-Toledo, Stumpf, V.J. and Neto, F.F.L., 1998. Regional rules of overpressure rift compartments in Campos Basin, *AAPG Bull.* 82, p. 1883-1884 (abstract).

Matthews, J.C., Helset, H.M. and Lander, R.H., 2000. Rates of pore volume loss in shales due to chemical compaction: implications for fluid pressures, presented at *AAPG International Conference and Exhibition, Bali, Indonesia*, October 15-18,

2000 (Abstract).

Mavko, G., Mukerji, T. and Dvorkin, J., 1998. *The rock physics handbook: tools for seismic analysis in porous media*, Cambridge University Press, 329 p.

McBride, B.C., Weimer, P. and Rowan, M.G., 1998. The effect of allochthonous salt on the petroleum systems of northern Green Canyon and Ewing Bank (offshore Louisiana), northern Gulf of Mexico, *AAPG Bull.*, v. 82, p. 1083-1112.

McCabe, P.J., Ryder, R.T. and Bishop, M.G., 2000. U.S. Geological Survey region 3 Asia Pacific – assessment summary. (http://pubs.ussgs.gov/dds/dds-060/).

McCaffrey, M.A, Abolins, P., Hoesni, M.J. and Huizinga, B.J., 1998. Geochemical characterisation of Malay Basin oils: some insight into effective petroleum systems, *Proceedings: 9th Regional Congress on Geology, Mineral and Energy Resources of Southeast Asia-GEOSEA '98* (abstract).

McKenzie, D., 1978. Some remarks on the development of sedimentary basins, *Earth Planet. Sci. Letts.*, 40, p. 25-32.

McTavish, R.A., 1978. Pressure retardation of vitrinite diagenesis, offshore Northwest Europe, *Nature*, 271, p. 648-650.

McTavish, R.A., 1998. The role of overpressure in the retardation of organic matter maturation, *Journal of Petroleum Geology*, 21, p. 153-186.

Meissner, F.F., 1978. Petroleum geology of the Bakken Formation, Williston Basin, North Dakota and Montana: *Proceedings of 1978 Williston Basin Symposium*, September24-27, Montana Geological Society, Billings, p. 207-227.

Metivier, F., Gaudemer, Y., Tapponier, P. and Klein, M., 1999. Mass accumulation rates in Asia during the Cenozoic, *Geophysical Journal International*, 137, p. 280-318.

Mitchell, A. and Grauls, D. (eds), 1998. Overpressures in petroleum exploration, Workshop proceedings, Bull. Centre Rech. Elf Explor. Prod., Memoir 22, 249 p.

Moretti, I., 1998. The role of faults in hydrocarbon migration, *Petroleum Geoscience,* v. 4, p. 81-94.

Morley, C.K., 2001. Combined escape tectonics and subduction rollback-back arc extension: a model for the evolution of Tertiary rift basins in Thailand, Malaysia and Laos, *J. Geol. Soc of London*, 158, p. 461-474.

Mouchet, J.P. and Mitchell, A., 1989, *Abnormal Pressures While Drilling. Manuels Techniques 2* , Elf Aquitaine pp. 287.

Mudford, B.S., 1988. Modeling the occurrence of overpressure on the Scotian Shelf, Offshore Eastern Canada, *Journal of Geophysical Research*, vol. 93, No. B7, p. 7845-7855.

Mudford, B.S. and Best, M.E., 1989. Venture gas field, offshore Nova Scotia: case study of overpressuring in region of low sedimentation rate, *AAPG Bulletin*, v.73, no. 11, p. 1383-1396.

Murphy, R.W., 1989. Inversion tectonics – a discussion. *Geological Society of London Special Publication,* 44, 336-337.

Nadeau, P.H., Peacor, D.R., Yan, J. and Hillier, S., 2002. I-S precipitation in pore space as the cause of geopressuring in Mesozoic mudstones, Egersund Basin, Norwegian continental shelf, *American Mineralogist*, v. 87, p. 1580-1589.

Nagao, T. and Uyeda, S., 1995. Heat-flow distribution in Southeast Asia with consideration of volcanic heat, *Tectonophysics,* p. 153-159.

Neuzil, C.E. (1994). How permeable are the clays and shales? *Water Resour. Res.*, 30, p. 145-150.

Ngah, K., 1990. Deposition and diagenesis of Oligocene-Lower Miocene sandstones in the southern Malay Basin, unpublished Ph.D. Thesis, University of London.

Ngah, K., Madon, M. and Tjia, H.D., 1996. Role of pre-Tertiary fractures in formation and development of the Malay and Penyu basins. In: Hall, R. and Blundell, D. (eds) *Tectonic Evolution of Southeast Asia*, Geol. Soc. Special Pub., No. 106, p. 281-289.

Norwegian Petroleum Directorate, 2004. Exploration wellbore: 6406/2-6. (http://www.npd.no/engelsk/cwi/pbl/en/wdss_index.htm).

Nygard, R., Gutierrez, M., Gautam, R and Hoeg, K., 2004. Compaction behaviour of argillaceous sediments as function of diagenesis, *Marine and Petroleum Geology*, p. 349-362.

O'Brien, N.R. and Slatt, R.M., 1990. *Argillaceous rock atlas*, Springer, 141 p.

O'Connell, J.K., Kohli, M. and Amos, S., 1993. Bullwinkle: A unique 3-D experiment, *Geophysics*, v. 58, No. 1, p. 167-176.

Osborne, M.J. and Swarbrick, R.E., 1997. Mechanisms for generating overpressure in sedimentary basins: a reevaluation, *AAPG Bulletin*, v. 81, No. 6, p. 1023-1041.

Osborne, M.J. and Swarbrick, R.E., 1999. Diagenesis in North Sea HPHT clastics reservoirs – consequences for porosity and overpressure prediction, *Marine and Petroleum Geology*, 16, p. 337-353.

Peters, K.E. and Cassa, M.R., 1994. Applied source rock geochemistry. In: Magoon, L.B. and Dow, W.G. (eds). The Petroleum System – From Source To Trap, *AAPG Memoir 60*, p. 93-117.

PETRONAS, 1999. *The Petroleum Geology and Resources of Malaysia,* , 655p.

Poelchau, H.S., 2001. Modeling an exhumed basin: a method for estimating eroded overburden, *Natural Resources Research*, vol. 10, no.1, p. 73-84.

Powers, M., 1967. Fluid release mechanisms in compacting marine mudrocks and their importance in oil exploration, *AAPG Bull.*, 51, p. 1240-1254.

Price, L.C. and Barker, C.E., 1985. Suppression of vitrinite reflectance in amorphous rich kerogen – a major unrecognized problem. *Journal of Petroleum Geology*, 8, p. 59-84.

Price, L.C. and Wenger, L.M., 1992. The influence of pressure on petroleum generation and maturation as suggested by aqueous pyrolysis, *Organic Geochemistry*, 19, p. 141-159.

Ramli, M.N., 1988. Stratigraphy and paleofacies development of Carigali's operating areas in the Malay Basin, South China Sea, *Bulletin Geological Society of Malaysia*, 22, p. 153-187.

Revil, A., Cathles III, L.M., Shosa, J.D., Pezard, P.A. and de Larouziere, F.D., 1998. Capillary sealing in sedimentary basins: A clear field example, *Geophysical Research Letters*, v. 25, no. 3, p. 389-392.

Rieke, H.H. III and Chilingarian, G.V., 1974. *Compaction of Argillaceous Sediments,* Developments in Sedimentology 16, Elsevier, Amsterdam.

Rubey, W.W. and Hubbert, M.K., 1959. Role of fluid pressure in mechanics of overthrust faulting, II: *Geological Society of America Bulletin*, v. 70, p. 166-205.

Sandal, S.T. (ed), 1996. The geology and hydrocarbon resources of Negara Brunei Darussalam, Brunei Shell Petroleum Company Sendirian Berhad and Brunei Museum, , Bandar Seri Begawan, 243 pp.

Scherer, F.C., 1980. Exploration in East Malaysia over past decade. In: Halbouty, M.T. (ed). Giant Oil and Gas Fields of the Decade 1968-1978. AAPG Memoir 30, p. 423-440.

Schimdt, G., 1973. Interstitial water composition and geochemistry of deep Gulf Coast shales and sandstones, *AAPG Bull.*, 57, p. 321-337.

Schneider, F. and Hay, S., 2001. Compaction model for quartzose sandstones application to the Garn Formation, Haltenbanken, Mid-Norwegian Continental Shelf, *Marine and Petroleum Geology*, 18, p. 833-848.

Schneider, F., Nadeau, P. and Hay, S., 2003. Model of shale permeability as a function of the temperature. Application to Mesozoic mudstones, Egersund Basin, Norwegian Continental Shelf, EAGE 65th Conference & exhibition, Stavanger, Norway, 2-5 June 2003.

Schneider, F., Potdevin, J.L., Wolf, S. and Faille, I., 1996. Mechanical and chemical compaction model for sedimentary basin simulators, *Tectonophysics*, 263, p. 307-317.

Schneider, F.J., Burrus, J. and Wolf, S., 1993. Modeling overpressure by effective-stress/porosity relationships in low-permeability rocks: Empirical artiface or physical reality?, in Dore, A.G., Augustson, J.H., Hermanrud, C., Stewart, D.J., and Sylta, O., (eds), *Basin Modelling: Advances, and Applications*, Norwegian Petroleum Society Special Publication 3, p. 333-341.

Sheldon, H.A. and Wheeler, J., 2003. Influence of pore fluid chemistry on the state of stress in sedimentary basins, *Geology*, v. 31, no. 1, p. 59-62.

Singh, I. and Ford, C.H., 1982, The occurrence, causes and detection of abnormal pressure in the Malay Basin, *Offshore South East Asia 82 Conference*, Singapore, p. 9-12.

Skar, T., van Balen, R. and Hansen, S., 1998. Overpressuring in Cretaceous shales on the Halten Terrace, offshore mid-Norway: nature and causes, Overpressures in Petroleum Exploration, Proceeding Workshop, Pau, 1998, *Bull. Centre Rech. Elf Explor. Prod., Mem.* 22, p. 69-75.

Skempton, A.W., 1970. The consolidationof clays by gravitational compaction, *Journal of the Geological Society of London*, 125, p. 373-411.

Slavin, V.I. and Smirnova, E.M, 1998. Abnormally high formation pressures: origin, prediction, hydrocarbon field development, and ecological problems, In: Law, B.E., Ulmishek, G.F. and Slavin, V.I. (eds) *Abnormal Pressures in Hydrocarbon Environments*, AAPG Memoir 70, p. 105-114.

Spencer, C. W., 1987, Hydrocarbon generation as a mechanism for overpressuring in Rocky-Mountain region: *AAPG Bulletin*, v. 71, p. 368-388.

Stump, B.B., Flemings, P.B., Finkbeiner, T. and Zoback, M.D., 1998. Pressure differences between overpressured sands and bounding shales of the Eugene Island 330 field (offshore Lousiana, USA) with implications for fluid flow induced by sediment loading. In: Mitchell, A. and Grauls, D., (eds*), Overpressure in Petroleum Exploration,* Proc. Workshop, Pau, April 1998, Bull. Centre Rech. Elf Explor. Prod., Mem. 22, p. 83-92.

Swarbrick, R.E., 2002. Challenges of porosity-based pore pressure prediction, *CSEG Recorder*, p.74-77.

Swarbrick, R.E., and Osborne, M., 1996, The nature and diversity of pressure transition zones*: Petroleum Geoscience*, v. 2, p. 111-116.

Swarbrick, R.E., and Osborne, M., 1998, Mechanisms that generate abnormal pressures: an overview, In: Law, B.E, Ulmishek, G.F. and Slavin, V.I. (eds), *Abnormal Pressures in Hydrocarbon Environments*, AAPG Memoir 70, AAPG, Tulsa, p. 13-34.

Swarbrick, R.E., Osborne, M.J. and Yardley, G.S., 2002. Comparison of overpressure magnitude resulting from the main generating mechanisms,. In: Huffman, A.R. and Bowers, G.L. (eds), Pressure regimes in sedimentary basins and their prediction: *AAPG Memoir 76*, p. 1-12.

Tada, R. and Siever, R., 1989. Pressure solution during diagenesis, *Ann. Rev. Earth Planet Sci*, 17, p. 89-118.

Tan, D.N.K., Rahman, A.H.A, Anuar, A., Bait, B. and Tho, C.K., 1999. West Baram Delta. . In: Leong, K.M. (ed), *The Petroleum Geology and Resources of Malaysia*, PETRONAS, p. 291-341.

Tapponier, P., Peltzer, G. and Armijo, R., 1986. On the mechanics of the collision between India and Asia, in Collision Tectonics. In: Coward, M.P. and Ries, A., *CollisionTectonics, Geol. Soc. Spec. Publ.*, 19, p.115-157.

Tapponier, P., Peltzer, G., Le Dain, A.Y., Armijo, R. and Cobbold, P. 1982. in Asia: new insights from simple experiments with plasticine, 10, p. 611-616.

Tenthorey, E., Scholtz, C.H., Aharonov, E. and Leger, A., 1998. Precipitation sealing and diagenesis- 1. Experimental results, *J. Geophyical. Research. B* 103, p. 23951-23967.

Thyne, G., 2001. A model for diagenetic mass transfer between adjacent sandstone and shale, *Marine and Petroleum Geology*, 18, p. 743-755.

Tigert, V. and Al-Shaieb, Z., 1990. Pressure seals – their diagenetic banding-patterns, *Earth-Science Reviews*, v. 29, p. 227-240.

Tingay, M.R.P., Hillis, R.R., Swarbrick, R.E., Mildren, S.D., Morley, C.K. and Okpere, E.C., 2000. The sonic and density log expression of overpressure in B runei Darussalam. In: Overpressure 2000 Workshop Proceeding, Drilling and Exploiting Overpressured Reservoirs, A Research Workshop for the Millenium, London, U.K., 4-6th April, 2000.

Tjia, H.D., 1994. Origin and tectonic development of Malay-Penyu-West Natuna basisn. In: PETRONAS Research & Scientific Services "Research for Business Excellence Seminar", Kuala Lumpur, 20-21 June 1994.

Tjia, H.D. and Liew, K.K., 1996. Changes in tectonic stress field in northern Sunda Shelf basins. In: Hall, R. and Blundell, D.J. (eds), *Tectonic Evolution of Southeast Asia*, Geological Society of London Special Publication, 106, p. 291-306.

Torre, M.D., Mahlman, R.F. and Ernst, W.G., 1997. Experimental study on the pressure dependance of vitrinite maturation. *Geochimica et Cosmochimica Acta*, 61, p.2921-2928.

Toxopeus, J.M.A.B., 1983. Selection criteria for the use of vitrinite reflectance as a maturity tool. In: Brooks, J (ed), *Petroleum Geochemistry and Exploration of Europe*. Geol. Soc. London Special Publication, 12, p. 295-307.

Traugott, M., 1996. The pore pressure Centroid Concept: reducing drilling risks. In: *Compaction and Overpressure Current Research*, 9-10 December, IFP, Paris (abstract).

Traugott, M., 1997. Pore/fracture pressure determinations in deep water, *Deepwater Technology Supplement to World Oil*, p. 68-70.

Trevena, A.S. and Clark, R.A., 1986. Diagenesis of sandstone reservoirs in the Pattani Basin, Gulf of Thailand, *AAPG Bull.*, 70, p. 299-308.

Ungerer, P., Burrus , J., Doligez, B., Chenet, P.Y. and Bessis,1990.Basin evaluation by integrated two-dimensional modelling of heat transfer, fluid flow, hydrocarbon generation, and migration, AAPG Bull, v. 74, No. 3, p. 309-335.

van Ruth, P., Hillis, R., Tingate, P. and Swarbrick, R., 2003. The origin of overpressure in 'old' sedimentary basins: an example from the Cooper Basin, Australia, *Geofluids*, 3, p. 125-131.

Van Ruth, P.J., Hillis, R.R. and Swarbrick, R.E., 2000. Mudweights, transient pressure tests, and the distribution of overpressure in the North West Shelf, Australia, *PESA Journal*, 28, p. 59-66.

Vandenbroucke, M., Behar, F. and Rudkiewicz, J.L., 1999. Kinetic modelling of petroleum formation and cracking: implications from the high pressure/high temperature Elgin Field (UK, North Sea), *Organic Geochemistry*, 30, p. 1105-1125.

Vik, E. and Hermanrud, C., 1993. Transient thermal effects of rapid subsidence in the Haltenbanken area. In: Dore et al. (eds), *Basin Modelling: Advances and Applications*, NPF Special Publication3, p. 107-117.

Waples, D.W. and A. Okui, 1992. Overpressuring and hydrocarbon expulsion, *AAPG Annual Meeting (Abstract)*, v.76, p. 137.

Waples, D. and Ramly, M., 1996. Geochemistry of gases in the Malay Basin, *Bulletin of the Geological Society of Malaysia*, 39, p. 241-258.

Waples, D.W. and Ramly, M., 1994. A simple statistical method for correcting and standardizing heat flows and subsurface temperatures derived from log and test data, *Bulletin of the Geological Society of Malaysia*, 37.

Waples, D.W., Ramly, M. and Leslie, W., 1995. Implications of vitrinite reflectance suppression for the tectonic and thermal history of the Malay Basin. AAPG International Conference & Exhibition, Kuala Lumpur, Malaysia, August 21-24, 1994. *Bulletin of the Geological Society of Malaysia*, 37, p. 269-284.

Ward, C.D., Coghill, K. and Broussard, M.D., 1994, The application of petrophysical data to improve pore and fracture pressure determination in North Sea Central Graben HPHT wells, *Presented at the SPE 69th Annual Technical Conference and Exhibition New Orleans*, LA. SPE 28297.

Wensaas, L., Shaw, H.F., Gibbons, K. Aagaard, P and Dypvik, H., 1994. Nature and causes of overpressuring in the mudrocks of the Gulfaks area, North Sea, *Clay Miner*als, v. 29, p. 439-449.

Weyl, P.K., 1959. Pressure solution and the force of crystallization: A phenomenological theory: *Journal of Geophysical Research* - Solid Earth, v. 64, p. 2001-2025.

White, A.J., Traugott, M.O. and Swarbrick, R.E., 2002. The use of leak-off tests as means of predicting minimum in-situ stress, *Petroleum Geoscience*, vol. 8, p. 189-193.

Wilkins, R.W.T., Wilmshurst, J.R., Rusell, N.J., Hladky, G., Ellacott, M.V. and Buckingham, C., 1992. Fluorescence alteration and the suppression of vitrinite reflectance. *Organic Geochemistry*, 18, p. 629-640.

Worden, R.H., Mayall, M.J. and Evans, I.J., 1997. Predicting reservoir quality during exploration: lithic grains, porosity and permeability in Tertiary clastic rocks of the South China Sea basin. In: Fraser, A.J., Matthews, S.J. and Murphy, R.W. (eds), *Petroleum Geology of Southeast Asia*, Geological Society Special Publication, No. 126, p. 107.

Yakzan, A.M., Harun, A, Nasib, B.M. and Morley, R.J., 1994. Integrated biostratigraphic zonation for the Malay Basin. Abstracts of AAPG International Conference & Exhibition, Kuala Lumpur, Malaysia, August 21-24, 1994, *AAPG Bull,* 78, p. 1170-1171.

Yang, Y. and Aplin, A.C., 1998. Influence of lithology and compaction on the pore size distribution and modelling permeability of some mudstones from the Norwegian margin, *Marine and Petroleum Geology*, 15, p. 163-175.

Yang, Y., Aplin, A.C. and Larter, S.R., 2004. Quantitative assessment of mudstone lithology using geophysical wireline logs and artificial neural networks, *Petroleum Geoscience*, vol. 10, p. 141-151.

Yardley, G., 1998, Can lateral transfer explain the high pressures in the Central North Sea? - Overpressures in petroleum exploration; Proc. Workshop, Pau, April 1998- Bull. Centre Rech. Elf Explor. Prod., Mem. 22, p. 201-206.

Yardley, G.S and Swarbrick, R.E., 2000. Lateral transfer: a source of additional overpressure? *Marine and Petroleum Geology*, v. 17, p. 523-537.

Yassir, N.A. and Bell, J.S., 1996. Abnormally high fluid pressures and associated and stress regimes in sedimentary basins, *SPE*, 48, 3, p. 5-10.

Yusoff, W.I.W., 1984. Heat flow study in the Malay Basin, CCOP Technical Publication, 15, p. 77-87.

Yusoff, W.I.W., 1993. Geothermics of the Malay Basin, offshore Malaysia, M.Sc. thesis, University of Durham, 213 pp,. (Unpublished).

Zainul, A.J.B., Misman, R.B. an Ali, A.J.B., 1999. Overview of petroleum resources of Malaysia. In: Leong, K.M. (ed), *The Petroleum Geology and Resources of Malaysia*, PETRONAS, p. 33-58.

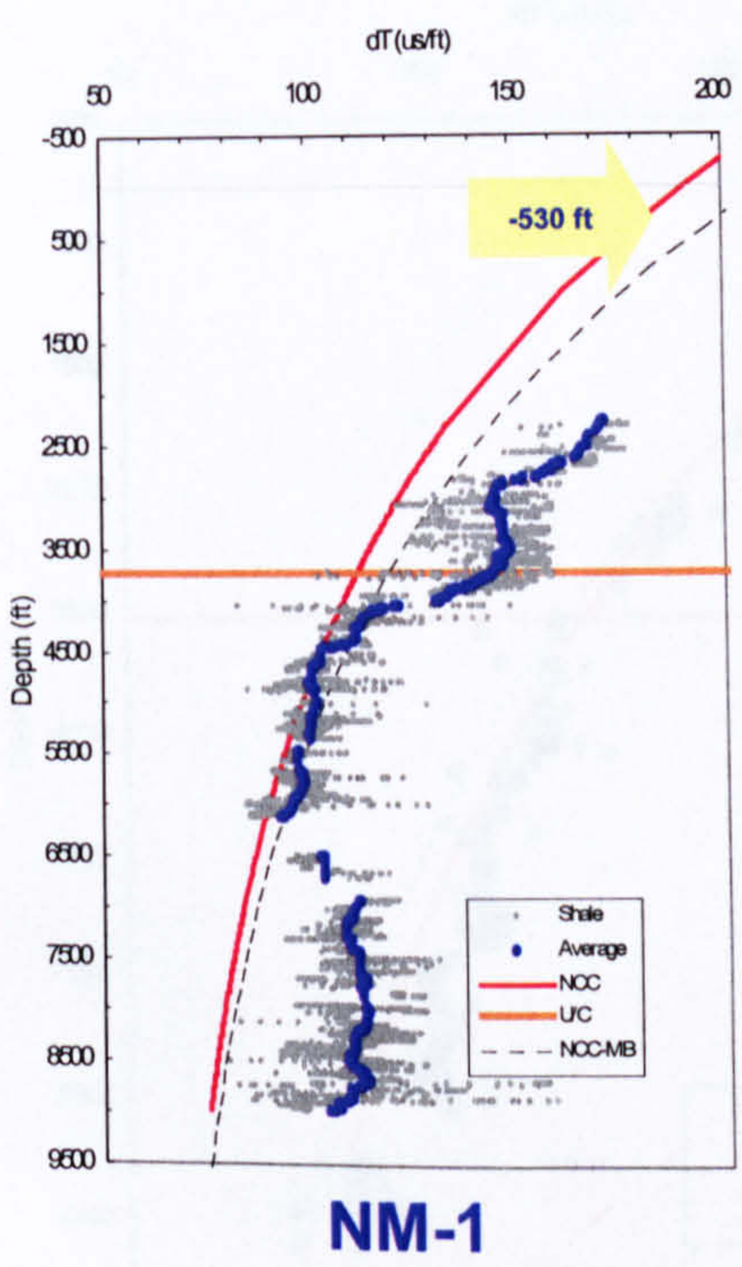
Zaunbrecher, M.L., 1994. Oil and gas accumulations of the offshore Barrow and Exmouth sub-basins – trends in hydrocarbon habitat. In: Purcell, P.G. and Purcell, R.R. (eds), The Sedimentary Basins of Western Australia, *Proceedings West Australian Basins Symposium, Perth, Western Australia*, p. 449-458.

Zou, Y-R. and Peng, P., 2001. Overpressure retardation of organic-matter maturation: a kinetic model and its application, *Marine and Petroleum Geology*, 18, p. 707-713.

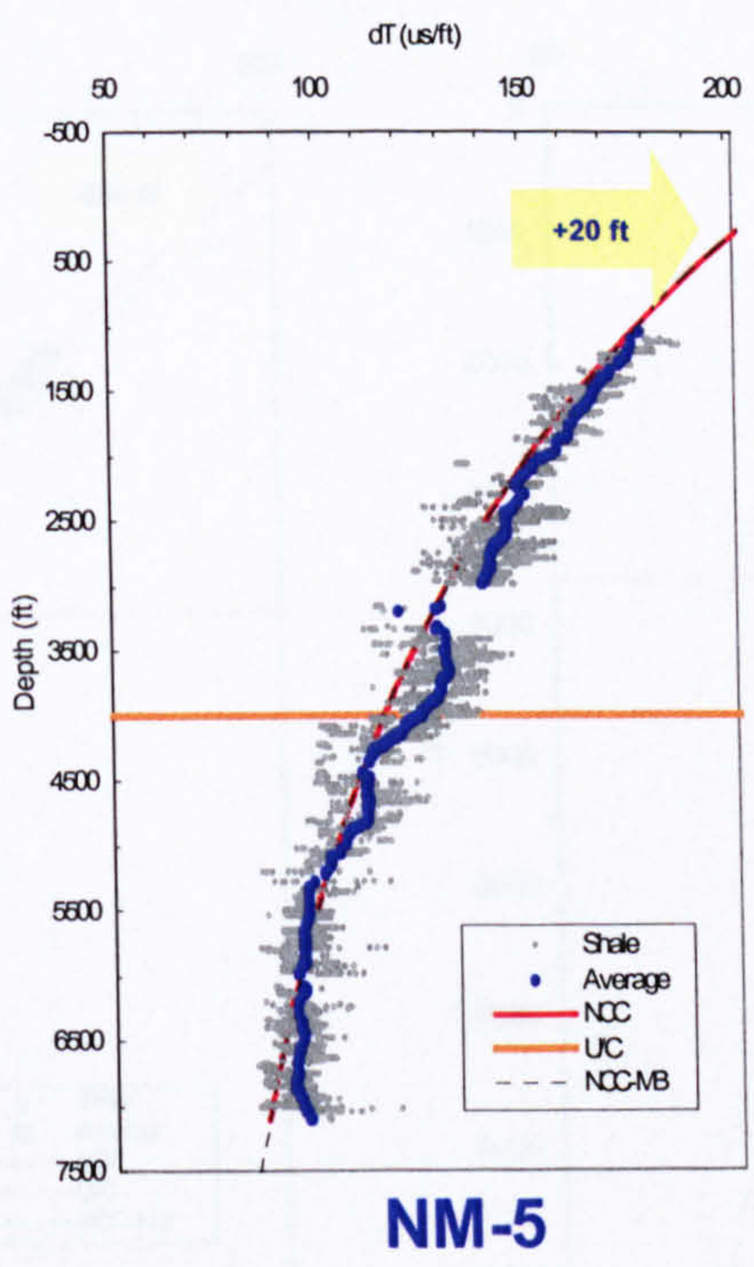
Appendix A:

Erosion Estimation from Sonic Logs

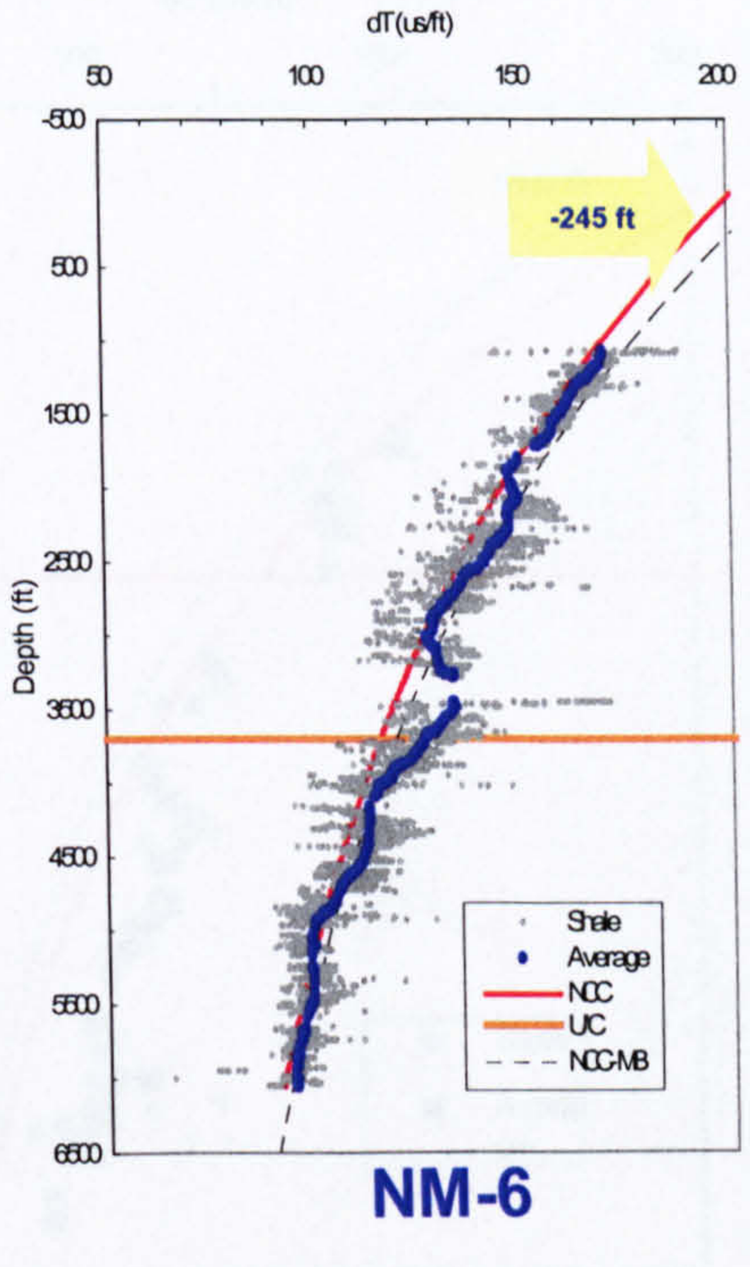
North Malay



NM-1

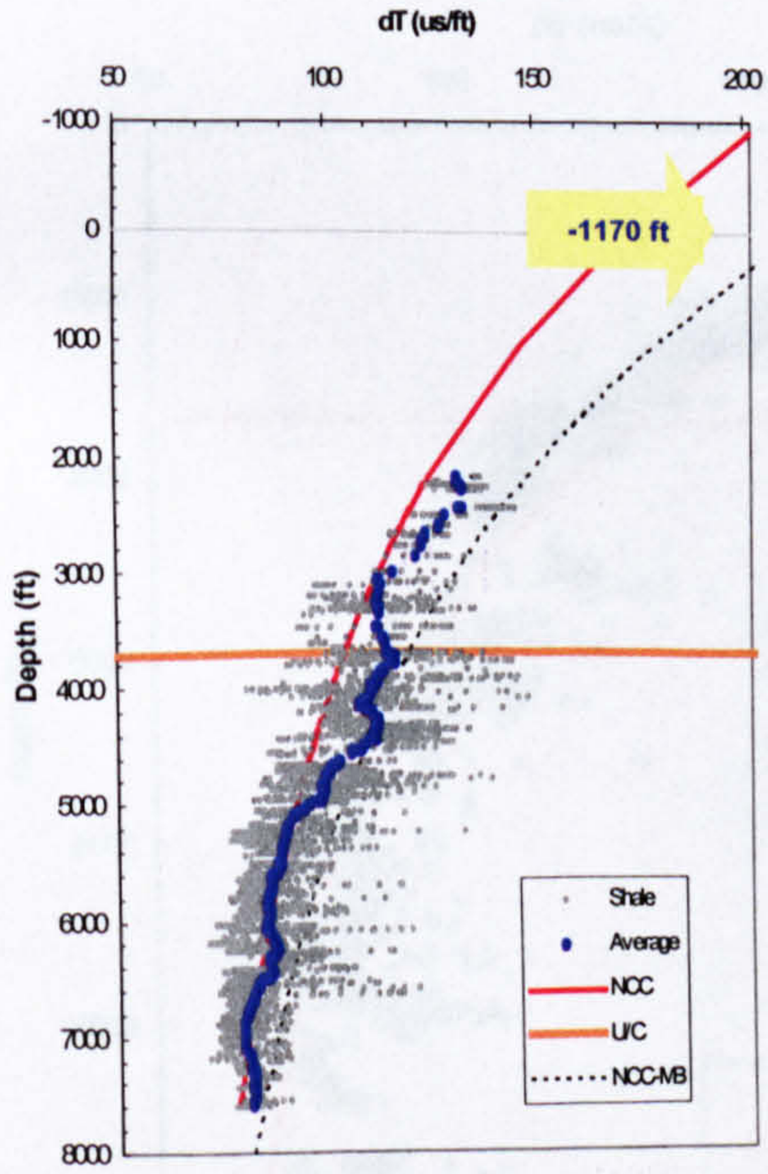


NM-5

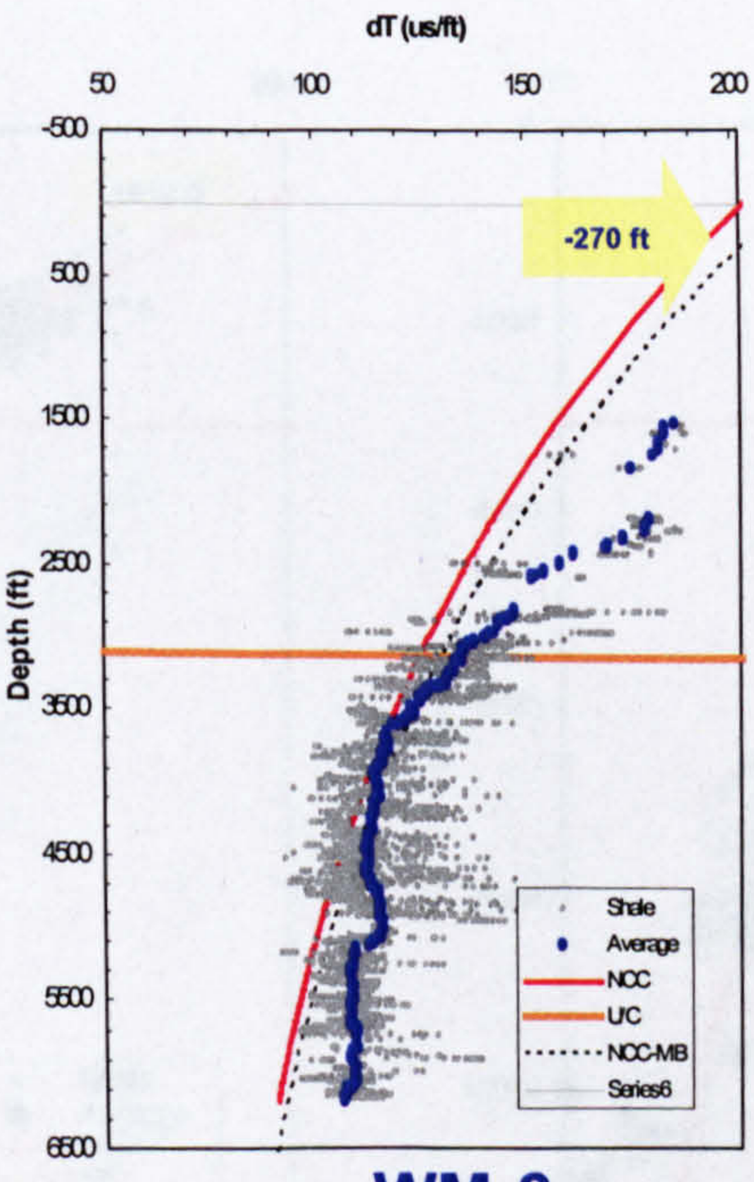


NM-6

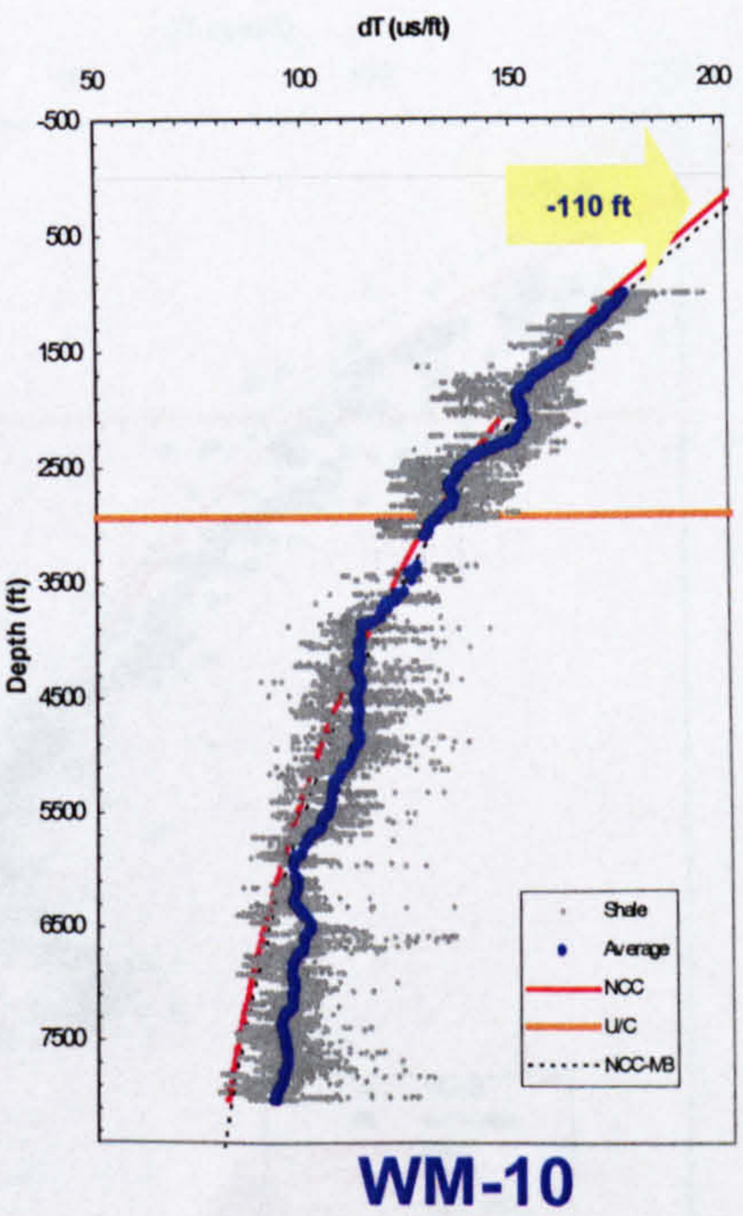
West Malay



WM-7

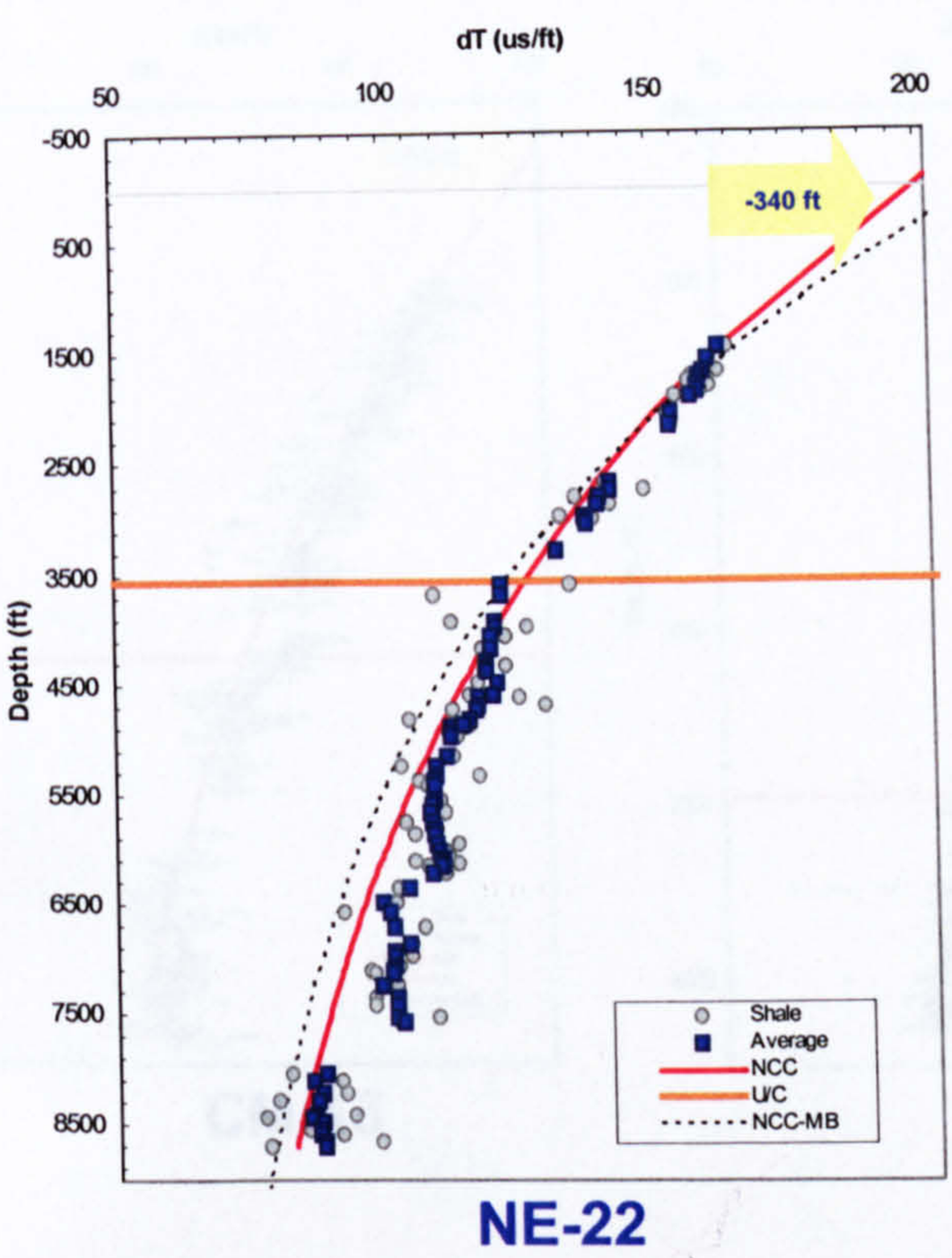


WM-8

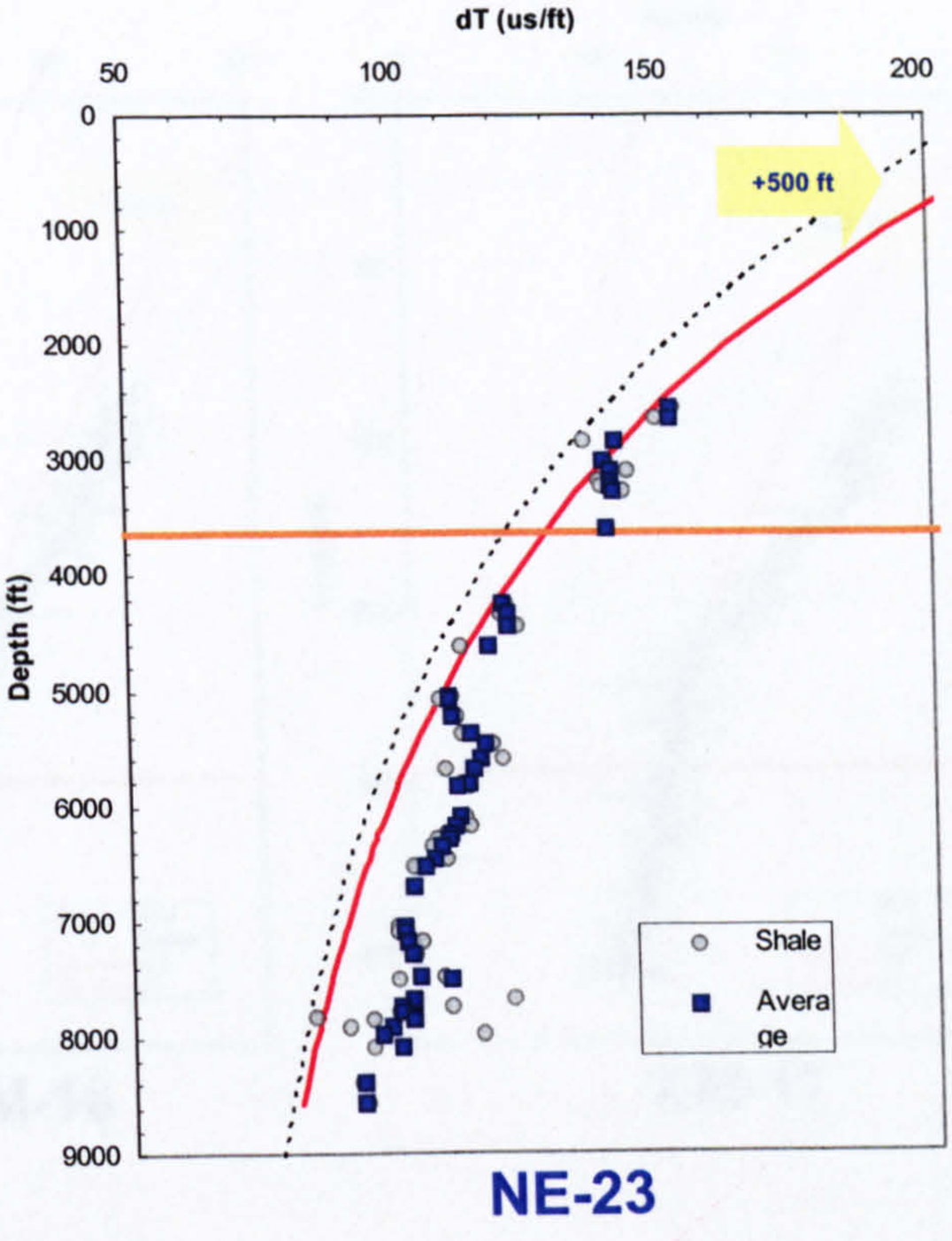


WM-10

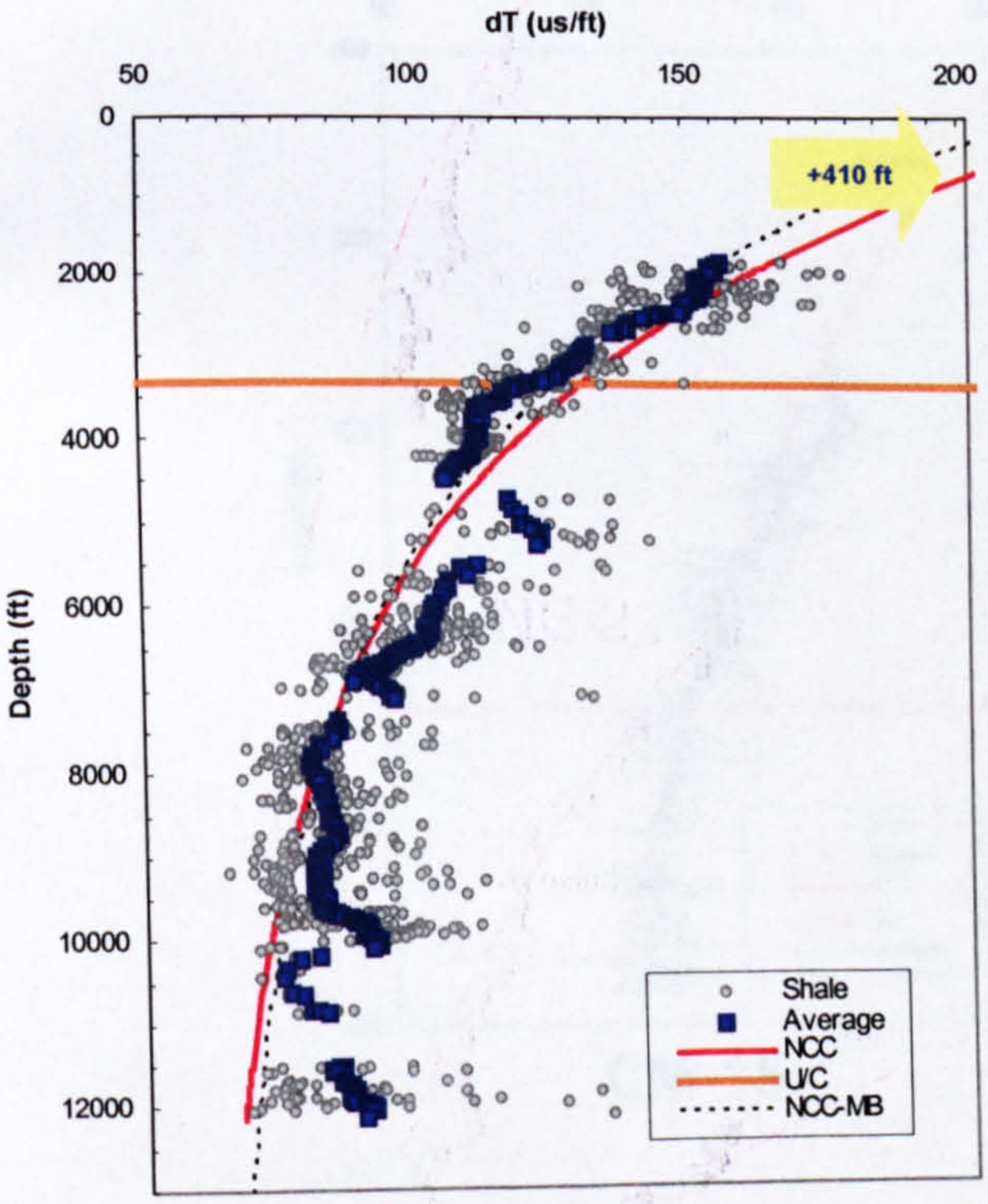
NE Malay



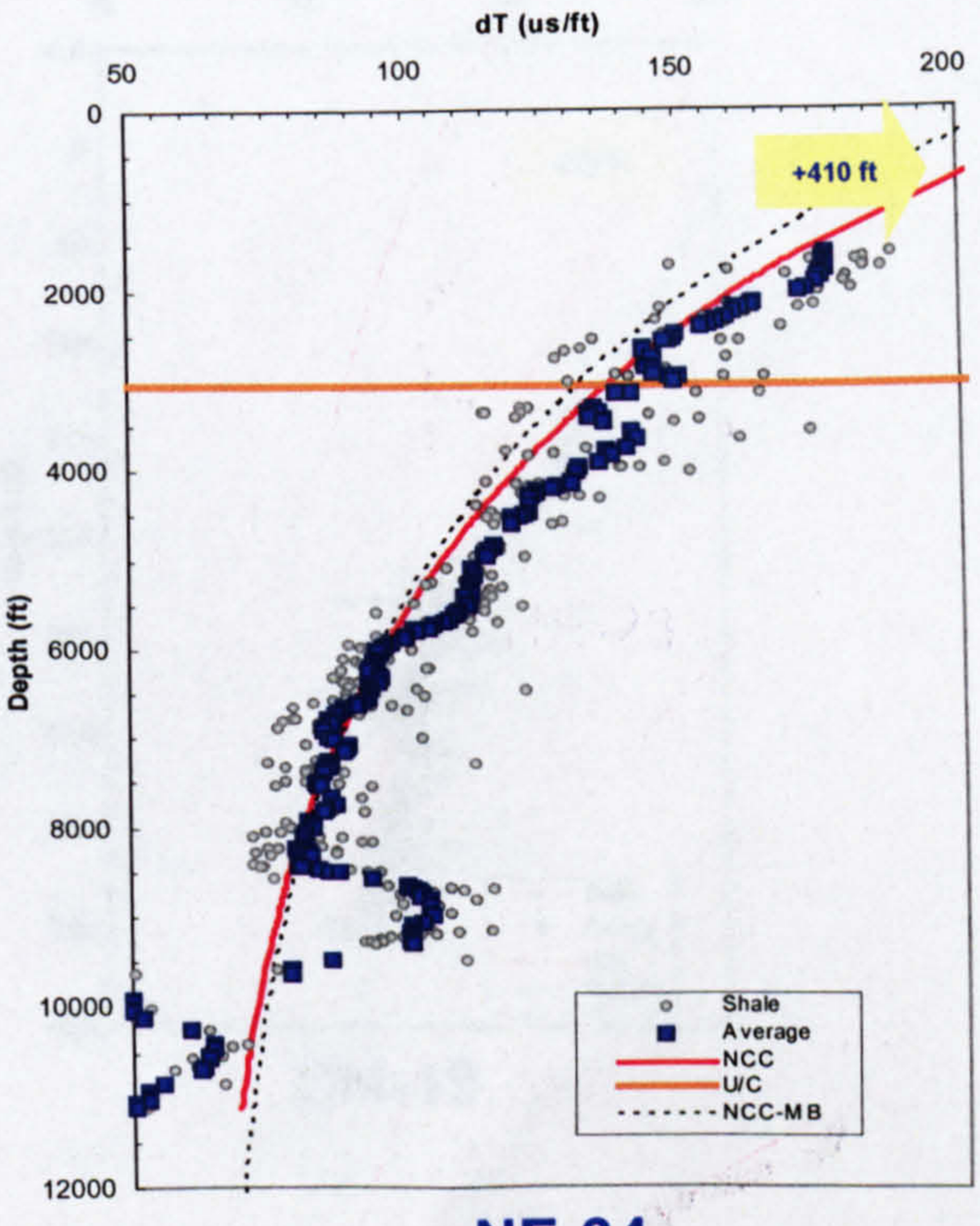
NE-22



NE-23

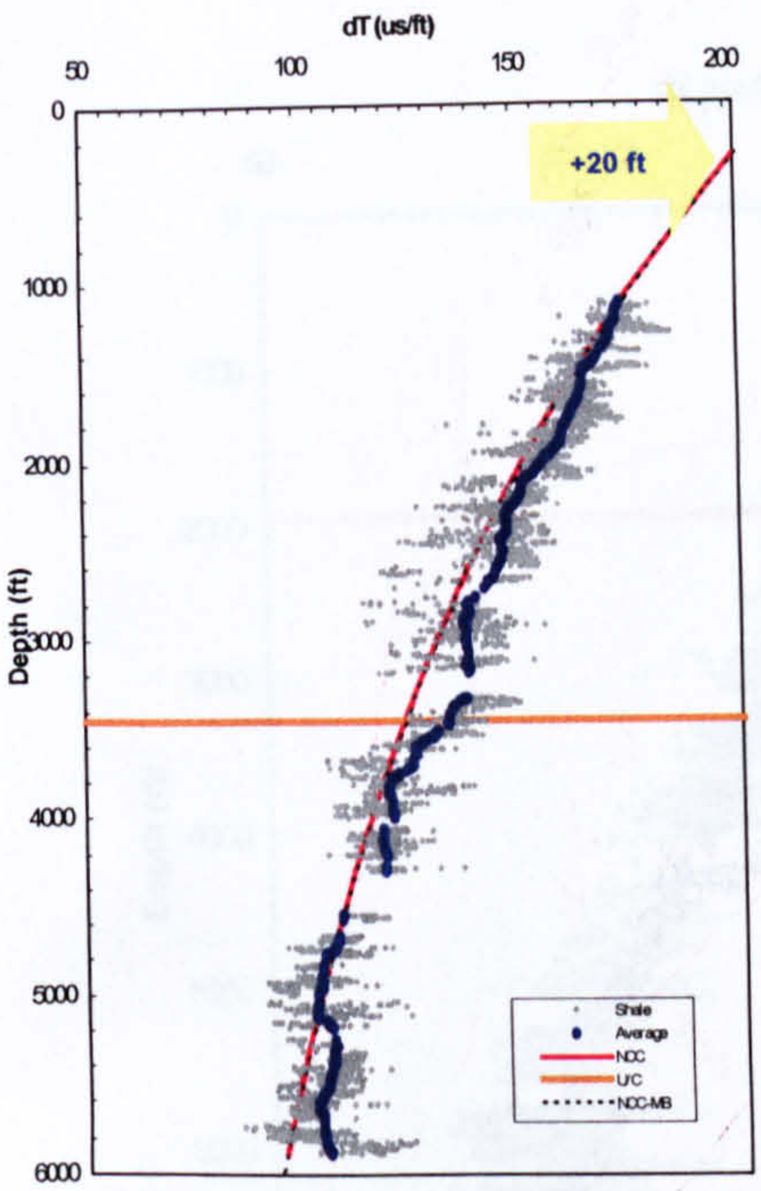


NE-33

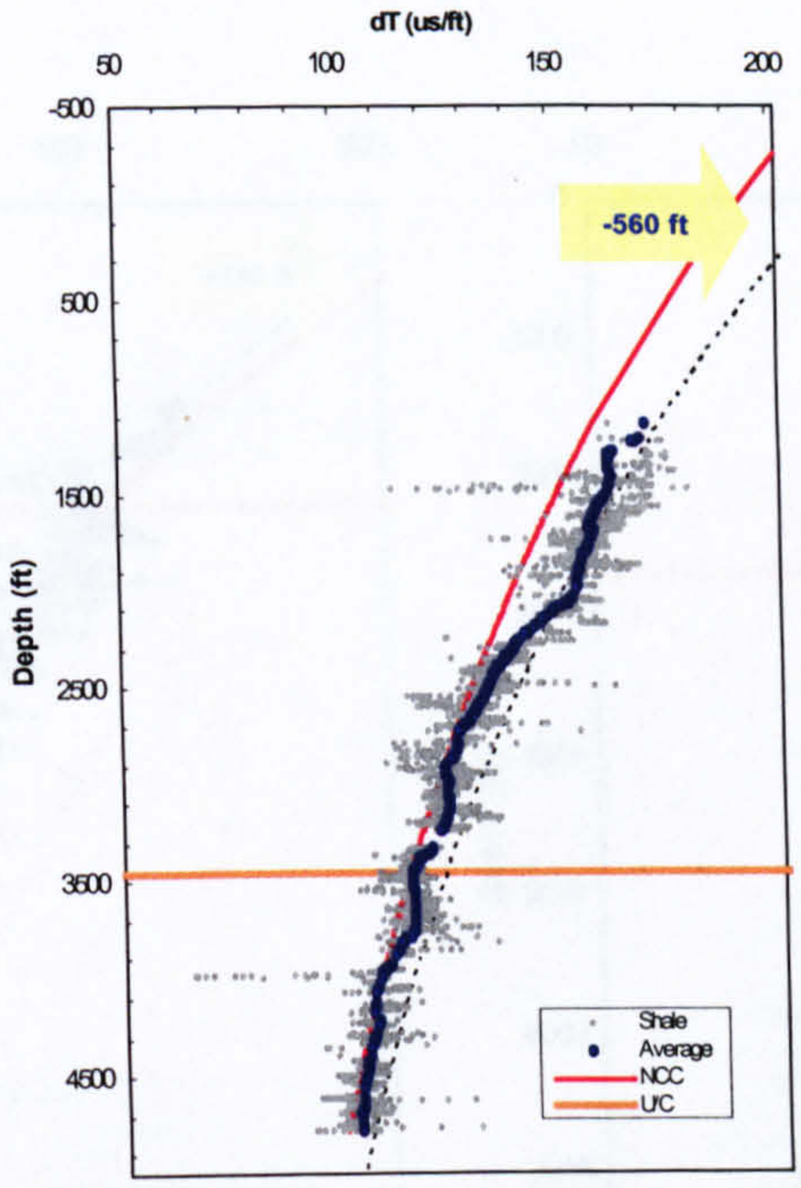


NE-34

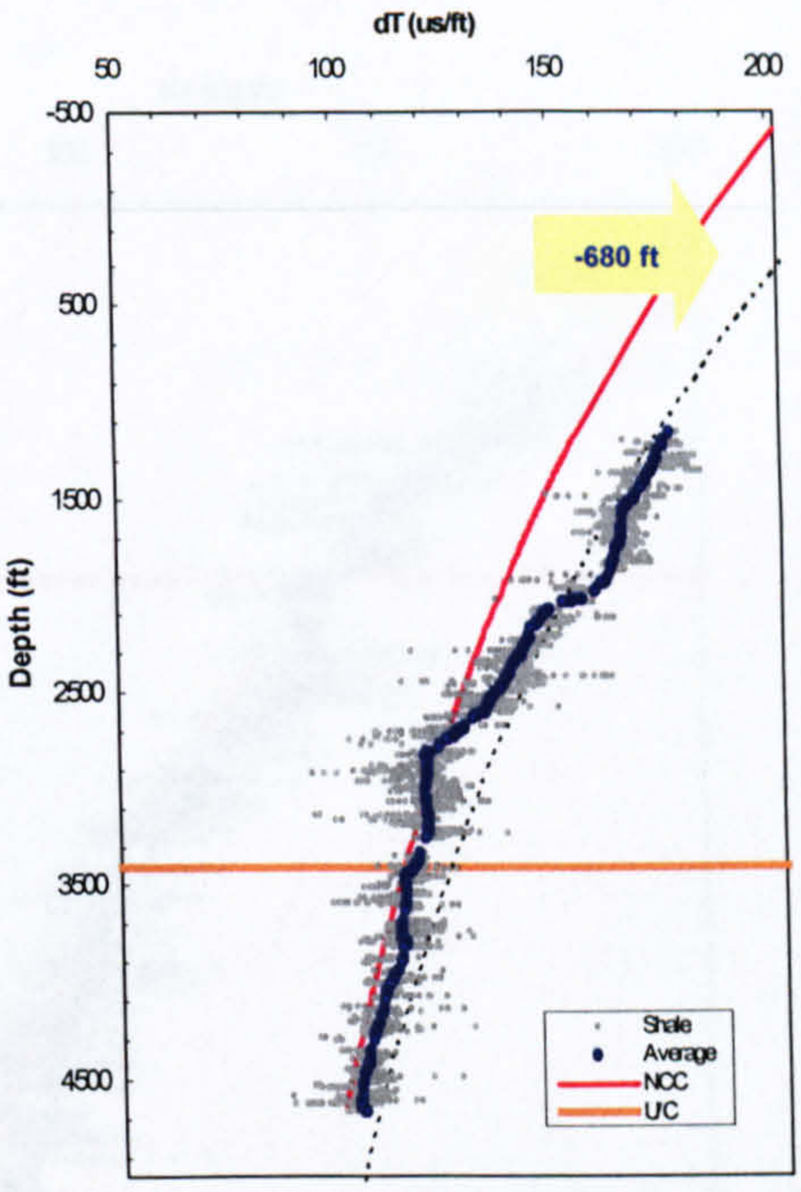
Central Malay



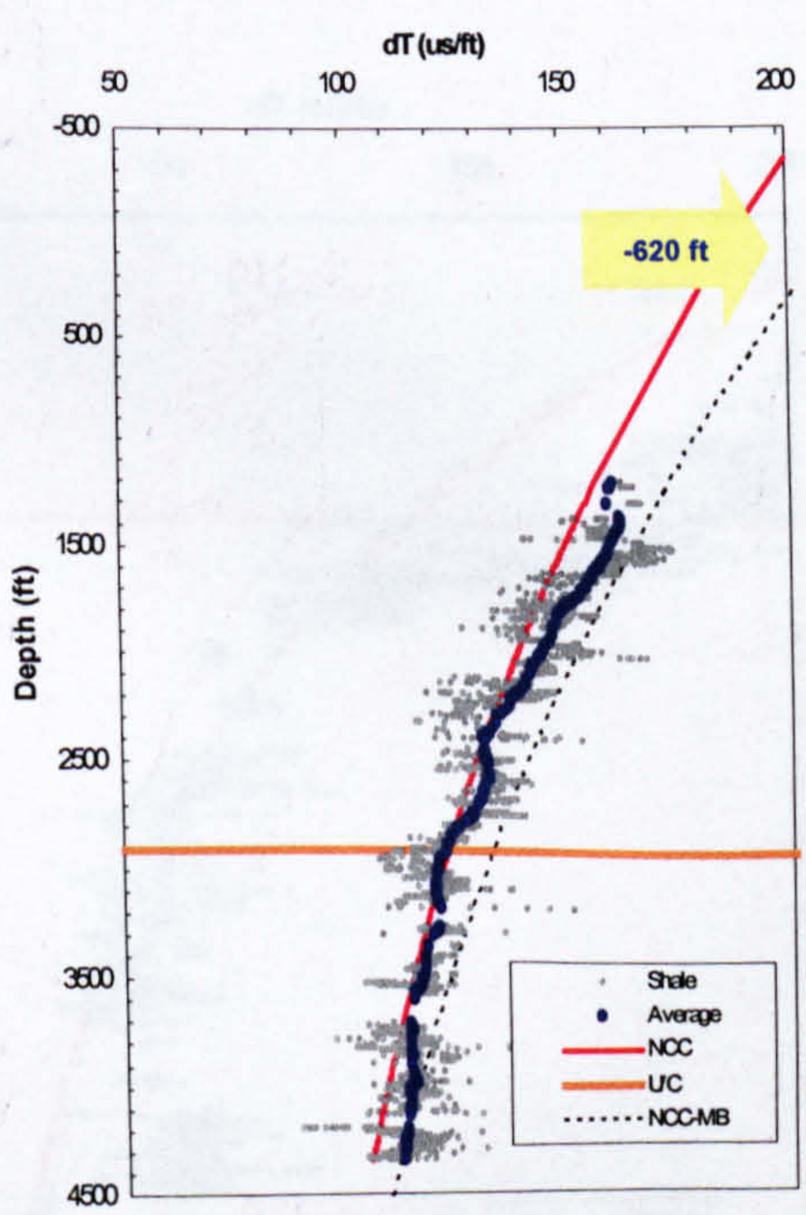
CM-15



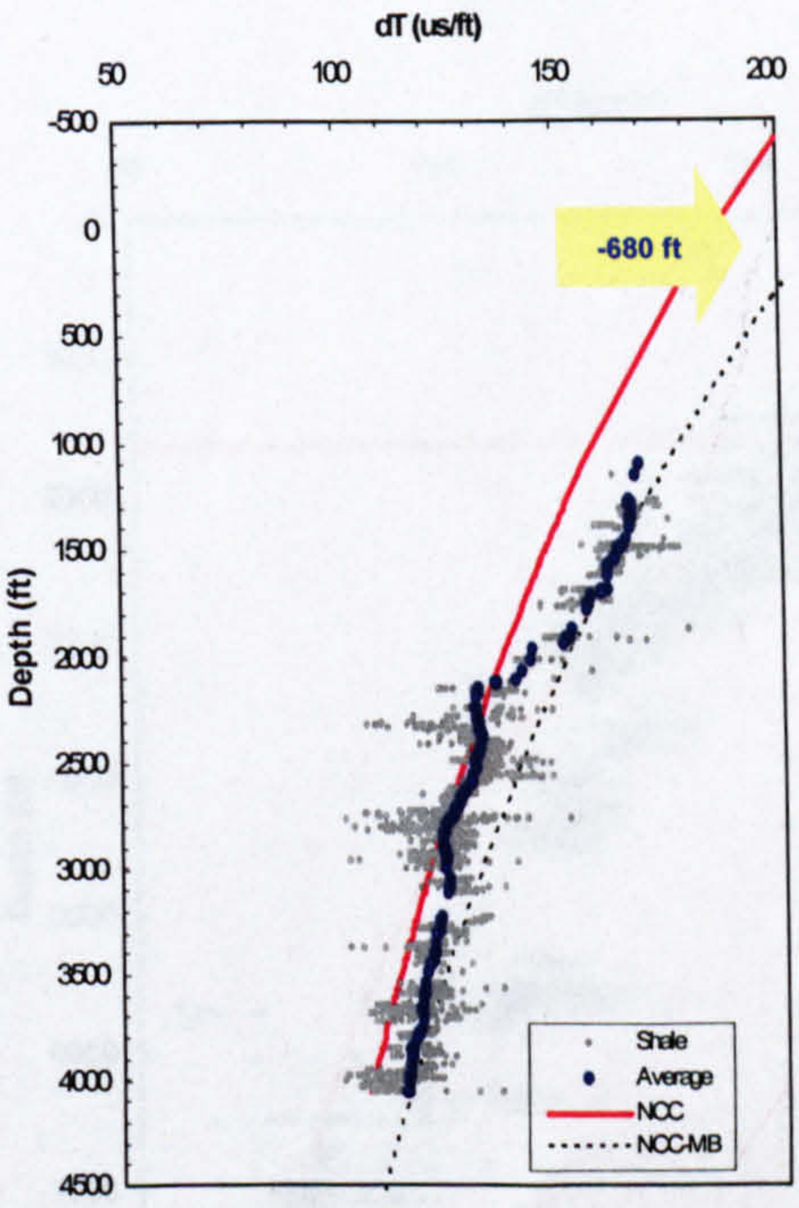
CM-16



CM-17

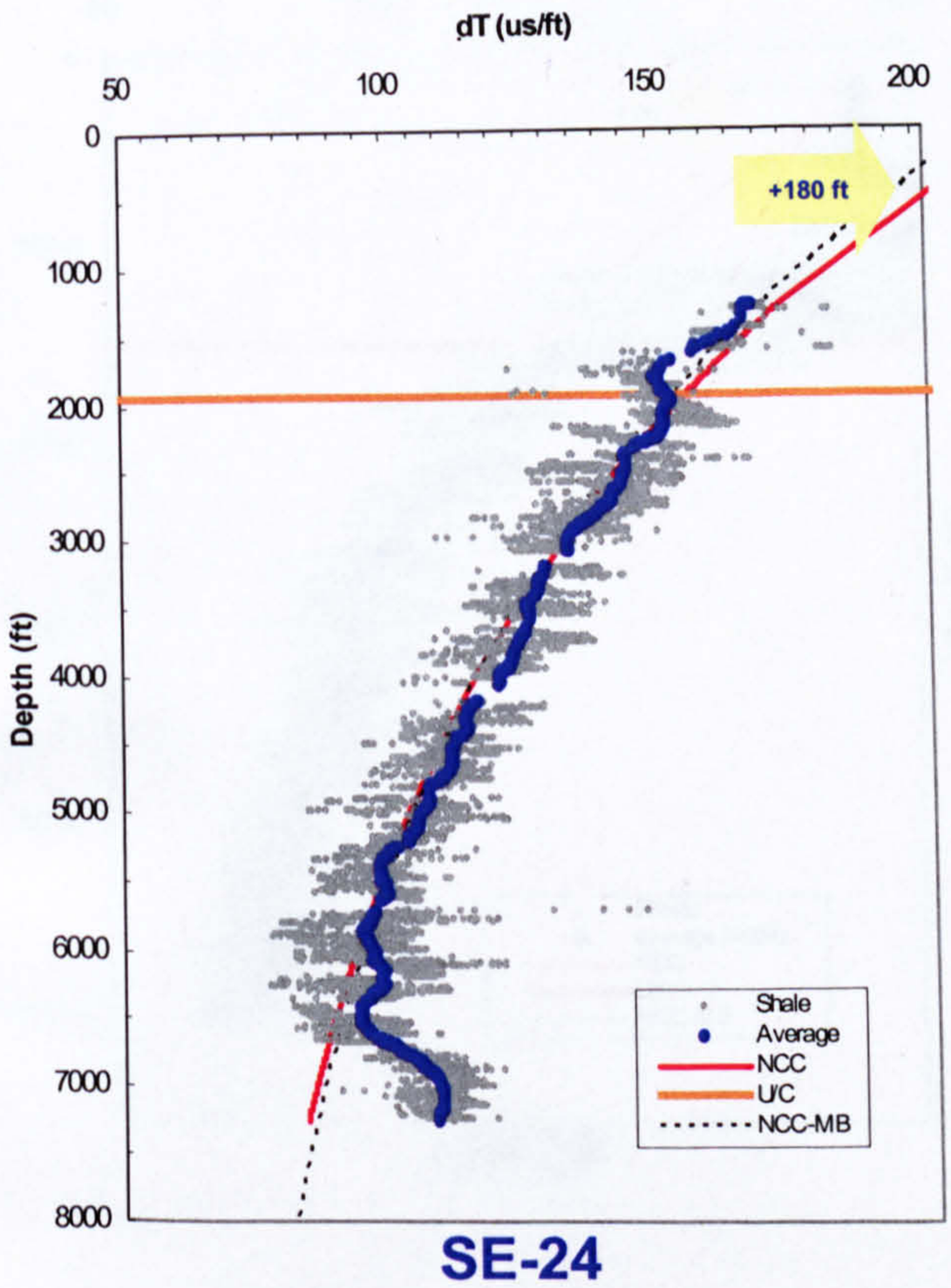


CM-18

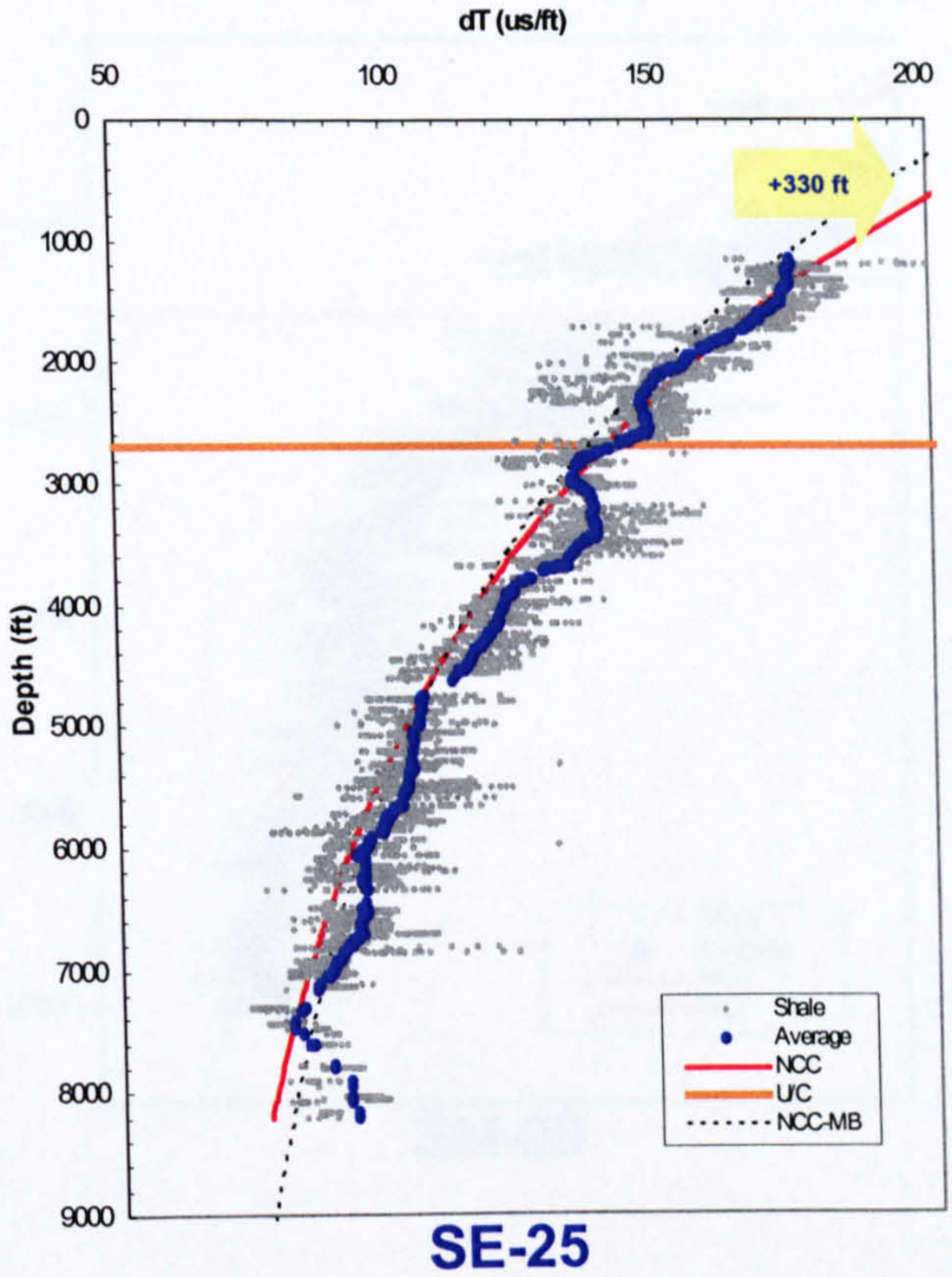


CM-19

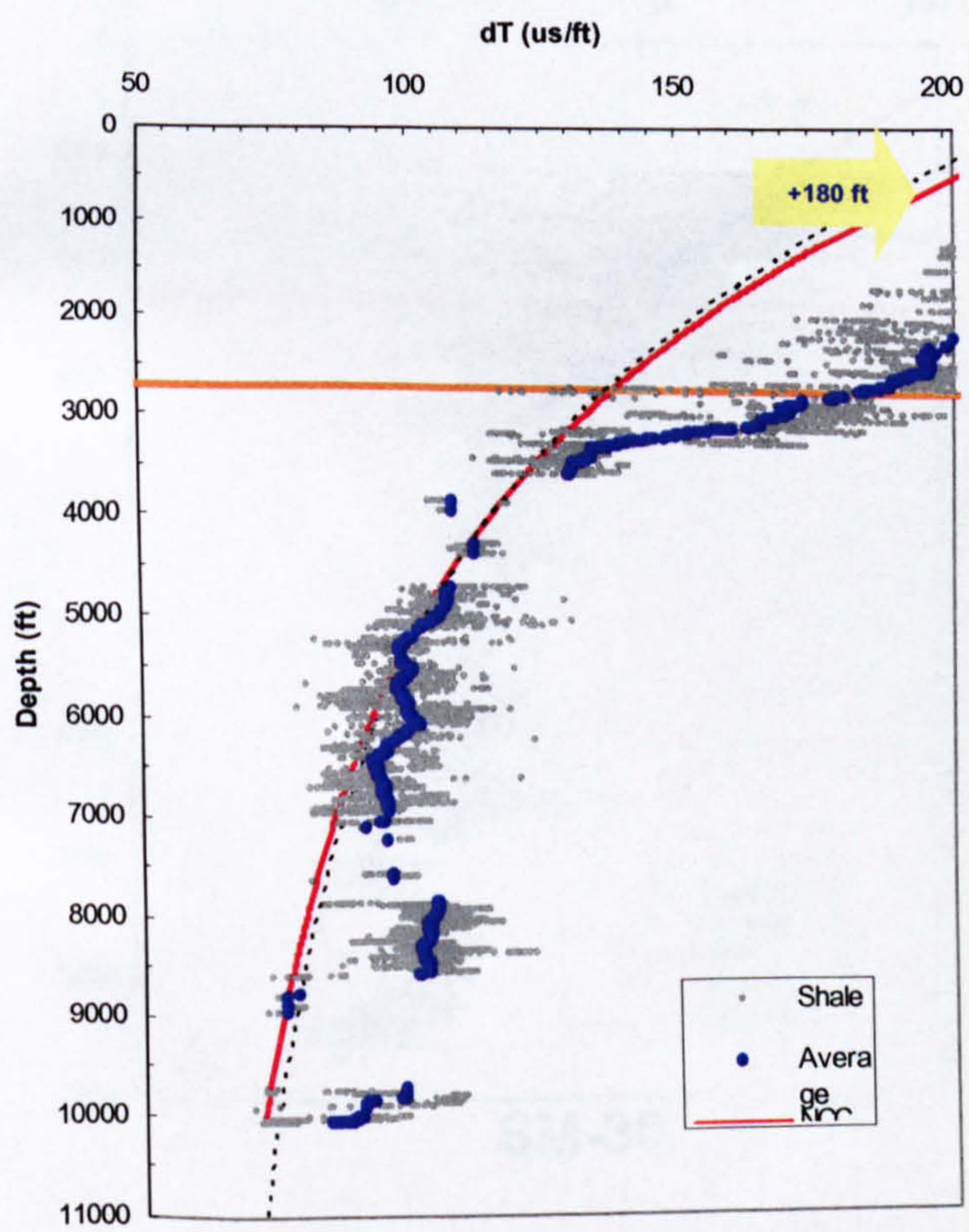
SE Malay



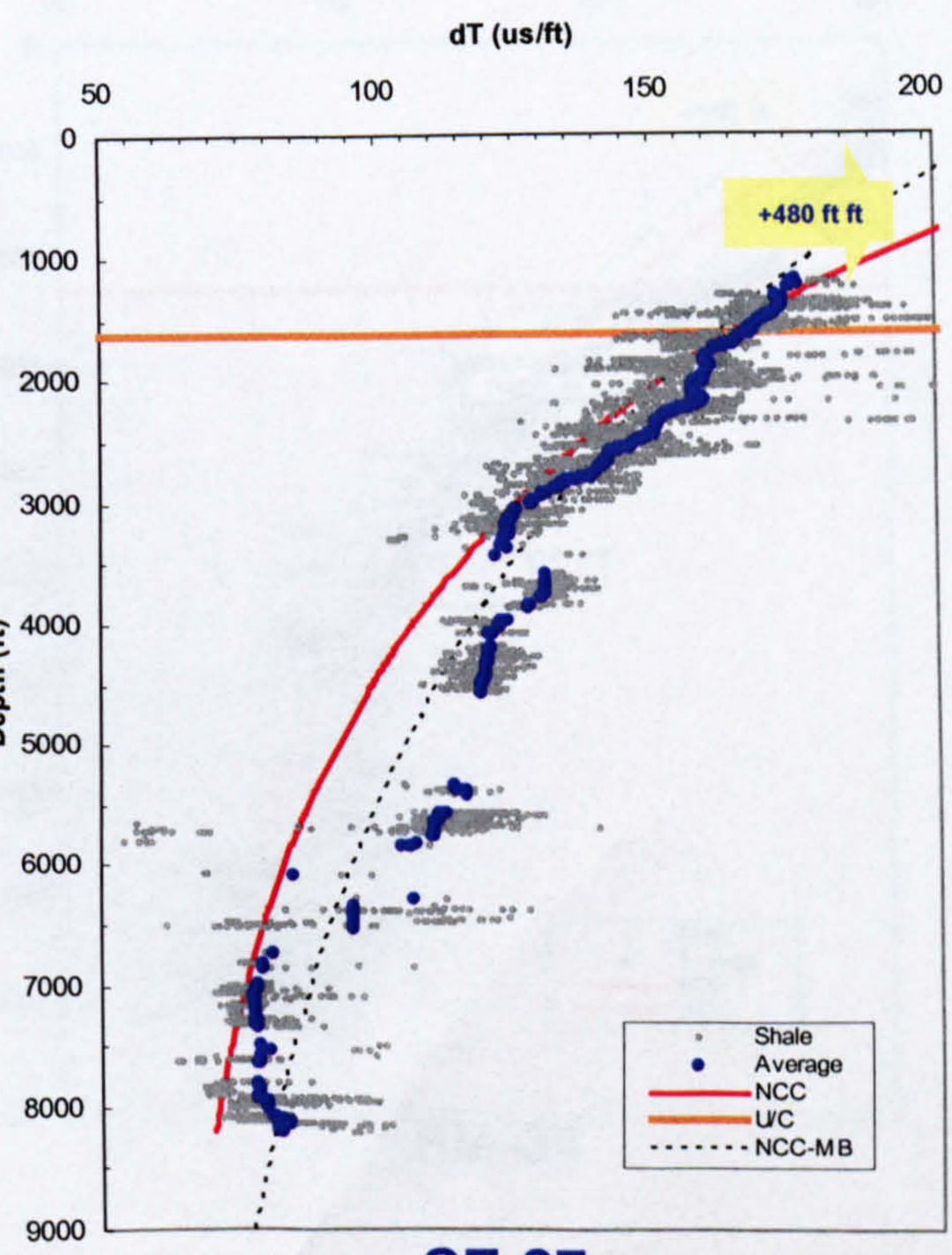
SE-24



SE-25

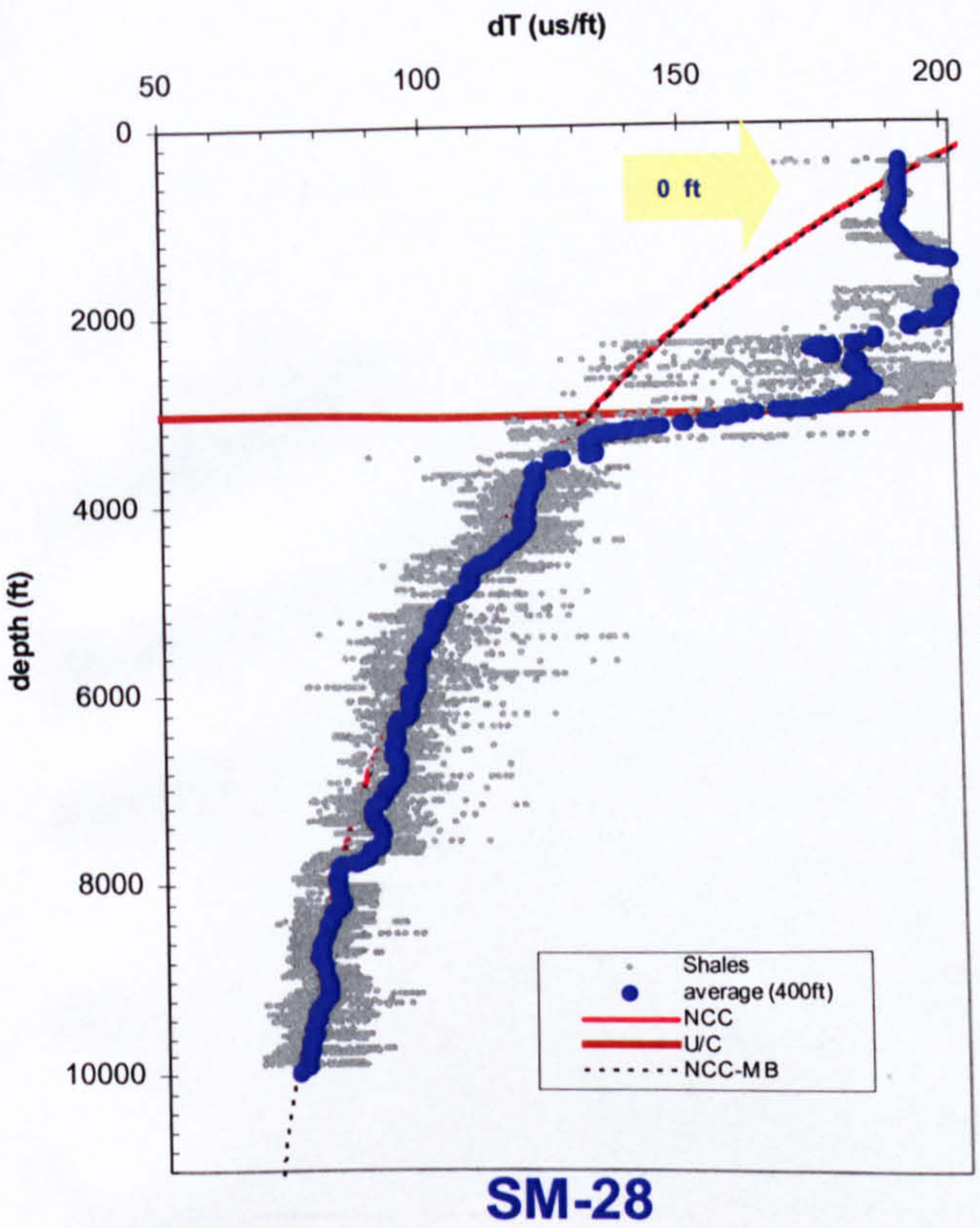


SE-26

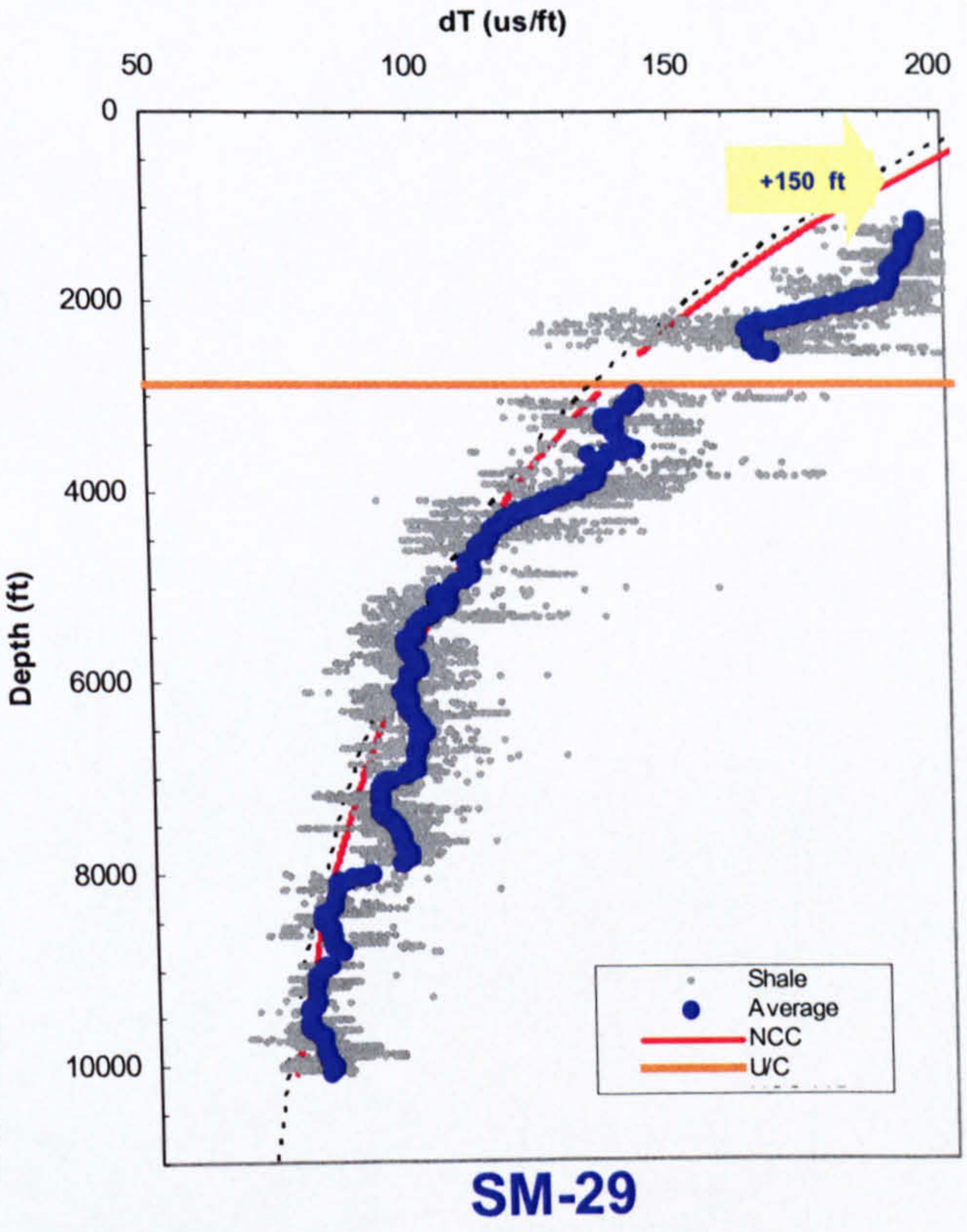


SE-27

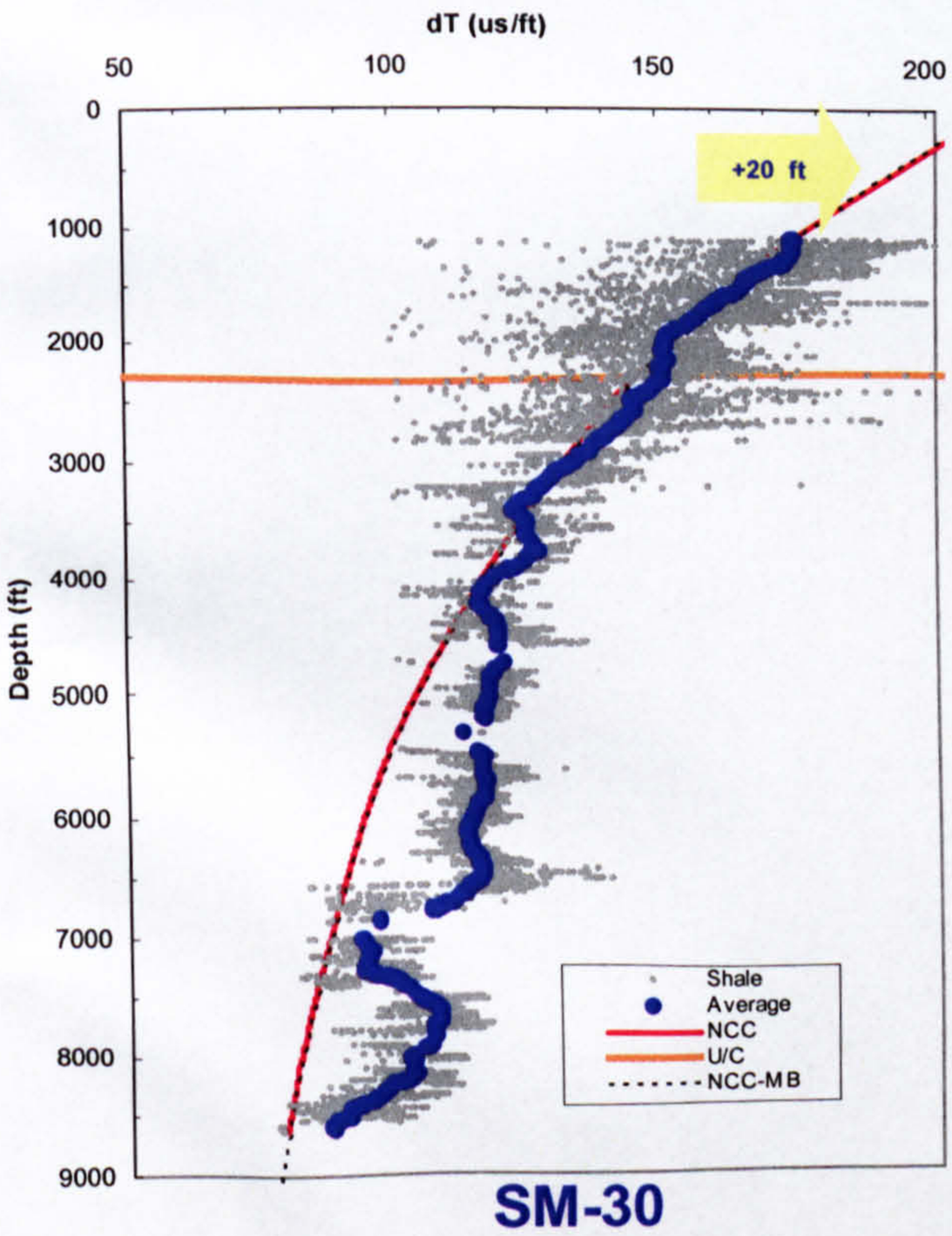
South Malay



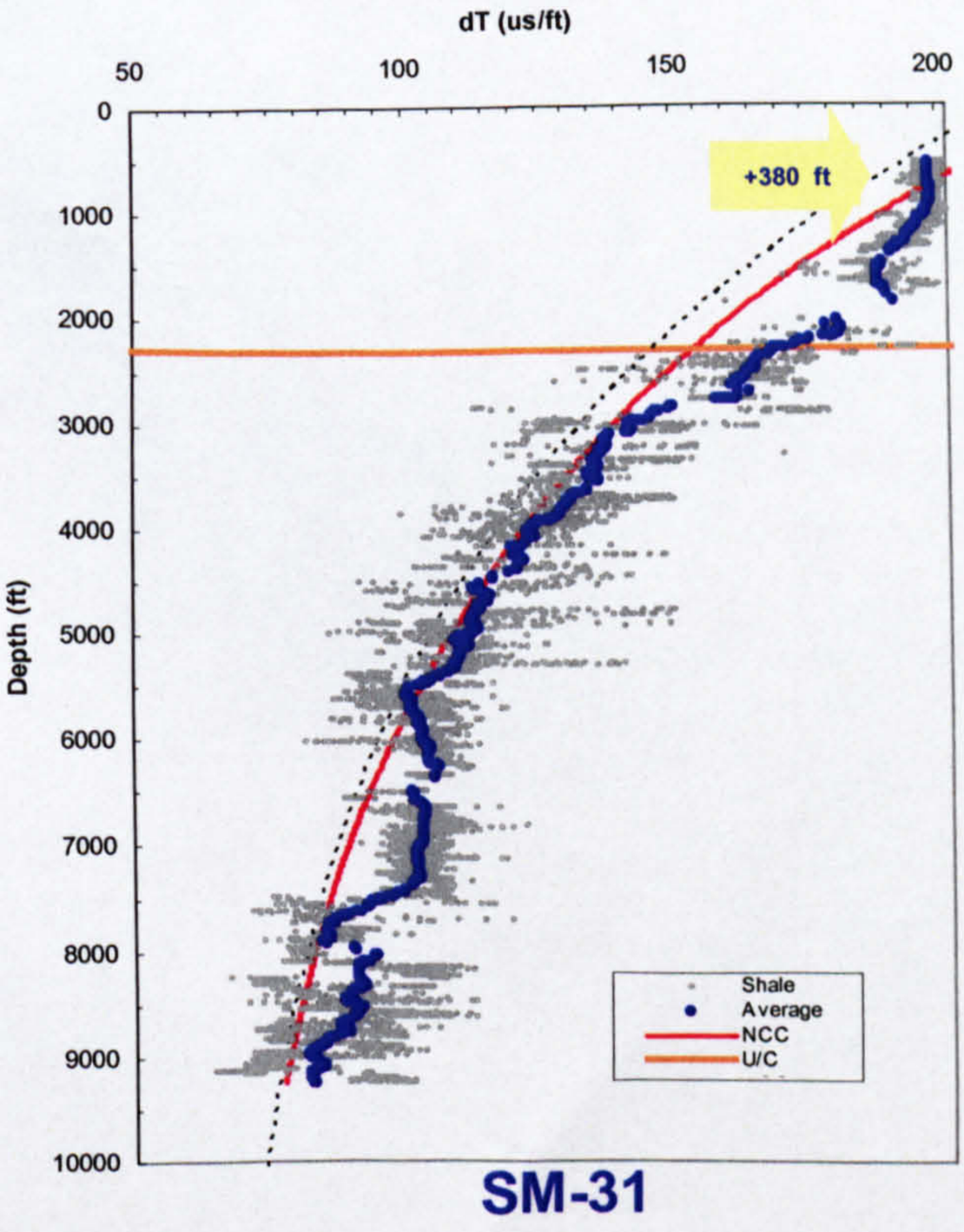
SM-28



SM-29



SM-30



SM-31